

Nano-Electrochemical studies of 2D Materials  
for Energy Storage and Conversion using  
Scanning Electrochemical Cell Microscopy

A thesis presented to

*School of Chemistry, Trinity College Dublin, The University of Dublin*

for the degree of

Doctor of Philosophy in Chemistry

by

Marc Brunet Cabré



Under supervision of:

Prof. Kim McKelvey & Prof. Paula E. Colavita

2023



# Declaration

I declare that this thesis has not been submitted as an exercise for a degree at this or any other university and it is entirely my own work.

I agree to deposit this thesis in the University's open access institutional repository or allow the Library to do so on my behalf, subject to Irish Copyright Legislation and Trinity College Library conditions of use and acknowledgement.

I consent the examiner retaining a copy of the thesis beyond the examining period, should they so wish (EU GDPR May 2018).

Marc Brunet Cabré, February 2023



---



# Acknowledgements

First and foremost, I would like to thank the thesis supervisors Prof. Kim McKelvey and Prof. Paula E. Colavita for all their enormous dedication, help and guidance put through the course of this thesis. Prof. McKelvey inducted me into the world of nano-electrochemistry which I became passionate about. Thanks to Prof. McKelvey I developed expertise on advanced nano-electrochemical methods and instrumentation. Moreover, Prof. McKelvey put the dedication and patience to teach me multiple skills, which are essential in the researcher toolbox, including communication, data analysis and coding skills. In 2020 Prof. McKelvey moved from Trinity College Dublin to Victoria University of Wellington, in New Zealand. At this moment Prof. McKelvey volunteered to continue supervising my thesis remotely. Since then, Prof. McKelvey has provided constant attendance, supervision and active engagement with the research work, far beyond any obligation and despite of distance and the 12 hour difference. For all those reasons, I am extremely grateful to Prof. McKelvey.

In 2020, I had the opportunity to join the physical chemistry group supervised by Prof. Colavita. Prof. Colavita provided a very warm welcome to her group and since day one, she engaged over supervision duties, actively contributed to the already open research projects, and proposed complementary projects. The Prof. Colavita group focuses on material research for electrochemical purposes, which allowed me to widen my knowledge beyond my PhD thesis focus on electrochemical methods. Over the course of this thesis, the expertise of Prof. Colavita and Prof. McKelvey groups has found a common path, and nowadays, there are multiple collaborations ongoing in both directions. I feel very fortunate to be at the crossroads between those collaborations and to have the opportunity to work and learn from both groups. Prof. Colavita has also been engaging towards disseminating my work in conferences, publication and award participation. I truly appreciate all the opportunities provided by Prof. Colavita. Finally, Prof. Colavita and Prof. McKelvey have always shown an enthusiastic approach toward fundamental aspects of research work, which I am interested in too. I really appreciate that they found the time (and patience) to discuss and share their knowledge about those fundamental questions.

I would like to thank the international collaborators Dr. Matej Velicky, Prof. Jens Anders and Dr. Denis Djeick, as well as Trinity College Dublin collaborators, Prof. Valeria Nicolosi and Dr. Dahnán Spurling for their contributions and the relevant insight provided over the research matters.

During this thesis I had the opportunity to mentor and work hand-by-hand with BSc and MSc students who were conducting their final year project. Many many thanks to Timothee Romano, Pietro Martinuz, Larry Brazel, Lua Henderson and Zijian Wang for your team spirit, dedication, and excellence work contribution.

The members of the Colavita group have become like a second family for the past year. The friendship and fellowship of Christian Schröder, Filippo Pota, Lua Henderson, Maida Aysla Costa de Oliveira, Hugo Nolan and Silvia Fogli have made many days much happier.

Tots els meus agraïment a la meva família, als Brunet i als Cabré, per la seva ajuda incondicional durant anys i anys i anys. De cor, moltíssimes gracies. Así, todos mis agradecimientos a mi pareja Laura Pilar Gomez Barrio, que definitivamente ha sido la persona más vital para el desarrollo de esta tesis y de mi persona en los últimos años. Mis infalibles amigos Natalia, Iñigo, Sara y Adrian que codo con codo, risa a risa, y a veces pena a pena, hemos ido tirando para adelante, muchísimas gracias. També vull agrair als Cartxofes i a tots aquells que la distància ens ha separat una mica, però no tant.

I express my gratitude to Trinity College Dublin for the funding and opportunity given to conduct this thesis. Finally, many thanks to the Dublin University Cycling Club and its cherished members for all those moments, rides and trips that become memorable.

# Summary

Electrochemical systems are of critical importance in modern society as they enable the conversion of electricity from renewable sources into chemicals and materials. The integration of nanomaterials in energy storage and conversion technologies has resulted in significant advancements, providing improved efficiency and performance to existing technologies while enabling the development of new, cutting-edge technologies. Electrochemical technologies that incorporate nanomaterials are expected to be widespread across industries and society in the years ahead. Understanding the electrochemical behaviour of nanomaterials is crucial, but it remains a challenge to decipher nanomaterial contributions in electrochemical systems that involve multiple physical and chemical phenomena. Recently, new electrochemical methods have emerged to allow the unambiguous characterisation of nanomaterials, the key to which is the isolation of single nanoscale objects or domains. Scanning Electrochemical Cell Microscopy (SECCM) is one such technique that focusses on the electrochemistry of single nanoscale entities. This thesis aims to use SECCM to study the fundamental behaviour of 2D nanomaterial systems relevant for energy storage and conversion and to contribute to the development of new methods for nano-electrochemical characterisation.

In the opening section of this thesis, electrochemical systems used for energy generation and storage are examined, as well as the role nanomaterials play in these technologies. This includes examples of state-of-the-art nanomaterials and electrochemical designs. The two-dimensional nanomaterials category (2D materials) has garnered attention for its potential in energy storage and conversion due to the large surface area and electrocatalytic properties that 2D materials present. Chapter 2 delves into techniques for studying 2D materials using SECCM, with a particular emphasis on SECCM instrumentation, its operations, and underlying principles. A major focus of this thesis is exploring various 2D materials of high significance for energy conversion and storage, with the aim of gaining a deeper understanding of their behaviour, which could be leveraged for further research and practical applications.

The first results chapter (Chapter 3) is dedicated to method and instrumentation development for nano-electrochemistry. Signal processing and current amplification in electrochemical setups are critical for providing the resolution required to measure the response of single nano-entities. Chapter 3 presents measurements made on a low-noise high-bandwidth custom-made transimpedance amplifier (current signal amplifier), specifically designed for the SECCM technique. The custom current amplifier was designed and manufactured by international collaborators, and the results presented in Chapter 3 showcase the testing of this device and the successful single-entity electrochemical characterisation at an unprecedented high bandwidth of 1 MHz.

The two-dimensional transition metal dichalcogenides (2D TMDCs) are an interesting nanomaterial for electrocatalytic applications, such as the hydrogen evolution reaction. 2D TMDCs are known to have a flake morphology with varying numbers of stacked TMDC layers. The previous literature is unclear how the morphology of 2D TMDCs, specifically the number of layers stacks, affects their electrochemical behaviour. To address this question, Chapter 4 isolates the electrochemical response of 2D TMDC basal planes with one, two, and three stacked layers using SECCM. The results show that not only does the electrochemical behaviour vary with the layer thickness and the electric contact, but there is also a strong correlation between the number of stacked layers, changes in the material's band gap, and its electrochemical behaviour. In Chapter 5, the discussion of the 2D TDMC morphology and electrochemical response correlation moves forward by identifying and characterising defective points and areas. By analysing the electrochemical response of defects, a better understanding is gained of how the response observed through nano-electrochemical methods translates to macroscale responses. Additionally, the method developed in Chapter 5 is noteworthy as it enables the detection of nanometre- and subnanometre- scale kinetically enhanced defects through electrochemical means alone.

Two-dimensional transition-metal carbides and nitrides, commonly referred to as MXenes, have garnered interest as electrode materials for supercapacitor applications because of their unique combination of properties. These materials exhibit a rich surface chemistry and good conductivity. In acidic electrolytes, the MXene surfaces display proton redox activity, leading to pseudocapacitive behaviour. Despite the presence of numerous experimental and computational studies that aim to understand the protonation and deprotonation mechanisms of MXene surfaces, the response of individual MXene flakes has not been thoroughly evaluated. To address this gap in the literature, Chapter 6 employs SECCM with sub-micrometre resolution to isolate the response of single MXene flakes. The results of this study bridge the gap between previous experimental reports, at the millimetre scale, and computational methods, at the nanometre scale. The unique electrochemical configuration achieved by SECCM has allowed us to observe a delocalised surface charging mechanism, of which there are no prior reports.





# Contents

CHAPTER 1: Introduction.....	1
1.1 Electrochemistry and energy conversion technologies .....	2
1.2 Electrochemical systems for energy conversion and storage.....	4
1.2.1 Energy conversion and open electrochemical systems.....	5
1.2.2 Energy storage and closed electrochemical systems .....	7
1.3 Nanomaterials in electrochemistry.....	8
1.3.1 Effects of scaling down the size of an electrochemical system.....	9
1.3.2 The new properties offered by nanomaterials.....	12
1.3.3 2D materials for energy storage and conversion .....	14
1.4 Characterizing nanomaterial electrochemical response .....	17
1.4.1 Bulk vs single entity electrochemistry .....	17
1.4.2 The family of SPEM techniques .....	19
1.4.3 Overview on nano-electrochemical studies via SECCM.....	22
1.5 Describing and modelling electrochemical phenomena at the nanoscale ....	24
1.5.1 Solution – Electrode interface on non-Faradaic processes .....	25
1.5.2 Electron transfer models .....	26
1.5.3 Mass transport processes .....	38
1.6 Aims of this thesis .....	43
References .....	44
CHAPTER 2: Experimental Methods.....	53
2.1 Electrochemical Methods.....	54
2.2 Single Barrel SECCM .....	59
2.2.1 SECCM instrumentation.....	60
2.2.2 The SECCM probe.....	63
2.2.3 SECCM operation methods .....	75
2.3 Surface morphology characterisation.....	81
2.3.1 Atomic Force Microscopy (AFM).....	81

2.3.2 Scanning electron microscopy (SEM).....	82
2.4 Finite element simulation for diffusive mass transport .....	84
2.4.1 Principle of finite element simulation method .....	84
2.4.2 Implementation of FES to resolve mass transport for SECCM probes.....	85
References.....	88

## CHAPTER 3: Single-Entity Electrochemistry at Microsecond Time Resolution .....

93

3.1 Introduction.....	94
3.1.1 Single-entity electrochemistry.....	94
3.1.2 Stochastic Collision Electrochemistry.....	95
3.1.3 Signal and resolution requirements for stochastic collision electrochemistry .	95
3.1.4 Bandwidth, gain, and noise during current amplification. ....	97
3.1.5 Integration of a custom current amplifier for stochastic collision electrochemistry with SECCM.....	97
3.1.6 Description of the behaviour of the transimpedance amplifier. ....	99
3.2 Aims.....	102
3.3 Methods .....	103
3.4 Results and Discussion .....	105
3.4.1 Characteristic noise response .....	105
3.4.2 Electrochemical Performance.....	113
3.4.3 Single Nano-Entity Electrochemistry.....	115
3.5 Conclusions.....	118
References.....	120

## CHAPTER 4: Electrochemical Kinetics as a Function of Transition-Metal Dichalcogenide Thickness.....

125

4.1 Introduction.....	126
4.1.1 Anisotropy of transition metal dichalcogenide crystals .....	126
4.1.2 Heterogeneity and nanoscale domains in 2D TMDC.....	127
4.1.3 Advances in 2D TMDC exfoliation .....	128
4.1.4 Localised electrochemical methods for the study of 2D TDMCs .....	129

4.1.5 Electronic contact of 2D materials: Bottom-contact vs. top-contact .....	131
4.1.6 Strategy to resolve electron transport on 2D TMDCs electrodes .....	132
4.2 Aims .....	134
4.3 Methods .....	135
4.4 Results and discussion.....	136
4.4.1 TMDC thickness characterisation.....	136
4.4.2 Local electrochemical measurements and morphology correlation .....	138
4.4.3 Modeling of linear sweep voltammogram curves.....	148
4.4.4 Fitting the simulated response to the gold surface response.....	155
4.4.5 Fitting the simulated response to different thicknesses of TMDCs.....	156
4.4.6 Discussion of the variation of the $k_{\max}$ parameter with layer thickness.....	160
4.5 Conclusions .....	165
References .....	167

## CHAPTER 5: Nanoscale Defects on 2D Transition Metal

Dichalcogenides .....	173
5.1 Introduction .....	174
5.1.1 Defects on 2D TMDCs .....	174
5.1.2 Methods for defect detection .....	175
5.1.3 Mass transport effects on kinetically enhanced defects.....	176
5.2 Aims .....	178
5.3 Methods .....	179
5.3.1 Electrochemical measurements.....	179
5.3.2 Simulation of disc and band electrodes in the SECCM probe.....	179
5.4 Results .....	181
5.4.1 Electrochemical mapping by SECCM.....	181
5.4.2 Anomalous current enhanced points and correlation with 2D TMDC morphological features .....	182
5.4.3 Analysis of diffusion-limited current plateaus for defect detection .....	184
5.4.4 Modeling single-point defect electrochemical response.....	190
5.4.5 Modeling the electrochemical response of a band defect .....	193
5.4.6 Identification of defects by SECCM: advantages, limitations, and nature of defects .....	194

5.5 Conclusions.....	196
References.....	198
Appendix.....	202
CHAPTER 6: Pseudocapacitance of MXene Monolayers at the Nanoscale .....	209
6.1 Introduction.....	210
6.1.1 2D material-based pseudocapacitors .....	210
6.1.2 MXene pseudocapacitance .....	212
6.1.3 Surface processes vs. Bulk processes. ....	214
6.1.4 Electrochemical isolation of MXene building blocks. ....	217
6.2 Aims.....	219
6.3 Methods .....	220
6.4 Results.....	223
6.4.1 Characterisation of the structure of MXene $Ti_3C_2T_x$ flakes .....	223
6.4.2 Identification of the region with MXene flakes for SECCM scanning .....	224
6.4.3 Morphological characterisation of MXene flakes in the SECCM scanned region.....	225
6.4.4 Assignment of SECCM point to $Ti_3C_2T_x$ flake morphology.....	228
6.4.5 Determination of cell geometric area .....	<b>Error! Bookmark not defined.</b>
6.4.6 Localised electrochemical measurements on $Ti_3C_2T_x$ flakes .....	231
6.4.7 Observation of the capacitive response in subregions of $Ti_3C_2T_x$ flakes. ....	233
6.4.8 Implications on the pseudocapacitive mechanism of MXenes.....	237
6.5 Discussion .....	238
6.6 Conclusion .....	240
Appendix.....	242
References.....	243
CHAPTER 7: Conclusion and Future work .....	251
APPENDIX: Published work.....	259



# Major symbols

## Roman symbols

Symbol	Meaning	Usual Units
<b>A</b>	(a) area of electrode (b) area	cm <sup>-2</sup> , μm <sup>-2</sup> , nm <sup>-2</sup>
<b>C<sub>p</sub></b>	input capacitance	pF
<b>c<sub>i</sub></b>	concentration of <i>i</i> species	M
<b>C</b>	capacitance	pF
<b>D<sub>i</sub></b>	diffusion coefficient	cm <sup>2</sup> s <sup>-1</sup>
<b>E<sup>0</sup></b>	standard potential	V
<b>E<sub>f</sub></b>	Fermi level	eV
<b>E<sub>g</sub></b>	band gap of semiconductor	eV
<b>E</b>	potential	V
<b>E<sub>a</sub></b>	activation energy	kJ
<b>F</b>	Faraday Constant	C mol <sup>-1</sup>
<b>f</b>	bandwidth	Hz
<b>ΔG<sup>0</sup><sub>i</sub></b>	standard Gibbs free energy change in a <i>i</i> chemical processes	kJ mol <sup>-1</sup>
<b>ΔG<sup>ts</sup><sub>i</sub></b>	standard Gibbs free energy change of transition state in a <i>i</i> chemical processes	kJ mol <sup>-1</sup>
<b>ΔG<sub>i</sub></b>	Gibbs free energy change in a <i>i</i> chemical processes	kJ mol <sup>-1</sup>
<b>I</b>	current	A
<b>J<sub>i</sub></b>	Flux of <i>i</i> species	cm/s
<b>K<sub>B</sub></b>	Boltzmann constant	eV K <sup>-1</sup>
<b>k<sup>0</sup></b>	Standard heterogeneous rate constant	cm s <sup>-1</sup>
<b>k<sub>i</sub></b>	rate constant of <i>i</i> species or <i>i</i> process	cm s <sup>-1</sup>
<b>k<sub>max</sub></b>	maximum rate of electron transfer	cm s <sup>-1</sup>
<b>L</b>	solution electric conductivity	S m <sup>-1</sup>

---

<b><i>n</i></b>	(a) number of elements (b) boundary normal (c) units of charge (electron charge) of a species	none none none
<b>Q</b>	charge	pC
<b>R</b>	gas constant	J mol <sup>-1</sup> K <sup>-1</sup>
<b>r</b>	radial distance, radius	nm
<b>S<sub>ΔV</sub></b>	intrinsic noise power spectral density	V <sup>2</sup> Hz <sup>-1</sup>
<b>S<sub>ΔI</sub></b>	input referred noise	A <sup>2</sup> Hz <sup>-1</sup>
<b>T</b>	temperature	K
<b>t</b>	time	s
<b>V</b>	potential	V
<b>v<sub>i</sub></b>	rate of species <i>i</i> reacting or <i>i</i> process	mols L <sup>-1</sup> s <sup>-1</sup>
<b>v<sub>n</sub></b>	nuclear frequency factor	s <sup>-1</sup>
<b>v</b>	sweep rate, scan rate	V/s
<b>x</b>	(a) Spatial coordinate (b) Tunnelling barrier thickness	nm
<b>z</b>	(a) Spatial coordinate (b) units of charge (electron charge) of a species	nm none

---

## Greek symbols

---

<b>Symbol</b>	<b>Meaning</b>	<b>Usual Units</b>
<b><i>κ<sub>el</sub></i></b>	electronic transmission coefficient	none
<b><i>ϕ<sub>i</sub></i></b>	workfunction of <i>i</i> electrode or redox species	eV
<b><i>α</i></b>	transfer coefficient	none
<b><i>β</i></b>	tunnelling decay constant	Å <sup>-1</sup>
<b><i>η</i></b>	overpotential	V
<b><i>λ</i></b>	reorganisation energy	eV
<b><i>ω</i></b>	Working frequency (bandwidth)	rad s <sup>-1</sup>

---



## Abbreviations

---

<b>Abbreviation</b>	<b>Meaning</b>
AFM	atomic force microscopy, atomic force microscope
BV	Butler-Volmer
CMOS	complementary metal-oxide semiconductor
CV	cyclic voltammogram
CVD	chemical vapour deposition
DOS	density of states
EC	electrochemistry, electrochemical
ECDL	electrochemical double layer
EC-SPM	electrochemical scanning probe microscopy
EDX, EDS	energy dispersive X-ray analysis
FES, FEM	finite element simulation, finite element methods
HER	hydrogen evolution reaction
HET	heterogeneous electron transfer
LSV	linear sweep voltammogram
MH	Marcus-Hush
PCB	printed circuit board
QRCE	quasi-reference counter electrode
SECCM	scanning electrochemical cell microscopy
SECM	scanning electrochemical microscopy
SEM	scanning electron microscopy
SICM	scanning ion-conductance microscopy
SPM	scanning probe microscopy
SSA	specific surface area
STM	scanning tunnelling microscopy
TEM	transmission electron microscopy
TIA	transimpedance amplifier

---

---

TMDC	transition metal dichalcogenide
UME	ultramicroelectrode
XRD	x-ray diffraction analysis

---

# List of Figures

## CHAPTER 1

**Figure 1.1:** Scheme of electrode, interface, solution system showing the electron transfer process between electron and redox active species.

**Figure 1.2:** Schematic of different types of electrode cell setups.

**Figure 1.3:** Ragone plot of the various electrochemical energy storing technologies, power density energy density.

**Figure 1.4:** Surface to volume ratio of a sphere across length-scale of nanometres to meters.

**Figure 1.5:** Mass transport on nanostructured systems

**Figure 1.6:** Examples of 0D, 1D, 2D and 3D nanomaterials. Red and grey contrast represent different nanomaterial types.

**Figure 1.7:** Schematic view of monoelement, non-metal nitride, metal dichalcogenide, metal halide, metal oxide, metal hydroxide, and perovskite 2D materials.

**Figure 1.8:** Number of citations received per year of the 50 most cited paper using the combination of key terms “1D material” or “2D material” with “Supercapacitor” or “Electrocatalyst”.

**Figure 1.9:** Comparison between bulk electrochemistry and single entity electrochemistry.

**Figures 1.10:** Representation of different scanning electrochemical probe techniques.

**Figures 1.11:** Schematic representation of Scanning electrochemical cell microscopy technique.

**Figure 1.12:** Scheme of the different equilibria involved in a Faradaic reaction with redox species in solution.

**Figure 1.13:** Potential and charge distribution at electrode-solution interface.

**Figure 1.14:** Representation of A-B equilibrium along the reaction coordinates.

**Figure 1.15:** Representation of reaction coordinates of  $A+e^- \leftrightarrow B$  equilibrium upon the application of an external potential (E).

**Figure 1.16:** Standard free energy state distribution profiles across the reaction coordinates for one electron transfer equilibrium  $A + e^- \leftrightarrow B$ .

**Figure 1.17:** Representation of the probability of crossing the activation energy barrier with respect to overpotential in the MH formalism.

**Figure 1.18:** Energy ( $\varepsilon$ ) distribution of the solution ( $W_A(\varepsilon)$  and  $W_B(\varepsilon)$ ) and electrode states ( $f(\varepsilon)_{electrons}$  and  $f(\varepsilon)_{holes}$ ) for different potential applied.

**Figure 1.19:** Normalised rate constants prediction respect overpotential applied for Butler-Volmer, Marcus-Hush and Gerischer formalism.

**Figure 1.20:** Example of distinguishable BV and MH domains based on parameters of well-known redox couple as Ruthenium Hexamine.

**Figure 1.21:** Diffusive mass transport on different geometries.

## CHAPTER 2

**Figure 2.1:** Schematic showing the circuit connections of different electrochemical system and reference electrode equilibrium principle.

**Figure 2.2:** Illustration of the I-t-E surface.

**Figure 2.3:** Potentiometric technique waveform and the resulting current response plotted as in function of time or potential for Potential steps, linear sweep voltammetry and cyclic voltammetry and for macroscale and microscale sized electrodes.

**Figure 2.4:** SECCM schematic setup and the different elements that form the instrument.

**Figure 2.5:** Mounting position of camera and light source relative to probe and sample.

**Figure 2.6:** Schematic of the signal processing protocol of SECCM instrument.

**Figure 2.7:** Schematic of a pipette tip indicating the main geometric parameters.

**Figure 2.8:** Schematic of capillary pulling of multiple cycles.

**Figure 2.9:** Electron microscopy images of pipette tip.

**Figure 2.10:** Schematic of setup for ion conductance measurement to determine pipette aperture.

**Figure 2.11:** Pipette aperture determination via bubbling point.

**Figure 2.12:** Diagram illustrating the combination of ion conductance and electron microscopy measurement for pipette aperture size determination.

**Figure 2.13:** Effect of pipette functionalization in droplet cell shape.

**Figure 2.14:** Schematic showing the self-filling processes of the pipette tapered end.

**Figure 2.15:** Current threshold position respect noise levels and current spike during droplet cell formation.

**Figure 2.16:** Scheme of electrochemical mapping procedure.

**Figure 2.17:** Scheme of two different methods for single nano-entity electrochemistry with SECCM.

**Figure 2.18:** Schematic of atomic force microscope (AFM) working principles.

**Figure 2.19:** Scheme of scanning electron microscopy (SEM) and energy dispersive spectroscopy (EDS) instrument. Illustration shows the different instrumentation elements and different types of interaction and their interaction volume.

**Figure 2.20:** Representation of linear combination base function implemented in finite element simulation.

**Figure 2.21:** SECCM axisymmetric model implemented in FES.

## CHAPTER 3

**Figure 3.1:** Schematic showing the relation between the number of entities measured in conventional ensemble base bulk electrochemical measurements (left) and single-entity electrochemistry (right).

**Figure 3.2:** Schematic of stochastic collision electrochemistry experiments showing a single nano-entity free diffusing that collides with an ultra-microelectrode, generating an electrochemical response.

**Figure 3.3:** Chronoamperometric current trace of nano impact oxidation of silver nanoparticles recorded at different bandwidths.

**Figure 3.4:** Schematic of the SECCM setup for single nano-entity measurements on custom transimpedance amplifier chip (TIA)

**Figure 3.5:** Photo of the PCB board, with the main components labelled.

**Figure 3.6:** Equivalent circuit for the custom TIA with pseudo-resistor feedback.

**Figure 3.7:** Flowchart diagram for the signal-noise analysis.

**Figure 3.8:** Current trace of one second length in open circuit showing intrinsic noise levels of the TIAs at different bandwidths.

**Figure 3.9:** Power spectral densities of the custom experimental setup.

**Figure 3.10:** Input-referred noise ( $S_{\Delta I}$ ) for the 80 kHz, 250 kHz, and 1 MHz TIAs in open and closed circuit configuration.

**Figure 3.11:** Cumulative integration of current densities in open and close circuit configuration for different bandwidths.

**Figure 3.12:** Maximized spectrum of the input-referred noise.

**Figure 3.13:** Intrinsic input-referred noise power spectral density of the opamp ( $S_{\Delta V}$ ).

**Figure 3.14:** Fitting of the Input-referred noise for open circuit and close circuit (red) and fitting.

**Figure 3.15:** Least square error from the fitting of input-referred noise curve.

**Figure 3.16:** Droplet cell formation detection on custom TIAs.

**Figure 3.17:** Cyclic voltammetry measurement over the gold contact pad for two different redox couples.

**Figure 3.18:** Current-trace of stochastic collision electrochemistry experiment on custom TIAs.

**Figure 3.19:** Chronoamperometry of single Ag nanoparticle collision and their respective blanks.

**Figure 3.20:** AFM of the gold electrode located on PCB near TIA showing that the surface of the Au electrode roughness.

## CHAPTER 4

**Figure 4.1:** Structure of TMDCs.

**Figure 4.2:** Images of 2D MoS<sub>2</sub> flakes produce with bottom-up and top-down approaches.

**Figure 4.3:** Calculated band structure for MoS<sub>2</sub> in bulk form and bidimensional form, differentiating stacks of 4 layers, 2 layers and monolayer.

**Figure 4.4:** Electrochemical response of 2D MoS<sub>2</sub> with different number of layers stacked.

**Figure 4.5:** Scheme of two possible contact modes for TMDCs.

**Figure 4.6:** Schematic of experimental setup.

**Figure 4.7:** Morphological characterisation 2D MoSe<sub>2</sub>

**Figure 4.8:** Morphological characterisation 2D MoS<sub>2</sub>.

**Figure 4.9:** Morphological characterisation 2D WSe<sub>2</sub>.

**Figure 4.10:** Morphological characterisation 2D WS<sub>2</sub>.

**Figure 4.11:** Histogram of droplet diameters determined from AFM images over different layer thicknesses of WS<sub>2</sub>, MoS<sub>2</sub>, WSe<sub>2</sub>, and MoSe<sub>2</sub>

**Figure 4.12:** Assignment of each grid point to surface type based on droplet cell residue location for WS<sub>2</sub> SECCM scan.

**Figure 4.13:** Assignment of each grid point to surface type based on droplet cell residue location for WSe<sub>2</sub> SECCM scan.

**Figure 4.14:** Assignment of each grid point to surface type based on droplet cell residue location for MoSe<sub>2</sub> SECCM scan.

**Figure 4.15:** Assignment of each grid point to surface type for MoS<sub>2</sub> SECCM scan.

**Figure 4.16:** LSV dataset for 1L, 2L and 3L WS<sub>2</sub>.

**Figure 4.17:** LSV dataset for 1L, 2L and 3L MoS<sub>2</sub>.

**Figure 4.18:** LSV dataset for 1L, 2L and 3L MoSe<sub>2</sub> and gold points contacting gold surface.

**Figure 4.19:** LSV dataset for 1L, 2L and 3L MoSe<sub>2</sub> and gold points contacting gold surface

**Figure 4.20:** Description of the FES model implemented for characterizing 2D TMDCs response.

**Figure 4.21:** LSVs on monolayer for different 2D TMDCs.

**Figure 4.22:** Linear sweep voltammograms recorded on WS<sub>2</sub> normalised by diffusion limiting current.

**Figure 4.23:** Integral of the overlapped function for anodic and cathodic processes

**Figure 4.24:** Fitting simulated LSVs to gold response.

**Figure 4.25:** Comparison of recorded and simulated LSVs for a range of  $k_{max}$  values.

**Figure 4.26:** Recorded and simulated LSVs on MoS<sub>2</sub> basal plane.

**Figure 4.27:** Recorded and simulated LSVs on MoSe<sub>2</sub> basal plane.

**Figure 4.28:** Recorded and simulated LSVs on WS<sub>2</sub> basal plane.

**Figure 4.29:** Recorded and simulated LSVs on WSe<sub>2</sub> basal plane.

**Figure 4.30:** Distribution logarithm of fitted  $k_{max}$  for all recorded LSVs.

**Figure 4.31:** Simulated LSVs with median  $k_{max,nL}$  extracted from fitting recorded LSVs on 1L, 2L, and 3L.

**Figure 4.32:**  $k_{max}$  values determined from fitting simulation to experimental data for different layer thickness.

**Figure 4.33:** Diagram of the tunnelling junction for monolayer of TMDC and stack of three layers of TMDC.

**Figure 4.34:**  $\beta_{Au-nL}$  values plotted against the band gap for 1-, 2-, and 3-layer MoS<sub>2</sub>, MoSe<sub>2</sub>, WS<sub>2</sub>, and WSe<sub>2</sub>

## CHAPTER 5

**Figure 5.1:** Plot of diffusion-limited current density with respect to the radius of active surface, showing the 1/radius relation, and illustration of equi-concentration lines around a kinetically enhanced defect.

**Figure 5.2:** Model of simulated 3D geometry.

**Figure 5.3:** Schematic of the SECCM experimental configuration and optical image of the sample surface before the SECCM measurements.

**Figure 5.4:** Average LSV response at different MoS<sub>2</sub> thicknesses and unmodified Au surface.

**Figure 5.5:** Electrochemical mapping of the electrochemical response for [Ru(NH<sub>3</sub>)<sub>6</sub>]<sup>3+</sup> on MoS<sub>2</sub> and the LSV responses at certain sample points.



**Figure 5.6:** Electrochemical mapping of the electrochemical response for  $[\text{Ru}(\text{NH}_3)_6]^{3+}$  on  $\text{MoSe}_2$  and the LSV responses at certain sample points.

**Figure 5.7:** Electrochemical mapping of the electrochemical response for  $[\text{Ru}(\text{NH}_3)_6]^{3+}$  on  $\text{WSe}_2$  and the LSV responses at certain sample points.

**Figure 5.8:** Electrochemical mapping of the electrochemical response for  $[\text{Ru}(\text{NH}_3)_6]^{3+}$  on  $\text{MoS}_2$  and the LSV responses at certain sample points.

**Figure 5.9:** Electrochemical mapping of the electrochemical response for  $[\text{Ru}(\text{NH}_3)_6]^{3+}$  on  $\text{WSe}_2$  and the LSV responses at certain sample points.

**Figure 5.10:** Finite element simulation results for a disk defect.

**Figure 5.11:** Finite element simulation results for a band defect.

## CHAPTER 6

**Figure 6.1:** Illustration of the three types of mechanism implemented in supercapacitors

**Figure 6.2:** Structure of MXenes ( $\text{M}_{n+1}\text{X}_n\text{T}_x$ ) and proton intercalation properties.

**Figure 6.3:** Deconvolution of a 3D Mxene capacitive I-V current into the contribution of surface and bulk capacitive currents.

**Figure 6.4:** Schematic of the SECCM configuration for measuring monolayer  $\text{Ti}_3\text{C}_2\text{T}_x$  flakes immobilized on a carbon supporting electrode surface.

**Figure 6.5:** A. X-ray diffractogram (XRD), Raman spectra and Energy dispersive X-ray spectroscopy (EDX) of  $\text{Ti}_3\text{C}_2\text{T}_x$  freestanding films.

**Figure 6.6:** Optical image of the substrate with  $\text{Ti}_3\text{C}_2\text{T}_x$  drop-cast.

**Figure 6.7:** AFM characterisation for MXene flakes.

**Figure 6.8:** SEM micrographs obtained after SECCM scans.

**Figure 6.9:** A. Identification and classification of SECCM grid points visualized in the SEM micrographs.

**Figure 6.10:** Distribution of the active geometric areas obtained from SEM images of electrolyte residues after SECCM.

**Figure 6.11:** First loop of cyclic voltammograms on carbon, mixed monolayer MXene and Carbon, and monolayer (basal-plane) MXene.

**Figure 6.12:** Second loop of cyclic voltammograms on carbon, mixed monolayer MXene and Carbon, and monolayer (basal-plane) MXene.

**Figure 6.13:** Representative cyclic voltammograms on a carbon surface and monolayer MXene flake, and histogram of the capacitance values of each individual SECCM grid point

**Figure 6.14: A.** Electron micrograph of sample surface flakes, specific gravimetric capacitance on monolayer  $\text{Ti}_3\text{C}_2\text{T}_x$  compared to the total area  $\text{Ti}_3\text{C}_2\text{T}_x$  flake, and specific gravimetric capacitance obtained by normalizing by the total mass of the monolayer flake.

**Figure 6.15:** Surface capacitance plotted against the area of  $\text{Ti}_3\text{C}_2\text{T}_x$  monolayer contacted.

# List of Tables

## CHAPTER 2

**Table 2.1:** Advantages and disadvantages of the different optical mounting system on SECCM.

**Table 2.2:** Characteristic electrochemical performance of SECCM probe in function of the pipette aperture

**Table 2.3:** Pulling parameters used on laser puller P-2000 from Sutter Instruments for fabrication of pipettes between 500 nm to 1000 nm.

**Table 2.4:** Summary of expected information displayed during measurement and/or key feature to evaluate on saved dataset by the user during SECCM operation.

**Table 2.5:** Coordinate that defined boundaries for Finite element simulation of SECCM probe and description of type of boundary conditions.

**Table 2.6:** Summary of variables used in finite element simulations of SECCM probes.

## CHAPTER 3

**Table 3.1:** Noise values for different TIAs bandwidth by root-mean-square calculation and from the integration of current densities.

**Table 3.2:** Input capacitance ( $C_p$ ) and thermal noise values used for curve fitting of input-referred noise of each TIAs bandwidth.

## CHAPTER 4

**Table 4.1:** Average droplet residue diameter and standard deviation for each 2D TMDC experiment.

**Table 4.2:** Number of points assigned to each layer thickness, number of points on defective areas, and number of points analysed for the kinetics study.

**Table 4.3:** Boundary conditions for finite element simulation of 2D TMDCs.

**Table 4.4:** Comparison of the pipette aperture diameter derived by the fitting finite element simulation geometry to the limiting current and the droplet size diameter measured by AFM on TMDCs.

**Table 4.5:** Median  $k_{max}$  and 25<sup>th</sup> and 75<sup>th</sup> percentiles for different number of layers stacked and TMDCs.

**Table 4.6:** Median prefactor,  $k_{max}$ , and the 25<sup>th</sup> and 75<sup>th</sup> percentiles in brackets.  $\beta_{Au-nL}$  derived for the median  $k_{max}$  of MoS<sub>2</sub>, MoSe<sub>2</sub>, WS<sub>2</sub> and WSe<sub>2</sub>. In brackets the  $\beta_{Au-nL}$  derived from the 25<sup>th</sup> and 75<sup>th</sup>  $k_{max}$  percentiles. Band gap reported of same TMDCs with different numbers of layers.

## CHAPTER 6

**Table 6.1:** MXene flake step-heights obtained from AFM images.

**Table 6.2:** Area of Ti<sub>3</sub>C<sub>2</sub>T<sub>x</sub> flakes as determined from SEM micrographs.

**Table 6.3:** Total number of SECCM points examined and classified according to the surface morphology probed.

**Table 6.4:** Area of Ti<sub>3</sub>C<sub>2</sub>T<sub>x</sub> flakes as determined from SEM micrographs and the equivalent mass of each flake

**Table 6.5:** Summary of capacitance values reported in literature for Ti<sub>3</sub>C<sub>2</sub>T<sub>x</sub> electrodes and comparison with the capacitance values reported in this thesis.





# CHAPTER 1

---

## Introduction

From nano- and single-entity electrochemistry to energy storage  
and conversion technologies

---

## 1.1 Electrochemistry and energy conversion technologies

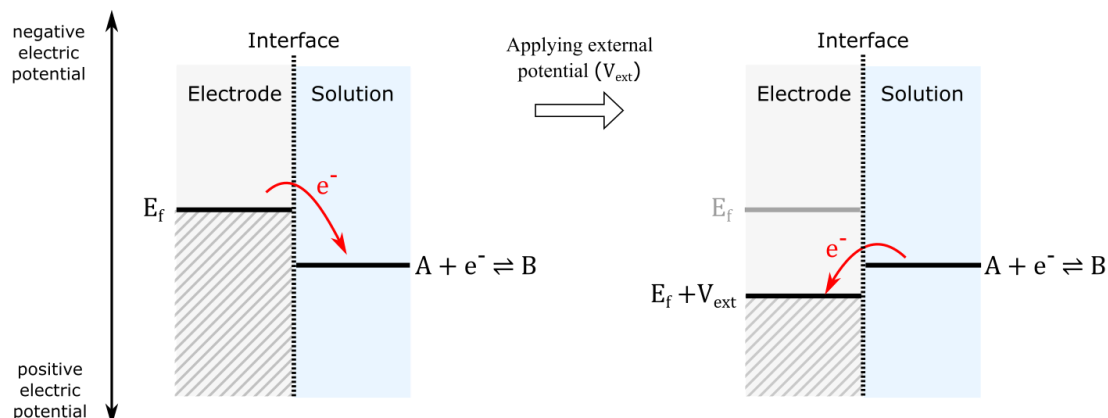
Electrochemistry is a branch of chemistry that deals with the interplay between electrical and chemical systems. Typical electrochemical systems enable carrying one or several physicochemical processes at the interface between a solid electron conductor phase (electrode) and a liquid ionic conductor phase (electrolyte). Other configurations such as solid-solid, liquid-liquid, or other interfaces are also possible to implement as electrochemical systems. The typical physicochemical processes of electrochemical systems involve conducting electrochemical reactions and/or accumulating/depleting charge carriers, resulting in the generation of currents in the electrochemical system. Electrochemical reactions involve electron transfer processes that allow the current to pass through the electrode and electrolyte interface. The species in the electrolyte phase that can give or donate electrons to the electrode are the redox-active species. Electrodes are typically conductor or semiconductor materials that can act as electron donors or receptors. Then, a broad description of electron transfer is of the processes that occur when the electron potential energy of the electron donor is equal to or greater than the electron potential energy of the acceptor, as shown in Figure 1.1. Electrochemical systems allow an external potential to be applied to the electrode, thus shifting the electron potential energy at the electrode, which in turn, enables control over the electron transfer process. Therefore, by applying an external potential it is possible to induce or quench the net transfer of charge at the interface, as shown in Figure 1.1.<sup>1</sup> The charge transfer can then be used to convert electrical work to stored energy in the form of chemical bonds, or the opposite, use energy stored in chemical bonds to provide electrical work.<sup>1,2</sup>

Electrochemical processes that involve electron transfer between the electrode and the electrolyte are called Faradaic processes. Electrochemical systems, however, can promote other physicochemical processes that do not involve electron transfer but result in current flows, these are referred to as non-Faradaic processes.<sup>1</sup> Examples of non-Faradaic processes are surface adsorption and desorption as well as charge accumulation at the electrode/electrolyte interface. These non-Faradaic processes could also represent a form of energy conversion or accumulation as a result of the coupling of electrical and chemical systems.<sup>3</sup>

Electrochemical systems are technologies of critical interest for modern society because they enable us to take advantage of electrical power from renewable sources and convert or store it into chemicals and materials. In this way, electrochemical systems can enable more effective and widespread use of renewable sources, which is essential for reducing reliance on fossil fuels and carbon emissions associated with human activities. Electrochemical technologies such as fuel cells, electrolyzers, and batteries already play a major role in the integration of renewables into energy grids and allow advancement towards electrification. The need to expand our use of electrochemical devices is widely recognised in policy initiatives such as the EU Renewable



Energy Directive (Directive 2009/28/EC) and the DOE Decarbonisation Roadmap (DOE/EE-2635). However, it remains a challenge to achieve mature technologies that are efficient, cost-effective, sustainable, and accessible to all without increasing pressure on natural resources that are scarce or whose supply is under threat for geopolitical reasons.<sup>2</sup>



**Figure 1.1:** Scheme of electrode, interface, solution system showing the electron transfer process between electron and redox active species. On the left side, the electron transfer occurs between the free electrons of the electrode with energy  $E_f$  and the solution species A, which is in equilibrium with B involving one electron transfer process. The energy level display in the solution refers to the equilibrium of the A and B species. On the right the energy of the electrons of the electrode have decreased as a result of application of external potential, favouring the electron transfer from the B species (in equilibrium with A involving an electron transfer) to the electrode.

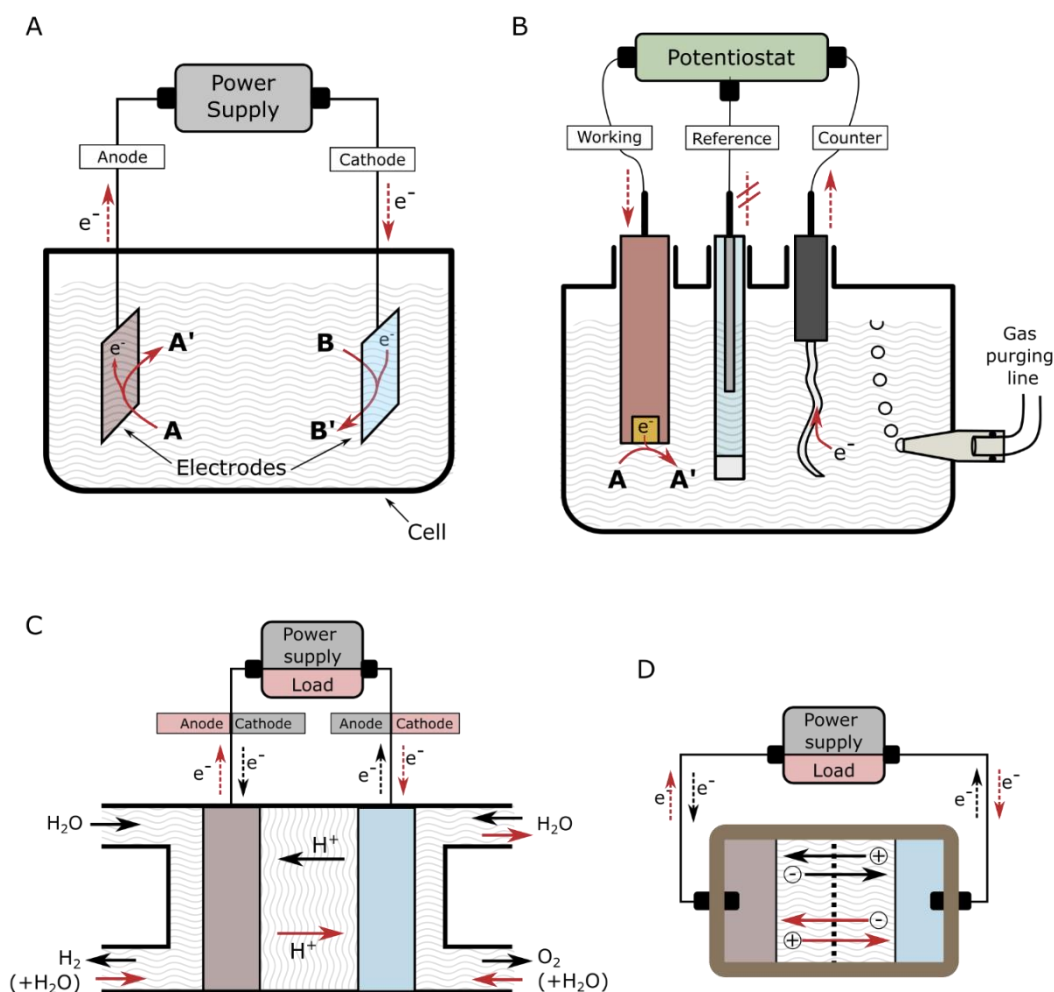
The introduction of nanomaterials into electrochemical energy storage and conversion technologies has boosted device performance, allowed technology development beyond scarce materials, and provoked the development of new electrochemical energy storage and conversion technologies. However, advanced nanomaterial-based electrochemical systems are significantly more intricate than classical electrochemical systems. Real-world devices require the nanomaterial-based components to be assembled into macroscale electrodes. Then, for the implementation of novel nanomaterial-based devices, it is crucial to understand and control the material properties from the nanoscale single entity level up to the macroscale material assembly level. Classical electrochemical methods are capable of characterising macroscale material assemblies. However, recent developments in nano-electrochemical methods allow electrochemical characterisation experiments directly on the single nano-entities, surpassing the barriers that classical electrochemical methods face with nanomaterial electrochemical characterisation.<sup>4</sup> Nano-electrochemical methods unlock a new range of possible measurements to provide in depth information about the behaviour of nanomaterials that are relevant for energy storage and energy conversion applications.

In this Introduction, I will first discuss common electrochemical systems used for energy conversion and storage technologies. In the following Section 1.3, I will discuss the role of nanomaterials in electrochemical systems, with a special focus on state-of-the-art nanomaterials for energy conversion and storage technologies. The nano-electrochemical characterisation techniques are presented in Section 1.4, including scanning electrochemical probe microscopy (SEPM) techniques such as scanning electrochemical cell microscopy (SECCM). The description of the mathematical models used to understand electrochemical behaviours is provided in Section 1.5. At the end of this introduction, in Section 1.6, the aims of this thesis are explained.

### **1.2 Electrochemical systems for energy conversion and storage.**

A basic schematic of an electrochemical system is shown in Figure 1.2 A. The different parts that constitute an electrochemical system are as follows: the cell for containing the electrolyte; electrodes made of metallic or semiconductor material that are inserted into the electrolyte; and the power supply for controlling the passage of electrical current through the electrode. Electrochemical systems are the site of an extensive number of different physical phenomena that might take place simultaneously; for example, charge and mass transport processes, electron transfer processes, charge carrier accumulation/depletion, chemical equilibria, etc. might all be at play during operation. Consequently, it is possible to find a variety of methodologies or electrochemical system configurations which differ significantly, as shown in the other schemes of Figure 1.2. For instance, more fundamental electrochemical studies often prefer 3-electrode cell setup, shown Figure 1.2 B; the 3-electrode setup allows to isolate the physical phenomena that occur only at one electrode (*i.e.* the working electrode) from the physical phenomena occurring in the rest of the cell.<sup>1</sup>

For energy storage and conversion applications, a 2-electrode setup is often used. Two large families of electrochemical system types can be distinguished: energy conversion devices, such as electrolyser or fuel cells, in which species can be incorporated or subtracted from the electrochemical cell, see Figure 1.2 C; and energy storage devices, such as batteries or capacitors, which are closed systems designed to work without the need of an external species supply, as shown in Figure 1.2 D. Energy conversion systems are used to transform electrical power into chemical energy that is stored elsewhere (or vice versa), while energy storage devices act as lone energy reservoirs.<sup>2</sup>



**Figure 1.2:** Schematic of different types of electrode cell setup. **A)** Two-electrode cell, **B)** three-electrode cell and **C)** open electrochemical setup characteristic for water electrolyzers and hydrogen fuel cells. Arrows indicated the flow of species and charges. The black colour code indicates the water electrolyser configuration and the red arrow indicates the hydrogen fuel cell configuration. **D)** Close electrochemical setup characteristic for batteries or capacitors. The encapsulation of the electrochemical cell is represented in brown. Arrows indicate the flow of charges. The black and red arrows indicate the charging and discharging processes, respectively.

### 1.2.1 Energy conversion and open electrochemical systems

Electrolytic cells are described as electrochemical systems in which the cell potential is negative ( $\Delta G > 0$ ) and work needs to be done to drive the reaction. Electrolytic cells can be used to synthesise valuable chemicals from precursors diluted in the electrolyte. Electrolytic cells can achieve energy conversion if the electrical work input is stored into chemical compounds that can be further used as fuel. Electrolytic cells for energy conversion often display an open electrochemical system, and thus the refreshing of reactant species allows recurrent fuel generation.

An example is electrolyzers, schematically shown in Figure 1.2 C, which can generate hydrogen ( $H_2$ ) from water (the precursor). Similar open electrochemical systems can be used for the inverse processes, *i.e.* generating electrical power from the consumption of chemical fuels, as in the case for fuel cells. Figure 1.2 C shows the scheme of an  $H_2$  fuel cell. Note that the components for both  $H_2$  electrolyzers and fuel cells can be shared. Often, the development of a fuel cell technology is intimately related to the development of the equivalent electrolytic cell.<sup>2</sup>

In an electrolytic cell, the electron transfer between the electrolyte species and the electrode surface is the process that enables energy conversion, from electrical work to chemical storage. The mechanism of electron transfer might depend on the interaction between the precursor and product species with the electrode surface. Generally, electrochemical reactions are classified as outer-sphere if the species involved in electron transfer do not interact strongly with the electrode surface; thus, the electron transfer is dependent only on the electron density at the electrode surface and independent of the chemical nature of the electrode surface. On the other hand, it is said to be inner-sphere if the species interact with the electrode surface prior to the electron transfer. Inner-sphere electron transfers can be expected to depend on the chemical state of the electrode surface.<sup>1</sup> Electron transfer of outer-sphere species is adiabatic and reversible, which would be ideal for energy conversion systems. Details on electron transfer mechanisms are provided in Section 1.5.2. The number of species that offer outer-sphere electron transfer behaviour is quite limited, often involve scarce elements (noble metals) or present other scalability limitations, such as high cost or poor long-term stability. As a consequence, the known outer-sphere species have limited application in scalable energy conversion technologies. Outer-sphere species, however, are widely used for fundamental studies, as their predictable behaviour and consistent responses are useful for comparing electrochemical systems.

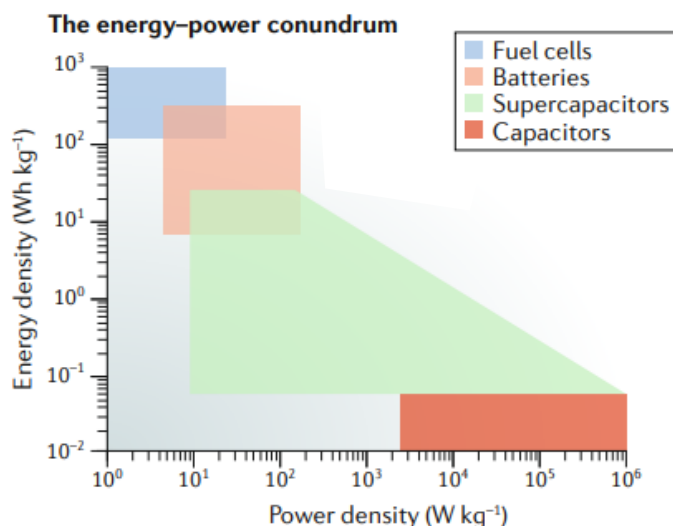
Energy conversion devices, *e.g.* electrolytic cells and fuel cells, generally rely on inner-sphere reactions and must satisfy requirements for scalability.<sup>5</sup> For example, vanadium oxide species, which display fast inner-sphere kinetics, are used for large scale redox flow batteries.<sup>6,7</sup> Electrolytic cells can reduce other very abundant species such as  $CO_2$ ,  $O_2$ ,  $N_2$ ,  $CH_4$ , etc. into valuable chemicals.<sup>8</sup> Generally, the inner-sphere processes present more complicated reaction pathways than other-sphere species. Inner-sphere electron transfer processes might involve multiple transition states, adsorption/desorption equilibria, radical generation, appearance of side reactions, etc. As a result, the design and optimisation of electrolytic cells require the development of electrode catalyst materials which target and favour a specific reaction mechanism, maximise kinetics and reduce side product formation.<sup>5</sup> High-efficient electrocatalyst materials are often reliant on scarce elements from the Earth's crust, which again limits their scalability. An example of a high-efficiency but scarce electrocatalyst material is platinum, which offers outstanding performance for water-splitting reactions. Nanomaterials are a great alternative to scarce elements

due to their great tunability, designability to mimic the physicochemical properties of scarce elements while utilising abundant elements from the Earth's crust, and therefore overcome the scalability requirements for electrocatalysts.<sup>9</sup> In summary, understanding the species / electrode surface interactions is key to develop electrochemical systems for the conversion of electrical energy into valuable chemicals. Advanced electrocatalytic materials are essential for finding cheaper alternatives to scarce Earth catalyst materials, and these materials usually incorporate nanostructured elements.

## 1.2.2 Energy storage and closed electrochemical systems

Electrochemical systems can be used as an energy storage reservoir. Energy storage devices use electrical work to drive a charge storage mechanism within the elements that constitute an electrochemical system (Figure 1.2 D). Because charging / discharging processes can be achieved without the need to remove or add species to the system, energy storage devices are portable technologies that can be easily integrated into an electrical grid.<sup>2,10</sup> Some examples of a classical and well-known system would be rechargeable batteries and electrochemical capacitors. Generally, battery charging involves a phase change of the electrode material, often mediated by electrolyte species. Meanwhile, capacitors are characterised for storing charge between the electrode and the electrolyte interface.<sup>3</sup> A detailed explanation of battery and capacitor charging mechanism and their differences is given in Chapter 6. Among the differences in the charging mechanism, batteries and capacitors can also be differentiated by their performance as energy storage devices. The key parameters that define charge storage technologies are the device's power density and energy density.<sup>11</sup>

The energy density refers to the total amount of energy that the system can store, also commonly referred to with respect to the weight (J/kg or Wh/kg) or volume (J/cm<sup>3</sup> or Wh/cm<sup>3</sup>) of the system. Power density refers to the rate at which energy can flow in and out of the system per amount of time and weight (W/kg) or volume of the system (W/cm<sup>3</sup>). Note that the relevance of which density metric is used, *i.e.*, gravimetric or volumetric, is subject to the interest of the final application. As shown in the Ragone plot in Figure 1.3, batteries are characterised for presenting a high energy density with low power density, whereas capacitors present a low energy density with high power density. Figure 1.3 also displays other supercapacitor technologies, which achieve a compromise between energy density and power density. Note that despite the variety and complementary characteristics of the different energy storage technologies, the fossil fuel based technologies provide a combined larger power density ( $> 10^6 \text{ W / kg}$ ) and larger energy density ( $> 10^3 \text{ Wh / kg}$ ) than any current electrochemical technologies. This highlights the demand for new or more advanced energy conversion and energy storage technologies.<sup>11</sup>



**Figure 1.3:** Ragone plot of the various electrochemical energy-storing technologies, power density energy density. Reproduced with permission from Sun, H. et al..<sup>11</sup>

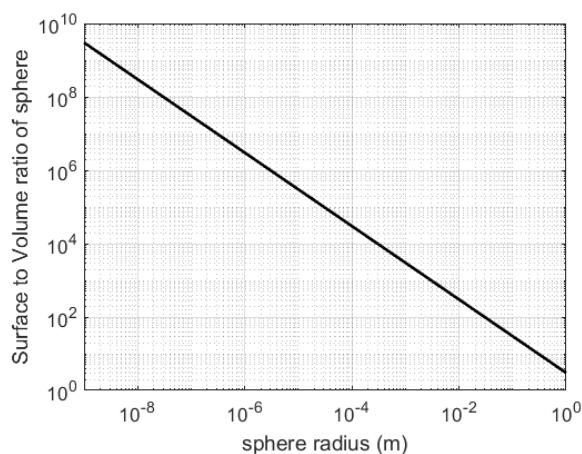
The closed nature of energy storage technologies, such as batteries or capacitors, make the mobility of charge carrier species paramount. The charge carrier mobility can limit the power density (charging/discharging rates) that a device can provide.<sup>11,12</sup> Carrier mobility can also affect the total energy density of the system; thus, if the charge carrier cannot reach certain regions of the system, the total energy storage capabilities are decreased. As a consequence, the design of energy storage devices goes through optimisation of charge carrier transport (among the development requirements of each system).<sup>4</sup> Energy storage devices benefit from presenting a nanostructured electrode architecture to improve charge carrier transport. Moreover, nanomaterials offer a high specific surface area, enlarging the size of the interface. As a result, the incorporation of nanomaterials facilitates the improvement of the performance for energy storage devices.

### 1.3 Nanomaterials in electrochemistry

Energy conversion and storage devices, such as batteries, supercapacitors, electrolyzers, or fuel cells, use nanomaterials to boost performance while simultaneously reducing the mass of material necessary.<sup>3</sup> A nanomaterial is a material in which at least one dimension is less than 100 nm. This very broad definition encompasses a wide variety of chemical structures. However, dimensions below 100 nm for electrochemical systems translate into drastic changes in the relative contributions of physical phenomena that determine the electrochemical response, independently of the chemistry of the specific nanomaterial itself.<sup>13</sup> This section will provide a broad overview of how nanomaterials can influence the response of electrochemical systems.

### 1.3.1 Effects of scaling down the size of an electrochemical system

Nanomaterials present a surface to volume ratio that is several orders of magnitude larger than their bulk counterparts, as shown in Figure 1.4 for a spherical particle. Nanomaterials have a high percentage of surface atoms compared to total atoms and a large specific surface area, which can both be exploited for energy storage and conversion devices. For example, electrolyzers benefit from the integration of nanomaterials by lowering the demand on catalyst loads, while preserving the active surface area.<sup>9</sup> Electrochemical capacitance depends on the interface area, thus the integration of nanostructured materials that provide larger interfacial areas results in a direct increase in electrochemical system capacitance.<sup>14</sup> Capacitance-based energy storage devices receive a massive gain in energy density from the incorporation of nanomaterials, becoming a new type of energy storage technology called supercapacitors, which bridges the performance gap between traditional batteries and capacitors.<sup>15</sup>



**Figure 1.4:** Surface-to-volume ratio of a sphere across a length scale of nanometres to metres.

The interfacial area between the liquid electrolyte and the solid species is increased by orders of magnitude when using nanomaterials. As a result, when nanomaterials are integrated into electrochemical systems, interface-dependent properties can potentially dominate the overall system behaviour. The properties offered by the interface can be exploited for energy storage and conversion devices. For instance, some transition metal or metal oxide materials present pseudocapacitive properties, *i.e.*, under certain electrochemical conditions the surface can store charge via bond formation with electrolyte species. Pseudocapacitance is a property that depends exclusively on surface properties and offers a charge storage mechanism that is suitable for applications in energy storage devices if electrode materials are designed to display a large specific surface area.<sup>16</sup> The large interface offered by nanomaterials can also affect the timescale over which certain electrochemical processes occur. For instance, electrochemical oxidation or corrosion of a metal is an interface-dependent process and, thus, the electrolyte species must interact with the surface of the metal. In the case of nanomaterials, the large surface to volume ratio results in the complete oxidation of single nanoparticles on microsecond to millisecond timescales.<sup>17</sup>

The incorporation of nanostructured objects and nanostructured interfaces have a huge impact on the displacement of species in the electrochemical system.<sup>4</sup> Section 1.5.3 provides descriptions of the different mass transport processes involved in electrochemical systems, which often require a careful approach and the usage of mathematical models. Without delving into such level of detail, the size of nanostructures and their tuneable geometry allow to optimize mass transport processes beyond the possibilities offered by bulk materials. To illustrate that, Figure 1.5 shows a simplistic model of systems displaying two phases with different mass transport properties (*e.g.* different species mobility or diffusion coefficient on different phases) and with structured and nonstructured interfaces. In the Figure 1.5 model, for example, the faster mass transport phase can be interpreted as a solution phase; and the slower mass transport phase can for instance be interpreted as an electrode phase during charge carrier intercalation. In Figure 1.5 A, the interphase is flat, *i.e.*, not structured. The total time that a species needs to travel along both phases to move from the points “a” to “aa” ( $t_{a \rightarrow aa}$ ) in the shortest distance possible can be described as:

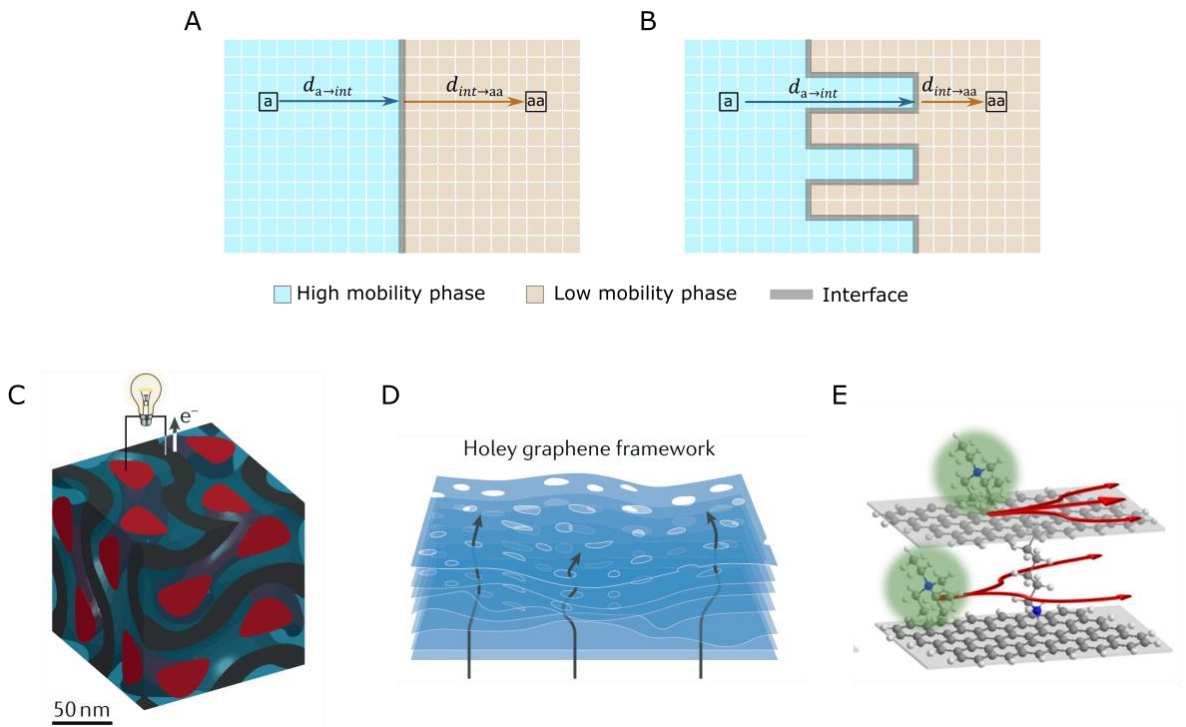
$$t_{a \rightarrow aa} = \frac{d_{a \rightarrow int}}{v_{i-sol}} + \frac{d_{int \rightarrow aa}}{v_{i-el}} \quad (\text{Eq. 1.1})$$

where  $d_{a \rightarrow int}$  is the distance from “a” to the interface,  $d_{int \rightarrow aa}$  from the interface to “aa”,  $v_{i-sol}$  is the average velocity at which species  $i$  move from “a” to the interface in the solution phase and  $v_{i-el}$  is the average velocity at which species  $i$  moves from the interface to the “aa” in the electrode phase. Note that for simplicity of the example, Figure 1.5 A and B show the case where the shortest distance travelled is also the fastest route and that the average displacement velocities are used instead of considering a description of diffusion and migration transport. For a structured interface, as shown in Figure 1.5 B, the distance the species need to travel ( $d$ ) along each phase to move from “a” to “aa” has changed. Thus, for Figure 1.5 B,  $d_{a \rightarrow int} > d_{int \rightarrow aa}$ , while species velocity are  $v_{i-sol} > v_{i-el}$ , as a result the overall time ( $t_{i \rightarrow ii}$ ) is smaller for the structured interface. Therefore, by only altering the geometry of the interface, a faster species displacement is achieved. Notice that for many other selected points from “a” to “aa”, a faster species displacement will also be achieved. A more general description of this phenomenon for different geometries can be found in White, H.S. *et al.* review paper.<sup>18</sup>

The performance of electrochemical energy storage devices often depends on the charge carrier displacement across different phases (*e.g.* anode, cathode, electrolyte, etc.). Interface geometry optimisation provides faster species displacement, which instigate faster charging/discharging rate and greater power densities. For instance, the 3D tri-contentious electrode assemblies shown in Figure 1.5 D minimise the displacement distance between phases. Additionally, the 3D holey graphene frameworks favour the formation of specific channels or paths for enhance charge carrier mobility; as shown in Figure 1.5 E<sup>11</sup>. A faster species displacement is achieved if the interface structures match the size of the charge carrier.<sup>18</sup> In energy storage systems, charge carriers are



commonly ions or polarisable species, which size is in the nanometre range. As a result, interface geometry optimisation strategies are widely implemented in energy storage devices by using a nanostructured electrode.<sup>11</sup> For example, pillared graphene materials show an improvement in capacitance performance when the charge carrier size is matched to the spacing between graphene layers,<sup>19</sup> as shown in Figure 1.5 E.



**Figure 1.5:** Mass transport in nanostructured systems. **A)** Displacement of species between points “a” to “aa” points across two phases, which have faster and slower mass transport properties and flat interface. **B)** Similar to A but with an interface presenting a non-flat structure. **C)** Illustration of a 3D tri-continuous nanolayer battery assembly. The anode, electrolyte, and cathode are coloured black, blue, and red, respectively. **D)** Illustration of a holey graphene framework that highlights the paths for charge mobility with black arrows. **E)** Illustration of a pillared graphene structure showing possible charge carrier mobilities (red arrows) along the spaced graphene layers. Reproduced with permission from Banda, H *et al.*<sup>19</sup>. C, and D are reproduced with permission from Sun, H. *et al.*<sup>11</sup>.

Optimisation of geometry in energy storage devices is very complex because it depends on many variables.<sup>20</sup> In recent years, computational tools have been developed to resolve geometry optimisation via simulation.<sup>21</sup> During my Ph.D., I contributed to a review paper on continuous simulations of 3D electrodes for battery applications. In continuous simulation, a set of initial geometric parameters are defined and the response of the system is simulated; iteratively the geometric parameters are varied and depending on device performance changes, the parameters are retained or discarded.<sup>22</sup>

In summary, nanostructured materials display high surface area to volume ratio, thus enhancing the relevance of interfacial properties and influencing the mass transport of species in solution to the surface, resulting in significant effects on the overall electrochemical response.

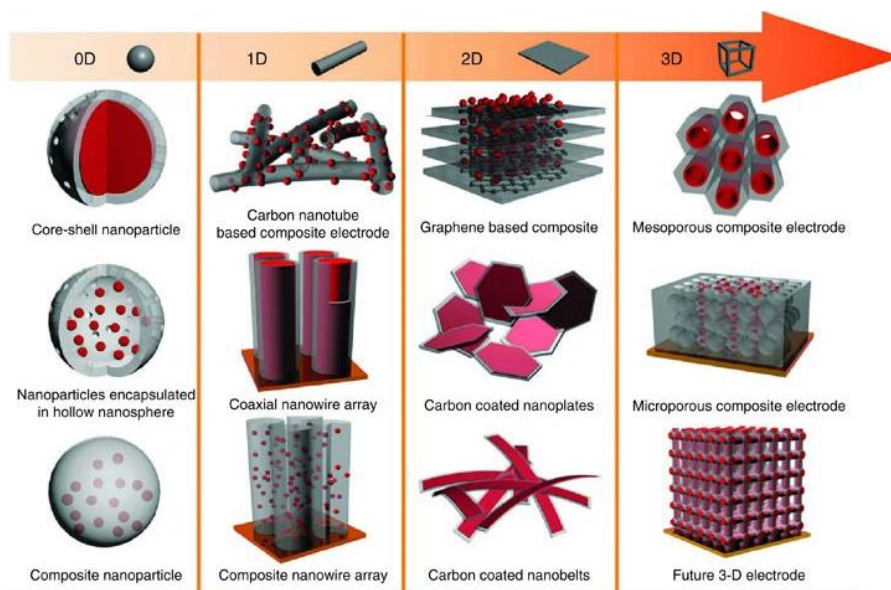
### 1.3.2 The new properties offered by nanomaterials

Scaling down the characteristic size of the material can produce changes in the intrinsic physicochemical properties of the material itself. Chemical structure, electronic structure, and optical properties can all be altered in low-dimensional materials, and characteristics that are important for electrochemical processes, such as state distributions, charge carrier concentration, and carrier mass and mobility, can also significantly depart from those observed in the counterpart bulk material. Quantum-confinement effects can also be observed; for instance, graphene has a unique conduction/valence band structure that differs from that of graphite, which allows for ballistic transport of electrons<sup>23</sup> and results in photoluminescence effects.<sup>24</sup>

The uniqueness of nanomaterials opens an enormous window of applications and custom-made materials with widely tuneable properties that can be leveraged to improve the design and performance of energy storage and conversion devices. For instance, surface chemistry properties of scarce elements can be matched with nanostructure non-scarce elements.<sup>25,26</sup> Note that material scarcity is not only a problem related to electrochemistry, thus many fields would also benefit from having larger stock of scarce earth elements.<sup>27</sup> The hydrogen evolution reaction (HER) is considered an important reaction for energy conversion technologies which rely on the usage of electrocatalyst. The HER electrocatalysts need to present a high work function to balance protons adsorption and hydrogen gas desorption, a high free charge carrier density that provides good conductivity and facilitate electron transfer kinetics, and great stability under acidic conditions.<sup>9</sup> Not many materials present the right set of properties, which are characteristic for the scarce and expensive elements of platinum group metals.<sup>28,29</sup> An alternative to offer the desired surface properties is the development of new catalysts by creating materials with hybrid properties.<sup>30,31</sup> For example, graphitic carbon is a good electron conductor, a stable material in acidic conditions and electrochemically relatively inert, but by introducing doping elements, such as embedded nitrogen, which present electron lone pairs, hydrogen absorption centres can be created. The resulting material then keeps the advantages of using a graphite base electrode, but with certain domains present specific activity toward proton chemistry.<sup>32</sup> Notice that the adequate interplay between different material domains is often reached if the domains are in the nanoscale size. Larger domains ( $> \mu\text{m}$ ) instead tend to create segregated phases with independent properties, and the benefits brought by material heterogeneity are negated.<sup>25</sup>

Single nanoscale entities can also match the properties characteristic of scarce materials. For example, two-dimensional transition metal dichalcogenides (2D TMDCs) have been shown to perform as efficient HER electrocatalysts thanks to the larger surface area of 2D materials, as well as the presence of electrocatalytic sites,<sup>33</sup> as detailed in Chapter 4. Moreover, nanoscale defects such as grain boundaries, lattice dislocations, heteroatoms, cracks, edges, etc. can lead to generation of local redox active centres while the overall physical properties of the nanomaterial material (*e.g.* conductivity) are preserved.<sup>34</sup> Thus, defect engineering facilitates to achieve, to tune and to enhance nanomaterial properties, which are greatly used in electrochemical systems as explored in Chapter 5. Single nanomaterial entities can also present unique combinations of electronic structure and surface chemistry which are not achievable in bulk materials. As explored in Chapter 6, MXenes (two-dimensional metal carbides and nitrides) present a metallic-like electronic structure, while presenting a surface chemistry closer to that of a metal oxide.

Energy conversion and storage devices often require macroscale sized electrodes to be operable for real-world applications. By combining one or more types of nanomaterial into assemblies, it is possible to achieve macroscale-sized electrodes using nanomaterials as building blocks. Nanomaterial assemblies, also called 3D nanostructures, generally consist of a scaffold made of one or more types of nanomaterials (2D, 1D, 0D) that can include or be decorated with other types of nanomaterials, as shown in Figure 1.6.<sup>13</sup> Examples of 0D materials are nanoparticles and quantum dots; nanotubes or nanorods are classified as 1D materials; while nanoflakes or monolayers are considered 2D nanomaterials. Nanomaterial assemblies offer an opportunity to bring different properties into electrochemical systems, so that a great variety of properties can be achieved through the fabrication of unique composite or hybrid materials. For example, nanostructured carbon-based scaffolds (*e.g.*, CNTs, graphene, platelets or pearls), which provide good conductivity, porosity, and chemical stability, often are combined or decorated with nanostructured inorganic materials (such as metal oxide, sulphides, carbides, or nitrides) that provide specific activity in charge storage mechanisms or electrocatalysis.<sup>35</sup>

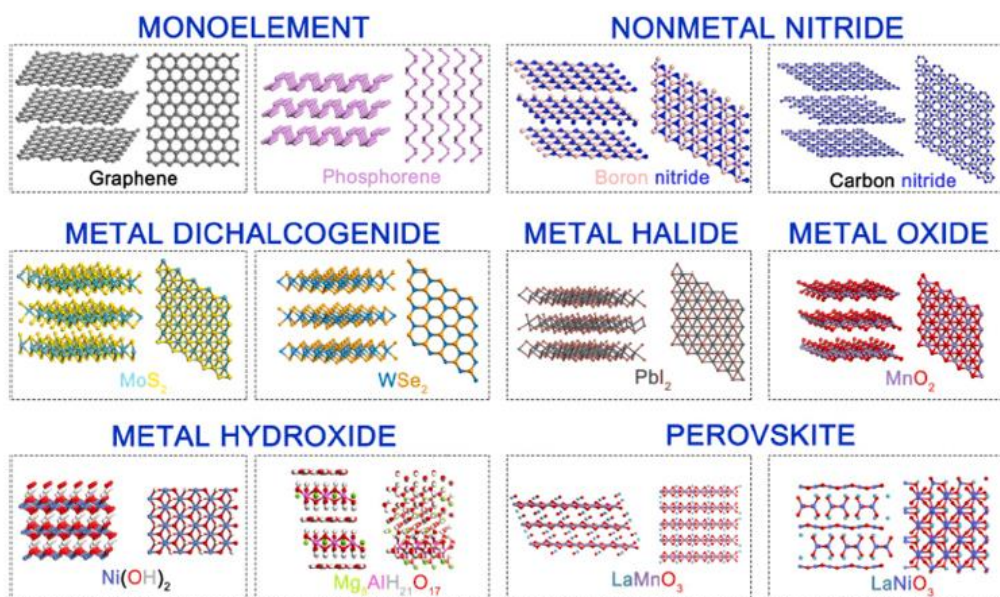


**Figure 1.6:** Examples of 0D, 1D, 2D and 3D nanomaterials. The red and grey contrasts represent different types of nanomaterials. Reproduced with permission from Lukatskaya, M. R. *et al.*<sup>13</sup>

### 1.3.3 2D materials for energy storage and conversion

Fundamental research on 2D materials and their applications in energy conversion and storage devices has been emerging in the last decade. 2D materials are usually presented in the form of flakes or nanosheets, allowing the entire surface to be exposed to the electrolyte and participate in electrochemical processes, achieving high theoretical specific surface areas.<sup>36</sup> The 2D flakes or nanosheets present two distinct domains: the basal plane and the edge. The basal plane is defined as the surface parallel to the flake plane and is characterised by atomic flatness. The basal plane of a 2D material often provides a uniform and well-defined surface with a low density of defects that can potentially be used for studying electrochemical mechanisms at the atomic level. The edges of 2D flakes are the “surfaces” perpendicular to the flakes plane and are characterised by having unsaturated coordination, being defective, and often presenting a heterogeneous structure and chemical composition. Edges often provide very distinct electrochemically active domains compared to the basal plane: dangling bonds, edge reconstructions and capping groups can be exploited as electrocatalytic centres.<sup>36,37</sup> However, notice that basal plane domains might present defects, introducing unsaturated coordination that could also act as a local reaction centre, provide a local charge carrier donor/acceptor, or become a scattering center.<sup>38</sup> Beyond those localised effects, the defects present in 2D materials might alter the overall electronic structure of the material, as is the case for doping effects.<sup>38</sup>

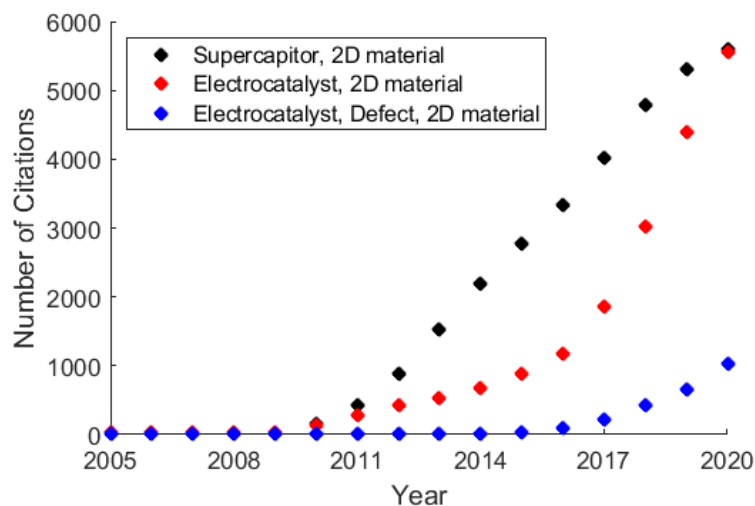
The family of 2D materials is very large, with hundreds of materials studied experimentally and others proposed by computational methods. Examples of 2D material structures are illustrated in Figure 1.7; a wide range of 2D materials have been studied for applications including the oxygen evolution reaction, the hydrogen evolution reaction, the CO<sub>2</sub> reduction reactions, photocatalytic water splitting, electrical double layer capacitors, pseudocapacitors, and batteries.<sup>36</sup> Integration of 2D materials in electrochemical energy conversion/storage devices often requires the material to be a conductor or semiconductor, and to manufacture a macroscale electrode the 2D material is assembled into a 3D nanostructure. The assembly into a 3D nanostructure is often a highly tuneable process that can influence final performance/properties; for instance, the resulting 3D nanostructure can be optimised to present high degree of connectivity between 2D flakes that maximise electrical conductivity and minimise resistive effects. Also, 3D nanostructures can be tuned to provide hierarchical porosity that generates sites for ion intercalation while enabling fast ion transport, thus enhancing the power/energy density of batteries and supercapacitors.<sup>11</sup>



**Figure 1.7:** Schematic view of monoelement, non-metal nitride, metal dichalcogenide, metal halide, metal oxide, metal hydroxide, and perovskite 2D materials. Reproduced with permission from Tao, H. *et al.*<sup>36</sup>

The application of 2D materials in energy storage and conversion can be evaluated by reviewing the literature. From the Web-of-Science database it is possible to compare the number of citations related to the combination of “2D material” with “Supercapacitor” or “Electrocatalyst”, as representative key terms. Figure 1.8 shows the total number of citations per year of the 50 articles most cited related to these key terms, which offers a qualitative means of comparing the increasing or decreasing trends in the number of studies on these topics over time. Figure 1.8 shows two main trends. First, the implementation of 2D materials in energy storage and conversion applications

such as electrocatalysts or supercapacitors has emerged just a few years after the first 2D material, graphene, was discovered in 2003. Second, supercapacitor applications emerge earlier than electrocatalyst applications for 2D materials. This might be a sign that electrocatalytic technologies are more complex than capacitor technologies, and thus require more mature knowledge about the material properties. Figure 1.8 also shows the result for the key term “Defect” in combination with “2D material” and “Electrocatalyst”. The trend observed in Figure 1.8 shows a very recent increase in the number of citations, which highlights the correlation between 2D electrocatalytic materials and the presence of defects.



**Figure 1.8:** Number of citations received per year of the 50 most cited articles using the combination of key terms “1D material” or “2D material” with “Supercapacitor” or “Electrocatalyst”. The green line represents the combination of the key terms “2D material” and “Electrocatalyst” and defects. All data have been obtained from the database Web-of-Science database on 29/11/2022.

In this thesis, two different 2D materials relevant for energy conversion and energy storage, 2D TDMCs and the MXenes, have been studied at the single entity and/or single active domain level. The work of this thesis on 2D material has focused on correlating the electrochemical response with the presence of morphological feature and electroactive domains, via nano-electrochemical methods. In Chapters 4 and 5 the electrochemical behaviour of 2D TDMCs with respect to morphological features such as number of layers stacked and defect presence, is experimentally measured and discussed. In Chapter 6 the pseudocapacitance response of the individual building blocks MXene based electrodes, *i.e.* single MXene flakes, is experimentally measured and discussed. The 2D TMDCs and MXenes are very different materials with very distinct structure and physicochemical properties. Understanding the 2D TMDC and MXene characteristic electrochemical behaviour relies on a detailed understanding of the structure and the physicochemical properties of these materials, and as such, these materials are discussed in the introductory section of their corresponding chapters.

## 1.4 Characterizing nanomaterial electrochemical response

The previous section described how electrochemical behaviour can be altered using nanomaterials. In this section, the instrumentation and methods used for characterising nanosized electrochemical systems are introduced.

### 1.4.1 Bulk vs single entity electrochemistry

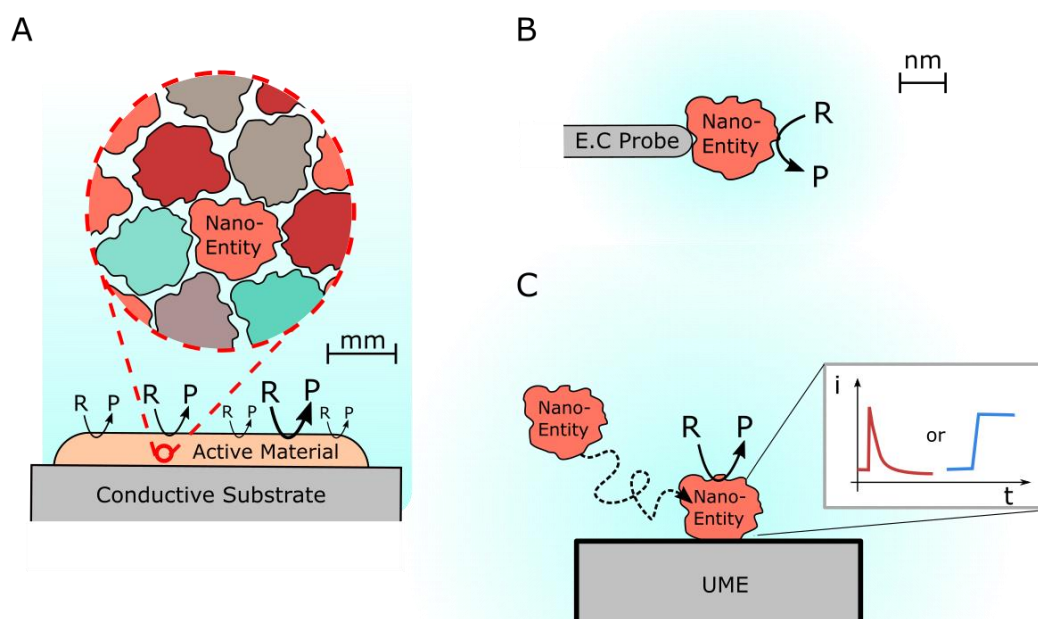
When nanomaterials were first introduced into electrochemical systems, the available electrochemical characterisation methods were designed for macroscale materials, leading to several challenges. Classical electrochemistry methods and instrumentation are designed to measure currents in the  $\mu\text{A}$ - $\text{mA}$  range, while currents associated with nano-entities are generally in the  $\text{pA}$ - $\text{nA}$  range. Classical electrochemical approaches need macroscale quantities of nanomaterials to produce sufficiently large currents to be compatible with equipment resolution, which is achieved by manufacturing electrodes based on an ensemble of a vast number of individual nano-entities. Then, the signal recorded and dataset generated from characterising nanomaterials with classical ensemble-based electrochemical methods is representative of the behaviour of the 3D nano-entity assembly, which might differ from the individual nano-entities behaviour. The behaviour of 3D nano-entity assemblies strongly depends on the exact architecture of the assembly. For instance, nanoscale ion-intercalation channels generated in a 3D nanostructure for a supercapacitor application affect the assembly performance.<sup>11</sup> Moreover, in 3D nano-entity assemblies, not all of the nano-entities are identical to each other and instead present a dispersion in size, shape and overall properties, as illustrated in Figure 1.9 A.<sup>17,39</sup> Therefore, the readouts of the classical ensemble-base electrochemical method have contributions of the average behaviour of the individual entities and contribution from the macroscale 3D assembly properties. Conventional ensemble-based electrochemical approaches are not best suited for direct determination of nanomaterial properties dispersion, for identifying details of the nanomaterial heterogeneity contributions, or for differentiating between the single-entity and the assembly contributions. Classical electrochemical methods can face temporal resolution limitations. The characteristic timescales used in classical electrochemical methods range from seconds to minutes (and even hours) while the single-entity electrochemistry phenomena typically occur at a shorter timescale, in the order of microseconds to milliseconds. Therefore, nanomaterial electrochemical methods need to account for resolving very short timescale signals.<sup>40</sup>

The properties of nanomaterials are intimately related to the morphology of the nanomaterial. Then, one of the key aspects for the electrochemical characterisation of nanomaterials is understanding the role of morphology.<sup>41</sup> Ensemble-based electrodes present distinct morphological features

ranging from nanometres, *i.e.*, on the scale of the single nano-entities, up to millimetres, *i.e.*, on the scale of the macroscale electrode. Bulk electrochemical methods might infer nanoscale morphology contributions utilising strategies such as impedance spectroscopy and circuit modelling, signal deconvolution or relying on microscopy / spectroscopy characterisation.<sup>17,42</sup> However, the additional morphological features on the micrometre and millimetre range created by the ensemble approach make resolving nanoscale morphology complex, and often information about nanoscale phenomena remain hinder. Some nanomaterials, moreover, present sub-single entity domains, which are distinct electroactive domains within a single-entity. Sub-single entity properties can dominate the electrochemical behaviour of the system. For instance, a single nano-entity like a 2D flake can present multiple electroactive domains like edges, basal-planes or defects. Another example of the limitations of ensemble-based methods is control over how the electrical contact of single entities is achieved, which can define the electrochemical response.<sup>43</sup>

A more detailed description of nanomaterial properties and the relation with nanoscale morphology can instead be obtained via characterisation methods that measure single nano-entities independently.<sup>17</sup> Single nano-entity electrochemistry (SEE) is a branch of the electrochemistry which isolates the electrochemical response of individual nanoparticles, 2D flakes, nanotubes, etc. as shown in Figure 1.9 B. The study and integration of nanomaterials in electrochemistry has been accompanied by the development of new electrochemical techniques and methods which characterise in an effective manner the electrochemical response of nanomaterials. A new generation of electrochemical techniques has been developed to measure in the length, time, and sensitivity scales that are adequate for nanomaterial characterisation. The most common approach for new techniques to overcome the difficulties of measuring at the nanoscale is to downscale the elements of the electrochemical system.<sup>17,39,44</sup> For instance, microscale-sized electrodes, also known as ultra-microelectrodes (UME), can be used to isolate the response of single entities dispersed in solution by stochastic collision electrochemistry, as illustrated in Figure 1.9 C (also see Chapter 3).<sup>45</sup> In addition to the downscaling of the electrochemical system elements, the family of scanning electrochemical probe microscopy (SEPM) techniques allows the spatial displacement of a micro- / nano- scale electrochemical probe which facilitate isolation of single entities. Thus, SEPM provides a platform to resolve SEE with nanometre spatial resolution for a wide spectrum of nanomaterial and electrochemical systems.<sup>17,39,44</sup>





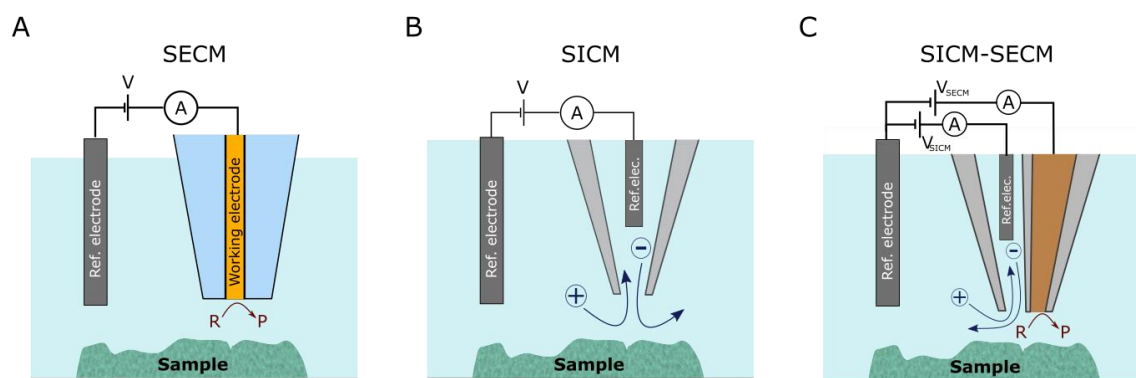
**Figure 1.9:** Comparison between bulk electrochemistry and single-entity electrochemistry. **A)** Electrode with a macroscale amount of heterogeneous nanomaterial with multiple reaction sites. “R” stands for reactant and “P” stands for product. **B)** Representation of a single nano-entity measurement with only a single reaction site. **C)** Example of a stochastic collision electrochemistry experiment in which the response of an individual nano-entity is isolated when it collides with the electrode surface, originating an electrochemical response.

### 1.4.2 The family of SPEM techniques

Scanning probe microscopy (SPM) techniques, such as atomic force microscopy (AFM) and scanning tunnelling microscopy (STM), were initially developed in the 1980s with the aim of obtaining topographic information on surfaces at the atomic level.<sup>46</sup> A description of the AFM working principle is reported in the Methods chapter, Section 2.3.1. The evolution of AFM and STM hardware instrumentation and software set the basis for the development of scanning electrochemical probe microscopy. The first studies using a movable probe to detect electrochemical phenomena date back to the 1970s by Isaacs, H. S. *et al.*<sup>47,48</sup> Since these first reports, the experimental and theoretical methodology of SEPM has evolved in parallel with other SPM techniques. In 1999 the first commercially available SECM equipment (CH Instruments) was released and since then multiple groups have incorporated SEPM techniques into their research methodology.<sup>49</sup> Henceforth, a dedicated family of SEPM instruments has been developed based on the principles of scanning probe microscopy. The expansion of SEPM methodology during the 1990s and 2000s was also related to advances in AFM instrumentation and methods. The initial development of the AFM technique led to the introduction of probes with multiple functionalities that are capable of probing the physicochemical properties of surfaces and interfaces with spatial

resolution, such as mechanical, electrical, or thermal properties. Further advances in conductive AFM (C-AFM) allowed one to measure surface density of states or perform localised surface modifications. The introduction of liquid-phase AFM technology, together with conductive AFM probes, allowed localised electrochemical measurements, which led to electrochemical AFM (EC-AFM) technologies. EC-AFM allows to perform electrochemistry with nanoscale resolution and nowadays is a powerful technique. Nevertheless, the EC-AFM demands a narrow set of experimental conditions to operate that might be limiting for some electrochemical experimental designs. Therefore, it is a complementary technique to the electrochemically focused family of SEPM techniques.<sup>49</sup>

SEPM is a family of probe-based electrochemistry techniques that can perform local electrochemical studies with nanometre to micrometre spatial resolution. The first SEPM approach developed was scanning electrochemical microscopy (SECM). As shown in Figure 1.10 A, SECM is based on placing a UME, acting as probe, in close proximity to the sample surface, so the signal readout depends on the local physicochemical properties and/or the morphology of the sample. Fine position and motion control on the SECM probe, achieved with piezo controllers and current feedback loops, allows one to obtain spatial information along the X, Y, and Z axes. The potential can be applied between the sample and the UME or between a reference electrode in solution and the UME. SECM has been widely reported for the study of electrochemically active domains with a resolution of a few  $\mu\text{m}$ .<sup>50</sup>



**Figures 1.10:** Representation of different scanning electrochemical probe techniques. **A)** SECM with an ultra-microelectrode as probe, **B)** SICM with a micropipette as probe, and **C)** SICM-SECM which combine in the same probe a micropipette and an ultra-microelectrode in the same probe. For all techniques shown, both the sample and probe are immersed in an electrolyte solution, which is represented with blue colouring.

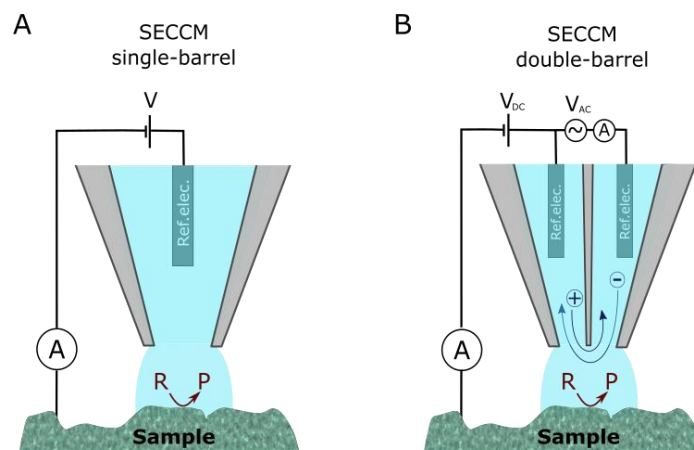
Other types of scanning electrochemical probe microscopy have been developed, sharing similar hardware and software but using different probe types. Scanning ion conductance microscopy (SICM) uses a hollow micropipette as a probe instead of the UME probe of SECM, as shown in Figure 1.10 B. Two electrodes are used, one placed inside the micropipette and a second one placed

in the bulk solution; this allows one to apply a potential difference between the inside and outside of the pipette so that an ion current is generated between the two electrodes through the aperture of the micropipette probe.<sup>51</sup> The aperture of the micropipette then acts as an ionic channel, and the current response generated is equivalent to the ion flow through the pipette aperture. SICM is sensitive to local variations in ionic concentration and is sensitive to distance when placed near the sample surface. SICM does not require a conductive sample but demands the same precise control over the probe position, achieved with a feedback loop over the ionic flow. SICM was originally used for the topological characterisation of samples that needed non-contact methods or immersion in solution, such as living cells.<sup>52</sup> More advanced configurations can be achieved by the combination of SICM and SECM, by coupling a micropipette and a UME in a single multifunctional probe, as in Figure 1.10 C. In the SICM-SECM technique, the UME can perform a controlled electrochemical redox characterisation, while the micropipette acting as an ionic channel provides information about the distance between the surface and the probe. SICM-SECM techniques can be used to perform simultaneous electrochemical and morphological mappings of the surface.<sup>50</sup>

The SECM and SICM techniques require that the probe and sample be immersed in solution and exposed to the electrolyte; however, this might not always be the most appropriate configuration. SECM or SICM-SECM often require the whole surface of the sample to be set at a given potential despite only a small surface region being interrogated. Setting the sample at a potential while the sample surface is exposed results in difficult control of surface termination/adsorbates, so that characterisation of the pristine surface is not always guaranteed. Complete immersion of the sample and probe can also restrict lateral resolution because of the mass transport effects (diffusion) of species in solution. Those problems have been addressed by the scanning droplet family of SEPM techniques, of which scanning electrochemical cell microscopy (SECCM) is the leading approach.<sup>50</sup>

SECCM is a recently developed technique first reported in 2010.<sup>53</sup> The SECCM probe uses a liquid meniscus at the end of a pipette to form a micro- or nano-scale electrochemical cell, when placed in close proximity to the sample surface. The meniscus, also called the droplet cell, only wets the desired area of study and the rest of the sample remains exposed to air, as shown in Figure 1.11. In SECCM the sample is commonly used as the working electrode. The electrolyte solution is enclosed inside the pipette and often contains the electroactive species. The pipette aperture of SECCM probes can be tuned from 10's of nanometre to 50's of micrometre conferring significant versatility and providing nanometre to micrometre spatial resolution.<sup>54</sup> The most versatile and commonly used SECCM probe types are single barrel micropipettes with a single electrode inserted, as illustrated in Figure 1.11 A, and double barrel micropipettes with one electrode inserted in each barrel, as shown in Figure 1.11 B. Both probe configurations can be used to apply a

potential difference between the pipette and the surface to enable electrochemical characterisation, but double barrel pipettes can also measure the ionic flow between the two barrels, which provides additional information about the droplet cell geometry.<sup>55</sup> Other SECCM probe designs and electrode placement geometries have been reported to fulfil specific experimental requirements or to enhance its performance toward specific tasks, often at the cost of versatility.<sup>56</sup> A description of the SECCM working principle is found in the Methods Chapter, Section 2.2.



**Figures 1.11:** Schematic representation of the scanning electrochemical cell microscopy technique for **A)** a single barrel pipette as a probe and **B)** a double barrel pipette as a probe. Note that neither the sample nor the probe are immersed in the electrolyte solution as the electrolyte is contained within the probe.

### 1.4.3 Overview of the SECCM driven nano-electrochemical studies

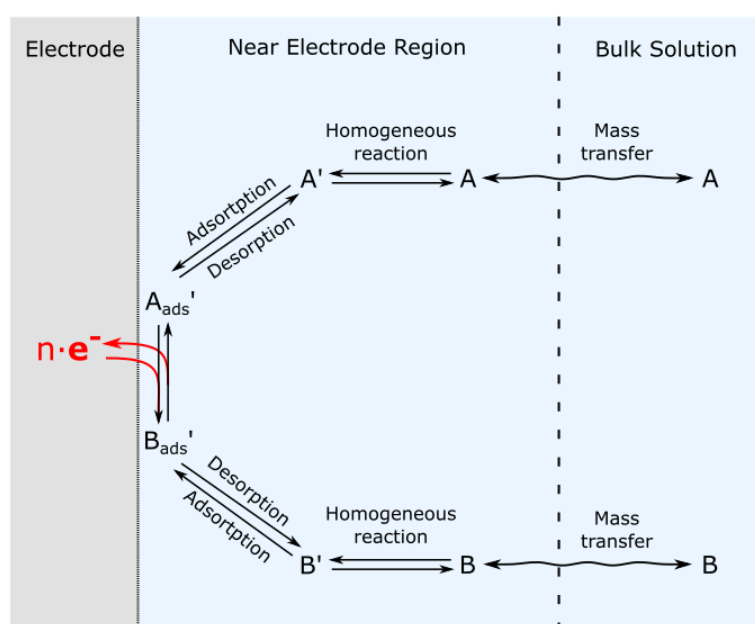
SECCM probes can isolate the electrochemical response of different surface domains or features, such as grain boundaries or morphological features, and single nano-entities, such as single nanoparticles or nanoclusters. Electrochemical measurements on nanoscale features or entities are relevant for multiple research topics and electrochemical disciplines. The SECCM research outcomes can be grouped into:

- Studies of grain boundary and facet dependent electrochemical properties on polycrystalline electrodes, including electrocatalytic and corrosion properties. For instance, Mariano *et al.* reported enhancement towards CO<sub>2</sub> reduction on gold grain boundaries;<sup>57</sup> Unwin *et al.* observed that the anodic dissolution of iron depends on grain boundaries exposed to electrolyte;<sup>58</sup> Ren *et al.* mapped the potential of zero charge (PZC) dependence on Pt grain boundaries.<sup>59</sup> For other studies reporting electrocatalysis dependence on grain boundaries and crystalline facets via SECCM, see ref. 60-63.

- Studies of 2D materials and electrochemical characterisation of layered crystals. SECCM has established correlations between the electrochemical response and morphological features of layered materials, such as basal planes, edges, and/or the number of layers. Unwin *et al.* quantified heterogeneous electron transfer behaviour of monolayer and multilayer graphene showing differences arising from the number of layers stacked,<sup>64</sup> and between the edge and basal plane domains.<sup>65</sup> Hill *et al.* reported the photoelectrochemical response 2D TMDCs via SECCM, showing strong correlation between morphological features and photoelectrochemical response.<sup>66</sup> For other studies on 2D materials via SECCM, see ref. 67 and 68.
- Electrochemical characterisation of single nano-entity electrocatalysts. Through SECCM, the electrochemical reactions of single nanoparticles or nanoclusters can be isolated and their electrochemical response can be correlated with the entity morphology.<sup>44</sup> Baker *et al.* studied the electrocatalytic activity in the HER and OER of individual gold nanoparticles with different morphology.<sup>69</sup> Recent single-entity electrocatalysis studies are reported by Dong. *et al.* on single NiFe<sub>2</sub>O<sub>4</sub> nanocrystals<sup>70</sup> and Hill. *et al.* on gold nanorods.<sup>71</sup> For other studies on single entity electrocatalysts, see ref. 72 and 73.
- Study of the nucleation processes at the single nano-entity level. SECCM can perform electrodeposition experiments which allow study of the nucleation of individual nano-entities.<sup>74,75</sup> The nucleation of single gas bubbles in the liquid electrolyte via conduction of electrochemical gas evolution with SECCM is also reported by Chen *et al.*.<sup>76-78</sup> The mobility of individual particles over the electrode/electrolyte has also been studied via SECCM.<sup>79</sup> For other related studies, see ref. 60 and 80.
- Patterning and surface modification at the nano- and microscale.<sup>81</sup> SECCM allows electrodepositing material on patterns with micrometre resolution thanks to the small and controlled contact area of the SECCM droplet cell.<sup>82-85</sup> It is possible to generate conductive patterning, *e.g.* metals or conductive polymers, that can be further used or implemented in a device.<sup>86-88</sup>
- Studies of single nano-entities with high temporal resolution. Stochastic collision electrochemistry, also called nano-impact electrochemistry, requires high temporal resolution.<sup>89,90</sup> The tuneable size of the pipette tapered end, its aperture and the small contact area offered by the droplet cell of the SECCM probe provides an alternative platform with respect to traditional UME experiments to achieve nano-impact measurements.<sup>91-95</sup>

## 1.5 Describing and modelling electrochemical phenomena at the nanoscale

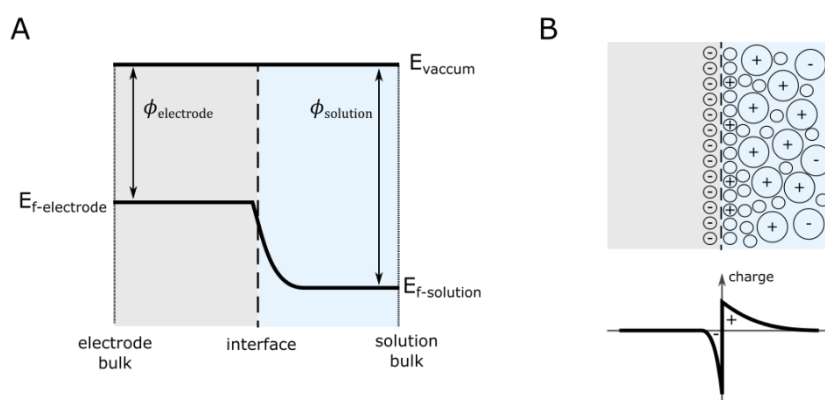
For a given electrochemical reaction  $A + e^- \rightleftharpoons B$ , Figure 1.12 shows the different steps involved in the Faradaic process, including: (i) the heterogeneous electron transfer processes that occur at the electrode surface; (ii) adsorption/desorption equilibria of species in solution, which could or might be controlled by the electrode potential; (iii) homogeneous chemical reactions near electrode surface between the diluted species ( $A'$  and  $B'$ ) and the species generated electrochemically ( $A$  and  $B$ ); (iv) mass transport of species between the near-electrode region, where there is a concentration gradient of the solvated species, and the bulk of the solution, where the concentration is constant. Each of the above equilibria steps has a defined rate constant. The current produced by the Faradaic process/reaction is often limited by the slowest of those equilibria, which is defined as the rate-determining step. Some of the above equilibria do not involve interactions with the electrode surface nor are dependent on the applied potential to the electrode. Therefore, when interpreting the electrochemical response and its relationship with the applied potential, the contribution and impact of all equilibria must be considered.<sup>1</sup> This section discusses mathematical models that can be used to understand Faradaic phenomena that present a dependence on electron transfer equilibria (Section 1.5.2) and mass transport equilibria (Section 1.5.3). Furthermore, limitations of the models and their applicability at different length scales are discussed, focussing on relevant phenomena for nanoscale electrochemistry. A brief description of non-Faradaic processes is provided in Section 1.5.1.



**Figure 1.12:** Scheme of the different equilibria involved in a Faradaic reaction with redox species in solution.

### 1.5.1 Solution – Electrode interface on non-Faradaic processes

Electrochemical systems are characterised by the presence of the electrode-electrolyte junction. Both the solution and the electrode possess their respective fermi levels, therefore upon electrode-electrolyte contact an electric field is established, as shown in Figure 1.13 A. The electric field will induce a local displacement of free charge carriers in both the electrode and solution; thus, the potential is constant in the bulk of electrode and solution once equilibrium is established after contact. Metallic electrodes generally have a large density of free charge carriers (free electrons and/or holes), and consequently, the electric field is confined to the vicinity of the electrode surface and does not extend significantly into the bulk of the electrode material. However, charge carriers in solution are ionic or polarisable species with concentrations that are typically much lower than those of free charge carriers in metals. As a result, ion accumulation/depletion occurs through a diffuse layer that extends 1-10's nm from the electrode surface to the solution phase, see Figure 1.13 B. This phenomenon, inherent in electrochemical setups, is described as the electrical double layer.<sup>1</sup>

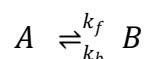


**Figure 1.13:** Potential and charge distribution at the electrode-solution interface **A)** Potential distribution showing an electric field across the interface, which is neutralised at the bulk of the solution and the electrode phases. **B)** Charge distribution at metallic electrode-solution interface showing double layer formation. Small circles with a charge sign represent the free charge carriers. The big circle with the charge sign represents hydrated charges. Circles without charge sign represent non-polarizable solvent species.

The dynamics of electrical double layers are complex.<sup>96</sup> Two key outcomes from the description of the solution-electrode interface that must be considered for describing current and potential dependencies are: first, the double-layer compensates the junction potential at the electrode interface, even if an external potential is applied, thus the bulk solution and bulk electrode potential differences are well defined and not affected by the junction. Second, the presence of the electrode-solution junction potential and the electrical double layer results in a capacitive effect at the electrode interface. Capacitive effects can generate currents in electrochemical systems and have an important impact on nanoscale electrochemistry, as explored in Chapters 3 and 6.

## 1.5.2 Electron transfer models

Faradaic currents are associated with processes that involve heterogeneous electron transfer (HET) between the solution and the electrode. HET occurs when the electron/s transition from occupied to unoccupied levels between the electrode and the electrolyte, resulting in either oxidation or reduction of species in solution. Electrochemical systems can control HET and its kinetics (rate of HET) by controlling the difference in potential between the electrode and the solution.<sup>1</sup> Electrochemical measurements can be used to extract information about HET kinetics; however, to derive kinetic parameters from electrochemical signals, a model is needed to describe the probability of observing HET and, in turn, a net current under a given set of conditions. As a first case, the example of a homogeneous equilibrium reaction might be considered, described by a general equation:



The rate of forward and backward reactions ( $v_f, v_b$  in  $\text{mols L}^{-1} \text{ s}^{-1}$ ) depend on the concentrations of A and B ( $C_A, C_B$  in  $\text{mols L}^{-1}$ ) and on rate coefficients ( $k_f, k_b$  in  $\text{s}^{-1}$ ) as follows:

$$v_f = k_f \cdot C_A \quad (\text{Eq. 1.2})$$

$$v_b = k_b \cdot C_B \quad (\text{Eq. 1.3})$$

The net rate of reaction ( $v_{net}$ ) is then:

$$v_{net} = v_f - v_b = k_f \cdot C_A - k_b \cdot C_B \quad (\text{Eq. 1.4})$$

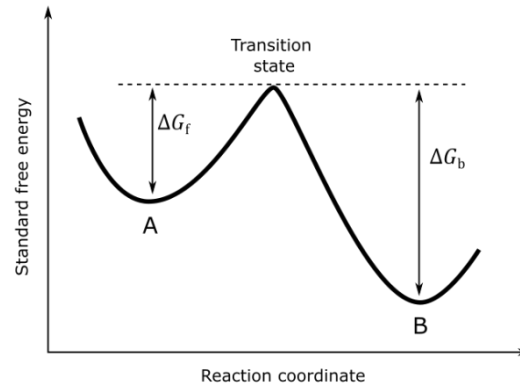
Assuming A and B present a Boltzmann distribution of states due to temperature and there is a reaction path between A and B with defined potential energy (*i.e.* the reaction coordinate) that connects A and B potential energy minima through a local maxima: describing an activation energy barrier ( $E_a$  in  $\text{J mol}^{-1}$ ), as shown in Figure 1.14, allows to express the rate constant ( $k_f$  and  $k_b$ ) by the Arrhenius equation.

$$k_i = k_i' \cdot e^{-E_a/RT} \quad (\text{Eq. 1.5})$$

where  $k'$  is the frequency factor (in  $\text{s}^{-1}$ ), R is the universal gas constant and T is temperature. The frequency factor ( $k'$ ) can be understood as the frequency at which the species attempts to cross the activation barrier.<sup>1,97</sup> The exponential term in the Arrhenius equation describes the probability of crossing the activation barrier of the reaction coordinate. The activation energy for A or B can be understood as the change in standard internal energy of species A or B to go from species potential energy minima to maxima. Then, the state of energy maxima is called the transition state.<sup>1</sup> The net reaction rate can be described in terms of the activation energy ( $\Delta G_i$ ) for the A and B species with respect to the transition state, as illustrated in Figure 1.14.

$$v_{net} = k_f' \cdot e^{-\Delta G_f/RT} \cdot C_A + k_b' \cdot e^{-\Delta G_b/RT} \cdot C_B \quad (\text{Eq. 1.6})$$





**Figure 1.14:** Representation of the A-B equilibrium along the reaction coordinates. The activation energies from A and B are defined as  $\Delta G_f$  and  $\Delta G_b$  respectively.

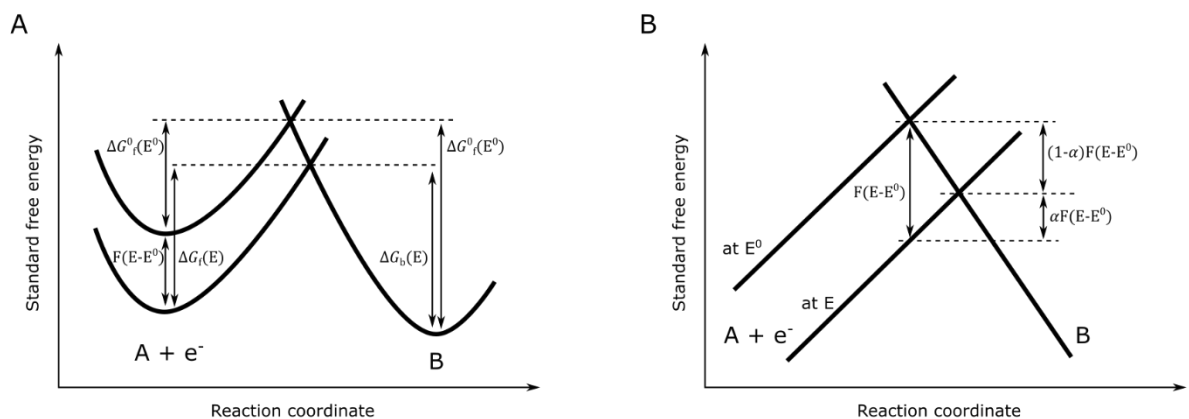
If the A-B equilibrium is achieved through an HET process with the surface of an electrode that acts as an electron source or drain, then, the net rate of reaction ( $v_{net}$ ) can be expressed as a net current ( $I_{net}$  in A):

$$I_{net} = zFA v_{net} \quad (\text{Eq. 1.7})$$

$$I_{net} = I_f - I_b = zFA (k_f \cdot C_A - k_b \cdot C_B) \quad (\text{Eq. 1.8})$$

### 1.5.2.1 Butler-Volmer formalism

Following the example given above ( $A + e^- \leftrightarrow B$ ), applying a potential to the electrode will shift the reaction coordinate, as shown in Figure 1.15. As a result, the applied potential ( $E$  in V) influences the HET and shifts the equilibrium of the A-B species.



**Figure 1.15:** Representation of the reaction coordinates of  $A + e^- \leftrightarrow B$  equilibrium upon the application of an external potential ( $E$ ). **A**) The change in reaction coordinate and activation energy by the applied potential **B**) Maximise representation of the region of A, which presents crossing of A and B reaction coordinates.

The influence of applied potential on rate constants ( $k_f, k_b$  in  $s^{-1}$ ) can be described as a function of the variation in activation energies. The Butler-Volmer formalism assumes a quadratic dependence of the Gibbs free energy with respect to the reaction coordinate. However, at the intersection point between the states of the two species involved in the equilibrium (*i.e.*, at the transition state), it is assumed that the variation of the energy profiles with the reaction coordinate is linear, as shown in Figure 1.15 B. This assumption simplifies the expressions used to describe changes in forward and backward activation energies with applied potential. Moreover, this allows us to define any activation energy  $\Delta G$  with respect to an activation energy  $\Delta G^0$ , which occurs at a given reference potential  $E_0$ .<sup>1</sup> Under these assumptions, the change in activation energy for a given applied potential  $E$  is defined as:

$$\Delta G_f(E) = \Delta G_f^0(E^0) + \alpha F(E - E^0) \quad (\text{Eq. 1.9})$$

$$\Delta G_b(E) = \Delta G_b^0(E^0) - (1 - \alpha)F(E - E^0) \quad (\text{Eq. 1.10})$$

where  $\alpha$  is the transfer coefficient.  $\alpha$  controls the influence that applied potential has over the relative changes in activation energy of the forward and backward reactions. As shown in Figure 1.15 B,  $\alpha$  describe the symmetry between the energy profile of A and B species around the transition state reaction.<sup>1</sup>

Equations 1.9 and 1.10 can be substituted into the expression for the activation energy in the Arrhenius expressions:

$$k_f = k_f' \cdot e^{-(\Delta G_f^0(E^0) + \alpha F(E - E^0))/RT} \quad (\text{Eq. 1.11})$$

$$k_b = k_b' \cdot e^{-(\Delta G_b^0(E^0) - (1 - \alpha)F(E - E^0))/RT} \quad (\text{Eq. 1.12})$$

Which can be rearranged also as:

$$k_f = k_f' \cdot e^{-(\Delta G_f^0(E^0))/RT} \cdot e^{-(\alpha F(E - E^0))/RT} \quad (\text{Eq. 1.13})$$

$$k_b = k_b' \cdot e^{-(\Delta G_b^0(E^0))/RT} \cdot e^{(1 - \alpha)F(E - E^0)/RT} \quad (\text{Eq. 1.14})$$

The terms that are independent of the applied potential can be used to define rate constants for the forward ( $k_f^0$ ) and backward ( $k_b^0$ ) reactions at  $E_0$ , yielding the following expressions:

$$k_f = k_f^0 \cdot e^{-(\alpha F(E - E^0))/RT} \quad (\text{Eq. 1.15})$$

$$k_b = k_b^0 \cdot e^{(1 - \alpha)F(E - E^0)/RT} \quad (\text{Eq. 1.16})$$

In the Butler-Volmer formalism, the reference potential,  $E^0$ , is the potential at which the reaction equilibrium results in equal concentrations of A and B species ( $C_A^0 = C_B^0$ ). Moreover, Butler-Volmer formalism also considers the case that at  $E^0$  the rates of reaction of the forward and backward steps ( $v_f^0, v_b^0$ ) are equal so that:

$$v_f^0 = v_b^0 \quad (\text{Eq. 1.17})$$

$$k_f^0 \cdot C_A^0 = k_b^0 \cdot C_B^0 \quad (\text{Eq. 1.18})$$

$$k_f^0 = k_b^0 \quad (\text{Eq. 1.19})$$

This allows us to define a *standard rate constant* ( $k^0$ ), which is interpreted as a measure of the kinetic facility/sluggishness of a reaction and indicates the speed at which equilibrium can be reached.<sup>1</sup> Thus, the forward and backward rate constants can be expressed in terms of  $k^0$ .

$$k_f = k^0 \cdot e^{-(\alpha F(E-E^0))/RT} \quad (\text{Eq. 1.20})$$

$$k_b = k^0 \cdot e^{(1-\alpha)F(E-E^0)/RT} \quad (\text{Eq. 1.21})$$

Taking into account the description of the net current given in Equation 1.8, now it is possible to describe the net current generated by the shift of the equilibrium  $A + e^- \leftrightarrow B$  in function of the applied potential:

$$I_{net} = zFA k^0 (e^{-(\alpha F(E-E^0))/RT} \cdot C_A - e^{(1-\alpha)F(E-E^0)/RT} \cdot C_B) \quad (\text{Eq. 1.22})$$

Measurements of the current at different potentials can thus be used to obtain information on A-B species and HET processes. Voltammetric electrochemical methods, such as cyclic voltammetry or potential steps, are often used to derive equilibrium kinetics. Details of voltammetric methods are provided in the Methods chapter, Section 2.1.

Assuming conditions of zero current ( $I_{net} = 0$ ) the following equalities can be derived:

$$e^{-(\alpha F(E-E^0))/RT} \cdot C_A = e^{(1-\alpha)F(E-E^0)/RT} \cdot C_B \quad (\text{Eq. 1.23})$$

$$-\frac{\alpha F(E-E^0)}{RT} + \ln(C_A) = \frac{(1-\alpha)F(E-E^0)}{RT} + \ln(C_B) \quad (\text{Eq. 1.24})$$

$$-\frac{F(E-E^0)(\alpha+(1-\alpha))}{RT} = \ln(C_B) - \ln(C_A) \quad (\text{Eq. 1.25})$$

$$\frac{F(E-E^0)}{RT} = -\ln(C_B) + \ln(C_A) \quad (\text{Eq. 1.26})$$

$$E = E^0 + \frac{RT}{F} \ln\left(\frac{C_A}{C_B}\right) \quad (\text{Eq. 1.27})$$

Equation 1.27 is the Nernst equation for one electron transfer ( $z=1$ ).

### 1.5.2.2 Limitations of the Butler-Volmer formalism in nano-electrochemistry

The Butler-Volmer (BV) kinetic model relies on a set of assumptions that often limit the potential window over which kinetic predictions are reasonable. The transition state along the reaction coordinate is defined as the point at which the potential energy profile of the reactant and the product cross; around the transition state, it is assumed that the energy dependence is linear and that a single parameter ( $\alpha$  the transfer coefficient) can describe the shape of the activation barrier. These assumptions are sensible for highly reversible and symmetric reactions (the energy profile of A and B species is similar around the transition state, thus  $\alpha \sim 0.5$ ). However, the system might approximate highly reversible and symmetric conditions only over a narrow overpotential window around equilibrium. Systems which display experimentally determined values outside the  $0.3 < \alpha < 0.7$  range suggest that they cannot be adequately described by a BV formalism. Similarly, the definition of the *standard rate constant* ( $k^0$ ) used in the current-overpotential equation (Eq. 1.22) relies on the assumption of equal reaction rates for forward and backward processes ( $v_f^0 = v_b^0$  and  $k_f^0 = k_b^0$ ) under standard conditions ( $C_A^0 = C_B^0$  and  $E = E^0$ ). The BV formalism extends the use of  $k^0$  for conditions where  $E \neq E^0$ , and at large overpotentials this assumption might effectively breakdown.

Second, the standard rate constant ( $k^0$ ) in the BV formalism integrates contributions from multiple physical quantities in a single term. The use of a single pre-exponential term limits the information that can be obtained about the HET processes that are undergoing at the electrode surface and their kinetics. Third, in the BV formalism the rate constants ( $k_f, k_b$ ) and the net current ( $I_{net}$ ) always vary exponentially with overpotential, even for very large overpotentials. As a consequence, the BV formalisms do not predict a kinetic limit with the applied potential. The application of the BV current-overpotential equation to describe the experimental observations of current-overpotential trends relies on the addition of mass transport effects to limit the current predictions. Experimental evidence shows that there is a limited increase in the rate constant with overpotential, even in the absence of mass transport limitations,<sup>98</sup> this is addressed by more sophisticated HET models that indeed predict a kinetic limit of the reaction rate constant ( $k_i$ ).<sup>99,100</sup> In practical terms, BV formalism can satisfactorily describe rate constants kinetics typically over a narrow potential windows of 10's to few 100's of mV; however, BV models remain widely used in electrochemistry. This is mainly due to the fact that for macroscale electrodes the potential range over which the current signal is not affected by mass transport is also of 10's to few 100's of mV. Therefore, the exponential dependencies of the BV current-overpotential equation can effectively model the experimental behaviour observed around the standard potentials ( $E^0$ ) on macroscale electrodes. At micro- /nano-scale electrodes, mass transport effects result in larger diffusion limited current density values (discussed in Section 1.5.3), which allows us to observe HET kinetic dependencies over larger overpotential window.<sup>101</sup>

### 1.5.2.3 Marcus-Hush formalism

The Marcus-Hush (MH) model is used to describe the kinetics of both homogenous and heterogeneous reactions. MH considers the molecular structure of the equilibrium species as well as their surrounding environment (*i.e.* the solvent).<sup>1</sup> MH formalism considers HET adiabatic processes in the absence of adsorption or strong interaction with the electrode. The electron transfer is defined to occur between two isoenergetic species without changes in nuclear configuration. The appropriate nuclear configuration must be reached to allow adiabatic electron transfer processes to occur with high probability. Thus, the species involved in the reaction have the same nuclear configuration before and after electron transfer.<sup>1</sup>

For the equilibrium reaction  $A + e^- \leftrightarrow B$ , where A and B present a quadratic change in energy *vs.* reaction coordinate, the Marcus-Hush model describes the rate constant as:

$$k_i = K_i \cdot \nu_n \cdot \kappa_{el} \cdot e^{-E_a/RT} \quad (\text{Eq. 1.28})$$

Compared to Equation 1.5, the pre-exponential factor is deconvoluted into a nuclear frequency factor ( $\nu_n$  in  $s^{-1}$ ), an electronic transmission coefficient ( $\kappa_{el}$ ) and the precursor equilibrium constant ( $K_i$ ),<sup>1,97</sup> which is described as:

$$K_i = \frac{C_i^{surface}}{C_i^{bulk}} \quad (\text{Eq. 1.29})$$

The transition state in the MH model is not described as an intersection of linear distribution of states, but considers the parabolic (quadratic) nature of the distribution. This assumption is based on the principle that nuclear oscillations can be described as simple harmonic oscillators with proportionality constant ( $k$ ).<sup>1</sup> The energy profile ( $G_i$ ) of  $i$  species along its reaction coordinate ( $q_i$ ) has parabolic dependence:

$$G_i(q_i) = G_i^o + \left(\frac{k}{2}\right) (q_i - q_i^o)^2 \quad (\text{Eq. 1.30})$$

The energy barrier ( $\Delta G_i^{ts}$ ) can be defined as a function of the energy for A ( $G_A$ ) and B ( $G_B$ ) species *vs.* their reaction coordinates ( $q_A$  and  $q_B$ ), as shown in Figure 1.16, yielding expressions:

$$\Delta G_i^{ts} = G_i(q^{st}) - G_i(q_i^o) = G_i^o + \left(\frac{k}{2}\right) (q^{st} - q_i^o)^2 - G_i^o + \left(\frac{k}{2}\right) (q_i^o - q_i^o)^2 \quad (\text{Eq. 1.31})$$

$$\Delta G_i^{ts} = \left(\frac{k}{2}\right) (q^{st} - q_i^o)^2 \quad (\text{Eq. 1.32})$$

The energy barrier  $\Delta G_i^{ts}$  can be related to the standard Gibbs free energy of the reaction ( $\Delta G_{A-B}^o$ ):

$$\Delta G_A^{ts} = \Delta G_B^{ts} + \Delta G_{A-B}^o \quad (\text{Eq. 1.33})$$

Substituting  $\Delta G_i^{ts}$  (Equation 1.32) into Equation 1.33 and assuming that both species, A and B, present identical force constants ( $k$ ),  $q^{ts}$  can be isolated:

$$q^{ts} = \frac{1}{2}(q_A^0 + q_B^0) - \frac{\Delta G_{A-B}^0}{k(q_A^0 - q_B^0)} \quad (\text{Eq. 1.34})$$

At this point, the activation energy ( $\Delta G_i^{st}$ ) can be defined without knowing the exact coordinate position of the transition state by substituting the expression of  $q^{ts}$  of Equation 1.34 into Equation 1.32. By introducing the reorganisation energy term ( $\lambda$  in eV) as:

$$\lambda = \frac{k}{2}(q_A^0 + q_B^0) \quad (\text{Eq. 1.35})$$

So, the final expression of the activation energy is:

$$\Delta G_i^{ts} = \frac{\lambda}{4} \left( 1 + \frac{\Delta G_{A-B}^0}{\lambda} \right)^2 \quad (\text{Eq. 1.36})$$

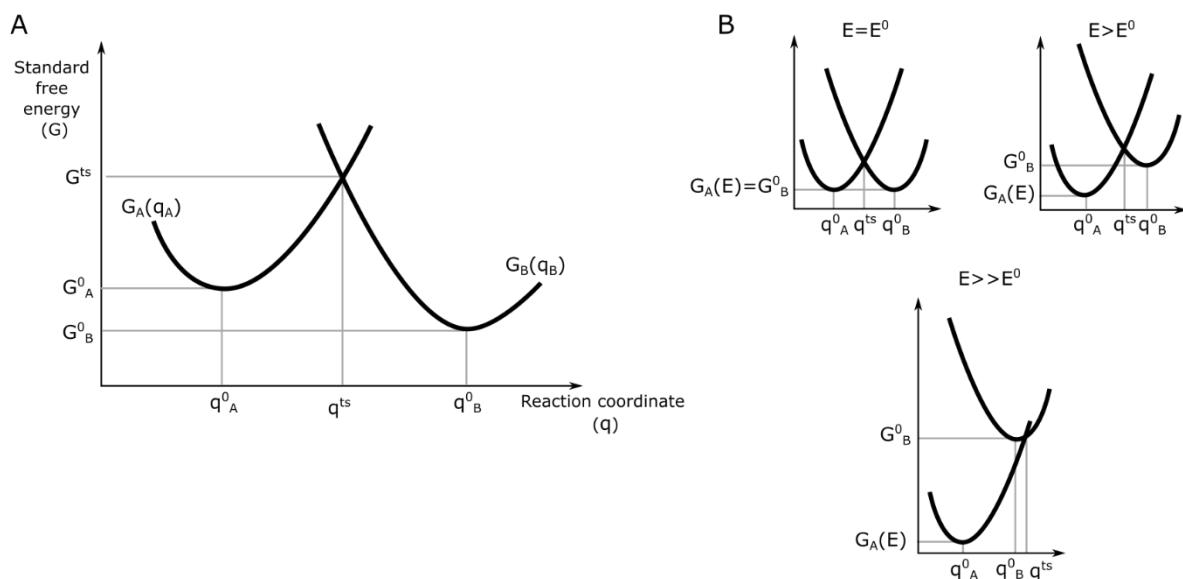
For the heterogeneous reaction  $A + e^- \leftrightarrow B$ , the standard free energy of the reaction,  $\Delta G_{A-B}^0$ , can be described as a function of the applied potential ( $E$ ) with respect to the standard potential ( $E^0$ ) of the reaction (see prior section 1.5.2.1), yielding an energy barrier expressed as:

$$\Delta G_i^{ts} = \frac{\lambda}{4} \left( 1 + \frac{F(E-E^0)}{\lambda} \right)^2 \quad (\text{Eq. 1.37})$$

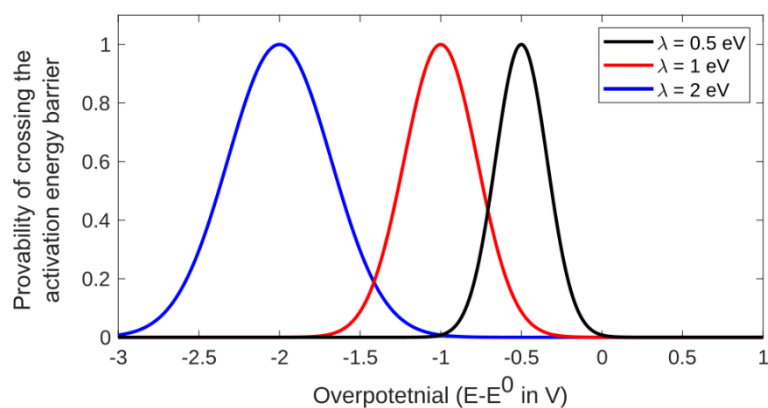
The resulting rate constant of the MH formalism (also see Equation 1.28) is therefore:

$$k_i = K_i \cdot v_n \cdot \kappa_{el} \cdot e^{-\frac{\lambda}{4} \left( 1 + \frac{F(E-E^0)}{\lambda} \right)^2 / RT} \quad (\text{Eq. 1.38})$$

The rate constant  $k_i$  in the MH formalism has pre-exponential terms ( $K_i, v_n, \kappa_{el}$ ) which do not depend on applied potential  $E$ , and an exponential term that includes a potential dependence. The exponential term of  $k_i$  vs.  $E$  trend has a Gaussian shape ranging from 0 to 1, as shown in Figure 1.17, while the magnitude of the  $k_i$  is defined by the pre-exponential terms. Notice that the rate constant increases first with exponential behaviour vs. overpotential, as predicted in the BV formalism; at larger overpotentials  $k_i$  transitions to a linear dependency and then plateaus for very large overpotentials, thus departing significantly from the BV model. As a consequence, the current-overpotential equation derived from the MH formalism saturates at high overpotentials. However, after saturation, the MH formalism predicts a current decrease, also called the inverted region, which occurs when the crossing point of energy profiles ( $q^{ts}$ ) occurs beyond the energy minima along the reaction coordinate ( $q^0$ ), as shown in Figure 1.16 B. The physical interpretation of this phenomenon is complex and the experimental evaluation of this behaviour is difficult because, at very high overpotentials, the current response is often dominated by other physical effects unrelated to HET kinetics.<sup>1</sup>



**Figure 1.16:** Standard free energy state distribution profiles across the reaction coordinates for one electron transfer equilibrium  $A + e^- \leftrightarrow B$ . **A)** Parabolic state distribution ( $G_A(q_A)$  and  $G_B(q_B)$ ), where the reaction coordinate positions with minimum standard free energy ( $q_i^0$ ) and transition state ( $q^{ts}$ ) are highlighted. **B)** State distribution for different applied potentials. The bottom figure shows that, for very large overpotentials, the intersection of parabolic distribution profiles ( $q^{ts}$ ) occurs beyond the reaction coordinate positions with minimum standard free energy ( $q_B^0$ ).



**Figure 1.17:** Representation of the probability of crossing the activation energy barrier with respect to overpotential in the MH formalism. The probability of crossing the energy barrier corresponds to the potential dependent term in the rate contact expression. Curbs plotted for different reorganisation energies, showing that for larger reorganisation energies, the probability of crossing the energy barrier decreases for the same overpotential.

Thanks to the MH formalism, the overpotential window over which the kinetics of HET can be described is increased to about 0.5 V to 1 V. The MH formalism includes additional details about the nature of the reorganisation energy ( $\lambda$ ) by articulating contributions from inner ( $\lambda_i$ ) and outer ( $\lambda_o$ ) components, which account the contributions from the nuclear configuration transformations

and from the solvent coordination transformations. Moreover, the MH formalism also accounts for additional free energy contributions, often included as work terms ( $w_i$ ).<sup>1,99</sup> Nevertheless, such details are not relevant to the interpretation and discussion of the result presented in thesis; the reader is referred to reference books in electrochemistry, such as ref. 1 and 99, for further discussion about reorganisation energy components.

#### 1.5.2.4 Gerischer formalism

The Gerischer formalism of charge transfer is based on the overlap of solution states and electrode states. The solution states ( $W_i$ ) are those of the species in solution involved in the reaction, *i.e.*, reactants and products. For the heterogeneous electron transfer equilibrium,  $A + e^- \leftrightarrow B$ , the solution states relevant to the model are  $W_A$ , of the electron acceptor, and  $W_B$  of the electron donor. Both species A and B have a Boltzmann distribution of electronic energies ( $\varepsilon$ ) according to their reorganisation energy contribution ( $\lambda$ ), as shown in the Figure 1.18. The electrode states ( $f_i$ ) are those of the free charge carriers in the solid electrode, *i.e.*, electrons and holes. Notice that the equilibrium of the A and B species can also be written as  $A \leftrightarrow B + h^+$ . The electrode charge carrier species  $f_{electrons}$  are electron donor or hole acceptor, and  $f_{holes}$  are electron acceptor or hole donor. The charge carrier species also have an electronic energy distribution ( $\varepsilon$ ) according to the density of state function of the solid electrode, as shown in the Figure 1.18. The Gerischer formalism assumes that adiabatic charge transfer between the solution and electrode states only occurs for isoenergetic donor-acceptor states.<sup>99</sup> The rate constant for the A and B species at equilibrium are  $k_f$  and  $k_b$  for the forward and backward reactions, respectively, are determined by the overall integrals:

$$k_f = k_{max-f} \cdot \int_{-\infty}^{\infty} W_A(\varepsilon) \cdot f(\varepsilon)_{electrons} \partial\varepsilon \quad (\text{Eq. 1.39})$$

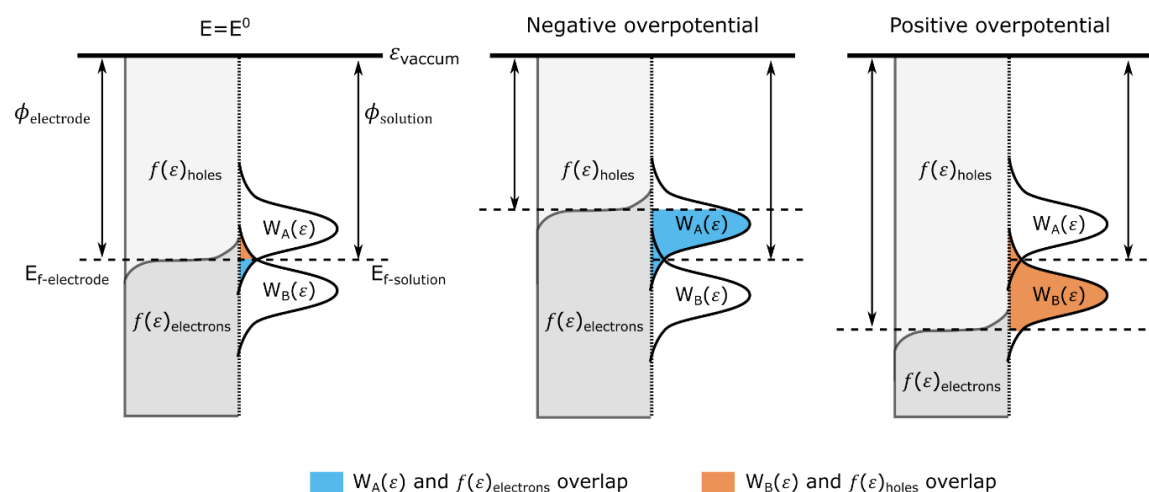
$$k_b = k_{max-b} \cdot \int_{-\infty}^{\infty} W_B(\varepsilon) \cdot f(\varepsilon)_{holes} \partial\varepsilon \quad (\text{Eq. 1.40})$$

where the pre-factor ( $k_{max}$ ) is the maximum rate of electron transfer. The prefactor can be decomposed into the nuclear frequency factor ( $\nu_n$  in  $s^{-1}$ ), electronic transmission coefficient ( $\kappa_{el}$ ) and the precursor equilibrium constant ( $K_i$ ), similar to the pre-exponential factor defined in the MH model. Details of the formulation of the electronic energy distribution of solution states ( $W_i(\varepsilon)$ ) and electrode states ( $f(\varepsilon)_i$ ) are provided in Chapter 4.

The Gerischer formalism introduces the applied potential ( $E$ ) to the electrode as a shift in the position of the fermi level of the electrode ( $E_{f-electrode}$ ). Therefore, the applied potential can directly change the overlap between states and consequently the reaction rates, as shown in the overlap function of Figure 1.18. For negative overpotentials, the  $E_{f-electrode}$  rises, leading to overlap between

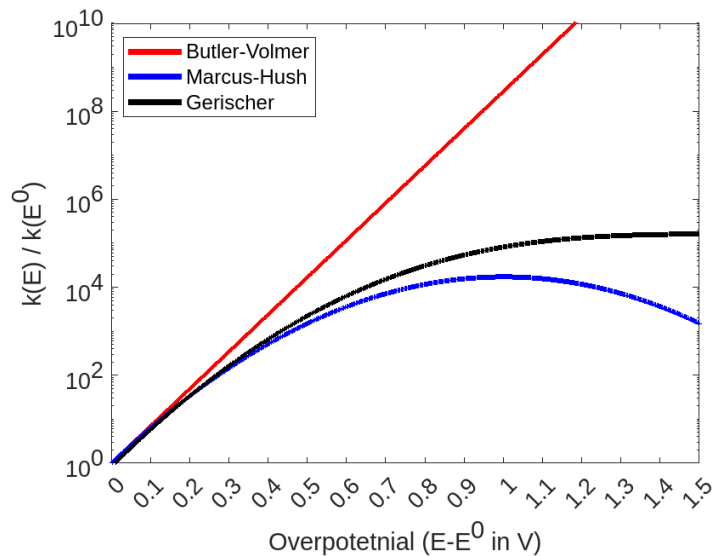


the occupied electrode states and the empty solution states ( $W_A(\varepsilon)$ ), leading to reduction of A species and formation of B species. For positive overpotentials, the overlap between the isoenergetic unoccupied electrode states and the occupied solution states ( $W_B(\varepsilon)$ ), favours the oxidation of B species into A species. At large overpotentials, either positive or negative, a complete overlap of the electrode and solution species is achieved, and from this point onwards, increasing the overpotential does not change the overlap integral. Therefore, at very large overpotential, the model predicts that the rate constant reaches a plateau.<sup>99</sup>



**Figure 1.18:** Energy ( $\varepsilon$ ) distribution of the solution ( $W_A(\varepsilon)$  and  $W_B(\varepsilon)$ ) and electrode states ( $f(\varepsilon)_{\text{electrons}}$  and  $f(\varepsilon)_{\text{holes}}$ ) for different potential applied. The resulting overlapped regions are highlighted in colour.

The evolution of the rate constant with the overpotential predicted by Butler-Volmer, Marcus Hush, and Gerischer's formalisms is summarised in Figure 1.19. Here, it can be clearly appreciated that for small overpotentials ( $\eta < 0.2$  V) the three theories predict very similar rate constants. For any potential above  $\sim 0.2$  V, the BV theory predicts much larger kinetic rates than MH or Gerischer. Between 0.2 V to 0.5 V overpotentials MH and Gerischer's formalism predict similar rate constants, but for large overpotentials ( $\eta > 0.5$  V) MH theory predicts slightly smaller rate constants than Gerischer's formalism. For very large overpotentials ( $\eta > 1$  V) the MH rate constant enters an inversion region while Gerischer predicts a plateau in the rate constant. The inverted regions should not occur in electron transfer reactions at metallic electrodes; therefore, Gerischer's formalism overcomes the problems of rate inversion and allows to describe HET kinetics for potentials far from equilibrium values. These conditions are relevant in semiconductor electrochemistry, as well as, for metallic electrodes that present a non-metallic bound layer on their surface.<sup>99,101</sup>



**Figure 1.19:** Normalised rate constants prediction respect overpotential applied for Butler-Volmer, Marcus-Hush and Gerischer formalism. The rate constants are normalised by rate constant at standard potential ( $E^0$ ) isolate overpotential dependencies and avoid pre-exponential factor contribution. Reorganisation energy ( $\lambda$ ) use of 1 eV.

### 1.5.2.5 Electron transfer kinetics in nanoscale electrochemistry

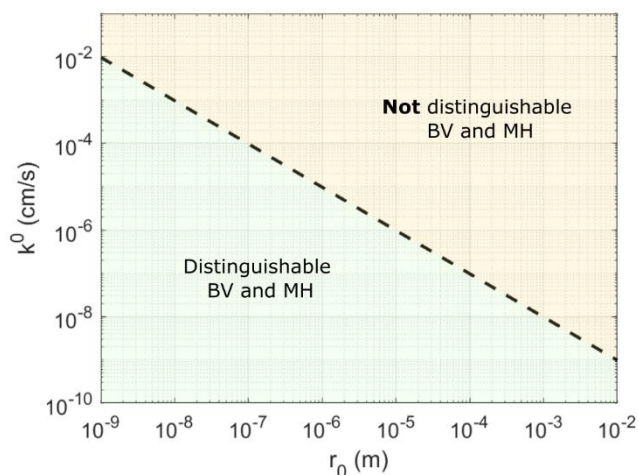
It is very common in the literature to use the BV formalism to derive kinetic rates.<sup>101</sup> As mentioned in Section 1.3.1 and expanded in the following Section 1.5.3, the mass transport on macroscale electrodes is expected to dominate the current-overpotential response even for small overpotentials. On macroscale electrodes, the region from which kinetic information can be extracted is very close to the standard potential, and therefore the BV formalism is an adequate model (see Figure 1.19). At nanoscale electrodes, mass transport rates are fast, allowing kinetics to dominate over a much larger overpotential window. However, it is not always clear under what conditions the MH or Gerischer formalisms might more accurately describe an experimental system (*i.e.* under which conditions reorganisation energy plays an important role). Based on mass transport considerations, Feldberg approximated the set of conditions under which it is adequate to use the BV formalism, and the conditions when it is better to implement a formalism which considers the effect of reorganisation energy (MH or Gerischer).<sup>101</sup> Feldberg proposed the relation:

$$\frac{k^0 r_0}{D_i} \leq 10 \left( \frac{1 - \frac{\lambda_i}{K_B T}}{10} \right) \quad (\text{Eq. 1.41})$$

where  $k^0$  is the standard rate constant as derived from Butler-Volmer formalism,  $r_0$  is the radius of the electrode,  $D_i$  is the diffusion coefficient and  $\lambda_i$  is the reorganisation energy of any given  $i$  species. If the left term is smaller than the right term, then mass transport effects allow reorganisation energy effects to be observed. The relation between  $k^0$  and  $r_0$  defined in

Equation 1.41 is represented in Figure 1.20, for a given  $D_i$  and  $\lambda_i$ . Figure 1.20 shows that for slower kinetics (smaller  $k^0$ ) and smaller radius electrodes, it is often better to describe the electrochemical kinetics using the MH or Gerischer's formalisms. On the other hand, for macroscale electrodes ( $> \text{mm}^2$ ) the BV formalism is indistinguishable from the MH or Gerischer formalism, unless the reaction kinetics are extremely sluggish. For such reasons in SEPM techniques, which probe size is typically in the  $\mu\text{m}$  range, the  $k^0/r_0$  ratio often is at the boundary of BV and MH/Gerischer representations.<sup>101</sup>

Notice, the  $k^0$  values shown in Figure 1.20 do not represent the pre-exponential factors of the reaction kinetics as derived from the MH formalism, but are the pre-exponential factors that will be obtained if fitting the current-overpotential response with the BV formalism. If BV is not adequate for fitting a given current-overpotential response (even if indistinguishable from MH implementation), the pre-exponential factor derived will not be representative of the kinetics of the system. Notice that because BV formalism predicts an indefinite exponential increase of current with overpotential, fitting current responses over large overpotential windows demands the use of very small pre-exponential factors to compensate.



**Figure 1.20:** Example of distinguishable BV and MH domains based on parameters of a well-known redox couple such as Ruthenium Hexamine, using diffusion coefficient ( $8 \cdot 10^{-6} \text{ cm}^2\text{s}^{-1}$ ),<sup>102</sup> and for  $[\text{Ru}(\text{NH}_3)_6]^{3+/2+}$  of 1 eV.<sup>103-105</sup>

### 1.5.3 Mass transport processes

As previously described, understanding mass transport is critical for interpreting electrochemical data. Three different types of mass transport are typically present in electrochemical systems: diffusion, migration, and convection. The general expression that defines the flux of species in electrochemical systems is described by the Nernst-Planck equation:

$$J_i = -D_i \nabla c_i - \frac{n_i F}{RT} D_i c_i \nabla \phi + c_i v \quad (\text{Eq. 1.42})$$

where  $J_i$  is the flux of the  $i$  diluted species,  $D_i$  is  $i$  diluted species diffusion coefficient,  $c_i$  is  $i$  diluted species concentration,  $n_i$  is  $i$  diluted species effective charge,  $v$  is the convection flux. The term  $D_i \nabla c_i$  refers to diffusive mass transport,  $\frac{z_i F}{RT} D_i c_i \nabla \phi$  refers to migration mass transport and term  $c_i v$  refers to the convective mass transport.<sup>1</sup>

Migration transport is associated with the displacement of charged or polarisable species in the presence of an electric field. Migrative transport demands the presence of an electric field, which in electrochemical systems originates between the electrode and electrolyte.<sup>1</sup> Upon the placement of an electrode, which has a defined work function, into an electrolyte solution, which also has a defined work function, an electric field originates due to the differences in the work function. The electrode work function can also be varied by the applied potential, which can lead to variation in the electric field between the electrode and solution. The electrolyte solution employed in an electrochemical system often contained diluted charged or polarisable species that are displaced by the electric fields, resulting in the accumulation or depletion of electrolyte charge in the region near the electrode surface. If the electrolyte contains excess charged or polarisable species, the concentration gradient in the near-electrode region generates an electric field that compensates for the difference between the work functions of the electrode and the solution; this effect is called the double layer (see Section 1.5.1). As a result, the net electric field in the bulk of the electrolyte solution is close to zero and the further migration effects of electrolyte species become negligible. The use of an excess of charged or polarisable species, called supporting electrolyte, is a common practise adopted in electrochemical measurements to avoid strong migration currents.<sup>1</sup> However, if the migration effects on the electrochemical systems are not negligible (often because of poor electrolyte conductivity), the migration current can often be expressed by linear mass-transfer system as:

$$I_{\text{migration}-i} = L \nabla \phi \quad (\text{Eq. 1.43})$$

where  $L$  is the solution electric conductivity (in  $\Omega^{-1} \text{m}^{-1}$ ) which is expressed in function of system cross-section area,  $A$  (in  $\text{m}^2$ ) as:

$$L = A \sum_i \frac{|n_i|^2 F^2 D_i}{RT} c_i \quad (\text{Eq. 1.44})$$

The experiments performed in this thesis are designed to avoid migration effects via the usage of a supporting electrolyte, and therefore migration effects are not discussed further.

Convective transport originates from the motion of the electrolyte solvent as a fluid, which causes displacement of diluted or dispersed species in the solvent. Convection effects can be forced or natural. Natural convection refers to the flow of the solution as a result of a local change in the densities of the solvent. For instance, in an electrochemical system natural convection can originate due to the electrochemical phenomena inducing a heat transfer process and varying the electrolyte density near the electrode surface.<sup>106</sup> Force convection refers to intentional mechanical stirring or agitation for creating fluid motion or flow. Hydrodynamic electrochemical methods use force convection to control the flow of species toward the electrode surface, overcoming possible uncontrolled natural convection effects.<sup>106</sup> For instance, the rotating disk electrode methods, use the electrode movement to force convection which ensure steady-state conditions during electrochemical observations.<sup>1,106</sup> In this thesis, no force convection method has been implemented and so, will not be further discussed. Natural convection in microscale electrochemical systems is complex and very dependent on geometry.<sup>107</sup>

For the SECCM experimental setups, as the main nano-electrochemical method used in this thesis, it is expected that the evaporation of the electrolyte solvent (water) from the droplet cell potentially induces thermal inhomogeneities across the SECCM probe. On the other hand, the reduced micro-nanoscale size of the droplet cell ensures fast heat dissipation, which minimises local natural convection effects. Because of the fast heat dissipation offered by microscale electrochemical systems, natural convection flows are often considered negligible. As far as knowledge of the author goes, there are no studies reporting or analysing the convection effects on the SECCM probe. Therefore, it is not straightforward to consider whether the contributions of thermal inhomogeneities originate a negligible or a non-negligible convective flow. In this thesis, precautions have been taken to minimise natural convection effects, such as ensuring that the different elements of the SECCM equipment and probe are at steady room temperature before measurement; minimising the length of electrochemical measurement;<sup>107</sup> and minimising the time the droplet cell is formed. Accounting these precautions measures are taken, the natural convection effects are considered negligible and are not further discussed in this thesis. Yet, the author considers that the development of a convection model for the SECCM probe, which allows to derive quantitative estimation of convective flow, would be an interesting topic for further research.

Diffusive mass transport originates from Brownian movement of species dissolved or dispersed in liquid or gas phase; thus, diffusive transport is intrinsic in electrochemical systems with liquid electrolytes.<sup>1</sup> As a consequence, most nano-electrochemical systems rely on diffusive mass transport to carry solution species towards/away from the electrode surface. In electrochemical systems, diffusive transport can be described according to Fick's second law:

$$\frac{\partial c_i}{\partial t} = D_i \nabla^2 c_i \quad (\text{Eq. 1.45})$$

where  $c_i$  and  $D_i$  is the concentration and diffusion of  $i$  species,  $t$  is time, and  $\nabla^2$  is the Laplacian operator. The Laplacian operator in Cartesian coordinates ( $x, y, z$ ) has the form:

$$\nabla^2 = \frac{\partial^2}{\partial x^2} + \frac{\partial^2}{\partial y^2} + \frac{\partial^2}{\partial z^2} \quad (\text{Eq. 1.46})$$

The Laplacian operator can take other forms depending on the coordinate reference system used (*e.g.* Cartesian, spherical, cylindrical, etc.) and the system dimensionality (1D, 2D, 3D). Disk-shaped ultra-microelectrodes ( $< 25 \mu\text{m}$  diameter) present a hemispherical diffusion front, as shown in Figure 1.21 B. The diffusion front can be understood as the concentration gradient that gives origin to the flux of species via diffusion. The symmetry of hemispherical diffusion processes allows to simplify the Laplacian operator to a 2D axisymmetric model as follows:

$$\nabla^2_{\text{hemispherical}} = \frac{\partial^2}{\partial r^2} + \frac{1}{r} \cdot \frac{\partial}{\partial r} + \frac{\partial^2}{\partial z^2} \quad (\text{Eq. 1.47})$$

where  $r$  is the radial distance and  $z$  is the normal distance. The number of variables in Equation 1.47 are reduced compared to Equation 1.46 and so, operating with the Laplacian becomes easier. On the other hand, bulk macroscale electrodes present a linear diffusion front, as shown in Figure 1.21 C. Note that the linear diffusion front of macroscale electrodes is equivalent to merging the hemispherical diffusion fronts of close packed smaller electrode, as also shown in Figure 1.21 C. Then, for macroscale electrodes, the Laplacian operator can be simplified to its linear form:

$$\nabla^2_{\text{linear}} = \frac{\partial^2}{\partial z^2} \quad (\text{Eq. 1.48})$$

To resolve diffusion processes in electrochemical systems, it is also necessary to impose a set of initial conditions that account for the initial state and boundary conditions. Boundary conditions relate concentration and concentration gradient to the system geometry; more details are provided in the Methods chapter, Section 2.4. Resolving the Laplacian operator differential equations on highly symmetrical systems with simple boundary and initial conditions might lead to analytical expressions.<sup>1</sup> For instance, a linear diffusion model for which the differential equation is:

$$\frac{\partial c_i(z,t)}{\partial t} = D_i \frac{\partial^2}{\partial z^2} c_i(z,t) \quad (\text{Eq. 1.49})$$

with only one diffusive  $i$  species, homogeneous initial condition (at time zero,  $\mathbf{c}_i = c_i^0$  for any possible  $\mathbf{z}$ ) and considering all  $i$  species that contact the electrode get consumed with one electron transferred ( $\mathbf{c}_i = \mathbf{0}$  at  $\mathbf{z} = 0$ , also see Figure 1.21 C) leads to the current-time response (Cottrell equation) and concentration profile analytical equations:

$$I(t) = nFAc_i^0 \sqrt{\frac{D_i}{\pi t}} \quad (\text{Eq. 1.50})$$

$$c_i(z, t) = c_i^0 \operatorname{erf} \left[ \frac{z}{2\sqrt{D_i t}} \right] \quad (\text{Eq. 1.51})$$

The Cottrell equation is very important for electrochemistry, as it predicts the current dependency with the square root of time which is easily observed in many electrochemical systems using a potential step (as described in the Methods chapter, Section 2.1). The linear diffusion model has, however, its limitations; the equation predicts that the diffusion front distance from the electrode increases indefinitely over time but clearly, a diffusion front much larger than the electrode size must become hemispherical rather than remain linear.<sup>1</sup> Consequently, the prediction of Cottrell equation that  $I(t \rightarrow \infty) = 0$  is never observed, and a certain diffusion limited current is reached after a given  $\Delta t$ . The analytical solutions of diffusion equations are then limited to geometry approximations and boundary conditions implemented; yet, they represent a valuable resource for the electrochemistry community because they have proven to provide reliable predictions over a wide range of electrochemical systems and conditions.

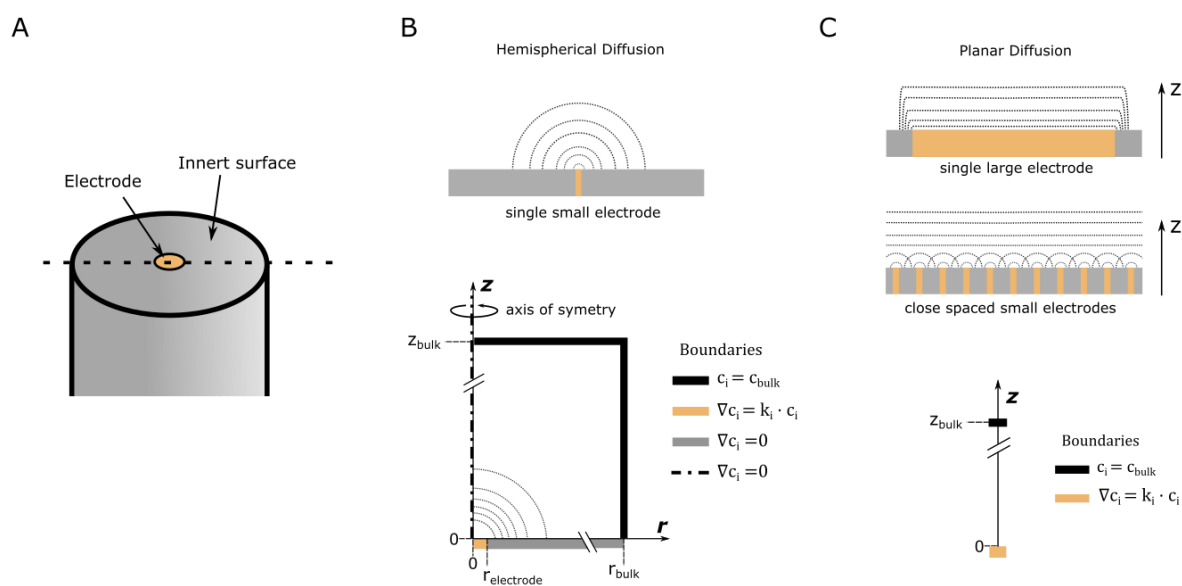
Other useful analytical expressions can be derived from the differential equations for microscale electrodes. Using the axisymmetric model of hemispherical diffusion (Eq. 1.47) and the boundary conditions described in Figure 1.21 B, it can be found that  $I(t \rightarrow \infty) \neq 0$ . At  $t \rightarrow \infty$  UMEs reach a steady state behaviour with constant current, or diffusion limited current ( $I_{diff.limited}$ ) which has the expression:

$$I_{diff.limited} = 4zFD_i c_{i-bulk} r \quad (\text{Eq. 1.52})$$

where  $r$  is the radius of the UME. Observation of a steady diffusion limited current is common for nano-electrochemical methods, including pipette-based techniques such as SECCM. However, the more complex geometry characteristic of SEPM techniques, as for instance for the SECCM probe, very often does not allow to obtain analytical expressions for diffusive transport.

For complex geometries or complex boundaries, resolving differential equations into an analytical expression is not a simple task, if even achievable. Complex geometries do not allow the reduction of the Laplacian operator into lower-dimensional forms. Moreover, common potentiometric methods (described in Methods chapter, Section 2.1) can introduce complex boundaries with additional dependencies. For instance, electrode/solution interface boundary during a cyclic voltammetry experiment describes the local changes in concentration depending on the kinetic rate ( $k_i$ ), which depend on the potential applied ( $E$ ) which vary over time according to scan-rate. Therefore, deriving analytical expression in complex systems is not always possible, or demands use of assumptions or simplifications which are system dependent, have limited range of applicability and that might turn unreliable across different length-scales. Instead, the prediction of diffusive transport on complex systems is often resolved by numerical methods.

The nano-electrochemical systems come into a variety of possible geometries, present geometric configuration in the micro-nanometre scale, and are not necessarily suitable for high-spatial symmetries modelling. Therefore, the nano-electrochemical system has complex diffusion processes, and the modelling of diffusion processes becomes easier by adopting numerical rather than analytical methods. Nowadays the computational power of modern PCs and the availability of dedicated software significantly facilitate the calculation tasks characteristic of numerical methods and can provide diffusion predictions on complex geometries in minutes. In Methods chapter Section 2.4, a description is provided of the Finite Element Simulation models implemented in this thesis for resolving mass transport for the SECCM probe.



**Figure 1.21:** Diffusive mass transport on different geometries. **A)** Schematic of a disk electrode showing the electrochemically active area in gold colour and the electrochemically inner surface in grey colour. **B)** At the top, schematic of the diffusion front towards a single small electrode showing a hemispherical shape. At the bottom, two-dimensional axisymmetric model of diffusion showing the boundary conditions and system geometry. **C)** Diagram of the diffusion front toward a single large electrode and toward the tightly packed small electrode, both showing a planar shape. At the bottom, a one-dimensional linear model of diffusion showing the boundary conditions and system geometry.



## 1.6 Aims of thesis

The transition to renewable energy sources requires crucial technologies for converting and storing energy, facilitating energy management and integration across society and industry. Several 2D materials have been successfully investigated to improve the performance and efficiency of energy storage/conversion devices, as well as to allow the development of new technologies. However, the nanoscale nature of 2D materials and their characteristic heterogeneity hinder an in-depth understanding of their electrochemical properties when characterised using conventional electrochemical methods. In particular, a better understanding is needed of how nanoscale behaviour translates into the macroscale electrochemical response. Advanced method development is needed to resolve those obstacles and obtain a much deeper understanding of nano-electrochemical systems.

The aim of this thesis is to use nano-electrochemical methods, primarily SECCM, for the study of 2D materials which are relevant for energy storage and conversion. This thesis also aims to contribute to the development of instrumentation and methods for nano-electrochemical characterisation. The work of this thesis includes:

- The development of high temporal resolution electrochemical instrumentation and methodology for single nano-entity electrochemistry, explored in Chapter 3.
- Characterisation of the electrochemical response 2D TMDCs. Exploring the electron transfer processes on different numbers of stacked layers, as detailed in Chapter 4.
- The development of methods for the detection of nanoscale defects on 2D materials via SECCM, as reported in Chapter 5.
- The isolation of the electrochemical response on of the building blocks of 2D MXene pseudocapactive electrodes, *i.e.* single MXene flakes, is explored in Chapter 6.

The investigation conducted in this thesis has contributed through the development of new methods to characterise 2D materials, as well as to identify the key aspects of 2D material electrochemical characterisation. This thesis also highlights the relevance of using advanced electrochemical methods to overcome challenges in nanomaterial characterisation. The results of this research have been communicated to the scientific community through four peer-review articles in well-recognised journals and through international conference presentations.

## References

- 1 Bard, A. J. & Faulkner, L. R. *Electrochemical methods: fundamentals and applications*. 2nd edn, (John Wiley & Sons, Inc., 2001).
- 2 Badwal, S. P., Giddey, S. S., Munnings, C., Bhatt, A. I. & Hollenkamp, A. F. Emerging electrochemical energy conversion and storage technologies. *Front. Chem.* **2**, 79 (2014). <https://doi.org/10.3389/fchem.2014.00079>
- 3 Gogotsi, Y. & Penner, R. M. Energy Storage in Nanomaterials - Capacitive, Pseudocapacitive, or Battery-like? *ACS Nano* **12**, 2081-2083 (2018). <https://doi.org/10.1021/acsnano.8b01914>
- 4 Pomerantseva, E., Bonaccorso, F., Feng, X., Cui, Y. & Gogotsi, Y. Energy storage: The future enabled by nanomaterials. *Science* **366** (2019). <https://doi.org/10.1126/science.aan8285>
- 5 Bard, A. J. Inner-sphere heterogeneous electrode reactions. Electrocatalysis and photocatalysis: the challenge. *J. Am. Chem. Soc.* **132**, 7559-7567 (2010). <https://doi.org/10.1021/ja101578m>
- 6 Parasuraman, A., Lim, T. M., Menictas, C. & Skyllas-Kazacos, M. Review of material research and development for vanadium redox flow battery applications. *Electrochim. Acta* **101**, 27-40 (2013). <https://doi.org/10.1016/j.electacta.2012.09.067>
- 7 Lv, Y. R. *et al.* Recent advances in metals and metal oxides as catalysts for vanadium redox flow battery: Properties, structures, and perspectives. *J. Mater. Sci. Technol.* **75**, 96-109 (2021). <https://doi.org/10.1016/j.jmst.2020.09.042>
- 8 Tang, C., Zheng, Y., Jaroniec, M. & Qiao, S. Z. Electrocatalytic Refinery for Sustainable Production of Fuels and Chemicals. *Angew. Chem. Int. Ed. Engl.* **60**, 19572-19590 (2021). <https://doi.org/10.1002/anie.202101522>
- 9 Peng, Y. *et al.* Recent Advances Regarding Precious Metal-Based Electrocatalysts for Acidic Water Splitting. *Nanomaterials* **12**, 2618 (2022). <https://doi.org/10.3390/nano12152618>
- 10 Liu, J. *et al.* Advanced Energy Storage Devices: Basic Principles, Analytical Methods, and Rational Materials Design. *Adv. Sci.* **5**, 1700322 (2018). <https://doi.org/10.1002/advs.201700322>
- 11 Sun, H. *et al.* Hierarchical 3D electrodes for electrochemical energy storage. *Nat. Rev. Mater.* **4**, 45-60 (2018). <https://doi.org/10.1038/s41578-018-0069-9>
- 12 Abraham, K. M. Prospects and Limits of Energy Storage in Batteries. *J. Phys. Chem. Lett.* **6**, 830-844 (2015). <https://doi.org/10.1021/jz5026273>
- 13 Lukatskaya, M. R., Dunn, B. & Gogotsi, Y. Multidimensional materials and device architectures for future hybrid energy storage. *Nat. Commun.* **7**, 12647 (2016). <https://doi.org/10.1038/ncomms12647>
- 14 Lavacchi, A., Miller, H. & Vizza, F. *Nanotechnology in Electrocatalysis for Energy*. (New York: Springer, 2013).
- 15 Raza, W. *et al.* Recent advancements in supercapacitor technology. *Nano Energy* **52**, 441-473 (2018). <https://doi.org/10.1016/j.nanoen.2018.08.013>

- 16 Fleischmann, S. *et al.* Pseudocapacitance: From Fundamental Understanding to High Power Energy Storage Materials. *Chem. Rev.* **120**, 6738-6782 (2020). <https://doi.org/10.1021/acs.chemrev.0c00170>
- 17 Baker, L. A. Perspective and Prospectus on Single-Entity Electrochemistry. *J. Am. Chem. Soc.* **140**, 15549-15559 (2018). <https://doi.org/10.1021/jacs.8b09747>
- 18 Long, J. W., Dunn, B., Rolison, D. R. & White, H. S. Three-dimensional battery architectures. *Chem. Rev.* **104**, 4463-4492 (2004). <https://doi.org/10.1021/cr0207401>
- 19 Banda, H. *et al.* Sparsely Pillared Graphene Materials for High-Performance Supercapacitors: Improving Ion Transport and Storage Capacity. *ACS Nano* **13**, 1443-1453 (2019). <https://doi.org/10.1021/acsnano.8b07102>
- 20 Zhang, D., Bertei, A., Tariq, F., Brandon, N. & Cai, Q. Progress in 3D electrode microstructure modelling for fuel cells and batteries: transport and electrochemical performance. *Prog. Energy* **1** (2019). <https://doi.org/10.1088/2516-1083/ab38c7>
- 21 Grazioli, D., Magri, M. & Salvadori, A. Computational modeling of Li-ion batteries. *Comput. Mech.* **58**, 889-909 (2016). <https://doi.org/10.1007/s00466-016-1325-8>
- 22 McKelvey, K., Cabre, M. B. & Paiva, A. E. Continuum simulations for microscale 3D batteries. *Curr. Opin. Electrochem.* **21**, 76-83 (2020). <https://doi.org/10.1016/j.coelec.2020.01.008>
- 23 Du, X., Skachko, I., Barker, A. & Andrei, E. Y. Approaching ballistic transport in suspended graphene. *Nat. Nanotechnol.* **3**, 491-495 (2008). <https://doi.org/10.1038/nnano.2008.199>
- 24 Zhu, S. J. *et al.* Photoluminescence mechanism in graphene quantum dots: Quantum confinement effect and surface/edge state. *Nano Today* **13**, 10-14 (2017). <https://doi.org/10.1016/j.nantod.2016.12.006>
- 25 Seh, Z. W. *et al.* Combining theory and experiment in electrocatalysis: Insights into materials design. *Science* **355** (2017). <https://doi.org/10.1126/science.aad4998>
- 26 Arvidsson, R. & Sanden, B. A. Carbon nanomaterials as potential substitutes for scarce metals. *J. Cleaner Prod.* **156**, 253-261 (2017). <https://doi.org/10.1016/j.jclepro.2017.04.048>
- 27 de Boer, M. A. & Lammertsma, K. Scarcity of rare earth elements. *ChemSusChem* **6**, 2045-2055 (2013). <https://doi.org/10.1002/cssc.201200794>
- 28 Zeradjanin, A. R., Grote, J. P., Polymeros, G. & Mayrhofer, K. J. J. A Critical Review on Hydrogen Evolution Electrocatalysis: Re-exploring the Volcano-relationship. *Electroanalysis* **28**, 2256-2269 (2016). <https://doi.org/10.1002/elan.201600270>
- 29 Hansen, J. N. *et al.* Is There Anything Better than Pt for HER? *ACS Energy Lett.* **6**, 1175-1180 (2021). <https://doi.org/10.1021/acsenerylett.1c00246>
- 30 Zhou, W. J. *et al.* Recent developments of carbon-based electrocatalysts for hydrogen evolution reaction. *Nano Energy* **28**, 29-43 (2016). <https://doi.org/10.1016/j.nanoen.2016.08.027>
- 31 Wang, J. *et al.* Carbon-based electrocatalysts for sustainable energy applications. *Prog. Mater. Sci.* **116** (2021). <https://doi.org/https://doi.org/10.1016/j.pmatsci.2020.100717>

- 32 Zhang, J., Xia, Z. & Dai, L. Carbon-based electrocatalysts for advanced energy conversion and storage. *Sci. Adv.* **1**, e1500564 (2015). <https://doi.org/10.1126/sciadv.1500564>
- 33 Mondal, A. & Vomiero, A. 2D Transition Metal Dichalcogenides-Based Electrocatalysts for Hydrogen Evolution Reaction. *Adv. Funct. Mater.* **32** (2022). <https://doi.org/10.1002/adfm.202208994>
- 34 Zhang, Y. Q. *et al.* Defect Chemistry on Electrode Materials for Electrochemical Energy Storage and Conversion. *Chemnanomat* **6**, 1589-1600 (2020). <https://doi.org/10.1002/cnma.202000437>
- 35 Iqbal, S., Khatoon, H., Hussain Pandit, A. & Ahmad, S. Recent development of carbon based materials for energy storage devices. *Mater. Sci. Energy Technol.* **2**, 417-428 (2019). <https://doi.org/10.1016/j.mset.2019.04.006>
- 36 Tao, H. C. *et al.* Two-dimensional materials for energy conversion and storage. *Prog. Mater. Sci.* **111** (2020). <https://doi.org/10.1016/j.pmatsci.2020.100637>
- 37 Chia, X. Y. & Pumera, M. Characteristics and performance of two-dimensional materials for electrocatalysis. *Nat. Catal.* **1**, 909-921 (2018). <https://doi.org/10.1038/s41929-018-0181-7>
- 38 Sun, T. *et al.* Defect chemistry in 2D materials for electrocatalysis. *Mater. Today Energy* **12**, 215-238 (2019). <https://doi.org/10.1016/j.mtener.2019.01.004>
- 39 Wang, Y., Shan, X. & Tao, N. Emerging tools for studying single entity electrochemistry. *Faraday Discuss.* **193**, 9-39 (2016). <https://doi.org/10.1039/c6fd00180g>
- 40 Robinson, D. A., Edwards, M. A., Ren, H. & White, H. S. Effects of Instrumental Filters on Electrochemical Measurement of Single-Nanoparticle Collision Dynamics. *Chemelectrochem* **5**, 3059-3067 (2018). <https://doi.org/10.1002/celc.201800696>
- 41 Ryu, C. H., Lee, H., Lee, H. & Ren, H. Learning from the Heterogeneity at Electrochemical Interfaces. *J. Phys. Chem. Lett.* **13**, 7838-7846 (2022). <https://doi.org/10.1021/acs.jpcllett.2c02009>
- 42 Shao, H. *et al.* Unraveling the Charge Storage Mechanism of Ti<sub>3</sub>C<sub>2</sub>TX MXene Electrode in Acidic Electrolyte. *ACS Energy Lett.* **5**, 2873-2880 (2020). <https://doi.org/10.1021/acseenergylett.0c01290>
- 43 Molina, N. Y., Pungsrissai, T., O'Dell, Z. J., Paranzino, B. & Willets, K. A. The Hidden Role of the Supporting Electrode for Creating Heterogeneity in Single Entity Electrochemistry. *Chemelectrochem* **9** (2022). <https://doi.org/10.1002/celc.202200245>
- 44 Wahab, O. J., Kang, M. & Unwin, P. R. Scanning electrochemical cell microscopy: A natural technique for single entity electrochemistry. *Curr. Opin. Electrochem.* **22**, 120-128 (2020). <https://doi.org/10.1016/j.coelec.2020.04.018>
- 45 Ren, H. & Edwards, M. A. Stochasticity in Single-Entity Electrochemistry. *Curr. Opin. Electrochem.* **25** (2021). <https://doi.org/10.1016/j.coelec.2020.08.014>
- 46 Loos, J. The art of SPM: Scanning probe microscopy in materials science. *Adv. Mater.* **17**, 1821-1833 (2005). <https://doi.org/10.1002/adma.200500701>
- 47 Isaacs, H. S. & Kissel, G. Surface Preparation and Pit Propagation in Stainless-Steels. *J. Electrochem. Soc.* **119**, 1628-& (1972). <https://doi.org/10.1149/1.2404061>

- 48 Engstrom, R. C., Weber, M., Wunder, D. J., Burgess, R. & Winkquist, S. Measurements within the diffusion layer using a microelectrode probe. *Anal. Chem.* **58**, 844-848 (2002). <https://doi.org/10.1021/ac00295a044>
- 49 Sun, P., Laforge, F. O. & Mirkin, M. V. Scanning electrochemical microscopy in the 21st century. *Phys. Chem. Chem. Phys.* **9**, 802-823 (2007). <https://doi.org/10.1039/b612259k>
- 50 Takahashi, Y., Kumatani, A., Shiku, H. & Matsue, T. Scanning Probe Microscopy for Nanoscale Electrochemical Imaging. *Anal. Chem.* **89**, 342-357 (2017). <https://doi.org/10.1021/acs.analchem.6b04355>
- 51 McKelvey, K., German, S. R., Zhang, Y. L., White, H. S. & Edwards, M. A. Nanopipettes as a tool for single nanoparticle electrochemistry. *Curr. Opin. Electrochem.* **6**, 4-9 (2017). <https://doi.org/10.1016/j.coelec.2017.06.006>
- 52 Korchev, Y. E. *et al.* Specialized scanning ion-conductance microscope for imaging of living cells. *J. Microsc.* **188**, 17-23 (1997). <https://doi.org/10.1046/j.1365-2818.1997.2430801.x>
- 53 Ebejer, N., Schnippering, M., Colburn, A. W., Edwards, M. A. & Unwin, P. R. Localized high resolution electrochemistry and multifunctional imaging: scanning electrochemical cell microscopy. *Anal. Chem.* **82**, 9141-9145 (2010). <https://doi.org/10.1021/ac102191u>
- 54 Ebejer, N. *et al.* Scanning electrochemical cell microscopy: a versatile technique for nanoscale electrochemistry and functional imaging. *Annu. Rev. Anal. Chem.* **6**, 329-351 (2013). <https://doi.org/10.1146/annurev-anchem-062012-092650>
- 55 Snowden, M. E. *et al.* Scanning electrochemical cell microscopy: theory and experiment for quantitative high resolution spatially-resolved voltammetry and simultaneous ion-conductance measurements. *Anal. Chem.* **84**, 2483-2491 (2012). <https://doi.org/10.1021/ac203195h>
- 56 Kang, M., Momotenko, D., Page, A., Perry, D. & Unwin, P. R. Frontiers in Nanoscale Electrochemical Imaging: Faster, Multifunctional, and Ultrasensitive. *Langmuir* **32**, 7993-8008 (2016). <https://doi.org/10.1021/acs.langmuir.6b01932>
- 57 Mariano, R. G., McKelvey, K., White, H. S. & Kanan, M. W. Selective increase in CO(2) electroreduction activity at grain-boundary surface terminations. *Science* **358**, 1187-1192 (2017). <https://doi.org/10.1126/science.aao3691>
- 58 Yule, L. C. *et al.* Nanoscale electrochemical visualization of grain-dependent anodic iron dissolution from low carbon steel. *Electrochim. Acta* **332** (2020). <https://doi.org/10.1016/j.electacta.2019.135267>
- 59 Wang, Y., Gordon, E. & Ren, H. Mapping the Potential of Zero Charge and Electrocatalytic Activity of Metal-Electrolyte Interface via a Grain-by-Grain Approach. *Anal. Chem.* **92**, 2859-2865 (2020). <https://doi.org/10.1021/acs.analchem.9b05502>
- 60 Wang, Y., Gordon, E. & Ren, H. Mapping the Nucleation of H(2) Bubbles on Polycrystalline Pt via Scanning Electrochemical Cell Microscopy. *J. Phys. Chem. Lett.* **10**, 3887-3892 (2019). <https://doi.org/10.1021/acs.jpcclett.9b01414>
- 61 Aaronson, B. D. *et al.* Pseudo-single-crystal electrochemistry on polycrystalline electrodes: visualizing activity at grains and grain boundaries on platinum for the Fe<sup>2+</sup>/Fe<sup>3+</sup> redox reaction. *J. Am. Chem. Soc.* **135**, 3873-3880 (2013). <https://doi.org/10.1021/ja310632k>

- 62 Shkirskiy, V. *et al.* Nanoscale Scanning Electrochemical Cell Microscopy and Correlative Surface Structural Analysis to Map Anodic and Cathodic Reactions on Polycrystalline Zn in Acid Media. *J. Electrochem. Soc.* **167** (2020). <https://doi.org/10.1149/1945-7111/ab739d>
- 63 Chen, C. H., Meadows, K. E., Cuharuc, A., Lai, S. C. & Unwin, P. R. High resolution mapping of oxygen reduction reaction kinetics at polycrystalline platinum electrodes. *Phys. Chem. Chem. Phys.* **16**, 18545-18552 (2014). <https://doi.org/10.1039/c4cp01511h>
- 64 Guell, A. G., Ebejer, N., Snowden, M. E., Macpherson, J. V. & Unwin, P. R. Structural correlations in heterogeneous electron transfer at monolayer and multilayer graphene electrodes. *J. Am. Chem. Soc.* **134**, 7258-7261 (2012). <https://doi.org/10.1021/ja3014902>
- 65 Guell, A. G. *et al.* Redox-dependent spatially resolved electrochemistry at graphene and graphite step edges. *ACS Nano* **9**, 3558-3571 (2015). <https://doi.org/10.1021/acsnano.5b00550>
- 66 Hill, J. W. & Hill, C. M. Directly Mapping Photoelectrochemical Behavior within Individual Transition Metal Dichalcogenide Nanosheets. *Nano Lett.* **19**, 5710-5716 (2019). <https://doi.org/10.1021/acs.nanolett.9b02336>
- 67 Bentley, C. L. *et al.* Electrochemical maps and movies of the hydrogen evolution reaction on natural crystals of molybdenite (MoS(2)): basal vs. edge plane activity. *Chem. Sci.* **8**, 6583-6593 (2017). <https://doi.org/10.1039/c7sc02545a>
- 68 Strange, L. E. *et al.* Investigating the Redox Properties of Two-Dimensional MoS(2) Using Photoluminescence Spectroelectrochemistry and Scanning Electrochemical Cell Microscopy. *J. Phys. Chem. Lett.* **11**, 3488-3494 (2020). <https://doi.org/10.1021/acs.jpcclett.0c00769>
- 69 Choi, M. *et al.* Probing Single-Particle Electrocatalytic Activity at Facet-Controlled Gold Nanocrystals. *Nano Lett.* **20**, 1233-1239 (2020). <https://doi.org/10.1021/acs.nanolett.9b04640>
- 70 Lu, X. *et al.* Direct Probing of the Oxygen Evolution Reaction at Single NiFe(2)O(4) Nanocrystal Superparticles with Tunable Structures. *J. Am. Chem. Soc.* **143**, 16925-16929 (2021). <https://doi.org/10.1021/jacs.1c08592>
- 71 Saha, P., Hill, J. W., Walmsley, J. D. & Hill, C. M. Probing Electrocatalysis at Individual Au Nanorods via Correlated Optical and Electrochemical Measurements. *Anal. Chem.* **90**, 12832-12839 (2018). <https://doi.org/10.1021/acs.analchem.8b03360>
- 72 Quast, T. *et al.* Single Particle Nanoelectrochemistry Reveals the Catalytic Oxygen Evolution Reaction Activity of Co(3) O(4) Nanocubes. *Angew. Chem. Int. Ed. Engl.* **60**, 23444-23450 (2021). <https://doi.org/10.1002/anie.202109201>
- 73 Tetteh, E. B. *et al.* Calibrating SECCM measurements by means of a nanoelectrode ruler. The intrinsic oxygen reduction activity of PtNi catalyst nanoparticles. *Nano Res.* **15**, 1564-1569 (2021). <https://doi.org/10.1007/s12274-021-3702-7>
- 74 Lai, S. C. S., Lazenby, R. A., Kirkman, P. M. & Unwin, P. R. Nucleation, aggregative growth and detachment of metal nanoparticles during electrodeposition at electrode surfaces. *Chem. Sci.* **6**, 1126-1138 (2015). <https://doi.org/10.1039/c4sc02792b>

- 75 Ornelas, I. M., Unwin, P. R. & Bentley, C. L. High-Throughput Correlative Electrochemistry-Microscopy at a Transmission Electron Microscopy Grid Electrode. *Anal. Chem.* **91**, 14854-14859 (2019). <https://doi.org/10.1021/acs.analchem.9b04028>
- 76 Liu, Y. *et al.* Visualization and Quantification of Electrochemical H<sub>2</sub> Bubble Nucleation at Pt, Au, and MoS<sub>2</sub> Substrates. *ACS Sens.* **6**, 355-363 (2021). <https://doi.org/10.1021/acssensors.0c00913>
- 77 Liu, Y., Lu, X., Peng, Y. & Chen, Q. Electrochemical Visualization of Gas Bubbles on Superaerophobic Electrodes Using Scanning Electrochemical Cell Microscopy. *Anal. Chem.* **93**, 12337-12345 (2021). <https://doi.org/10.1021/acs.analchem.1c02099>
- 78 Deng, X. *et al.* Direct measuring of single-heterogeneous bubble nucleation mediated by surface topology. *Proc. Natl. Acad. Sci. U.S.A.* **119**, e2205827119 (2022). <https://doi.org/10.1073/pnas.2205827119>
- 79 Ustarroz, J. *et al.* Mobility and Poisoning of Mass-Selected Platinum Nanoclusters during the Oxygen Reduction Reaction. *Acs Catal.* **8**, 6775-6790 (2018). <https://doi.org/10.1021/acscatal.8b00553>
- 80 Jin, C., Liu, Y.-L., Shan, Y. & Chen, Q.-J. Scanning Electrochemical Cell Microscope Study of Individual H<sub>2</sub> Gas Bubble Nucleation on Platinum: Effect of Surfactants. *Chin. J. Anal. Chem.* **49**, e21055-e21064 (2021). [https://doi.org/10.1016/s1872-2040\(21\)60096-8](https://doi.org/10.1016/s1872-2040(21)60096-8)
- 81 Oswald, E., Palanisamy, K. & Kranz, C. Nanoscale surface modification via scanning electrochemical probe microscopy. *Curr. Opin. Electrochem.* **34** (2022). <https://doi.org/10.1016/j.coelec.2022.100965>
- 82 Bentley, C. L., Kang, M. & Unwin, P. R. Scanning Electrochemical Cell Microscopy (SECCM) in Aprotic Solvents: Practical Considerations and Applications. *Anal. Chem.* **92**, 11673-11680 (2020). <https://doi.org/10.1021/acs.analchem.0c01540>
- 83 Oseland, E. E. *et al.* Surface patterning of polyacrylamide gel using scanning electrochemical cell microscopy (SECCM). *Chem. Commun.* **52**, 9929-9932 (2016). <https://doi.org/10.1039/c6cc05153g>
- 84 Aaronson, B. D., Garoz-Ruiz, J., Byers, J. C., Colina, A. & Unwin, P. R. Electrodeposition and Screening of Photoelectrochemical Activity in Conjugated Polymers Using Scanning Electrochemical Cell Microscopy. *Langmuir* **31**, 12814-12822 (2015). <https://doi.org/10.1021/acs.langmuir.5b03316>
- 85 Rahman, M. M., Tolbert, C. L., Saha, P., Halpern, J. M. & Hill, C. M. On-Demand Electrochemical Fabrication of Ordered Nanoparticle Arrays using Scanning Electrochemical Cell Microscopy. *ACS Nano* **16**, 21275-21282 (2022). <https://doi.org/10.1021/acsnano.2c09336>
- 86 McKelvey, K., O'Connell, M. A. & Unwin, P. R. Meniscus confined fabrication of multidimensional conducting polymer nanostructures with scanning electrochemical cell microscopy (SECCM). *Chem. Commun.* **49**, 2986-2988 (2013). <https://doi.org/10.1039/c3cc00104k>
- 87 Patten, H. V. *et al.* Electrochemical "read-write" microscale patterning of boron doped diamond electrodes. *Chem. Commun.* **51**, 164-167 (2015). <https://doi.org/10.1039/c4cc07830f>

- 88 Zhan, D., Yang, D., Zhu, Y., Wu, X. & Tian, Z. Q. Fabrication and characterization of nanostructured ZnO thin film microdevices by scanning electrochemical cell microscopy. *Chem. Commun.* **48**, 11449-11451 (2012). <https://doi.org/10.1039/c2cc35809c>
- 89 Bartlett, T. R., Sokolov, S. V. & Compton, R. G. Electrochemical Nanoparticle Sizing Via Nano-Impacts: How Large a Nanoparticle Can be Measured? *ChemistryOpen* **4**, 600-605 (2015). <https://doi.org/10.1002/open.201500061>
- 90 Cheng, W. & Compton, R. G. Electrochemical detection of nanoparticles by 'nano-impact' methods. *TrAC, Trends Anal. Chem.* **58**, 79-89 (2014). <https://doi.org/10.1016/j.trac.2014.01.008>
- 91 Ustarroz, J., Kang, M., Bullions, E. & Unwin, P. R. Impact and oxidation of single silver nanoparticles at electrode surfaces: one shot versus multiple events. *Chem. Sci.* **8**, 1841-1853 (2017). <https://doi.org/10.1039/c6sc04483b>
- 92 Bentley, C. L., Kang, M. & Unwin, P. R. Time-Resolved Detection of Surface Oxide Formation at Individual Gold Nanoparticles: Role in Electrocatalysis and New Approach for Sizing by Electrochemical Impacts. *J. Am. Chem. Soc.* **138**, 12755-12758 (2016). <https://doi.org/10.1021/jacs.6b08124>
- 93 Kang, M. *et al.* Time-Resolved Detection and Analysis of Single Nanoparticle Electrocatalytic Impacts. *J. Am. Chem. Soc.* **137**, 10902-10905 (2015). <https://doi.org/10.1021/jacs.5b05856>
- 94 Chen, C. H. *et al.* Impact of Surface Chemistry on Nanoparticle-Electrode Interactions in the Electrochemical Detection of Nanoparticle Collisions. *Langmuir* **31**, 11932-11942 (2015). <https://doi.org/10.1021/acs.langmuir.5b03033>
- 95 Kleijn, S. E. *et al.* Landing and catalytic characterization of individual nanoparticles on electrode surfaces. *J. Am. Chem. Soc.* **134**, 18558-18561 (2012). <https://doi.org/10.1021/ja309220m>
- 96 Schmickler, W. & Santos, E. *Interfacial Electrochemistry*. (Springer Science & Business Media, 2010).
- 97 He, Z. D., Chen, Y. X., Santos, E. & Schmickler, W. The Pre-exponential Factor in Electrochemistry. *Angew. Chem. Int. Ed. Engl.* **57**, 7948-7956 (2018). <https://doi.org/10.1002/anie.201800130>
- 98 Becka, A. M. & Miller, C. J. Electrochemistry at Omega-Hydroxy Thiol Coated Electrodes .3. Voltage Independence of the Electron-Tunneling Barrier and Measurements of Redox Kinetics at Large Overpotentials. *J. Phys. Chem.* **96**, 2657-2668 (1992). [https://doi.org/DOI 10.1021/j100185a049](https://doi.org/DOI%2010.1021/j100185a049)
- 99 Memming, R. *Semiconductor Electrochemistry*. (John Wiley & Sons, 2015).
- 100 Liu, Y. W. & Chen, S. L. Theory of Interfacial Electron Transfer Kinetics at Nanometer-Sized Electrodes. *J. Phys. Chem. C* **116**, 13594-13602 (2012). <https://doi.org/10.1021/jp300696u>
- 101 Feldberg, S. W. Implications of Marcus-Hush theory for steady-state heterogeneous electron transfer at an inlaid disk electrode. *Anal. Chem.* **82**, 5176-5183 (2010). <https://doi.org/10.1021/ac1004162>



- 102 Wang, Y. J., Limon-Petersen, J. G. & Compton, R. G. Measurement of the diffusion coefficients of  $[\text{Ru}(\text{NH}_3)_6]^{3+}$  and  $[\text{Ru}(\text{NH}_3)_6]^{2+}$  in aqueous solution using microelectrode double potential step chronoamperometry. *J. Electroanal. Chem.* **652**, 13-17 (2011). <https://doi.org/10.1016/j.jelechem.2010.12.011>
- 103 Velicky, M. *et al.* Electron transfer kinetics on natural crystals of MoS<sub>2</sub> and graphite. *Phys. Chem. Chem. Phys.* **17**, 17844-17853 (2015). <https://doi.org/10.1039/c5cp02490k>
- 104 Ghosh, S. & Hammes-Schiffer, S. Calculation of Electrochemical Reorganization Energies for Redox Molecules at Self-Assembled Monolayer Modified Electrodes. *J. Phys. Chem. Lett.* **6**, 1-5 (2015). <https://doi.org/10.1021/jz5023784>
- 105 Royea, W. J., Hamann, T. W., Brunshwig, B. S. & Lewis, N. S. A comparison between interfacial electron-transfer rate constants at metallic and graphite electrodes. *J. Phys. Chem. B* **110**, 19433-19442 (2006). <https://doi.org/10.1021/jp062141e>
- 106 Compton, R. G. & Banks, C. E. *Understanding Voltammetry*. (World Scientific, 2018).
- 107 Novey, J. K. & Compton, R. G. Thermal convection in electrochemical cells. Boundaries with heterogeneous thermal conductivity and implications for scanning electrochemical microscopy. *Phys. Chem. Chem. Phys.* **19**, 12759-12775 (2017). <https://doi.org/10.1039/c7cp01797a>



# CHAPTER 2

---

## Experimental Methods

---

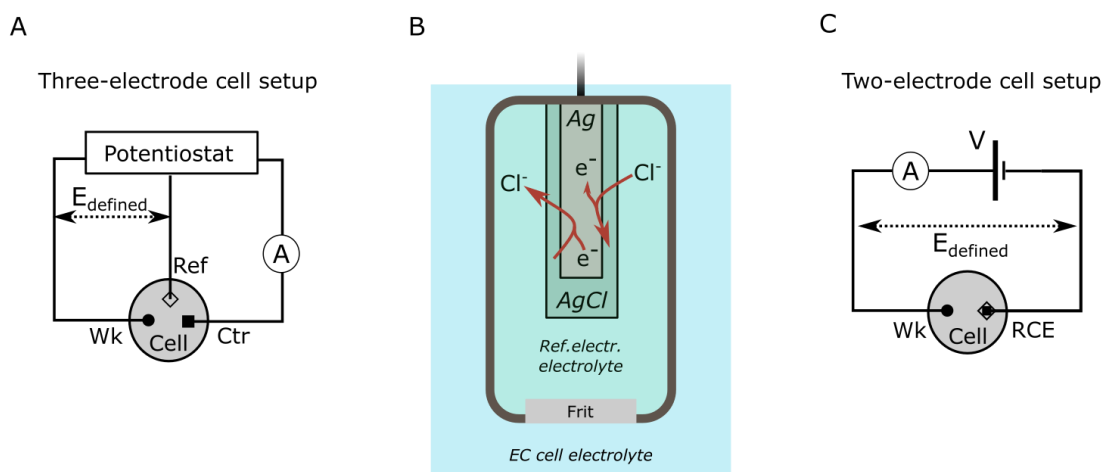
## 2.1 Electrochemical Methods

To interrogate and measure an electrochemical system with the aim of obtaining information about its behaviour, different electrochemical methods can be implemented. As detailed in the introductory chapter, the electrochemical current generated in an electrochemical system can depend on the potential applied to the electrodes. Then, by controlling the potential applied to the electrodes while monitoring the current, it is possible to obtain information about current-potential dependencies. Electrochemical methods based on applying defined potentials to an electrode and observing the resulting current response are called voltammetric techniques. In order to achieve a well-defined potential on the electrodes without the perturbations from the physicochemical phenomena ongoing on the electrochemical cell, voltammetric techniques are often carried out using a potentiostat instrument and a three-electrode cell setup, which includes working, counter and reference electrode. A schematic of the basic three-electrode cell circuit using a potentiostat is shown in Figure 2.1 A. The potentiostat function ensures there is a defined potential difference between the working electrode and the reference electrode while allowing the necessary current between the counter electrode and the working electrode to ensure electroneutrality in solution. Then, the function of the reference electrode is to provide a stable reference potential in the electrochemical cell against which the working electrode potential can be defined.

Reference electrodes achieve a defined stable potential (defined workfunction) by carrying a chemical equilibrium involving HET with a defined workfunction. Reference electrode equilibria must present fast HET kinetics to provide zero-charge transfer resistance.<sup>1</sup> In this manner, the potential at which the working electrode is set refers to the potential difference with respect to the fix equilibria potential of the reference electrode. The potentiostat also prevents any large current from being driven through the reference electrode, which could affect its defined equilibrium potential. There are different reference electrode architectures, and for this thesis, it has been usually used a reference electrode consisting of a metallic electrode inserted in an electrolyte solution. The electrolyte solution needs to contain the electroactive species, such the HET equilibrium between the metal electrode and the diluted species is established. Electrolyte species also need to be concentrated enough to provide a constant makeup, so that the HET equilibria is maintained. In Figure 2.1 B is shown a schematic of a reference electrode base of  $\text{Ag}_{(s)} + \text{Cl}^{-}_{(aq)} \rightleftharpoons \text{AgCl}_{(s)} + e^{-}$  equilibria, as used for the experiments of Chapters 3, 4 and 5. For the experiments in Chapter 6, the Pd-H<sub>2</sub> reference electrode is used. Pd-H<sub>2</sub> HET equilibrium is based on the electrochemically driven intercalation of H atoms in the crystalline lattice of Pd.<sup>2,3</sup>

For microscale sized working electrodes, the current passed through the system is small enough (pA to nA) that if current is driven through the reference electrode, this will not change its composition over the time course of a typical experiment and so maintain a constant equilibrium

potential. Therefore, for small electrodes the potentiostat can be operated in a two-electrode configuration with a working electrode and a combined reference-counter electrode (RCE),<sup>4</sup> as shown in Figure 2.1 C.

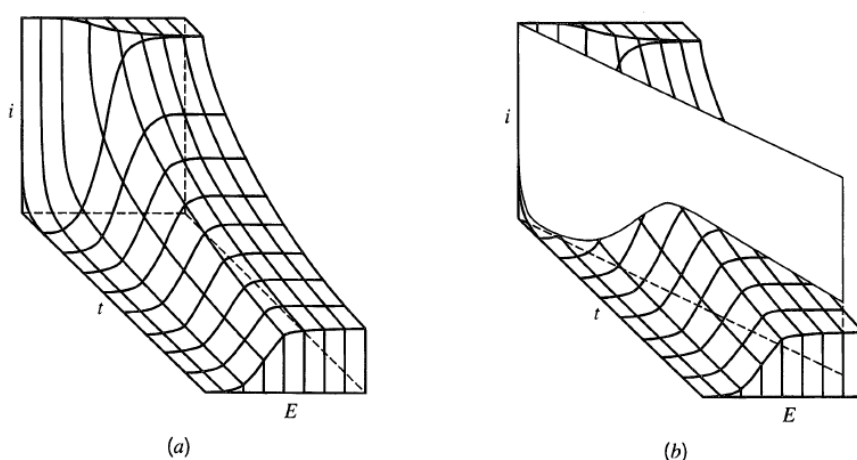


**Figure 2.1:** Schematic showing the circuit connections of different electrochemical systems and the equilibrium principle of the reference electrode. **A)** Schematic of a three-electrode cell using a potentiostat. **B)** Schematic of an Ag/AgCl based reference electrode, showing the forward and backward equilibrium reactions with red arrows. **C)** Schematic of two electrode cell with RCE. For A and C, *Wk* refers to the working electrode, *Ctr* refers to the counter electrode, *Ref* refers to the working electrode, *RCE* refers to the reference counter electrode, *A* inside a white circle refers to the current reader, and *V* to a DC potential source.

The Introduction chapter, Section 1.5.2, details how the current generated from the HET processes vary with the applied potential. However, the current predictions from HET models do not account for the current-time dependencies imposed by mass transport effects, capacitive effects, and their interaction with the variation of applied potential over time. Then when interrogating electrochemical systems with voltammetric methods, the current (*I*), time (*t*) and potential (*E*) dependencies need to be accounted for, which can be pictured as a three dimensional *I-t-E* surface,<sup>1</sup> as shown in Figure 2.2.

By applying different potential profiles to the working electrode, different regions of the *I-t-E* surface can be interrogated. On *potential steps*, the potential is stationary for a given period of time and could be set to another value for another period of time. The applied *E-t* function is a step function, as shown in Figure 2.3. The term *chronoamperometry* is also used when measuring stationary potential. For a stationary working electrode potential, it is measured the current-time (*I-t*) dependencies which arise from the capacitive currents and Faradaic currents from Nernstian reaction. In *potential steps*, capacitive currents are characterised by their large magnitude over a short duration of time, either on macroscale and nanoscale electrodes, as shown in Figure 2.3. Nernstian reactions at stationary potentials are characterised for presenting constant electron

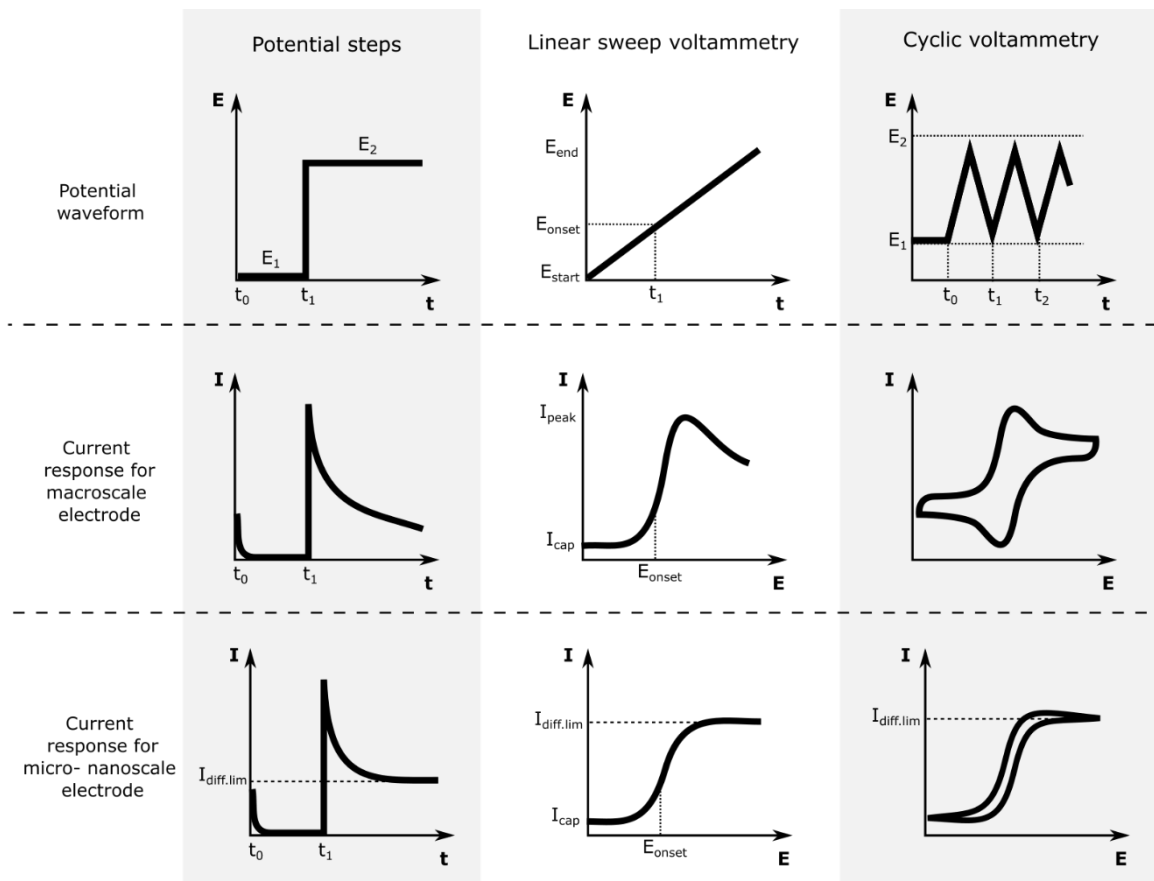
transfer kinetics, nevertheless the Nernstian currents might vary over time due to mass transport effects. For the macroscale electrode, linear mass transport generates Nernstian currents that decay over time defined by the Cottrell equation (see the Introduction chapter, Section 1.5.3) and shown in Figure 2.3. On a micro- nanoscale electrodes, it is expected that the hemispherical mass transport led to an initial Nernstian current decay, and after diffusion limiting current plateau is reached (see Introduction chapter, Section 1.5.3), as displayed in Figure 2.3. Information about electron transfer kinetics and the I-t-E surface can be obtained by performing multiple potential steps over a potential window around the equilibrium potential. In this thesis, *chronoamperometry* has been employed for carrying out stochastic collision electrochemistry experiments, as detailed in Chapter 3.



**Figure 2.2:** **A)** Illustration of the current dependence over potential and time for an HET reaction, also called I-t-E surface. **B)** Illustration of the region asked by a linear sweep voltammogram (white panel) over the I-t-E surface. Reproduced with permission from Bard, A.J. *et al.* <sup>1</sup>.

In *voltammetry* experiments, the potential is 'continuously changed' by performing a potential sweep over a defined potential window at a given sweep rate. *Voltammetry* allows one to obtain information about the electron transfer kinetics and reaction reversibility, mass transport effects, and capacitance and resistance effects in a single experiment without the data analysis requirements of potential steps. Figure 2.3 shows the characteristic E-t ramp function of a *linear sweep voltammogram* (LSV), which slope is defined by the sweep rate, also called the scan rate,  $v$  (in  $\text{V s}^{-1}$ ). Generally, LSVs are employed to evaluate potential dependence processes, and thus, LSVs are commonly plotted as I-E curves. Figure 2.3 shows a typical Faradaic current response for a Nernstian reaction, which highlights the Faradaic current variation depending on HET kinetics around the equilibrium or onset potential. When studying Nernstian reactions with *voltammetry*, mass transport effects often dominate the current response at high overpotentials. In Figure 2.3 is shown the expected current response for a macroscale electrode with linear diffusion and the expected current response for a micro- nanoscale electrode with hemispherical diffusion. The region of the I-t-E surface interrogated by an LSVs is shown in Figure 2.2 B. Notice that the sweep

rate plays an important role in the region of the I-t-E surface that is being interrogated. For instance, faster sweep rates interrogate regions of the I-t-E surface close to early times, making mass transport and capacitance effects more noticeable. On the other hand, slower scan rates interrogate later times, more resembling steady potential response and being less affected by mass transport or capacitive effects. LSVs have been employed to evaluate the electron transfer kinetics on 2D TMDCs, as detailed in Chapters 4 and 5.



**Figure 2.3:** Characteristic waveforms of potentiometric techniques for potential steps, linear sweep voltammetry, and cyclic voltammetry measurements. The current responses are plotted with respect to time or potential applied, for macroscale and microscale sized electrodes.

The potential ramp function can be reversed at the end of the LSV and further potential ramps can be added consecutively, as shown in Figure 2.3. This experimental procedure is called *cyclic voltammetry* (CV). CV enables comparing forward and backward cycle response and evaluating the response over multiple cycles, information that is not provided by the LSVs. For instance, by comparing forward and backward cycle capacitances, quantitative determination can be obtained. During a potential sweep it is expected that capacitive current contributions ( $I_{cap}$ ) to be:

$$I_{cap} = C \cdot v \quad (\text{Eq. 2.1})$$

where  $I_{cap}$  is the capacitive current,  $C$  is the capacitance and  $v$  the sweep rate.

The forward and backward sweeps have  $v$  values of opposite sign, resulting in current contribution of the opposite sign. CV allows the capacitive contributions to be isolated from any offsetting currents by subtracting the charge contributions of the forward and backward cycles. Charge contributions are obtained by integrating current over time, as:

$$Q_{forward/backward} = \int I_{forward/backward} dt \quad (\text{Eq. 2.2})$$

$$Q_{forward} - Q_{backward} = Q_{cap} \quad (\text{Eq. 2.3})$$

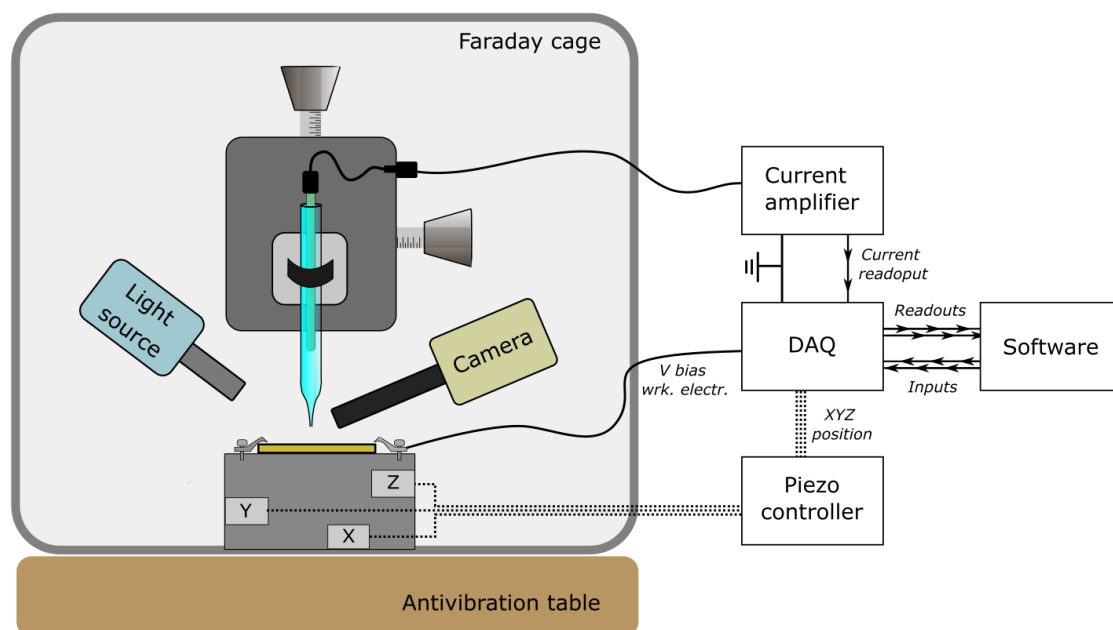
$$C = \frac{Q_i}{V_i} = \frac{Q_{cap}}{2 \cdot E_{window}} \quad (\text{Eq. 2.4})$$

In this thesis cyclic voltammetry has been employed for evaluating MXene 2D materials pseudocapacitive response, as detailed in Chapter 6. CVs and voltammetry methods can be used to extract many different types of information about the electrochemical system, and so is a very popular technique in the electrochemistry field. The reader is referred to the article of Dempsey *et al.* in ref. 5 for a brief summary of CV technique, and to the book of Compton & Banks ref. 6 for an extended and detailed explanation about voltammetric techniques, including CVs. There are other commonly used electrochemical methods, such as galvanostatic or impedance spectroscopy, that are essential for any electrochemist toolbox, but have not been employed for the work presented in this thesis. The reader is referred to ref. 1 for a detailed explanation of other electrochemical methods.



## 2.2 Single Barrel SECCM

As introduced in Introduction chapter, Section 1.4.2, SECCM is a scanning electrochemical probe microscopy technique, which via the formation of micro- nanoscale electrochemical cell (droplet cell), the electrochemical response of micro- nanoscale domains of a surface are isolated. SECCM is often used to perform electrochemical characterisation of nanoscale entities. SECCM measurements require the fulfilment of multiple tasks, often including: SECCM probe preparation, probe alignment with sample features, probe-sample approach for droplet cell formation, performing electrochemical measurements utilising electrochemical methods, signal processing and signal recording. Often an SECCM measurement involves the repetition of all those tasks several times to measure multiple points on the surface for mapping the electrochemical response of an area. To complete all those tasks, it is required the SECCM probe fabrication and characterisation, the use of specific SECCM hardware instrumentation and the use of software to operate and synchronize the electrochemical measurements, the probe displacement and the data recording.<sup>7</sup> In the following sections, it is provided the description of the SECCM experimental methods implemented for this thesis, as well as the comparison with alternative SECCM methods provided in literature.



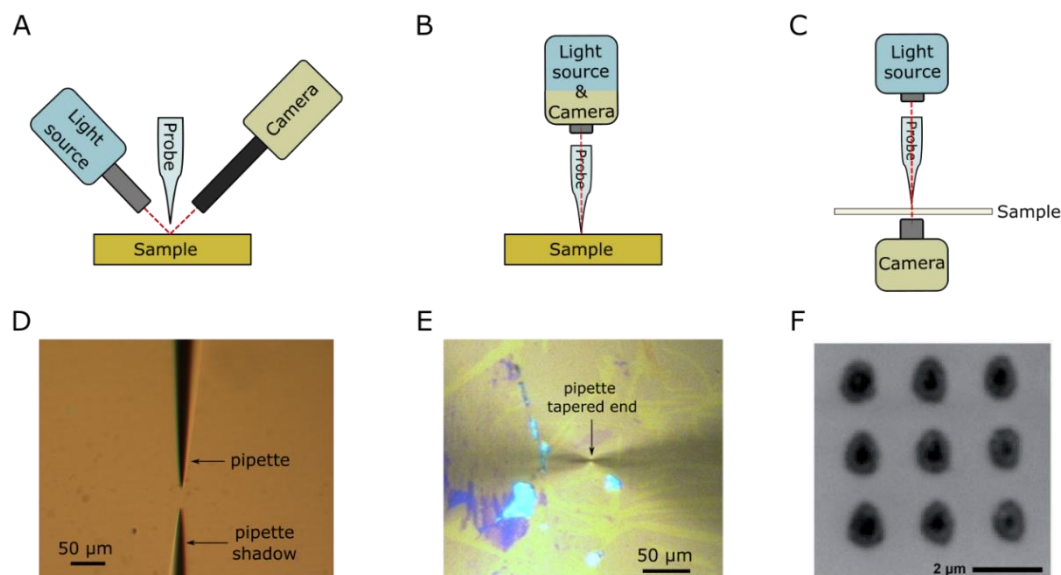
**Figure 2.4:** SECCM schematic setup and the different elements that make up the instrument. The different elements are connected by wires that indicate the information carried: in solid line the wires that connect the elements of the electrochemical cells, in dotted lines the wires that connect the piezoelectric actuators, and the arrowed lines display the input and output information of the system and its direction. DAQ stands for data acquisition board.

## 2.2.1 SECCM instrumentation

In Figure 2.4 is shown a schematic of a general single barrel pipette SECCM setup indicating the multiple instrumentation components. SECCM components can be grouped into modules, according to the functionality they provide, having the optical system, the mechanical displacement module, the signal processing module, and the SECCM probe. In the following subsection, each of the components of each module and their operation are described, except the SECCM probe, which is discussed independently in Section 2.2.2.

### 2.2.1.1 Optical system

The optical system is composed of a light source with controllable brightness and a camera (usually the camera requires a relatively long working distance of  $> 2$  cm). The optical system must provide images of the sample and the end of the probe for manual alignment of the probe. The distinct morphological features of the sample generally need to be recognisable optically. Because the regions SECCM can typically scan are 10's of micrometres in size, the optical system must be capable of providing resolution over the sample surface of at least 10's  $\mu\text{m}$  features. Consequently, the magnification required for the camera is at least  $\times 10$ , with a  $\times 20$  magnification typically used. The purpose of the optical system is to identify the relative position of the SECCM (pipette end) with respect to the sample surface. There are different possible mounting positions for the camera and light source,<sup>7-9</sup> as shown in Figure 2.5. The advantages and disadvantages of each mounting position are summarised in Table 2.1.



**Figure 2.5:** Mounting position of the camera and light source relative to the probe and the sample. **A)** In-plane mounting, **B)** Vertical mounting and **C)** Transmission mounting. The red dashed lines indicate the optical path. Images of pipette over sample surface collected with **D)** in-plane mounting, **E)** vertical mounting, and **F)** transmission mounting.

**Table 2.1:** Advantages and disadvantages of the different optical mounting systems on SECCM.

	<b>Advantages</b>	<b>Disadvantages</b>
<b>In-plane mounting</b> (Figure 2.5 A)	<p>Provides a good vertical resolution of the sample-to-pipette distance, thanks to the pipette shadow visible on the surface (see Figure 2.5 D).</p> <p>Facilitate the displacement and approach procedure of the pipette.</p> <p>The optical system can be mounted independently of the rest of the equipment.</p> <p>Lenses require a working distance of about 5 cm.</p>	<p>The camera has a tilt angle with respect to the surface. Therefore, it is not possible to bring the whole surface into focus at once.</p> <p>The in-plane alignment of the light source, probe, and camera is required prior to operation.</p> <p>Sensitive to sample reflectivity.</p>
<b>Vertical mounting</b> (Figure 2.5 B)	<p>Great XY resolution of the sample surface without probe mounted.</p> <p>Similar configuration to that used in optical microscopies. Brings versatility to the equipment that can also be used for standard optical microscopy measurements.</p>	<p>The XY resolution decreases when the SECCM probe is mounted, with the probe intersecting the optical path producing aberrations in the image (see Figure 2.5 E).</p> <p>Determining the distance sample-to-pipette (Z-resolution) is possible but difficult, making the pipette approach more complex.</p> <p>Requires an optical lens with a very long working distance (&gt;10 cm).</p>
<b>Transmission mounting</b> (Figure 2.5 C)	<p>The highest XY resolution among the different mounting positions (see Figure 2.5 F).</p> <p>Allow transmission and spectroscopic measurements.</p>	<p>Requires working with transparent samples and transparent substrates.</p> <p>Might require an additional optical system for probe positioning.</p> <p>The integration with other components of the system that might interfere with the optical path should be considered.</p>

### 2.2.1.2 Mechanical displacement module

The relative movement between the probe and the sample is commonly achieved with micropositioners for displacements in the  $\mu\text{m}$  to mm range, and piezoelectric actuators for displacements in the range nm to  $\mu\text{m}$  range. The micropositioner facilitates the location of the probe in the region of interest and the positioning of the probe within the range of the piezoelectric actuators. The coarse pipette approach often allows to set the end of the pipette at few  $10^1$ 's of  $\mu\text{m}$  distance from the sample surface (see Figure 2.5 D). The micropositioner can be operated manually or by a servo motor. The final pipette approach and droplet cell formation require fine control over pipette movement on the nanometre range. Piezoelectric actuators allow the user to set a fixed

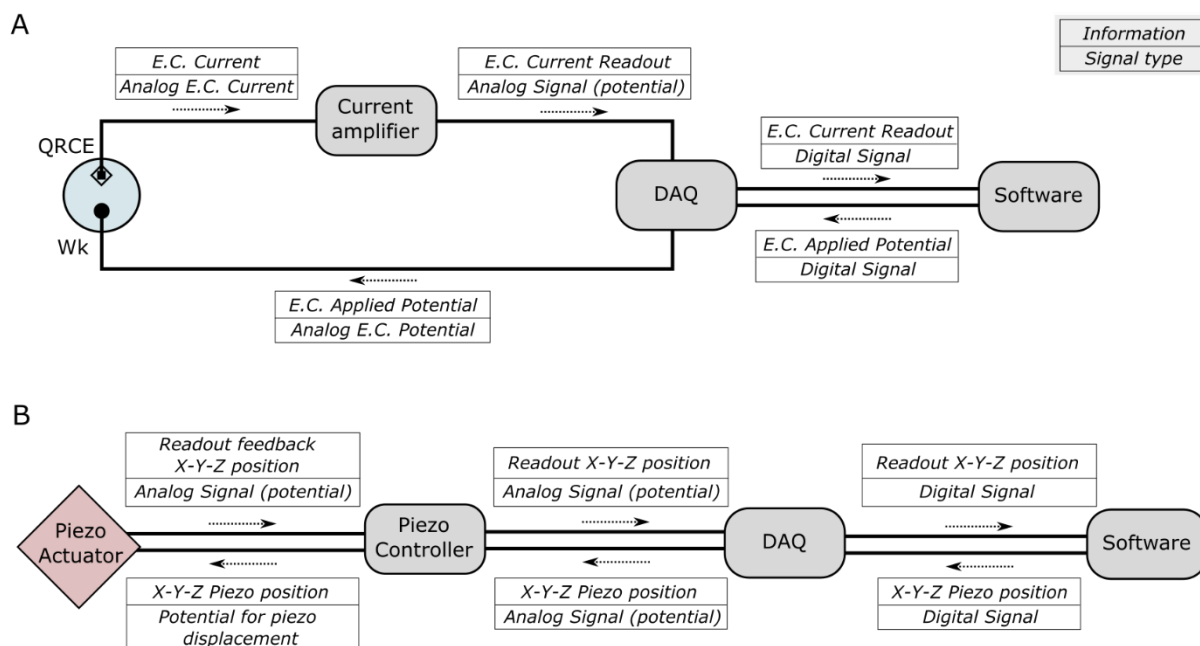
pipette approach rate (e.g. 100 nm/s) and coupled with a current-based feedback loop, allow for the detection of the droplet cell formation. Piezoelectric actuators are also in charge of maintaining the pipette at a given distance from the surface during electrochemical measurements.

The mechanical actuator can be installed in a variety of configurations. For example, the SECCM implementation on the ParkSystems NX10 (used in this thesis) controls the X-Y displacement by moving the sample and the Z displacement by the movement of the probe. Any other possible configuration, such as X-Y-Z displacement occurring on the probe or the sample, are equally valid. The displacement of the piezoelectric actuator is regulated by a piezo controller, as shown in Figure 2.4. However, piezoelectric actuators suffer from uncontrolled displacement or “drift” over time.<sup>10</sup> Once the pipette is in close proximity over the electrode surface (100’s nm) the piezoelectric drift might cause pipette crashing or droplet cell instability. A popular practise implemented by the SECCM user is to minimise the time in which the pipette is in close proximity to the surface.

### 2.2.1.3 Signal processing module

Carrying out electrochemical measurements demands managing potential and current signals. The electrochemical input/output signals of the SECCM equipment are ultimately managed by a software-controlled device. Nevertheless, software operates in a binary code that needs to be translated into the analogue signal characteristic of electrochemical cells. Then, any electrochemical system demands a signal processing and conversion procedure. Figure 2.6 A schematic illustrates the information and signal type in each connection between the elements that make up the SECCM equipment used in this thesis. The elements that form the signal processing module are the current amplifier, a data acquisition board (DAQ) and software controlled device (PC, FPGA card, etc). The mechanical displacement module also operates with analogue signals which are ultimately controlled by software. The schematic of the signal conversion procedure for the mechanical displacement module is provided in Figure 2.6 B.

As shown in Figure 2.6 A, the current amplifier transforms the analogue current signal generated on the working electrode (pA to nA) into a scaled potential analogue signal (e.g. -10 to +10V) thanks to a transimpedance gain. The current amplifier transimpedance gain used for SECCM instrumentation is often around  $10^8 - 10^{11}$  V/A. The role of the current amplifier is critical thus transform the experimental observable (current) into a readout. The current amplifier architectures, features and performance are discussed in detail in Chapter 3. For the displacement module, shown in Figure 2.6 B, the X-Y-Z positions are defined by the software, the DAQ transforms the digital signals from the software into analogue signals. The piezo controller amplifies the analogue signal from the DAQ to the potential required for displacement of the piezo actuators. The displacement module often includes position readout signals, which are used to verify the piezo actuator function.



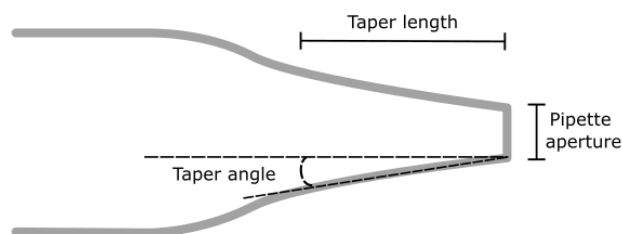
**Figure 2.6:** Schematic of the signal processing protocol of the SECCM instrument for **A)** the electrochemical system and for **B)** the mechanical displacement module. The different elements that contribute to signal conversion are marked with a coloured shape. Each connection between elements shows the type of information and signal carried.

The data acquisition board acts as an interface between the analogue signals and the digital signal. For SECCM equipment, the DAQs must have multiple input and output ports in analogue and digital signals. The software controls all the processes that undergo the SECCM. For this thesis, two different SECCM equipments have been used, a commercially available instrument (Park NX10) that is controlled by SmartScan software and a self-made instrument controlled by the Warwick Electrochemical Scanning Probe Microscopy (WEC-SPM) platform written in LabView.

### 2.2.2 The SECCM probe

Micro- or nano-pipettes filled with electrolyte solution are the probes for SECCM. The pipette geometry is intimately linked with the scale of the nano-domain that is being interrogated, as well as the transport of chemical species through the pipette tip to the sample surface. The pipette aperture, the taper angle (also called half-cone angle) and the taper length are the main parameters that define the SECCM probe, as indicated in Figure 2.7. For SECCM purposes, the pipette aperture ranges between 50 nm to 50  $\mu\text{m}$  and the taper length can be from millimetres to 100's of  $\mu\text{m}$ . Notice that those two geometric parameters can vary orders of magnitude, resulting in very different SECCM probes that target different nano- or micro-electrochemical measurements. Commonly, the tapered angle is a less variable parameter ranging between 5 - 15 degrees.<sup>11</sup>

The pipette aperture is the main parameter for controlling the droplet cell size. In each SECCM experiment, the pipette aperture needs to be carefully selected, targeting the encapsulation within the droplet cell of the nanostructure and morphological features desired. Pipettes about 20-100 times larger than the feature desired to probe provide the best electrochemical contrast, as discussed in Chapter 5. The merits of smaller or larger pipettes are summarised in Table 2.2.



**Figure 2.7:** Schematic of a pipette tip indicating the main geometric parameters: the pipette aperture, the taper angle, and the taper length.

**Table 2.2:** Characteristic electrochemical performance of the SECCM probe as a function of the pipette aperture.

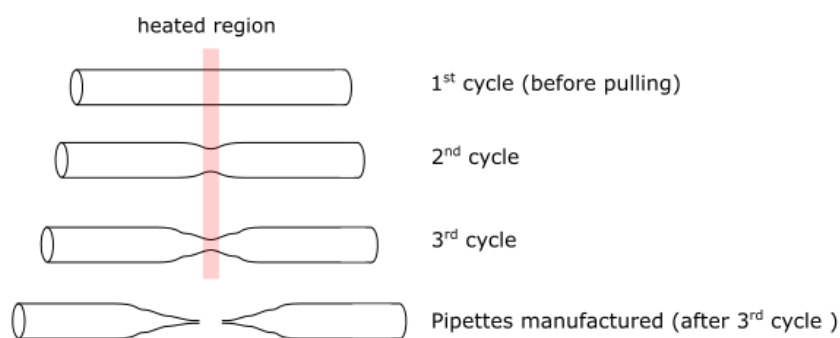
<b>Smaller pipette aperture</b>	<b>Larger pipette aperture</b>
Higher mass transport rates.	Lower mass transport rates
Smaller magnitude currents	Larger current magnitudes
Greater lateral (XY) resolution.	Lower lateral (XY) resolution.
When perform electrochemical mapping, longer time of scan for large areas.	When perform electrochemical mapping, short time of scan for large areas.
Small probability of leakage and good droplet cell stability.	Higher probability of leakage, and droplet cell more sensitive to surface morphology.

The fabrication of pipettes by capillary pulling (detailed in Section 2.2.2.1) fixes the taper angle of the pipette within the  $5^\circ - 15^\circ$  range.<sup>11,12</sup> The relatively narrow range of possible taper angles demands adjustment of the tapered length for the manufacturing of pipettes with smaller or larger apertures. Thus, increasing the tapered length results in smaller pipette apertures.<sup>12</sup> However, a too long tapered length might impact the SECCM measurements. The high aspect ratio of a long tapered channel ( $>100$ 's  $\mu\text{m}$  length with diameter  $< 1 \mu\text{m}$ ) can affect the ion conductance, resulting in the appearance of resistive effects and migration mass transport.<sup>13</sup> Under the condition of low solution conductance (low concentration of the supporting electrolyte) long tapered lengths are undesirable. Long tapered lengths also make filling the pipette difficult with trapped air bubbles in the tapered region. Formation of an air bubble must always be avoided, or the bubble must be eliminated prior to performing a SECCM scan to avoid solution conductivity issues. Further details regarding the electrolyte filling process and air bubble generation can be found in Section 2.2.2.4.

In contrast with other SPM methods, SECCM probes are generally single-use probes. It is common for the user to need several probes to find the optimum SECCM probe and attempt a SECCM measurement. The following sections describe the pipette fabrication processes, the pipette characterisation methods and how the pipettes are used as SECCM probe.

### 2.2.2.1 Pipette fabrication: Capillary pulling

The standardised method to fabricate micro-nano pipettes is capillary pulling. Capillary pulling consists of heating the centre of the capillary close to its melting point while pulling the capillary ends apart. This method thins the centre of the capillary, in one or multiple cycles of heating and pulling, until the capillary breaks, forming two tapered pipettes, as shown in Figure 2.8. There are different capillary puller technologies, such as a laser puller or a CO<sub>2</sub> thermal heater, as well as several commercial instruments. Most capillary puller instrumentation offers a range of programmable parameters (heating condition, pulling strength, number of cycles, etc.) that allow tuning of the pipette geometry. Unfortunately, the processes of bringing a capillary close to melting point and pulling are extremely sensitive to multiple factors that are often difficult to control and/or remain obscure to the user. For example, ambient conditions or particular equipment conditions affect the resulting pipette pulling geometry.<sup>12</sup> As a consequence, there is no single "parameter recipe" to pull a capillary to obtain a given pipette geometry, even when using the same equipment model and the same capillary specification.<sup>12</sup>



**Figure 2.8:** Schematic of capillary pulling of multiple cycles.

The design of the capillary pulling recipe involves setting the heating and pulling condition along a multiple number of cycles. An example of pulling design could be three cycle steps, as shown in Table 2.3. The first two cycles aim to reduce the diameter of the capillary in its centre, and a final cycle (often with stronger pulling) breaks the capillary and forms the tapered end of the pipette. Note that the capillary gets thinner in each cycle, reducing its mass in the centre, and thus making heating processes faster. It is recommended to design capillary pulling with the least possible number of cycles and/or maximising thinning of capillary in each step. This practise results in a more consistent pipette geometry over different capillary pulls. Following the same principle, tuning of pipette geometry is recommended to adjust only the parameters of the last cycle.

Some published literature provides guidelines for how to produce pipettes from capillary pulling<sup>12,14</sup> or report the recipe and capillary used to obtain given pipette size.<sup>15</sup> First attempts to pull a given pipette geometry might be based on reported pulling parameters for the same equipment and capillary used. Adjustment, or at the very least fine-tuning, of the pulling recipe is almost always required to achieve a consistent pulling of the desired pipette geometry. In Table 2.3 it is summarize the parameters used to pull the pipettes used as SECCM in the thesis with a P-2000 laser puller (Sutter Instruments Inc.). Table 2.3 shows the pulling procedure used in this thesis to manufacture pipettes with consistent aperture ranging between 500 nm to 1000 nm diameter.

**Table 2.3:** Pulling parameters used on the laser puller P-2000 from Sutter Instruments for fabrication of pipettes between 500 nm and 1000 nm. *Heat* refers to the heating power in arbitrary units. *Fil* refers to the width of the heated region from the capillary centre, in arbitrary units. *Vel* refers to the glass viscosity threshold from which heating stops, in arbitrary units. *Del* refers to the time between heating stop and pulling starts, in milliseconds. *Pull* refers to the pull strength in arbitrary units. The third-cycle pulling strength parameter (pull) is adjusted to larger values to produce smaller apertures, or smaller values to produce larger apertures opposite.

<b>N° cycle</b>	<b>Heat</b>	<b>Fil</b>	<b>Vel</b>	<b>Del</b>	<b>Pull</b>
<b>1<sup>st</sup></b>	600	4	30	150	20
<b>2<sup>nd</sup></b>	500	4	30	150	60
<b>3<sup>rd</sup></b>	450	3	30	135	45-80

One of the common issues facing pipette pulling is consistency of the pipette geometry over different pulls. In addition to optimising the pulling parameters, the equipment conditions have a huge influence on the sensitive pulling process. If the equipment condition changes, a given optimised pull recipe may not produce the desired pipette geometry. For example, the pulling strength can vary if the elements that make up the pulling system (pullies, ropes, and motors) age or accumulate dirt. Moreover, the laser pullers reflective mirror can become dirty with dirt/grease sputtered from the capillary, causing a variation in heating performance. It is recommended that users keep the capillary pulling equipment in a pristine condition. Examples of good practises are: ensuring an adequate clean space for the equipment, not moving the equipment once installed, operating always with clean gloves and replacing them often, and ensuring cleanliness of capillary used. Furthermore, maintenance, cleaning and calibration as indicated by equipment manufacturer are essential.

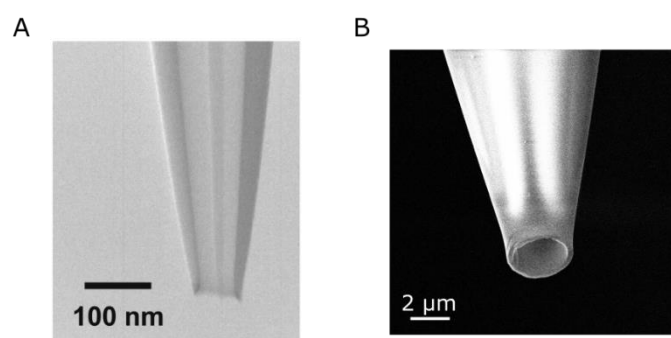


### 2.2.2.2 Characterisation of pipette geometry

The nanoscale dimensions of pipettes used for SECCM do not allow optical characterisation of pipette geometry. Electron microscopy provides direct imaging of the pipette tip with accurate determination of the pipette aperture and tapered angle values. However, there are other alternative or complementary methods for pipette characterisation which require less sophisticated equipment. Alternatives to electron microscopy rely on observation of the pore-like behaviour of the nanopipette to determine its aperture.<sup>15</sup> Simpler methods of determining the aperture of the pipette are particularly convenient for the SECCM user, as they allow fast evaluation of the geometry of the pipette prior to the SECCM scan. The following sections introduce pipette aperture determination by electron microscopy, *ionic conductivity* and *bubble point* methods.

#### 2.2.2.2.1 Electron microscopy determination

Transmission electron microscopy (TEM) or scanning electron microscopy (SEM) provides direct imaging of pipette tips, as shown in Figure 2.9, from which the geometric parameters can be measured. It should be noted that measuring any sample under an electron microscope requires adequate sample preparation. For borosilicate or quartz pipettes, electron conduction paths are necessary to avoid charge-accumulation effects that distort the image. For instance, silver paste can be used to make a conductive surface near the end of the pipette.



**Figure 2.9.** Electron microscopy images of pipette tips by A) TEM and B) SEM. “A” is reproduced with permission from Momotenko, D. *et al.*<sup>15</sup>

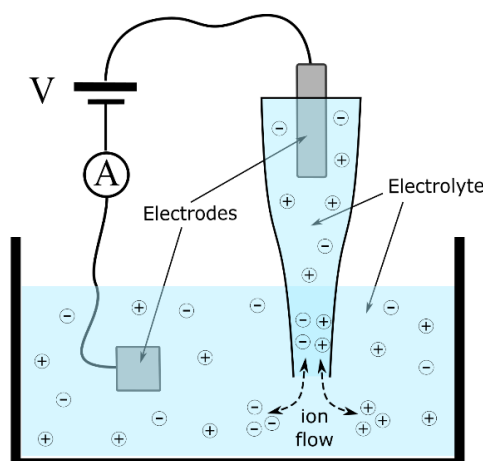
#### 2.2.2.2.2 Ion conductance determination

It is possible to estimate pipette aperture electrochemically by measuring the ion conductivity through the pipette, as is used in scanning ion-conductance microscopy (SICM). As illustrated in the setup schematic in Figure 2.10, the pipette is filled with a salt electrolyte solution (*e.g.* 100 mM KCl) and an Ag/AgCl electrode is inserted into the back end of the pipette. The pipette tip is immersed in a solution containing the same electrolyte solution and another electrode.

The electrodes must be connected to a potentiostat or similar device (as described in Section 2.1). Using a voltammetric technique, we can measure the current generated by the migration of ions through the pipette aperture and its dependence on potential. The current-potential slope is the conductance, or its inverse the resistance, offered by the pipette aperture to the flow of ions, which can be related with the pipette aperture by the following expression:

$$R_{ap} = \frac{1}{L \cdot \pi \cdot r_i \cdot \tan(\alpha)} \quad (\text{Eq. 2.5})$$

where  $R_{ap}$  is the access resistance of the pipette aperture,  $L$  is the solution electric conductivity,  $r_i$  is the pipette aperture radius and  $\alpha$  is the pipette tapered angle.<sup>16,17</sup> If the tapered angle is known, or just assuming tapered angles between 5 to 15 degrees, the Equation 2.5 provides an estimated of pipette aperture. This method allows fast pipette aperture estimation and qualitative comparison between pipettes of different batches. Ion conductance determinations are often convenient for the SECCM user because of the familiarity with the electrochemical setup required.



**Figure 2.10:** Schematic of setup for ion conductance measurement to determine pipette aperture

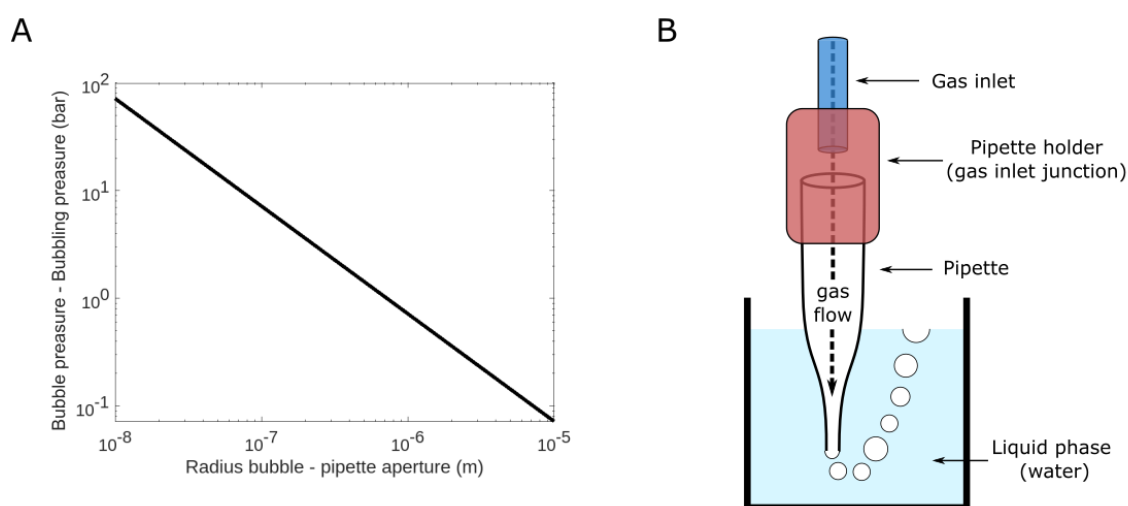
#### 2.2.2.2.3 Bubbling point determination

Passing a gas through the pipette aperture can generate gas bubbles inside a liquid phase, if the gas pressure is high enough. As described by the Young-Laplace effect for spherical bubbles, the phase pressure differences ( $\Delta P$ ) can be related to the surface tension between the two phases ( $\sigma$ ) and the radius of the bubble ( $r$ ),<sup>18</sup> expressed as:

$$\Delta P = \frac{2\sigma}{r} \quad (\text{Eq. 2.6})$$

Based on Equation 2.6, in Figure 2.11 A the relation between the bubble radius and the pressure difference is shown for the air bubble in water; however, other solvents can be used as the liquid phase with methanol being a popular choice.<sup>18</sup> Micro- nano-scaled pipettes will generate bubble

sizes similar to their aperture when immersed in a liquid phase.<sup>18</sup> Estimate of pipette aperture can then be obtained from the gas pressure at which a pipette starts to produce bubbles when immersed in a liquid.<sup>19</sup> Figure 2.11 B shows a schematic of the setup required to conduct bubbling pressure measurement. As shown in Figure 2.11 B, the pipette holder acts as a junction between the pipette and the gas line. First, the pipette is inserted into the liquid phase (commonly water) without any gas flow or pressure applied. Then, the gas pressure is gradually increased as long as no bubbling is observed from the pipette ends. The bubbling pressure is determined as the pressure at which bubbles that form at the end of the pipette can be observed. Notice that the bubbling pressure for pipettes below 1  $\mu\text{m}$  radius is in the few bar range, as shown in Figure 2.11 A. Therefore, the bubbling point determination of SECCM probes requires a pipette-to-gas line clamping setup that can withstand these high pressures.



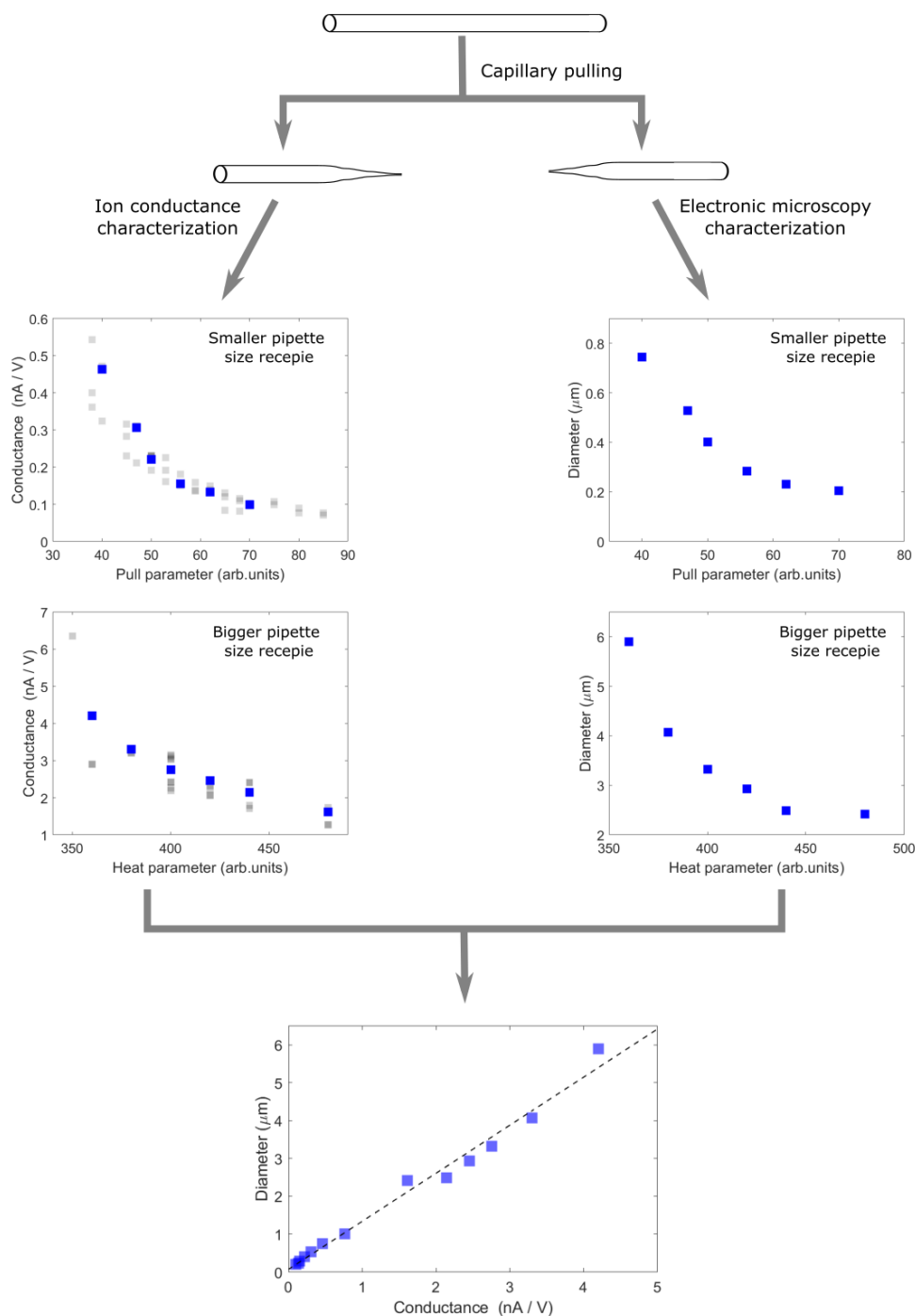
**Figure 2.11:** Pipette aperture size determination via the bubbling point method. **A)** Pressure of an air bubble in a water phase (surface tension of  $72 \text{ mN m}^{-2}$  at  $298\text{K}$ ) as a function of its size, determined using the Young-Laplace effect. **B)** Schematic of the setup to measure the bubbling point and determine the pipette aperture.

#### 2.2.2.2.4 Combination of pipette characterisation methods.

The ion conductance or bubbling point methods are fast to perform and provide precise measurement. However, both methods do not provide a direct measurement of pipette geometry, but rely on the usage of physical models to derive the pipette aperture. As a result, pipette geometry determinations may have a lack of accuracy, despite the good precision of the measurement. The accuracy of ion conductance or bubbling point methods can be optimised if complemented with electron microscopy, which provides direct determination of pipette geometry with the expense of being more complex and time consuming.

## Chapter 2

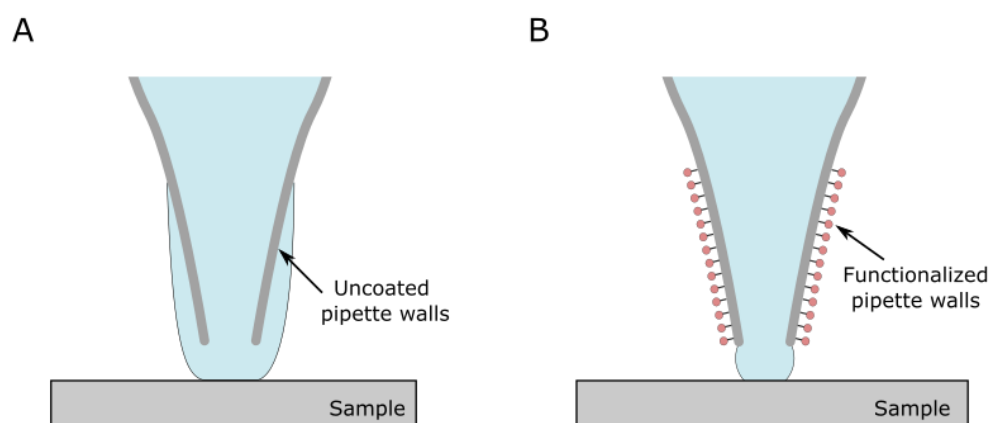
Notice that two pipettes with the same aperture (a pipette pair) are generated in a single capillary pull. If one pipette is characterised via an indirect determination method, *e.g.* ion conductance, and the other pipette via a direct determination method such as electron microscopy, both determinations can be correlated. By characterising multiple pipettes pairs of different geometry by direct and indirect methods, trends between pipette aperture, capillary pulling condition and indirect method observation can be related, as shown in Figure 2.12. An empirical equation can be derived by polynomial fitting, as shown in Figure 2.12 for ion conductance observation and pipette aperture determination. After this correlation, pipette aperture determination by ion conductance can provide fast, accurate and precise determination of pipette aperture.



**Figure 2.12:** Diagram illustrating the combination of ion conductance and electron microscopy measurement for pipette aperture size determination. From a single capillary pull two pipettes (a pipette pair) with same aperture are obtained. The point represented in blue corresponds to a dataset of pipette pairs; one pipette is characterised by ion conductance (left) and the other by electron microscopy (right). Pipette pair characterisation enable correlation of both measurements and derivation of an empirical equation via polynomial fitting, as shown in the bottom graph. The points represented in grey illustrate the trend and dispersion of ion conductance measurement for multiple pipettes pulled with different pulling parameters. The graphs display a dataset obtained as part of this thesis work.

### 2.2.2.3 Pipette hydrophobic functionalization

The pipette material, either borosilicate or quartz glass, is typically hydrophilic materials that, due to surface tension forces, can cause wetting of the external size of the pipette during the formation of the SECCM droplet cell,<sup>20</sup> as shown in Figure 2.13 A. The distorted droplet cell produced by this phenomenon changes the mass transport, leading to complex data interpretation of the electrochemical response, and causes inconsistent droplet cell size and leakage of the electrolyte solution from the pipette to the sample surface. To enhance the stability of the droplet cells, it is possible to apply a hydrophobic coating on the outside of the pipette,<sup>7</sup> as shown in Figure 2.13 B. The external hydrophobic coating is achieved by immersing the pipette in a solution that contains a hydrophobic functionalisation agent, while a gas flow is passed through the pipette, ensuring that the solution only contacts outside of the pipette.<sup>21</sup> The setup necessary is the same as necessary for the bubbling point determination, Figure 2.11 B. In this thesis, dichlorodimethylsilane is used as a hydrophobic functionalisation agent (diluted 1/20 in chloroform).



**Figure 2.13:** Effect of pipette functionalisation on the shape of the droplet cell. **A)** Schematic of a droplet cell distorted due to the wetting of the external pipette walls. **B)** Schematic showing that a hydrophobic coating on the external pipette walls promotes a stable and confined droplet cell.

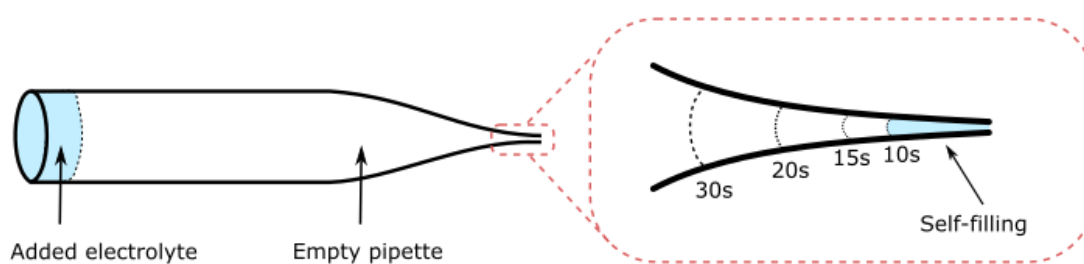
### 2.2.2.4 Filling the pipette with electrolyte solution

The preparation of the SECCM probe involves filling the pipette with electrolyte, creating a continuous solution from the SECCM droplet cell to the QRCE. This task is often performed with the help of a syringe and a micro-filler, a flexible needle with diameter small enough to be inserted from the open end of the pipette. However, the small diameter of pipetted taper region limits the access from the micro-filler to the end of the pipette. Instead, the tapered end of the pipette is self-filled due to the high hydrophilicity of pipette material (glass, borosilicate, quartz, etc.).

The self-filling process is not very easily controlled by the user. If electrolyte solution is inserted with the micro-filler directly into the taper end, the self-filling processes might occur too abruptly,

trapping gas bubbles in the pipette taper end. Gas bubbles should always be avoided, as they interrupt the conductivity of the solution. The use of a desktop optical microscope (with x10 magnification) is essential to evaluate the adequate filling of the pipettes. From my experience developed during the thesis, gradual self-filling decreases the chances of bubble formation. For gradual self-filling, a small droplet of electrolyte solution is inserted into the open end of the pipette, as shown in Figure 2.14. After a waiting roughly 30 seconds, a progressive self-filling of the tapered end without bubbles is observed.

The self-filling process occurs because of the high hydrophilicity of glass. However, any surface that is exposed to the atmosphere becomes covered by adsorbed hydrocarbons in a few hours or days, significantly reducing the hydrophilicity of the surface.<sup>22-25</sup> Then, the hydrophilicity of the pipette changes over time. From my experience, pipettes preserved in a closed container (as for instance, a Petri dish) hold good self-filling behaviour for about two weeks from their pulling time. Pipettes older than two weeks might present an inconsistent or non-self-filling process in the tapered region, resulting in gas bubble formation or the impossibility of filling the pipette completely.



**Figure 2.14:** Schematic showing the self-filling processes of the tapered end of the pipette. The electrolyte is added in the pipette open end, and the tapered end is self-filled. Maximised image showing that filling takes several seconds to complete.

### 2.2.2.3 The QRCE

After the pipette is filled with the electrolyte solution, the RCE can be inserted through the open end of the pipette to complete the assembly of the SECCM probe. In case of using an unprotected wire as quasi reference counter electrode (QRCE), such as chloridized silver wire or a PdH<sub>2</sub> wire, some measures should be taken in order to not compromise the stability of the QRCE and not induce contamination of the QRCE into the solution.<sup>4,26</sup> The insertion of the QRCE should be carefully done without scraping the wire against the walls of the pipette which can scratch the QRCE material off.<sup>4</sup> It is recommended to maximise the distance between the QRCE and the aperture of the pipette, thus even in case of small solution contamination, the electrolyte solution around the tapered region of the pipette and droplet cell remains pristine for as long as few hours.<sup>4,26</sup>

From the experience generated in this thesis, it is more convenient to first mount the filled pipette on the pipette holder of the SECCM equipment, then make electrical connection with QRCE and last step insert the QRCE gently.

In this thesis, an Ag/AgCl no-leak RCE and two types of QRCE, Ag/AgCl and Pd-H<sub>2</sub> wires, have been used. Ag/AgCl wire QRCE is self-fabricated by immersing an Ag wire in a commercial bleach solution for 2 minutes and then rinsing with DI water. The bleach forms an AgCl coating around the wire, as shown in Figure 2.1 B. When the Ag/AgCl wire is placed inside the electrolyte filled pipette, the Ag/AgCl wire is in direct contact with the electrolyte solution, thus it is usually necessary that the solution contains diluted Cl<sup>-</sup> ions for achieving the  $\text{Ag} + \text{Cl}^- \rightleftharpoons \text{AgCl} + \text{e}^-$  equilibrium. The presence of Cl<sup>-</sup> ions in the electrolyte solution does not suit all electrochemical experimental designs. For instance, Cl<sup>-</sup> ions can cause corrosion processes on many metal surfaces under anodic conditions. A commercial Ag/AgCl no-leak electrode (Innovative Instrument Ltd., commercial code LF-1-45) specially designed for fitting into pipettes or capillaries (outer diameter of 0.5 mm) was used in this thesis as RCE for the situation where Cl<sup>-</sup> needs to be avoided. The few commercially available Ag/AgCl no leak electrodes always have a bulky rigid connection that sits on top of the pipette. Unfortunately, this connection element makes commercially available no-leak electrodes not suitable for SECCMs with vertical aligned optical systems (see Section 2.2.1.1). Therefore, if SECCMs are operated with vertically aligned optical systems, a wire QRCE is the suitable option.

For SECCM measurement in an acidic electrolyte, a Pd-H<sub>2</sub> wire was used as a QRCE. Pd-H<sub>2</sub> QRCE are self-prepared and requires a conditioning step. For that, the Pd wire and a Pt counter electrode are immersed in acidic electrolyte solution (same concentration as used in the SECCM measurement) and a -3V bias is applied between these electrodes for 5 minutes.<sup>3</sup> The Pd wire acts as a cathode and the Pt counter electrode as anode. This process forces protons in solution to intercalate inside the Pd, resulting in the Pd wire being "charged" with protons. When the wire is placed inside the filled pipette, part of the 'charged' protons in the Pd wire are realised forming H<sub>2</sub> micro-bubbles. On the surface of the Pd-wire it is achieved the equilibrium  $\text{Pd} - \text{H}_x \rightleftharpoons \text{Pd} + \text{H}_2 + \text{e}^-$ .

In summary, achieving good SECCM probes requires optimised pipette geometry and careful pipette pulling. Once the pipette geometry is established, it is recommended to plan the SECCM experiments so that the pipette pulling, pipette functionalisation, and SECCM measurements are carried out within the same day. This ensures pristine pipette hydrophilicity on the inside walls for a good electrolyte self-filling of the pipette tapered end. Next, the correct RCE or QRCE for the desired electrolyte must be used, which may include QRCE preconditioning processes if necessary. During SECCM operation, evaporation occurs from the droplet cell, which can cause precipitation of the electrolyte salts; therefore, low electrolyte concentrations are often used.



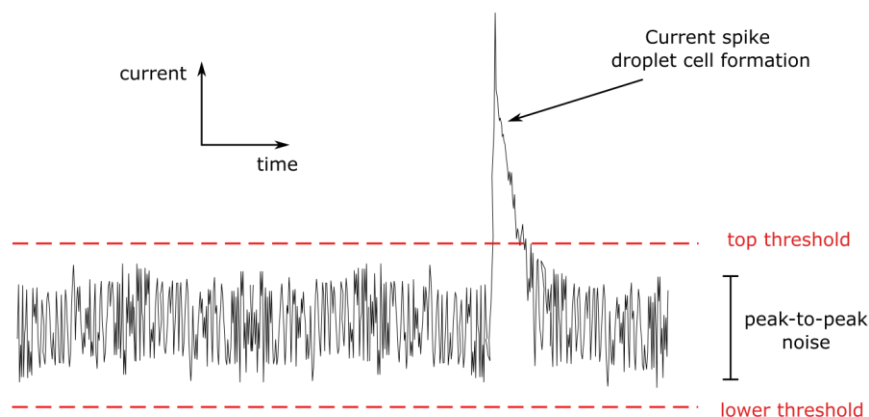
### 2.2.3 SECCM operation methods

Previous method sections have discussed the instrumental and signal processing aspects of SECCM. This section introduces the procedures for setting and operating the SECCM equipment. The following subsections explain the pipette approach and droplet cell formation procedure, electrochemical mapping procedure, and the procedure for carrying single nano-entity electrochemistry with SECCM. The user roles during SECCM operation are described in the last subsection.

#### 2.2.3.1 Pipette approach and droplet cell formation procedures

To perform an electrochemical measurement with SECCM, a droplet cell needs to first be formed on the surface. To form the SECCM droplet cell, the SECCM probe is approached perpendicularly towards the surface at a constant speed (typically 100 nm/s) until the droplet contacts the underlying surface. Note that there is no direct contact between the pipette and the sample surface during SECCM measurements. Thus, the droplet cell forms when the pipette is at a distance of around one pipette aperture radius from the surface.<sup>7</sup> Because a region of the sample surface becomes wetted upon the formation of the droplet cell, a double layer is immediately formed at the newly created interface, generating a current spike. The position of the pipette at which the droplet cell is formed is detected by the current spike, which triggers a feedback loop to immediately stop the movement of the pipette. Therefore, during the pipette approach, the software code continuously evaluates the current response and uses a current threshold to determine whether the current spike has been produced or not.

The current spike generated by droplet cell formation is small in magnitude and short in time, typically arising from the double layer charging of a surface of a  $\mu\text{m}$  size area. As a consequence, the current thresholds need to be set close to the current background noise signal, as shown in Figure 2.15. If the current threshold is set far beyond the background noise levels, the current spike may not reach the threshold and may not activate the “stop-approach” feedback loop, resulting in the pipette crashing into the electrode surface. Incorrect current threshold values are a common cause of pipette crashing. Decreasing the open circuit noise levels allows us to set a lower current threshold that favours detection of the current spike. However, reducing noise levels via decreasing the sampling frequency (*i.e.*, averaging points over longer times) might not be beneficial, as the short duration current spike of double layer formation can be lost. It is possible to increase the magnitude of the current spike by enlarging the double layer formation process, either by applying a potential during the approach or by utilising larger pipette apertures that increase the area of the droplet cell. After successful droplet cell formation, the pipette movement is stopped and the pipette position is maintained during the course of subsequent measurements.



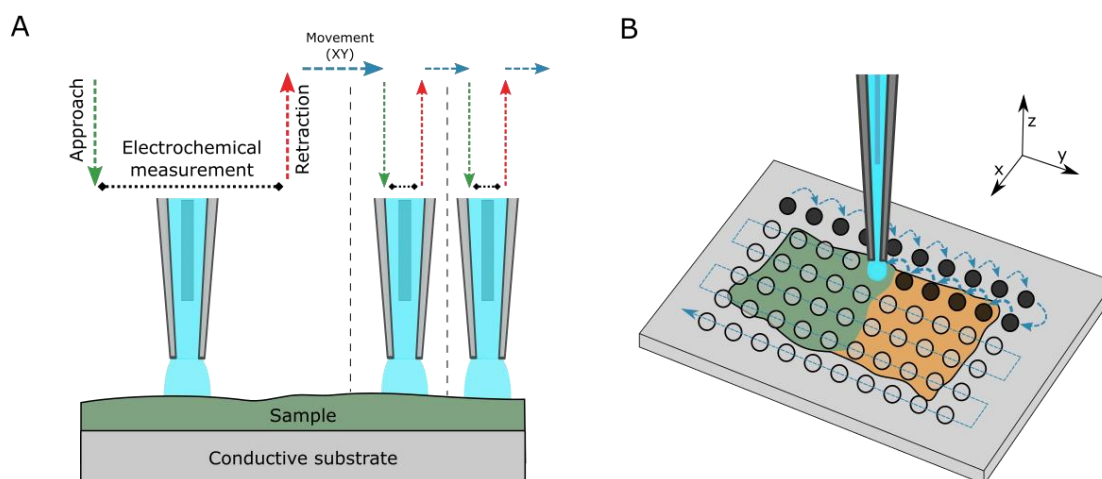
**Figure 2.15:** Current trace during pipette approach showing the current threshold setting above and below background noise. The current trace has a current spike generated upon droplet cell formation that is greater than the threshold, leading to a stop on the pipette approaching movement.

### 2.2.3.2 Electrochemical mapping procedure

SECCM can perform electrochemical measurements at multiple points on the surface of the sample. Measurement of electrochemical responses at multiple points and their correlation with the XY position is known as electrochemical mapping. As shown in Figure 2.16 A, the SECCM operation mode can be automated by software, repeating point-by-point the commands to approach the pipette, perform electrochemical measurements, retract the pipette, and move to new XY positions. Usually, electrochemical mappings are performed defining an array of points on the sample surface, as shown in Figure 2.16 B. One of the main advantages of SECCM compared to other EC-SPM techniques is that the surface is not exposed to electrolyte or potential differences prior to electrochemical measurement. Therefore, each of the responses collected in an electrochemical mapping corresponds to a pristine sample surface. Another advantage is that SECCM usually leaves a small residue of dried electrolyte on the sample surface, this being a footprint of the area contacted with the droplet cell. Using complementary microscopy techniques (typically AFM or SEM) the droplet cell residues can be imaged, allowing us to determine the exact location of each measurement.

The resolution of the mapping depends on the probe size which determines the minimum distance between grid points. To always measure uncontacted sample surface and maximise resolution, the spacing between points should be slightly larger than the diameter of the droplet cell. This prevents the formation of droplets on previous droplet cell residues, which can cause droplet cell instability. It is common practise to establish a spacing between points of at least  $\times 1.5$  of the expected droplet cell size.

Like other SPM techniques, the size of the electrochemically mapped areas is often limited by the time and resolution of the measurement, rather than by the capabilities of probe displacement of the SECCM equipment. For example, a common SECCM size grid of  $20 \times 20 \mu\text{m}$  with a relatively low lateral resolution of  $2 \mu\text{m}$  (*i.e.* grid spacing of  $2 \mu\text{m}$ ) requires measuring at 100 individual points. Taking into account that 30 seconds are spent per point, the total mapping time would be about 50 minutes. The same measurement with a larger grid size of  $40 \times 40 \mu\text{m}$ , or a greater lateral resolution of  $1 \mu\text{m}$ , implies measuring 400 points and more than 3 hours of measurement. Long SECCM electrochemical mappings are complex because the electrolyte solution evaporates from the pipette and pipette functionalisation becomes affected by electrolyte, which might result in droplet cell instability. The overall measurement time can be minimised by reducing the time spent per point. Common practises involve utilising faster approaching rates (for instance,  $1000 \text{ nm/s}$  instead of the safer  $100 \text{ nm/s}$ ), decreasing the distance the pipette is retracted between points, or setting a fast XY displacement speed (for instance,  $20 \mu\text{m/s}$ ). Note that faster pipette displacements often come at a higher risk of crashing the pipette. Another possibility is to design electrochemical measurements of a shorter duration if the experimental requirements allow. For instance, the voltammetry experiment can be shortened by utilising faster scan rates, decreasing the potential window, or implementing linear sweep voltammograms instead of cyclic voltammograms. A SECCM electrochemical mapping procedure optimised for short time duration can archive  $< 5 \text{ s}$  per point.<sup>3</sup> Finally, note that mapping larger sample surface areas increases the risk of encountering a not pristine region of the sample surface that might cause pipette crashing or droplet cell leakage.

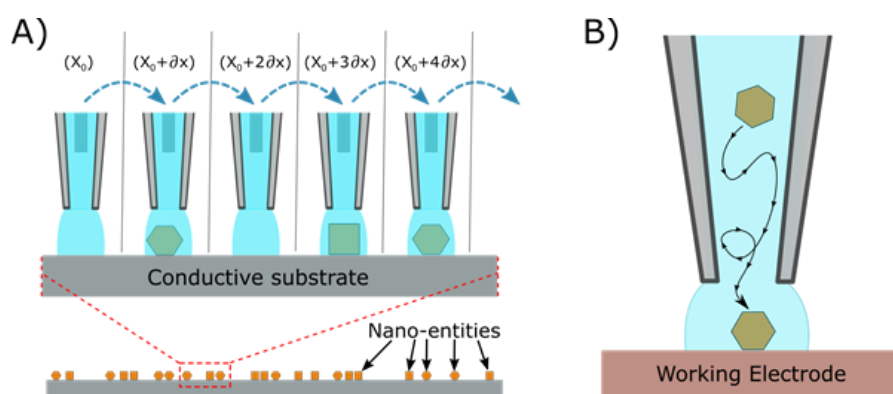


**Figure 2.16:** Scheme of electrochemical mapping. **A)** Showing the command sequences for each of the points probed. **B)** Grid of points over the sample surface illustrating the isolation of the electrochemical response of two different sample domains, displayed in green and yellow colouring. The conductive inert substrate is displayed in grey colouring. The black circles illustrate grid points that have been already measured, while the clear circles indicate following programmed grid points that will be measured along the mapping.

## 2.2.3.3 Single nano-entity electrochemistry with SECCM

The small droplet cell architecture of SECCM and the electrochemical mapping approach can be used to enclose individual nano-entities deposited on a surface,<sup>27</sup> as shown in Figure 2.17 A. However, to adequately isolate nano-entities with the SECCM droplet cell, the nano-entities must already be spatially isolated over the conductive surface. Therefore, the type of measurement shown in Figure 2.16 A, requires a prior optimisation of the nano-entity deposition processes. In this thesis, drop-casting of nano-entity colloidal solution is used to deposit isolated nano-entities. The substrate also plays a key role and requires to be conductive (for single barrel pipettes), to present a roughness smaller than the nano-entity characteristic size, and to be electrochemical inert (*i.e.*, not induce an electrochemical response at the electrochemical conditions the nano-entity does).

Single nano-entity electrochemistry can also be performed for entities dispersed within the electrolyte solution of the SECCM probe, as shown in Figure 2.17 B. The tapered end of the pipet acts as a channel that restricts the movement of the dispersed entities; thus, upon the formation of the droplet cells, individual entities can enter the droplet cell and interact with the electrode surface. The same principle is used for stochastic collision electrochemistry with UMEs. Performing stochastic collision electrochemistry with SECCM is often more complex than with a UME-based setup. However, SECCM allows for the use of any flat conductive surface as a working electrode. Also, note that the UME manufacturing procedure often restricts the variability in the geometry, material, size, and type of electrical connections. Then, SECCM allows for a complementary stochastic electrochemistry technique suitable for experiments which require custom electrochemical instrumentation.<sup>27</sup>



**Figure 2.17:** Scheme of two different methods for single nano-entity electrochemistry with SECCM **A)** Characterisation of single entities isolated over a substrate via electrochemical mapping **B)** Characterisation of single entities dispersed in the SECCM probe via stochastic collision electrochemistry.

#### 2.2.3.4 Role of the user

Like in other microscopy, spectroscopic or SPM techniques, the SECCM user must supervise the execution of multiple tasks and have an active role during the measurement. Among following the methods description, the user must be capable of evaluating if the data or information being collected is sensible or if otherwise, adjusting instrumentation parameters or changing methods is required. SECCM instrumentation provides information as current trace, X-Y-Z piezo position and optical images. The SECCM user must be able to evaluate the quality of the experiment based on the live information displayed, as well as perform fast data analysis and/or plotting while operating the equipment. A popular analogy would be the operation of an optical microscope; the user is constantly observing the image generated and adjusting focus, brightness, contrast, filters, etc. until the final image acquisition. In Table 2.4 provides a brief summary of the information the SECCM user should expect and account for during the SECCM operation, classified according to the operation procedures described in the previous sections.

The detection of unexpected responses during the SECCM operation is common, especially when implementing a new experimental procedure or testing new pipette geometries. The user should evaluate the experimental setting used and modify the methods accordingly. Note that different SECCM equipment might provide different information to the user while operating; consequently, there is no single procedure to evaluate SECCM operation.

**Table 2.4:** Summary of the expected information displayed during measurement and/or key feature to evaluate in the saved dataset by the user during SECCM operation.

<b>Pipette approach</b>	<b>Current trace</b>	Constant unfluctuating current with constant noise levels, until droplet cell formation, then an abrupt current spike from droplet cell formation should be observed, see Figure 2.15. The current spike should be abrupt, any sign of prior smaller peaks or prior current fluctuation in current trace is strong indicative of incorrect threshold setting (see Figure 2.15) or pipette crashing. The current spike should only present a fast exponential decay shape over time. No other current response, but an exponential decay to the same background current should be observed after droplet cell formation. The presence of other spikes or current fluctuations is indicative of droplet cell instabilities.
	<b>X-Y-Z position</b>	Fixed X-Y position values and Z position changing at a constant pace during the approach. The Z position should be exactly stopped once the current spike is observed with a minimal time delay between those. On observation of the current spike, X-Y-Z should remain a fixed value.
	<b>Optical image</b>	During approach pipette displacement is slow and of a few $\mu\text{m}$ , thus any optical change would be difficult to observe. However, if the user observed any vibration or shake on the pipette, it is indicative of the pipette crashing with the sample surface.
<b>Electrochemical measurements while droplet cell is formed</b>	<b>Current trace</b>	Smooth current changes and transitions without the presence of any abrupt and sharp peak. The presence of sharp peaks is indicative of droplet cell leaking.
	<b>X-Y-Z position</b>	Fixed X-Y-Z values. Considering the pipette tip sits at approximately one pipette aperture radius distance from the sample surface, evaluate if the Z-drift during the EC measurement is smaller than the pipette aperture.
	<b>Optical image</b>	No visual changes are expected. If around the pipette end there are changes in colouring (often darker) is indicative of droplet cell leaking.
<b>Electrochemical mapping</b>	Most of the information observed for a single point should be reproduced at the rest of the points of the grid, unless the expected differences due to sample heterogeneity. Any other distinct information or features on current, piezo position, or optical image are indicative of inconsistent droplet cells. For a flat sample, the Z distance at which droplet cell is formed should be equal in each point, if the Z distance increases it is an indication of pipette crashing. If the sample presents large morphological features or the sample surface is tilted with respect to the XY movement plane of the probe, the Z distance of droplet cell formation is then expected to vary.	

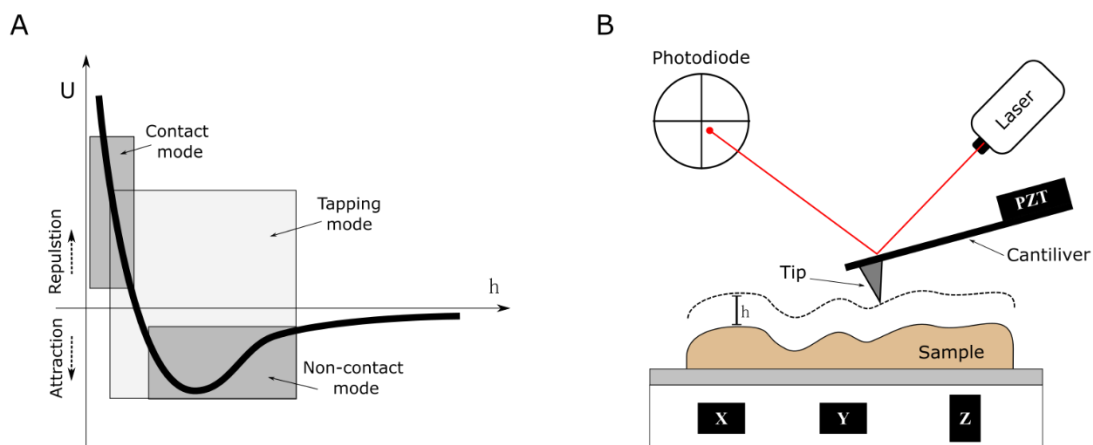
## 2.3 Surface morphology characterisation

SECCM provides detail electrochemical information on discrete surface points. From SECCM mapping, it is also possible to generate maps of the sample topography, but typically at low spatial resolution. As a consequence, to resolve surface morphology with nanometre resolution, other characterisation techniques such as atomic force microscopy (AFM) or Scanning electron microscopy (SEM) are employed.

### 2.3.1 Atomic Force Microscopy (AFM)

AFM is an SPM base technique that can measure surface profiles. AFM typically has a subnanometre resolution on the Z axis and a resolution of a few nanometres on the X and Y axis.<sup>28</sup> The common SPM nature of AFM and SECCM facilitates sample compatibility with both techniques, providing complementary information. Indeed, the hardware of AFM and SECCM can be mostly shared, with the exception of the probe and electrochemical signal processing elements.

The AFM working principle consists of placing a sharp tip that sits at the end of a cantilever at a very close proximity to the surface. The type of interaction between the tip and the sample depends on the distance between the tip and the sample surface, as shown in the distance-interaction curve shown in Figure 2.18 A. Non-contact mode imaging occurs when the tip is positioned at a distance for electrostatic attraction, contact-mode when the tip sits in the electrostatic repulsion regime, and tapping mode if the tip both attractive and repulsive regimes. For non-contact and tapping mode, the cantilever oscillating at its resonance frequency and the electrostatic attraction or repulsion forces which depends on tip/surface distance affect the oscillating amplitude or phase. The position and oscillation of the tip are constantly monitored; thus, any change in the amplitude and/or phase is detected and used as input for a tip repositioning feedback loop. Usually, for imaging purposes the feedback loop of non-contact and tapping mode is set to ensure a constant distance between tip and surface along the scan. In this manner, when the tip moves across the surface (XY) and encounters morphological features (Z), the tip copies the profile, obtaining morphological information, and preventing the tip from crashing, as shown in Figure 2.18 B. In contact mode, the probe does not oscillate and remains constantly in contact with the sample surface. The different surface morphology deflects the cantilever, which is being monitored.<sup>28</sup> In this thesis, non-contact mode AFM with amplitude feedback is typically used to map sample surfaces.



**Figure 2.18:** Schematic of atomic force microscope (AFM) working principles. **A)** Diagram of the repulsion and attractive forces as a function of the tip-sample distance and the corresponding regime of AFM scanning modes. **B)** Schematic of AFM instrumentation with main components: the cantilever with the scanning tip at its end and piezo actuator for controlling cantilever oscillation, the laser and photodiode which measure cantilever oscillation and deflection, and the piezo actuator that provides X-Y-Z displacement. Tip profile along the scan in constant distance ( $h$ ) mode indicated with a dashed line.

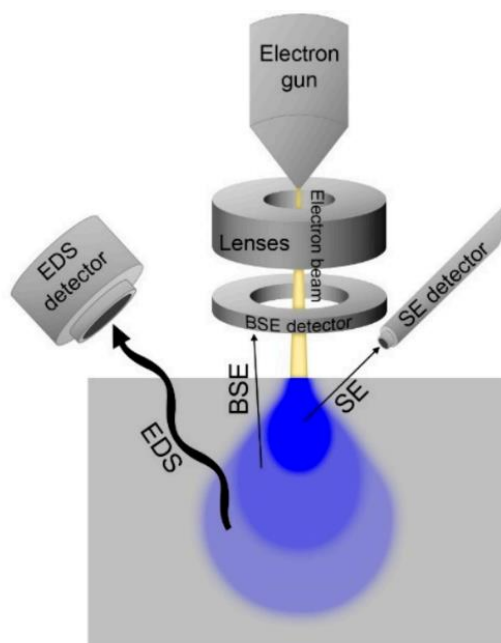
### 2.3.2 Scanning electron microscopy (SEM)

Scanning electron microscopy (SEM) is a type of microscopy that provides surface imaging with topographical information with nanometre resolution. As shown in Figure 2.19, SEM uses an incident electron beam to scan the sample surface while one or multiple detectors, which are positioned over the sample surface, collect the electrons resulting from incident beam and sample interaction. The electrons of the beam are generated from an electron source, typically a thermionic or field emission source. After that, the electrons are accelerated to a given energy (typically 1 to 10 keV), the electron beam is controlled by a set of electromagnetic lenses that allow focus control, aberration correction, etc.<sup>29</sup>

SEM can use backscattered and secondary electrons for image generation. Secondary electrons (SE) originate from inelastic interaction with the near-surface atoms; therefore, they are depth sensitive and provide detailed information about sample topography. The backscattered electrons (BSE) originate from elastic scattering within an interaction volume. The elastic scattering depends on the atomic number, and therefore BSE provides a great contrast on surface composition. On the other hand, BSE are less sensitive with depth and offer less contrast with topography than the SE. For morphological characterisation of an SECCM sample, both types of imaging results are useful; thus, BSE provides greater contrast with droplet cell residue, and SE provides greater topographical detail of the sample nanostructure.



The electron beam interaction with the sample surface can knock out electrons from the inner shells of the atoms, which generate the outer shell atoms to relax by emitting X-ray radiation. X-ray emission can be detected and provides spectroscopic information about the atomic number of sample atoms. Spatial information about the element composition of the sample can be given if the electron beam scans the sample while X-rays are collected.<sup>29</sup> This technique is called energy dispersive X-ray analysis, often abbreviated EDX or EDS, and has been used for element characterisation in this thesis.



**Figure 2.19:** Scheme of SEM and EDS. The illustration shows the different instrumentation elements and different types of interaction and their interaction volume. Reproduced with permission from Giurlani, W. *et al.*<sup>30</sup>

## 2.4 Finite element simulation for diffusive mass transport

The transport of diluted species in solution to the electrode surface needs to be understood to study the electrochemical signals, as detailed in the Introduction chapter, Section 1.5.3. Mass transport can be described with the Nernst-Planck differential equation. SECCM, and other nano-electrochemical systems, present complex geometries that do not allow for analytical resolution of the mass transport differential equations. Instead, numerical methods can be used to approximate mass transport phenomena. Modern PCs offer great computational power and offer dedicated software to facilitate numerical approximation calculation tasks. The following sections detail how the finite element simulation method can be used for approximating mass transport in SECCM experiments.

### 2.4.1 Principle of finite element simulation method

The numerical resolution of multivariable differential equations (DE) can be approximated if the domains along which the variables are described are discretised, *i.e.* if the range of values a variable can take within a system geometry and boundary conditions is defined. The finite number of elements generated in the domain allow to approximate the DE at each element with other functions which have more facile numerical solution.

Taking a simple example, the concentration profile,  $c$ , at the region near the electrode surface for a system dominated by linear diffusion transport is often describe as 1D system (also described as Equation 1.51 in Introduction chapter) as:

$$c(z, t) = c_i^0 \operatorname{erf} \left[ \frac{z}{2\sqrt{D_i t}} \right] \quad (\text{Eq. 2.7})$$

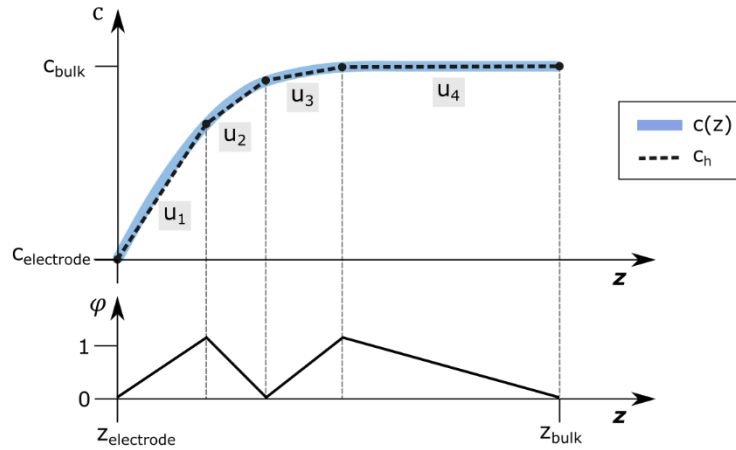
where  $c_i^0$  and  $D_i$  are constants. For a given time ( $t = \text{constant}$ ), the concertation profile is only dependent on the distance to the electrode surface  $z$ .  $c(z)$  function is plotted in Figure 2.20.  $c(z)$  can also be approximated by linear combination base function ( $c_h$ ):

$$c(z) \approx c_h \quad (\text{Eq. 2.8})$$

$$c_h = \sum_n u_n \varphi_n(z) \quad (\text{Eq. 2.9})$$

where  $\varphi_n(z)$  is the base function (represented black line in Figure 2.20) and  $u_n$  are the set of coefficient which approximates  $c_h$  to  $c(z)$ . To fulfil a good approximation of  $c(z)$  from  $\varphi_n(z)$ , the range along variable  $z$  is expressed become discretized, forming  $n$  elements and  $n + 1$  nodes. For each element, the  $u_n$  coefficient that approximate  $\varphi_n(z)$  to  $c(z)$  can be calculated. In this manner

function  $c_h$  is generated, as shown in Figure 2.20. Notice that the more nodes the greater the resolution and greater similarity between  $c_h$  and  $c(z)$ . A larger number of nodes also come at cost of more  $u_n$  coefficient to be calculated. On the other hand, not enough nodes and elements or inappropriate node distribution might lead to poor approximations. Therefore, the distribution of elements and nodes, also called mesh, needs to be adequate for approximating  $c_h$  to  $c(z)$ . This methodology is the basis of finite element methods (FEM), which can be extended over larger dimensional systems, and resolve spatial and time-dependent physical properties described by DE. Modern dedicated FEM software, such as COMSOL Multiphysics, has implemented advanced numerical methods resolution, which facilitate the user tasks to define the geometry, boundaries, and physical DE that govern the system, as well as various mesh, solver, and simulation parameters. It is out of the scope of the thesis to provide a general description of the FEM principles and mathematical formulation; the reader is referred to ref. 31-35 for further details on the implementation of FEM in electrochemical systems.



**Figure 2.20:** Representation of a linear combination base function  $c_h$  (black dashed line) approximating an analytical function  $c(z)$  (solid blue line).  $c_h$  is a linear combination of basis function  $\varphi_n$  (black solid line) with coefficient  $u$ .  $c(z)$  is the Cottrell equation at given time ( $t = ct$ ) represented between electrode surface ( $z_{electrode}$ ) and bulk solution ( $z_{electrode}$ ).

#### 2.4.2 Implementation of FES to resolve mass transport for SECCM probes

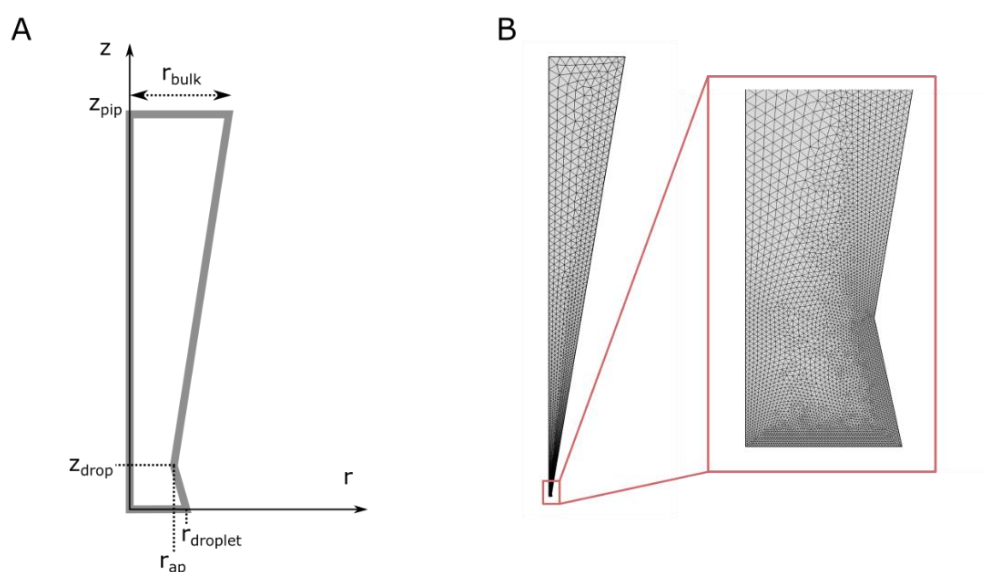
In this thesis, finite element simulations (FES) were performed on COMSOL Multiphysics software to solve the local concentration variation of electroactive species. Using FES, it has been possible to understand and quantify the electrochemical response observed during SECCM experiments. The time-dependent diffusional mass transport was simulated using Fick's second law of diffusion, which is given by:

$$\frac{\partial c}{\partial t} - D\nabla^2 c = 0 \quad (\text{Eq.2.8})$$

The cylindrical nature of the SECCM probe favours the implementation of 2D axisymmetric model geometry, which has been implemented on most of the FES shown in this thesis. The coordinates that define the geometry of the model are described in Table 2.5. A schematic of the resulting geometry is shown in Figure 2.21 A. Table 2.6 summarises the set of variables used to describe the model simulated, including geometry variables, mesh variables, transport of diluted species variables, and variables related to reaction kinetics.

**Table 2.5:** Cylindrical coordinates ( $r$  and  $z$ ) used to describe the SECCM probe boundaries in the finite element simulation and the description of the mass transport conditions for each boundary.

Boundary	$r$	$z$	Mass transport condition
Axisymmetric axis	$0 \rightarrow 0$	$0 \rightarrow z_{\text{drop}} + z_{\text{pip}}$	-
Bulk solution	$0 \rightarrow r_{\text{bulk}}$	$z_{\text{drop}} + z_{\text{pip}} \rightarrow z_{\text{drop}} + z_{\text{pip}}$	$c = c_{\text{bulk}}$
Pipette wall	$r_{\text{bulk}} \rightarrow r_{\text{ap}}$	$z_{\text{drop}} + z_{\text{pip}} \rightarrow z_{\text{drop}}$	$J = 0$ (No flux)
Droplet cell – air interface	$r_{\text{ap}} \rightarrow r_{\text{drop}}$	$z_{\text{drop}} \rightarrow 0$	$J = 0$ (No flux)
Working electrode (Sample active surface)	$r_{\text{drop}} \rightarrow 0$	$0 \rightarrow 0$	$J = v_{\text{net}} = k \cdot c$



**Figure 2.21:** SECCM axisymmetric model implemented in FES. **A)** Schematic showing the FES geometry boundaries and related variables. **B)** FES mesh generated for the geometric domain simulated. Magnification around the SECCM droplet cell, showing a greater mesh resolution.

**Table 2.6:** Summary of the variables used in finite element simulations of the SECCM probes.

Variable symbol	Description
$c$	Concentration of the diluted species
$c_{\text{bulk}}$	Concentration of the diluted species ( $c$ ) of the electrolyte the pipette is filled with.
$D$	Diffusion coefficient
$k$	Rate constant
$r_{\text{ap}}$	Pipette aperture radius
$r_{\text{bulk}}$	Radius of boundary domain with concentration equal to bulk concentration. $r_{\text{bulk}} = z_{\text{pip}} \cdot \tan(\alpha)$ .
$r_{\text{drop}}$	Droplet cell radius
$z_{\text{drop}}$	Droplet cell height – often $z_{\text{drop}} = r_{\text{drop}}$
$z_{\text{pip}}$	Height of pipette simulated – often $z_{\text{pip}} = 100 \cdot r_{\text{ap}}$
$\alpha$	Degrees of pipette tapered angle – often $10^\circ$

The mesh divides the simulation domain (the area contained within the geometrical boundaries imposed) into a finite number of elements. The mesh should distribute the elements according to the resolution requirements of the physical simulation. In this thesis, mass transport has been simulated accounting only for diffusive mass transport, and so the mesh must be optimised to provide greater density of element on the areas which present a greater concentration gradient. On SECCM probes, the region with a greater concentration gradient is the droplet cell. Thus, the upper part of the pipet acts only as a reservoir of species. To account for the greater concentration gradient regions, the geometric boundaries corresponding to the working electrode and droplet cell were set with a minimum mesh element size 1/100 of the droplet cell radius. The rest of the mesh is generated by tessellation processes, as shown in Figure 2.21 B.

The mass transport boundary conditions are summarised in Table 2.5. Briefly: the pipette wall and droplet cell-air interface have a no flux boundary; the domain defined as the bulk solution has constant concentration ( $c = c_{\text{bulk}}$ ) and allows flux of species; and the working electrode can have a species flux according to the reaction rate expressions derived in the Introduction Chapter, Section 1.5.2. The reaction rate equations, derived from the different electron transfer models, are described in detail in Chapters 4 and 5. As the initial condition, it is defined that the whole simulated domain has a concentration equal to the bulk solution boundary ( $c = c_{\text{bulk}}$ ).

## References

- 1 Bard, A. J. & Faulkner, L. R. *Electrochemical methods: fundamentals and applications*. 2nd edn, (John Wiley & Sons, Inc., 2001).
- 2 Vasile, M. J. & Enke, C. G. The Preparation and Thermodynamic Properties of a Palladium-Hydrogen Electrode. *J. Electrochem. Soc.* **112** (1965). <https://doi.org/10.1149/1.2423713>
- 3 Daviddi, E., Gonos, K. L., Colburn, A. W., Bentley, C. L. & Unwin, P. R. Scanning Electrochemical Cell Microscopy (SECCM) Chronopotentiometry: Development and Applications in Electroanalysis and Electrocatalysis. *Anal. Chem.* **91**, 9229-9237 (2019). <https://doi.org/10.1021/acs.analchem.9b02091>
- 4 Bentley, C. L., Perry, D. & Unwin, P. R. Stability and Placement of Ag/AgCl Quasi-Reference Counter Electrodes in Confined Electrochemical Cells. *Anal. Chem.* **90**, 7700-7707 (2018). <https://doi.org/10.1021/acs.analchem.8b01588>
- 5 Elgrishi, N. *et al.* A Practical Beginner's Guide to Cyclic Voltammetry. *J. Chem. Educ.* **95**, 197-206 (2017). <https://doi.org/10.1021/acs.jchemed.7b00361>
- 6 Compton, R. G. & Banks, C. E. *Understanding Voltammetry*. (World Scientific, 2018).
- 7 Ebejer, N. *et al.* Scanning electrochemical cell microscopy: a versatile technique for nanoscale electrochemistry and functional imaging. *Annu. Rev. Anal. Chem.* **6**, 329-351 (2013). <https://doi.org/10.1146/annurev-anchem-062012-092650>
- 8 Valavanis, D. *et al.* Hybrid scanning electrochemical cell microscopy-interference reflection microscopy (SECCM-IRM): tracking phase formation on surfaces in small volumes. *Faraday Discuss.* **233**, 122-148 (2022). <https://doi.org/10.1039/d1fd00063b>
- 9 Saha, P., Hill, J. W., Walmsley, J. D. & Hill, C. M. Probing Electrocatalysis at Individual Au Nanorods via Correlated Optical and Electrochemical Measurements. *Anal. Chem.* **90**, 12832-12839 (2018). <https://doi.org/10.1021/acs.analchem.8b03360>
- 10 Husain, M., Boudier, T., Paul-Gilloteaux, P., Casuso, I. & Scheuring, S. Software for drift compensation, particle tracking and particle analysis of high-speed atomic force microscopy image series. *J. Mol. Recognit.* **25**, 292-298 (2012). <https://doi.org/10.1002/jmr.2187>
- 11 Jiao, Y., Zhuang, J., Li, F., Zheng, Q. & Gao, Z. Analysis and improvement of positioning reliability and accuracy of theta pipette configuration for scanning ion conductance microscopy. *Ultramicroscopy* **224**, 113240 (2021). <https://doi.org/10.1016/j.ultramic.2021.113240>
- 12 Zhang, S., Li, M., Su, B. & Shao, Y. Fabrication and Use of Nanopipettes in Chemical Analysis. *Annu. Rev. Anal. Chem.* **11**, 265-286 (2018). <https://doi.org/10.1146/annurev-anchem-061417-125840>
- 13 Snowden, M. E. *et al.* Scanning electrochemical cell microscopy: theory and experiment for quantitative high resolution spatially-resolved voltammetry and simultaneous ion-conductance measurements. *Anal. Chem.* **84**, 2483-2491 (2012). <https://doi.org/10.1021/ac203195h>

- 14 Kececi, K., Dinler, A. & Kaya, D. Review-Nanopipette Applications as Sensors, Electrodes, and Probes: A Study on Recent Developments. *J. Electrochem. Soc.* **169** (2022). <https://doi.org/10.1149/1945-7111/ac4e58>
- 15 Perry, D., Momotenko, D., Lazenby, R. A., Kang, M. & Unwin, P. R. Characterization of Nanopipettes. *Anal. Chem.* **88**, 5523-5530 (2016). <https://doi.org/10.1021/acs.analchem.6b01095>
- 16 Rheinlaender, J. & Schaffer, T. E. An Accurate Model for the Ion Current-Distance Behavior in Scanning Ion Conductance Microscopy Allows for Calibration of Pipet Tip Geometry and Tip-Sample Distance. *Anal. Chem.* **89**, 11875-11880 (2017). <https://doi.org/10.1021/acs.analchem.7b03871>
- 17 Zhu, C., Huang, K., Siepser, N. P. & Baker, L. A. Scanning Ion Conductance Microscopy. *Chem. Rev.* **121**, 11726-11768 (2021). <https://doi.org/10.1021/acs.chemrev.0c00962>
- 18 Tognoni, E., Baschieri, P., Ascoli, C., Pellegrini, M. & Pellegrino, M. Characterization of tip size and geometry of the pipettes used in scanning ion conductance microscopy. *Micron* **83**, 11-18 (2016). <https://doi.org/10.1016/j.micron.2016.01.002>
- 19 Bowman, C. L. & Ruknudin, A. M. Quantifying the geometry of micropipets. *Cell. Biochem. Biophys.* **31**, 185-206 (1999). <https://doi.org/10.1007/BF02738172>
- 20 Shao, Y. & Mirkin, M. V. Voltammetry at micropipet electrodes. *Anal. Chem.* **70**, 3155-3161 (1998). <https://doi.org/10.1021/ac980244q>
- 21 Yule, L. C., Bentley, C. L., West, G., Shollock, B. A. & Unwin, P. R. Scanning electrochemical cell microscopy: A versatile method for highly localised corrosion related measurements on metal surfaces. *Electrochim. Acta* **298**, 80-88 (2019). <https://doi.org/10.1016/j.electacta.2018.12.054>
- 22 Yamamoto, T., Okubo, M., Imai, N. & Mori, Y. Improvement on hydrophilic and hydrophobic properties of glass surface treated by nonthermal plasma induced by silent corona discharge. *Plasma Chem. Plasma Process.* **24**, 1-12 (2004). <https://doi.org/10.1023/B:PCPP.0000004878.61688.4d>
- 23 Guo, W. *et al.* Effect of Airborne Hydrocarbons on the Wettability of Phase Change Nanoparticle Decorated Surfaces. *ACS Nano* **13**, 13430-13438 (2019). <https://doi.org/10.1021/acsnano.9b06909>
- 24 Kozbial, A., Zhou, F., Li, Z., Liu, H. & Li, L. Are Graphitic Surfaces Hydrophobic? *Acc. Chem. Res.* **49**, 2765-2773 (2016). <https://doi.org/10.1021/acs.accounts.6b00447>
- 25 Prydatko, A. V., Belyaeva, L. A., Jiang, L., Lima, L. M. C. & Schneider, G. F. Contact angle measurement of free-standing square-millimeter single-layer graphene. *Nat. Commun.* **9**, 4185 (2018). <https://doi.org/10.1038/s41467-018-06608-0>
- 26 Li, Y., Morel, A., Gallant, D. & Mauzeroll, J. Ag(+) Interference from Ag/AgCl Wire Quasi-Reference Counter Electrode Inducing Corrosion Potential Shift in an Oil-Immersed Scanning Micropipette Contact Method Measurement. *Anal. Chem.* **93**, 9657-9662 (2021). <https://doi.org/10.1021/acs.analchem.1c01045>
- 27 Wahab, O. J., Kang, M. & Unwin, P. R. Scanning electrochemical cell microscopy: A natural technique for single entity electrochemistry. *Curr. Opin. Electrochem.* **22**, 120-128 (2020). <https://doi.org/10.1016/j.coelec.2020.04.018>

- 28 Binnig, G., Quate, C. F. & Gerber, C. Atomic force microscope. *Phys. Rev. Lett.* **56**, 930-933 (1986). <https://doi.org:10.1103/PhysRevLett.56.930>
- 29 Vernon-Parry, K. D. Scanning electron microscopy: an introduction. *III-Vs Review* **13**, 40-44 (2000). [https://doi.org:10.1016/s0961-1290\(00\)80006-x](https://doi.org:10.1016/s0961-1290(00)80006-x)
- 30 Giurlani, W., Berretti, E., Innocenti, M. & Lavacchi, A. Measuring the Thickness of Metal Coatings: A Review of the Methods. *Coatings* **10** (2020). <https://doi.org:10.3390/coatings10121211>
- 31 Cutress, I. J., Dickinson, E. J. F. & Compton, R. G. Analysis of commercial general engineering finite element software in electrochemical simulations. *J. Electroanal. Chem.* **638**, 76-83 (2010). <https://doi.org:10.1016/j.jelechem.2009.10.017>
- 32 Vyroubal, P., Maxa, J., Kazda, T. & Vondrak, J. The Finite Element Method in Electrochemistry - Modelling of the Lithium-Ion Battery. *ECS Trans.* **48**, 289-296 (2014). <https://doi.org:10.1149/04801.0289ecst>
- 33 Dickinson, E. J. F., Ekstrom, H. & Fontes, E. COMSOL Multiphysics (R) : Finite element software for electrochemical analysis. A mini-review. *Electrochem. Commun.* **40**, 71-74 (2014). <https://doi.org:10.1016/j.elecom.2013.12.020>
- 34 Giaccherini, A. *et al.* Finite Elements Analysis of an Electrochemical Coating Process of an Irregularly Shaped Cathode with COMSOL Multiphysics®. *ECS Trans.* **64**, 1-8 (2015). <https://doi.org:10.1149/06435.0001ecst>
- 35 Lavacchi, A. *et al.* Cyclic voltammetry simulation at microelectrode arrays with COMSOL Multiphysics (R). *J. Appl. Electrochem.* **39**, 2159-2163 (2009). <https://doi.org:10.1007/s10800-009-9797-2>







# CHAPTER 3

## Single-Entity Electrochemistry at Microsecond Time Resolution

---

Stochastic collision electrochemistry requires high-resolution and high-bandwidth current amplification due to the low magnitude and short duration of single nano-entity current signals. Increasing the current amplifier bandwidth, however, leads to increased current noise levels, which in turn may obscure the current signal generated from stochastic collision electrochemistry experiments. The key to minimising current noise when operating at high bandwidth is to achieve an experimental design which minimises the input capacitance to the current amplifier. In this chapter, a new strategy is reported to minimise input capacitance to a current amplifier using a movable microscale electrochemical cell, formed at the end of a micropipette using a scanning electrochemical cell microscopy approach, to conduct electrochemical experiments in close proximity ( $\sim 300 \mu\text{m}$ ) to a custom-designed transimpedance amplifier. The electrochemical performance of the experimental design presented here is demonstrated via the electro-oxidation of single Ag nanoparticles, detected at unprecedented bandwidths of up to 1 MHz.

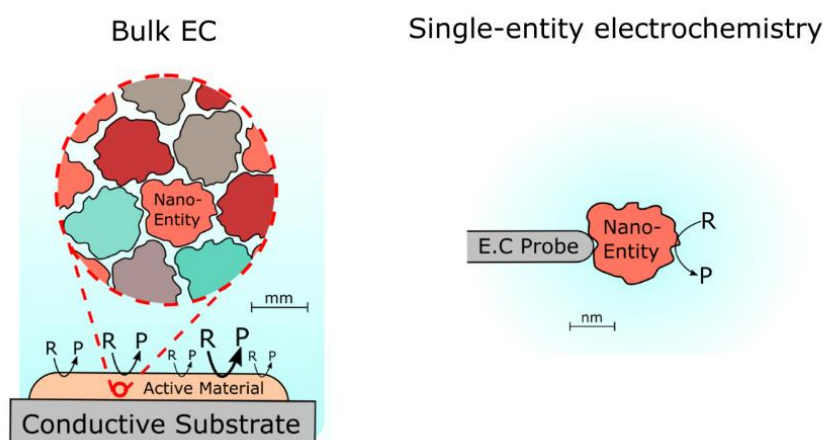
---

## 3.1 Introduction

### 3.1.1 Single-entity electrochemistry

Single-entity electrochemistry (SEE) refers to the study of the electrochemical response of individual objects or units, isolating a single-entity response by time or spatial constraints, or a combination of both. There are several reasons to pursue a single-entity approach in electrochemistry. First, the observed electrochemical response for any given bulk electrochemical system depends on the response of many individual entities, for instance, single molecules, single enzymes, single particles, single cells, etc. Thus, the measurement of the electrochemical response from single entities will provide information on how the individual entities respond as an ensemble, resulting in the observed bulk behaviour. Second, SEE provides fundamental insights into electrochemistry at the nanoscale and enables the development of further concepts and technologies. Third, SEE can provide a deeper understanding of the underlying chemical processes and underpin mechanistic understanding that might become hindered at the bulk scale, as proven in several recent publications.<sup>1</sup> An extensive discussion of the state-of-the-art in nanomaterial electrochemistry approaches and techniques can be found in Introduction, Section 1.3.

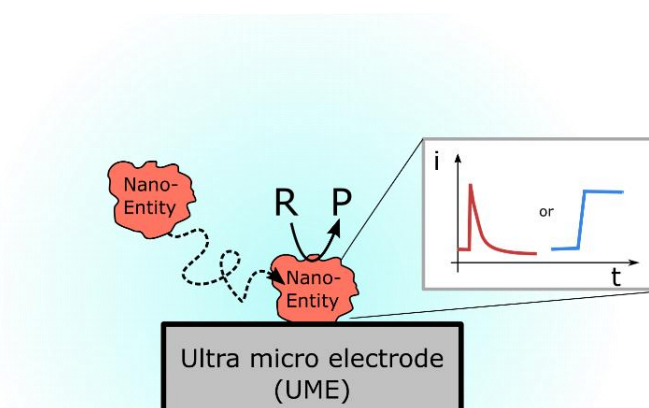
SEE characterisation has excelled in assessing the effect of heterogeneity within the individual entities which compose a system into the electrochemical response. Conventional ensemble-based electrochemical approaches average the electrochemical response over many entities, and in doing so obscure the effects of sample heterogeneity and the exact relationship between entity structure and its electrochemical activity. The key to unravelling these relationships is the development of SEE techniques, which aim at one single entity at a time, as illustrated in Figure 3.1. To date, this has been achieved most successfully using stochastic collision electrochemistry experiments.<sup>2-4</sup>



**Figure 3.1:** Schematic showing the relation between the number of entities measured in conventional ensemble base bulk electrochemical measurements (left) and single-entity electrochemistry (right).

### 3.1.2 Stochastic collision electrochemistry

In stochastic collision electrochemistry, the entities desired to characterise are dispersed and freely diffuse in solution; when they collide with the surface of a micro- or nano-scale electrode, they make electrical contact and induce an electrochemical response.<sup>2,5</sup> Due to the small electrode size (< 10  $\mu\text{m}$  diameter) and by controlling the concentration of the entities in solution, individual collision events can be separated in time. A schematic of a stochastic collision electrochemistry experiment is shown in Figure 3.2. This approach is one of the simplest experimental setups to achieve single-entity electrochemistry; moreover, it provides high throughput. Over 10's of seconds, the experimenter can measure 1000's of single entities, providing robust statistics while continuing to work at a single entity level.



**Figure 3.2:** Schematic of stochastic collision electrochemistry experiments showing a single nano-entity free diffusing that collides with an ultra-microelectrode, generating an electrochemical response.

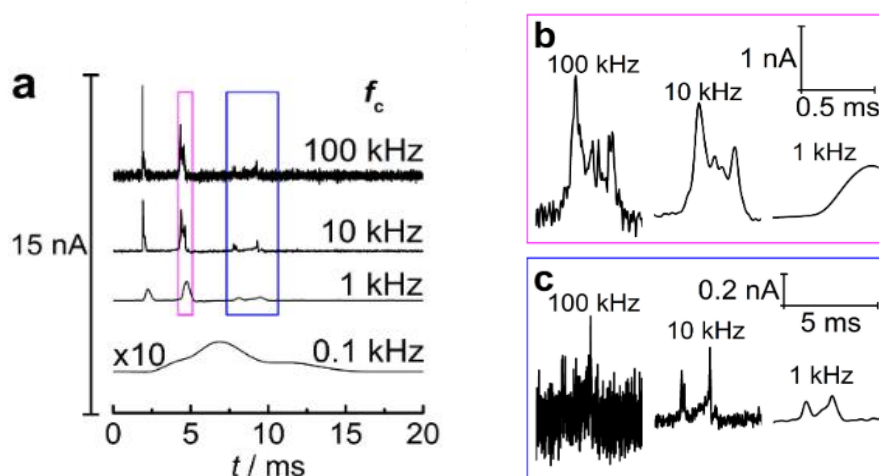
The stochastic collision electrochemistry approach is also known as nanoimpact electrochemistry<sup>6,7</sup> or electrocatalytic amplification<sup>8,9</sup> depending on the nature of the electrochemical signal. Examples include hydrogen evolution measured in single Pt nanoparticles and clusters,<sup>10</sup> reduction and oxidation of single Ag nanoparticles,<sup>11,12</sup>  $\text{H}_2\text{O}_2$  oxidation measured in single IrOx nanoparticles,<sup>13,14</sup> single collisions of toluene-in-water emulsion droplets,<sup>15</sup> oxygen reduction in single enzymes,<sup>16</sup> or the collision of single red blood cells with an electrode surface.<sup>17</sup>

### 3.1.3 Signal and resolution requirements for stochastic collision electrochemistry

In stochastic collision electrochemistry of nanomaterials, or for any other single-entity electrochemistry approach, the current signals generated are on the order of femtoamperes (fA) to picoamperes (pA). Thus, typically a single nano-entity is only capable of inducing small signals.

Single-entity collision events with the electrode surface are also characterised by their short time duration, with the induction of an electrochemical response lasting from microseconds ( $\mu\text{s}$ ) to milliseconds ( $\text{ms}$ ). For example, the entire duration of an IrOx nanoparticle collision is less than 1 ms,<sup>13,14</sup> RuOx nanoparticle collisions occur over 300  $\mu\text{s}$ ,<sup>18</sup> and Ag nanoparticle oxidation collisions occur over 10's of milliseconds with many individual collision events during this time.<sup>19</sup> The characteristic current signal generated during a stochastic collision experiment differs significantly from that expected from bulk electrochemical systems, which are characterised by currents in the microampere range or above ( $> \mu\text{A}$ ) and time-scales greater than a second ( $> \text{s}$ ).

Instrumentation for stochastic collision electrochemistry, or for any other SEE experiment, should be capable of processing small and short signals, thus providing high current magnification, high bandwidth, and low noise level. Otherwise, limitations on instrumentation might interfere and distort the electrochemical signal, provoking a mismatch between the signal acquired and the Faradaic process ongoing at the electrode surface. White H. S. *et al.* showed the distortion produced by instrumental limitations on time resolution (*i.e.* bandwidth limitation) when recording single-entity events, as reproduced in Figure 3.3.<sup>20</sup> Thus, stochastic collision electrochemistry measurements with limited temporal resolution could compromise the interpretation of the resulting current signal.<sup>21</sup>



**Figure 3.3:** a) Chronoamperometric current trace of nano-impact oxidation of silver nanoparticles recorded experimentally at 200kHz current amplifier bandwidth and filtered using a low-pass Bessel filter. The Bessel filter emulates current traces being recorded with current amplifiers with slower bandwidth with cut-off frequencies of 100kHz, 10kHz, 1kHz and 100Hz. The pink and blue rectangles indicate the regions shown in B and C, respectively. b) and c) magnification of the current trace within pink and blue rectangles. Comparison of current traces at different bandwidths illustrates the distortion in the recorded signal and the resulting loss of information produced when using the current amplifier without enough time resolution. Figure reproduced with permission from White H.S. *et al.*<sup>20</sup>

### 3.1.4 Bandwidth, gain, and noise during current amplification.

Measurement of electrochemical signals on the fA to pA current scale requires a high magnification current amplifier. However, current magnification (*i.e.* gain) results in a trade-off with time resolution (*i.e.* bandwidth). Thus, the limited time response of high-gain current amplifiers often limits the temporal resolution of SEE measurements. For example, commercial current amplifiers operating with an amplification factor of 1 V/nA (1 G $\Omega$ ) have bandwidths of 10 kHz to 50 kHz, but when moving to a greater current amplification factor of 1 V/pA (1 T $\Omega$ ) the bandwidth of the current amplifier can drop to just 0.1 Hz (for example, with the DDPCA-300 from FEMTO).

The current bandwidth and amplifier scale are intimately linked, with efforts to increase the bandwidth introducing higher current noise, which obscures the target electrochemical signal.<sup>22</sup> One possible strategy is to minimise the noise contribution of the system; thus, for equal gain, it is possible to boost the bandwidth. One of the main factors that contributes to noise levels in the current amplifier is the input capacitance, which depends on the parasitic capacitance of the connection cables, the stray capacitances in the current amplifier, as well as the capacitance contributions from the electrochemical cell.<sup>23</sup>

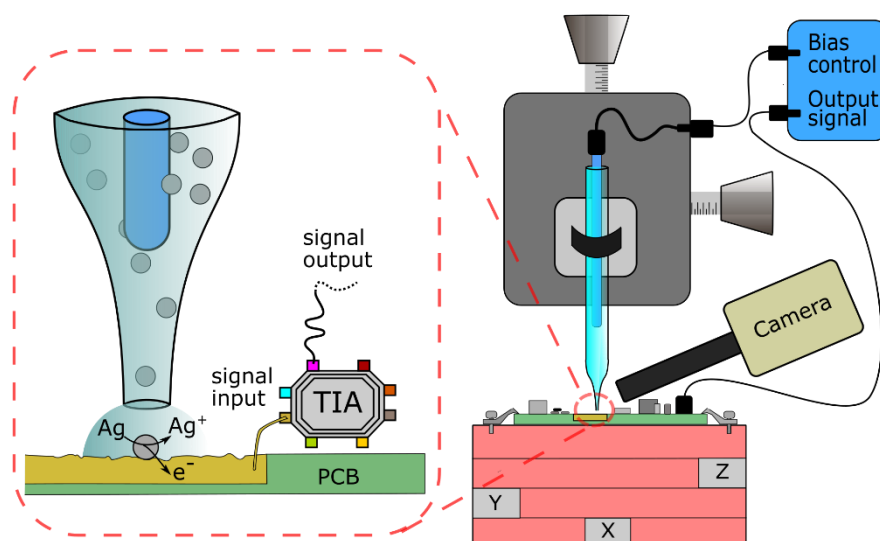
Research efforts have been aimed at producing amplifiers with high bandwidth and high sensitivity, leading to the development of direct measurement strategies in which the current is generated in close proximity to the amplifier.<sup>24</sup> This strategy minimises capacitance contributions from connections/contacts and effectively minimises noise levels. For example, custom current amplifiers have incorporated nanopores and electrodes into the current amplifier chip itself,<sup>25</sup> integrated large electrochemical cells onto the current amplifier,<sup>26</sup> or fabricated arrays of nanoscale electrodes on the current amplifier.<sup>27</sup> However, such design specificity often limits the versatility of the equipment.

### 3.1.5 Integration of a custom current amplifier for stochastic collision electrochemistry with SECCM

Coupling a custom current amplifier optimised for minimum input capacitance and minimum number of connections, with electrochemical systems optimised for single-entity measurements, is a challenging design task. SECCM offers a mobile microscale electrochemical cell that can be formed on any flat conductive surface.<sup>28</sup> Using SECCM as an electrochemical probe, it is possible to design a current amplifier where the working electrode surface is simplified to a metallic contact pad printed on a circuit board, as illustrated in Figure 3.4. This configuration minimises the connections needed to the ultimate stage, so that the working electrode can be placed < 1 mm away from the current amplifier chip. Also, SECCM can easily achieve an electrochemical contact area < 5  $\mu\text{m}^2$ , thus reducing the contribution of the electrochemical cell to the input capacitance.

The instrumentation design proposed here, which is exemplified in the scheme shown in Figure 3.4, minimises input capacitance while reducing the overall output noise levels of the current amplifier, thus enabling an increased current amplifier bandwidth, as required for single nano-entity measurements. Furthermore, several different single-entity electrochemistry measurements have been previously achieved by SECCM.<sup>29</sup> Therefore, such an instrumentation design could be potentially versatile for multiple single nano-entity measurements.

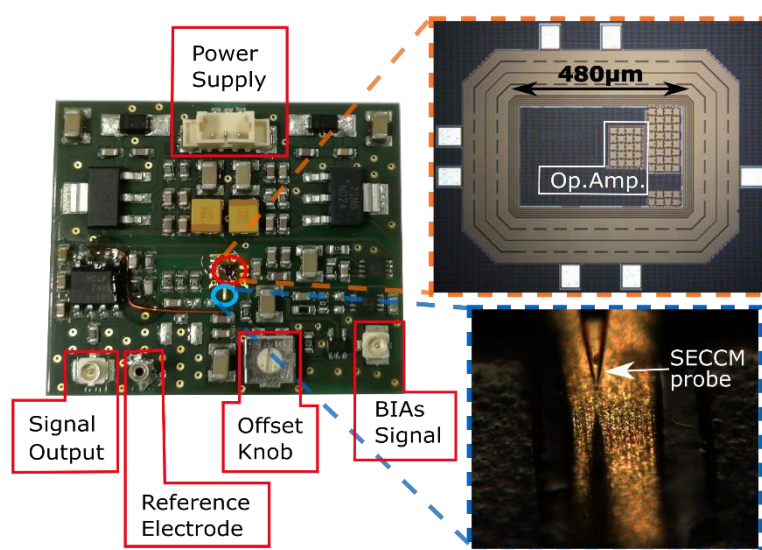
Briefly, the instrumentation design of Figure 3.4 consists of a set of micropositioners that can move the pipette up to 10's micrometres distance from the gold electrode, helped with an external optical camera. Fine displacement is achieved using an XYZ piezoelectric positioner stage. A programmable data acquisition card running a custom LabVIEW code is used for data recording and piezoelectric positioner control. A hollow glass capillary pulled to a sharp point in a laser puller is used to form a micropipette. The micropipette is filled with solution (for instance, containing dispersed nano-entities) and a quasi-reference counter electrode (QRCE) is inserted at the top end. After positioning the probe on the gold contact pad of the PCB board, cyclic voltammetry or chronoamperometry experiments could be performed. A more detailed description of the SECCM experimental setup can be found in the Methods chapter, Section 2.2.



**Figure 3.4:** On the left, a schematic of single nano-entity measurements of silver nanoparticle oxidation using SECCM to form an electrochemical cell over the gold printed pad on a PCB board, which is located in close proximity to the transimpedance amplifier chip (TIA). On the right, a schematic of the complete SECCM setup showing the movable parts, such as micro positioner controllers and x-y- piezo actuators, connections, and camera. Figure adapted with permission from Brunet Cabré, M. *et al.*.<sup>30</sup>



The custom current amplifier, schematic shown in Figure 3.5 and whose details have been previously presented,<sup>31</sup> is used for the readout of the current signal. The current amplifier shown in Figure 3.5 uses active pseudo-resistor feedback that allows for large and adjustable transimpedance values with minimum stray capacitance for maximum bandwidth. The current amplifier chip (a transimpedance amplifier) is mounted on a PCB (5 cm × 5 cm) that provides all required power supplies and signal connections to the chip, as shown in Figure 3.5. A gold trace is located at 300 μm from the chip input on the PCB board. Thanks to the SECCM probe, the gold trace is accessible as the working electrode for electrochemical experiments, as shown in Figure 3.5. A more detailed description of the current amplifier chip and PCB board is given in Section 3.3.

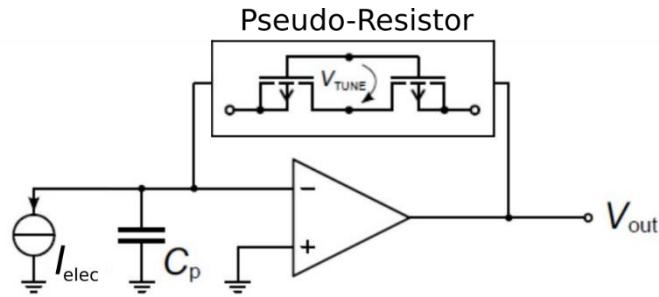


**Figure 3.5:** Photo of the PCB board, with the main components labelled. The top-right magnification is a photo of the transimpedance amplifier (TIA) chip. The bottom-right magnification is a photo of the gold electrode on the PCB with a micropipette positioned a few micrometres from its surface. Figure adapted with permission from Brunet Cabré, M. *et al.*<sup>30</sup>

### 3.1.6 Description of the behaviour of the transimpedance amplifier.

Current amplifiers are devices that provide a readout of AC or DC currents by converting the current signal into a potential signal, which could be further read by a data acquisition board. Operational amplifiers based on transimpedance amplification are a type of current sensor that provide a great trade-off between noise, bandwidth, and linearity (required for DC measurements). Single-entity electrochemical characterisation generally uses chronoamperometry or voltammetry techniques that produce DC signals. Therefore, transimpedance amplifiers (TIAs) are very well suited for SEE signal processing requirements. TIAs are also commonly used in biomedical and

material science applications.<sup>20</sup> The equivalent circuit of a TIA is shown in Figure 3.6, where the closed feedback loop with a pseudo-resistor element is shown. The close-loop feedback element provides gain and amplification power. There are several elements, such as resistance or capacitors, that could be used as feedback elements. For the work presented, a pseudo-resistive feedback element was used. The pseudo-resistive element is composed of multiple CMOS and achieves the best performance when sensing low currents and high bandwidth, as demanded in single-entity electrochemistry. The current amplifier was designed and constructed as part of Denis Djecik's Ph.D. work at the University of Stuttgart; I was provided with these custom current amplifiers for my SECCM experiments, but I was not involved in their design or construction. Details on circuitry and TIAs architecture are thus outside the scope of this thesis; the reader is referred to the work of Anders, J. *et al.* for further information.<sup>31,32</sup>



**Figure 3.6:** Equivalent circuit for the custom TIA with pseudo-resistor feedback, including the input capacitance ( $C_p$ ), input current source equivalent to adjacent electrode pad ( $I_{elec}$ ), internal pseudo-resistor with tuning circuit ( $V_{TUNE}$ ) and output voltage ( $V_{out}$ ). Figure adapted with permission from Brunet Cabré, M. *et al.*<sup>30</sup>

The noise levels (output noise) of a TIA with a pseudo-resistive feedback element can be approximated by Equation 3.1 description.<sup>32</sup>

$$S_{\Delta I} \approx \frac{4kT}{R_{tot}} + \omega^2 C_p^2 S_{\Delta V} \quad (\text{Eq. 3.1})$$

where  $S_{\Delta I}$  is the input-referred noise power spectral density ( $A^2/Hz$ ) at the TIA's output. The input-referred current noise is obtained by the Fourier analysis of the recorded current traces, then the power of the signal is represented as a function of the frequency. The input-referred noise power spectral density,  $S_{\Delta I}$ , is indicative of the noise contribution at each frequency.  $R_{tot}$  is the total equivalent resistance of the pseudo-resistor feedback, which defines the amplification magnitude (gain) of the system.  $\omega = 2\pi f$  is working frequency (rad/s) where  $f$  is bandwidth (Hz).  $C_p$  is the input capacitance (F).  $S_{\Delta V}$  is the intrinsic microchip opamp noise power spectral density ( $V^2/Hz$ ).  $S_{\Delta V}$  only depends on the TIAs chip architecture and it can be measured separately.  $k$  is Boltzman's constant and  $T$  is temperature.

The term  $\frac{4kT}{R_{tot}}$  of Equation 3.1 corresponds to the thermal noise for resistive feedback TIA and represents the noise floor (or minimum out noise) of the current amplifier chip. The  $\omega^2 C_p^2 S_{\Delta V}$  term describes the capacitive shaped contribution of the opamp noise. Note that this later term has quadratic dependence on bandwidth, as well as input capacitance, and, as a consequence, minimising input capacitance favours an increase in bandwidth without increases in output noise levels.

## 3.2 Aims

In this chapter, a new approach for conducting stochastic collision electrochemistry experiments at a high bandwidth extending from DC to the MHz range is reported. A moveable microscale electrochemical cell (3  $\mu\text{m}$  in diameter) formed at the end of a glass micropipette, as for SECCM, is used to conduct electrochemical experiments with minimum stray capacitance. The moveable microscale electrochemical cell allowed to perform stochastic collision electrochemistry experiments on a gold trace of a printed circuit board, directly next to the contact pad of a custom-designed transimpedance amplifier (TIA). With this instrumental design, the electrochemical experiment is brought to close proximity (with a single connection point) to the TIA, reducing contact capacitances and improving current noise levels. Moreover, it is compatible with other current amplifier chip design and with single nano-entity measurement allowed by SECCM equipment.

The experiments and results displayed in this chapter aim, first, to evaluate the noise levels and input capacitance of the proposed instrumentation design. Second, validate that the proposed instrumentation design can effectively conduct electrochemical measurements, including chronoamperometry and cyclic voltammetry. Third, probe single-entity electrochemistry and perform single silver nanoparticle oxidation at unprecedented bandwidth (up to 1MHz).

This project was carried out in collaboration with Prof. Jens Anders's research group at the Institute of Smart Sensors at the University of Stuttgart. The design and fabrication of the current amplifier chip and its integration on the PCB were carried out by PhD student Denis Djekic from the University of Stuttgart. The electrochemical characterisation and experimental work with SECCM, including single nano-entity measurements, have been carried out by the author of this thesis.

### 3.3 Methods

A custom electrochemical scanning probe microscope (EC-SPM) was used to perform localised microscale electrochemical cell measurements, shown in Figures 3.4 and 3.5. Positioning of the micropipette probe is achieved using manual micropositioners (XYZ differential adjusters, Thorlabs), while the fine displacement of the PCB board is achieved using an XYZ piezoelectric positioner stage (NanoCube P611.3 with LVPZT-Amplifier controller, Physik Instrumente). The EC-SPM is situated in a Faraday cage supported on an optical table. A field-programmable gate array (FPGA) data acquisition card (USB-7855R, National Instruments) that runs a custom LabVIEW code (LabVIEW 2018, National Instruments) was used for data recording and piezoelectric positioner control.

A custom TIA, schematic shown in Figure 3.5 and whose details have been previously presented,<sup>25</sup> was used for the readout of the current signal. The TIA uses active pseudoresistor feedback that allows for large, adjustable transimpedance values with a minimum stray capacitance for maximum bandwidth. The TIA was fabricated using commercial silicon-on-insulator (SOI) CMOS technology, which further minimises stray capacitances and thereby maximises the achievable bandwidth. The TIA was mounted as bare dies, i.e. without package, on a PCB (5cm x 5cm) that provides all the required power supply and signal connections to the TIA chip, as shown in Figure 3.5. The TIA's transimpedance value is adjustable via an external resistor on the PCB. A subsequent shelving filter is used to further extend the bandwidth by providing increased gain at high frequencies. Three different TIA settings with bandwidths of 80 kHz, 250 kHz and 1 MHz were used, while the last two feature the bandwidth extension circuit. Electrochemical experiments were carried out on a gold trace situated 300  $\mu\text{m}$  from the TIA input on the PCB.

A hollow glass capillary pulled to a sharp point in a laser puller (P-2000, Sutter Instruments) was used to form a micropipette. The 3.5  $\mu\text{m}$  diameter aperture micropipettes were made from a borosilicate capillary (BF150-86-7.5, Sutter Instruments) with internal and external diameters of 0.86 mm and 1.5 mm, respectively. The micropipette was filled with solution using a microfil (MF34G-5, World Precision Instruments), while filtered with PTFE 0.45  $\mu\text{m}$  syringe filter (FisherBrand). The quasi-reference electrode was inserted into the top end (an Ag/AgCl wire in this case) to form a movable microscale electrochemical cell for localised electrochemical measurements, as is used in SECCM measurements. The micropipette tip was positioned within 10's of micrometres of the gold electrode with the help of an external optical camera (PL-B776U, Pixelink), as shown in Figure 3.4. The micropipette tip was then vertically approached to the gold electrode surface using piezoelectric positioners until the electrochemical cell formed between the tip and the surface. The contact with the gold electrode surface was detected via the capacitive current spike produced by the formation of the electrical double layer on the gold electrode surface.

## Chapter 3

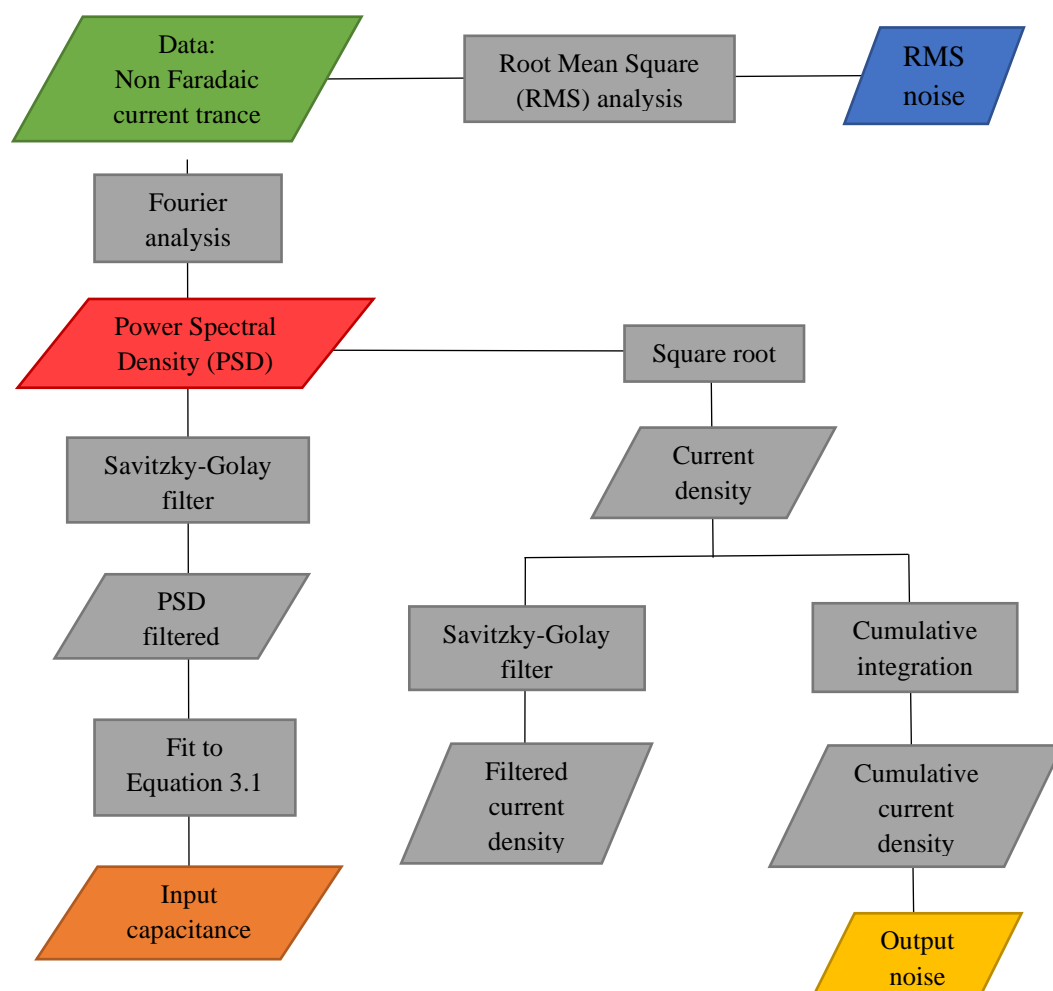
When this signal was detected, the vertical movement of the pipette was stopped. After positioning the probe on the electrode surface, cyclic voltammetry or chronoamperometry experiments were performed.

Silver nanoparticles (100 nm in diameter, 0.02 mg of Ag/mL in 2 mM sodium citrate) were purchased from STREM Chemicals. A solution of  $1.8 \times 10^9$  silver nanoparticles/ml dispersed in 10 mM  $\text{NaNO}_3$  (VWR Chemicals) and 4 mM sodium citrate (Sigma-Aldrich) was used for Ag nanoparticle oxidation experiments. Solutions of 1 mM potassium hexacyanoferrate (II) trihydrate (Honeywell) or 1 mM hexamine ruthenium trichloride (JMC) in 20 mM KCl (VWR Chemicals) were also prepared and used. All solutions were made using ultrapure water with resistivity greater than 18 M $\Omega$ .

## 3.4 Results and Discussion

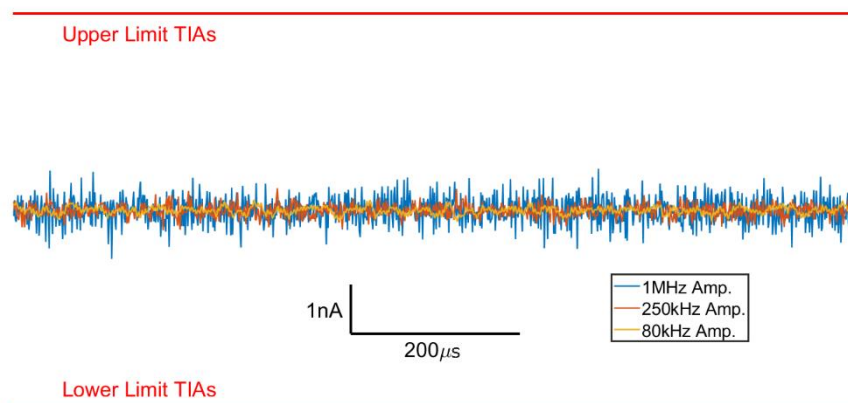
### 3.4.1 Characteristic noise response

Three different TIAs were used for microscale cell measurements, each with a different bandwidth (80 kHz, 250 kHz, 1 MHz) and always using a sampling frequency of 1 MHz, which is the limit of the data acquisition card. The characteristic signal and noise response of the instrumentation (custom TIA and SECCM) were assessed from 10 seconds current traces in both open and closed circuit conditions, in the absence of any Faradaic current. This analysis allowed an evaluation of the contribution of the double layer capacitance at the microscale droplet/Au electrode interface to the overall TIAs noise response. The flowchart diagram displayed in Figure 3.7 shows the complete signal-noise analysis carried out in this section, as well as the main results.



**Figure 3.7:** Flowchart diagram for the signal-noise analysis. The rhomboids indicate datasets, and the rectangles their operation processes. In green, the input dataset obtained by chrono-amperometry measurements. In blue, read, orange, and yellow are the corresponding outputs of the different data analysis processes.

Open circuit current traces of 1 s duration for different bandwidth current amplifier are shown in Figure 3.8, where the noise levels are smaller than the maximum positive or negative readout currents of the TIAs. The RMS current noise at open circuit is 22.2 pA for the 80 kHz current amplifier, 88.8 pA current noise for the 250 kHz current amplifier and 196 pA for the 1 MHz TIA.



**Figure 3.8:** Current trace of one second length in open circuit showing intrinsic noise levels of the TIAs bandwidth of 80 kHz in yellow line, 250 kHz in the orange line and 1 MHz blue line. The red lines represent the range of currents that TIAs can amplify. Figure adapted with permission from Brunet Cabré, M. *et al.*<sup>30</sup>

For the two-electrode setup used here, the open circuit RMS noise corresponds to the intrinsic noise level. When the microscale electrochemical cell is formed over the Au pad (*i.e.* close circuit noise), the noise levels reflect those under operation conditions. Therefore, closed circuit current noise relies on the intrinsic noise from the current amplifier plus noise induced from the electrochemical cell, such as from the double-layer capacitance at the droplet-electrode interface. The RMS current noise in closed circuit is 22.9 pA for 80 kHz TIAs, 89.2 pA for 250 kHz TIAs, and 197 pA for 1 MHz TIAs. The difference in noise values obtained for open and closed circuits is below 1 pA for all TIAs. All RMS noise values for open and close circuits and their differences are summarised in Table 3.1. Both datasets for open circuit and closed circuits correspond to blank current traces without any Faradaic current induced, obtained with 10 mM KCl solution. The relatively small increase in RMS noise upon contact with the microscale electrochemical cell indicates that the current noise is dominated by the intrinsic current noise of the current amplifier and does not arise significantly from the electrochemical cell.

The power spectral density (PSD) of the open and closed circuit current traces are displayed in Figure 3.9 (in blue colour) for 80 kHz, 250 kHz and 1 MHz bandwidth TIAs. The PSD curves are smoothed by a third-order Savitzky-Golay filter with a frame length of 1001 points. Figure 3.9 shows that the filtered PSD curves (in orange) are representative of the input-referred noise variation.



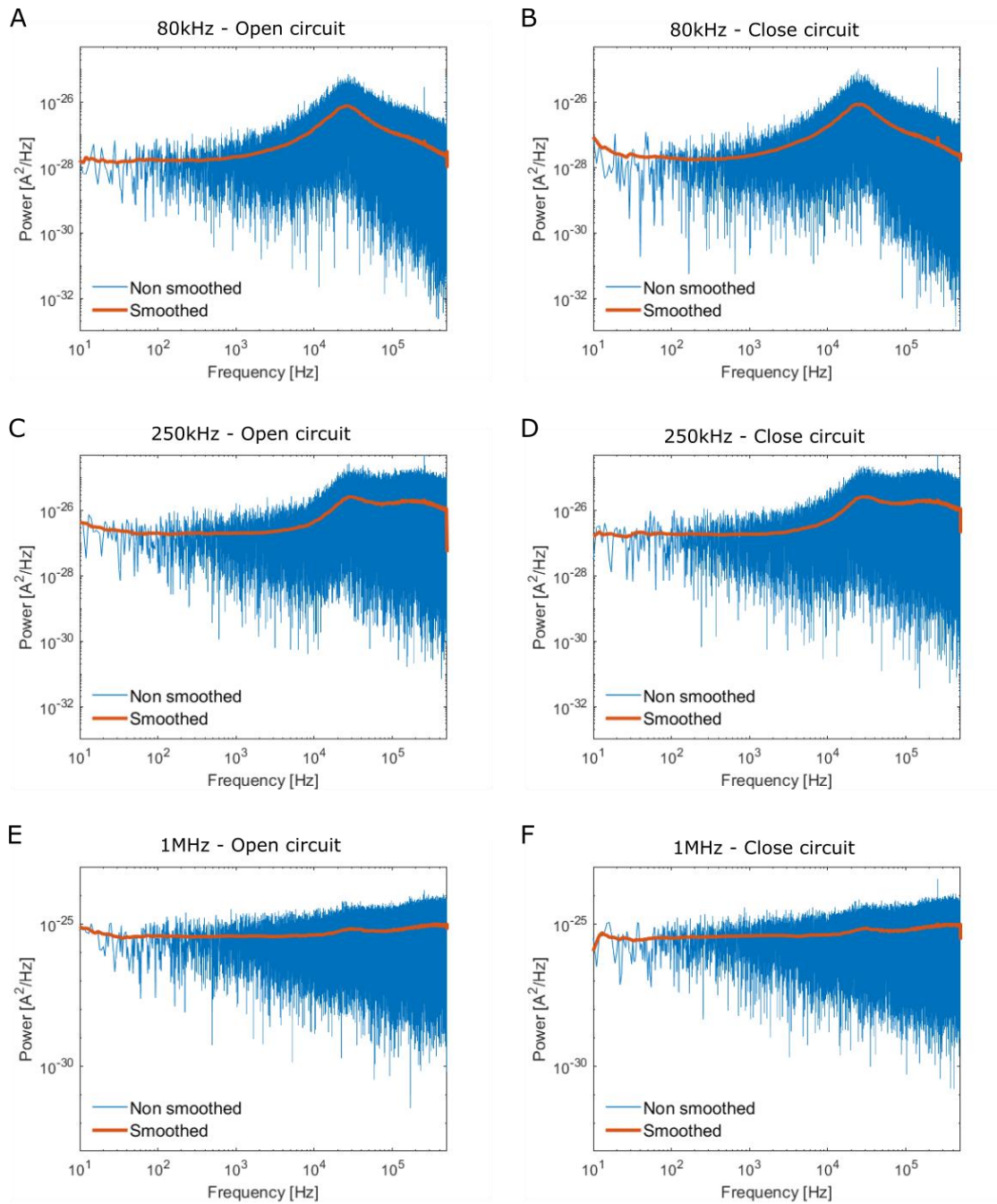
**Table 3.1:** Noise values for different TIAs bandwidth by root-mean-square calculation and from the integration of current densities.

TIAs Bandwidth	Noise deduced by RMS treatment			Noise deduced from current density cumulative integration		
	Open circuit (pA)	Close Circuit (pA)	Noise difference (pA)	Open Circuit (pA)	Close Circuit (pA)	Noise difference (pA)
80 kHz	22.2	22.9	+ 0.7	22.2	23.0	+ 0.8
250 kHz	88.9	89.2	+ 0.3	88.8	89.2	+ 0.4
1 MHz	196	197	+ 1.0	196	197	+ 1.0

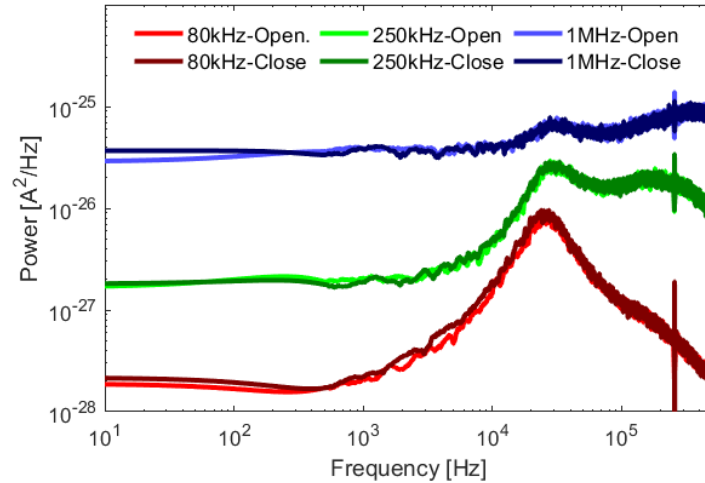
In Figure 3.10, the power spectral density is plotted for the three current amplifier bandwidths tested. The input-referred noise floor ( $< 1$  kHz) of 80 kHz TIA is  $1.5 \cdot 10^{-28}$  A<sup>2</sup>/Hz, within the same regime of the expected thermal noise of an equivalent 250 M $\Omega$  resistor feedback amplifier ( $6 \cdot 58^{-29}$  A<sup>2</sup>/Hz), derived from thermal noise term ( $4kT/R_{tot}$ ) of Equation 3.1. Above 1 kHz, the input-referred noise is dominated by the capacitive opamp noise (second term of Equation 3.1) and noise peaks at 20 kHz, as shown in Figure 3.10 A and B. Notice that, for frequencies greater than approximately 10 kHz, the capacitive noise contributions are quenched thanks to the use of a pseudo-resistive feedback element. Instead, a pure capacitive feedback element on the TIAs would keep a quadratic growth of noise.

In Figure 3.10 it is observed that the noise floor (thermal noise) increases when the TIAs bandwidth is increased. This is an unexpected result, as the noise floor should be independent of the bandwidth, as stated in Equation 3.1. Unfortunately, the larger noise floor on the 250 kHz and 1 MHz bandwidth TIAs will contribute to the noise levels during current amplification. The origin of this behaviour is intrinsic of the current amplifier as both open- or closed-circuit measurements contain this trend. The collaborators from the Prof. Jens Ander group, which designed the TIA, suggested that the larger thermal noise might be related to the integration of the operational amplifier chip within the PCB board circuitry. The TIA's transimpedance value is adjustable via an external resistor on the PCB. A subsequent shelving filter is used to further extend the bandwidth by providing increased gain at high frequencies. The 250 kHz and 1 MHz TIAs feature such bandwidth extension circuits which might be the cause of the floor noise increase.

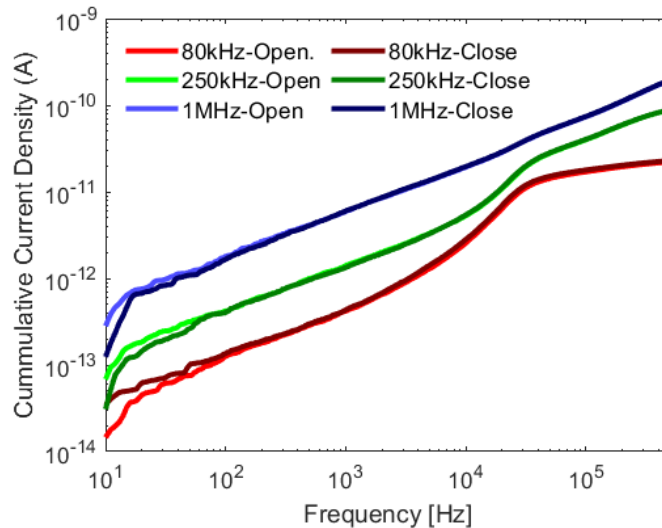
The square root of the input-referred noise gives the current density (with units A/ $\sqrt{\text{Hz}}$ ) and is integrated over the frequency domain to provide the TIAs output noise. In Figure 3.11 the cumulative integration of the current density is shown, which highlights the difference in noise floor (low frequency) of different bandwidth TIAs. The total TIA output noise values are shown in Table 3.1 and show good agreement ( $< 0.1$  pA difference) with the reported RMS noise.



**Figure 3.9:** Power spectral densities (blue) and smoothed (orange) by third order Savitzk-Golay filter with frame length of 1001 points for **A.** 80 kHz TIAs in open circuit, **B.** 80 kHz TIAs in close circuit, **C.** 250 kHz TIAs in open circuit, **D.** 250 kHz TIAs in close circuit, **E.** 1 MHz TIAs in open circuit and **F.** 1 MHz TIAs in close circuit. Figure adapted with permission from Brunet Cabré, M. *et al.*<sup>30</sup>

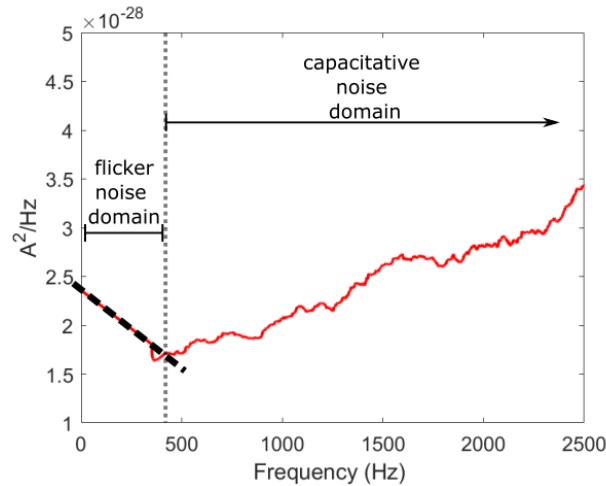


**Figure 3.10:** Input-referred noise ( $S_{\Delta I}$ ) for the 80 kHz, 250 kHz, and 1 MHz TIAs in open and closed circuit configuration. Figure adapted with permission from Brunet Cabré, M. *et al.*<sup>30</sup>



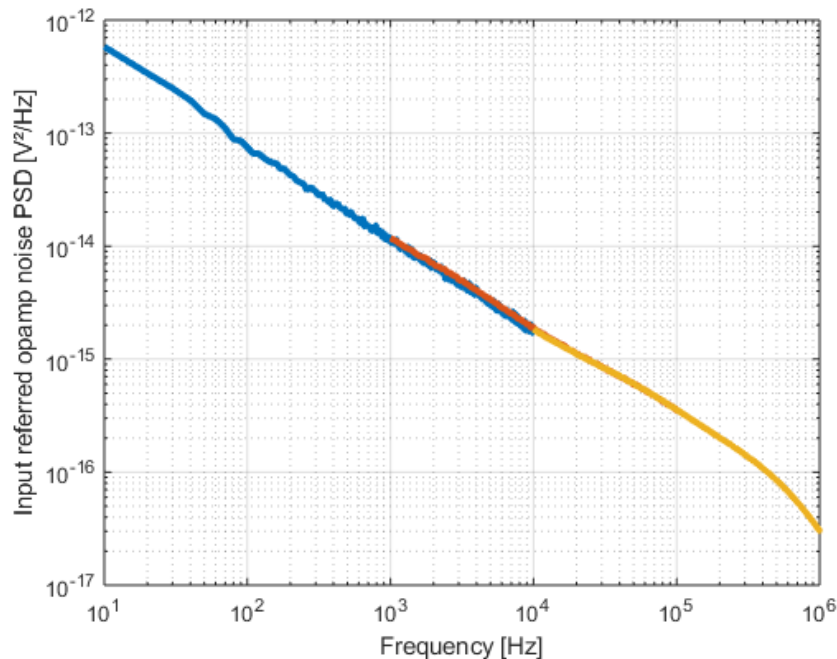
**Figure 3.11:** Cumulative integration of current densities for 80 kHz TIAs in open circuit (light red) and close circuit (dark red), 250 kHz TIA in open circuit (light green) and close circuit (dark green) and 1 MHz TIAs for open circuit (light blue) and close circuit (dark blue). Figure adapted with permission from Brunet Cabré, M. *et al.*<sup>30</sup>

To calculate the input capacitance, Equation 3.1 can be used to fit the section of input-referred noise region dominated by the capacitive opamp noise. For very low frequencies ( $< 400$  Hz) the noise contribution is dominated by flicker noise, as shown in Figure 3.12. The flicker noise domain is not included in the equation fitting. For high frequencies ( $> 5$  kHz for 80 kHz TIA,  $> 10$  kHz for 250 kHz TIA and  $> 20$  kHz for 1 MHz TIA) the input-referred noise is affected by the pseudocapacitive feedback element which reduced the input capacitance parasitic contribution, as previously discussed, and regions above those frequencies are then not considered for the fitting.



**Figure 3.12:** Maximized spectrum of the input-referred noise ( $S_{\Delta I}$ ) for low frequencies. Below 400 Hz it is observed that there is an increase in noise, which is related to the flicker noise domain.

To derive input capacitance from Equation 3.1 fitting, it has been used:  $f = 80$  kHz or 250 kHz or 1 MHz ( $\omega = 2\pi f$ ),  $T = 298$  K and  $S_{\Delta V}$  as reported in Figure 3.13. Notice,  $S_{\Delta V}$  is frequency dependent and has been measured prior, as shown in Figure 3.13. Thermal noise has also been adjusted to the observed value for each TIAs bandwidth, as reported in Table 3.2.



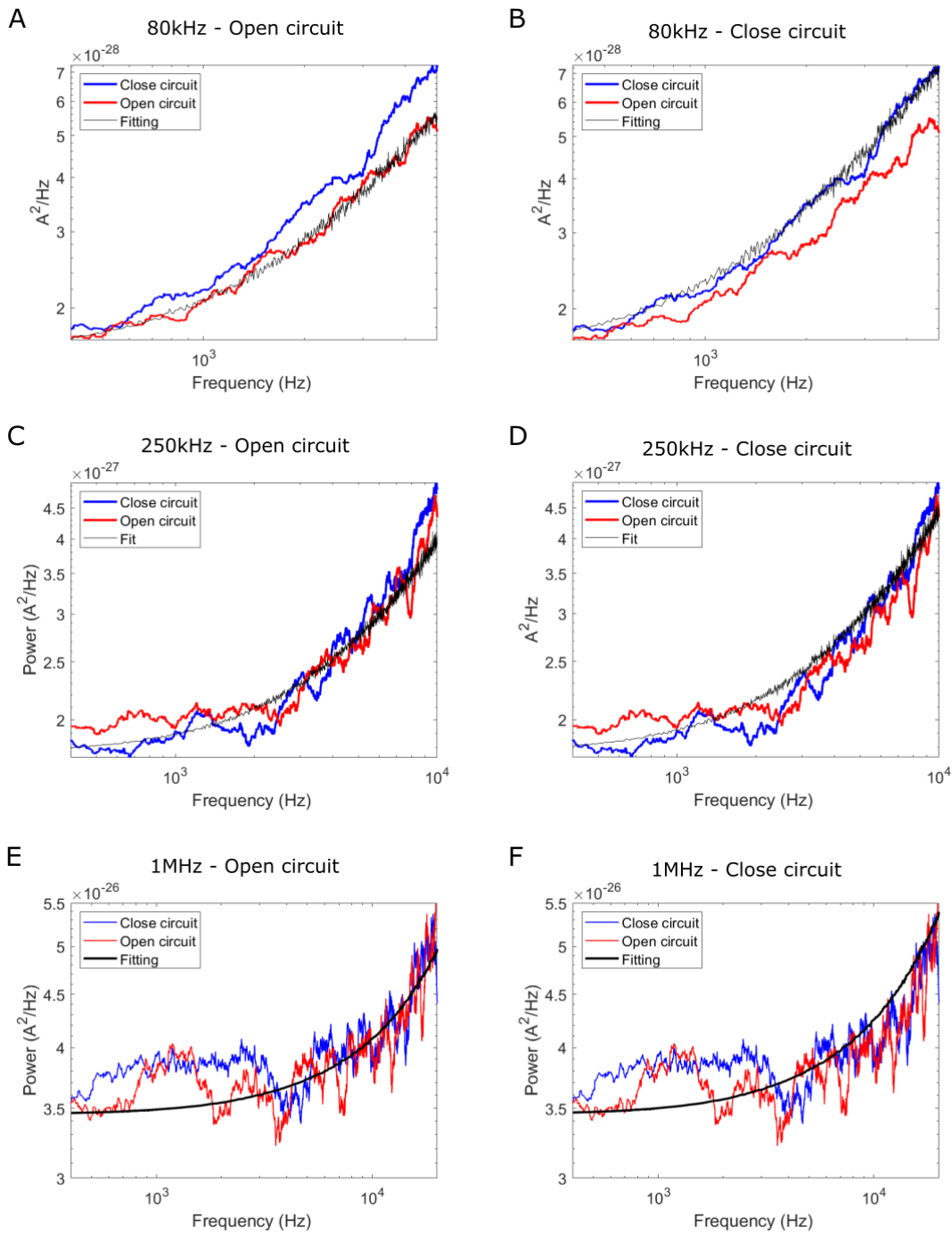
**Figure 3.13:** Intrinsic input-referred noise power spectral density of the opamp ( $S_{\Delta V}$ ). Obtained by averaging 80 measurements of the open-input TIA with shorted feedback pseudoresistor. The noise is dominated by flicker noise, as is typical for CMOS opamps. Measurement was assets for three frequency domains, from 10 Hz to 10 kHz displayed in blue, from 1 kHz to 100 kHz in orange, and 10 kHz to 1 MHz in yellow. Figure adapted with permission from Brunet Cabré, M. *et al.*<sup>30</sup>

The input capacitances ( $C_p$ ) deduced from fitting Equation 3.1 to PSD are displayed in Table 3.2. The curve fittings for the three different TIAs bandwidth tested in the open and closed circuit are shown in Figure 3.14. The optimal value of the input capacitance which adjusts Equation 3.1 to PSD has been found by least squares error, as shown in Figure 3.15.

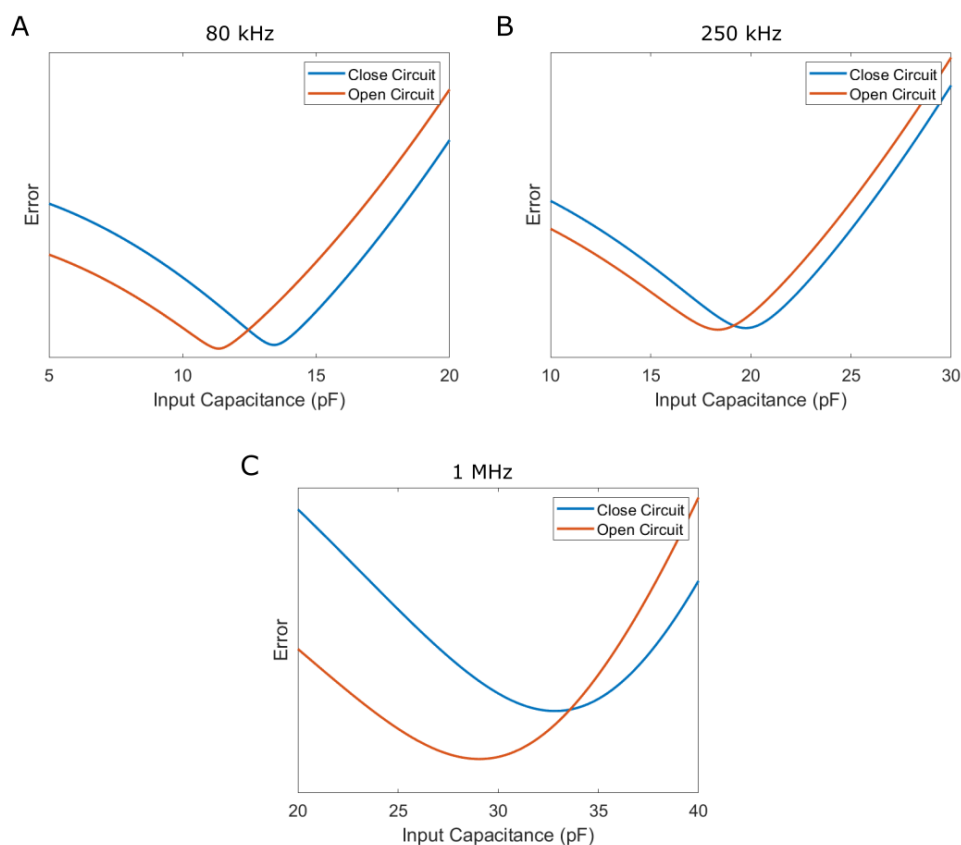
As shown in Table 3.2, for 80 kHz TIAs there is a difference of 2.1 pF between close- and open-circuit capacitance. The open circuit input capacitance arises from circuitry and connections. Therefore, the additional capacitance observed in the close circuit can be attributed to the electrochemical cell formation. The electrochemical cell capacitance depends on the electrolyte, the electrode material, and the area of the electrode in contact with the solution, which is expected to be similar regardless of the TIA bandwidth. The droplet diameter is approximately equal to pipette aperture ( $3.5 \mu\text{m}$ )<sup>28</sup> and therefore the capacitance per unit area is approximately 20-25  $\mu\text{F}/\text{cm}^2$ , which is in agreement with the expected value for double-layer capacitance on an Au electrode in 10 mM KCl (between 15  $\mu\text{F}/\text{cm}^2$  to 40  $\mu\text{F}/\text{cm}^2$ ).<sup>33</sup> The electrochemical cell capacitance obtained from fitting the input-referred noise of the 250 kHz and 1 MHz TIAs are 1.4 pF and 3.8 pF respectively. The values for the three current amplifiers are then of the same order of magnitude, and the difference observed between them might be attributed to variation in the electrochemical contacted area. When a micropipette probe is used, it is common to see a variation in the droplet cell size; this is caused by the variance in the aperture size of the manufactured pipettes. As shown in Table 3.2, the main contribution to the input capacitance arises from the intrinsic capacitance of the TIA (open circuit) rather than the electrochemical capacitance of the cell. This is possible because of the small electrochemical cell size that can be achieved by the use of an SECCM probe.

**Table 3.2:** Input capacitance ( $C_p$ ) and thermal noise values used for curve fitting of input-referred noise of each TIAs bandwidth with Equation 3.1.

TIAs Bandwidth	Input Capacitance			Thermal noise ( $\text{A}^2/\text{Hz}$ )
	Open Circuit (pF)	Close Circuit (pF)	EC Cell capacitance (pF)	
80 kHz	11.35	13.43	2.08	$1.50 \cdot 10^{-28}$
250 kHz	17.82	19.50	1.39	$1.75 \cdot 10^{-27}$
1 MHz	29.05	32.83	3.78	$3.45 \cdot 10^{-26}$



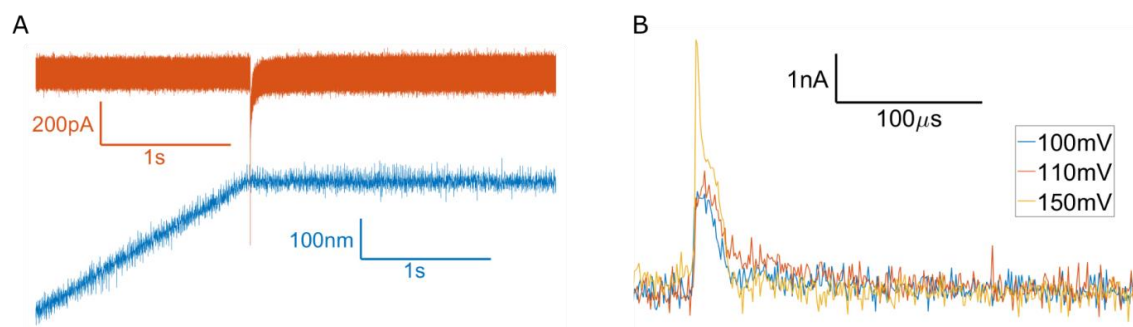
**Figure 3.14:** Input-referred noise for open circuit (blue) and close circuit (red) and fitting with Equation 3.1 (black). For 80 kHz TIAs, bandwidth fitting to **A)** open circuit and **B)** close circuit. For 250 kHz TIAs bandwidth fitting to **C)** open circuit and **D)** close circuit. For 1MHz TIAs bandwidth fitting to **E)** open circuit and **F)** close circuit. Figure adapted with permission from Brunet Cabré, M. *et al.*<sup>30</sup>



**Figure 3.15:** Least square error obtained for the fitting of input-referred noise curve and with Equation 3.1 for a range of input capacitance values. **A)** for 80 kHz TIAs, **B)** 250 kHz TIAs, and **C)** for 1MHz TIAs.

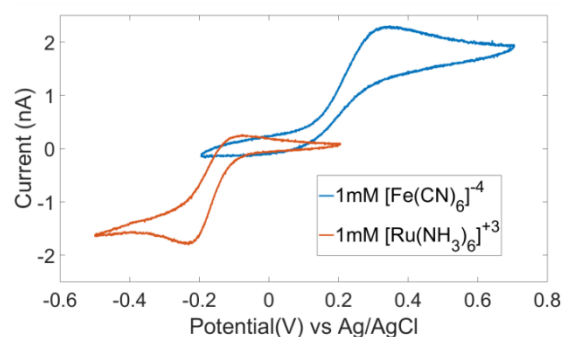
### 3.4.2 Electrochemical Performance

The formation of the electrochemical cell is achieved by approaching the micropipette tip with respect to the gold electrode pad printed on the PCB board until the droplet cell is formed. Droplet cell formation is detected via the double layer formation current upon wetting of the electrode surface. A typical current-time trace and the corresponding vertical position-time trace during a micropipette landing are shown in Figure 3.16 A indicating the ability to land a micro-scale electrochemical cell directly on an Au electrode next to a TIA input on a PCB.<sup>28</sup> The current-time signal recorded for double layer formation upon the very initial contact between the probe droplet and the gold electrode surface is shown in Figure 3.16 B for the bandwidth of 1 MHz and different applied potentials. Double layer formation occurs over a very short time period, estimated to be 50  $\mu\text{s}$  in a 10 mM solution,<sup>34</sup> and therefore is very often obscured due to bandwidth limitations, especially on the micro and nano scales. Using a micropipette approach on a high bandwidth current amplifier enables the initial stages of double layer formation (and any ion absorption processes that could occur on the initial contact of solution with an electrode surface) to be measured with high resolution.



**Figure 3.16:** Droplet cell formation detection on custom TIAs. **A)** Concurrent current-time and vertical position-time traces recorded during the pipette approach, for an approach rate of 200 nm/s, a 3.5  $\mu\text{m}$  aperture diameter micropipette, 80 kHz bandwidth TIA and an approaching potential of  $-0.5\text{ V vs. Ag/AgCl}$ . Upon detection of the double-layer charging current, the vertical movement of the probe was halted automatically via a control feedback loop running of the FPGA-DAQ card. **B)** Current signal response due to double layer formation upon contact of a 400 nm diameter probe droplet containing 10 mM KCl with a 1 MHz current amplifier at three different potentials (*vs. Ag/AgCl* reference electrode). Figure adapted with permission from Brunet Cabré, M. *et al.*<sup>30</sup>

To demonstrate the ability to conduct electrochemistry directly on the TIA electrode, cyclic voltammetry measurements with two different redox couples, 1 mM Ruthenium Hexamine ( $[\text{Ru}(\text{NH}_3)_6]^{+3}$ ) and 1 mM ferricyanide ( $[\text{Fe}(\text{CN})_6]^{-4}$ ), were performed. The resulting voltammograms are shown in Figure 3.17, which shows the expected electrochemical behaviour; the  $[\text{Ru}(\text{NH}_3)_6]^{+3}$  reduction to  $[\text{Ru}(\text{NH}_3)_6]^{+2}$  is observed around  $-0.15\text{ V vs Ag/AgCl}$  (*ca.*  $0.1\text{ V vs SHE}$ ) and  $[\text{Fe}(\text{CN})_6]^{-4}$  oxidation to  $[\text{Fe}(\text{CN})_6]^{-3}$  around  $+0.2\text{ V vs Ag/AgCl}$  (*ca.*  $+0.4\text{ V vs SHE}$ ).<sup>35</sup> The shape of the voltammogram, typical for SECCM probes, has a well-defined diffusion-limited current which is indicative of a lack of any resistive potential drop.<sup>35</sup> The instrumentation design proposed in this chapter (custom TIA + SECCM) can conduct potentiometric metric measurements within 300  $\mu\text{m}$  of the TIA circuit.



**Figure 3.17:** Cyclic voltammetry measurement on the TIA's gold contact pad for two different redox couples, 1 mM  $[\text{Fe}(\text{CN})_6]^{-4}$  and 1 mM  $[\text{Ru}(\text{NH}_3)_6]^{+3}$ , both in 20 mM KCl supporting electrolyte and obtained with a scan rate of 1 V/s. Figure adapted with permission from Brunet Cabré, M. *et al.*<sup>30</sup>



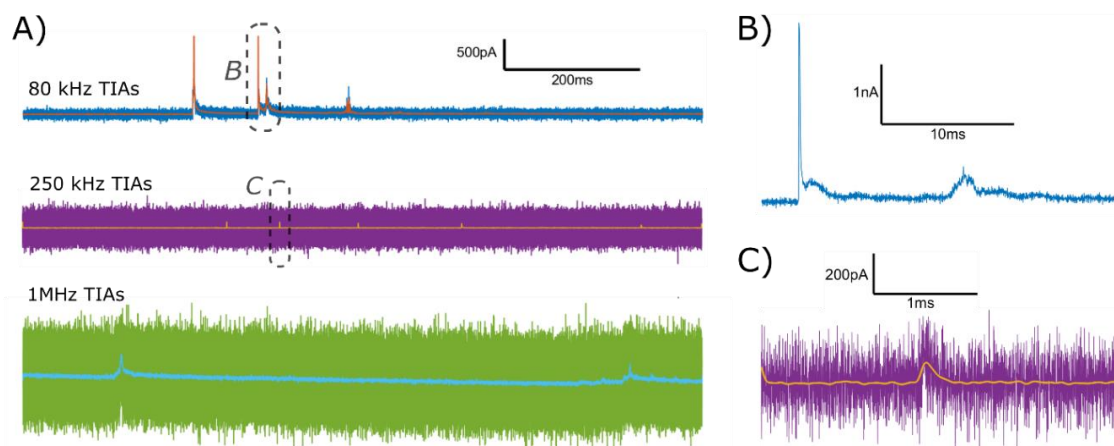
### 3.4.3 Single Nano-Entity Electrochemistry

To test single nano-entity electrochemistry on the instrumentation, we conducted stochastic collision experiments for the electrochemical oxidation of silver nanoparticles. Several studies have previously analysed nanoimpact oxidation of silver nanoparticles and found that time resolution is essential to resolve the interactions of the silver nanoparticle with the electrode surface.<sup>6,11,12,19,21,36–39</sup> Furthermore, this experiment typically produces current spikes that range between 10's pA and few nA, which are suitable for the current magnification (4 nA/V) of the TIAs. To conduct nanoimpact oxidation of silver nanoparticles a solution containing freely diffusing Ag nanoparticles was loaded into the micropipette probes, and a potential of +1 V vs. Ag/AgCl was applied to the gold electrode surface. When the droplet cell was in contact with the Au electrode surface, the oxidation of the single nanoparticles could be observed when the electrode was held at a sufficiently oxidising potential. Ag nanoparticles typically undergo multiplex electro-oxidation, with multiple peaks attributed to the Brownian motion of Ag nanoparticles in solution,<sup>36,39</sup> although the exact nature of the multiplex behaviour is still under debate.<sup>37</sup>

As expected, multiple short nA-scale current spikes were observed when the micropipette probe containing Ag nanoparticles was brought into contact with the Au electrode. Typical current-time traces, which display the characteristic current spikes of Ag nanoparticle electro-oxidation on the three different TIA (80 kHz, 250 kHz, and 1 MHz) are shown in Figure 3.18 A. A filtered current-time trace is also included, filtered with a bilinear transformed Bessel filter with a 10 kHz cut-off frequency and 5<sup>th</sup> order pole to preserve the amplitude responses, emulating a low bandwidth current amplifier response.<sup>20,38</sup> One Ag nanoparticle oxidation event, is defined as a group of multiple short-time anodic peaks which ceases over time. With the 80 kHz TIA an oxidation event was observed approximately every 20 seconds. Each event is composed of multiple peaks above 1 nA with a total duration of fractions of a second, as shown in Figure 3.18 A. Each individual anodic peak lasts a few milliseconds, as shown by the maximised current trace of Figure 3.17 B. The integrated charge over the whole event, *i.e.* accounting for the multiple peaks, is ~4 pC. The theoretical charge for the complete oxidation of 100 nm silver NPs to Ag<sup>+</sup> is 4.9 pC (assuming Ag to Ag<sup>+</sup> oxidation of 100 nm diameter nanoparticles with 10.5 g/cm<sup>3</sup> density and atomic weight 107 g/mol). Therefore, it is concluded that single Ag nanoparticles were fully oxidised during the collision event by undergoing multiple partial oxidations and that one nanoparticle was fully oxidised approximately every 20s.

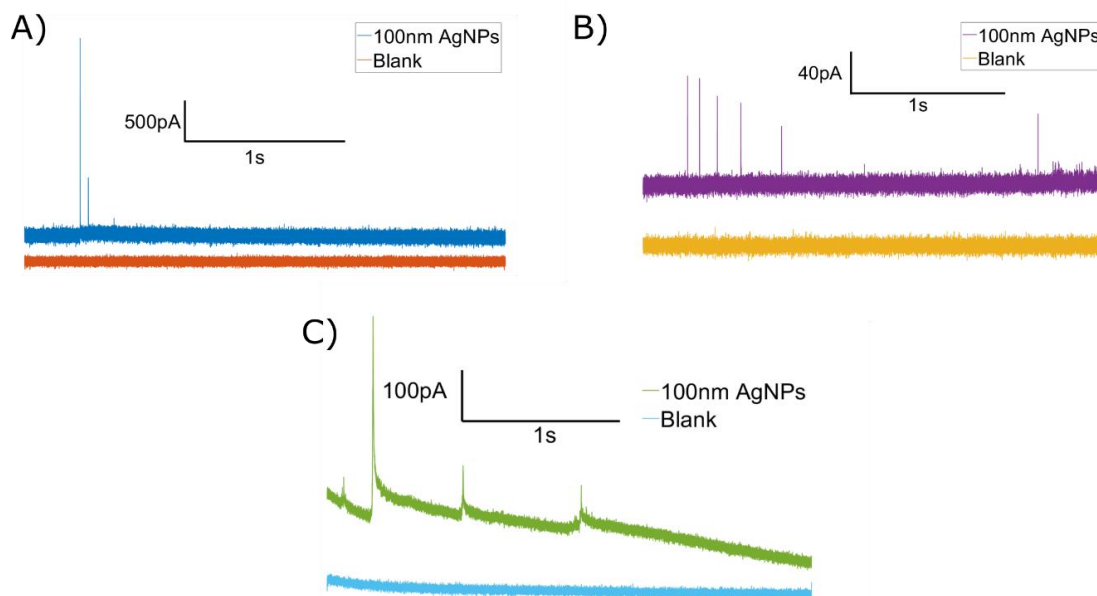
With the 250 kHz TIA, Ag nanoparticle collision signals constitute a longer duration event with numerous smaller current spikes, as shown in Figure 3.18 A and C. In this case, the integrated charge (~0.3 pC) is lower than the value expected from full nanoparticle oxidation, suggesting only

partial oxidation of the 100 nm diameter Ag nanoparticle. Finally, for the 1 MHz TIA, single long oxidation peaks are observed, with the integrated charge ( $\sim 2 - 4$  pC) indicating that some events undergo partial and some complete oxidation of the nanoparticle. The current trace that reproduces the same experimental condition but without silver nanoparticles dispersed in the electrolyte solution, shows no spikes in current trace as displayed in Figure 3.19.

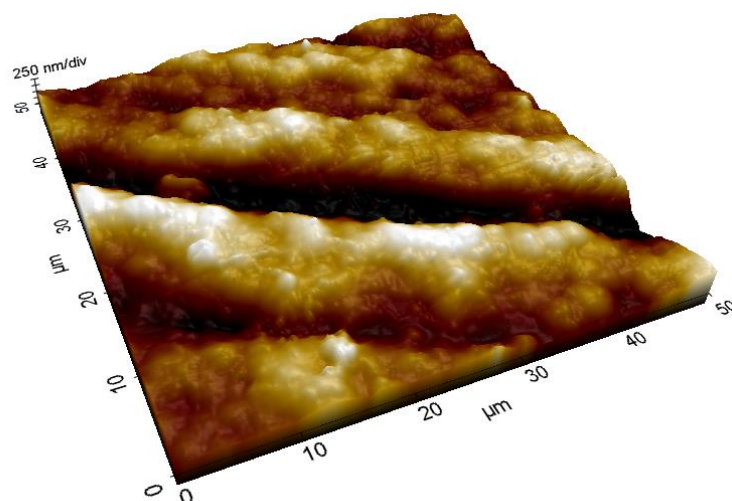


**Figure 3.18:** Current-trace of the stochastic collision electrochemistry experiment on custom TIAs. **A)** Chronoamperometry of single Ag nanoparticle collision and oxidation for three different bandwidth TIA's (80 kHz, 250 kHz, 1 MHz). The current spikes correspond to nanoparticle impact and oxidation. The 10 kHz Bessel-filtered signal is also displayed. **B)** Magnification of chronoamperometry on 80 kHz TIA, the complex behaviour of the signal is attributed to multiple Ag nanoparticle collision/oxidation events. **C)** Magnification of chronoamperometry with 250 kHz TIA showing the current generated by nano-impacts and partial oxidation of a single Ag nanoparticle. Figure adapted with permission from Brunet Cabré, M. *et al.*<sup>30</sup>

The oxidation of Ag nanoparticles on the three different current amplifiers shows differences in spike shape and magnitude. This result is somehow unexpected, as different TIAs bandwidth should not affect the Faradaic process undergoing on the electrode surface. Thus, higher bandwidth TIAs are expected to provide only greater time resolution over a similar type of current signal. However, previous studies reported that the oxidation processes of Ag NPs are highly sensitive to the electrode surface state, which affects the electron transfer processes leading to different current trace signals.<sup>38,40</sup> It is plausible that the gold electrode pads of different current amplifiers have slightly different surfaces due to the manufacturing process. The surface of the gold pad has been characterised by AFM, which has shown that the surface of the electrode has a relatively rough and uneven surface topography, as shown in Figure 3.20. Single entity electrochemistry measurement could be very sensitive to surface chemistry, and thus good control of the surface state is required. The surface morphology indicates that the gold printed pad electrode might not be the most adequate implementation for the working electrode, and further research in custom TIAs should integrate different contact pads design.



**Figure 3.19:** Chronoamperometry of single Ag nanoparticle collision and their respective blanks (without nanoparticle in solution) for three different bandwidth TIA's **A)** 80 kHz current trace with silver nanoparticles (blue) and without (orange). **B)** 250 kHz current trace with nanoparticles (purple) and without (yellow). **C)** 1 MHz current trace with nanoparticles (green) and without (blue). The 250 kHz and 1 MHz current traces have been filtered using a bilinear transformed Bessel filter with a 10 kHz cut-off frequency. Figure adapted with permission from Brunet Cabré, M. *et al.*<sup>30</sup>



**Figure 3.20:** AFM of the gold electrode located on PCB near TIA showing that the surface of the Au electrode is relatively rough (RMS roughness of 0.38  $\mu\text{m}$ ). Figure adapted with permission from Brunet Cabré, M. *et al.*<sup>30</sup>

### 3.5 Conclusions

In this chapter, a new experimental approach for single entity electrochemistry up to microsecond temporal resolution has been developed. The combination of a custom transimpedance amplifier with a micropipette SECCM probe allowed electrochemical measurements (voltammetry and chronoamperometry) at 300  $\mu\text{m}$  from the current amplifier, minimising connections, input capacitance, and noise levels. The low noise levels allowed measurements of picoamp scale currents up to a bandwidth of 1 MHz.

The contribution of the electrochemical cell to the overall current noise was evaluated, showing a minor contribution. Thus, because of the small, controlled size offered by the micropipette probe approach (SECCM), it is possible to achieve minimum noise increases when this electrochemical system is connected to the current amplification system. However, detailed analysis of noise levels by power spectral density spectrum revealed that the floor noise levels increased for higher-bandwidth TIAs. This unexpected observation suggested issues with the circuit integration on the PCB board of high bandwidth TIA chips. A second generation of TIA chips has been designed by our collaborators at the University of Stuttgart. Once the amplifiers are manufactured, future work would involve testing and evaluating the electrochemical response of the improved current amplifiers.

Nano-impact oxidation of silver nanoparticles demonstrates that single entity electrochemistry is possible with the three TIAs tested: 80 kHz, 250 kHz, and 1 MHz bandwidth. The chronoamperometric response observed for the oxidation of silver nanoparticles was distinct on the three different current amplifiers tested, which might be related to the surface state of the gold electrode pad. The next generation of current amplifiers aims to replace the printed gold pad with a ball bond as the input electrode. The gold ball can be flattened and polished, ensuring a pristine electrode surface. Furthermore, the gold ball bond could be deposited directly on the TIA chips, thus reducing the distance between the TIA and electrode contacts from 300  $\mu\text{m}$  to  $< 50 \mu\text{m}$ .

There is a wide range of SEE experiments which can benefit from the high temporal resolution instrumentation presented in this chapter. For instance, studying the diffusion and adsorption of nanoparticles or other nano-entities to electrode surfaces;<sup>41,42</sup> time evolution of nanoscale phases formation, such as nanobubbles during electrocatalyst;<sup>43</sup> or even single bioanalyte testing such as time real-time hybridisation of DNA, single vesicle formation, or determining kinetic heterogeneity of enzyme activity over time.<sup>44,45</sup> The research presented in this chapter is focused on technique development. The improved performance of the next generation TIAs will allow further SEE experiments to be developed.

## Authorship Statement

This chapter is an extended adaptation of the work presented in the publication:

*Microscale electrochemical cell on a custom CMOS transimpedance amplifier for high temporal resolution single-entity electrochemistry.*

Brunet Cabre, M.; Djekic, D.; Romano, T.; Hanna, N.; Anders, J. and McKelvey, K.  
*ChemElectrochem*, 2020, 7, 4724 – 4729.

The publication encompasses graphic table of content is the cover feature displayed in the 23/2020 issue of ChemElectroChem journal. The publication and the cover feature could be found in the Appendix section of the thesis.

Electrochemical experiments, data analysis, and manuscript writing were carried out by the first author of the publication, MBC, as part of the Ph.D. thesis presented here.

Co-authors D.D. and N. H. developed and manufactured the custom-designed transimpedance amplifier, as part of their Ph.D. and MSc project, respectively. T.R. contributed to the optimisation of micropipette manufacturing optimisation and obtention of preliminary electrochemical data, as part of his MSc project. J.A. supervised and led the development of the transimpedance amplifier and contributed to the experimental design.

The corresponding author, K.M. supervised and led the experimental design for the acquisition of electrochemical data, provided guidance over data analysis, and contributed to manuscript drafting and correction.

## References

1. Baker, L. A. Perspective and Prospectus on Single-Entity Electrochemistry. *J. Am. Chem. Soc.* **140**, 15549–15559 (2018) <https://doi.org/10.1021/jacs.8b09747>.
2. Peng, Y.-Y., Qian, R.-C., Hafez, M. E. & Long, Y.-T. Stochastic Collision Nanoelectrochemistry: A Review of Recent Developments. *ChemElectroChem* **4**, 977–985 (2017) <https://doi.org/10.1002/celec.201600673>.
3. Anderson, T. J. & Zhang, B. Single-Nanoparticle Electrochemistry through Immobilization and Collision. *Acc. Chem. Res.* **49**, 2625–2631 (2016) <https://doi.org/10.1021/acs.accounts.6b00334>.
4. Patrice, F. T., Qiu, K., Ying, Y.-L. & Long, Y.-T. Single Nanoparticle Electrochemistry. *Annual Rev. Anal. Chem.* **12**, 347–370 (2019) <https://doi.org/10.1146/annurev-anchem-061318-114902>.
5. Ma, C. *et al.* Dynamically imaging collision electrochemistry of single electrochemiluminescence nano-emitters. *Chem. Sci.* **9**, 6167–6175 (2018) <https://doi.org/10.1039/C8SC02251H>.
6. Kätelhön, E. *et al.* Understanding Nano-Impact Current Spikes: Electrochemical Doping of Impacting Nanoparticles. *J. Phys. Chem. C* **120**, 17029–17034 (2016) <https://doi.org/10.1021/acs.jpcc.6b04289>.
7. Cheng, W. & Compton, R. G. Electrochemical detection of nanoparticles by ‘nano-impact’ methods. *TrAC, Trends Anal. Chem.* **58**, 79–89 (2014) <https://doi.org/10.1016/j.trac.2014.01.008>.
8. Bard, A. J., Zhou, H. & Kwon, S. J. Electrochemistry of Single Nanoparticles via Electrocatalytic Amplification. *Isr. J. Chem.* **50**, 267–276 (2010) <https://doi.org/10.1002/ijch.201000014>.
9. Alligrant, T. M., Dasari, R., Stevenson, K. J. & Crooks, R. M. Electrocatalytic Amplification of Single Nanoparticle Collisions Using DNA-Modified Surfaces. *Langmuir* **31**, 11724–11733 (2015) <https://doi.org/10.1021/acs.langmuir.5b02620>.
10. Kim, J., Dick, J. E. & Bard, A. J. Advanced Electrochemistry of Individual Metal Clusters Electrodeposited Atom by Atom to Nanometer by Nanometer. *Acc. Chem. Res.* **49**, 2587–2595 (2016) <https://doi.org/10.1021/acs.accounts.6b00340>.
11. Hao, R., Fan, Y. & Zhang, B. Electrochemical Detection of Nanoparticle Collision by Reduction of Silver Chloride. *J. Electrochem. Soc.* **163**, H3145–H3151 (2016) <https://doi.org/10.1149/2.0191604jes>.
12. McKelvey, K., Robinson, D. A., Vitti, N. J., Edwards, M. A. & White, H. S. Single Ag nanoparticle collisions within a dual-electrode micro-gap cell. *Faraday Discuss.* **210**, 189–200 (2018) <https://doi.org/10.1039/C8FD00014J>.
13. Zhou, M., Yu, Y., Hu, K., Xin, H. L. & Mirkin, M. v. Collisions of Ir Oxide Nanoparticles with Carbon Nanopipettes: Experiments with One Nanoparticle. *Anal. Chem.* **89**, 2880–2885 (2017) <https://doi.org/10.1021/acs.analchem.6b04140>.
14. Kwon, S. J., Fan, F.-R. F. & Bard, A. J. Observing Iridium Oxide (IrO<sub>x</sub>) Single Nanoparticle Collisions at Ultramicroelectrodes. *J. Am. Chem. Soc.* **132**, 13165–13167 (2010) <https://doi.org/10.1021/ja106054c>.

15. Kim, B.-K., Boika, A., Kim, J., Dick, J. E. & Bard, A. J. Characterizing Emulsions by Observation of Single Droplet Collisions—Attoliter Electrochemical Reactors. *J. Am. Chem. Soc.* **136**, 4849–4852 (2014) <https://doi.org/10.1021/ja500713w>.
16. Sekretaryova, A. N., Vagin, M. Yu., Turner, A. P. F. & Eriksson, M. Electrocatalytic Currents from Single Enzyme Molecules. *J. Am. Chem. Soc.* **138**, 2504–2507 (2016) <https://doi.org/10.1021/jacs.5b13149>.
17. Ho, T. L. T., Hoang, N. T. T., Lee, J., Park, J. H. & Kim, B.-K. Determining mean corpuscular volume and red blood cell count using electrochemical collision events. *Biosens. Bioelectron.* **110**, 155–159 (2018) <https://doi.org/10.1016/j.bios.2018.03.053>.
18. Kang, M. *et al.* Time-Resolved Detection and Analysis of Single Nanoparticle Electrocatalytic Impacts. *J. Am. Chem. Soc.* **137**, 10902–10905 (2015) <https://doi.org/10.1021/jacs.5b05856>.
19. Zhang, F., Edwards, M. A., Hao, R., White, H. S. & Zhang, B. Collision and Oxidation of Silver Nanoparticles on a Gold Nanoband Electrode. *J. Phys. Chem. C* **121**, 23564–23573 (2017) <https://doi.org/10.1021/acs.jpcc.7b08492>.
20. Robinson, D. A., Edwards, M. A., Ren, H. & White, H. S. Effects of Instrumental Filters on Electrochemical Measurement of Single-Nanoparticle Collision Dynamics. *ChemElectroChem* **5**, 3059–3067 (2018) <https://doi.org/10.1002/celec.201800696>.
21. Ma, H., Zhong, C. B., Ying, Y.-L. & Long, Y.-T. Seeing Is Not Believing: Filtering Effects on Random Nature in Electrochemical Measurements of Single-Entity Collision. *ACS Meas. Sci. Au* (2022) <https://doi.org/10.1021/acsmesuresciau.2c00004>.
22. Lu, S.-M., Peng, Y.-Y., Ying, Y.-L. & Long, Y.-T. Electrochemical Sensing at a Confined Space. *Anal. Chem.* **92**, 5621–5644 (2020) <https://doi.org/10.1021/acs.analchem.0c00931>.
23. Fraccari, R. L. *et al.* High-bandwidth detection of short DNA in nanopipettes. *Faraday Discuss.* **193**, 459–470 (2016) <https://doi.org/10.1039/C6FD00109B>.
24. Hartel, A. J. W. *et al.* High bandwidth approaches in nanopore and ion channel recordings - A tutorial review. *Anal. Chim. Acta.* **1061**, 13–27 (2019) <https://doi.org/10.1016/j.aca.2019.01.034>.
25. Carminati, M., Ferrari, G., Ivanov, A. P., Albrecht, T. & Sampietro, M. Design and characterization of a current sensing platform for silicon-based nanopores with integrated tunneling nanoelectrodes. *Analog. Integr. Circuits. Signal Process.* **77**, 333–343 (2013) <https://doi.org/10.1007/s10470-013-0193-9>.
26. Rosenstein, J. K., Wanunu, M., Merchant, C. A., Drndic, M. & Shepard, K. L. Integrated nanopore sensing platform with sub-microsecond temporal resolution. *Nat. Methods.* **9**, 487–492 (2012) <https://doi.org/10.1038/nmeth.1932>.
27. Lemay, S. G. *et al.* High-Frequency Nanocapacitor Arrays: Concept, Recent Developments, and Outlook. *Acc. Chem. Res.* **49**, 2355–2362 (2016) <https://doi.org/10.1021/acs.accounts.6b00349>.
28. Ebejer, N. *et al.* Scanning Electrochemical Cell Microscopy: A Versatile Technique for Nanoscale Electrochemistry and Functional Imaging. *Annu. Rev. Anal. Chem.* **6**, 329–351 (2013) <https://doi.org/10.1146/annurev-anchem-062012-092650>.
29. Bentley, C. L., Kang, M. & Unwin, P. R. Scanning electrochemical cell microscopy: New perspectives on electrode processes in action. *Curr. Opin. Electrochem.* **6**, 23–30 (2017) <https://doi.org/10.1016/j.coelec.2017.06.011>.

30. Brunet Cabré, M. *et al.* Microscale Electrochemical Cell on a Custom CMOS Transimpedance Amplifier for High Temporal Resolution Single Entity Electrochemistry\*\*. *ChemElectroChem* **7**, 4724–4729 (2020) <https://doi.org/10.1002/celc.202001083>.
31. Djekic, D., Ortmanns, M., Fantner, G. & Anders, J. A tunable, robust pseudo-resistor with enhanced linearity for scanning ion-conductance microscopy. in *2016 IEEE International Symposium on Circuits and Systems (ISCAS)* 842–845 (IEEE, 2016). <https://doi.org/10.1109/ISCAS.2016.7527372>.
32. Djekic, D. *et al.* A transimpedance amplifier using a widely tunable PVT-independent pseudo-resistor for high-performance current sensing applications. in *ESSCIRC 2017 - 43rd IEEE European Solid State Circuits Conference* 79–82 (IEEE, 2017). <https://doi.org/10.1109/ESSCIRC.2017.8094530>.
33. Srinivasan, S. Electrode/electrolyte interfaces: structure and kinetics of charge transfer. Chapter in *Fuel Cells*. 27–92 (Springer US, 2006).
34. Morrow, R., McKenzie, D. R. & Bilek, M. M. M. The time-dependent development of electric double-layers in saline solutions. *J. Phys. D. Appl. Phys.* **39**, 937–943 (2006) <https://doi.org/10.1088/0022-3727/39/5/007>.
35. Bard, A. J. *Electrochemical methods: fundamentals and applications*. 2nd edn, (John Wiley & Sons, Inc., 2001).
36. Robinson, D. A. *et al.* Collision Dynamics during the Electrooxidation of Individual Silver Nanoparticles. *J. Am. Chem. Soc.* **139**, 16923–16931 (2017) <https://doi.org/10.1021/jacs.7b09842>.
37. Sundaresan, V., Monaghan, J. W. & Willets, K. A. Visualizing the Effect of Partial Oxide Formation on Single Silver Nanoparticle Electrodissolution. *J. Phys. Chem. C* **122**, 3138–3145 (2018) <https://doi.org/10.1021/acs.jpcc.7b11824>.
38. Ustarroz, J., Kang, M., Bullions, E. & Unwin, P. R. Impact and oxidation of single silver nanoparticles at electrode surfaces: one shot versus multiple events. *Chem. Sci.* **8**, 1841–1853 (2017) <https://doi.org/10.1039/C6SC04483B>.
39. Oja, S. M. *et al.* Observation of Multippeak Collision Behavior during the Electro-Oxidation of Single Ag Nanoparticles. *J. Am. Chem. Soc.* **139**, 708–718 (2017) <https://doi.org/10.1021/jacs.6b11143>.
40. Defnet, P. A., Anderson, T. J. & Zhang, B. Stochastic collision electrochemistry of single silver nanoparticles. *Curr. Opin. Electrochem.* **22**, 129–135 (2020) <https://doi.org/10.1016/j.coelec.2020.06.004>.
41. Feng, J. Electrochemistry probed one molecule at a time. *Curr. Opin. Electrochem.* **34**, 101000 (2022) <https://doi.org/10.1016/j.coelec.2022.101000>.
42. Bentley, C. L., Kang, M. & Unwin, P. R. Nanoscale Surface Structure–Activity in Electrochemistry and Electrocatalysis. *J. Am. Chem. Soc.* **141**, 2179–2193 (2019) <https://doi.org/10.1021/jacs.8b09828>.
43. Chen, Q., Zhao, J., Deng, X., Shan, Y. & Peng, Y. Single-Entity Electrochemistry of Nano- and Microbubbles in Electrolytic Gas Evolution. *J. Phys. Chem. Lett.* **13**, 6153–6163 (2022) <https://doi.org/10.1021/acs.jpcllett.2c01388>.
44. Zhang, J.-H. & Zhou, Y.-G. Nano-impact electrochemistry: Analysis of single bioentities. *TrAC, Trends Anal. Chem.* **123**, 115768 (2020) <https://doi.org/10.1016/j.trac.2019.115768>.



45. Baker, L. A. Perspective and Prospectus on Single-Entity Electrochemistry. *J. Am. Chem. Soc.* **140**, 15549–15559 (2018) <https://doi.org/10.1021/jacs.8b09747>.
46. Cullen, R. J. *et al.* Spontaneous grafting of nitrophenyl groups on amorphous carbon thin films: A structure-reactivity investigation. *Chem. of Mater.* **24**, 1031–1040 (2012) <https://doi.org/10.1021/cm2030262>.
47. Zhang, P. *et al.* In Situ Ice Template Approach to Fabricate 3D Flexible MXene Film-Based Electrode for High Performance Supercapacitors. *Adv. Funct. Mater.* **30**, (2020) <https://doi.org/10.1002/adfm.202000922>.
48. Wang, J., Polleux, J., Lim, J. & Dunn, B. Pseudocapacitive contributions to electrochemical energy storage in TiO<sub>2</sub> (anatase) nanoparticles. *J. Phys. Chem. C* **111**, 14925–14931 (2007) <https://doi.org/10.1021/jp074464w>.



# CHAPTER 4

## Electrochemical Kinetics as a Function of Transition-Metal Dichalcogenide Thickness

---

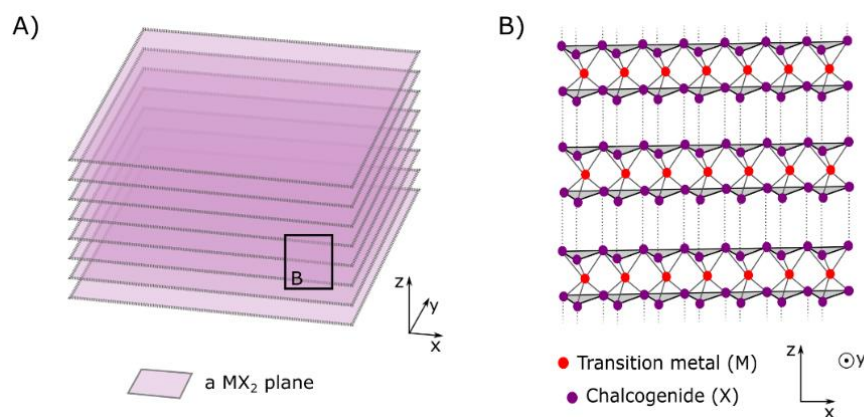
Two-dimensional transition metal dichalcogenides are used as electroactive materials for electrochemical and electrocatalytic applications. However, it remains unclear how the thickness of the transition metal dichalcogenide influences the electrochemical response measured at its surface. Scanning electrochemical cell microscopy (SECCM) is used to assess the electrochemical response of different thicknesses of bottom-contacted MoS<sub>2</sub>, MoSe<sub>2</sub>, WS<sub>2</sub>, and WSe<sub>2</sub> towards the simple outer-sphere redox couple [Ru(NH<sub>3</sub>)<sub>6</sub>]<sup>3+/2+</sup> with submicron spatial resolution. A detailed analysis, coupling mass transport and electrochemical kinetics, reveals that the electrochemical response can be described using an electron tunnelling barrier, which scales with the band gap of the two-dimensional transition metal dichalcogenide. The results suggest that the interpretation of the electrochemical and electrocatalytic responses on transition metal dichalcogenide-covered electrodes should account for the through-layer electron transport kinetics.

---

## 4.1 Introduction

### 4.1.1 Anisotropy of transition metal dichalcogenide crystals

Transition metal dichalcogenides (TMDCs) are materials that have a characteristic layered crystal structure. Each TMDC layer presents an  $\text{MX}_2$  configuration, where M is a transition metal element, *i.e.* Mo, V, W, etc. which is coordinated to X, being a chalcogenide element, *i.e.*, S, Se, etc. As shown in Figure 4.1, the two  $\text{MX}_2$  layers interact via Van der Waals forces (VdW), while metal (M) and chalcogenide (X) are covalently bonded. The characteristic TMDC crystalline structure with stronger intra-layer bonding and weaker inter-layer interaction makes this material anisotropic. The anisotropic behaviour of the bulk TMDC crystal influences macroscopic properties, including electrochemical behaviour.<sup>1,2</sup> Pumera, M. *et al.* showed that depending on which  $\text{MoS}_2$  crystal facet was exposed to electrolyte, different electron transfer kinetics were observed for outer-sphere redox mediators. Pumera's study shows that when the crystallographic edge-plane is exposed to electrolyte the kinetics are enhanced relative to when the basal-plane is exposed.<sup>3,4</sup> Similar enhancement of the Hydrogen Evolution Reaction (HER) kinetics on the crystallographic edge-planes of the  $\text{MoS}_2$  crystal compared to its crystallographic basal-plane have also been observed.<sup>5,6</sup>



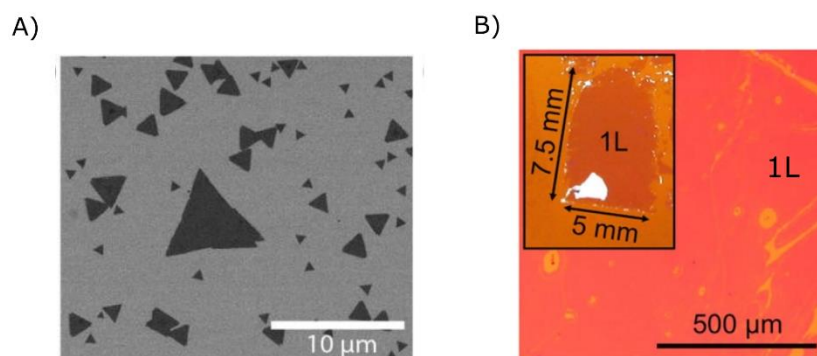
**Figure 4.1:** Structure of TMDCs **A)** Schematic crystal layered structure of TMDCs represented by  $\text{MX}_2$  planes. The black square indicates the cross section displayed in B. **B)** Schematic of the cross-section of a few  $\text{MX}_2$  planes stacked, highlighting the strong and short bonding for M-X coordination and the weaker VdW interaction between the X groups of the  $\text{MX}_2$  layers.

The anisotropic structure of TMDC also enables crystal exfoliation into mono- and few-layer two-dimensional (2D) sheets. The resulting 2D TMDC sheets are a completely new nanomaterial that has unique electronic, chemical, and mechanical properties.<sup>7</sup> For example, a monolayer of  $\text{MoS}_2$  presents a characteristic electronic structure with a direct band gap of 1.9 eV while the bulk crystal exhibits an indirect and smaller band gap of 1.2 eV.<sup>8</sup> The properties of 2D TMDCs have

been harnessed in electronic, spintronic, photonic, and energy conversion technologies.<sup>8-12</sup> Of particular interest here is the use of 2D TMDCs as active materials for electrochemical and electrocatalytic applications.<sup>13-15</sup> Examples of 2D TMDCs used in electrochemical applications include electrode materials for Li-ion batteries,<sup>16</sup> electrodes for supercapacitors,<sup>17,18</sup> and electrocatalysts for the hydrogen evolution reaction (HER).<sup>14,19-22</sup> Further details of the implementation of 2D material in energy storage and conversion devices can be found in Introductory chapter, Section 1.3.3.

#### 4.1.2 Heterogeneity and nanoscale domains in 2D TMDC

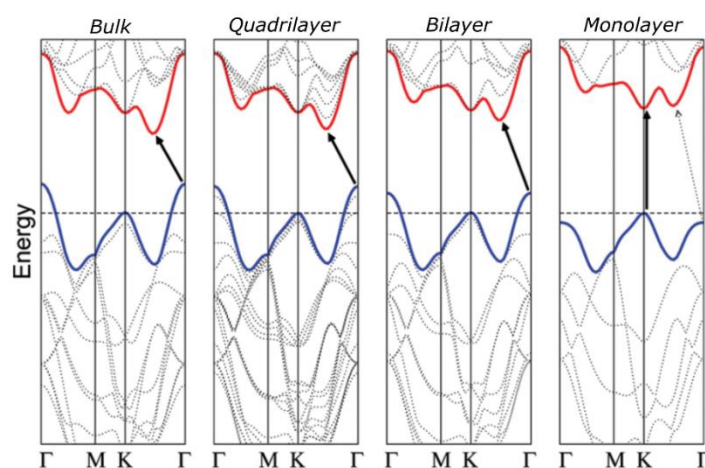
The 2D forms of TMDC can be achieved using top-down approaches, such as mechanical exfoliation of bulk crystals, or bottom-up approaches, such as chemical vapour deposition.<sup>13</sup> For both cases, the preparation of TMDCs in their 2D form typically yields heterogeneous samples with variable flake size, geometry, and thickness (number of single layers stacked), as shown in Figure 4.2. If manufacturing methods produce heterogeneous material, different domains with their characteristic electrochemical response can then be expected.



**Figure 4.2:** Images of 2D MoS<sub>2</sub> flakes produced by bottom-up and top-down approaches. **A)** SEM image of CVD-grown 2D MoS<sub>2</sub> flakes (dark contrast) on an Al<sub>2</sub>O<sub>3</sub> substrate (bright contrast). The images observed various discrete flakes with different geometry and sizes. This method produced a heterogeneous coverage of the substrate at the micrometre range. Reproduced with permission from Bergeron, H. *et al.*<sup>23</sup> **B)** Optical image of monolayer MoS<sub>2</sub> obtained by mechanical exfoliation on a gold surface. The inserted optical image shows the size of the monolayer region, which can be as large as a few mm<sup>2</sup>. Reproduced with permission from Velický, M. *et al.*<sup>24</sup>

The number of stacked TMDC layers strongly affects the electronic structure and the electrochemistry of the stacked material.<sup>13,24,25</sup> In the case of 2D MoS<sub>2</sub> for example, the largest band gap is observed for monolayer flakes, with values gradually decreasing with the number of layers, as shown in Figure 4.3. For 2D MoS<sub>2</sub> flakes with more than 5 layers stacked (approx. 4 nm thick), the band gap becomes very close to that of bulk MoS<sub>2</sub> crystals. The isolation and

electrochemical investigation of specific TMDC thicknesses remain a significant challenge, primarily because the flake size and active electrochemical domains of 2D TMDCs are in the nanometre to few micrometre scale range. It is difficult to prepare homogeneous mono- and few-layer flakes larger than tens of microns in lateral size, which are suitable for electrochemical measurements. However, recent advances in exfoliation methods, as well as the application of localised electrochemical methods, facilitate the study of the different nanoscale electrochemically active domains that are characteristic of such heterogeneous materials.<sup>24,26,27</sup>



**Figure 4.3:** Calculated band structure for MoS<sub>2</sub> in bulk form and bidimensional form, differentiating stacks of 4 layers, 2 layers and monolayer. The red line highlights the conduction band, the blue line highlights the valence band, and the black arrows indicate the smaller excitonic transition through the band gap. The indirect exciton transition occurs across a small band gap for bulk MoS<sub>2</sub>, while direct and large band gap transitions occur in monolayer MoS<sub>2</sub>. The quadrilayer and bilayer structures present an intermediate electronic structure configuration between the bulk and monolayer extremes. Reproduced with permission from Splendiani, A. *et al.*<sup>28</sup>

### 4.1.3 Advances in 2D TMDC exfoliation

One of the strategies to overcome difficulties in electrochemical characterisation of 2D TMDCs is to enlarge the size of the domains, by manufacturing larger homogeneous 2D TMDCs samples with fewer domains and larger characteristic lengthscales.<sup>13</sup>

Gold-mediated exfoliation is a mechanical exfoliation technique from bulk crystal, developed by collaborator Dr. Matěj Velický, which allows millimetre sized monolayer flakes to be fabricated. Gold-mediated exfoliation is achieved by placing a bulk layered TMDC crystal over a gold substrate: the outer layer of the crystal interacts with the gold substrate and if this interaction is

stronger than the TMDC inter-layer interaction strength, only the monolayer or few layers will be attached to the Au substrate surface once the crystal is removed.<sup>24</sup> Gold has high surface energy and displays strong interactions with TMDCs, but can be easily passivated by airborne adsorption.<sup>29</sup> If a TMDC crystal is placed on a freshly prepared gold surface (prior to any air exposure) a strong interaction between the substrate and the bulk crystal can be achieved, leading to the formation of large area 2D TMDCs coverage over 100's of micrometres sizes.<sup>24</sup> An example of the resulting gold substrate covered with mm size monolayer MoS<sub>2</sub> is displayed in Figure 4.2 B.

#### 4.1.4 Localised electrochemical methods for the study of 2D TMDCs

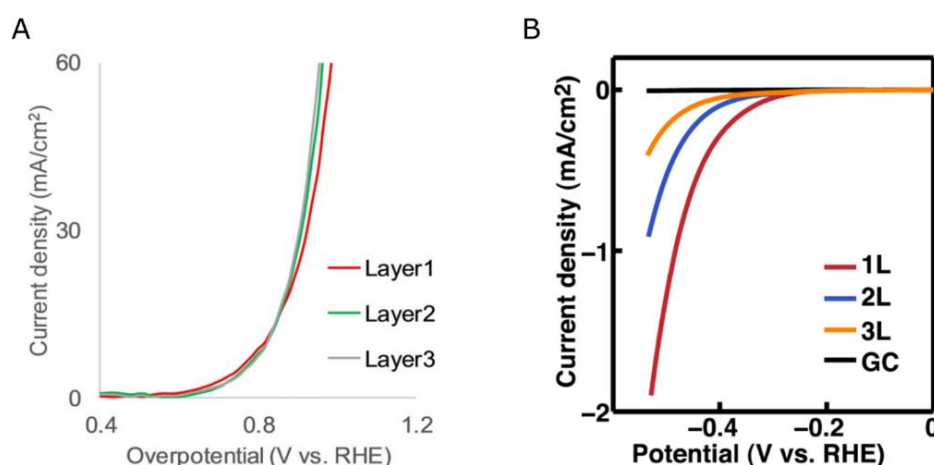
Large monolayer TMDCs domains can be obtained using state-of-the-art exfoliation techniques, however other electrochemically active domains, such as layer stacks  $\geq 2$  layers, layer boundaries and defects, remain close to or below the micrometre range.<sup>30</sup> Therefore, a spatial resolution in the micrometre range is still required from electrochemical measurements if desired to investigate any other domain than monolayer.

Scanning electrochemical probe microscopy techniques are particularly well suited to isolate the electrochemical activity of nano- and micro- scale domains.<sup>31,32</sup> Scanning electrochemical cell microscopy (SECCM) allows electrochemical mapping with a spatial resolution of tens to hundreds of nanometres using a nanodroplet electrochemical cell located at the end of a nanopipette.<sup>33-35</sup> A key advantage of a SECCM approach is the localised measurement at the area of interest, without electrochemical activation of the entire sample surface by its exposure to the electrolyte, as is the case in macroscale electrochemistry or scanning electrochemical microscopy. Furthermore, SECCM can be combined with complementary microscopy approaches, such as atomic force microscopy (AFM), to correlate the electrochemical activity with surface morphology. Combining SECCM and AFM techniques, Unwin, P. *et al.* have previously studied the electrocatalytic activity of bulk crystals of TMDCs that have well-defined terraces and edges.<sup>6,36</sup> These studies investigated HER on the surface of top-contacted TMDCs (MoS<sub>2</sub> and WS<sub>2</sub>), showing an enhanced electrocatalytic activity at the edge compared to the basal plane terraces.

Local electrochemical methods have also been implemented to study the 2D form of TMDCs. Takahashi, Y. *et al.* recently used SECCM with an impressive 20 nm resolution to characterise different 2D TMDCs (a few-layer MoS<sub>2</sub>, as well as heterostructures of MoS<sub>2</sub> and WS<sub>2</sub>) bottom-contacted, confirming an increased HER activity at the edge planes of MoS<sub>2</sub>, but showing no significant differences in HER activity for different number of TMDC layers, as shown in Figure 4.4 A.<sup>37</sup> However, other studies, which also conducted localised electrochemical measurements, reported different electrochemical activity depending on the number of 2D TMDCs

layers stacked. Cao, L. *et al.* reported clear differences in HER activity for bottom-contacted Monolayer (1L), Bilayer (2L) and Trilayer (3L) MoS<sub>2</sub>, as shown in Figure 4.4 B. Notice the disparity in current magnitude and potential window of the voltammograms shown in Figure 4.4 A with respect to Figure 4.4 B, despite the fact that both responses are acquired with SECCM and assigned to HER on few layer MoS<sub>2</sub>. Collaborator Velický, M. *et al.* previously measured the electrochemical and photoelectrochemical response of 2D MoS<sub>2</sub> of an insulating substrate (*i.e.* top-contacted) towards the reduction of the [Ru(NH<sub>3</sub>)<sub>6</sub>]<sup>3+/2+</sup> redox couple using a microdroplet electrochemical cell.<sup>38</sup> This study showed the significant effect of the number of layers (comparing monolayer, 3-4 layers, 5-10 layers, and bulk) on the electrochemical response.

Despite the novelty of the above studies that used local electrochemical methods on 2D materials, extracting conclusions from them remains challenging due to the very distinct behaviours observed and the use of different methods to establish electrical contact to the sample, top-contact, or bottom-contact. The electrical contact mode can indeed affect the observed electrochemical behavior of 2D TMDCs, as discussed in detail in this chapter.

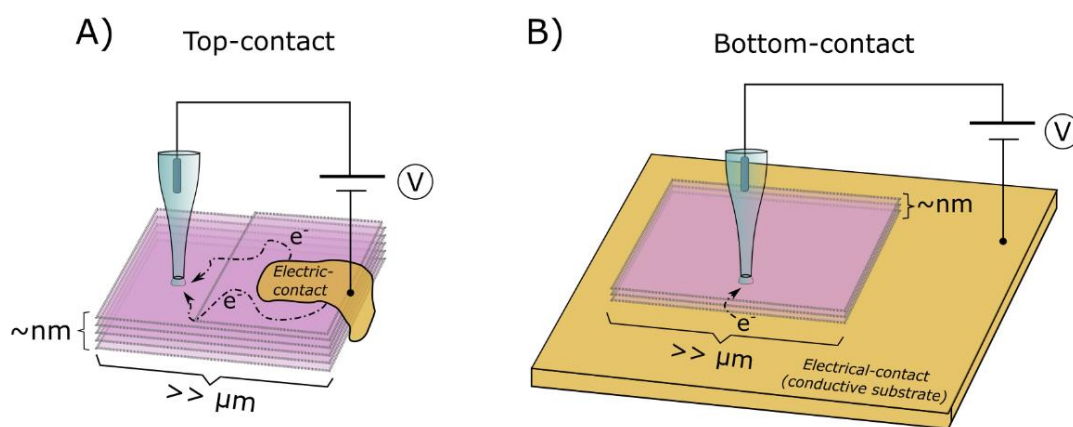


**Figure 4.4:** Electrochemical response of 2D MoS<sub>2</sub> with different number of layers stacked. **A)** Voltammograms showing equal cathodic current density and HER overpotential on different numbers of MoS<sub>2</sub> layers stacked. Reproduced with permission from Takahashi, Y. *et al.*<sup>37</sup> **B)** Voltammograms showing different cathodic current density and HER activity of different number of MoS<sub>2</sub> layers stacked. Reproduced with permission from Yu, Y. *et al.*<sup>25</sup>



### 4.1.5 Electronic contact of 2D materials: Bottom-contact vs. top-contact

In the case of catalysts with high aspect ratio, such as 2D materials, the way the connection is established, and the potentials applied define the path for electron transport. For 2D materials, it is possible to study their properties by establishing either a top-contact or a bottom-contact. As shown in Figure 4.5 A, in a top-contact configuration, electrical contact is made with the top layer of the 2D material stack (and/or with its side), usually using a conductive adhesive and a metallic wire. The top-contact configuration forces charge transfer (from electrode material to solution species or *vice versa*) to occur at a distance from the electrical contact.<sup>13</sup> For TMDCs, lateral electron transport occurs along the layers due to the high in-plane electrical conductivity.<sup>39</sup> In a bottom-contact configuration, however, electrical contact is established through the supporting metallic substrate on which the 2D layers are immobilised. As shown in Figure 4.5 B, this configuration provides homogeneous contact through the whole plane of the 2D material with respect to the location at which the electron transfer processes take place. This configuration forces charge transport to occur between the metallic substrate and the top 2D layer, where the electrochemical reaction takes place. Therefore, in a bottom-contacted 2D material, the interlayer electron transport can influence the electrochemical response.<sup>13</sup> In this chapter, the effect of electron transport through a different number of stacked TMDC layers on the electrochemical kinetics is described in detail.



**Figure 4.5:** Scheme of two possible contact modes for TMDCs. The 2D TMDC stacks are shown in pink. **A)** Top-contact configuration where electric contact is established with the top and/or side of the 2D TMDC located at least a few 100's  $\mu\text{m}$  from the electrochemical measurement. The electron flow indicates in plane conductivity. **B)** Bottom-contact configuration where electric contact is established by the conductive substrate, which is nanometres from the location of the electrochemical measurement.

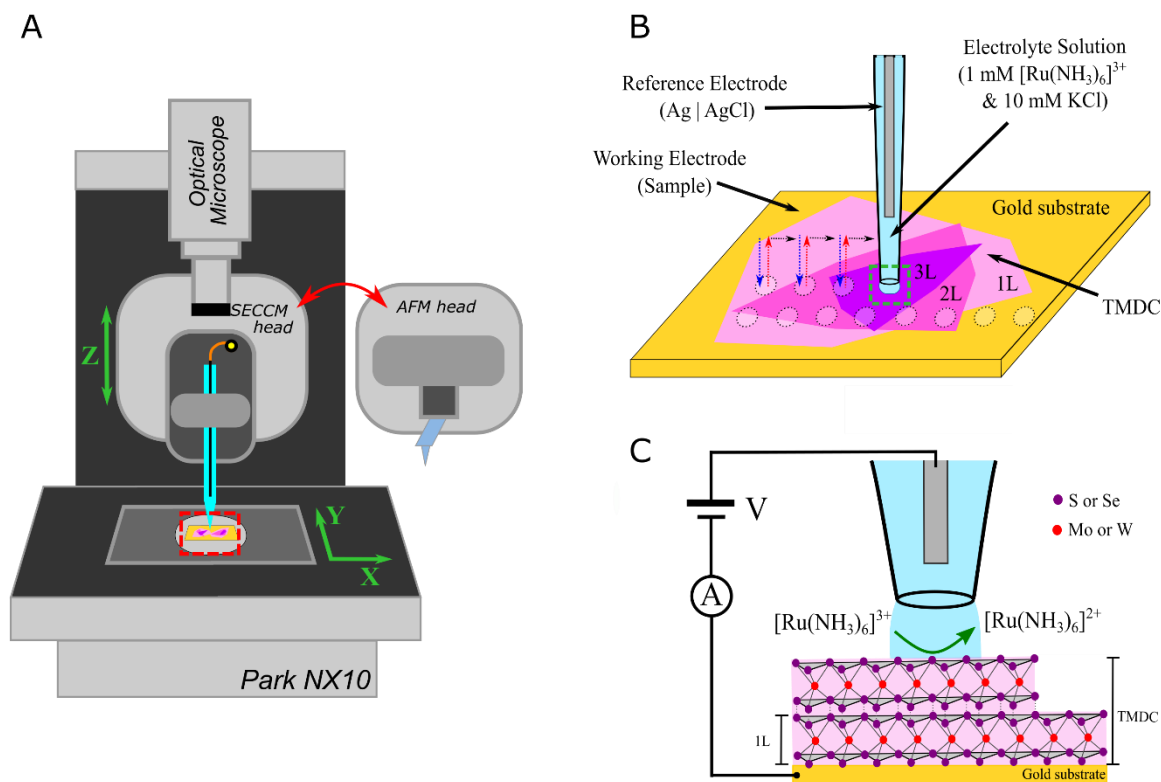
A very recent manuscript by Unwin, P. *et al*, published shortly after the work presented in this chapter was completed, used graphene supported on copper to explore the role of electron transfer in bottom-contacted 2D materials for outer-sphere redox couples.<sup>40</sup> Their work shows that in

bottom-contact configuration the electron transfer rate is dependent on the number of layers of graphene. Thus, the number of graphene layers effectively varies the properties of the electrode/electrolyte interface in bottom-contact configuration, and thus affects the kinetics of adiabatic electron transfer. For bottom-contacted 2D TMDCs, previous studies do not convey how electron transport/contact mode affects the electrochemical reaction.<sup>40</sup> Furthermore, previous 2D TMDCs studies focused on HER activity determinations, rather than the study of fundamental adiabatic processes. Some publications pointed out that electron transport between the conductive substrate and the 2D TMDC could be the rate-limiting step in HER electrocatalysis, suggesting that the kinetics of the HER relies on electron hopping between the MoS<sub>2</sub> layers.<sup>25</sup> However, a recent report of HER on bottom-contacted MoS<sub>2</sub> observed no significant dependence of the electrocatalytic response on either the electron transport, or the number of stacked layers.<sup>37</sup> Therefore, a clear scientific question arises about how the layer thickness and the bottom-contact affect the electrochemical response of a TMDC, and which role is played by the charge transport mechanism.

#### 4.1.6 Strategy to resolve electron transfer on 2D TMDCs electrodes

Gold exfoliated TMDCs produce large areas of bottom-contacted basal planes of 2D TMDCs with well-defined number of layers stack. By coupling this type of sample with local electrochemical measurement, such as SECCM, it is possible to isolate the electrochemical response of those basal planes, *i.e.* monolayer, bilayer, trilayer, etc. This experimental configuration allowed to probe the influence of electron transport and the number of stacked layers on the electrochemical response. Moreover, correlation of electrochemical response and sample morphology could be achieved by AFM.

HER is an inner sphere multistep reaction whose overall rate on TMDC electrodes is proposed to depend on chemical steps involving surface-adsorbate intermediates. However, the complexity and catalytic nature of the HER might hinder the effect of through-layer electron transport on the electrochemical response. If the electron transfer process is mediated instead by using a well-defined outer sphere redox couple (only sensitive to the density of electronic states), the system will be better suited to assess the dependence of the electrochemical response on the number of TMDC layers. Figure 4.6 illustrates a schematic of such an experimental setup.



**Figure 4.6:** Schematic of experimental setup. **A)** Schematic of the ParkSystems NX10 instrument featuring an SECCM probe and an exchangeable AFM probe head. **B)** Schematic of the SECCM nanopipette probe mapping the electrochemical response of the TMDC surface. **C)** Schematic of the nanodroplet-based electrochemical cell (located at the end of an SECCM probe), showing the electrochemical reaction taking place at the surface of the 2D TMDC, the structure of the 2D TMDC and the electrical contact with the Au substrate. Reproduced with permission from Brunet Cabré, M. *et al.*<sup>41</sup>

## 4.2 Aims

In this chapter, I explore the dependence of the electrochemical response of 2D TMDCs on layer thickness, with the aim of providing new knowledge and understanding on the role of electron transport towards future applications of 2D TMDCs as electrocatalysts. To conduct this study, it was essential to work with 2D TMDC samples that present large and homogeneous basal plane domains. A collaborator and expert in TMDC exfoliation, Dr. Matej Velicky provided different gold-mediated exfoliated 2D TMDCs studied (MoS<sub>2</sub>, MoSe<sub>2</sub>, WS<sub>2</sub> and WSe<sub>2</sub>) that meet these requirements.

This chapter is structured by first presenting sample morphological characterisation and layer thickness determination by optical microscopy and atomic force microscopy (AFM). Local electrochemical measurements performed with the SECCM technique were then carried out to evaluate the reduction of [Ru(NH<sub>3</sub>)<sub>6</sub>]<sup>3+/2+</sup>, an outer-sphere redox couple, on the top surface of bottom-contacted 2D TMDCs. SECCM scan grids aim to provide several voltammetric measurements on each layer thickness studied (monolayer, bilayer and trilayer) for the different 2D TMDCs studied. Moreover, SECCM combined with further AFM provided a correlation of the electrochemical response to the surface morphology, allowing the observation of trends between the electrochemical response and the number of stacked layers.

For a quantitative comparison between electrochemical kinetics and morphology of the 2D TMDCs, the system was modelled using finite element simulations, which account for mass transport effects and include a description of electron transfer kinetics. By fitting the simulations to the recorded voltammograms, kinetic parameters of electron transfer were derived. Finally, the last section of this chapter discusses the relation between the electrode transfer kinetics and the changes in electronic structure arising from changes in the number of TMDC layers stacked.

### 4.3 Methods

Hexaammineruthenium (III) chloride ( $[\text{Ru}(\text{NH}_3)_6]\text{Cl}_3$ ) was purchased from JMC Corporation (South Korea). Potassium chloride ( $\text{KCl}$ ,  $\geq 99.5\%$ ) was obtained from VWR Chemicals (USA). All chemicals were used as received. Distilled water with a resistivity of  $18 \text{ M}\Omega \text{ cm}$  was used to prepare the solution of  $10 \text{ mM KCl}$  and  $1.0 \text{ mM } [\text{Ru}(\text{NH}_3)_6]^{3+}$ . All procedures were carried out at room temperature.

Samples of transition metal dichalcogenides ( $\text{MX}_2$ ,  $\text{M} = \text{Mo}$  or  $\text{W}$  and  $\text{X} = \text{S}$  or  $\text{Se}$ ) were prepared by our collaborator Dr. Velický via mechanical exfoliation of bulk crystals on Au substrates, as previously reported.<sup>24</sup> The bottom-contact electrical connection to the TMDCs was established via the gold substrate.

Optical, AFM, and SECCM measurements were acquired on a Park NX10 instrument (Park Systems, South Korea). AFM images were obtained in non-contact mode (NCM) with a PPP NCHR cantilever type (force constant =  $42 \text{ N/m}$ , resonance frequency =  $330 \text{ kHz}$ , Nanosensors).

The SECCM probes were made of single-barrelled nanopipettes with a  $300 - 600 \text{ nm}$  aperture radius. Nanopipettes were fabricated from single-barrelled borosilicate capillaries ( $1.5 \text{ mm O.D}$  and  $0.86 \text{ mm I.D.}$ , BF150-86-7.5, Sutter Instrument, USA) using a P-2000 laser puller (Sutter Instrument, USA). The nanopipettes were filled with a solution of  $1 \text{ mM } [\text{Ru}(\text{NH}_3)_6]^{3+}$  in  $10 \text{ mM KCl}$  (sufficient supporting electrolyte for nanoscale electrochemical measurements)<sup>42</sup> using a pipette filler (MicroFil MF34G-5, World Precision Instruments, USA); prior to this, the electrolyte was filtered through a  $0.45 \mu\text{m}$  syringe filter (PTFE membrane, Fisher Scientific, USA). An Ag/AgCl wire quasi reference counter electrode was inserted into the top end of the nanopipette.

SECCM measurements were performed using the ParkSystem NX10 system. The SECCM probe was aligned with the sample area on the surface using the NX10 opticals and the LSVs were then recorded on a pre-programmed squared grid, with individual measurement spots spaced at  $1.5 \mu\text{m}$ . A hopping mode was used in which the probe was approached vertically toward the sample surface at a speed of  $0.3 \mu\text{m/s}$  and a potential of  $-0.8 \text{ V}$  until contact between the nanopipette droplet and the surface was established. The contact was detected as the appearance of a double layer charging current and immediate  $[\text{Ru}(\text{NH}_3)_6]^{3+}$  reduction, with a threshold of  $5 \text{ pA}$ . At this point, the vertical movement of the probe was stopped immediately and LSVs were recorded in the potential range of  $+0.2 \text{ V}$  to  $-0.8 \text{ V}$  at a speed of  $1 \text{ V/s}$ . After the electrochemical measurement is complete, the nanopipette was retracted and moved to the next sample point on the grid.

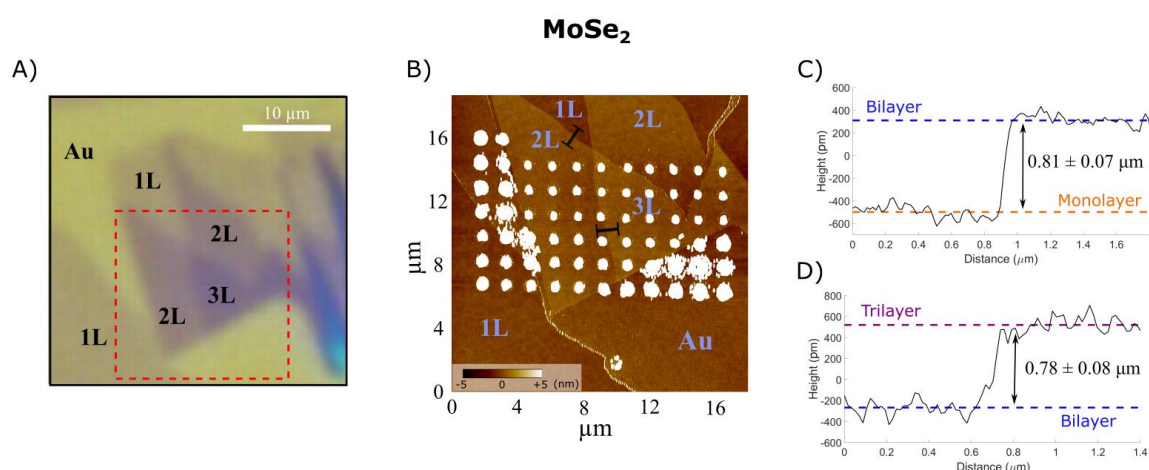
Simulations of the nano-electrochemical cell at the end of the SECCM probe were performed in COMSOL Multiphysics (COMSOL 5.2, Sweden).

## 4.4 Results and discussion

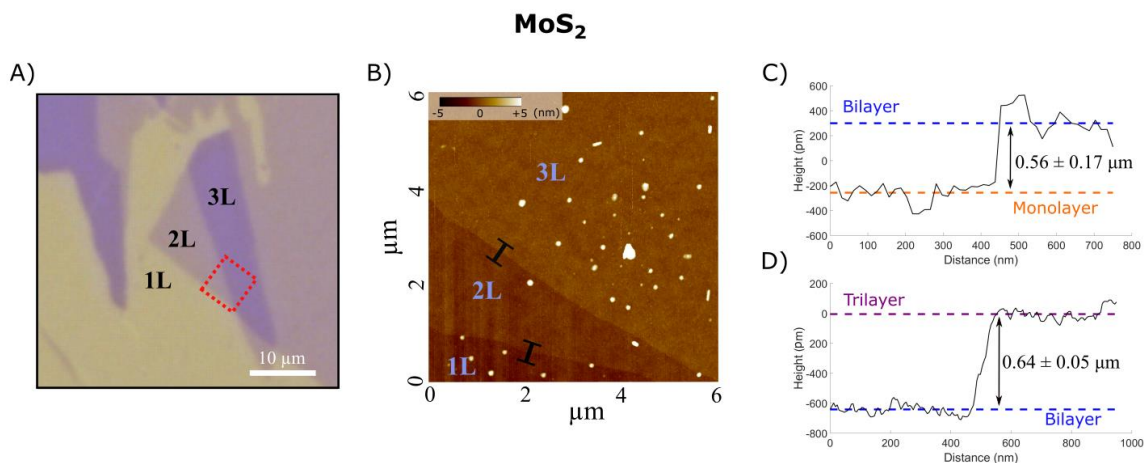
### 4.4.1 TMDC thickness characterisation

Samples consisting of 2D flakes of MoS<sub>2</sub>, MoSe<sub>2</sub>, WS<sub>2</sub>, and WSe<sub>2</sub> on an Au substrate were prepared by the collaborator Dr. Velický by gold-assisted mechanical exfoliation.<sup>24</sup> The samples were shipped to Trinity College Dublin for the rest of the experimental work. The regions of the Au substrate coated with TMDC flakes of a different number of layers could be optically distinguished, as shown for MoSe<sub>2</sub> in Figure 4.7 A. The optical contrast and colour of the flakes change with the different number of layers of MoSe<sub>2</sub> stacked.<sup>43</sup> Similar results were obtained for MoS<sub>2</sub>, WSe<sub>2</sub>, and WS<sub>2</sub>, as reported in Figures 4.8 to 4.10 A respectively.

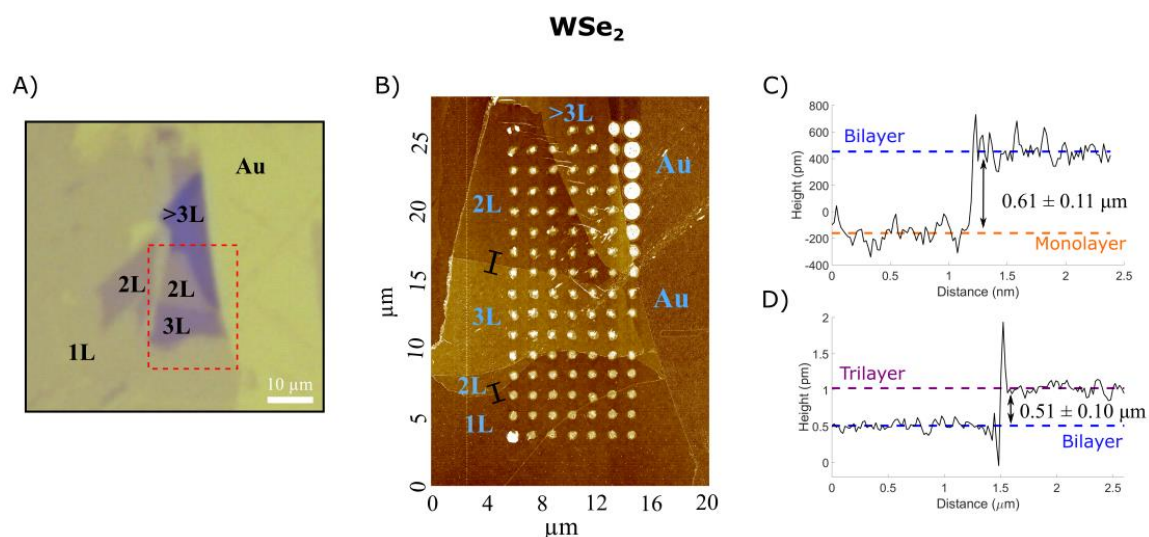
The optical images were used to locate surface regions containing various TMDCs thicknesses (1L-3L) prior to SECCM characterisation. AFM was used to corroborate the layer assignment from the step-height profiles obtained after the SECCM measurement, as shown in Figure 4.7 B. Step-height profiles of 1L/2L and 2L/3L areas displayed in Figure 4.7 C and D yield monolayer thickness of *ca.* 0.81 nm and 0.78 nm, in agreement with previous monolayer MoSe<sub>2</sub> estimates from AFM ( $\sim$ 0.85 nm).<sup>44</sup> The step-height from Au to 1L could not be clearly determined due to the roughness of the gold surface. AFM images and step-height profiles for the MoS<sub>2</sub>, WSe<sub>2</sub>, and WS<sub>2</sub> samples are displayed in Figures 4.8 to 4.10 respectively. The measured layer thicknesses agree with previous studies of different TMDCs and support the optical analysis.<sup>24,45-47</sup>



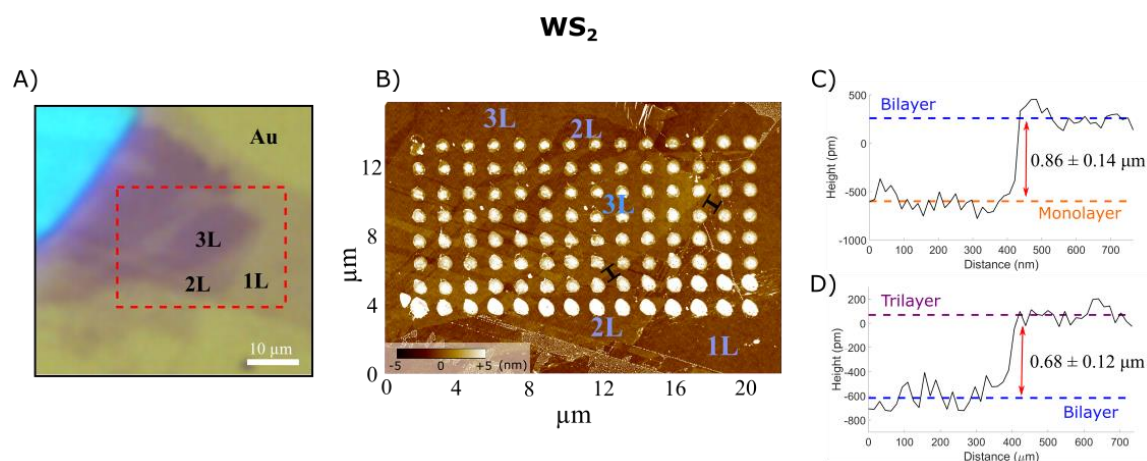
**Figure 4.7:** Morphological characterisation 2D MoSe<sub>2</sub>. **A)** Optical image of MoSe<sub>2</sub> crystals with different numbers of layers stacked. **B)** AFM image of a region depicted by the red rectangle in part A. The AFM was measured after the SECCM measurements and, therefore, revealed the electrolyte residues at the areas of contact between the droplet and the surface. **C)** and **D)** line profiles of the 1L/2L and 2L/3L boundaries, respectively, taken from the areas shown by the black lines in B). Step-height was calculated as the difference of the average terrace height (dashed coloured lines).



**Figure 4.8:** Morphological characterisation 2D MoS<sub>2</sub>. **A)** Optical image of MoS<sub>2</sub> flakes of different layer thickness. **B)** AFM image of the region depicted in A as a red rectangle, prior to the SECCM measurement. **C)** and **D)** Line profiles (solid line) for layer boundaries from monolayer to bilayer, and from bilayer to trilayer, respectively. Step-height was deduced from the difference of the terrace average height (dashed lines).



**Figure 4.9:** Morphological characterisation 2D WSe<sub>2</sub>. **A)** Optical image of WSe<sub>2</sub> flakes of different layer thickness. **B)** AFM image of the region depicted in A as a red rectangle, after SECCM measurement. **C)** and **D)** Line profiles (solid line) for layer boundaries from monolayer to bilayer, and from bilayer to trilayer, respectively. Step-height was deduced from the difference of the terrace average height (dashed lines).



**Figure 4.10:** Morphological characterisation 2D WS<sub>2</sub>. **A)** Optical image of WS<sub>2</sub> of different layer thickness. **B)** AFM image of the region depicted in A as a red rectangle, after SECCM measurement. **C)** and **D)** Line profiles (solid line) for layer boundaries from monolayer to bilayer, and from bilayer to trilayer, respectively. Step-height was deduced from the difference of the terrace average height (dashed lines).

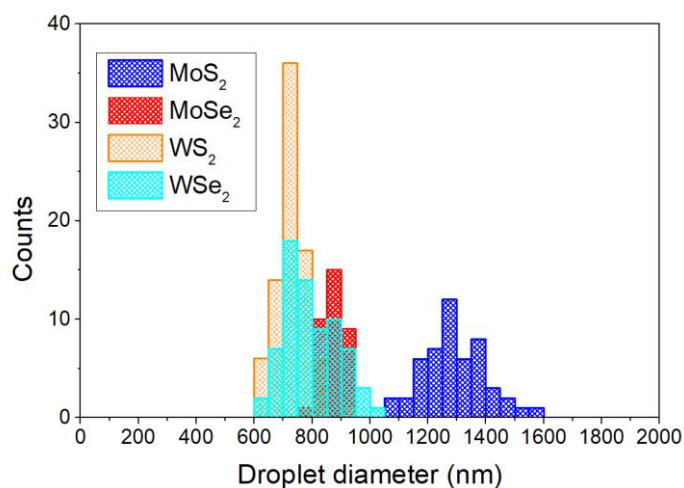
#### 4.4.2 Local electrochemical measurements and morphology correlation

SECCM electrochemical mapping was performed using a single barrel nanopipette probe of approximately 800 nm diameter. An Ag/AgCl wire immersed in the electrolyte solution was used as the reference electrode. Linear sweep voltammograms (LSVs) for the reduction of [Ru(NH<sub>3</sub>)<sub>6</sub>]<sup>3+</sup> to [Ru(NH<sub>3</sub>)<sub>6</sub>]<sup>2+</sup> were obtained with a regular grid of sample points spaced at 1.5 μm intervals on all four TMDC materials (MoS<sub>2</sub>, MoSe<sub>2</sub>, WS<sub>2</sub>, WSe<sub>2</sub>); multiple measurements were performed on each surface type (Au, 1L, 2L, and 3L). The AFM images shown in Figures 4.7 to 4.10 B, which were obtained after the SECCM measurements, reveal salt residues left at the points of contact between the SECCM droplet and the surface after water evaporation.

The droplet/surface contact area for each SECCM point was estimated from the AFM images by measuring the diameter of the droplet residue. The distribution of the droplet diameter measured for all TMDC samples is shown in Figure 4.11. The average estimates and their corresponding standard deviation are reported in Table 4.1, where similar droplet sizes are observed for the MoSe<sub>2</sub>, WS<sub>2</sub>, and WSe<sub>2</sub> SECCM measurements. The droplet size depends on the pipette aperture, and the pipette aperture is expected to have a slight variation between different pipettes. The variability in the aperture of the pipette is due to the nature of the pipette pulling process (see Methods Section 2.2.2). A new pipette was used for each SECCM measurement; therefore, a small variation in the average droplet size between each of the TMDC is expected, as observed for MoSe<sub>2</sub>, WS<sub>2</sub> and WSe<sub>2</sub>. The average droplet size of MoS<sub>2</sub>, however, is found to be



considerably larger at approximately  $1.30 \pm 0.11 \mu\text{m}$  in diameter. The larger droplet size observed on  $\text{MoS}_2$  was found to be due to a larger pipette aperture, which was determined from the diffusion-limited current on  $\text{MoS}_2$  as detailed later in Section 4.4.3.1 of this chapter. In conclusion, droplet size has only a narrow dispersion regardless of the TMDC thickness, which is consistent with the wetting behaviour of TMDCs surfaces after exposure to air.<sup>48,49</sup> Grid points sampled on bare gold surfaces (see the  $\text{MoSe}_2$  and  $\text{WSe}_2$  samples in Figures 4.7 and 4.9) exhibited the largest droplet contact size, which can be attributed to the higher hydrophilicity of Au compared to the TMDCs.<sup>29,49</sup>



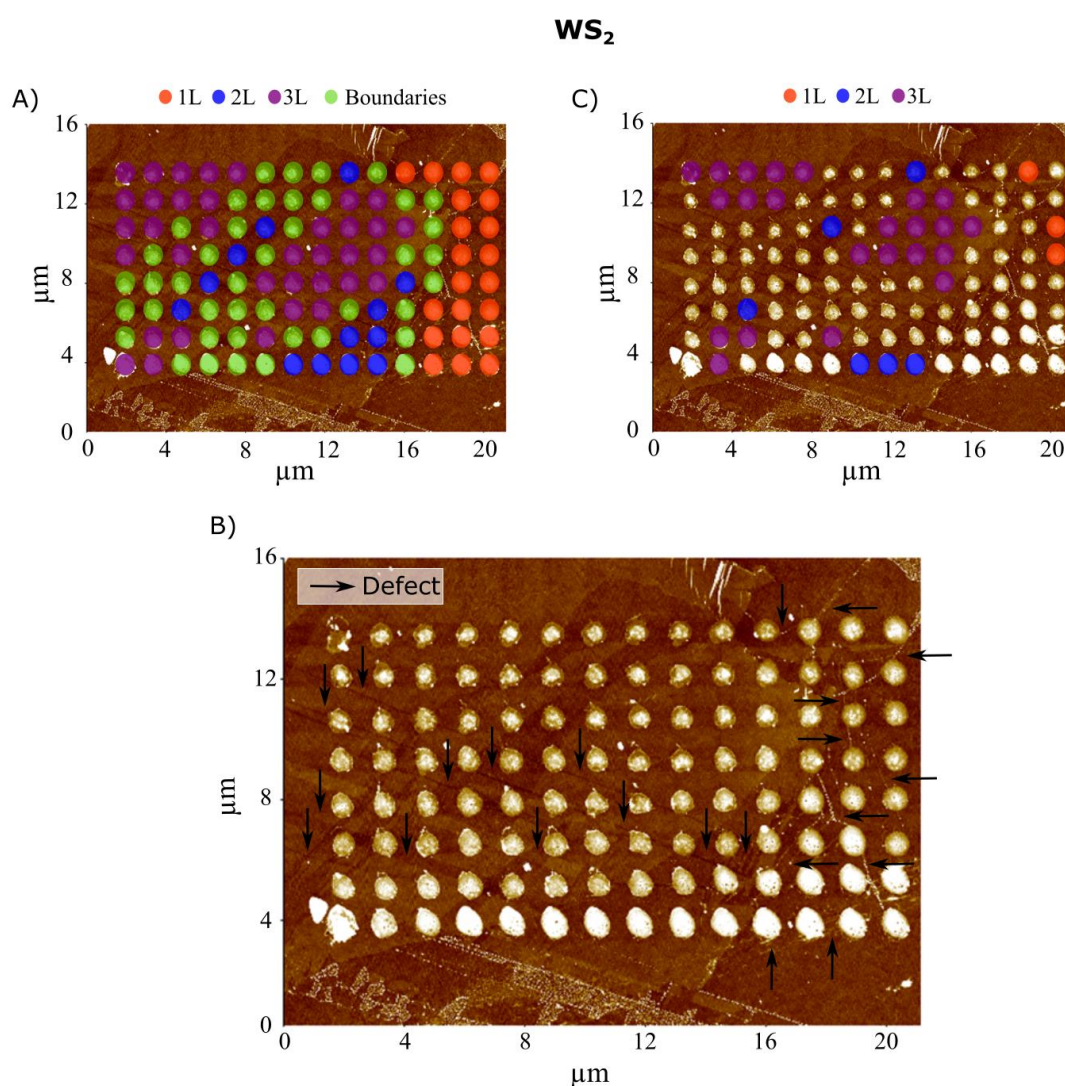
**Figure 4.11:** Histogram of droplet diameters determined from AFM images over different layer thicknesses of  $\text{WS}_2$ ,  $\text{MoS}_2$ ,  $\text{WSe}_2$ , and  $\text{MoSe}_2$ .

**Table 4.1:** Average droplet residue diameter and standard deviation for each 2D TMDC experiment. Average performed over all the droplet cell residues on TMDCs basal plane.

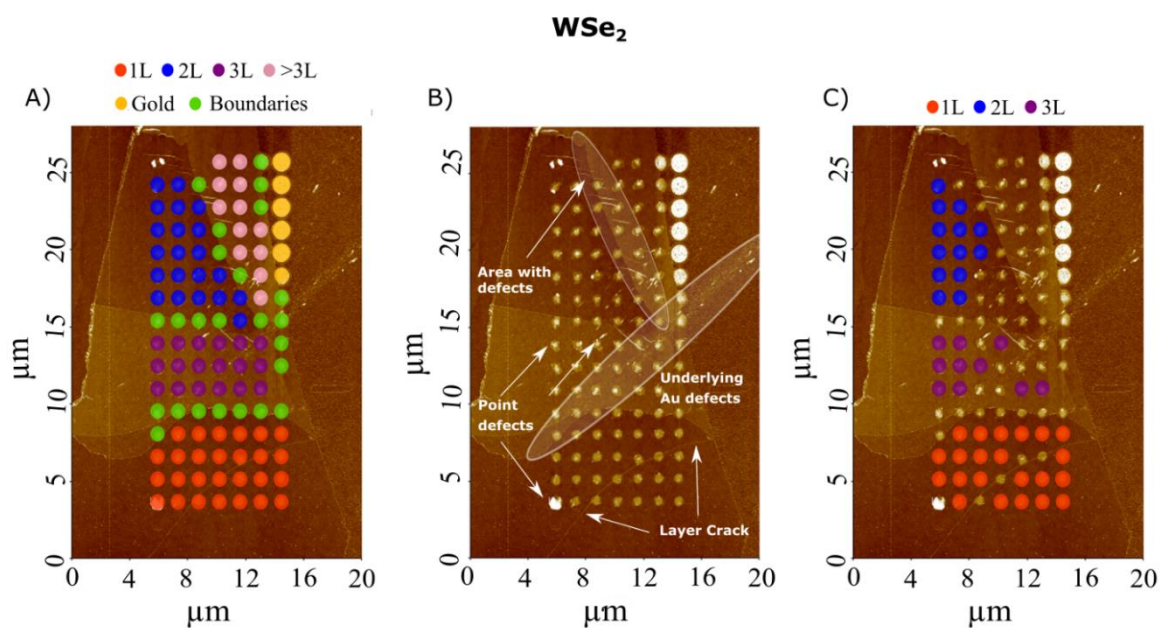
TMDCs	Mean (nm)	Standard deviation (nm)
$\text{MoS}_2$	1287	$\pm 109$
$\text{MoSe}_2$	807	$\pm 47$
$\text{WS}_2$	729	$\pm 52$
$\text{WSe}_2$	795	$\pm 90$

The salt residues observed on AFM images could be used to correlate each recorded LSV with a specific TMDC surface morphology contacted in terms of, for instance, TMDC thickness or presence of a direct contact to the gold surface. The points were then classified by the 'surface type' contacted as: gold, number of TMDC layer contacted and layer boundaries. Figures 4.12 to 4.14 A show AFM images for  $\text{WS}_2$ ,  $\text{WSe}_2$  and  $\text{MoSe}_2$  samples, respectively, recorded after the SECCM

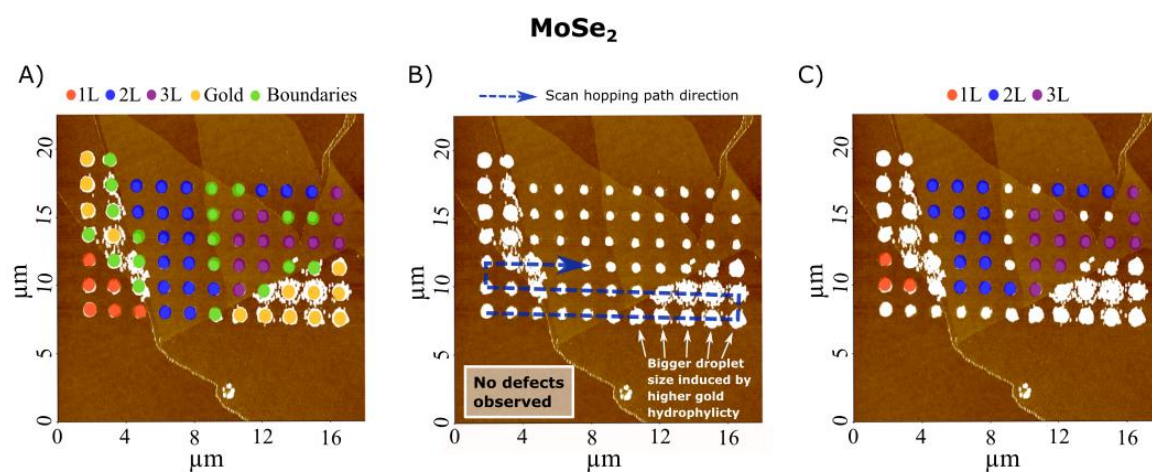
measurements, where the sampled areas are colour coded to reflect the corresponding surface type contacted. AFM imaging also revealed various forms of defects and surface irregularities, such as linear morphological features (which can be indicative of cracks in the 2D flakes) or defects in the underlying Au substrate, as shown in Figure 4.12 to 4.14 B. These morphological features are distinct from the expected for the TMDCs pristine basal plane. The Figures 4.12 to 4.14 C highlight the points that appear to be only contacting the pristine TMDC basal plane surface. The relative spacing ( $1.5\ \mu\text{m}$ ) of the SECCM point grid was identical for all four TMDCs. Due to the greater wetting on  $\text{MoS}_2$ , a larger fraction of the sample became covered by salt residues, which rendered the AFM analysis of the surface type unreliable. Therefore, we employed optical microscopy to assign the surface type to each SECCM point, as detailed in Figure 4.15.



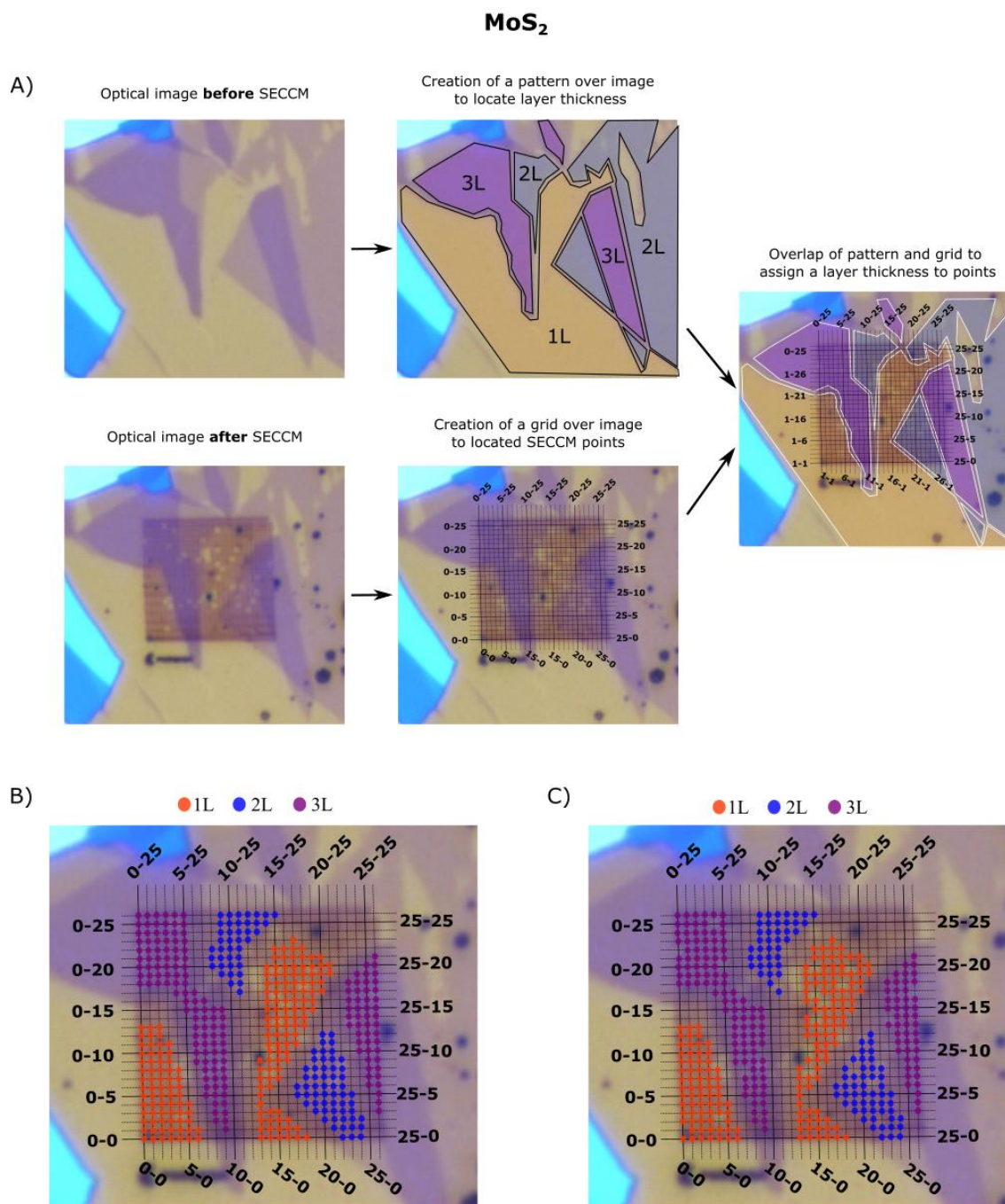
**Figure 4.12:** Assignment of each grid point to surface type based on the location of the droplet cell residue on the  $\text{WS}_2$  SECCM grid scan. **A)** Colour-coded surface type assignment over the AFM image showing the SECCM point grid on  $\text{WS}_2$ . **B)** Enlarged AFM image of A) that reveals multiple defects on  $\text{WS}_2$  layers, highlighted by black arrows. **C)** Colour-coded layer-thickness assignment excluding the points located over boundaries/defects. Sample points affected by these defects were excluded from the LSVs analysis. Reproduced with permission from Brunet Cabré, M. *et al.*<sup>41</sup>



**Figure 4.13:** Assignment of each grid point to the surface type based on the location of the droplet cell residue for the  $\text{WSe}_2$  SECCM grid scan. **A)** Colour-coded surface type assignment over the AFM image showing the SECCM point grid on  $\text{WSe}_2$ . **B)** AFM image of A) which reveals a variety of sample defects observed on the  $\text{WSe}_2$  sample, highlighted with white arrows. **C)** Colour-coded layer-thickness assignment excluding the points located over boundaries/defects. The sample points affected by these defects were excluded from the LSVs analysis.



**Figure 4.14.** Assignment of each grid point to surface type based on the location of the droplet cell residue for the  $\text{MoSe}_2$  SECCM scan. **A)** Colour-coded surface type assignment over the AFM image showing the SECCM point grid on  $\text{MoSe}_2$ . **B)** AFM image showing that the droplets enlarge once in contact with the bare gold surface. The LSVs corresponding to the six first points, located before the first gold contact, show a smaller limiting current, as seen in Figure 4.18 for 1L. These six points were not considered for LSV analysis. No defects were observed in this region, therefore, the rest of points assigned to 1L, 2L and 3L were accounted for in the analysis. **C)** Colour-coded layer-thickness assignment excluding the points located over boundaries/defects.

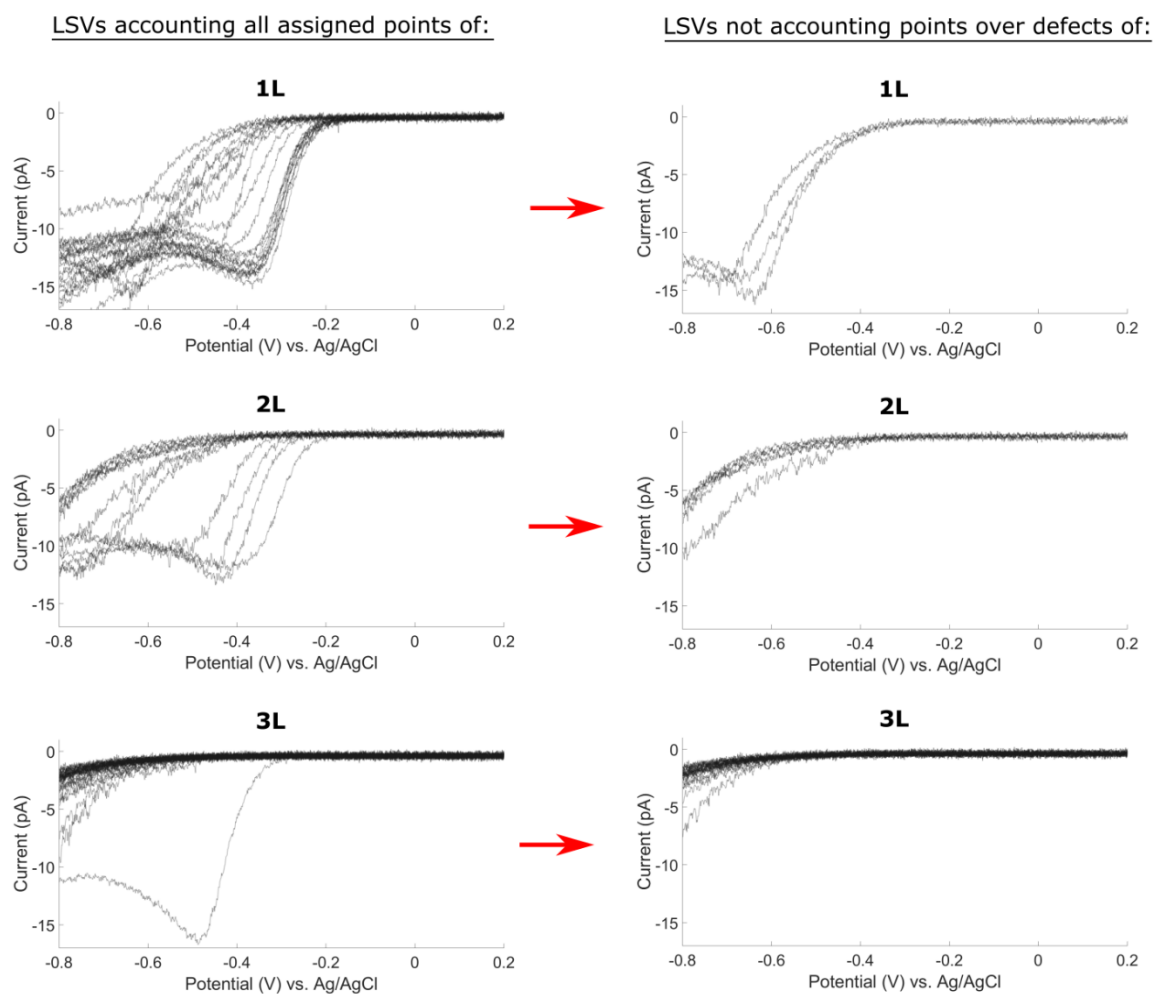


**Figure 4.15:** Assignment of each grid point to surface type for the MoS<sub>2</sub> SECCM scan. **A)** Detailed scheme for locating the each SECCM point of the grid based on the optical images of the same area before and after SECCM. **B)** Colour-coded layer-thickness assignment on the optical image showing the SECCM point grid on MoS<sub>2</sub>. **C)** Colour-coded layer-thickness assignment excluding the points where the pipette failed to approach the surface and form the droplet cell, leading to zero-current LSVs, observed in Figure 4.17.

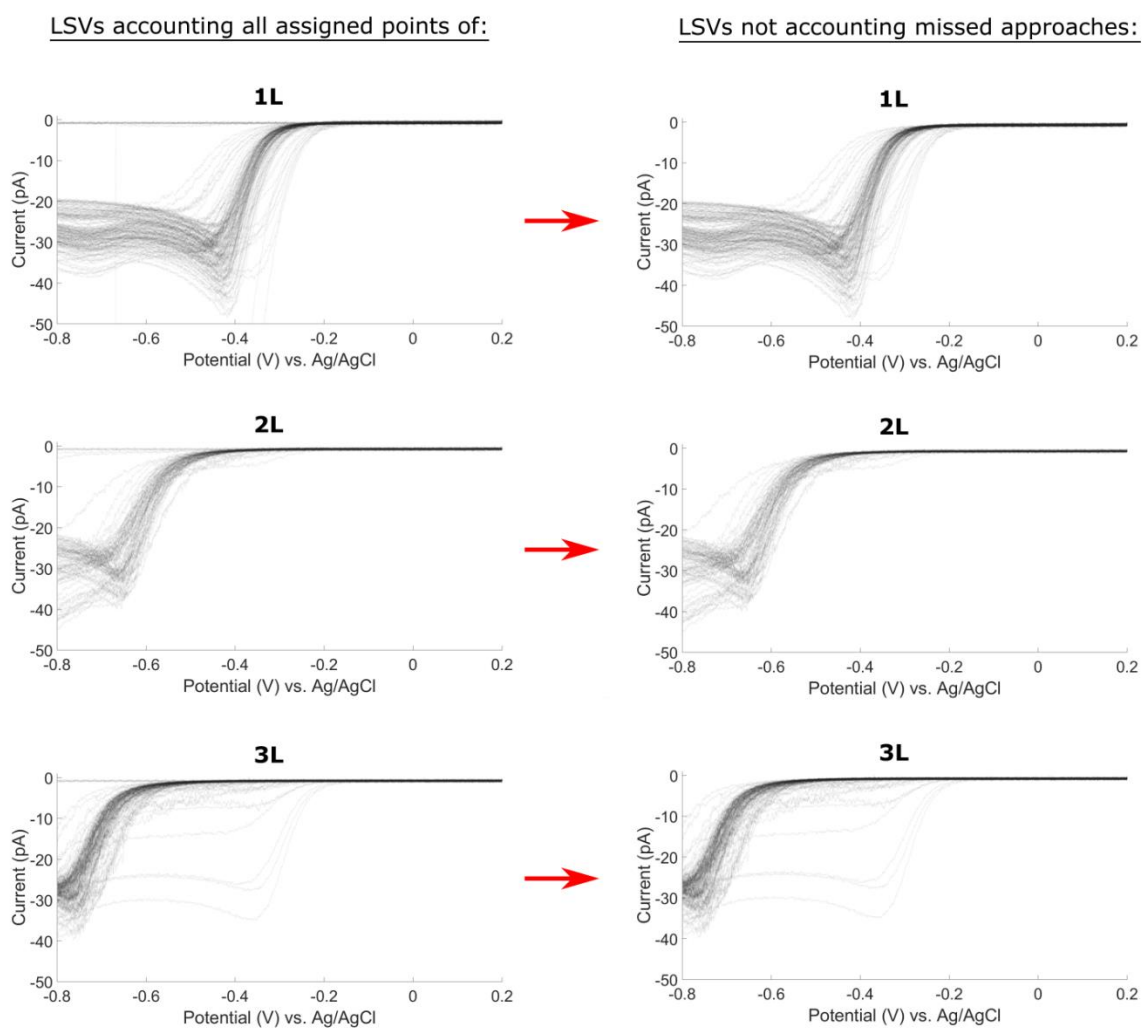
On the left side of Figure 4.16-4.19, all LSV curves recorded over the basal plane for the four TMDCs studied are shown and classified by the number of layers stacked. However, some of these droplet cells contacted distinct morphological features, *i.e.* defects, which are likely to affect the electrochemical response, see Figures 4.12 to 4.14 B. The LSV curves recorded at those points were therefore excluded from the analysis of the electrochemical response as a function of the TMDC thickness. As a consequence, the above procedure resulted in multiple LSV curves obtained at pristine regions of the basal planes and are classified by monolayer (1L), bilayer (2L) and trilayer (3L) thickness, as shown on the left side of Figures 4.16-4.19.

The LSV datasets shown in Figures 4.16 to 4.19, obtained by either including or excluding points over defects, show the dependence of the electrochemical behaviour on the TMDC layer thickness. However, the LSVs collected at the defect sites are noticeably different from those on the pristine basal plane, presenting lower cathodic overpotentials and resembling the Au surface response, as shown in Figure 4.18 and 4.19. Only once the LSVs of the pristine basal plane are taken into account, shown on the right side of Figure 4.16-4.19, lower dispersion on the voltammogram curves is observed for each layer thickness and the characteristic response of each TMDC and layer thickness becomes more apparent. Defective areas generally show faster apparent kinetics; therefore, if measurements were conducted with an electrochemical system which cannot isolate the response of a pristine basal plane, *i.e.*, a more macroscopic approach, the defective areas would not be avoidable, resulting in an overall enhanced apparent kinetics.

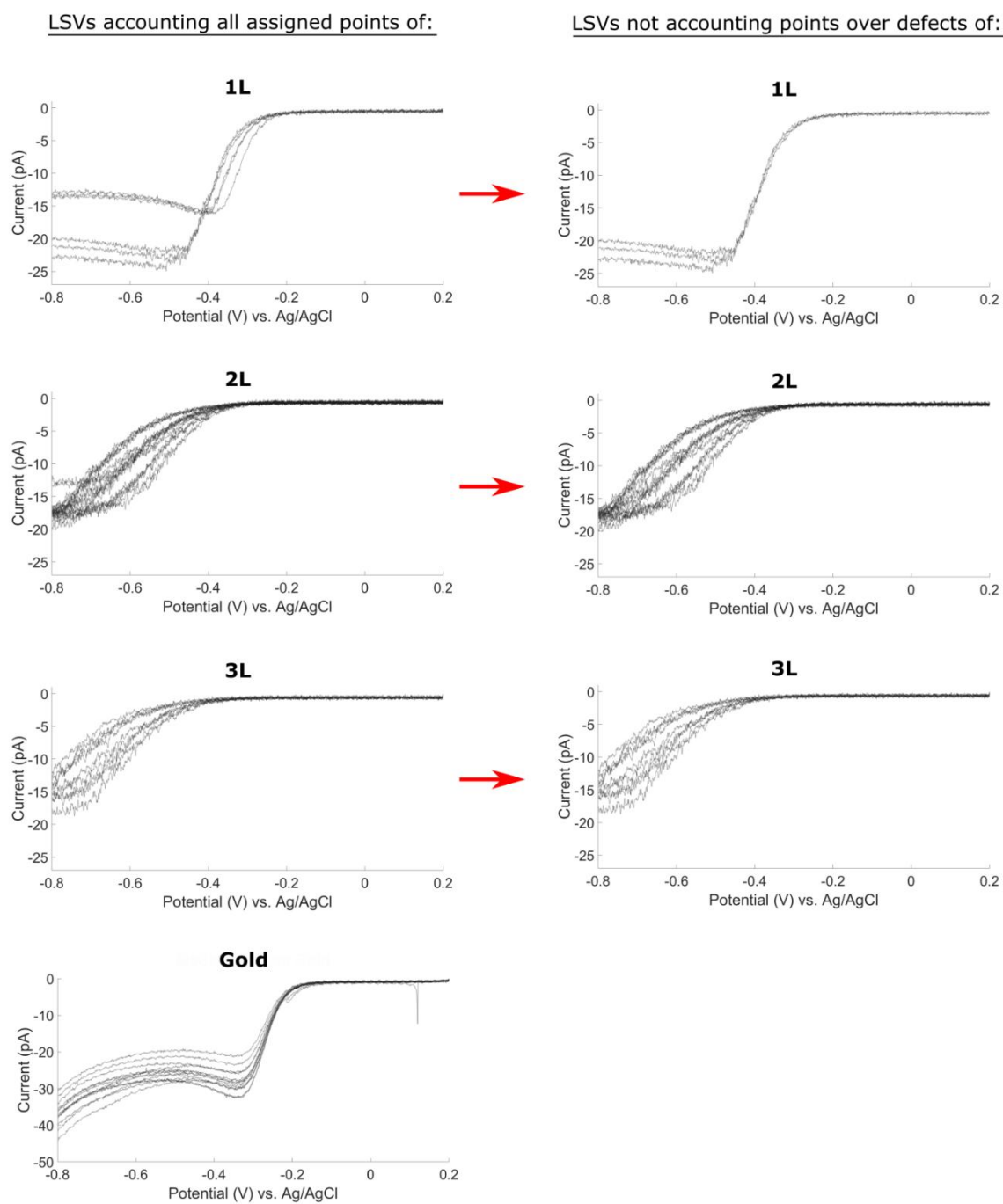
Both AFM and optical microscopy indicate that several LSV measurements were obtained at boundaries between different layer thicknesses (such as Au-1L, 1L-2L, Au-2L, 1L 3L boundaries). However, the dearth of data from the boundaries prevents us from drawing any strong conclusions and leaves the analysis of these types of surface morphologies to future work. Details on the points accounted and excluded are given in Table 4.2.

**WS<sub>2</sub>**

**Figure 4.16:** LSV dataset for 1L, 2L and 3L WS<sub>2</sub>. Left: LSVs including all the assigned points (Figure 4.12 A), right: LSVs excluding the points on defects (Figure 4.12 C).

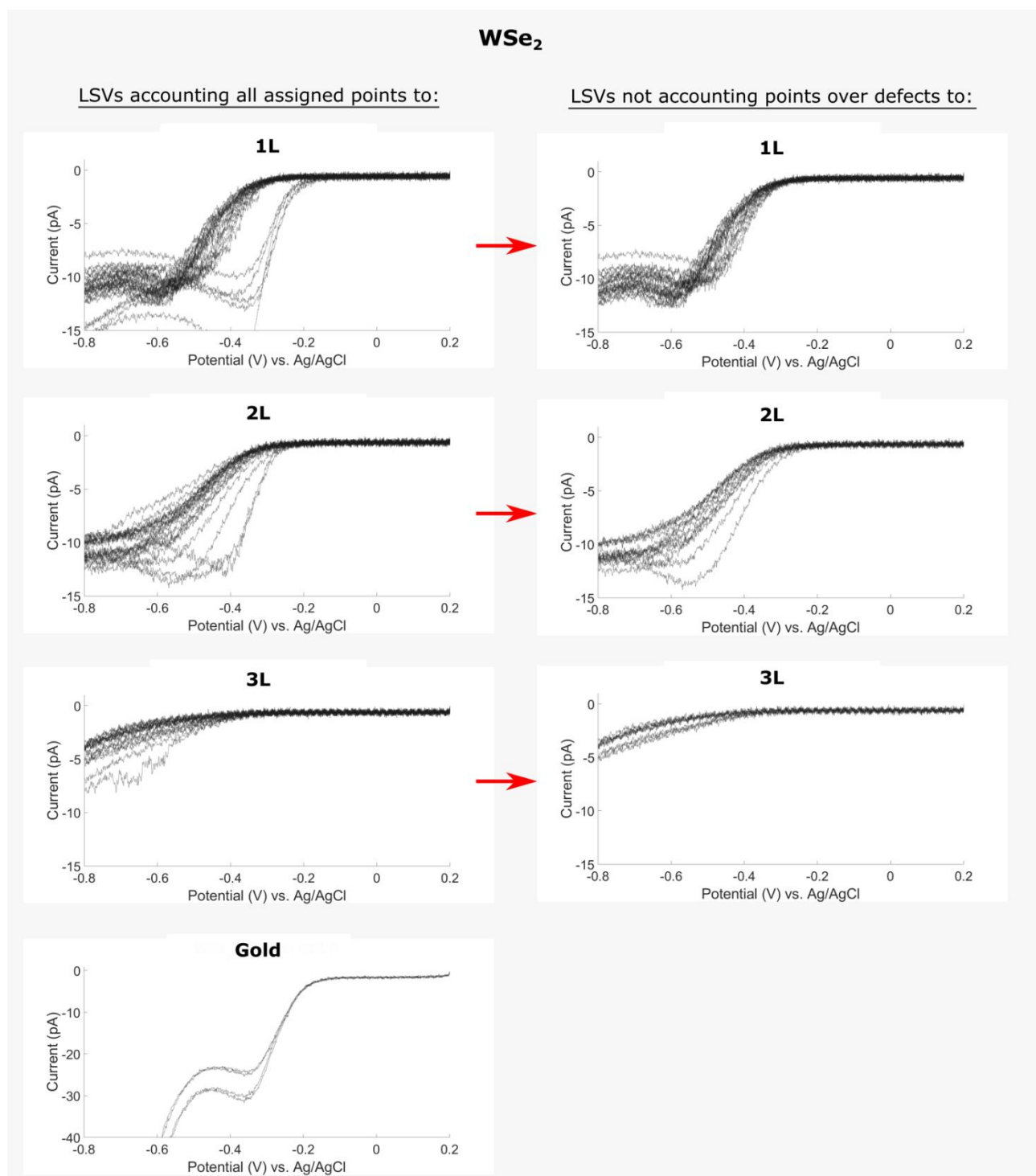
**MoS<sub>2</sub>**

**Figure 4.17:** LSV dataset for 1L, 2L and 3L MoS<sub>2</sub>. Left: LSVs including all the assigned points (Figure 4.15 B), right: LSVs excluding the points where the pipette fails to approach the surface (Figure 4.15 C).

**MoSe<sub>2</sub>**

**Figure 4.18:** LSV dataset for 1L, 2L and 3L MoSe<sub>2</sub> and gold points contacting gold surface. Left: LSVs including all assigned points for (Figure 4.14 A), right: LSVs excluding the points that coincide with defects and contacted gold (Figure 4.14 C).





**Figure 4.19:** LSV dataset for 1L, 2L and 3L  $MoSe_2$  and gold points contacting gold surface. Left: LSVs including all the assigned points (Figure 4.13 A), right: LSVs excluding the points that coincide with defects and contacted gold (Figure 4.13 C).

**Table 4.2:** Number of points assigned to each layer thickness, number of points on defective areas (including the percentage of the total number of points assigned), and number of points analysed for the kinetics study.

	<b>1L</b>			<b>2L</b>			<b>3L</b>		
	Assigned	Defective	Analysed	Assigned	Defective	Analysed	Assigned	Defective	Analysed
MoS <sub>2</sub>	178	13 (7.3%)	165	97	7 (7.2%)	90	148	7 (4.7%)	141
MoSe <sub>2</sub>	6	3 (50%)	3	18	2 (11.1%)	16	12	0 (0%)	12
WS <sub>2</sub>	21	18 (85.7%)	3	12	6 (50%)	6	36	13 (36.1%)	23
WSe <sub>2</sub>	27	5 (7.1%)	22	21	8 (38.1%)	13	18	8 (44.4%)	10

#### 4.4.3 Modelling of linear sweep voltammogram curves

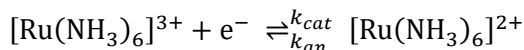
The LSVs in Figures 4.16-4.19 show that the  $[\text{Ru}(\text{NH}_3)_6]^{3+}$  reduction occurs at lower cathodic overpotentials on thinner stacks, *i.e.* on fewer number of stacked layers, for the four TMDCs studied. Furthermore, different overpotentials and overall different voltammetric responses are observed for the same number of layers stacked but different 2D TMDCs. To quantify those differences, voltammetric curves are fitted to a simulated response, which allows for the derivation of kinetic parameters. Mass transport effects on the SECCM micropipette can contribute significantly to voltammetric curves, therefore, mass transport cannot be excluded.<sup>33</sup> A finite element simulation was used to describe the transient diffusional transport of  $[\text{Ru}(\text{NH}_3)_6]^{3+/2+}$  in the SECCM probe Figure 4.20. This model also included the electron transfer kinetics at the sample surface, implemented in the boundary flux domain displayed in Figure 4.20 B.

##### 4.4.3.1 Description of finite element simulation model

Finite element simulation (FES) was performed on the COMSOL Multiphysics 5.3a software. A scheme of the simulated geometry is shown in Figure 4.20 A and B. In Table 4.3, the coordinates of all boundaries are listed, according to the parameters defined in Figure 4.20. Simulations were carried out with triangular mesh elements, with maximum element size of 1/5 of bulk solution boundary, minimum element size of 15 nm, growth rate of 1.05 and curvature factor of 0.3. The highest resolution was achieved around the solution / electrode interface and the meniscus / air interface boundaries by setting a maximum element size of 1/100 of the  $r_{pip}$  and a growth rate

of 1.02. Figure 4.20 C shows the typical mesh used. Further explanations on mass transport and FES are provided in the Introduction chapter, Section 1.5.3 and Methods chapter, Section 2.4.

The reaction simulated at the solution/electrode interface boundary is:

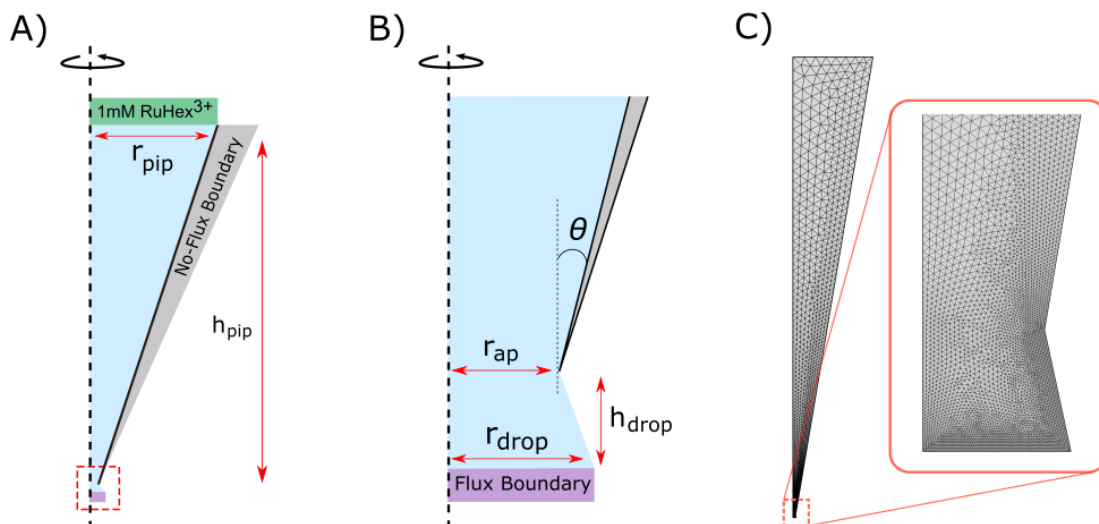


with  $k_{cat}$  and  $k_{an}$  as described in the Section 4.4.3.3 by Gerischer formalism.

The time-dependent diffusion equation cast in axisymmetric cylindrical coordinates is solved in the interior of the blue domain illustrated in Figure 4.20 by Fick's diffusion equation, Equation 4.1.

$$\frac{\partial c_i}{\partial t} = \nabla \cdot (D_i \nabla c_i) \quad (\text{Eq. 4.1})$$

where  $c_i$  is the concentration of  $[\text{Ru}(\text{NH}_3)_6]^{2+/3+}$  and  $D_i$  the diffusion coefficient set to be identical for reduced and oxidized species ( $8 \times 10^{-6} \text{ cm}^2 \text{ s}^{-1}$ ).<sup>50</sup> Boundary conditions of the transport of diluted species are listed in Table 4.3.

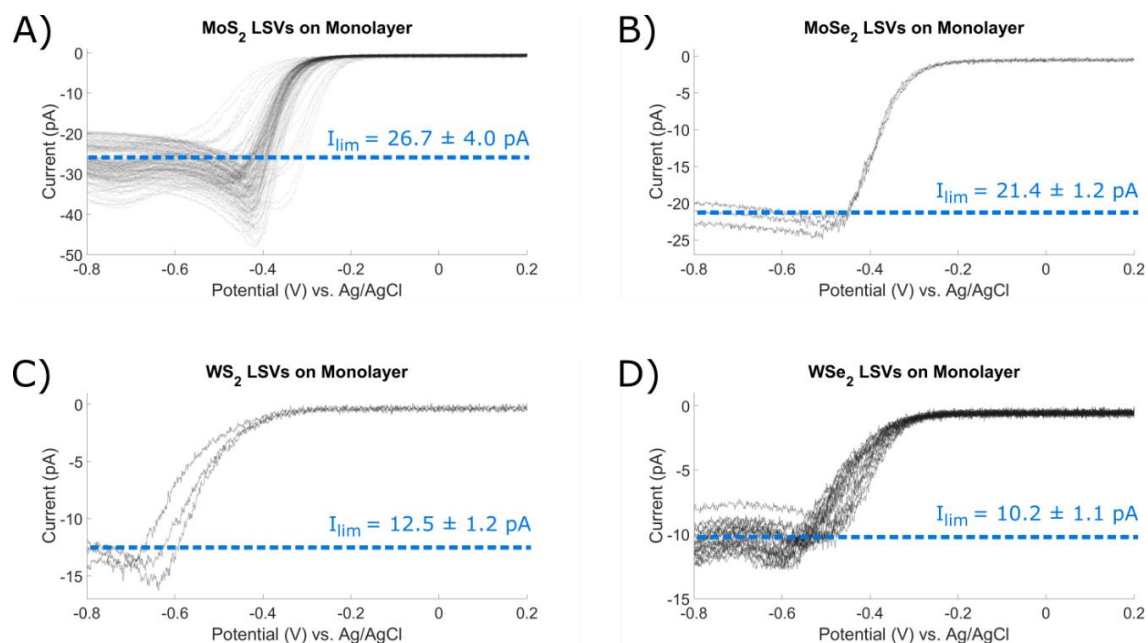


**Figure 4.20:** Description of the FES model implemented to characterise the response of 2D TDMCs. **A)** Schematic of a 2D axisymmetric pipette and droplet model implemented in finite element simulation. The solution with an initial concentration of 1 mM  $[\text{Ru}(\text{NH}_3)_6]^{3+}$  is shown in blue. The boundary region with a constant bulk concentration is shown in green. The pipette wall shown in grey is implemented in the simulation as a no-flux boundary. The simulated fraction of the pipette is equal to  $h_{\text{pip}} = 50 \mu\text{m}$ . **B)** Enlarged schematic of the nanopipette tip area. The electrode boundary where the species flux is defined by electrochemical kinetics is shown in purple. The pipette aperture angle,  $\theta$  is set to  $10^\circ$ . The pipette aperture radius is defined as  $r_{\text{ap}}$ . The droplet radius measured from AFM images is included in the geometry as  $r_{\text{drop}}$ . The distance between the end of the pipette and the substrate,  $h_{\text{drop}}$ , is set equal to  $r_{\text{ap}}$ . **C)** The mesh used for the finite element simulation, with higher resolution mesh grid around the droplet/surface contact.

**Table 4.3:** Boundary conditions for finite element simulation of 2D TMDCs. Geometric parameters are described in Figure 4.20.

Boundary Description	Coordinates		Boundary condition
	$\mathbf{z}$	$\mathbf{r}$	
Axis of Symmetry	$0 \leq \mathbf{z} \leq h_{pip}$	0	$0 = \nabla c$
Bulk Solution	$h_{pip}$	$0 \leq \mathbf{r} \leq r_{pip}$ ( $r_{pip} = r_{ap} + h_{pip} \cdot \tan(10^\circ)$ )	$c_{3+} = c_{bulk\ 3+} = 1mM$ $c_{2+} = c_{bulk\ 2+} = 0mM$
Pipette Wall	$h_{drop} \leq \mathbf{z} \leq h_{pip}$ (where $h_{drop} = r_{ap}$ )	$\mathbf{r} = r_{ap} + \mathbf{z} \cdot \tan(10^\circ)$	$J = 0$ (No flux)
Meniscus/ Air interface	$0 \leq \mathbf{z} \leq h_{drop}$	$\mathbf{r} = \mathbf{z} \cdot (r_{ap} - r_{drop})/h_{drop} + r_{drop}$	$J = 0$ (No flux)
Solution / Electrode interface	0	$0 \leq \mathbf{r} \leq r_{drop}$	$\nabla c_{3+} = -k_{cat} \cdot c_{3+} + k_{an} \cdot c_{2+}$ $\nabla c_{2+} = k_{cat} \cdot c_{3+} - k_{an} \cdot c_{2+}$

The variable geometric parameters used in the model ( $r_{drop}$  and  $r_{ap}$ ) are modified for each specific SECCM probe geometry used, thus accounting for different mass transport effects on the different TMDC measurements.  $r_{ap}$  is obtained by evaluating the diffusion limiting current observed on each TMDC measurement. All LSV curves obtained on monolayer surfaces show a diffusion-limited current, as shown in Figure 4.21. An estimate of the diffusion-limited current was calculated as the average of the LSV current at the cathodic end of the potential window (-0.8 V), as shown in Figure 4.21. This value was subsequently used to determine the pipette aperture size ( $r_{ap}$ ) by fitting the diffusion limited current with a finite element model of the SECCM probe. The pipette aperture radius ( $r_{ap}$ ) was 620 nm, 550 nm, 300 nm, and 290 nm for the MoS<sub>2</sub>, MoSe<sub>2</sub>, WS<sub>2</sub>, and WSe<sub>2</sub> SECCM measurements, respectively.  $r_{drop}$  is obtained from the average diameter of the salt residues left on the surface observed by AFM (Figure 4.12-4.14) and reported in Table 4.1. The pipette geometrical values used for the finite element simulation, and the ratio  $r_{drop}/r_{ap}$  are summarised in Table 4.4. The ratio is around unity for all the TMDC measurements, indicating that the droplet size is determined by the aperture diameter and that only minor spreading of the SECCM droplet takes place upon contact with the surface.



**Figure 4.21:** LSVs on 1L of **A)** MoS<sub>2</sub>, **B)** MoSe<sub>2</sub>, **C)** WS<sub>2</sub> and **D)** WSe<sub>2</sub> showing diffusion limited current regime. The diffusion limiting current value is shown in the blue dashed line.

**Table 4.4:** Comparison of the pipette aperture diameter derived by the fitting finite element simulation geometry to the limiting current and the droplet size diameter measured by AFM on TMDCs. As reported in Figure 4.21 and Figure 4.11 respectively. The table also includes the ratio between these two parameters, indicating the spread of the electrochemical droplet cell.

TMDCs	Pipette aperture diameter ( $r_{ap}$ )	Droplet size diameter ( $r_{drop}$ )	$r_{drop}/r_{ap}$
MoS <sub>2</sub>	1280nm	$1287 \pm 109$ nm	1.01
MoSe <sub>2</sub>	1100nm	$807 \pm 47$ nm	0.73
WS <sub>2</sub>	600nm	$729 \pm 52$ nm	1.22
WSe <sub>2</sub>	480nm	$795 \pm 90$ nm	1.65

## 4.4.3.2 Discussion of models for heterogeneous electron transfer.

In the dataset presented in Figure 4.16-4.19, the bilayer and trilayer surfaces present later  $[\text{Ru}(\text{NH}_3)_6]^{3+}$  reduction onset than the monolayer. For  $\text{MoS}_2$ ,  $\text{MoSe}_2$ ,  $\text{WS}_2$ , and  $\text{WSe}_2$  the shape of the waveform changes as number of layers increases. Butler-Volmer (BV) kinetics can be used to extract the electron transfer rate,<sup>51</sup> as described in Equation 4.2.

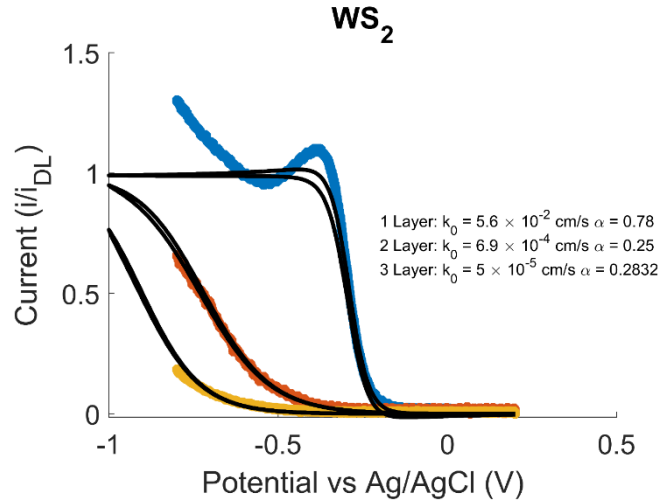
$$I = z \cdot F \cdot C_{ox} \cdot k^0 \left[ \exp\left(\frac{(1-\alpha)z\eta}{K_B T}\right) - \exp\left(\frac{\alpha z\eta}{K_B T}\right) \right] \quad (\text{Eq. 4.2})$$

where  $I$  is current at flux boundary, where  $z$  is the number of electrons in the reaction,  $F$  is Faraday's constant,  $C_{ox}$  is the concentration of  $[\text{Ru}(\text{NH}_3)_6]^{3+}$  at the electrode surface,  $k^0$  is the equilibrium rate constant,  $\alpha$  is the transfer factor,  $\eta$  is the overpotential,  $K_B$  is Boltzmann's constant and  $T$  is the temperature. A detailed description of the Butler-Volmer formalism can be found in the Introduction chapter, Section 1.5.2.1.

I have attempted to produce simulated voltammograms that reproduce the bilayer and trilayer responses by using the BV formalism (Eq. 4.2) at the flux boundary of the FES model (described in Figure 4.20) with  $z = 1$  ( $[\text{Ru}(\text{NH}_3)_6]^{3+}$  reduction to  $[\text{Ru}(\text{NH}_3)_6]^{2+}$ ),  $\eta = -0.19$  V vs Ag/AgCl (0.1 M KCl),  $T = 298$  K.  $k_0$  and  $\alpha$  are free parameters to adjust simulation.  $C_{ox}$  and  $I$  are given by implementation of FES model of diffusion and BV formalism.

As shown in Figure 4.22 for  $\text{WS}_2$ , very small values of  $\alpha$  ( $<0.3$ ) are needed to match our simulated voltammograms with our experimental voltammograms. The need to use  $\alpha$  values that deviate from 0.5 is indicative of the BV formalism failing to model the electrochemical system, and generally suggests, that the reaction rate determining process is not the heterogeneous electron transfer.<sup>52</sup> For instance, reactions involving non-adiabatic electron transfer process, multi-electron transfers process or adsorption/desorption mechanism lead to  $\alpha$  different than 0.5. However, as theoretically predicted by Feldberg<sup>53</sup> and recently verified experimentally,<sup>54</sup> Butler-Volmer formalism does not always correctly describe the waveforms obtained with a ultramicroelectrode for a reaction with slow kinetics and a limiting step that is still a heterogeneous electron transfer.

The more general Marcus-Hush/Gerischer formalism is instead better suited to the derivation of the HER rate constants under high mass transport and slow HET kinetics.<sup>53</sup> A detailed description of BV, Marcus-Hush and Gerischer formalism is found in the Introduction chapter, Section 1.5.2. Specifically, in Sections 1.5.2.2 and 1.5.2.5 it is discussed the limitations of the Butler-Volmer model in nano-electrochemistry. Thus, the rate of heterogeneous electron transfer (HET) could be determined by implementing the Marcus-Hush/Gerischer formalism, instead of BV, on the flux boundary of the FES model to describe the electrochemical kinetics. The Marcus-Hush and Gerischer formalisms are presented in the Introduction chapter, Sections 1.5.2.3 and 1.5.2.4.



**Figure 4.22:** Linear sweep voltammograms recorded on WS<sub>2</sub> normalised by diffusion limiting current for monolayer (blue), bilayer (yellow) and trilayer (yellow). Simulated voltammograms (black) using BV formalism in FES model. The parameters  $k_0$  and alpha ( $\alpha$ ) are used to obtain a similar voltammogram for each number of layers stacked.

#### 4.4.3.3 Details of Gerischer electron transfer kinetics model

In the Marcus-Hush/Gerischer formalism, the kinetics of HET can be described by considering the overlap between the isoenergetic electronic states of the electrode and the redox species in solution (electronic coupling in the Marcus-Hush formalism). Therefore, the kinetics of cathodic electron transfer ( $k_{cat}$ ) is given by the overlap between isoenergetic occupied states at the electrode ( $f(E)_{occupied}$ ) and empty electron acceptor states in the solution ( $W_{ox}$ ).<sup>52</sup> Likewise, the anodic kinetics ( $k_{an}$ ) is determined by the overlap of isoenergetic filled electron donor states ( $W_{red}$ ) in the solution and unoccupied states in the electrode ( $f(E)_{unoccupied}$ ). Therefore, the cathodic and anodic kinetic rates can be written as follows:

$$k_{cat} = k_{max} \cdot \int_{-\infty}^{\infty} W_{ox}(E) \cdot f(E)_{occupied} \partial E \quad (\text{Eq. 4.3})$$

$$k_{an} = k_{max} \cdot \int_{-\infty}^{\infty} W_{red}(E) \cdot f(E)_{unoccupied} \partial E \quad (\text{Eq. 4.4})$$

where the integration parameter  $E$  is the electron energy (in eV), and the prefactor,  $k_{max}$ , is the maximum rate of electron transfer.<sup>52</sup>

The solution states ( $W_{ox}$  and  $W_{red}$ ) are described by normalised Gaussian distributions and the electrode states ( $f(E)_{occupied}$  and  $f(E)_{unoccupied}$ ) are described by normalised Fermi-Dirac distributions for free electrons in a metal,<sup>52</sup> as shown in Equation 4.5 to 4.8.

$$W_{ox}(E) = \frac{1}{\sqrt{4\pi kT\lambda}} \cdot \exp\left(\frac{-(E-E^0+\lambda)^2}{4\lambda K_B T}\right) \quad (\text{Eq. 4.5})$$

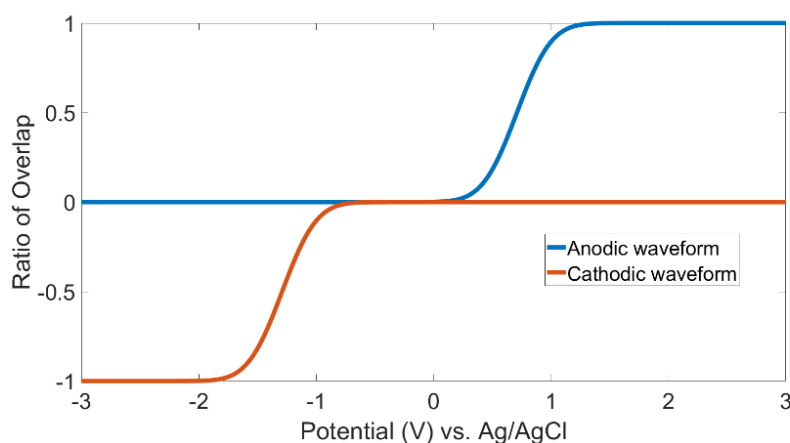
$$W_{red}(E) = \frac{1}{\sqrt{4\pi kT\lambda}} \cdot \exp\left(\frac{-(E-E^0-\lambda)^2}{4\lambda K_B T}\right) \quad (\text{Eq. 4.6})$$

$$f(E)_{occupied} = \frac{1}{1 + \exp\left(\frac{(E-E_f)}{K_B T}\right)} \quad (\text{Eq. 4.7})$$

$$f(E)_{unoccupied} = 1 - f(E)_{occupied} \quad (\text{Eq. 4.8})$$

Where  $E$  is the electron energy (in eV),  $E^0$  is the energy corresponding to the standard redox potential,  $E_f$  is the Fermi level of the working electrode and  $\lambda$  is the reorganisation energy of the redox couple. Note that when the electrochemical cell is set with an applied potential equal to 0 V, the working electrode work-function is equal to the reference electrode work-function. An applied potential between the working electrode and the reference electrode shifts the Fermi level position and changes the overlap between the electrode and solution states.

The overlap integrals for anodic and cathodic processes, as described in Equations 4.3 and 4.4, were calculated by numerical integration, obtaining two waveforms (for anodic and cathodic processes), which describe the ratio of the overlap of the reacting redox species as a function of the applied potential. Waveforms, shown in Figure 4.23, range from 0 to 1 and assume a metallic electrode with flat DOS and reorganisation energy ( $\lambda$ ) for  $[\text{Ru}(\text{NH}_3)_6]^{3+/2+}$  of 1 eV.<sup>4,55,56</sup>



**Figure 4.23:** Integral of the overlapped function for anodic and cathodic processes, which describe the ratio of reacting redox species (ratio of overlap) versus the applied potential. For this representation, a standard redox potential ( $E^0$ ) of -0.29 V is used.



Thus, the total current can be implemented in the flux boundary of the finite element simulation model as described in Equations 4.9 to 4.11:

$$i = i_{an} - i_{cat} \quad (\text{Eq. 4.9})$$

$$i_{an} = zF \cdot C_{red} \cdot k_{an} = nF \cdot C_{red} \cdot k_{max} \cdot \int W_{red}(E) \cdot f(E)_{unoccupied} \partial E \quad (\text{Eq. 4.10})$$

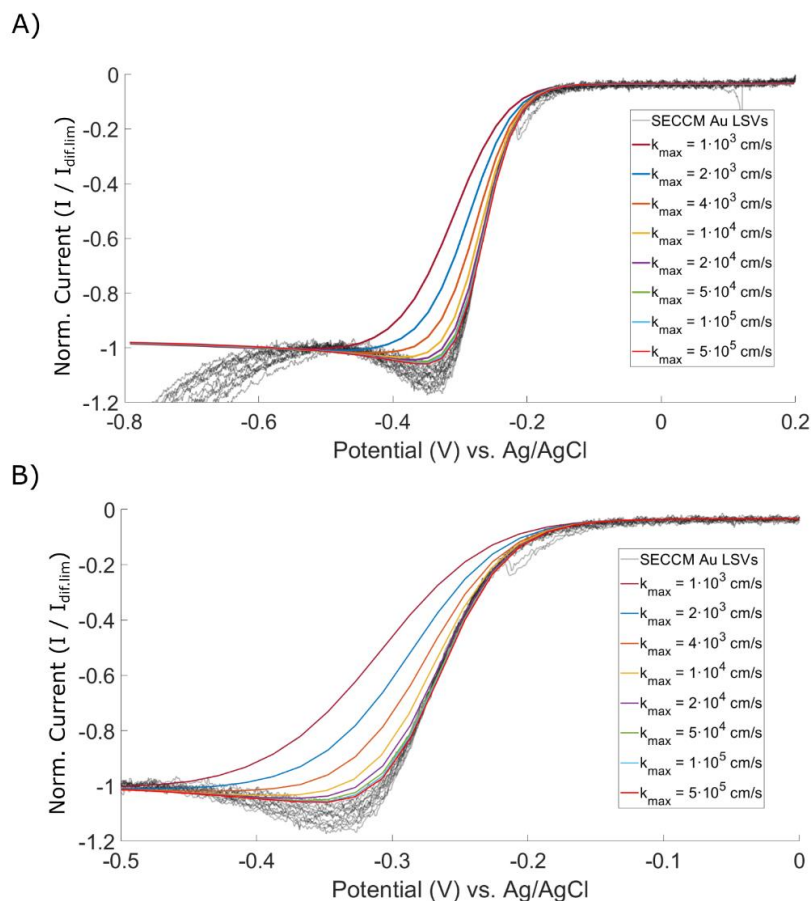
$$i_{cat} = zF \cdot C_{ox} \cdot k_{cat} = nF \cdot C_{ox} \cdot k_{max} \cdot \int W_{ox}(E) \cdot f(E)_{occupied} \partial E \quad (\text{Eq. 4.11})$$

where  $z = 1$  is the number of electrons in the reaction,  $F$  is Faraday's constant,  $C_{red}$  is the concentration of  $[\text{Ru}(\text{NH}_3)_6]^{2+}$  at the electrode surface,  $C_{ox}$  is the concentration of  $[\text{Ru}(\text{NH}_3)_6]^{3+}$  at the electrode surface and  $k_{max}$  is the maximum rate of electron transfer.

#### 4.4.4 Fitting the simulated response to the gold surface response

To find the differences in the HET rate for the different thicknesses of TMDC, the standard redox potential ( $E^0$ ) must first be defined.  $[\text{Ru}(\text{NH}_3)_6]^{3+/2+}$  standard redox potential vs. sat. Ag/AgCl is  $-0.10 \text{ V}$ .<sup>51</sup> However, we used a silver wire immersed in a 10 mM KCl solution as a quasi-reference counter electrode, thus some variation in the reference electrode potential with respect to saturated Ag/AgCl is expected. To find  $E^0$ , the simulated response is fitted to the response measured on bare gold (exposed substrate), as this provides faster HET than at any of the 2D TMDCs measured.<sup>24,40</sup> A standard redox potential  $E^0 = -0.29 \text{ V}$  vs Ag/AgCl wire best matches the simulated response to the experimental data, as shown in Figure 4.24. This implies that the Ag/AgCl wire has an equilibrium potential of  $-0.19 \text{ V}$  vs. sat. Ag/AgCl, which agrees with the expected shift when using the 10 mM concentration KCl solution Ag/AgCl reference electrode ( $-0.18 \text{ V}$  vs. sat. Ag/AgCl).<sup>57</sup>

For the bare gold surface,  $k_{max,Au}$  was determined to be at least  $2 \times 10^4 \text{ cm/s}$ , as shown in Figure 4.24 B. Note that  $k_{max}$  values greater than  $2 \times 10^4 \text{ cm/s}$  yielded simulated LSV curves that were no longer distinguishable. The  $k_{max,Au}$  value is close to the pre-exponential frequency factor for the adiabatic heterogeneous electron transfer dominated by the reorganisation energy predicted by the Marcus-Hush theory ( $10^4$ – $10^5 \text{ cm/s}$ )<sup>58,59</sup> and also to the experimentally determined value ( $1.1 \times 10^5 \text{ cm/s}$ ) obtained for  $[\text{Ru}(\text{NH}_3)_6]^{3+/2+}$  on bare gold.<sup>60</sup>

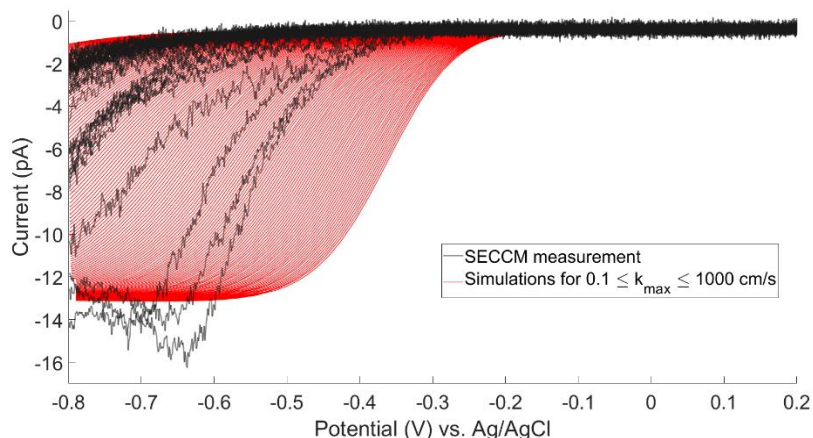


**Figure 4.24:** Fitting of the simulated LSVs to the gold EC response. **A)** Normalised experimental LSVs recorded on the gold surface in black and simulated LSVs response for a range of  $k_{max}$  values, in colour code, and  $E^0 = -0.29$  V. **B)** Enlarged version of A with potential window from 0V to -0.5V, showing that for  $k_{max}$  above  $2 \times 10^4$  cm/s the simulated LSVs shape is almost identical and resembles the response of the bare gold substrate. The finite element simulation uses droplet size measured over gold (see Figures 4.13 and 4.14) and a pipette aperture as derived in Table 4.4.

#### 4.4.5 Fitting the simulated response to different thicknesses of TMDCs.

The simulated LSVs were matched with the experimental data recorded on different TMDC thicknesses using only  $k_{max}$  as the fitting parameter. Matching the simulation to each individual experimental LSV over the kinetic region (up to 1/3 of the diffusion-limited current) by adjusting  $k_{max}$  allows us to estimate the apparent  $k_{max}$  on the different layers ( $k_{max,nL}$  for  $nL$ ). To perform the matching for each TMDC (*i.e.* each pipette and droplet geometry), a set of simulated LSVs was generated using a range of  $k_{max}$  from 0.1 cm/s to 1000 cm/s, as shown in Figure 4.25. Each measured LSV was then compared to the simulated LSVs by least squares regression in the kinetic region of the LSV (*i.e.* across the potential range until the current reached 1/3 of the diffusion

limiting current). A  $k_{max}$  fitting value was obtained for each recorded LSV. The median  $k_{max}$  for each TMDC and layer thickness and the corresponding 25<sup>th</sup> and 75<sup>th</sup> percentiles are reported in Table 4.5. Simulated LSVs corresponding to median and percentiles of  $k_{max}$  are displayed over measured LSVs in Figures 4.26 - 4.29 for MoS<sub>2</sub>, MoSe<sub>2</sub>, WS<sub>2</sub> and WSe<sub>2</sub>, respectively.

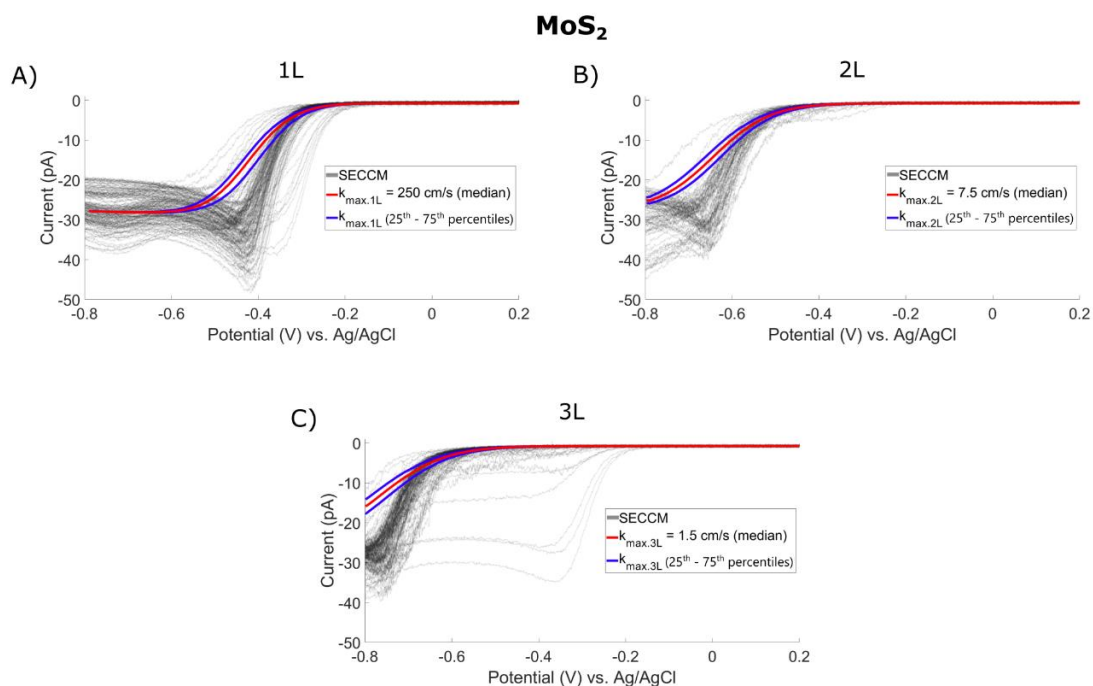


**Figure 4.25:** Comparison of recorded and simulated LSVs for a range of  $k_{max}$  values. In black, each LSV obtained in the pristine basal plane of WS<sub>2</sub> for 1L, 2L, and 3L. In red, set of simulated LSVs for a range of  $k_{max}$  between 0.1 and 1000 cm/s that were compared by least squares with each individual LSV recorded on WS<sub>2</sub>. Note that the simulated LSVs are generated from a model that accounts probe geometry ( $r_{ap}$  and  $r_{drop}$ ) used on WS<sub>2</sub> SECCM scan. Other SECCM scans of TMDCs account for different probe geometry, resulting in another simulated LSV dataset.

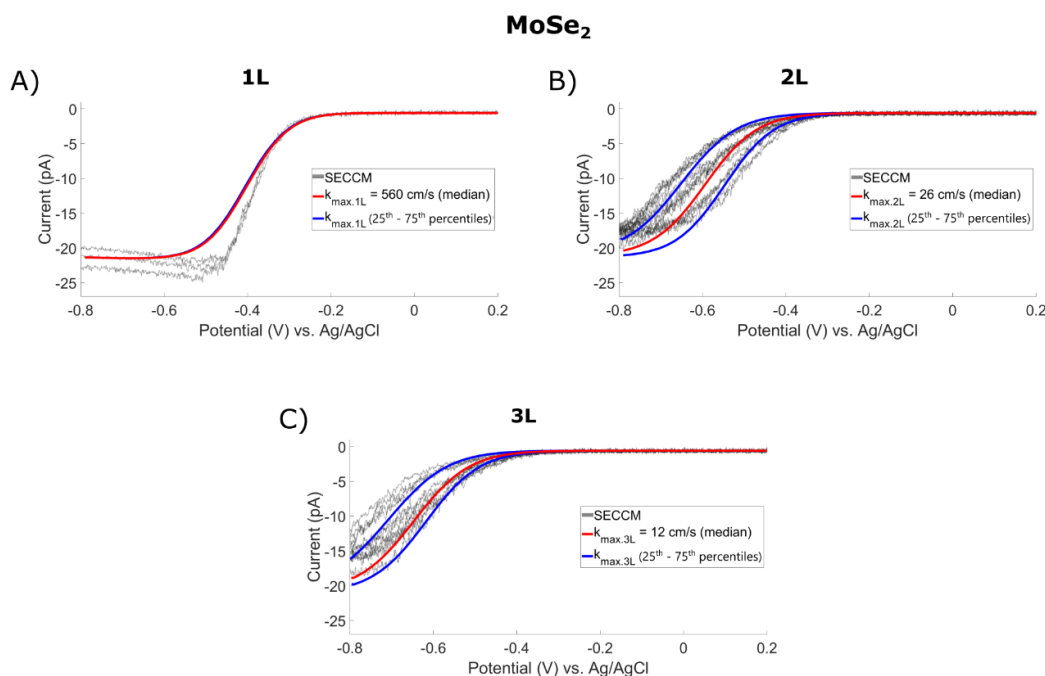
Note that there is an uneven number of LSVs collected for each surface type and each TMDC studied (count reported Table 4.2). Thus, in some TMDCs and surface types, it has been possible to fit over 100 LSVs, as for 1L MoS<sub>2</sub>, while other TMDC surface types yielded a much smaller number of LSVs, for instance, 1L WS<sub>2</sub> yielded only 3 LSVs. The distribution of the logarithm of  $k_{max}$  for 1L, 2L, and 3L MoS<sub>2</sub>, displayed in Figure 4.30 A, can be approximated by a normal distribution. However, the lack of points on other surface types, such as 1L and 2L WS<sub>2</sub>, as shown in Figure 4.30 B, is not sufficient to analyse the  $k_{max}$  distribution.

**Table 4.5:** Median  $k_{max}$  and 25<sup>th</sup>/75<sup>th</sup> percentiles for different number of layers stacked and TMDCs.

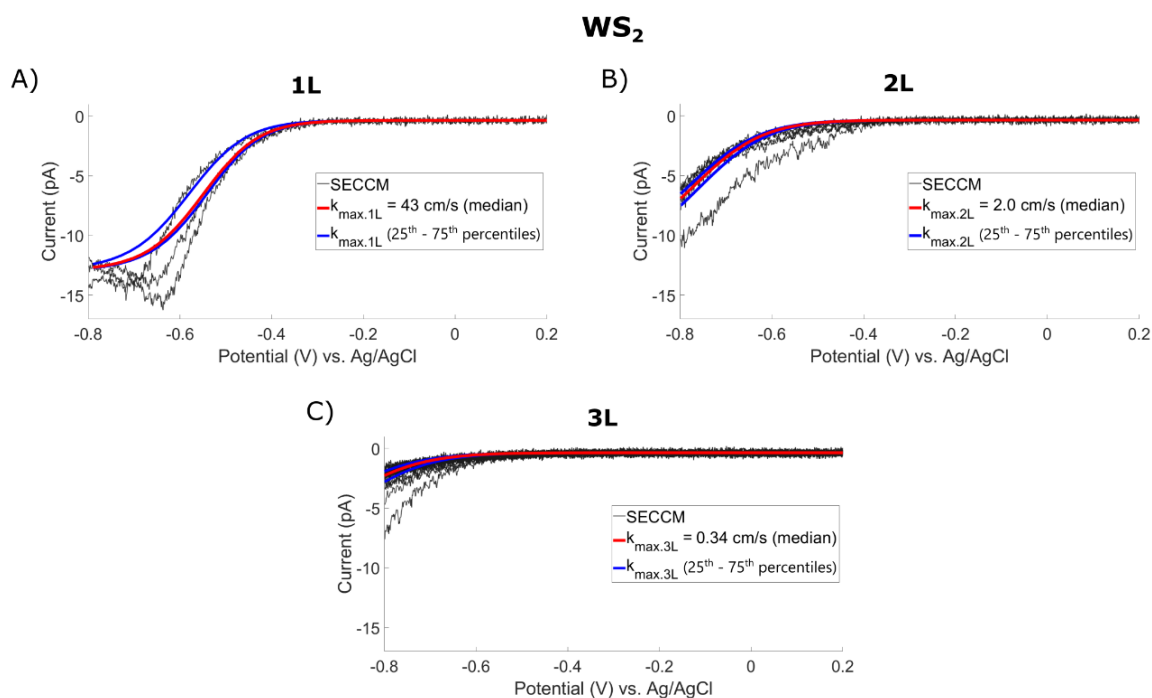
	$k_{max,1L}$ (cm/s)			$k_{max,2L}$ (cm/s)			$k_{max,3L}$ (cm/s)		
	25 <sup>th</sup>	50 <sup>th</sup>	75 <sup>th</sup>	25 <sup>th</sup>	50 <sup>th</sup>	75 <sup>th</sup>	25 <sup>th</sup>	50 <sup>th</sup>	75 <sup>th</sup>
<b>MoS<sub>2</sub></b>	193	246	350	5.92	7.47	9.43	1.16	1.46	1.84
<b>MoSe<sub>2</sub></b>	534	558	558	11.2	25.5	52.7	5.27	11.6	18.4
<b>WS<sub>2</sub></b>	26.6	42.9	49.0	1.74	1.96	2.33	0.269	0.340	0.455
<b>WSe<sub>2</sub></b>	103	142	184	97.1	123	174	0.601	0.916	2.33



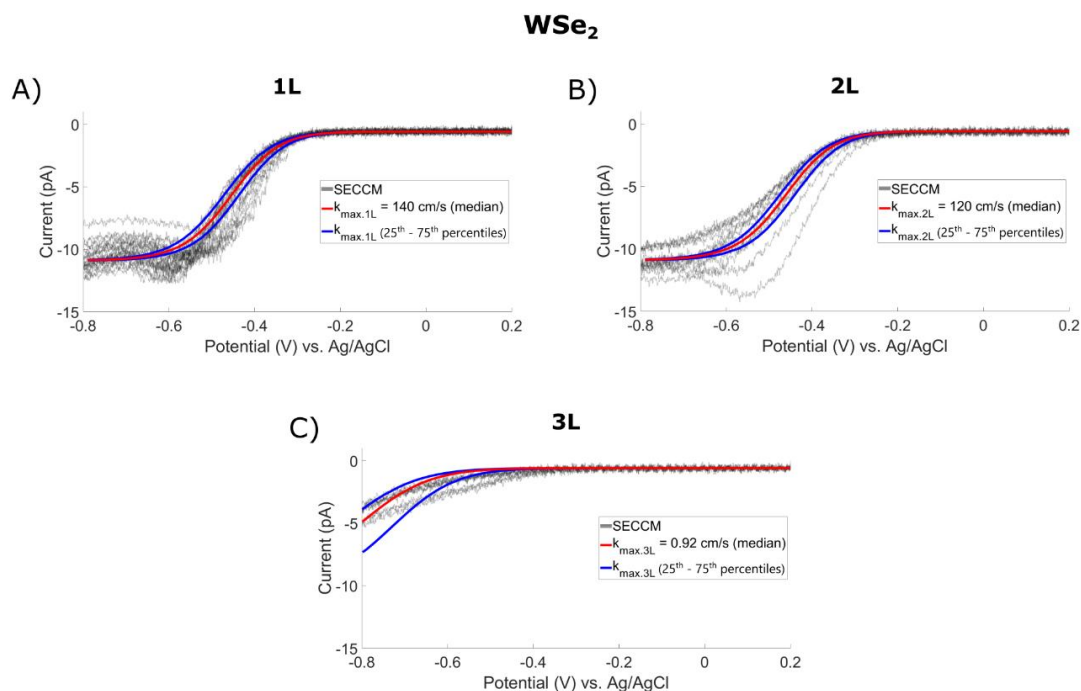
**Figure 4.26:** Recorded and simulated LSVs on MoS<sub>2</sub> basal plane. For **A)** 1L **B)** 2L and **C)** 3L of MoS<sub>2</sub>, with the experimental data shown in black, the simulated response corresponding to the median  $k_{\max}$  in red, and the simulated response corresponding to the 25<sup>th</sup> and 75<sup>th</sup> percentiles of  $k_{\max}$  in blue. Dataset formed by 165, 90 and 141 fitted LSVs with  $k_{\max}$  values for 1L, 2L and 3L respectively.



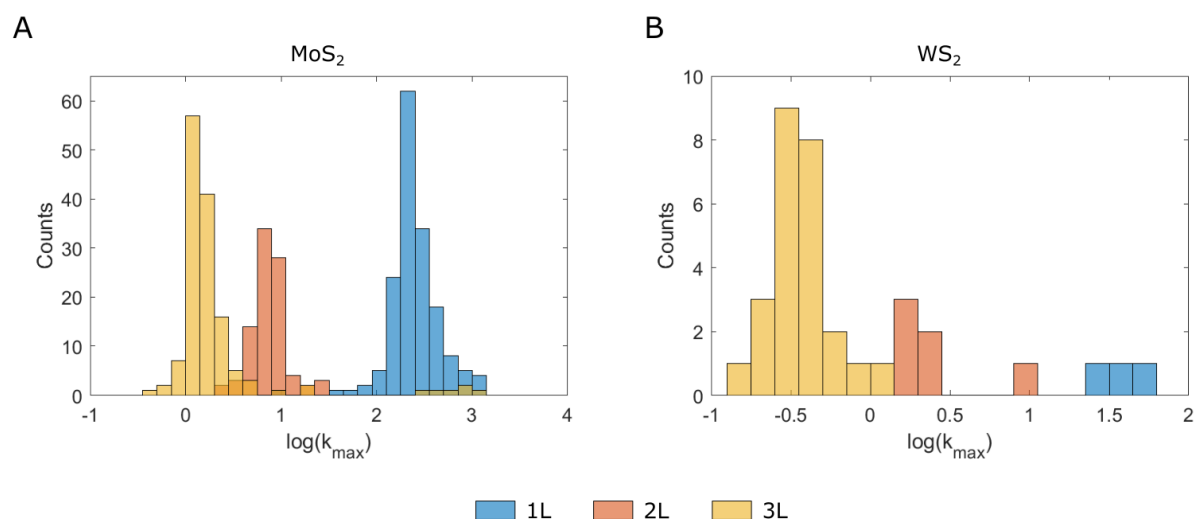
**Figure 4.27:** Recorded and simulated LSVs on MoSe<sub>2</sub> basal plane. For **A)** 1L **B)** 2L and **C)** 3L of MoSe<sub>2</sub>, with the experimental data shown in black, the simulated response corresponding to the median  $k_{\max}$  in red, and the simulated response corresponding to the 25<sup>th</sup> and 75<sup>th</sup> percentiles of  $k_{\max}$  in blue. Dataset formed by 3, 16 and 12 fitted LSVs with  $k_{\max}$  values for 1L, 2L and 3L respectively.



**Figure 4.28:** Recorded and simulated LSVs on WS<sub>2</sub> basal plane. For on **A)** 1L **B)** 2L and **C)** 3L of WS<sub>2</sub>, with the experimental data shown in black, the simulated response corresponding to the median  $k_{\max}$  in red, and the simulated response corresponding to the 25<sup>th</sup> and 75<sup>th</sup> percentiles of  $k_{\max}$  in blue. Dataset formed by 3, 16 and 12 fitted LSVs with  $k_{\max}$  values for 1L, 2L and 3L respectively. Reproduced with permission from Brunet Cabré, M. *et al.*<sup>41</sup>



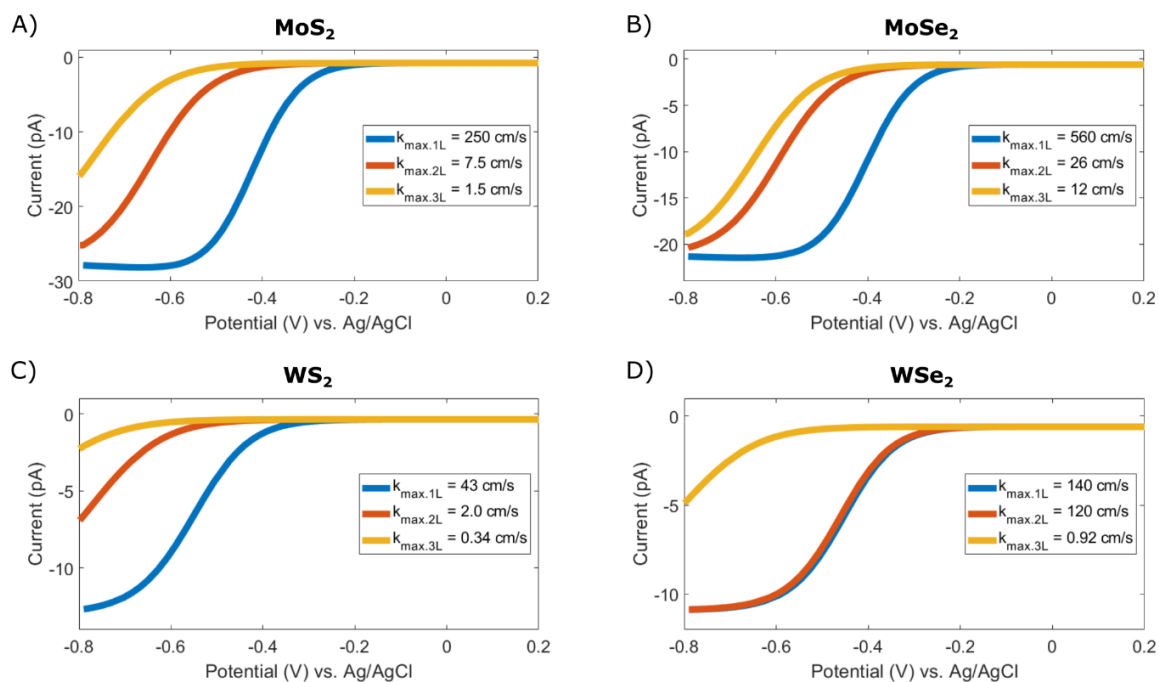
**Figure 4.29:** Recorded and simulated LSVs on WSe<sub>2</sub> basal plane. For **A)** 1L **B)** 2L and **C)** 3L of WSe<sub>2</sub>, with the experimental data shown in black, the simulated response corresponding to the median  $k_{\max}$  in red, and the simulated response corresponding to the 25<sup>th</sup> and 75<sup>th</sup> percentiles of  $k_{\max}$  in blue. Dataset formed by 22, 13 and 10 fitted LSVs with  $k_{\max}$  values for 1L, 2L and 3L respectively.



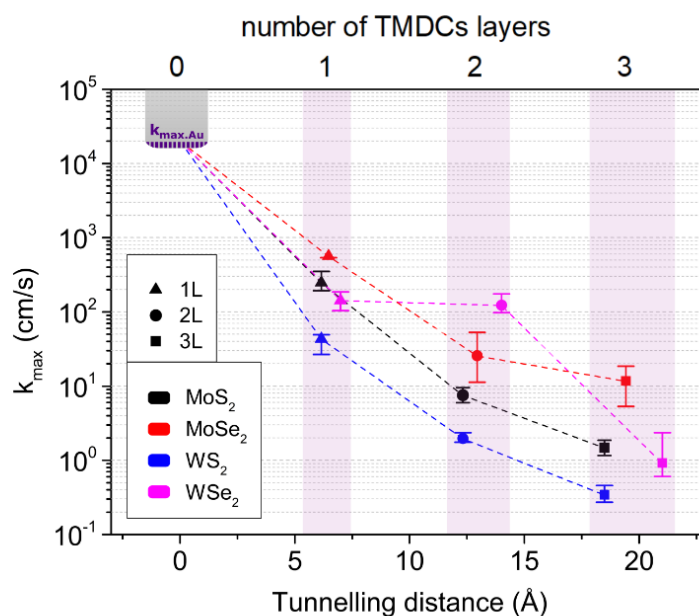
**Figure 4.30:** Logarithmic distribution of the fitted  $k_{max}$  for all recorded LSVs. **A)** MoS<sub>2</sub> with 165, 90 and 141  $k_{max}$  values for 1L, 2L and 3L, respectively; **B)** WS<sub>2</sub> with 3, 6 and 23  $k_{max}$  values for 1L, 2L and 3L, respectively. The graphs show that if there are enough points on a given surface type, a log-normal distribution of  $k_{max}$  is observed.

#### 4.4.6 Discussion of the variation of the $k_{max}$ parameter with layer thickness

To provide an overview picture, the simulated LSVs with median  $k_{max}$  value for the four TMDCs and different number of stacked layers are displayed in Figure 4.31. The [Ru(NH<sub>3</sub>)<sub>6</sub>]<sup>3+</sup> reduction kinetics slows down with the increasing number of layers of TMDCs, which is consistent with previous work on the HER with 2D TMDC electrodes.<sup>25</sup> To view the trend of  $k_{max}$ , in Figure 4.32 the median  $k_{max,nL}$  values extracted for all four materials studied, MoS<sub>2</sub>, WS<sub>2</sub>, MoSe<sub>2</sub>, and WSe<sub>2</sub>, are plotted versus the layer number. The responses on all four materials are similar and indicate a decrease in  $k_{max}$  with an increase in layer thickness, except for  $k_{max,2L}$  for WSe<sub>2</sub>, which is significantly larger compared to the other TMDCs studied, although it remains unclear why this is the case.



**Figure 4.31:** Simulated LSVs with median  $k_{max,nL}$  extracted from fitting recorded LSVs on 1L, 2L, and 3L. For **A)** MoS<sub>2</sub> **B)** MoSe<sub>2</sub> **C)** WS<sub>2</sub> and **D)** WSe<sub>2</sub>. Each TMDC displayed a different limiting current according to variation of the observed droplet size, which explains the varying scale of the y-axes. Reproduced with permission from Brunet Cabré, M. *et al.*<sup>41</sup>

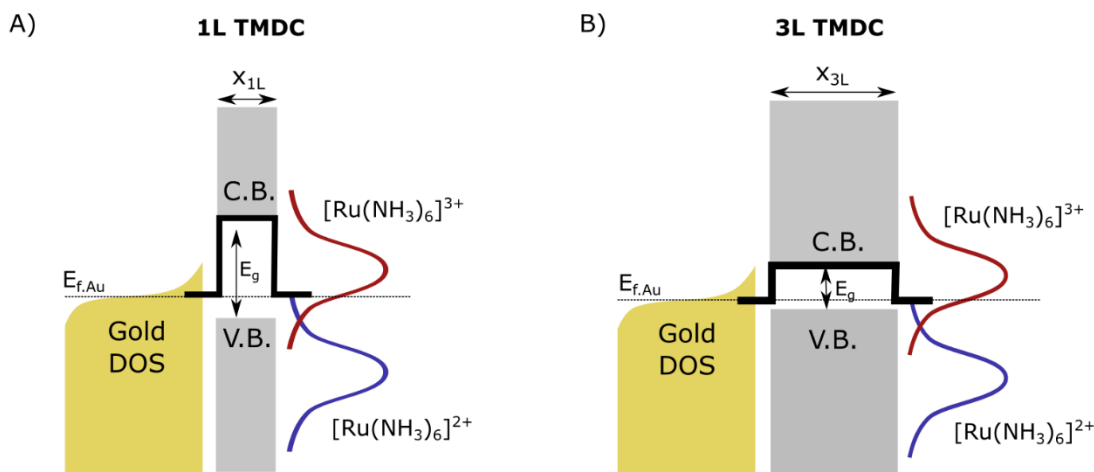


**Figure 4.32:**  $k_{max}$  values determined by fitting the simulation response to the experimental data for different layer thickness. The solid points correspond to each  $k_{max}$  value and dashed lines are displayed to guide the eye. Error bar correspond to  $k_{max}$  values for the 25<sup>th</sup> and 75<sup>th</sup> percentiles. Reproduced with permission from Brunet Cabré, M. *et al.*<sup>41</sup>

According to the Gerischer model for heterogeneous electron transfer, the prefactor  $k_{max}$  scales with the electronic transmission coefficient, which represents the probability of the electron transfer.<sup>52,58-60</sup> An electron tunnelling barrier arising from the TMDC material itself would reduce the transmission coefficient, and so reduce  $k_{max}$ , as the number of layers increases. Previously, an electron tunnelling barrier model was used to evaluate photocurrents obtained for 2D MoS<sub>2</sub> in a bottom-contact configuration,<sup>61</sup> and has also been used to assess HER kinetics on mono and few-layer MoS<sub>2</sub>.<sup>25</sup> A diagram of a tunnelling barrier model with electron transfer can be found in Figure 4.33 A. Assuming that tunnelling is the dominant process leading to a decrease in  $k_{max}$ , the  $k_{max,nL}$  on  $n$  layers of TMDC can be described as:

$$k_{max,nL} = k_{max,Au} \cdot \exp(-\beta \cdot x \cdot n) \quad (\text{Eq. 4.12})$$

where  $\beta$  is the tunnelling decay constant,  $x$  is the TMDCs layer thickness ( $x = 6.15 \text{ \AA}$  for MoS<sub>2</sub>,  $6.47 \text{ \AA}$  for MoSe<sub>2</sub>,  $6.16 \text{ \AA}$  for WS<sub>2</sub> and  $7.00 \text{ \AA}$  for WSe<sub>2</sub>)<sup>13</sup>,  $n$  is the number of TMDCs layers.



**Figure 4.33:** Diagram of the tunnelling junction for a **A)** monolayer of TMDC and **B)** stack of three layers of TMDC.  $E_{f,Au}$  is the Fermi level of the gold substrate,  $E_g$  is the band gap of the 2D TMDC for  $n$  layers,  $x_{1L}$  and  $x_{3L}$  represent the thickness of the stack of TMDC.

The tunnelling decay constant,  $\beta$ , values for  $[\text{Ru}(\text{NH}_3)_6]^{3+}$  reduction on different layer stacks for MoS<sub>2</sub>, MoSe<sub>2</sub>, WS<sub>2</sub>, and WSe<sub>2</sub> found from Eq. 4.12 are reported in Table 4.6. The four different TMDCs have tunnelling decay constants in the range  $1.0 - 0.4 \text{ \AA}^{-1}$ , which vary significantly depending on total thickness. The  $\beta$  values are consistent for 2D TMDCs, which have previously been estimated to have tunnelling decay constants of  $0.512 \text{ \AA}^{-1}$ .<sup>62</sup> The data in Table 4.6 show that the tunnelling decay constant,  $\beta$ , decreases with increasing numbers of layers for all four TMDCs. However, the  $k_{max,nL}$  values do not follow an exponential decay with an increase in layer thickness as we might expect if each additional layer added an identical electron tunnelling barrier, see Figure 4.32. Instead, the kinetics are faster for a larger number of layers than would be predicted by a tunnelling model with a constant  $\beta$ .



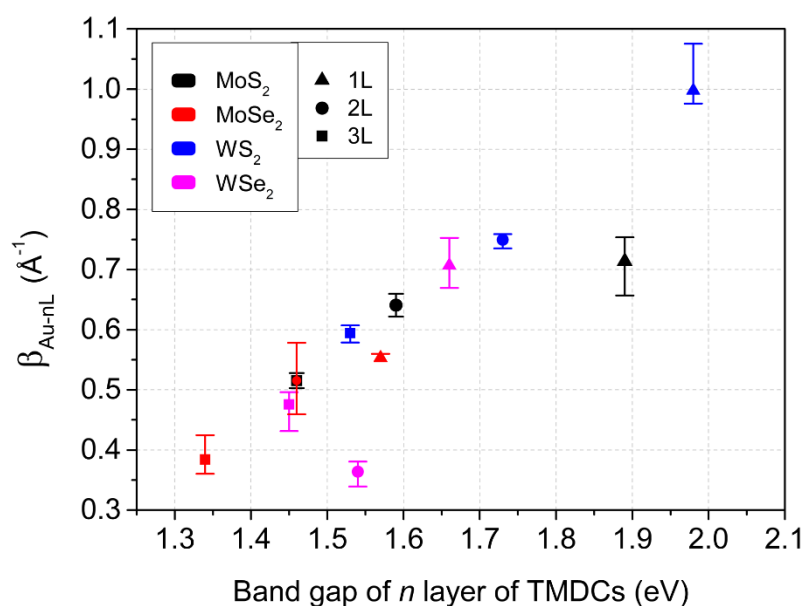
**Table 4.6:** Median prefactor,  $k_{max}$ , the 25<sup>th</sup> and 75<sup>th</sup> percentiles in brackets.  $\beta_{Au-nL}$  derived from Equation 4.12 for the median  $k_{max}$  of MoS<sub>2</sub>, MoSe<sub>2</sub>, WS<sub>2</sub> and WSe<sub>2</sub>. In brackets the  $\beta_{Au-nL}$  derived from the 25<sup>th</sup> and 75<sup>th</sup>  $k_{max}$  percentiles. The band gap is reported for the same TMDCs with different numbers of layers (1L, 2L and 3L).<sup>13</sup>

	$k_{max-nL}$ (cm/s)			$\beta_{Au-nL}$ (Å <sup>-1</sup> )			Band gap (eV)		
	1L	2L	3L	1L	2L	3L	1L	2L	3L
MoS <sub>2</sub>	250 [190 350]	7.5 [5.9 9.4]	1.5 [1.2 1.8]	0.71 [0.66 0.75]	0.64 [0.62 0.66]	0.52 [0.50 0.53]	1.89	1.59	1.46
MoSe <sub>2</sub>	560 [530 560]	26 [11 53]	12 [5.2 18]	0.55 [0.55 0.56]	0.51 [0.46 0.58]	0.38 [0.36 0.42]	1.57	1.46	1.34
WS <sub>2</sub>	43 [27 49]	2.0 [1.7 2.3]	0.34 [0.27 0.45]	1.00 [0.98 1.07]	0.75 [0.74 0.76]	0.59 [0.58 0.61]	1.98	1.73	1.53
WSe <sub>2</sub>	140 [103 184]	120 [97 170]	0.92 [0.60 2.3]	0.71 [0.67 0.75]	0.36 [0.34 0.38]	0.48 [0.43 0.50]	1.66	1.54	1.45

The electronic band structure of TMDCs depends on the number of stacked layers.<sup>63-65</sup> The band gap of MoS<sub>2</sub>, MoSe<sub>2</sub>, WS<sub>2</sub>, and WSe<sub>2</sub> increases with the decreasing layer number (< 5L) due to the strong quantum confinement in thin layers.<sup>65,66</sup> The larger band gap of thinner layers should lead to an increase in the tunnelling barrier height, and therefore larger tunnelling decay constants ( $\beta$ ). On the contrary, the smaller band gap of thicker layers should lead to smaller tunnelling decay constants. The tunnelling barriers diagrams presented in Figure 4.33 A and B illustrate changes in tunnelling barrier height with the number of layers stacked. Indeed, the tunnelling decay constants derived and listed in Table 4.6 agree with this trend.

The  $\beta_{Au-nL}$  values describe the  $n$ -layers of TMDCs acting as a single tunnelling barrier, thus  $\beta_{Au-nL}$  can be compared with the band gaps reported for  $n$ -layers of TMDCs (also displayed in Table 4.6).<sup>13</sup> From Table 4.6, we observe a correlation between  $\beta_{Au-nL}$  values and band gap on the different layer thickness of TMDCs. For example, of the TMDCs studied, WS<sub>2</sub> has the largest band gap and WS<sub>2</sub> also showed the largest tunnelling decay constant,  $\beta_{Au-nL}$ , values. Likewise, of the materials we considered, MoSe<sub>2</sub> has the smallest band gap and shows the smallest  $\beta_{Au-nL}$  values. In fact, we observe a strong correlation between the band gap values sourced from the literature<sup>13</sup> and the measured tunnelling decay constant,  $\beta_{Au-nL}$ , values, as shown in Figure 4.34. These findings are supported by the recent work by Lee, H. *et al.*, who experimentally determined the tunnelling barrier height on the different number of layers (1-5L) of MoS<sub>2</sub> on gold using conducting AFM.<sup>67</sup> The barrier height maximum is observed for 1L, then decreases and stabilises at > 5L, in good agreement with the values reported in Table 4.6 obtained, in this case, with the electron transfer of an outer-sphere redox probe.

From the results reported in this chapter, it is concluded that the electrochemical response on few-layer 2D TMDCs, in a bottom-contacted configuration, depends on the electron transport process through the TMDC layers. This electron transport is strongly influenced by the electronic structure of the 2D TMDCs, with larger band gaps resulting in a larger decrease in  $k_{max}$  with each additional layer, and therefore a higher electron tunnelling barrier. However, 2D TMDCs with fewer layers stacking show faster electron transport kinetics due to a narrower tunnelling barrier, despite having a larger tunnelling decay constant. As a consequence, bottom-contacted 2D TMDC samples with a heterogeneous number of stacked layers will produce an electrochemical response dominated by monolayer activity at lower overpotentials but with increasing activity of thicker layers at higher overpotentials (assuming there is no diffusional overlap). These findings suggest that the electrochemical response of the TMDC electrode surfaces is profoundly affected by the mode of contact established on the electrodes. This has implications for the interpretation of electrochemical and, importantly, electrocatalytic experiments at TMDC nanoarchitectures. Through-layer or within-layer electron transport must be considered when interpreting the performance of TMDC materials for the HER or other reactions of relevance to advanced electrochemical applications.



**Figure 4.34:**  $\beta_{Au-nL}$  values plotted against the band gap for 1-, 2-, and 3-layer MoS<sub>2</sub>, MoSe<sub>2</sub>, WS<sub>2</sub>, and WSe<sub>2</sub>.<sup>13</sup> Error bar correspond to  $\beta_{Au-nL}$  derived from  $k_{max}$  values for the 25<sup>th</sup> and 75<sup>th</sup> percentiles. Reproduced with permission from Brunet Cabré, M. *et al.*.<sup>41</sup>

## 4.5 Conclusions

In this chapter, SECCM has been used to quantify the effect of the number of stacked layers of 2D TMDCs (MoS<sub>2</sub>, MoSe<sub>2</sub>, WS<sub>2</sub>, WSe<sub>2</sub>) on the electrochemical response of the [Ru(NH<sub>3</sub>)<sub>6</sub>]<sup>3+/2+</sup> redox couple. Combining SECCM and AFM allowed us to precisely determine the exact nature of the underlying 2D material at each sample point, and to quantify the electrochemical response on the different numbers of layers. There is a significant difference in the electrochemical response on the different numbers of stacked layers, with more facile kinetics observed on thinner stacks of all four materials.

Kinetic dependence was assessed by comparison with a finite element simulation that coupled the diffusional mass transport of [Ru(NH<sub>3</sub>)<sub>6</sub>]<sup>3+/2+</sup> in the nanopipette probe with the Gerischer description of electrochemical kinetics. We quantified the rate of electron transfer on a different number of stacked layers of four TMDCs by fitting a simulated response to the experimentally measured LSVs by only varying the maximum kinetic rate,  $k_{max}$ . MoS<sub>2</sub>, MoSe<sub>2</sub>, WS<sub>2</sub>, and WSe<sub>2</sub> all show a decrease in the electron transfer rate constant as the number of layers increases.

Trends in the electron transfer rates were described by considering an electron tunnelling barrier arising from the TMDC itself. This allowed us to extract the apparent tunnelling decay constants,  $\beta$ , which range over 1.0 - 0.4 Å<sup>-1</sup> across all TMDC materials tested; these values are consistent with those reported for tunnelling decay constants of 2D TMDCs by other groups.<sup>62,67</sup>

The pre-factor,  $k_{max}$ , decays more slowly than we would expect if each additional layer added an identical electron tunnelling barrier. Therefore, the previously reported tunnelling barrier model for HER on a few-layer MoS<sub>2</sub>, where the tunnelling decay constant was not affected by the number of TMDCs layers,<sup>25</sup> is insufficient to explain the experimental data. The correlation observed between band gap and tunnelling decay constant suggests that non-exponential decay of rate constants is due to a change in the electronic properties of the tunnelling barrier, resulting from band gap changes as a function of the number of stacked layers of TMDCs. Therefore, the variation in the electronic structure of the 2D material affects the electron transport to such an extent that we can observe the effect in the electrochemical measurements.

The electrochemical behaviour observed on the 2D TMDCs surface is clearly heterogeneous, but thanks to AFM it was possible to determine and classify which points contacted only pristine basal plane, which facilitated observation of the electrochemical trends. Nevertheless, it has been observed that points which contacted other morphological features of 2D TMDCs, such as layer boundaries or defects, also presented characteristic electrochemical responses. In the following chapter, the role of other morphological features in the electrochemical response will be discussed.

## Authorship Statement

This chapter is an extended adaptation of the work presented in the publication:

*Electrochemical kinetics as a function of transition metal dichalcogenide thickness.*

Brunet Cabré, M.; Esmeraldo Paiva, A.; Velický, M.; Colavita, P.E. and McKelvey, K.

*Electrochimica Acta*, 2021, 393, 139027.

This publication is reproduced in the appendix section of the thesis.

Electrochemical experiments, data analysis, and manuscript writing were performed by the first author of the publication, M.B.C., as part of the Ph.D. thesis presented here.

Co-author A.E.P. contributed to the development of the experimental work with 2D TMDCs as part of his Ph.D. thesis. M.V. as a group collaborator, manufactured the 2D TMDCs samples used in this chapter and supervised manuscript writing. P.E.C. provide guidance over data analysis and results discussion.

The corresponding author, K.M. led and supervised the experimental design for the acquisition of electrochemical data. K.M contributed and supervised the data analysis processes, manuscript drafting and correction.

## References

- 1 Chia, X., Ambrosi, A., Sofer, Z., Luxa, J. & Pumera, M. Catalytic and charge transfer properties of transition metal dichalcogenides arising from electrochemical pretreatment. *ACS Nano* **9**, 5164-5179 (2015). <https://doi.org/10.1021/acsnano.5b00501>
- 2 Bentley, C. L., Kang, M. & Unwin, P. R. Nanoscale Structure Dynamics within Electrocatalytic Materials. *J. Am. Chem. Soc.* **139**, 16813-16821 (2017). <https://doi.org/10.1021/jacs.7b09355>
- 3 Tan, S. M. *et al.* Pristine Basal- and Edge-Plane-Oriented Molybdenite MoS<sub>2</sub> Exhibiting Highly Anisotropic Properties. *Chemistry* **21**, 7170-7178 (2015). <https://doi.org/10.1002/chem.201500435>
- 4 Velicky, M. *et al.* Electron transfer kinetics on natural crystals of MoS<sub>2</sub> and graphite. *Phys. Chem. Chem. Phys.* **17**, 17844-17853 (2015). <https://doi.org/10.1039/c5cp02490k>
- 5 Jaramillo, T. F. *et al.* Identification of active edge sites for electrochemical H<sub>2</sub> evolution from MoS<sub>2</sub> nanocatalysts. *Science* **317**, 100-102 (2007). <https://doi.org/10.1126/science.1141483>
- 6 Bentley, C. L. *et al.* Electrochemical maps and movies of the hydrogen evolution reaction on natural crystals of molybdenite (MoS(2)): basal vs. edge plane activity. *Chem. Sci.* **8**, 6583-6593 (2017). <https://doi.org/10.1039/c7sc02545a>
- 7 Manzeli, S., Ovchinnikov, D., Pasquier, D., Yazyev, O. V. & Kis, A. 2D transition metal dichalcogenides. *Nat. Rev. Mater.* **2**, 17033-17048 (2017). <https://doi.org/10.1038/natrevmats.2017.33>
- 8 Wang, Q. H., Kalantar-Zadeh, K., Kis, A., Coleman, J. N. & Strano, M. S. Electronics and optoelectronics of two-dimensional transition metal dichalcogenides. *Nat. Nanotechnol.* **7**, 699-712 (2012). <https://doi.org/10.1038/nnano.2012.193>
- 9 Choi, W. *et al.* Recent development of two-dimensional transition metal dichalcogenides and their applications. *Mater. Today* **20**, 116-130 (2017). <https://doi.org/10.1016/j.mattod.2016.10.002>
- 10 Pomerantseva, E., Bonaccorso, F., Feng, X., Cui, Y. & Gogotsi, Y. Energy storage: The future enabled by nanomaterials. *Science* **366** (2019). <https://doi.org/10.1126/science.aan8285>
- 11 Ahmadi, M. *et al.* 2D transition metal dichalcogenide nanomaterials: advances, opportunities, and challenges in multi-functional polymer nanocomposites. *J. Mater. Chem. A* **8**, 845-883 (2020). <https://doi.org/10.1039/c9ta10130f>
- 12 Wei, Z. M. *et al.* Various Structures of 2D Transition-Metal Dichalcogenides and Their Applications. *Small Methods* **2**, 1800094-1800094 (2018). <https://doi.org/10.1002/smt.201800094>
- 13 Velický, M. & Toth, P. S. From two-dimensional materials to their heterostructures: An electrochemist's perspective. *Appl. Mater. Today* **8**, 68-103 (2017). <https://doi.org/10.1016/j.apmt.2017.05.003>
- 14 Chia, X., Eng, A. Y., Ambrosi, A., Tan, S. M. & Pumera, M. Electrochemistry of Nanostructured Layered Transition-Metal Dichalcogenides. *Chem. Rev.* **115**, 11941-11966 (2015). <https://doi.org/10.1021/acs.chemrev.5b00287>

- 15 Chhowalla, M. *et al.* The chemistry of two-dimensional layered transition metal dichalcogenide nanosheets. *Nat. Chem.* **5**, 263-275 (2013). <https://doi.org:10.1038/nchem.1589>
- 16 Stephenson, T., Li, Z., Olsen, B. & Mitlin, D. Lithium ion battery applications of molybdenum disulfide (MoS<sub>2</sub>) nanocomposites. *Energy Environ. Sci.* **7**, 209-231 (2014). <https://doi.org:10.1039/c3ee42591f>
- 17 Ratha, S. & Rout, C. S. Supercapacitor electrodes based on layered tungsten disulfide-reduced graphene oxide hybrids synthesized by a facile hydrothermal method. *ACS Appl. Mater. Interfaces* **5**, 11427-11433 (2013). <https://doi.org:10.1021/am403663f>
- 18 da Silveira Firmiano, E. G. *et al.* Supercapacitor Electrodes Obtained by Directly Bonding 2D MoS<sub>2</sub> on Reduced Graphene Oxide. *Adv. Energy Mater.* **4** (2014). <https://doi.org:10.1002/aenm.201301380>
- 19 Zhu, Z. *et al.* Ultrathin Transition Metal Dichalcogenide/3d Metal Hydroxide Hybridized Nanosheets to Enhance Hydrogen Evolution Activity. *Adv. Mater.* **30**, e1801171 (2018). <https://doi.org:10.1002/adma.201801171>
- 20 Fu, Q. *et al.* 2D Transition Metal Dichalcogenides: Design, Modulation, and Challenges in Electrocatalysis. *Adv. Mater.* **33**, e1907818 (2021). <https://doi.org:10.1002/adma.201907818>
- 21 Lin, L. X. *et al.* Engineered 2D Transition Metal Dichalcogenides-A Vision of Viable Hydrogen Evolution Reaction Catalysis. *Adv. Energy Mater.* **10** (2020). <https://doi.org:10.1002/aenm.201903870>
- 22 Lu, Q., Yu, Y., Ma, Q., Chen, B. & Zhang, H. 2D Transition-Metal-Dichalcogenide-Nanosheet-Based Composites for Photocatalytic and Electrocatalytic Hydrogen Evolution Reactions. *Adv. Mater.* **28**, 1917-1933 (2016). <https://doi.org:10.1002/adma.201503270>
- 23 Bergeron, H. *et al.* Chemical vapor deposition of monolayer MoS<sub>2</sub> directly on ultrathin Al<sub>2</sub>O<sub>3</sub> for low-power electronics. *Appl. Phys. Lett.* **110** (2017). <https://doi.org:10.1063/1.4975064>
- 24 Velicky, M. *et al.* Mechanism of Gold-Assisted Exfoliation of Centimeter-Sized Transition-Metal Dichalcogenide Monolayers. *ACS Nano* **12**, 10463-10472 (2018). <https://doi.org:10.1021/acsnano.8b06101>
- 25 Yu, Y. *et al.* Layer-dependent electrocatalysis of MoS<sub>2</sub> for hydrogen evolution. *Nano Lett.* **14**, 553-558 (2014). <https://doi.org:10.1021/nl403620g>
- 26 Desai, S. B. *et al.* Gold-Mediated Exfoliation of Ultralarge Optoelectronically-Perfect Monolayers. *Adv. Mater.* **28**, 4053-4058 (2016). <https://doi.org:10.1002/adma.201506171>
- 27 Magda, G. Z. *et al.* Exfoliation of large-area transition metal chalcogenide single layers. *Sci. Rep.* **5**, 14714 (2015). <https://doi.org:10.1038/srep14714>
- 28 Splendiani, A. *et al.* Emerging photoluminescence in monolayer MoS<sub>2</sub>. *Nano Lett.* **10**, 1271-1275 (2010). <https://doi.org:10.1021/nl903868w>
- 29 Smith, T. The Hydrophilic Nature of a Clean Gold Surface. *J. Colloid Interface Sci.* **75**, 51-55 (1980). [https://doi.org:10.1016/0021-9797\(80\)90348-3](https://doi.org:10.1016/0021-9797(80)90348-3)
- 30 Huang, Y. *et al.* Universal mechanical exfoliation of large-area 2D crystals. *Nat. Commun.* **11**, 2453 (2020). <https://doi.org:10.1038/s41467-020-16266-w>

- 31 Bentley, C. L. *et al.* Nanoscale Electrochemical Mapping. *Anal. Chem.* **91**, 84-108 (2019). <https://doi.org/10.1021/acs.analchem.8b05235>
- 32 Bentley, C. L., Kang, M. & Unwin, P. R. Nanoscale Surface Structure-Activity in Electrochemistry and Electrocatalysis. *J. Am. Chem. Soc.* **141**, 2179-2193 (2019). <https://doi.org/10.1021/jacs.8b09828>
- 33 Snowden, M. E. *et al.* Scanning electrochemical cell microscopy: theory and experiment for quantitative high resolution spatially-resolved voltammetry and simultaneous ion-conductance measurements. *Anal. Chem.* **84**, 2483-2491 (2012). <https://doi.org/10.1021/ac203195h>
- 34 Ebejer, N. *et al.* Scanning electrochemical cell microscopy: a versatile technique for nanoscale electrochemistry and functional imaging. *Annu. Rev. Anal. Chem.* **6**, 329-351 (2013). <https://doi.org/10.1146/annurev-anchem-062012-092650>
- 35 Ebejer, N., Schnippering, M., Colburn, A. W., Edwards, M. A. & Unwin, P. R. Localized high resolution electrochemistry and multifunctional imaging: scanning electrochemical cell microscopy. *Anal. Chem.* **82**, 9141-9145 (2010). <https://doi.org/10.1021/ac102191u>
- 36 Tao, H. C. *et al.* Two-dimensional materials for energy conversion and storage. *Prog. Mater. Sci.* **111** (2020). <https://doi.org/10.1016/j.pmatsci.2020.100637>
- 37 Takahashi, Y. *et al.* High-Resolution Electrochemical Mapping of the Hydrogen Evolution Reaction on Transition-Metal Dichalcogenide Nanosheets. *Angew. Chem. Int. Ed. Engl.* **59**, 3601-3608 (2020). <https://doi.org/10.1002/anie.201912863>
- 38 Velicky, M. *et al.* Photoelectrochemistry of Pristine Mono- and Few-Layer MoS<sub>2</sub>. *Nano Lett.* **16**, 2023-2032 (2016). <https://doi.org/10.1021/acs.nanolett.5b05317>
- 39 Liao, W. *et al.* Interface engineering of two-dimensional transition metal dichalcogenides towards next-generation electronic devices: recent advances and challenges. *Nanoscale Horiz* **5**, 787-807 (2020). <https://doi.org/10.1039/c9nh00743a>
- 40 Liu, D. Q. *et al.* Adiabatic versus non-adiabatic electron transfer at 2D electrode materials. *Nat. Commun.* **12**, 7110 (2021). <https://doi.org/10.1038/s41467-021-27339-9>
- 41 Brunet Cabré, M., Paiva, A. E., Velický, M., Colavita, P. E. & McKelvey, K. Electrochemical kinetics as a function of transition metal dichalcogenide thickness. *Electrochim. Acta* **393** (2021). <https://doi.org/10.1016/j.electacta.2021.139027>
- 42 Li, X., Batchelor-McAuley, C., Laborda, E. & Compton, R. G. Aqueous Voltammetry in the Near Absence of Electrolyte. *Chemistry* **23**, 15222-15226 (2017). <https://doi.org/10.1002/chem.201703525>
- 43 Taghavi, N. S. *et al.* Thickness determination of MoS<sub>2</sub>, MoSe<sub>2</sub>, WS<sub>2</sub> and WSe<sub>2</sub> on transparent stamps used for deterministic transfer of 2D materials. *Nano Res.* **12**, 1691-1695 (2019). <https://doi.org/10.1007/s12274-019-2424-6>
- 44 Shaw, J. C. *et al.* Chemical vapor deposition growth of monolayer MoSe<sub>2</sub> nanosheets. *Nano Res.* **7**, 511-517 (2014). <https://doi.org/10.1007/s12274-014-0417-z>
- 45 Park, J., Kim, M. S., Cha, E., Kim, J. & Choi, W. Synthesis of uniform single layer WS<sub>2</sub> for tunable photoluminescence. *Sci. Rep.* **7**, 16121 (2017). <https://doi.org/10.1038/s41598-017-16251-2>

- 46 Liu, B. *et al.* Chemical Vapor Deposition Growth of Monolayer WSe<sub>2</sub> with Tunable Device Characteristics and Growth Mechanism Study. *ACS Nano* **9**, 6119-6127 (2015). <https://doi.org/10.1021/acsnano.5b01301>
- 47 Zhang, Y. *et al.* On Valence-Band Splitting in Layered MoS<sub>2</sub>. *ACS Nano* **9**, 8514-8519 (2015). <https://doi.org/10.1021/acsnano.5b03505>
- 48 Chow, P. K. *et al.* Wetting of mono and few-layered WS<sub>2</sub> and MoS<sub>2</sub> films supported on Si/SiO<sub>2</sub> substrates. *ACS Nano* **9**, 3023-3031 (2015). <https://doi.org/10.1021/nn5072073>
- 49 Kozbial, A., Gong, X., Liu, H. & Li, L. Understanding the Intrinsic Water Wettability of Molybdenum Disulfide (MoS<sub>2</sub>). *Langmuir* **31**, 8429-8435 (2015). <https://doi.org/10.1021/acs.langmuir.5b02057>
- 50 Wang, Y. J., Limon-Petersen, J. G. & Compton, R. G. Measurement of the diffusion coefficients of [Ru(NH<sub>3</sub>)<sub>6</sub>]<sup>3+</sup> and [Ru(NH<sub>3</sub>)<sub>6</sub>]<sup>2+</sup> in aqueous solution using microelectrode double potential step chronoamperometry. *J. Electroanal. Chem.* **652**, 13-17 (2011). <https://doi.org/10.1016/j.jelechem.2010.12.011>
- 51 Bard, A. J. & Faulkner, L. R. *Electrochemical methods: fundamentals and applications*. 2nd edn, (John Wiley & Sons, Inc., 2001).
- 52 Memming, R. *Semiconductor Electrochemistry*. (John Wiley & Sons, 2015).
- 53 Feldberg, S. W. Implications of Marcus-Hush theory for steady-state heterogeneous electron transfer at an inlaid disk electrode. *Anal. Chem.* **82**, 5176-5183 (2010). <https://doi.org/10.1021/ac1004162>
- 54 Velicky, M. *et al.* Electron Tunneling through Boron Nitride Confirms Marcus-Hush Theory Predictions for Ultramicroelectrodes. *ACS Nano* **14**, 993-1002 (2020). <https://doi.org/10.1021/acsnano.9b08308>
- 55 Royea, W. J., Hamann, T. W., Brunshwig, B. S. & Lewis, N. S. A comparison between interfacial electron-transfer rate constants at metallic and graphite electrodes. *J. Phys. Chem. B* **110**, 19433-19442 (2006). <https://doi.org/10.1021/jp062141e>
- 56 Ghosh, S. & Hammes-Schiffer, S. Calculation of Electrochemical Reorganization Energies for Redox Molecules at Self-Assembled Monolayer Modified Electrodes. *J. Phys. Chem. Lett.* **6**, 1-5 (2015). <https://doi.org/10.1021/jz5023784>
- 57 Liu, J. *et al.* Advanced Energy Storage Devices: Basic Principles, Analytical Methods, and Rational Materials Design. *Adv. Sci.* **5**, 1700322 (2018). <https://doi.org/10.1002/advs.201700322>
- 58 Hupp, J. T. & Weaver, M. J. Experimental estimate of the electron-tunneling distance for some outer-sphere electrochemical reactions. *J. Phys. Chem.* **88**, 1463-1467 (2002). <https://doi.org/10.1021/j150652a004>
- 59 He, Z. D., Chen, Y. X., Santos, E. & Schmickler, W. The Pre-exponential Factor in Electrochemistry. *Angew. Chem. Int. Ed. Engl.* **57**, 7948-7956 (2018). <https://doi.org/10.1002/anie.201800130>
- 60 Becka, A. M. & Miller, C. J. Electrochemistry at .omega.-hydroxy thiol coated electrodes. 3. Voltage independence of the electron tunneling barrier and measurements of redox kinetics at large overpotentials. *J. Phys. Chem.* **96**, 2657-2668 (2002). <https://doi.org/10.1021/j100185a049>



- 61 Son, Y. *et al.* Layer number dependence of MoS<sub>2</sub> photoconductivity using photocurrent spectral atomic force microscopic imaging. *ACS Nano* **9**, 2843-2855 (2015). <https://doi.org/10.1021/nn506924j>
- 62 Datta, K. & Khosru, Q. D. M. Simulation of thin-TFETs using transition metal dichalcogenides: effect of material parameters, gate dielectric on electrostatic device performance. *J. Comput. Electron.* **16**, 228-239 (2017). <https://doi.org/10.1007/s10825-017-0978-7>
- 63 Wang, K. C. *et al.* Control of interlayer physics in 2H transition metal dichalcogenides. *J. Appl. Phys.* **122** (2017). <https://doi.org/10.1063/1.5005958>
- 64 Park, J. H. *et al.* Scanning Tunneling Microscopy and Spectroscopy of Air Exposure Effects on Molecular Beam Epitaxy Grown WSe<sub>2</sub> Monolayers and Bilayers. *ACS Nano* **10**, 4258-4267 (2016). <https://doi.org/10.1021/acs.nano.5b07698>
- 65 Trainer, D. J. *et al.* Inter-Layer Coupling Induced Valence Band Edge Shift in Mono- to Few-Layer MoS<sub>2</sub>. *Sci. Rep.* **7**, 40559 (2017). <https://doi.org/10.1038/srep40559>
- 66 Yun, W. S., Han, S. W., Hong, S. C., Kim, I. G. & Lee, J. D. Thickness and strain effects on electronic structures of transition metal dichalcogenides: 2H-MX<sub>2</sub> semiconductors (M=Mo, W; X=S, Se, Te). *Phys. Rev. B* **85**, 1-5 (2012). <https://doi.org/10.1103/PhysRevB.85.033305>
- 67 Lee, H. *et al.* Layer-Dependent Interfacial Transport and Optoelectrical Properties of MoS<sub>2</sub> on Ultraflat Metals. *ACS Appl. Mater. Interfaces* **11**, 31543-31550 (2019). <https://doi.org/10.1021/acsami.9b09868>



# CHAPTER 5

## Nanoscale Defects on 2D Transition Metal Dichalcogenides

---

Translating nano-electrochemical behaviour to bulk electrochemical response requires to account for the response of all possible electroactive domains present on a surface. In the previous chapter, only the pristine basal plane response of 2D transition metal dichalcogenides was discussed. However, defects are often found on commonly used electrode surfaces, and two-dimensional transition metal dichalcogenides are not an exception. This chapter explores how nanometre and sub-nanometre scale defects can be detected electrochemically using scanning electrochemical cell microscopy (SECCM). On mechanically exfoliated MoS<sub>2</sub>, isolated anomalous electrochemical responses are found in the basal plane for outer-sphere redox couples. These anomalous sample points display faster electrochemical kinetics, with a diffusion-limited current plateau, compared to those of the surrounding sample points. The analysis of the electrochemical current suggests that the defects are equivalent to disk-shaped defects with radii of tens of nanometres, or to one-dimensional defects with nanometre to sub-nanometre widths. These results demonstrate that we can effectively isolate and electrochemically amplify the response from individual defects on a sample surface using SECCM, revealing features below the optical diffraction limit that would normally require high-resolution electron microscopy or scanning tunnelling microscopy to detect.

---

## 5.1 Introduction

### 5.1.1 Defects on 2D TMDCs

Electrochemically active surfaces are generally not perfect and homogeneous. Understanding the electrode surface as a defect-free single crystalline plane of a monocrystalline material is not representative of a real electrochemical system.<sup>1,2</sup> Instead, most of the electrode surface presents a variety of nanoscale morphological features such as vacancies, adatoms, grain boundaries, and impurities. The presence of such morphological features, or defects, strongly influences the physicochemical properties of the surface and subsequently the electrochemical response.<sup>3-5</sup> Two-dimensional (2D) transition metal dichalcogenides (TMDCs) are not an exception and defects are common on these surfaces.<sup>6-8</sup>

In recent years, the field of defect engineering in 2D materials has expanded largely thanks to its ability to tune the electrocatalytic performance of electrode materials. For the case of 2D TMDCs, several defect engineering studies consider the catalytic performance towards the hydrogen evolution reaction (HER).<sup>9,10</sup> The influence of defect engineering on other types of reaction has also been considered in other studies: Li, H. J. *et al.* assessed the role of the defects in WSe<sub>2</sub> base electrodes for Li-sulfide ion battery applications;<sup>11</sup> Zeng, L. *et al.* introduced defect vacancies by doping on MoS<sub>2</sub> to promote the nitrogen reduction reaction (NRR);<sup>12</sup> or, Jin, H. *et al.* reported that metal doping of MoS<sub>2</sub> provides a new catalytic centre for electrochemical CO<sub>2</sub> reduction.<sup>13</sup> A description of the influence of nanoscale features in the electrochemical response is provided in the Introduction chapter, Section 1.3.

In Chapter 4 we discussed the characteristic outer-sphere electrochemical response of the [Ru(NH<sub>3</sub>)<sub>6</sub>]<sup>2+/3+</sup> redox couple on 2D TMDCs basal planes. However, the electrochemical response of morphological features, such as boundaries or defects, was not evaluated. The study in Chapter 4 was possible due to the selective wetting of the electrode surface offered by SECCM. However, the bulk electrochemical system used in application devices does not present selective wetting and defects contribute to the overall electrochemical response. To understand the overall electrochemical performance of 2D TMDCs electrodes, it is then essential to isolate and evaluate the contribution of such defects to the response. Often, this involves defect detection, physical characterisation of the defect, and characterisation of the electrochemical response of the defect.<sup>14,15</sup>

### 5.1.2 Methods for defect detection

Defect detection can be achieved by physical characterisation techniques. For example, collective average responses originating from several defects on a surface could be detected by photoemission spectroscopy,<sup>16</sup> Raman spectroscopy or photoluminescence.<sup>17</sup> Individual morphological defects with a size of a few nanometres could be identified by atomic force microscopy (AFM)<sup>18</sup> or scanning electron microscopy (SEM).<sup>19</sup> Detection mapping of individual atomic-size defects, however, requires high-resolution techniques, such as high-resolution transmission electron microscopy (TEM)<sup>20</sup> or scanning tunnelling microscopy (STM).<sup>21</sup> Defect detection by electrochemical means is more challenging, as the signal produced by ensemble based (bulk) electrochemical approaches averages the response from all active sites and thus makes it difficult to identify heterogeneity present at the surface.<sup>22</sup> Compared to the limitations of bulk approaches, electrochemical scanning probe microscopy (EC-SPM) techniques can isolate the response from nanoscale domains, becoming the most suitable candidate for defect electrochemical detection.<sup>14</sup> A description of methods for characterising nanoscale features response is provided in Introduction chapter, Section 1.4. Such approaches have been used in several studies of 2D materials,<sup>23-28</sup> and used in Chapter 4 of this thesis.

However, EC-SPM techniques typically require complementary microscopy maps such as AFM, SEM, or optical microscopy to correlate the electrochemical response with surface morphological features.<sup>29</sup> However, these approaches can be limiting and thus assignment requires relatively large surface features to be resolved by microscopy techniques. Furthermore, atomic-size features would require the use of high-resolution techniques, such as TEM or STM, that are challenging to interface with electrochemical methods.<sup>5</sup> Sample preparation requirements for TEM and STM often make sample and/or instrumentation for electrochemical characterisation incompatible.<sup>29</sup>

There have been recent advances towards better instrumental integration of electrochemical measurements and TEM or STM techniques. For instance, Bentley, C. L. *et al.* have performed scanning electrochemical cell microscopy (SECCM) on a TEM grid.<sup>30</sup> Also, some studies achieved in-situ TEM characterisation of the electrode surface while performing electrochemical measurements.<sup>31</sup> Those examples and similar efforts, achieved correlation between electrochemical response and high-resolution morphological characterisation needed for defect detection, but require a very specific instrumental development and have limited applicability.<sup>31-34</sup>

### 5.1.3 Mass transport effects on kinetically enhanced defects

Electrochemistry is unique in that mass transport effects can amplify the size of the spatial region that is affected by a point-like change in the electrode surface. In classical electrochemical methods this had been demonstrated, *e.g.* by Amatore *et al.*, when discussing the effect of pin-hole defects on the waveform at SAM-modified electrodes;<sup>35</sup> In those studies it is highlighted that the hemi-spherical diffusion front of pin-holes below 10 nm in size can provide mass transfer rates about 3 orders of magnitude larger than the equivalent semi-infinite planar diffusion rate.<sup>36</sup> This occurs because diffusion limited current of a circular electrode with a hemispherical diffusion field depends linearly on its radius, as shown in Equation 5.1. However, the electrode area depends on the squared radius. Therefore, the diffusion-limited current density has a 1/*r* dependency, as shown in Equation 5.2. As represented in Figure 5.1 A, smaller electrodes have a greater diffusion-limited current density. Moreover, the interplay between the timescale used for potential steps/sweeps and the size of a diffusion front can be leveraged to increase the characteristic length scale of the observed effects.<sup>37</sup>

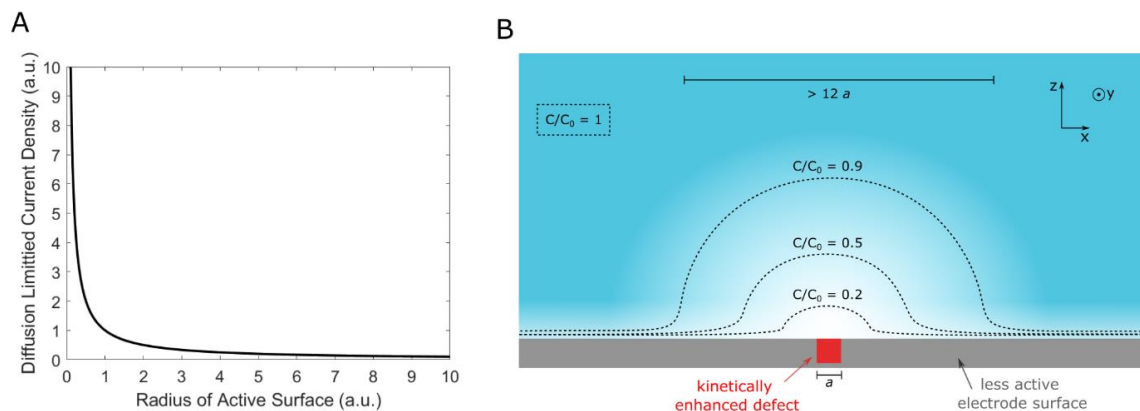
$$i_{diff.lim} = 4zrDFc \quad (\text{Eq 5.1})$$

$$i_{diff.lim-density} = \frac{i_{diff.lim}}{Area} = \frac{4zDFc}{\pi r} \quad (\text{Eq 5.2})$$

where *z* is the number of electrons transferred in the reaction, *r* is the equivalent radius of the defect, *D* is the diffusion coefficient, *F* is the Faraday constant, and *c* is the concentration of the bulk solution.

Mass transport effects coupled with modern nano-electrochemical techniques, such as EC-SPM, can achieve single defect detection and amplify the characteristic length of active nanoscale regions in the current response.<sup>38-40</sup> For example, SECCM has been used to detect single pinholes of < 10 nm on passivating layers<sup>41</sup> and the presence of defects on 2D materials (graphene supported on copper) has been observed.<sup>23</sup>

Note that previous studies based on SECCM evaluated only defects that present enhanced kinetics with respect to the surrounding material, as illustrated in Figure 5.1 B. Thus, to benefit from mass transport effects, the defect must have enhanced electrochemical kinetics. This constrains the type of defect that can be detected electrochemically; however, kinetically enhanced defects are expected to contribute the most to the bulk electrochemical response and are the most interesting from an electrocatalytic perspective.



**Figure 5.1:** **A.** Plot of diffusion-limited current density with respect to the radius of active surface, showing the  $1/\text{radius}$  relation. **B.** Illustration of equi-concentration lines around a kinetically enhanced defect (red) that consumes reactant species 'c' faster than the surrounding electrode surface (grey). The equi-concentration lines help to visualise the hemispherical diffusion front of the defect and the semi-infinite planar diffusion front of the surrounding electrode surface. The size of the defect 'a' is highlighted with respect to the region where the concentration is depleted below 90% of the bulk concentration ' $c_0$ ', which is greater than 12 times the electrode size.

## 5.2 Aims

To obtain a complete picture of the electrochemical response of 2D TMDCs, we need to characterise the different electrochemical active domains present at their surfaces. The behaviour of the basal plane domain was reported in Chapter 4, but the surface of 2D TMDCs also contains layer boundaries and defective domains. Defective domains on 2D material surfaces are expected to present different physicochemical properties compared to basal plane domains, resulting in different electrochemical responses. The detection and isolation of electrochemical responses arising from defects represents a significant challenge and often rely on additional physical characterisation. However, the small contact area (approx.  $1 \mu\text{m}^2$ ) offered by SECCM combined with mass transport effects can amplify the characteristic length scale of defects in the current response.

In this chapter, the presence of individual defects with enhanced electrochemical kinetics in 2D materials is explored using a SECCM approach. First, I will explore if the presence of kinetically enhanced domains is correlated with the presence of morphological features characteristic of 2D TMDCs observed by physical characterisation, such as layer boundaries, number of layers stacked, etc.. Then, the characteristic electrochemical response of kinetically enhanced domains will be analysed and correlated with the size and shape of the defect.

In this chapter, it is shown that it is possible to identify defects with enhanced electrochemical kinetics, with characteristic sizes ranging from a few angstroms to a few nanometres scale on different TMDCs:  $\text{MoS}_2$ ,  $\text{MoSe}_2$ , and  $\text{WSe}_2$ . These defects are too small to be easily mapped via optical or even atomic force microscopy and would normally require TEM or STM approaches for their identification. This means that SECCM is thus uniquely sensitive to the presence of sub-nanometre defects with enhanced kinetics at the material's surface (including 2D materials) that otherwise would remain hidden.



## 5.3 Methods

### 5.3.1 Electrochemical measurements

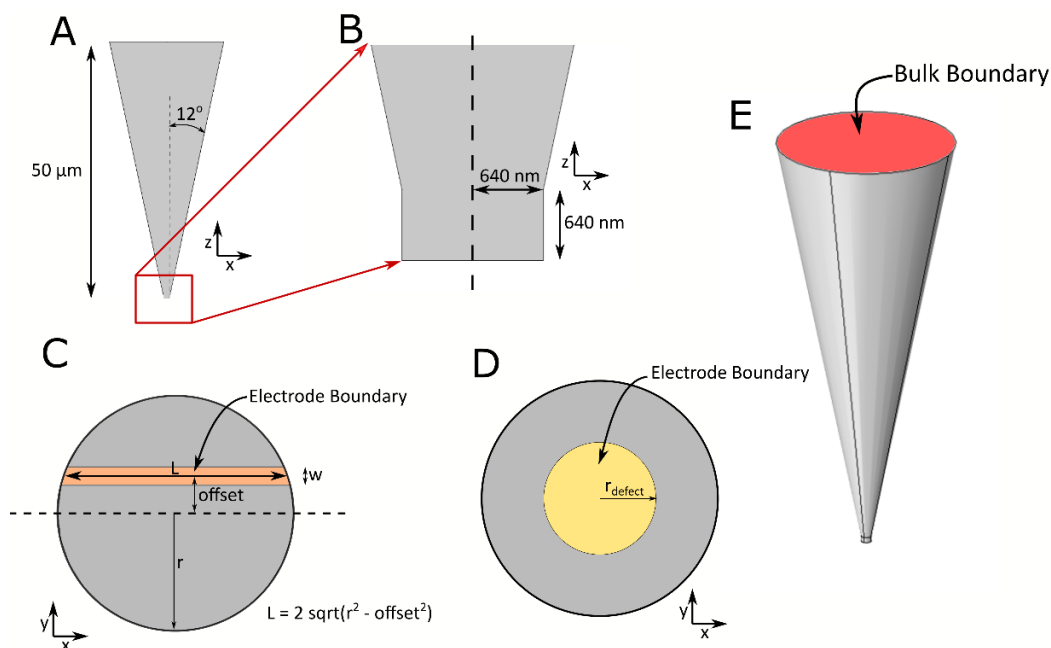
2D MoS<sub>2</sub>, MoSe<sub>2</sub> and WSe<sub>2</sub> samples were prepared on Au electrode surfaces by mechanical exfoliation of TMDC bulk crystals.<sup>42</sup> Electrical contact with the sample was established via the underlying Au. Optical and SECCM measurements were made using a Park NX10 instrument (Park Systems, South Korea). The SECCM tips were fabricated from glass capillaries (1.5 mm O.D and 0.86 mm I.D., BF150-86-7.5, Sutter Instruments, USA) using a P-2000 laser puller (Sutter Instrument, USA) to form a 640 nm radius single-barreled nanopipette. The SECCM tips were filled with 1.0 mM [Ru(NH<sub>3</sub>)<sub>6</sub>]Cl<sub>3</sub> (JMC Corporation, South Korea) in 10 mM KCl (VWR Chemicals, USA). A chloridized Ag wire was used as an Ag/AgCl quasi-reference counter electrode and was inserted into the top end of the nanopipette. SECCM measurements were made at an array of equally spaced points (1.5 μm apart) in hopping mode. Upon contact between the nanodroplet at the end of the SECCM tip, a linear sweep voltammogram (LSV) of the one electron reduction of [Ru(NH<sub>3</sub>)<sub>6</sub>]<sup>3+</sup> to [Ru(NH<sub>3</sub>)<sub>6</sub>]<sup>2+</sup> was conducted on the sample surface with a fast sweep rates ranging from 0.2 to 1 V s<sup>-1</sup>. All potentials are reported respect the Ag/AgCl quasi-reference counter electrode.

### 5.3.2 Simulation of disc and band electrodes in the SECCM probe

The diffusional transport of [Ru(NH<sub>3</sub>)<sub>6</sub>]<sup>3+</sup> and [Ru(NH<sub>3</sub>)<sub>6</sub>]<sup>2+</sup> to a band electrode that transects the SECCM probe was simulated in a time-dependent 3-dimensional finite element simulation using COMSOL Multiphysics. The circular defects, *i.e.* disc electrode, were simulated using a 2-dimensional axisymmetric model. The time-dependent diffusional transport of [Ru(NH<sub>3</sub>)<sub>6</sub>]<sup>3+</sup> and [Ru(NH<sub>3</sub>)<sub>6</sub>]<sup>2+</sup> within the nanopipette and the SECCM droplet was simulated using Fick's second law of diffusion, which is given by:

$$\frac{\partial c_i}{\partial t} - D_i \nabla^2 c_i = 0 \quad (\text{Eq. 5.3})$$

where  $c_i$  is the concentration of either [Ru(NH<sub>3</sub>)<sub>6</sub>]<sup>2+</sup> or [Ru(NH<sub>3</sub>)<sub>6</sub>]<sup>3+</sup>,  $D_i$  is the diffusion coefficient for either [Ru(NH<sub>3</sub>)<sub>6</sub>]<sup>2+</sup> ( $1.2 \times 10^{-5} \text{ cm}^2 \text{ s}^{-1}$ ) or [Ru(NH<sub>3</sub>)<sub>6</sub>]<sup>3+</sup> ( $8.4 \times 10^{-6} \text{ cm}^2 \text{ s}^{-1}$ ),<sup>43</sup> and  $t$  is time. The 3-dimensional geometry in which the concentration of [Ru(NH<sub>3</sub>)<sub>6</sub>]<sup>2+/3+</sup> was simulated is shown in Figure 5.2.



**Figure 5.2:** Model of simulated 3D geometry. **A:** Side view of the 3D geometry, showing the cone angle ( $12^\circ$ ) of the SECCM tip and the height of the simulation ( $50\ \mu\text{m}$ ). **B:** Zoom of the end of the SECCM probe, showing the droplet radius ( $640\ \text{nm}$ ) and the droplet height ( $640\ \text{nm}$ ). **C:** Geometry of the bottom of the droplet with a band electrode of length  $L$  and width  $w$ . The band electrode is offset from the centre of the droplet. The relation between the band length and its offset respect is  $L = 2\sqrt{r^2 - offset^2}$ . **D:** Geometry of the bottom of the droplet cell with a circular defect. **E:** 3D geometry of the SECCM simulation domain, including labelling of the bulk boundary.

All boundaries of the simulation domain, see Figure 5.2, were set as no-flux boundaries ( $-n \cdot J_i = 0$ , where  $n$  is the boundary normal and  $J_i$  is the flux of either  $[\text{Ru}(\text{NH}_3)_6]^{2+}$  or  $[\text{Ru}(\text{NH}_3)_6]^{3+}$ ) except:

- the bulk boundary (labelled in Figure 5.2 E) at which the concentration of  $[\text{Ru}(\text{NH}_3)_6]^{2+}$  was set to 0 mM and the concentration of  $[\text{Ru}(\text{NH}_3)_6]^{3+}$  was set to 1 mM.
- the band electrode (labelled in Figure 5.2 C) or the circular defect (labelled in Figure 5.2 D) at which the flux of  $[\text{Ru}(\text{NH}_3)_6]^{2+/3+}$  was defined by Butler-Volmer kinetics given by

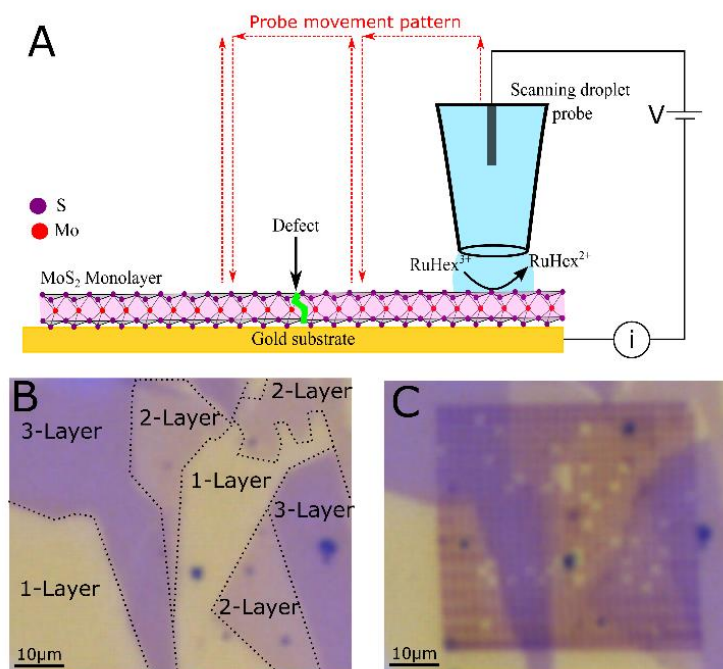
$$I = I_0 \left( c_{[\text{Ru}(\text{NH}_3)_6]^{2+}} \cdot e^{\frac{(1-\alpha)F\eta}{RT}} - c_{[\text{Ru}(\text{NH}_3)_6]^{3+}} \cdot e^{-\frac{\alpha F\eta}{RT}} \right) \quad (\text{Eq. 5.4})$$

where  $I$  is the current density,  $I_0 = Fk^0$ ,  $F$  is the Faraday constant,  $k^0$  is the standard heterogeneous electron transfer rate constant, which was set at  $10\ \text{cm s}^{-1}$ ,  $C_{[\text{Ru}(\text{NH}_3)_6]^{2+}}$  is the concentration of  $[\text{Ru}(\text{NH}_3)_6]^{2+}$  at the electrode boundary,  $C_{[\text{Ru}(\text{NH}_3)_6]^{3+}}$  is the concentration of  $[\text{Ru}(\text{NH}_3)_6]^{3+}$  at the electrode boundary,  $\alpha = 0.5$ ,  $R$  is the ideal gas constant,  $T = 298\ \text{K}$ ,  $\eta = E - E^0$ , where  $E^0 = -0.25\ \text{V}$  and  $E$  is the electrode potential that was ramped between 0 V and  $-0.5\ \text{V}$  at  $1\ \text{V s}^{-1}$  for the time dependent LSV simulation.

## 5.4 Results

### 5.4.1 Electrochemical mapping by SECCM

The starting point for the identification and morphology characterisation of defects is the dataset of electrochemical mappings of MoS<sub>2</sub> surfaces presented in Chapter 4. In summary, a 640 nm radius single-barreled nanopipette was used to map the one electron reduction of [Ru(NH<sub>3</sub>)<sub>6</sub>]<sup>3+</sup> to [Ru(NH<sub>3</sub>)<sub>6</sub>]<sup>2+</sup> on the MoS<sub>2</sub> surface using a hopping mode SECCM, as illustrated in Figure 5.3 A. Optical images of the MoS<sub>2</sub> sample in the region of SECCM mapping are shown in Figures 5.3 B and C before and after SECCM experiments, respectively. The region of interest contains mono-, bi-, and tri-layer MoS<sub>2</sub> immobilised on the underlying Au electrode surface, as determined by optical microscopy displayed in Figure 5.3 B.<sup>44</sup> The MoS<sub>2</sub> layers appear to be continuous in the optical images. In Chapter 4, the voltammetric analysis obtained on MoS<sub>2</sub> and other 2D TMDCs is reported, showing how the electrochemical kinetics of the [Ru(NH<sub>3</sub>)<sub>6</sub>]<sup>3+/2+</sup> couple depends on the number of 2D TMDC layers and, ultimately, the band gap of the 2D TMDC.<sup>45</sup> From this dataset, the electrochemical responses are examined at individual sample points to identify nanoscale defects at the sample surface.

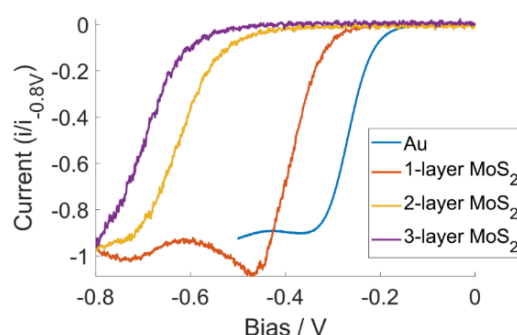


**Figure 5.3:** A. Schematic of the SECCM experimental configuration, in which we use a 640 nm radius single-barreled nanopipette filled with 1 mM [Ru(NH<sub>3</sub>)<sub>6</sub>]<sup>3+</sup> and 10 mM KCl electrolyte solution to conduct a series of LSVs over the sample surface (which is either mono-, bi-, or tri-layer MoS<sub>2</sub>) in a SECCM configuration. The probe movement pattern during the hopping mode scanning

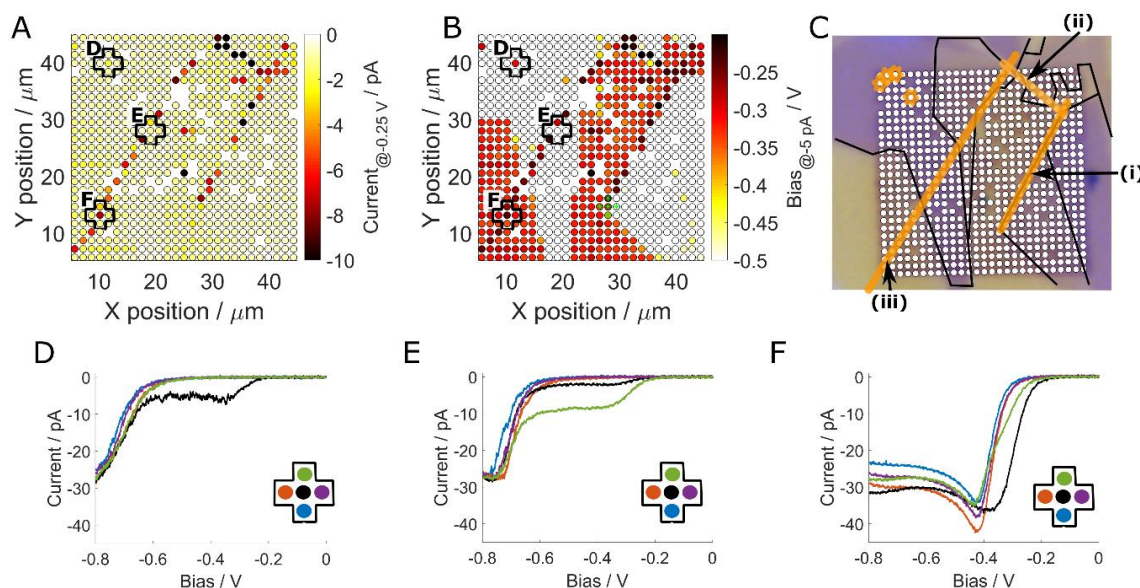
is shown in red. A bias (V) is applied between the QRCE inserted inside the SECCM droplet probe and the Au-supported MoS<sub>2</sub> sample and the current is measured through the sample surface. **B.** Optical image of the sample surface before the SECCM measurements, with the regions of different MoS<sub>2</sub> thicknesses labelled. **C.** Optical image of the sample surface after the SECCM experiments, showing the salt deposits left over from the SECCM imaging, which were used to assign the MoS<sub>2</sub> thickness (monolayer, bilayer, trilayer) for each LSV measurement. Note that at some sample points the SECCM droplet did not contact the sample surface because of early activation of the automatic feedback loop prior to the droplet contacting the sample surface. In those points there are no salt deposits left, and these can be identified as bright spots in the optical image. Reproduced with permission from Brunet Cabré, M. *et al.*<sup>46</sup>

### 5.4.2 Anomalous current enhanced points and correlation with 2D TMDC morphological features

Figure 5.5 A shows a map of the current obtained at -0.25 V from LSV curves measured at each position/pixel in the probed array; the -0.25 V bias is sufficient to drive [Ru(NH<sub>3</sub>)<sub>6</sub>]<sup>3+</sup> reduction at metallic Au surfaces, but insufficient to observe reduction at most MoS<sub>2</sub> surfaces, as shown in Figure 5.4 and reported in Chapter 4. Figure 5.5 A shows certain sample points (shown in orange/red/black) that display current magnitudes that are significantly larger than those observed in the surrounding pixels (shown in yellow/white). Figure 5.5 B shows a map of the applied bias required to observe a current of -5 pA at each pixel, which indicates that the points identified in Figure 5.5 A are also prominent in this constant current map and require lower biases to drive the same current than neighbouring pixels. Later in this chapter, Section 5.4.4, it is detailed why the current threshold of -5 pA was chosen because it provides sufficient contrast for visualising the defective points.



**Figure 5.4:** Average LSV response at different MoS<sub>2</sub> thicknesses and unmodified Au surface normalised by current at -0.8 V. The bias potential is given with respect to the Ag/AgCl QRCE.



**Figure 5.5:** **A:** Map of the electrochemical response for  $[\text{Ru}(\text{NH}_3)_6]^{3+}$  reduction showing the current measured at a bias of  $-0.25$  V, sufficient to drive  $[\text{Ru}(\text{NH}_3)_6]^{3+}$  reduction on Au but not on a  $\text{MoS}_2$  surface. The LSV responses at the sample points within regions D-F as shown in part D-F, respectively. **B:** Map of the electrochemical response showing the bias required to maintain a current of  $-5$  pA. The LSV responses at the sample points within regions D-F as shown in part D-F, respectively. **C:** Composite optical image showing the alignment of the defect features on the surfaces. **D-F:** LSV response at sample regions D-F shown in parts A and B, respectively. Sweep rate used  $1 \text{ V s}^{-1}$ . Reproduced with permission from Brunet Cabré, M. *et al.*<sup>46</sup>

Both Figures 5.5 A and B identify positions that yield deviations in current/bias relative to the surrounding sample points; these are highlighted and overlapped with the optical image in Figure 5.5 C. Several of these positions/pixels are aligned along the  $\text{MoS}_2$  edges, such as those labelled i) and ii) in Figure 5.5 C. Therefore, the  $\text{MoS}_2$  edges appear to be associated with anomalous outer-sphere electrochemical responses, although not all edges show these anomalous responses. The enhanced electrochemical response at the  $\text{MoS}_2$  edge has been previously reported for the hydrogen evolution reaction.<sup>25,47</sup> Therefore, we observe for the first time that the enhanced edge activity in 2D TMDCs also occurs for outer-sphere redox processes.

However, it is not always the case that anomalous electrochemical responses are associated with the  $\text{MoS}_2$  edges. For example, the line of anomalous electrochemical responses labelled iii) in Figure 5.5 C is not associated with a  $\text{MoS}_2$  edge. The anomalous sample points that are not associated with an  $\text{MoS}_2$  edge suggest that other 1-dimensional defects, *e.g.*, dislocation, grain boundaries, or even physical cracks in  $\text{MoS}_2$  are at the origin of their responses.<sup>10,48</sup> We also observed discrete sample points with enhanced electrochemical currents, that are isolated and do not belong to a line of anomalous sample points, such as the point labelled D in Figure 5.5 A and B. These anomalous sample points suggest that the electrochemical response is associated with point defects at the  $\text{MoS}_2$  sample surface, which cannot be identified optically.

Figures 5.5 D-F show the LSV responses measured in three regions, labelled D-F of panel 5.5 A and B, respectively; the LSVs of all 728 sample points are shown in the Appendix of this Chapter. Figure 5.5 D shows the electrochemical response on trilayer MoS<sub>2</sub>; this position is not part of a line of anomalous sample points. A significantly enhanced electrochemical response for [Ru(NH<sub>3</sub>)<sub>6</sub>]<sup>3+</sup> reduction is observed at one point in Figure 5.5 D relative to that of the surrounding sample points: a current plateau at approximately -5.5 pA between -0.35 and -0.7 V, while biases below -0.7 V are insufficient to drive the [Ru(NH<sub>3</sub>)<sub>6</sub>]<sup>3+</sup> reduction on the tri-layer MoS<sub>2</sub>. The next two sample regions, whose LSVs are shown in Figure 5.5 E and F, lie along the lines of the anomalous sample points(iii): region E is located on a trilayer MoS<sub>2</sub>, while region F is located on a monolayer MoS<sub>2</sub> (Figure 5.3 B could help visualise the number of layers stacked on points E and F). Note that two of the sample points in Figure 5.5 E show an anomalous electrochemical behaviour.

The onset biases for [Ru(NH<sub>3</sub>)<sub>6</sub>]<sup>3+</sup> reduction that we observe at the anomalous sample points are identical to those observed at an Au electrode surface, see Figure 5.4. This suggests that the enhanced electrochemical kinetics for the [Ru(NH<sub>3</sub>)<sub>6</sub>]<sup>3+/2+</sup> redox couple on the anomalous sample points is equivalent and indistinguishable to that of a metallic Au surface.

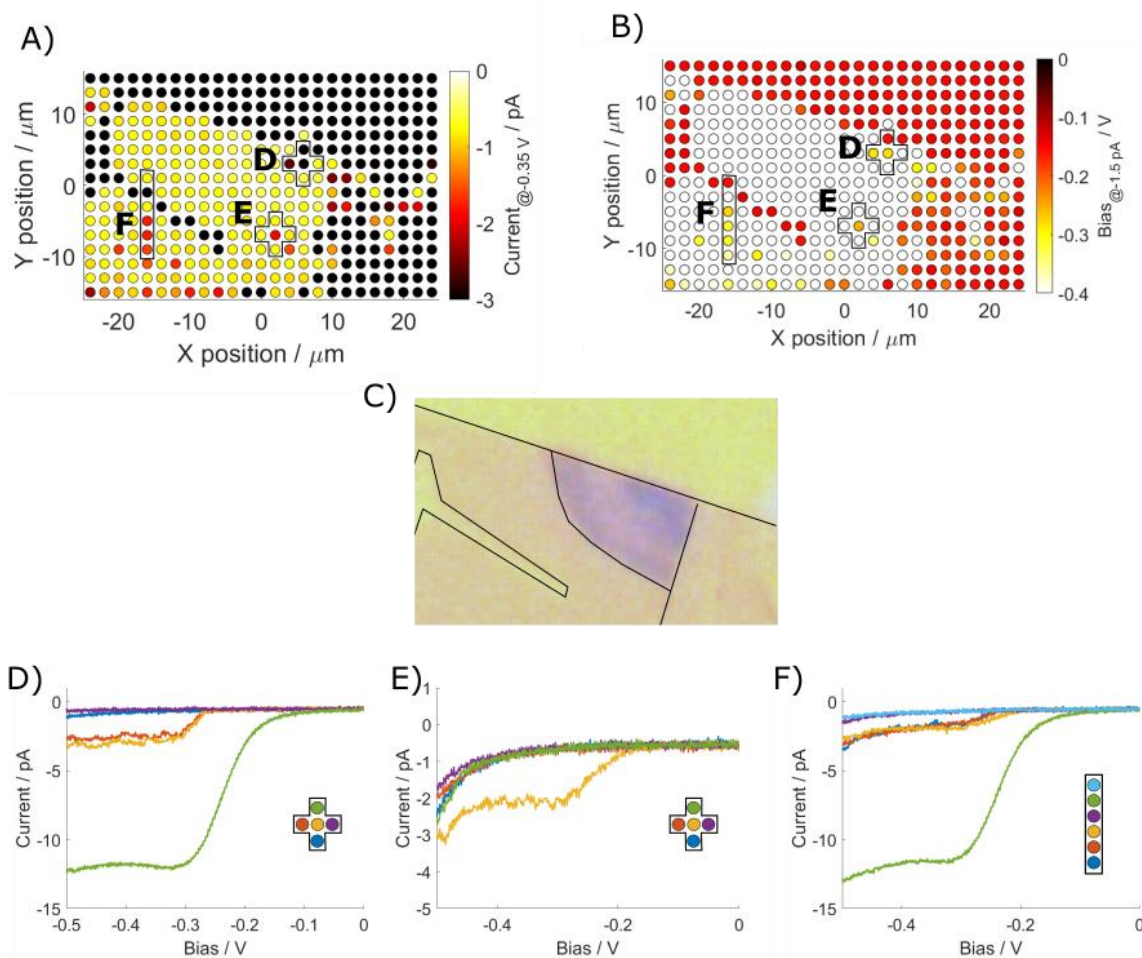
### 5.4.3 Analysis of diffusion-limited current plateaus for defect detection

A plateau in the reductive current at approximately -27 pA is observed in all the LSVs when applying a bias sufficient to drive the reduction of [Ru(NH<sub>3</sub>)<sub>6</sub>]<sup>3+</sup> ( $\leq -0.8$  V on tri-layer,  $< -0.7$  V on bi-layer,  $< -0.4$  V on mono-layer, and  $< -0.25$  V on Au, (see Figure 5.4 and Figure 5.5 D-F), due to the diffusion-limited transport of [Ru(NH<sub>3</sub>)<sub>6</sub>]<sup>3+</sup> to the MoS<sub>2</sub> surface. In a SECCM configuration, the magnitude of the diffusion-limited current at higher overpotentials depends on the concentration of [Ru(NH<sub>3</sub>)<sub>6</sub>]<sup>3+</sup>, the diffusion coefficient, the contact area between the SECCM nanodroplet and the sample surface, as well as the geometry of the SECCM probe.<sup>40</sup> The current plateau at the defect points shown in Figure 5.5 D and E is observed at much lower biases (ca. -0.25 V), which is consistent with the electrochemical response for [Ru(NH<sub>3</sub>)<sub>6</sub>]<sup>3+</sup> reduction on a sufficiently metallic surface. However, the current plateaus are well below the -27 pA observed at higher overpotentials, namely -5.5 pA for the point in Figure 5.5 D, and -8.5 pA and -2 pA for the points in Figure 5.5 E. In Figure 5.5 F the anomalous sample point, in black, shows a response at a much lower bias, but does not display a lower current plateau. In all LSVs (Figure 5.5 D, E and F) at higher biases, the current then reaches the -27 pA diffusion-limited current. This suggests that a small portion of the nanodroplet contact area is exposed to a surface defect with enhanced kinetics.

Note that the observation of a current plateau of smaller magnitude than expected based on droplet cell size, indicates that the diffusion layer associated with the defect site must be smaller than the one resulting from the total contacted area of the MoS<sub>2</sub> surface. Importantly, larger defects will lead to plateau currents that approach the maximum limiting current.

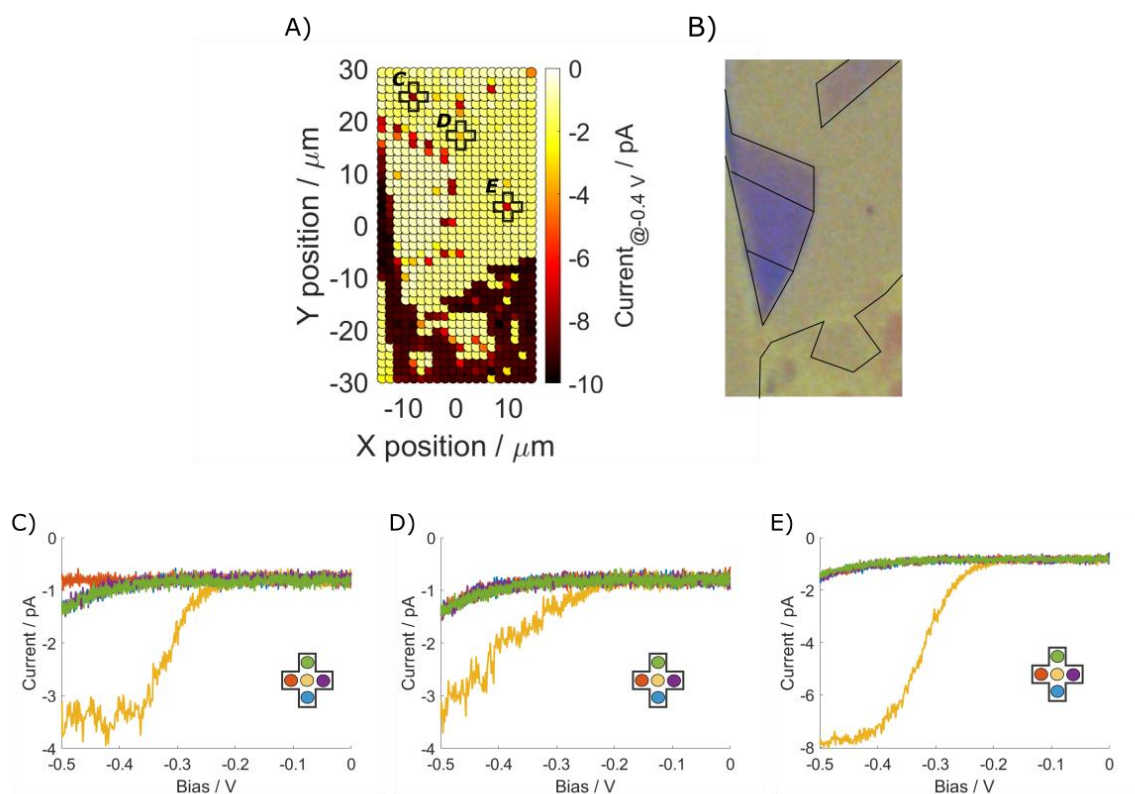
Additional SECCM maps on MoSe<sub>2</sub>, WSe<sub>2</sub> and other MoS<sub>2</sub> samples are shown in Figures 5.6 to 5.9, and anomalous points were observed on all samples. In Figures 5.6, 5.7 and 5.8 some of the enhanced points are aligned with morphological features, such as layer edges, while other enhanced sample points could not be correlated with any morphological features evident from optical microscopy. The characteristic current plateaus shown in Figure 5.5 for MoS<sub>2</sub> (*i.e.* with smaller magnitude than expected based on droplet cell size) are observed as well in the MoSe<sub>2</sub> and WSe<sub>2</sub> samples, as displayed in Figures 5.6 and 5.7. Another surface region of the same MoS<sub>2</sub> sample (same sample as Figure 5.5), has been map by SECCM and displays current plateaus with a lower current magnitude than the droplet diffusion limiting current, as shown in Figure 5.8. In another scanned region of the WSe<sub>2</sub> sample, shown in Figure 5.9, the current plateaus of a smaller magnitude are not observed, but lower onset potentials are clearly displayed for a series of points. Note that some of those points are not aligned with any discernible morphological feature, *e.g.* Figure 5.9 F.

The characteristic anomalous behaviour observed on different surface regions of MoS<sub>2</sub>, MoSe<sub>2</sub>, and WSe<sub>2</sub> indicates that kinetically enhanced defects could be commonly detected on mechanically exfoliated 2D TMDCs.

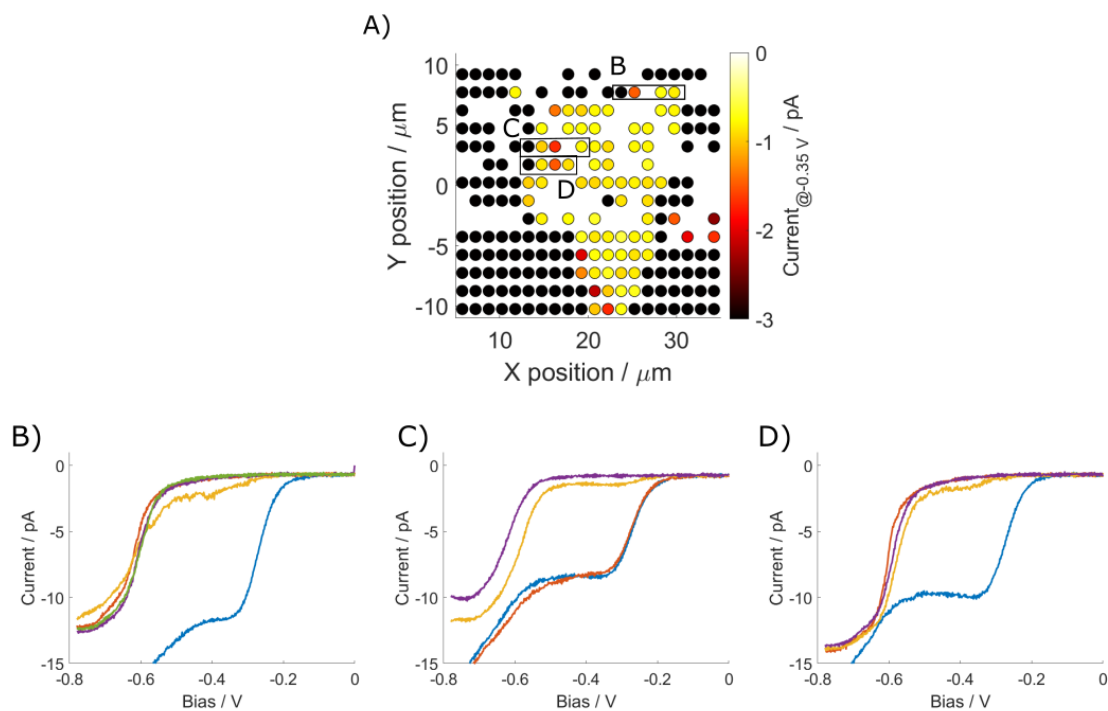


**Figure 5.6:** **A.** Map of the electrochemical response for [Ru(NH<sub>3</sub>)<sub>6</sub>]<sup>3+</sup> reduction on a MoSe<sub>2</sub> sample, showing the current measured at a bias of -0.35 V. The LSV responses at the sample points within the regions D-F are shown in D-F, respectively. **B.** Map of the electrochemical response showing the bias required to obtain a current of -1.5 pA. The LSV responses at the sample points within regions D-F as shown in part D-F, respectively. **C.** Composite optical image showing the position region F, which does not align with any morphological features of the sample surfaces. **D-F.** LSV response at sample regions D-F shown in parts A and B, respectively.

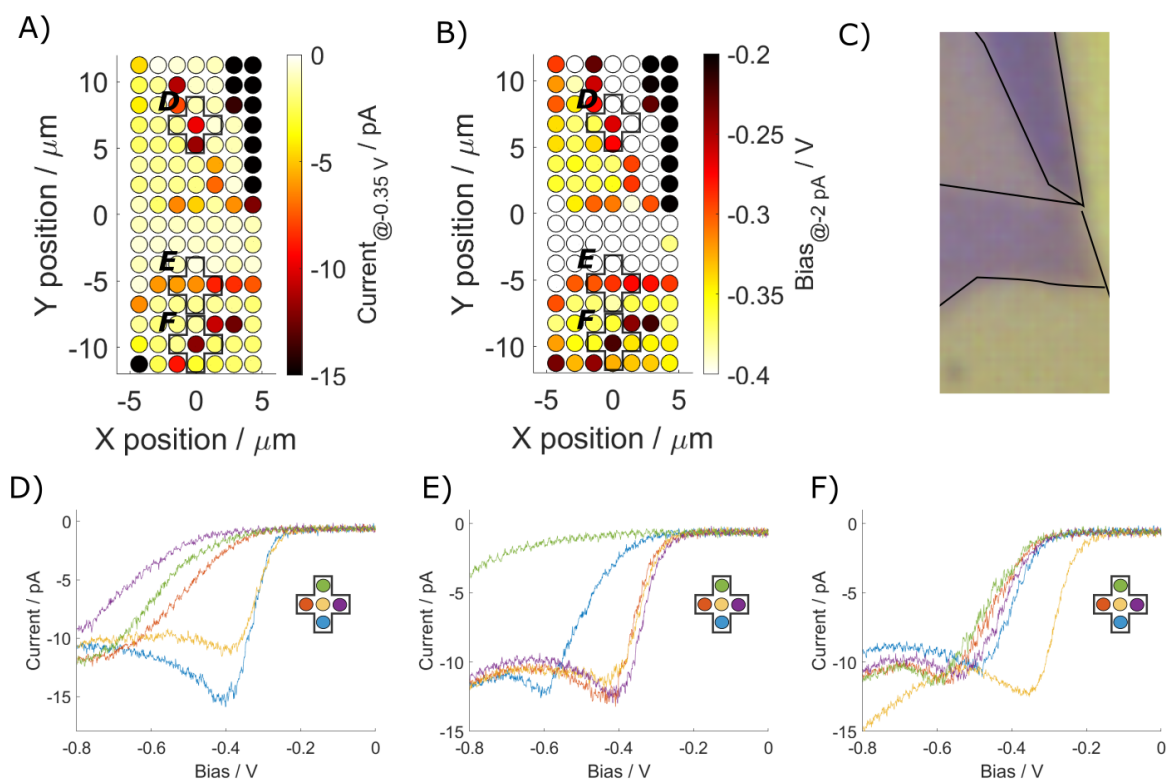




**Figure 5.7:** **A:** Map of the electrochemical response for  $[\text{Ru}(\text{NH}_3)_6]^{3+}$  reduction on a  $\text{WSe}_2$  sample, showing the current measured at a bias of  $-0.4$  V. The LSV responses at the sample points within the regions C-E are shown in C-E, respectively. **B:** Composite optical image showing the alignment of the defect features on the surfaces. **C-E.** LSV response at the sample regions C-E shown in part A.



**Figure 5.8:** **A.** Map of the electrochemical response for  $[\text{Ru}(\text{NH}_3)_6]^{3+}$  reduction on a  $\text{MoS}_2$  sample, showing the current measured at a bias of  $-0.35$  V. The LSV responses at the sample points within the regions B-D as shown in part B-D, respectively. Note that many sample points did not result in the SECCM droplet contacting with the sample (*i.e.* false hops) and appear as missing data points. The missed contacts from the SECCM probe are due to early activation of the automatic feedback loop prior to the droplet contact with the sample surface **B-D.** LSV response at sample regions B-D shown in part A.



**Figure 5.9:** **A:** Map of the electrochemical response for  $[\text{Ru}(\text{NH}_3)_6]^{3+}$  reduction on a  $\text{WSe}_2$  sample, showing the current measured at a bias of  $-0.35$  V. The LSV responses at the sample points within the regions D-F as shown in part D-F, respectively. **B:** Map of the electrochemical response showing the bias required to maintain a constant current of  $-2$  pA. The LSV responses at the sample points within regions D-F as shown in part D-F, respectively. **C:** Composite optical image showing the alignment of the defect features on the surfaces. Notice that (iv) alignment of current enhanced points could not be correlated with any morphological feature. **D-F:** LSV response at sample regions D-F shown in parts A and B, respectively.

#### 5.4.4 Modeling single-point defect electrochemical response

A first approach to understand the observed current plateaus is to calculate the size of the equivalent disc-shaped site on the surface of the TMDC, which would give rise to such a diffusion-limited current. Therefore, this first approximation does not yet consider the mass transport limitations imposed by the SECCM droplet configuration, but could be a good approximation for defects much smaller than the SECCM droplet.<sup>49</sup> In this case the diffusion-limited current  $i_{diff,lim}$  is described by hemispherical diffusion, as shown in Equation 5.1,<sup>37</sup> with  $z = 1$ ,  $D = 8.4 \times 10^{-6} \text{ cm}^2 \text{ s}^{-1}$  for the  $[\text{Ru}(\text{NH}_3)_6]^{3+}$ ,<sup>43</sup> and  $c = 1 \text{ mM}$  as the bulk solution concentration of  $[\text{Ru}(\text{NH}_3)_6]^{3+}$ .

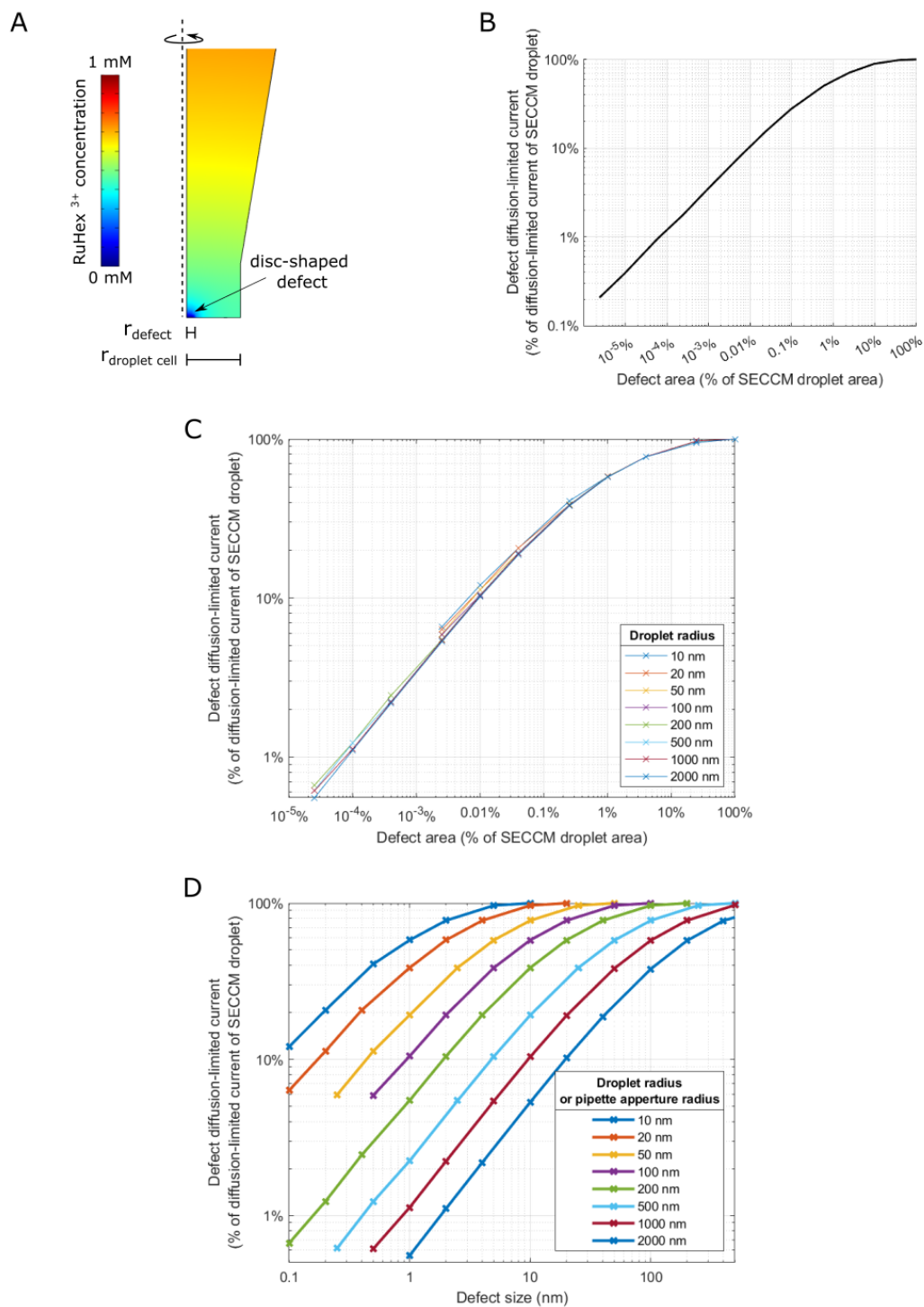
Using Equation 5.1 it is determined that a diffusion-limited current of  $-5.5 \text{ pA}$  observed in Figure 5.5 D is equivalent to a defect with radius of  $17 \text{ nm}$ . Likewise, the diffusion-limited currents of  $-8.5 \text{ pA}$  and  $-2 \text{ pA}$  in Figure 5.5 E correspond to defects with radii of  $26 \text{ nm}$  and  $6 \text{ nm}$ , respectively. The defect in Figure 5.5 F gives a diffusion-limited current plateau that is of the same magnitude as the  $[\text{Ru}(\text{NH}_3)_6]^{3+}$  reduction on the entire contacted  $\text{MoS}_2$  surface, suggesting that this defect is  $> 83 \text{ nm}$  in radius. Similarly, defects observed on  $\text{MoSe}_2$  have  $6 - 8 \text{ nm}$  radii approximately, see Figure 5.6 D-F. The current plateaus observed on  $\text{WSe}_2$ , displayed in Figures 5.7 C and E, correspond to  $10$  and  $25 \text{ nm}$  radii. This simple analysis suggests that the observed anomalous electrochemical responses can be generated by nanoscale kinetically enhanced defects on TMDC surfaces. The percentage of the defect area with respect to the SECCM droplet contact area ranges from  $0.01\%$  ( $6 \text{ nm}$  defect) to  $0.16\%$  ( $26 \text{ nm}$  defect) and their estimated sizes are well below the diffraction limit and therefore impossible to detect optically.

The above estimates of the defect size and diffusion limited current do not consider the effect of diffusion within the SECCM probe geometry. Solving the problem of diffusion for particular geometries can be a complex task, and it often does not yield analytical expressions, and, instead, numerical approaches must be adopted to approximate their description.<sup>50</sup> The relationship between a circular defective area in the SECCM droplet and the relative diffusion-limited current was simulated by finite element methods. A simplified axisymmetric representation of the model is shown in the scheme of Figure 5.10 A, where the diffusion limiting current is simulated as a function of  $r_{defect}$  size. The complete description of the model is given in the methods of this chapter, Section 5.3.2. The results of the simulations are shown in Figure 5.10 B, highlighting that a defect only needs to be present in a small fraction of the droplet cell area to give a large and measurable electrochemical response. Similar relationships to those in Figure 5.10 B are obtained regardless of the absolute droplet area, as shown in Figure 5.10 C.

However, by changing the pipette aperture (*i.e.*, changing the droplet size), a defect of a given size will result in a different limiting current relative to the maximum value expected. Therefore, it is possible to optimise the droplet size by modifying the pipette aperture to achieve the best contrast

for the detection of differently sized defects. Figure 5.10 D shows the ratio of diffusion limiting current expected for each combination of nanoscale defect size and pipette aperture. This plot enables the identification of which droplet size would provide the best contrast to detect defects of different sizes. We tentatively estimate that a kinetically enhanced defect which provides a diffusion-limited current between the 10 - 50 % of the droplet diffusion-limited current will provide good contrast with respect to the surrounding points. A response below 10 % might be compromised by noise levels, and a response above 50 % is too close to the diffusion limited current of the entire droplet to be readily distinguished. Note that only for currents below 50% of the diffusion limiting value, there is a linear relation between the defect area and the defect diffusion limiting current. For instance, a 10 nm defect would be best detected using a droplet whose radius is between 200 nm and 1000 nm. For a 1 nm sized defect, optimal contrast would be obtained with a droplet between 20 nm and 100 nm in radius.

The diffusion limiting current observed during the MoS<sub>2</sub> electrochemical mapping was  $-27$  pA (see Figure 5.5 D-F), and for representing the bias at which a current threshold is reached, the best defect contrast was achieved using  $-5$  pA (see Figure 5.5 B). This threshold current represents approx. 20% of the diffusion-limiting current, therefore within the range found to provide better contrast for defect identification.

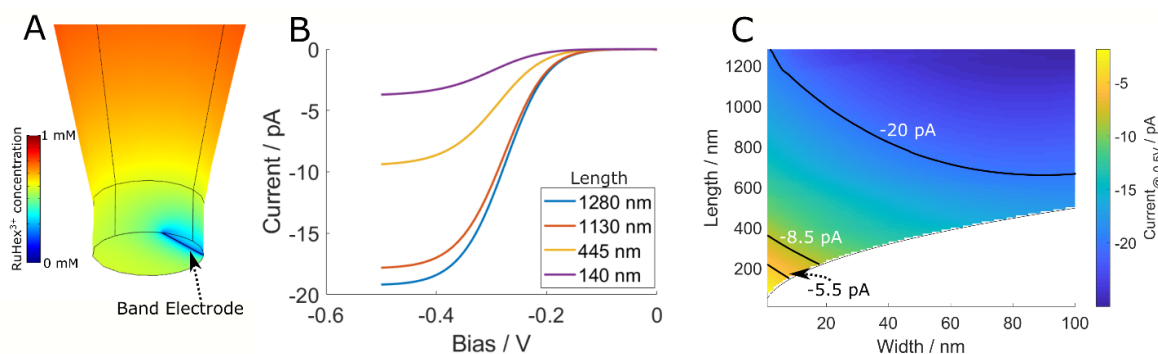


**Figure 5.10:** **A.** Simulated axisymmetric two-dimensional concentration profile of  $[\text{Ru}(\text{NH}_3)_6]^{3+}$  for a disc-shape defect. **B.** Relationship between the size of a planar circular defect and the resulting diffusion-limited current, compared to the size and diffusion-limited current of the entire SECCM droplet. **C.** Simulated relationship between the size of a planar circular defect and the droplet radius. The relative diffusion-limited current, with respect to the SECCM droplet diffusion-limited current, is independent of the droplet radius. Note that the droplet radius is equivalent to the pipette aperture used. **D.** Relationship between the size of a planar circular defect and the resulting diffusion-limited current compared for different droplet sizes. Figure adapted with permission from Brunet Cabré, M. *et al.*<sup>46</sup>

### 5.4.5 Modeling the electrochemical response of a band defect

The anomalous sample points that are arranged in lines (see Figure 5.5 E, Figure 5.6 F or Figure 5.9 F) might more accurately be described by linear defects in the TMDC sample surface (such as dislocations, grain boundaries, or cracks). The electrochemical response of a linear defect that traverses through the SECCM droplet can be approximated by a band electrode with a width  $w$  that traverses the SECCM droplet for a length  $L$ . The time-dependent current response for band electrodes which transverse the SECCM droplet is simulated for different widths, with an LSV at 1 V/s, see Section 5.3.2 for computational details. A typical simulated concentration profile for a 1 nm wide band electrode, which is offset from the centre of the SECCM droplet, is shown in Figure 5.11 A. The simulated response for a 1 nm wide band electrode traversing the SECCM droplet with different offsets from the centre, and thus with correspondingly different electrochemically active lengths, is shown in Figure 5.11 B. The simulations highlight that the length of the band electrode inside the SECCM droplet has a large influence on the observed response. Although in the case of our measurements there is uncertainty on the exact length of the line defect traversing the SECCM droplet, simulating a range of different band electrode sizes allows us to construct a map of all possible width-length combinations that can give rise to a given current plateau, as shown in Figure 5.11 C. A current plateau of -8.5 pA in a linear defect, as observed in Figure 5.5 E, could be obtained only with an electrode band width of less than 20 nm. Similarly, a current plateau of -2 pA would require an electrode band width of less than 1 nm (which is the minimum band width that we simulated). This analysis suggests that the linear defects would be on the scale of a single nanometre or a few-atoms wide.

The analysis provides an estimate of the electrochemical response of kinetically enhanced defects on 2D TMDCs using a SECCM approach. The conventional diffusion-based voltammetric theory (Equation 5.1) used here has limitations when considering nanoscale electrochemical interfaces,<sup>49</sup> namely for electrode radii smaller than 5 nm the electron transfer kinetics manifested could be different compared to macroscale electrodes.<sup>51,52</sup> Still, this diffusion-based theory has been used to describe the electrochemical response down to single atoms.<sup>53</sup> Our simulation results highlight that nanoscale defects, which represent a minor portion of the contacted area ( $< 0.01\%$ ), have a major impact on the electrochemical response. Note that the defect size calculations are based on the diffusion limiting current value, which depends on diffusion properties along the SECCM probe and not on the electron transfer kinetics of the defects. Therefore, the special conditions of small wetting areas and mass transport offered by SECCM allow the detection of nanoscale electrochemically enhanced domains, which are not easily detectable with other characterisation techniques compatible with electrochemical analysis.



**Figure 5.11:** **A.** Simulated 3-dimensional concentration profile of  $[\text{Ru}(\text{NH}_3)_6]^{3+}$  at a band electrode with 1 nm width offset from the centre of the 640 nm-radius SECCM droplet (with a band electrode length of 798 nm). **B.** Simulated LSV responses for a 1 nm wide band electrode transecting a 640 nm radius SECCM droplet with different lengths at a bias of  $-0.5$  V. **C.** Map of the limiting current at  $-0.5$  V for different widths and lengths of the band electrode in a 640 nm radius SECCM droplet. The contours indicate the combination of band width and length, which gives rise to currents of  $-20$  pA,  $-8.5$  pA, and  $-5.5$  pA, respectively. The lower limit of the electrode length is visible as the curve that separates the white area from the rest of the map. This limit is defined as the entire band electrode width at its centre point being just contained within the disc of the SECCM droplet. Reproduced with permission from Brunet Cabré, M. *et al.*<sup>46</sup>

#### 5.4.6 Identification of defects by SECCM: advantages, limitations, and nature of defects

This chapter has provided a new method to detect and understand the electrochemical response of defects in 2D materials. Identification and mapping of sites that display enhanced electrochemical activity remain a significant challenge and are of great relevance for TMDCs applications. The activity of 2D electrode materials is highly dependent on their local atomic structures, presence of under-coordinated sites, boundaries and/or impurities; but only some of these features are readily identified based on structural and topographic probes. The method implemented in this chapter used the special mass transport conditions of SECCM to evaluate the contribution of the defect to the electrochemical response from the diffusion limiting current regime. This is advantageous because the response does not depend on the kinetics of the reaction, just on the diffusion-limited mass transport. To the best of the author's knowledge, the work presented here is the first to report mapping of kinetically enhanced defects with high spatial resolution coupled to analysis/modelling of their size and shape based on diffusion limited currents. Moreover, defects on 2D TMDCs with enhanced electrochemical kinetics do not necessarily align with morphological features, which is different from that observed in previous studies.<sup>42,47</sup>



The method implemented here allows to assess the defect size, but does not provide further information on the defect nature. Our analysis is based purely on the electrochemical response, and there are multiple reasons why a structural nanoscale defect could provide enhanced kinetics. For instance, a structural defect can: produce a local change in electron density, become a catalytic centre due to dangling bonds, or expose the underlying materials to the electrolyte.<sup>3,10</sup> For the case of a crack in the bottom-contacted 2D TMDCs on Au, it is expected that the underneath metal contact that becomes exposed to the electrolyte will present faster kinetics. Despite the similarity observed between gold and the kinetically enhanced defect onset potential, it cannot be distinguished whether the defects detected correspond to exposure of the underneath metal by a crack or by a defect of another nature.

Still, the approach presented here could differentiate between defects with a smaller size and higher activity and defects with a larger size and lower activity. The key here is the fact that while the higher/lower activity of the defect should affect only the onset potential, the size of the defect will alter only the size of the diffusion-limiting current. Differences in kinetics at the defect sites are expected to affect the shape of the voltammogram. Large defects with slow kinetics will present more cathodic current onsets than those observed in defects with fast kinetics. At high overpotentials, a diffusion limited current will be reached that is dependent on defect size. It is acknowledged that discrimination of the different defects based on the current plateau might not be highly accurate, particularly between extremes, however, it provides a good semi-quantitative comparison. Defect points are detected by the presence on the voltammogram of a current-plateau smaller than the diffusion limiting current of the SECCM probe. We conclude that this behaviour is observed because there is a small area with enhanced kinetics whose diffusion layer front is smaller than that of the entire SECCM droplet cell. All calculations of defect size are based on the diffusion-limiting current, which depends on the diffusion properties of the redox species, and are independent of the electron transfer kinetics peculiarities of the defect.

## 5.5 Conclusions

SECCM mapping of the electrochemical reduction of  $[\text{Ru}(\text{NH}_3)_6]^{3+}$  on TMDC samples allowed us to identify defects. These defects give rise to electrochemical responses, which are equivalent to disc-shaped defects with radii of tens of nanometres in size, or to band electrodes of nanometer to sub-nanometre widths. Our results highlight that a SECCM-based approach can isolate and amplify the electrochemical response from surface features that are orders of magnitude smaller than the SECCM probe size, enabling us to detect features electrochemically that are well below the diffraction limit and therefore impossible to detect optically.

Importantly, the results of Chapter 5 also highlight the impact of nanoscale defects on the overall observed electrochemical response on seemingly defect-free 2D material. Only a very small defect needs to be present to dominate the electrochemical response of the entire surface area. This suggests that careful interpretation of electrocatalysis results on 2D TMDC materials is required, where the dominant response may not be the intrinsic electrocatalytic response of the material, but the electrocatalytic response of the defects present in the material. On the other hand, this results also underline that it is only needed to introduce a very low density of defects into our sample surface to effectively alter the electrocatalytic properties.

## Authorship Statement

This chapter is an extended adaptation of the work presented in the publication:

*Electrochemical Detection of Isolated Nanoscale Defects in 2D Transition Metal  
Dichalcogenides*

Brunet Cabre, M.; Esmeraldo Paiva, A.; Velický, M.; Colavita, P. E. and McKelvey, K.  
*The Journal of Physical Chemistry C*, 2022, 126, 28, 11636-11641.

This publication is reproduced in the appendix section of the thesis.

Electrochemical experiments, data analysis, and manuscript writing were carried out by the first-author of the publication, M.B.C, as part of the Ph.D. thesis presented here.

Co-authors A.E.P. contributed to development of the experimental work with 2D TMDCs as part of their Ph.D. thesis. M.V. as a group collaborator manufactured the 2D TMDCs samples used in this chapter and supervised manuscript writing. P.E.C. provided guidance over data analysis and results discussion. P.E.C supervised manuscript writing.

Corresponding author K.M. supervised and led the experimental design for the acquisition of electrochemical data. K.M also contributed to the data analysis processes, manuscript drafting, and correction.

## References

- 1 Davies, T. J., Moore, R. R., Banks, C. E. & Compton, R. G. The cyclic voltammetric response of electrochemically heterogeneous surfaces. *J. Electroanal. Chem.* **574**, 123-152 (2004). <https://doi.org/10.1016/j.jelechem.2004.07.031>
- 2 Zhang, Y. Q. *et al.* Defect Chemistry on Electrode Materials for Electrochemical Energy Storage and Conversion. *Chemnanomat* **6**, 1589-1600 (2020). <https://doi.org/10.1002/cnma.202000437>
- 3 Sun, T. *et al.* Defect chemistry in 2D materials for electrocatalysis. *Mater. Today Energy* **12**, 215-238 (2019). <https://doi.org/10.1016/j.mtener.2019.01.004>
- 4 Schweke, D., Mordehovitz, Y., Halabi, M., Shelly, L. & Hayun, S. Defect Chemistry of Oxides for Energy Applications. *Adv. Mater.* **30**, e1706300 (2018). <https://doi.org/10.1002/adma.201706300>
- 5 Hu, Z. *et al.* Two-dimensional transition metal dichalcogenides: interface and defect engineering. *Chem. Soc. Rev.* **47**, 3100-3128 (2018). <https://doi.org/10.1039/c8cs00024g>
- 6 Wang, Q. H., Kalantar-Zadeh, K., Kis, A., Coleman, J. N. & Strano, M. S. Electronics and optoelectronics of two-dimensional transition metal dichalcogenides. *Nat. Nanotechnol.* **7**, 699-712 (2012). <https://doi.org/10.1038/nnano.2012.193>
- 7 Choi, W. *et al.* Recent development of two-dimensional transition metal dichalcogenides and their applications. *Mater. Today* **20**, 116-130 (2017). <https://doi.org/10.1016/j.mattod.2016.10.002>
- 8 Wei, Z. M. *et al.* Various Structures of 2D Transition-Metal Dichalcogenides and Their Applications. *Small Methods* **2**, 1800094-1800094 (2018). <https://doi.org/10.1002/smt.201800094>
- 9 Mondal, A. & Vomiero, A. 2D Transition Metal Dichalcogenides-Based Electrocatalysts for Hydrogen Evolution Reaction. *Adv. Funct. Mater.* **32** (2022). <https://doi.org/10.1002/adfm.202208994>
- 10 Dong, S. & Wang, Z. G. Grain Boundaries Trigger Basal Plane Catalytic Activity for the Hydrogen Evolution Reaction in Monolayer MoS<sub>2</sub>. *Electrocatalysis* **9**, 744-751 (2018). <https://doi.org/10.1007/s12678-018-0485-z>
- 11 Li, H. J. *et al.* Quantitatively regulating defects of 2D tungsten selenide to enhance catalytic ability for polysulfide conversion in a lithium sulfur battery. *Energy Storage Mater.* **45**, 1229-1237 (2022). <https://doi.org/10.1016/j.ensm.2021.11.024>
- 12 Zeng, L., Chen, S., van der Zalm, J., Li, X. & Chen, A. Sulfur vacancy-rich N-doped MoS<sub>2</sub> nanoflowers for highly boosting electrocatalytic N<sub>2</sub> fixation to NH<sub>3</sub> under ambient conditions. *Chem. Commun.* **55**, 7386-7389 (2019). <https://doi.org/10.1039/c9cc02607j>
- 13 Jin, H. *et al.* Emerging Two-Dimensional Nanomaterials for Electrocatalysis. *Chem. Rev.* **118**, 6337-6408 (2018). <https://doi.org/10.1021/acs.chemrev.7b00689>
- 14 Bentley, C. L., Kang, M. & Unwin, P. R. Nanoscale Surface Structure-Activity in Electrochemistry and Electrocatalysis. *J. Am. Chem. Soc.* **141**, 2179-2193 (2019). <https://doi.org/10.1021/jacs.8b09828>

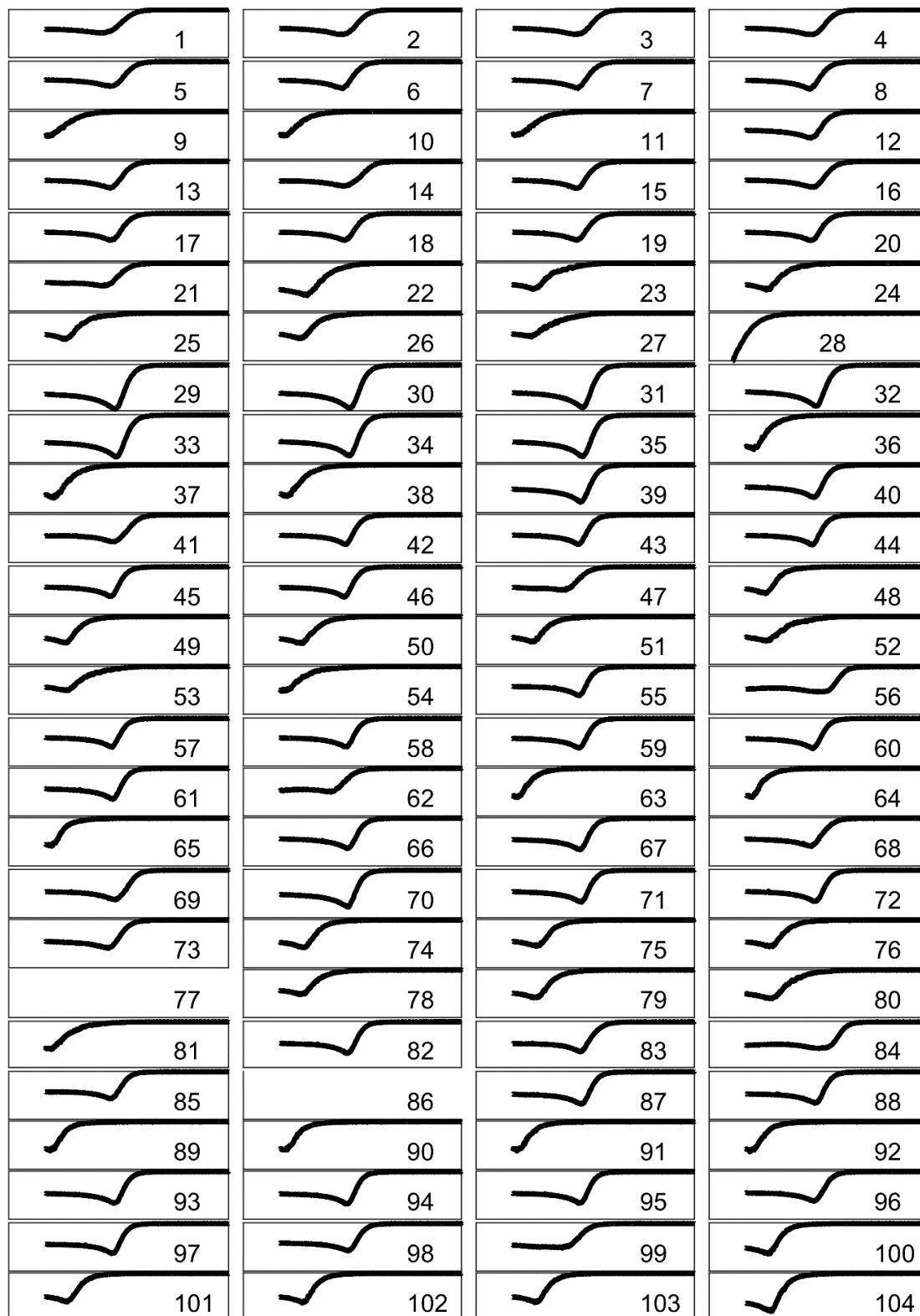
- 15 Pfisterer, J. H. K., Baghernejad, M., Giuzio, G. & Domke, K. F. Reactivity mapping of nanoscale defect chemistry under electrochemical reaction conditions. *Nat. Commun.* **10**, 5702 (2019). <https://doi.org/10.1038/s41467-019-13692-3>
- 16 Syari'ati, A. *et al.* Photoemission spectroscopy study of structural defects in molybdenum disulfide (MoS<sub>2</sub>) grown by chemical vapor deposition (CVD). *Chem. Commun.* **55**, 10384-10387 (2019). <https://doi.org/10.1039/c9cc01577a>
- 17 Chee, S. S. *et al.* Atomic Vacancy Control and Elemental Substitution in a Monolayer Molybdenum Disulfide for High Performance Optoelectronic Device Arrays. *Adv. Funct. Mater.* **30** (2020). <https://doi.org/10.1002/adfm.201908147>
- 18 Santos, S., Barcons, V., Christenson, H. K., Font, J. & Thomson, N. H. The intrinsic resolution limit in the atomic force microscope: implications for heights of nano-scale features. *PLoS One* **6**, e23821 (2011). <https://doi.org/10.1371/journal.pone.0023821>
- 19 Gianola, D. S., Ben Britton, T. & Zaefferer, S. New techniques for imaging and identifying defects in electron microscopy. *MRS Bull.* **44**, 450-458 (2019). <https://doi.org/10.1557/mrs.2019.125>
- 20 Aryeetey, F., Ignatova, T. & Aravamudhan, S. Quantification of defects engineered in single layer MoS<sub>2</sub>. *RSC Adv.* **10**, 22996-23001 (2020). <https://doi.org/10.1039/d0ra03372c>
- 21 Vancso, P. *et al.* The intrinsic defect structure of exfoliated MoS<sub>2</sub> single layers revealed by Scanning Tunneling Microscopy. *Sci. Rep.* **6**, 29726 (2016). <https://doi.org/10.1038/srep29726>
- 22 Wong, R., Batchelor-McAuley, C., Yang, M. & Compton, R. G. Electrochemical Heterogeneity at the Nanoscale: Diffusion to Partially Active Nanocubes. *J. Phys. Chem. Lett.* **13**, 7689-7693 (2022). <https://doi.org/10.1021/acs.jpcllett.2c01922>
- 23 Liu, D. Q. *et al.* Adiabatic versus non-adiabatic electron transfer at 2D electrode materials. *Nat. Commun.* **12**, 7110 (2021). <https://doi.org/10.1038/s41467-021-27339-9>
- 24 Guell, A. G. *et al.* Quantitative nanoscale visualization of heterogeneous electron transfer rates in 2D carbon nanotube networks. *Proc. Natl. Acad. Sci. U.S.A.* **109**, 11487-11492 (2012). <https://doi.org/10.1073/pnas.1203671109>
- 25 Takahashi, Y. *et al.* High-Resolution Electrochemical Mapping of the Hydrogen Evolution Reaction on Transition-Metal Dichalcogenide Nanosheets. *Angew. Chem. Int. Ed. Engl.* **59**, 3601-3608 (2020). <https://doi.org/10.1002/anie.201912863>
- 26 Zhong, J. H. *et al.* Quantitative correlation between defect density and heterogeneous electron transfer rate of single layer graphene. *J. Am. Chem. Soc.* **136**, 16609-16617 (2014). <https://doi.org/10.1021/ja508965w>
- 27 Bentley, C. L. *et al.* Correlating the Local Electrocatalytic Activity of Amorphous Molybdenum Sulfide Thin Films with Microscopic Composition, Structure, and Porosity. *ACS Appl. Mater. Interfaces* **12**, 44307-44316 (2020). <https://doi.org/10.1021/acsami.0c11759>
- 28 Hill, J. W. & Hill, C. M. Directly Mapping Photoelectrochemical Behavior within Individual Transition Metal Dichalcogenide Nanosheets. *Nano Lett.* **19**, 5710-5716 (2019). <https://doi.org/10.1021/acs.nanolett.9b02336>

- 29 Kalinin, S. V. *et al.* Toward Electrochemical Studies on the Nanometer and Atomic Scales: Progress, Challenges, and Opportunities. *ACS Nano* **13**, 9735-9780 (2019). <https://doi.org:10.1021/acsnano.9b02687>
- 30 Ornelas, I. M., Unwin, P. R. & Bentley, C. L. High-Throughput Correlative Electrochemistry-Microscopy at a Transmission Electron Microscopy Grid Electrode. *Anal. Chem.* **91**, 14854-14859 (2019). <https://doi.org:10.1021/acs.analchem.9b04028>
- 31 Han, C., Islam, M. T. & Ni, C. In Situ TEM of Electrochemical Incidents: Effects of Biasing and Electron Beam on Electrochemistry. *ACS Omega* **6**, 6537-6546 (2021). <https://doi.org:10.1021/acsomega.0c05829>
- 32 Al-Temimy, A. *et al.* Spatially resolved X-ray absorption spectroscopy investigation of individual cation-intercalated multi-layered Ti<sub>3</sub>C<sub>2</sub>T<sub>x</sub> MXene particles. *Appl. Surf. Sci.* **530** (2020). <https://doi.org:10.1016/j.apsusc.2020.147157>
- 33 Ma, X. Y., Luo, W., Yan, M. Y., He, L. & Mai, L. Q. In situ characterization of electrochemical processes in one dimensional nanomaterials for energy storages devices. *Nano Energy* **24**, 165-188 (2016). <https://doi.org:10.1016/j.nanoen.2016.03.023>
- 34 Zeng, Z. C. *et al.* Electrochemical Tip-Enhanced Raman Spectroscopy. *J. Am. Chem. Soc.* **137**, 11928-11931 (2015). <https://doi.org:10.1021/jacs.5b08143>
- 35 Amatore, C., Saveant, J. M. & Tessier, D. Charge-Transfer at Partially Blocked Surfaces - a Model for the Case of Microscopic Active and Inactive Sites. *J. Electroanal. Chem.* **147**, 39-51 (1983). [https://doi.org:Doi 10.1016/S0022-0728\(83\)80055-2](https://doi.org:Doi 10.1016/S0022-0728(83)80055-2)
- 36 Saito, Y. A Theoretical Study on the Diffusion Current at the Stationary Electrodes of Circular and Narrow Band Types. *Rev. Polarogr.* **15**, 177-187 (1968). <https://doi.org:10.5189/revpolarography.15.177>
- 37 Bard, A. J. & Faulkner, L. R. *Electrochemical methods: fundamentals and applications*. 2nd edn, (John Wiley & Sons, Inc., 2001).
- 38 Williams, C. G., Edwards, M. A., Colley, A. L., Macpherson, J. V. & Unwin, P. R. Scanning micropipet contact method for high-resolution imaging of electrode surface redox activity. *Anal. Chem.* **81**, 2486-2495 (2009). <https://doi.org:10.1021/ac802114r>
- 39 Ebejer, N. *et al.* Scanning electrochemical cell microscopy: a versatile technique for nanoscale electrochemistry and functional imaging. *Annu. Rev. Anal. Chem.* **6**, 329-351 (2013). <https://doi.org:10.1146/annurev-anchem-062012-092650>
- 40 Snowden, M. E. *et al.* Scanning electrochemical cell microscopy: theory and experiment for quantitative high resolution spatially-resolved voltammetry and simultaneous ion-conductance measurements. *Anal. Chem.* **84**, 2483-2491 (2012). <https://doi.org:10.1021/ac203195h>
- 41 Payne, N. A. & Mauzeroll, J. Identifying Nanoscale Pinhole Defects in Nitroaryl Layers with Scanning Electrochemical Cell Microscopy. *Chemelectrochem* **6**, 5439-5445 (2019). <https://doi.org:10.1002/celc.201901394>
- 42 Velicky, M. *et al.* Mechanism of Gold-Assisted Exfoliation of Centimeter-Sized Transition-Metal Dichalcogenide Monolayers. *ACS Nano* **12**, 10463-10472 (2018). <https://doi.org:10.1021/acsnano.8b06101>































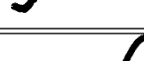























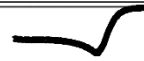
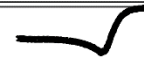






















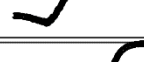











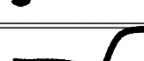
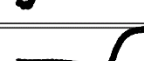












- 43 Wang, Y. J., Limon-Petersen, J. G. & Compton, R. G. Measurement of the diffusion coefficients of  $[\text{Ru}(\text{NH}_3)_6]^{3+}$  and  $[\text{Ru}(\text{NH}_3)_6]^{2+}$  in aqueous solution using microelectrode double potential step chronoamperometry. *J. Electroanal. Chem.* **652**, 13-17 (2011). <https://doi.org/10.1016/j.jelechem.2010.12.011>
- 44 Taghavi, N. S. *et al.* Thickness determination of  $\text{MoS}_2$ ,  $\text{MoSe}_2$ ,  $\text{WS}_2$  and  $\text{WSe}_2$  on transparent stamps used for deterministic transfer of 2D materials. *Nano Res.* **12**, 1691-1695 (2019). <https://doi.org/10.1007/s12274-019-2424-6>
- 45 Brunet Cabré, M., Paiva, A. E., Velický, M., Colavita, P. E. & McKelvey, K. Electrochemical kinetics as a function of transition metal dichalcogenide thickness. *Electrochim. Acta* **393** (2021). <https://doi.org/10.1016/j.electacta.2021.139027>
- 46 Cabré, M. B., Paiva, A. E., Velický, M., Colavita, P. E. & McKelvey, K. Electrochemical Detection of Isolated Nanoscale Defects in 2D Transition Metal Dichalcogenides. *J. Phys. Chem. C* **126**, 11636-11641 (2022). <https://doi.org/10.1021/acs.jpcc.2c01656>
- 47 Bentley, C. L. *et al.* Electrochemical maps and movies of the hydrogen evolution reaction on natural crystals of molybdenite ( $\text{MoS}_2$ ): basal vs. edge plane activity. *Chem. Sci.* **8**, 6583-6593 (2017). <https://doi.org/10.1039/c7sc02545a>
- 48 van der Zande, A. M. *et al.* Grains and grain boundaries in highly crystalline monolayer molybdenum disulphide. *Nat. Mater.* **12**, 554-561 (2013). <https://doi.org/10.1038/nmat3633>
- 49 Sun, Y. *et al.* On the Applicability of Conventional Voltammetric Theory to Nanoscale Electrochemical Interfaces. *J. Phys. Chem. C* **113**, 9878-9883 (2009). <https://doi.org/10.1021/jp902311h>
- 50 Dickinson, E. J. F., Ekstrom, H. & Fontes, E. COMSOL Multiphysics (R) : Finite element software for electrochemical analysis. A mini-review. *Electrochem. Commun.* **40**, 71-74 (2014). <https://doi.org/10.1016/j.elecom.2013.12.020>
- 51 Feldberg, S. W. Implications of Marcus-Hush theory for steady-state heterogeneous electron transfer at an inlaid disk electrode. *Anal. Chem.* **82**, 5176-5183 (2010). <https://doi.org/10.1021/ac1004162>
- 52 Liu, Y. W. & Chen, S. L. Theory of Interfacial Electron Transfer Kinetics at Nanometer-Sized Electrodes. *J. Phys. Chem. C* **116**, 13594-13602 (2012). <https://doi.org/10.1021/jp300696u>
- 53 Zhou, M., Bao, S. & Bard, A. J. Probing Size and Substrate Effects on the Hydrogen Evolution Reaction by Single Isolated Pt Atoms, Atomic Clusters, and Nanoparticles. *J. Am. Chem. Soc.* **141**, 7327-7332 (2019). <https://doi.org/10.1021/jacs.8b13366>



















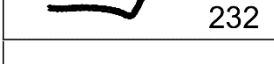
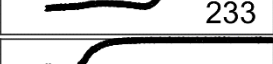













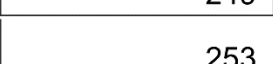
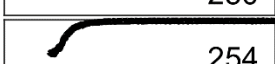
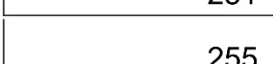





















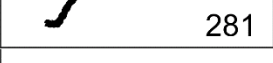


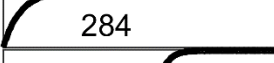




















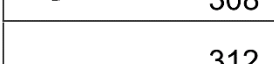







## Appendix






























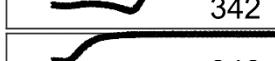










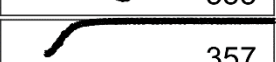








































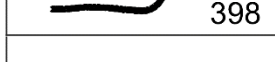









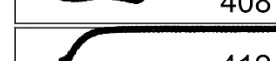












LSVs for each point of the SECCM mapping of MoS<sub>2</sub>. LSVs are numbered with respect to the order collected and displayed with a current scale of 0 – 50 pA and a potential scale of 0.2 to -0.8 V vs Ag/AgCl


























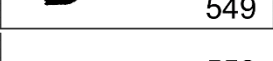
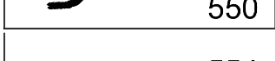

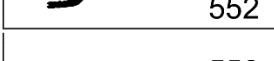


















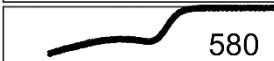








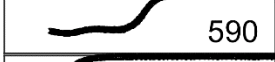











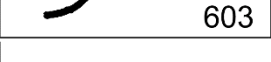














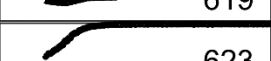














































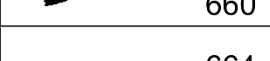



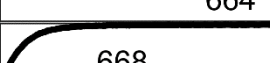
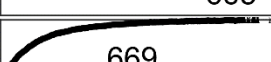


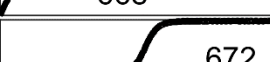






























































 105	 106	 107	 108
 109	 110	 111	 112
 113	 114	 115	 116
 117	 118	 119	 120
 121	 122	 123	 124
 125	 126	 127	 128
 129	 130	 131	 132
 133	 134	 135	 136
 137	 138	 139	 140
 141	 142	 143	 144
 145	 146	 147	 148
 149	 150	 151	 152
 153	 154	 155	 156
 157	 158	 159	 160
 161	 162	 163	 164
 165	 166	 167	 168
 169	 170	 171	 172
 173	 174	 175	 176
 177	 178	 179	 180
 181	 182	 183	 184
 185	 186	 187	 188
 189	 190	 191	 192
 193	 194	 195	 196
 197	 198	 199	 200
 201	 202	 203	 204
 205	 206	 207	 208

 209	 210	211	 212
 213	 214	 215	 216
 217	 218	 219	 220
 221	222	 223	224
 225	 226	227	 228
 229	 230	231	 232
 233	 234	 235	236
 237	 238	 239	 240
 241	 242	 243	 244
 245	 246	 247	248
 249	 250	 251	 252
253	 254	255	 256
 257	 258	 259	 260
 261	 262	 263	 264
 265	266	 267	 268
 269	 270	 271	 272
 273	 274	 275	276
 277	 278	 279	 280
 281	 282	283	 284
285	 286	 287	 288
 289	290	 291	 292
 293	 294	 295	 296
 297	 298	 299	 300
 301	 302	 303	 304
 305	 306	 307	 308
 309	 310	 311	312

 313	 314	 315	 316
 317	 318	 319	 320
 321	 322	 323	 324
 325	 326	 327	 328
 329	 330	 331	 332
 333	 334	 335	 336
 337	 338	 339	 340
 341	 342	 343	 344
 345	 346	 347	 348
 349	 350	 351	 352
 353	 354	 355	 356
 357	 358	 359	 360
 361	 362	 363	 364
 365	 366	 367	 368
 369	 370	 371	 372
 373	 374	 375	 376
 377	 378	 379	 380
 381	 382	 383	 384
 385	 386	 387	 388
 389	 390	 391	 392
 393	 394	 395	 396
 397	 398	 399	 400
 401	 402	 403	 404
 405	 406	 407	 408
 409	 410	 411	 412
 413	 414	 415	 416

 521	522	 523	 524
 525	526	527	 528
 529	 530	 531	 532
 533	 534	 535	 536
 537	 538	 539	 540
 541	 542	 543	 544
 545	 546	 547	 548
 549	 550	 551	 552
553	554	 555	556
 557	 558	 559	560
 561	 562	 563	 564
 565	 566	 567	 568
 569	 570	 571	 572
573	 574	 575	 576
 577	 578	 579	 580
 581	 582	583	 584
 585	 586	 587	 588
 589	 590	 591	 592
 593	 594	595	 596
 597	 598	 599	 600
 601	 602	 603	 604
 605	 606	607	 608
 609	 610	 611	 612
 613	 614	 615	 616
 617	 618	 619	 620
 621	 622	 623	 624

 625	 626	 627	 628
 629	 630	 631	 632
 633	 634	 635	 636
 637	 638	 639	 640
 641	 642	 643	 644
 645	 646	 647	 648
 649	 650	 651	 652
 653	 654	 655	 656
 657	 658	 659	 660
 661	 662	 663	 664
 665	 666	 667	 668
 669	 670	 671	 672
 673	 674	 675	 676
 677	 678	 679	 680
 681	 682	 683	 684
 685	 686	 687	 688
 689	 690	 691	 692
 693	 694	 695	 696
 697	 698	 699	 700
 701	 702	 703	 704
 705	 706	 707	 708
 709	 710	 711	 712
 713	 714	 715	 716
 717	 718	 719	 720
 721	 722	 723	 724
 725	 726	 727	 728



# CHAPTER 6

## Pseudocapacitance of MXene Monolayers at the Nanoscale

---

Since 2020 more than 700 articles have been published on the emerging field of MXene base capacitors, demonstrating the outstanding performance of this 2D material for supercapacitor application. Several experimental and computational works have attempted to explain the boost in MXene pseudocapacitive behaviour in acidic electrolytes. The debate has been partly caused by the scale disparity between previous electrochemical observations, based on bulk macroscale electrodes ( $> \text{mm}^2$ ), and computational methods, which can only afford to simulate a few  $\text{nm}^2$  of the system.

In this chapter, I explored the electrochemical response of the building blocks of the MXene base electrode: monolayer MXene flakes. The experimental approach is based on nano-micro- electrochemical technique, achieving electrochemical contact with subregions of MXene flakes ( $<1 \text{um}^2$ ) but observing pseudocapacitive charging of the whole MXene flake ( $> 5 \text{um}^2$ ). Such observation is directly derived from the current mechanistic description of MXene pseudocapacitive charging, which depends on ion-intercalation. Instead, it is proposed the existence of proton conduction channels that extend beyond the area contacted by our probe. Thus, in the particular electrochemical configuration studied, the MXene pseudocapacitance is controlled by proton transport over the MXene surface.

---

## 6.1 Introduction

### 6.1.1 2D material-based pseudocapacitors

The transition to a low-carbon economy based on renewable energy requires the development of energy storage technologies. Supercapacitors, characterised by both high-power density and high-energy density, bridge the gap between rechargeable batteries and more traditional parallel-plate capacitors.<sup>1</sup> A General description of energy storage technologies is provided in Introduction chapter, Section 1.2.2. Supercapacitors store energy by accumulating charge at the electrode-solution interface, and the capability of storing charge is defined by the capacitance ( $C$ ) as:

$$C = Q/V \quad (\text{Eq.6.1})$$

where  $Q$  is charge storage at the electrode surface and  $V$  is the electric potential difference applied.

There are different mechanisms by which charge accumulation can be achieved in a supercapacitor, and the simplest mechanism is based on the formation of an electrochemical double layer (ECDL) at the electrode interface. The double-layer capacitance can be approximated by the Helmholtz model as:

$$C = \epsilon_r \epsilon_0 A/d \quad (\text{Eq.6.2})$$

where  $\epsilon_r$  is the dielectric constant of the electrolyte at the interface,  $\epsilon_0$  is the vacuum permittivity,  $A$  is the electrode surface available for electrolyte ions and  $d$  is the effective electrochemical double layer thickness (Debye length).<sup>2</sup> ECDL mechanism of charge storage in supercapacitors is the same as used in more traditional electrochemical double-layer capacitors, but supercapacitor electrodes are differentiated by providing a much larger specific surface and taking advantage of electrode nanostructure.<sup>3,4</sup> To achieve a high specific active area and therefore high specific capacitance, ECDL supercapacitor materials often have engineered porous architectures, as shown in Figure 6.1 A. The porosity is designed to follow hierarchical pore sizes (macropores > 50 nm, mesopores 2–50 nm and micropores < 2 nm) to maximise the specific area while providing pathways for the ions to access most of the surface.<sup>5</sup> Examples are graphene aerogel electrodes, which have shown outstanding performance as supercapacitors thanks to their ultra-low density, porosity, electrical conductivity and stability, achieving capacitances greater than 300 F/g. Aerogel electrodes take advantage of the high surface area of 2D materials micro- nano- sheets (*e.g.* monolayer graphene, with 2630 m<sup>2</sup>/g specific surface area) to assemble a 3D network which presents a given degree of porosity.<sup>6</sup>

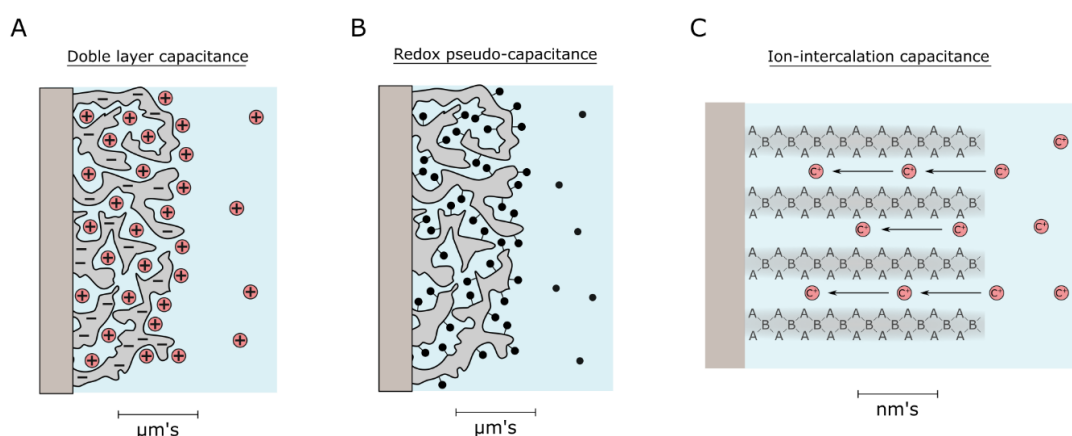


The other mechanism to store charge at electrode-solution interfaces is pseudocapacitance.<sup>3</sup> Pseudocapacitance is based on Faradaic charge transfer to surface species (including adsorption of species from electrolyte) which presents reversible redox cycling, as shown in Figure 6.1 B. The chemical nature of the pseudocapacitance mechanism allows storage of a charge density greater than that of ECDL supercapacitors. However, charge storage on pseudocapacitors is potential dependent, and thus, charging/discharging processes are subjected to the potential window defined by the nature of the redox process. Pseudocapacitors also benefit from having a large specific surface area and an engineered nanostructure, which facilitates the mobility of electrolyte species. Therefore, similar approaches towards manufacturing of electrode materials with 3D porous architectures are used for pseudocapacitors, as shown in the illustration of Figure 6.1 B.<sup>7,8</sup>

Ion-intercalation processes can also lead to pseudocapacitive charge storage and have been implemented recently in supercapacitor electrodes.<sup>3</sup> Classically, an ion-intercalation charge mechanism is defined by the Faradaic process which forces electrolyte ions into the crystal lattice of the electrode materials, inducing a phase change. Note that such a classic definition does not limit charge storage to the electrode-solution interface but through the bulk of the electrode material.<sup>7,8</sup> Ion-intercalation is widely used in batteries and generally does not offer high-power densities.<sup>3</sup> However, since the early 2000s several studies reported nanostructured materials that facilitate ion-intercalation processes through designed channels, achieving fast intercalation and increased power densities (100's to 1000's  $\text{W kg}^{-1}$ ).<sup>9-11</sup> For example, graphene aerogel-based supercapacitors have an outstanding specific capacitance, high physical and chemical stability, and present a hierarchical pore structure that facilitates ion transport to ensure fast charge/discharge rates. Moreover, the tunable porosity and interlayer distance of the graphene aerogel enables the use of a wide variety of ions for charge storage.<sup>6</sup>

With current state-of-the-art nanostructured electrodes, the differences between battery and supercapacitor electrodes that operate via ion-intercalation become blurred.<sup>7</sup> Previous interpretations described the charge storage mechanism that occurs at the electrode-electrolyte interface as capacitive, while the battery charge storage mechanism was accompanied by a phase transition of the electrode material. However, the hierarchical porous nanostructure of modern supercapacitor electrodes challenges conventional distinctions, because the boundary between electrode and solution (*i.e.* the interface) is no longer clearly identifiable. On the electrolyte solution side, the hierarchical nanochannels or nanopores could contain variable amounts of electrolyte, as low as a discrete number of electrolyte molecules; thus, establishing the spatial limit between the bulk electrolyte and the confined electrolyte is not possible. On the electrode material side, the nanostructured material (*e.g.*, a monolayer of a 2D material) might present all or most of its atoms exposed to the solution interface, thus becoming impossible to clearly differentiate between the electrode interface domain and the electrode bulk domain. The impossibility of

defining the limits of the electrode-electrolyte interfaces makes it ambiguous to state whether there is / is not a phase transition in electrode materials during pseudocapacitive ion-intercalation charging. As a consequence, the electrode-electrolyte interface is effectively extended throughout the entire supercapacitor electrode material; see the schematics of Figure 6.1 C. Moreover, it is challenging to classify the pseudocapacitive active species (*e.g.* redox species or ions) solely on the basis of their contribution to adsorption or intercalation processes. Terms such as 'shallow adsorption', 'deep adsorption', 'extrinsic pseudocapacitance', 'intrinsic pseudocapacitance', 'surface processes' or 'bulk processes' have been used in the literature in an attempt to discriminate different pseudocapacitive behaviours observed.<sup>7</sup>



**Figure 6.1:** Illustration of the three types of mechanism implemented in supercapacitors. **A.** High surface area electrochemical double layer, **B.** redox/adsorption pseudocapacitance, and **C.** intercalation pseudocapacitance.

In summary, 2D materials have been used extensively for supercapacitor applications, as they excel in providing large specific surface areas and assembling into aerogels and porous materials. The development of new supercapacitor technology depends on the development of new materials, and this is supported by the precise understanding of the physical nature of the electrochemical charge storage mechanism.<sup>6,7</sup>

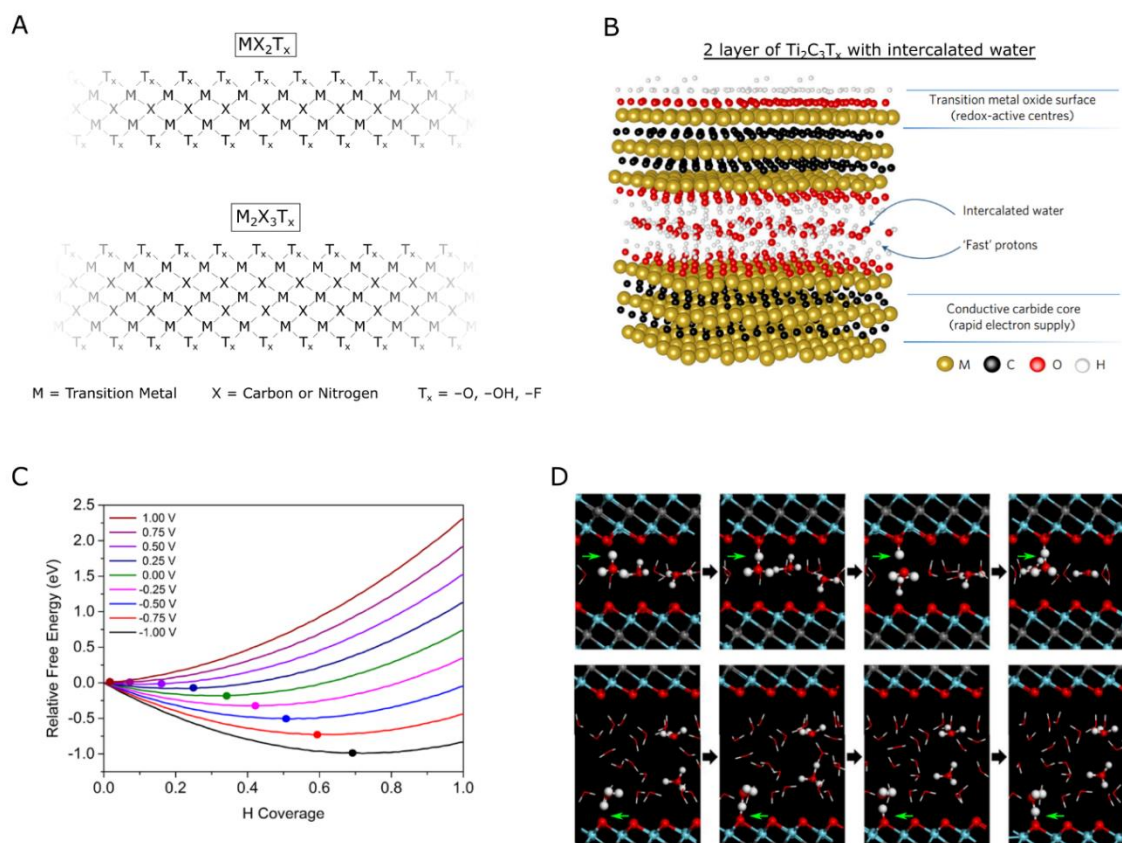
### 6.1.2 MXene pseudocapacitance

MXenes are recently discovered two-dimensional materials from the family of transition metal carbides, nitrides and carbon-nitrides. MXenes are obtained from the exfoliation of a ternary MAX phase ( $M_{n+1}AX_n$ ), where M is a transition metal, X is a carbon or nitrogen, and A is a group XIII or XIV element. The exfoliation processes consists of a selective etching of the A element of the MAX phase, resulting in the formation of  $M_{n+1}X_nT_x$  flakes, where  $T_x$  is the terminal group and  $n$  is the number of M-X layers, as illustrated in Figure 6.2 A.<sup>12</sup> The terminal group ( $T_x$ ) is typically defined as  $-O$  or  $-OH$ , however, due to the exfoliation processes often involving HF, it is common

that terminal group  $-F$  could be found on 10-40% of  $T_x$  sites. The MXenes flakes present simultaneously in-plane metallic conductivity (for  $Ti_3C_2T_x$  up to 10 kS/cm) and a redox-active metal-oxide-like surface chemistry, making them an interesting material for electrochemical applications. Among other applications,<sup>13</sup> MXenes exhibit excellent performance as supercapacitors. The nanoscale 2-dimensional nature of MXene flakes yields a high specific surface area. MXene flakes also present a negatively charged surface, given by electronegative terminal groups ( $T_x$ ), resulting in a very hydrophilic behaviour.<sup>14</sup> MXene flakes can be assembled in 3-dimensional architectures generating porous hierarchical structures, thus allowing fast ion-intercalation processes.<sup>15</sup> Nevertheless, they can be differentiated from other 2D supercapacitor materials, such as graphene aerogels, by simultaneously presenting pure metallic conductivity, redox-active surfaces and fast ion-intercalation availability.<sup>16</sup> Note that pristine graphene does not present a metal-like electronic structure, nor a redox-active surface.

Titanium carbide MXenes ( $Ti_3C_2T_x$ ) can be obtained by facile exfoliation, exhibit high stability and allow several electrode architectures, with capacitances of approximately 250 F/g or 1500 F/cm<sup>3</sup> in acid electrolyte.<sup>15,17,18</sup> The enhanced specific capacitance observed in proton-containing electrolytes, compared to salt-based electrolytes, opened the debate about the nature of MXene capacitance and their charging mechanism. The current state-of-the-art describes the origin of charge storage of  $Ti_3C_2T_x$  in acid electrolytes as fast intercalation of ions in the interlayer spaces coupled with the change in the oxidation state of the Ti and protonation of the oxygen functional groups ( $T_x \rightarrow -O$  to  $-OH$ ), see Figure 6.2 B.<sup>19-23</sup> The charging mechanism of MXene under acidic conditions has been extensively discussed in the literature, mainly using computational tools, such as DFT or molecular dynamic simulations, to model the experimental behaviour observed in MXene macroscale electrodes.<sup>20,22,24-27</sup> For instance, DFT studies reported the potential windows at which MXene surface proton coverage phases ( $T_x \rightarrow -O$  or  $-OH$ ) is the thermodynamically favourable, as shown in Figure 6.2 C.<sup>22</sup> Molecular dynamics simulation studies explained the proton intercalation as a proton-hopping Grotthuss mechanism between the water intercalated within the MXene interlayer, as well as fast proton exchange between the  $Ti_3C_2T_x$  surface and water, as shown in Figure 6.2 D.<sup>24</sup>

Despite a good alignment between computational predictions and experimental observations, there is a difference of several orders in the scale of domain size used for computational and experimental macroscale electrodes. Computational studies can only afford to model a small portion of a few nm<sup>2</sup> of a MXene flake. Meanwhile, most experimental data of  $Ti_3C_2T_x$  pseudocapitance in acid electrolytes have relied on macroscale electrodes (typically 0.1 cm<sup>2</sup> or larger in size) which consist of millions of 2D flakes arranged in 3D architectures (porous films, hydrogels, aerogels, or foams). Therefore, in the current state-of-the-art a microscale characterisation of the MXene flakes electrochemical response is missing.



**Figure 6.2:** **A.** Structure of MXenes ( $\text{M}_{n+1}\text{X}_n\text{T}_x$ ) for  $n = 1$  (top) and  $n = 2$  (bottom). **B.** Structure of two  $\text{Ti}_3\text{C}_2\text{T}_x$  flakes separated by intercalated water, enabling a proton conduction mechanism. Reproduced with permission from Lukatskaya *et al.*<sup>18</sup> **C.** Gibbs free energy of  $\text{Ti}_3\text{C}_2\text{T}_x$  MXene in acidic media respect the proton coverage ( $\text{T}_x = -\text{O}$  or  $-\text{OH}$ ) for different applied potentials (vs. SHE), showing that more cathodic potential favours greater proton coverage. Reproduced with permission from Zhan, C. *et al.*<sup>22</sup> **D.** Represented with ball-and-stick model: short time snapshots (1ps) of water and protons confined between two  $\text{Ti}_3\text{C}_2\text{T}_x$  flakes ( $\text{T}_x = -\text{O}$ ), showing the fast exchange of protons between water and  $\text{T}_x$  groups. Obtained by first-principle molecular dynamic simulation, with one layer of confined water displayed for the top sequence and two layers of water for the bottom sequence. Reproduced with permission from Sun, Y. *et al.*<sup>24</sup>

### 6.1.3 Surface processes vs. Bulk processes.

Designing a MXene-based, or any other nanomaterial-based, electrochemical storage device for real-world applications requires a choice of macroscale configuration of the electrode.<sup>7,8</sup> There are a relevant number of prior experimental studies that aim to optimize the device performance by achieving 3D MXene architectures that favour mass transport and enhance their specific or volumetric capacitance.<sup>15</sup> However, the use of macroscale MXene electrodes means that the measured capacitance results from the average response of millions of MXene flakes at once.

Thus, conventional bulk ensemble electrochemical approaches can obscure information and details about the charging mechanism of single MXene flakes. Moreover, the responses obtained from macroscale electrochemical strategies can also be affected by mass transport effects within the electrode volume. It is a classical electrochemical problem that the mass transport effects limit the information that can be obtained about the Faradaic process at the electrode surface, *i.e.*, the MXene surface charging processes for this study.<sup>28</sup> (please see also the Introduction chapter, Section 1.3.1).

Several approaches have attempted to provide fundamental understanding of pseudocapacitive mechanisms while utilising macroscale supercapacitor architectures, by decoupling the intrinsic contribution of the electrode surface to charge storage (surface processes) from the contribution of 3D electrode architecture (bulk processes).<sup>18,29-33</sup> A variety of techniques, methods, and models have been implemented to deconvolute the capacitive  $V$  curves of 3D macroscale electrodes based on a range of materials, including MXenes, into distinct contributions from surface and bulk processes.<sup>29-33</sup> These methods use differences in timescales and time dependencies: surface processes occur at shorter timescales while bulk processes display longer characteristic timescales.<sup>31,33-35</sup> To the best of the author's knowledge, no quantitative determination of MXene charging timescales has been reported in the literature yet. The mathematical model used to deconvolute I-V curves of macroscale electrodes, described by Dunn *et al.*, correlates the capacitive currents ( $I_C$ ) with the I-V curve sweep rate dependency.<sup>35</sup>

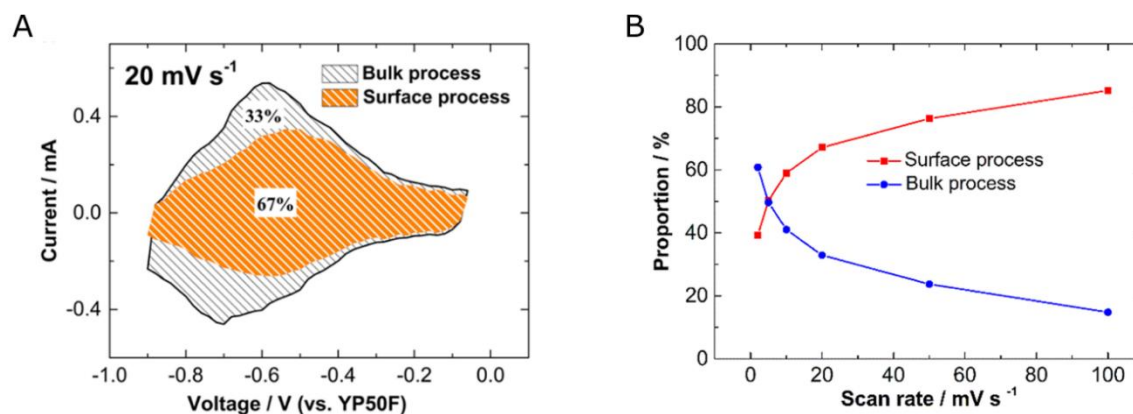
$$I_C = av^b \quad (\text{Eq. 6.1})$$

where  $v$  is the sweep rate and  $a$  and  $b$  are adjustable parameters. Notice that if  $b = 0.5$  the current is proportional to the square root of the scan rate, resembling the current dependency of Nernstian systems under semi-infinite linear diffusion. Otherwise, if  $b = 1$ , the capacitive current has a linear relationship with the scan rate, resembling double-plate capacitive response. The  $b$ -values can be determined from the slope of the plot of  $\log I_C$  vs.  $\log v$ . Dunn *et al.* observed that at different potentials the  $b$ -values fluctuate between 0.5 and 1, suggesting that at a given potential the current can be described as the linear combination of  $b = 1$  and  $b = 0.5$  processes.<sup>30</sup>

$$I_C (V) = s_1 v + s_2 v^{1/2} \quad (\text{Eq. 6.2})$$

where  $s_1$  and  $s_2$  are fitting parameters. Thus, finding the ratio between  $s_1$  and  $s_2$  that fits the current at each potential can be used to quantify the fractional contribution due to capacitive surface processes ( $b = 1$ ) and to diffusion-limited processes ( $b = 0.5$ ). The above equations are widely used as a standard measure to evaluate the kinetics of energy storage materials. On MXenes, it is well known that  $T_x$  groups present a very fast redox kinetics, while experimental observations on macroscale MXene electrodes have also shown a slower capacitive behaviour, which has been attributed to mass transport and ion-intercalation mechanisms. The mathematical model described

in Equation 6.2 was implemented on MXene pseudocapacitance  $I$ - $V$  curves to deconvolute and differentiate between fast surface ( $b=1$ ) and slower bulk ( $b=0.5$ ), as shown in Figure 6.3 A.<sup>33</sup> Shao, H. *et al.* obtained the contribution of the surface and bulk processes to the total charge storage and its dependence on the scan rate, for a 3D MXene electrode under acidic conditions, as shown in Figure 6.3 B.<sup>33</sup>



**Figure 6.3:** **A.** Deconvolution of a 3D MXene capacitive  $I$ - $V$  current (black) into the contribution of surface and bulk capacitive currents, in orange and grey, respectively. Voltamogram performed under acidic electrolyte conditions. **B.** Total charge contribution of the surface and bulk processes for different scan rates, showing that bulk processes dominate charge contribution at slow scan rates while surface processes dominate fast scan rates. A and B are reproduced with permission from Shao, H. *et al.*.<sup>33</sup>

Nevertheless, Dunn *et al.* mathematical model only considers two possible charging processes and relies on describing transport of species, *i.e.* bulk processes, as one-dimensional linear diffusion-limited process, which is not necessarily suitable for modelling the response of 3D hierarchical porous structures that also allow for intercalation. As pointed out in other publications, deconvolution can be implemented by including other transport mechanisms and variables in the Dunn model, such as porous media transport and hemispherical diffusion. However, the increasing number of variables of the more sophisticated deconvolution approaches makes the resolution of their equations complex, with the possibility of nonunique solutions. Moreover, even with those expanded models, often not enough detail is provided to capture the complex electrochemical charging nature of 3D electrode architectures.<sup>31-33</sup> As a consequence, despite the fact that mathematical models for  $I$ - $V$  curve deconvolution offer an interesting and promising approach to study the charge storage mechanisms of faradic and capacitive electrodes, further efforts beyond deconvolution strategies are needed to build the connection between the electrochemical response and the underlying physicochemical processes.

#### 6.1.4 Electrochemical isolation of MXene building blocks.

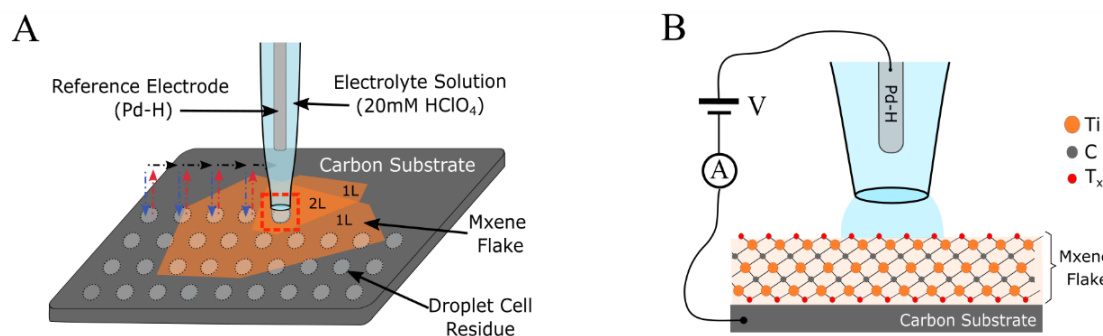
To provide a deeper understanding of the MXene charging mechanism, the acquisition of MXene electrochemical response at the micro- or nanoscale could facilitate a comparison of experimental data with computational methods, which operate on similar scales ( $\text{nm}^2$ ). Electrochemical scanning probe microscopy (EC-SPM) techniques could isolate the electrochemical response from small domains within the  $\text{nm}^2$  to  $\mu\text{m}^2$  range.<sup>36</sup> MXene flakes are up to a few  $\mu\text{m}$ 's in lateral size,<sup>28,37</sup> therefore, by implementing EC-SPM techniques it could be plausible to measure the electrochemical response of individual building blocks that constitute MXene electrodes, *i.e.*, a single monolayer MXene flakes.

Isolation of the electrochemical response of a single MXene flake by EC-SPM might be advantageous to avoid any mass transport effect related with the 3D architecture of macroscale electrodes and thus remove the contributions from bulk processes. Thus, having direct access to the response of a discrete monolayer in the absence of MXene stacking/assembly, enables the unambiguous assignment of the observed charging behaviour to “surface processes” exclusively, without any further deconvolution of the I-V curves. Moreover, single-flake electrochemistry could potentially identify any characteristic behaviour of single MXene flakes, which becomes obscured by the averaging effect occurring at the macroscale electrode. The implementation of EC-SPM methods also allows us to identify heterogeneity in the response across different MXene flakes.

SECCM, as a member of the family of EC-SPM techniques, might be the ideal candidate for isolating the capacitive response of a single MXene flake because of its ability to achieve controlled partial wetting of the working electrode. Therefore, the clear contact area achieved by SECCM allows for an unambiguous correlation between the electrochemical response and single flake morphology.<sup>38,39</sup> Moreover, the clear determination of the area wetted by the electrolyte allows further quantification of the electrochemical response in terms of current or capacitance density. The SECCM probe offers a defined mass transport of diluted species toward the electrode surface; the SECCM probe acts as a species reservoir and the pipette tapered end acts as a mass transport channel perpendicular to the electrode surface.<sup>36</sup> The SECCM characteristics are then of great advantage for comparison of the nano- or micro- scale electrochemical measurement with prior state-of-the-art experimental and computational literature. Further details about SECCM and other EC-SPM techniques are given in the Introduction chapter, Section 1.4.2.

To quantify the intrinsic electrochemical pseudocapacitive response of the monolayer  $\text{Ti}_3\text{C}_2\text{T}_x$  MXene, it is isolated the capacitive response on  $0.3 \mu\text{m}^2$  regions of monolayer  $\text{Ti}_3\text{C}_2\text{T}_x$  MXene flakes immobilised on a carbon supporting electrode using SECCM, as shown in Figure 6.4 A. Through SECCM electrochemical mapping, cyclic voltammograms are measured on a regular grid of sample points spaced  $1.80 \mu\text{m}$  apart on a region of monolayer  $\text{Ti}_3\text{C}_2\text{T}_x$  flakes. Cyclic

voltammograms were acquired on both  $\text{Ti}_3\text{C}_2\text{T}_x$  flakes and the surrounding carbon substrate, allowing us to compare the response on different flakes, different parts of the same flake, and control sample points on the carbon substrate. As shown in Figure 6.4 B, probing individual 2D MXene flakes supported on a carbon electrode with SECCM provides a bottom-contact configuration that has not been tested before for MXenes.



**Figure 6.4:** **A.** Schematic of the SECCM configuration to measure monolayer  $\text{Ti}_3\text{C}_2\text{T}_x$  flakes immobilised on the surface of a carbon supporting electrode. SECCM-based cyclic voltammogram measurements were conducted in a hopping mode, with the probe movement pattern shown in coloured arrows (blue approach, red retract, and black move to next measurement position). **B.** Schematic of the end of SECCM probe, highlighting the nanoscale electrochemical droplet cell and the two-electrode electrochemical cell configuration. Reproduced with permission from Brunet Cabré, M. *et al.*<sup>40</sup>.



## 6.2 Aims

The aim of this chapter is to measure the pseudocapacitance response of the building blocks of MXene electrode supercapacitors, *i.e.*, individual monolayer MXene flakes. The approach taken in this chapter will allow a comparison of the pseudocapacitive behaviour observed on monolayer flakes with the macroscale electrode response. Therefore, the measurement will bridge the gap between previous macroscale experimental approaches and computational studies.

To achieve the aim of this chapter, I first developed an experimental protocol that isolates single MXene flakes on a flat, conductive surface suitable for nano-electrochemical techniques. The electrochemical mapping, achieved by SECCM, is then used to isolate the electrochemical response of subregions of MXene flakes. A careful analysis of electrochemical data and morphological characterisation allowed the isolation of the response from the monolayer basal planes, edges, and layer stacks. Those results allow for a discussion of pseudocapacitive behaviour on those different morphological features.

## 6.3 Methods

**Chemicals.** Perchloric acid (HClO<sub>4</sub>, Fluka Analytical, 67-72%) was used as supplied by the manufacturer. All solutions were made with Millipore water with a high resistivity of 18 MΩ cm. All procedures were carried out at room temperature.

**Preparation of carbon substrates.** Carbon substrates were synthesised on SiO<sub>2</sub>/Si wafers substrates by sputtering deposition followed by graphitisation under an inert atmosphere. The SiO<sub>2</sub>/Si wafers (300 nm thermal oxide) were first cleaned with piranha solution (3:1 H<sub>2</sub>SO<sub>4</sub>/H<sub>2</sub>O<sub>2</sub>) and then rinsed with Millipore water and dried under nitrogen prior to sputter deposition. Deposition was carried out as previously reported;<sup>46</sup> briefly, amorphous carbon thin films were deposited in a dc-magnetron sputtering chamber (Torr International, Inc.) using a graphite target at a base pressure  $< 2 \times 10^{-6}$  mbar for 40 min using Ar as deposition gas (50 sccm,  $1-2 \times 10^{-2}$  mbar). The films were subsequently graphitised at 900 ° C in a tube furnace (Carbolite Gero) under N<sub>2</sub> flow for 60 minutes, yielding  $73 \pm 3$  nm thick carbon electrodes. All of the carbon substrates used in this chapter were manufactured integrally by Ph.D. student Christian Schröder.

**Preparation of Ti<sub>3</sub>C<sub>2</sub>T<sub>x</sub> stock solution:** 20 ml of 9 M HCl (Sigma) were added into a PTFE vented vessel containing 1.6g of LiF powder (Sigma). To allow the dissolution of the LiF powder, the solution was stirred at 400 rpm for 10 minutes while the vessel was placed in an oil bath at 35 °C. Keeping the vessel in the oil bath while stirring the solution, a total of 1 g of MAX Ti<sub>3</sub>AlC<sub>2</sub> phase (Carbon-Ukraine ltd.) was added to the solution in small fractions, allowing the temperature to stabilise between additions and minimising overheating of the solution. To achieve a complete etching of the MAX phase, the solution was kept at 35°C and stirred at 400 rpm for 24 hours. After this time, the solution was diluted with deionised water and centrifuged 5 minutes at 5000 rpm. The supernatant was discarded, the sediment was redispersed in deionised water, and centrifuged again for 5 minutes at 5000 rpm. This process was repeated until the solution was pH 6. The solution was then vortex for 30 minutes to ensure delamination of multilayer Ti<sub>3</sub>C<sub>2</sub>T<sub>x</sub> flakes in monolayer Ti<sub>3</sub>C<sub>2</sub>T<sub>x</sub> flakes. After vortex, the solution was centrifugated 30 min at 1500 rpm, collecting the supernatant that contained the monolayer flakes. A final centrifugation step for 1 hour at 5000 rpm was used to concentrate the monolayer flakes in the sediment, which was redispersed to obtain a 4 g/ml stock solution of Ti<sub>3</sub>C<sub>2</sub>T<sub>x</sub> flakes. The Ti<sub>3</sub>C<sub>2</sub>T<sub>x</sub> synthesis method described here was previously reported by Borghetti, M. *et al.*<sup>41</sup> The Ti<sub>3</sub>C<sub>2</sub>T<sub>x</sub> stock solution used in this chapter was manufactured by Ph.D. student Dahnian Spurling.

**Preparation of monolayer MXene flakes supported on carbon electrodes.** The stock solution was diluted with distilled water down to 10 µg/ml. The Ti<sub>3</sub>C<sub>2</sub>T<sub>x</sub> stock and aliquots were bubbled with argon to degas the solution and the flask was filled with argon to store the solution in an inert atmosphere. 2 µl of the diluted solution were drop-cast onto carbon substrates within the first 24 h

from the obtention of the MXene stock solution. The sample was dried overnight in air, resulting in a region within the drop-cast area with single MXene flakes on a carbon substrate, which stabilised the bottom-contact connection. Electrochemical measurements were carried out within 1 day from the drop-cast.

**Instruments.** Optical, atomic force microscopy (AFM), and scanning electrochemical cell microscopy (SECCM) measurements were acquired on a Park NX10 (Park Systems, South Korea). The AFM images were obtained in a non-contact mode (NCM) with a PPP-NCHR cantilever type (force constant = 42 N/m, resonance frequency = 330 kHz, Nanosensors). AFM and SECCM measurements were performed in a room with temperature control. The temperature and humidity inside the SECCM and AFM faraday cage were recorded for 7 days (see Appendix Figure A1 at the end of this chapter) with a mean temperature of  $22.6 \pm 0.2$  °C and relative humidity between 40 - 60 %RH. Scanning electron microscopy (SEM) images were acquired with ZEISS Ultra plus with the secondary electron detectors, SE2 and In-Lens, at an acceleration voltage of 3 kV. Energy dispersive X-ray spectroscopy (EDX) was performed on Zeiss Ultra Plus field-emission SEM at an acceleration voltage of 10 keV with a 20mm<sup>2</sup> Oxford Inca EDX detector. X-ray diffraction (XRD) was obtained using the powder diffractometer Bruker D8 Discovery, in  $\theta/2\theta$  configuration and range of 3–75 ° at 2 ° min<sup>-1</sup>. Raman spectroscopy measurements were acquired using a WITec Alpha 300R instrument with a 633 nm He-Ne laser source and 1800 lines/mm grating. Structural characterisation measurements (EDX, Raman, and XRD) were performed on the as-synthesised Ti<sub>3</sub>C<sub>2</sub>T<sub>x</sub> thin film produced by vacuum filtration. The EDX, XRD, and Raman characterisation performed in this chapter were manufactured integrally by Ph.D. student Dahnna Spurling. The SEM characterisation performed in this chapter was performed with the help of Ph.D. student Dahnna Spurling.

**Probe preparation.** Single-barrelled nanopipettes with an aperture radius of approximately 400 nm were used as SECCM probe. The nanopipettes were fabricated from single-barrelled borosilicate capillaries (1.5 mm O.D. and 0.86 mm I.D., BF150-86-7.5, Sutter Instrument, USA) using a P-2000 laser puller (Sutter Instrument, USA). Using a pipette filler (MicroFil MF34G-5, World Precision Instruments, USA) the nanopipette was filled with 20 mM HClO<sub>4</sub>. A Pd-H<sub>2</sub> quasi reference counter electrode (QRCE) was inserted at the top end of the pipette; prior to this, a Palladium wire (0.25 mm diameter, 5 cm long, PD005130, Goodfellow, UK) was biased at -3 V vs. a Pt counter electrode in 20 mM HClO<sub>4</sub> solution for 15 min to yield the Pd-H<sub>2</sub> quasi reference electrode.<sup>38,42</sup> Pd-H<sub>2</sub> QRCE was calibrated against standard calomel electrode (SCE) after SECCM scan with a read of -191mV, which corresponds of Pd-H<sub>2</sub> of +50mV vs standard hydrogen electrode (SHE).

**Scanning protocol.** Electrochemical SECCM measurements were performed over a region of the sample where monolayer Ti<sub>3</sub>C<sub>2</sub>T<sub>x</sub> flakes were immobilised, as identified by optical microscopy.

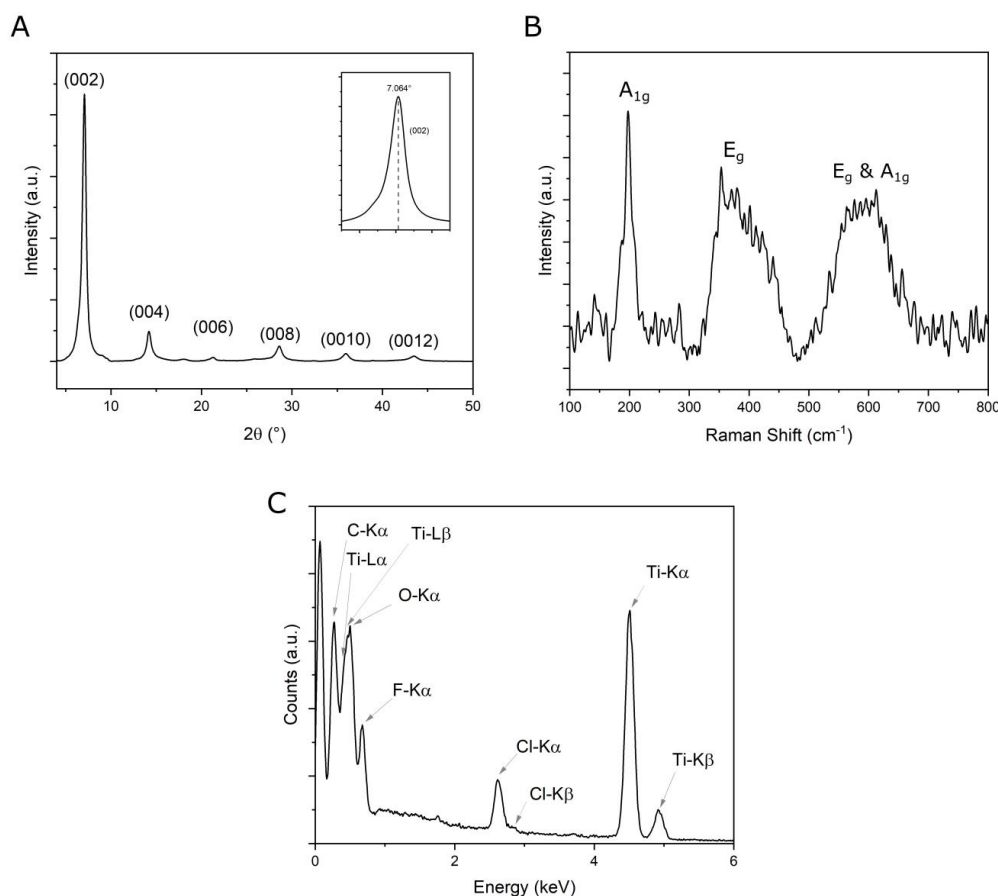
SECCM imaging was carried out on a regular grid of sample points spaced  $1.8\ \mu\text{m}$  apart. At each SECCM sample point two cyclic voltammograms were measured between  $+0.500\ \text{V}$  and  $-1.000\ \text{V}$  vs.  $\text{Pd-H}_2$  at a scan rate of  $0.500\ \text{V/s}$ . A hopping mode was used in which the probe was approached vertically toward the sample surface at a speed of  $0.200\ \mu\text{m/s}$  and a potential of  $-0.500\ \text{V}$  was held until contact was established between the nanopipette droplet and the surface. The contact was detected as the appearance of a double layer charging current that exceeded a defined absolute threshold current of  $3.0\ \text{pA}$ . After the pipette approach and droplet cell formation, the potential was changed to  $+0.500\ \text{V}$  and after a holding time of  $2.0\ \text{s}$ , two voltammetry cycles were recorded; then the pipette was retracted and moved to the next sample point of the predefined grid.

## 6.4 Results

### 6.4.1 Characterisation of the structure of MXene $Ti_3C_2T_x$ flakes

To characterise the MXene flakes produced by MAX phase exfoliation, a set of spectroscopic and diffraction techniques were carried out; results shown here are reported courtesy of Mr. Dahnian Spurling from the Nicolosi group. First, three free-standing films were made from individual MXene flakes prepared by vacuum filtration using the  $Ti_3C_2T_x$  stock dispersion (4 mg/ml). Each film was characterised only by one technique: EDX, Raman, or XRD. The sample was pristine prior to each of the characterisation techniques to avoid potential damage from prior characterisation methods to affect further measurements.

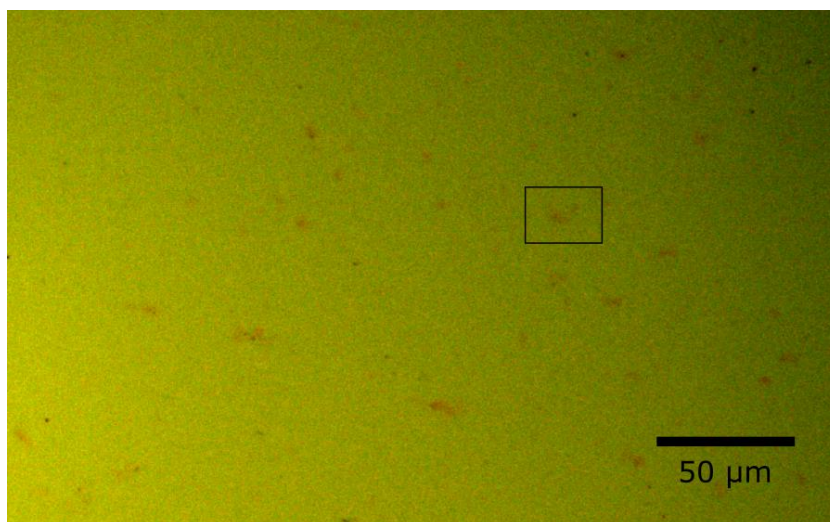
The X-ray diffractogram (XRD) of the  $Ti_3C_2T_x$  free-standing films, shown in Figure 6.5 A, shows the characteristic (0 0 2) peak at  $7.064^\circ$  and its reflections up to (0 0 12). XRD indicates that the freestanding film is formed of bidimensional  $Ti_3C_2T_x$  flakes.<sup>37</sup> There is no trace of an anatase ( $TiO_2$ ) peak at around  $2\theta = 25^\circ$  and no other characteristic MAX phase peaks are observed. Therefore, it is concluded that the stock solution contains only  $Ti_3C_2T_x$  flakes. The Raman spectra shown in Figure 6.5 B also indicates the bidimensional  $Ti_3C_2T_x$  that forms the freestanding film with the presence of  $A_{1g}$  and  $E_g$  peaks.<sup>43</sup> The EDX spectra with the corresponding elements assigned to each peak, displayed in Figure 6.5 C, indicate only the presence of elements characteristic of the  $Ti_3C_2T_x$  flakes, namely  $T_x = -O$ ,  $-F$  and  $-Cl$ . Note that  $-Cl$  results from the exfoliation procedure implemented with the use of LiF salt in combination with HCl.<sup>37</sup>



**Figure 6.5:** **A.** X-ray diffractogram (XRD) of freestanding  $\text{Ti}_3\text{C}_2\text{T}_x$  films. The diffractogram shows the characteristic peak (0 0 2) at  $7.064^\circ$  and its reflections up to (0 0 12).<sup>37</sup> **B.** Raman spectra of the freestanding  $\text{Ti}_3\text{C}_2\text{T}_x$  film. Spectra show characteristic peaks:  $A_{1g}$  at  $200\text{ cm}^{-1}$ ,  $E_g$  within the region of  $230 - 470\text{ cm}^{-1}$  and both  $E_g$  and  $A_{1g}$  in the region of  $580 - 730\text{ cm}^{-1}$  region.<sup>43</sup> **C.** Energy dispersive X-ray spectroscopy (EDX) of  $\text{Ti}_3\text{C}_2\text{T}_x$  freestanding films. Spectra show the presence of the surface group atoms. No Al trace is observed suggesting complete MXene exfoliation. The observed halogen elements (F, Cl) observed are introduced during the exfoliation of the MAX phase with LiF and HCl solution.<sup>37</sup> Data provided courtesy of Mr. Dahnian Spurling.

#### 6.4.2 Identification of the region with MXene flakes for SECCM scanning

Optical images were used to locate the region of the carbon substrate that displayed supported  $\text{Ti}_3\text{C}_2\text{T}_x$  flakes, as shown in Figure 6.6. The red features were identified as MXene flakes over the carbon substrate, which present a yellowing colouring. Once the region was identified, SECCM electrochemical mappings were conducted over a red feature. After SECCM, physical characterisation was conducted by AFM and SEM. All experimental results presented in this chapter are performed over the region marked with a black square in the optical image displayed in Figure 6.6.

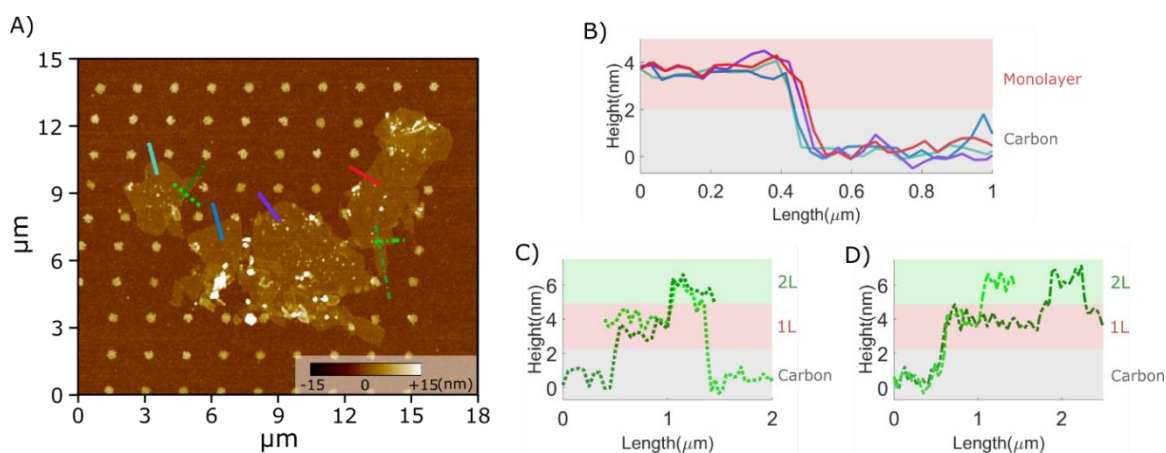


**Figure 6.6:** Optical image of the substrate with  $\text{Ti}_3\text{C}_2\text{T}_x$  drop-cast. The yellow background is the carbon substrate, and the red features are the MXene flakes. Black square indicates the region of the sample where the experiments were conducted.

### 6.4.3 Morphological characterisation of MXene flakes in the SECCM scanned region

The morphology of the  $\text{Ti}_3\text{C}_2\text{T}_x$  flakes was determined by a combination of AFM and SEM, both of which were performed after SECCM probing. The AFM image in Figure 6.7 A shows four distinct MXene flakes supported on the carbon thin film electrode; the circular features distributed in a square grid correspond to inorganic residues left by the SECCM droplet cell. Figure 6.7 B shows four height profiles measured at the step-edges between the carbon substrate and the basal plane of  $\text{Ti}_3\text{C}_2\text{T}_x$  flakes, corresponding to four different flakes, as indicated using solid lines in Figure 6.7 A. The average step-height was found to be  $3.4 \pm 0.4$  nm (see Table 6.1). The  $\text{Ti}_3\text{C}_2\text{T}_x$  monolayer thickness, according to TEM studies and DFT calculations of prior published literature, is estimated to be 0.98 nm;<sup>44-46</sup> however, experimental AFM step-heights typically reported for  $\text{Ti}_3\text{C}_2\text{T}_x$  monolayers supported on  $\text{SiO}_2$  are in the range 2-3 nm.<sup>47-50</sup> These larger values of step-height observed via AFM are commonly attributed to a combination of the nature of the substrate/2D material interface, the presence of adsorbates on 2D materials and possible instrumental factors.<sup>50-52</sup> Adsorbed water layers and/or water trapped in the interlayer between monolayer and substrate, are a characteristic of deposited  $\text{Ti}_3\text{C}_2\text{T}_x$  monolayers, as is also the case for other 2D materials discussed in the literature.<sup>52-54</sup> Furthermore, a recent study observed that AFM step-height profiles of  $\text{Ti}_3\text{C}_2\text{T}_x$  monolayers vary depending on the exfoliation procedure used because of differences in surface functionalities ( $\text{T}_x$ ), leading to variable densities of adsorbed water at their surface.<sup>49</sup> Therefore, AFM thickness determinations of  $\text{Ti}_3\text{C}_2\text{T}_x$  monolayers are

highly dependent on the presence of adsorbates and on the specific substrate of choice. Based on the combined AFM and SEM characterisation (detailed below) the step-height of  $3.4 \pm 0.4$  nm measured between the carbon substrate and the MXene flake, can be attributed to a monolayer of  $\text{Ti}_3\text{C}_2\text{T}_x$  with the presence of a water adlayer and, probably, also of an interlayer trapped between the flake and the carbon substrate.



**Figure 6.7:** AFM characterisation for MXene flakes. AFM image taken after SECCM. **A.** AFM map of MXene flakes, also showing left over SECCM droplet residues. Solid coloured lines indicate regions where step profiles from carbon to monolayer were taken. The dotted lines indicate regions where step profiles from carbon to monolayer to bilayer were taken. **B.** Step profiles from the carbon surface to the monolayer MXene surface. **C.** and **D.** Step profiles from the carbon surface to the monolayer surface and to the bilayer surface.

**Table 6.1:** MXene flake step-heights obtained from AFM images.

$\text{Ti}_3\text{C}_2\text{T}_x$ Morphology		Step-height (nm)	Standard deviation (nm)
Carbon to monolayer MXene	Profile 1	3.35	0.29
	Profile 2	3.35	0.29
	Profile 3	3.59	0.38
	Profile 4	3.39	0.32
	<i>Mean</i>	<i>3.42</i>	<i>0.35</i>
Monolayer to bilayer MXene	Profile 1	1.85	0.48
	Profile 2	2.47	0.61
	Profile 3	2.22	0.50
	Profile 4	2.59	0.55
	<i>Mean</i>	<i>2.28</i>	<i>0.63</i>

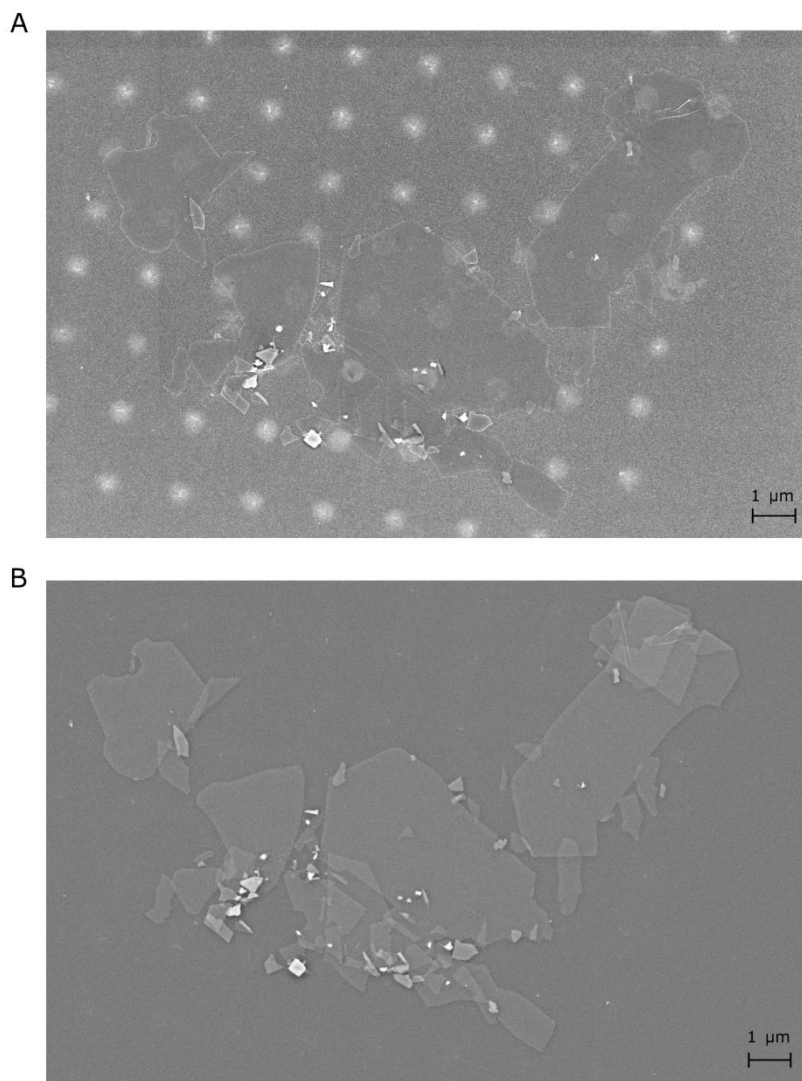


Figure 6.7 A also shows that some of the monolayer flakes are immobilized overlapping each other, resulting in bilayer regions. The height profiles from carbon to monolayer and to bilayer were acquired in regions indicated in Figure 6.7 A by a dotted line, and are plotted in Figures 6.7 C and D. The step-height from monolayer to bilayer was found to be  $2.28 \pm 0.63$  nm (see Table 6.1), considerably smaller than the step-height values obtained for carbon (substrate) to monolayer. This is in good agreement with observations from other studies, where reported step-height values for monolayer to bilayer are considerably smaller than for substrate to monolayer.<sup>49</sup>

SEM imaging was performed using the In-Lens and Secondary Electron (SE2) detectors. The In-Lens detector, see Figure 6.8 A, clearly resolves the locations of electrolyte residues on the sample. This enabled us to assign the composition of the surface at each SECCM measurement point, and its classification as being on either carbon, or  $\text{Ti}_3\text{C}_2\text{T}_x$  flakes, as detailed in Section 6.4.4 below. In Figure 6.8 B, the SE2 detector provided clear contrast that allowed us to determine the number of  $\text{Ti}_3\text{C}_2\text{T}_x$  layers stacked on the substrate, with areas with overlapping flakes being clearly differentiated as brighter regions. Four isolated flakes with an area larger than  $5 \mu\text{m}^2$  were identified in Figure 6.8 B (also see Figure 6.14 A), and their areas are reported in Table 6.2. The four larger flakes and most of the smaller flakes consist of the same number of layers. Given that the exfoliation method used achieves a monolayer yield of 80%,<sup>55</sup> the secondary electron SEM micrograph corroborates the assignment of the four largest  $\text{Ti}_3\text{C}_2\text{T}_x$  flakes as a monolayer.

**Table 6.2:** Area of  $\text{Ti}_3\text{C}_2\text{T}_x$  flakes as determined from SEM micrographs.

Flake label	Flake size ( $\mu\text{m}^2$ )
(i)	$5.87 \pm 0.03$
(ii)	$5.13 \pm 0.03$
(iii)	$15.43 \pm 0.09$
(iv)	$14.14 \pm 0.04$

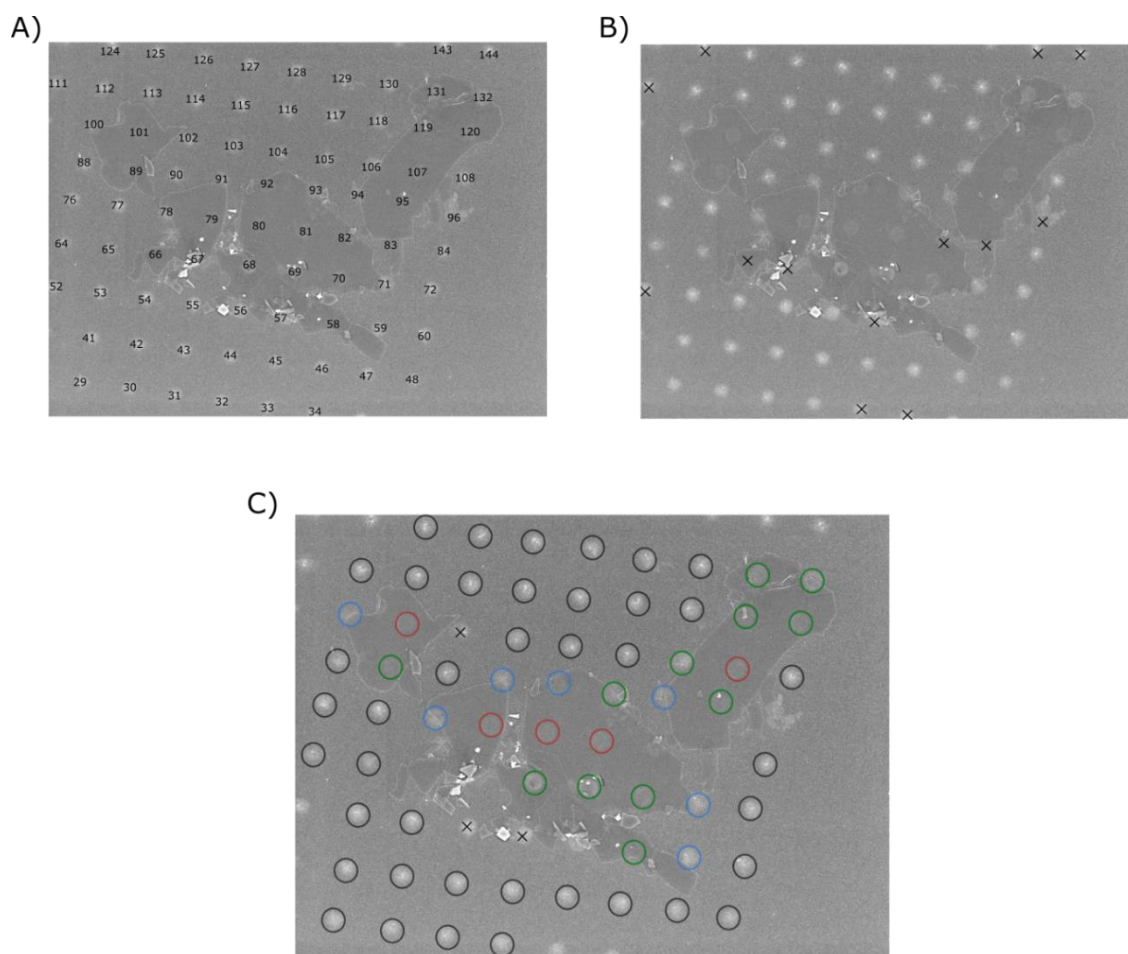


**Figure 6.8:** SEM micrographs obtained after SECCM scans. **A.** Image obtained with the In-Lens detector. **B.** Image obtained with the secondary electron detector (SE2).

#### 6.4.4 Assignment of SECCM point to $\text{Ti}_3\text{C}_2\text{T}_x$ flake morphology

Electrolyte residues are a common feature of SECCM mapping that enable identification of the area contacted and probed by the SECCM droplet cell.<sup>36</sup> Thus, the relative positions of residue points are used to correlate the electrochemical response with the surface morphology probed in each case. Figure 6.9 A identifies a total of 80 points of the SECCM grid that are visible over the area imaged in the SEM micrograph; of these, 67 points present a well-defined circular geometry that is suitable for area normalisation to current densities, while the remaining 13 points are indicated with crosses in Figure 6.9 B. Based on the locations in the SEM micrograph, the electrochemical responses of these 67 points were assigned to that of either the carbon substrate (40 points) or  $\text{Ti}_3\text{C}_2\text{T}_x$  MXene (24 points). For the remaining 3 points, it is not possible to

unambiguously establish if the droplet cell was in contact with the MXene flake, therefore these 3 points (marked with a cross in Figure 6.9 C) were excluded from further analysis. The contrast of the SE2 detector further enabled us to discriminate whether contact with  $\text{Ti}_3\text{C}_2\text{T}_x$  was established exclusively on the monolayer basal plane (5 points, in red), on the edge of a monolayer (7 points, in blue), or on a multilayer region (12 points, in green). The classification of all 64 points according to the above four morphologies is shown in Figure 6.9 C, and a summary of the number of points for each category is reported in Table 6.3.



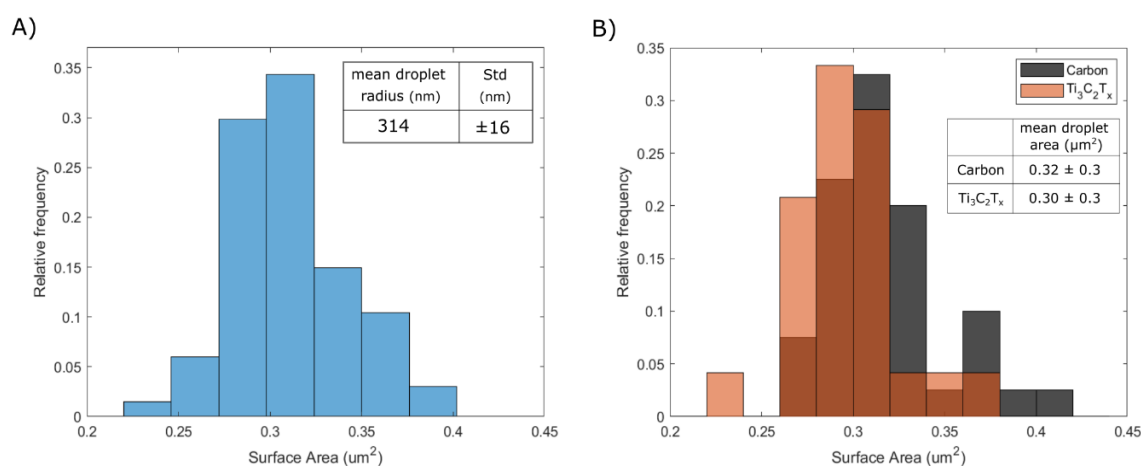
**Figure 6.9:** **A.** Identification of all SECCM grid points visualised in the SEM micrographs; each point is indicated with the corresponding numbered position in the grid. **B.** Identification of points without a well-defined circular geometric area (black cross). **C.** Classification of points with a well-defined circular geometric area and non-ambiguous contact, respect the surface contacted; only carbon contact (black circle), only monolayer basal-plane contact (red circle), partial carbon and partial monolayer contact (blue circle) and partial or complete multilayer contact (green circle). For three points (black crosses) it is ambiguous if they contact only carbon or if there is partial contact of carbon and partial contact of monolayer contact.

**Table 6.3:** Total number of SECCM points examined and classified according to the surface morphology probed.

	<b>Number of points</b>
Points visualized in SEM micrograph	80
Points with a well-defined geometric area	67
Points with well-defined surface contact	64
<i>Surface morphology contacted</i>	
Ti <sub>3</sub> C <sub>2</sub> T <sub>x</sub> - Monolayer basal-plane	5
Ti <sub>3</sub> C <sub>2</sub> T <sub>x</sub> - Carbon and Monolayer	7
Ti <sub>3</sub> C <sub>2</sub> T <sub>x</sub> - Multilayer Stack	12
Ti <sub>3</sub> C <sub>2</sub> T <sub>x</sub> - Total	24
Carbon	40

### 6.4.5 Determination of cell geometric area

The electrochemically active geometric area was estimated from the diameter of each residue observed in the SEM images displayed in Figure 6.8 A. The distribution of the area values obtained is shown in Figure 6.10 A. The average area contacted by the droplet cell was found to be  $0.31 \pm 0.02 \mu\text{m}^2$ . The well-defined circular geometry observed for the majority of electrolyte residues and the narrow distribution of the electrochemical surface area values confirm that the SECCM droplet cell maintains a regular shape and does not spread over the contacted surface during measurements. Figure 6.10 B shows the geometric area distributions observed for the carbon and Ti<sub>3</sub>C<sub>2</sub>T<sub>x</sub> regions; the distributions display maxima at similar positions and mean values within their errors, indicating consistent droplet sizes at the two types of surface.



**Figure 6.10:** Distribution of the active geometric areas obtained from SEM images of electrolyte residues after SECCM. **A.** Distribution of area values for all points with well-defined circular shape (N = 67). **B.** Overlap histogram showing distributions of droplet area values for points that correspond to the carbon (N = 40, in black) and Ti<sub>3</sub>C<sub>2</sub>T<sub>x</sub> (N = 24, in brown) regions.

### 6.4.6 Localised electrochemical measurements on $\text{Ti}_3\text{C}_2\text{T}_x$ flakes

Cyclic voltammograms (CV) in acid electrolyte (20 mM  $\text{HClO}_4$ ) were measured at each probed point, between + 0.5 V and – 1.0 V vs. Pd- $\text{H}_2$  at 0.5 V/s; two cycles were recorded in all cases. As shown in Figures 6.11 and 6.12, the voltammograms obtained at each point can be classified by the first or second cycle response and by the surface morphology contacted: only carbon contact, only monolayer basal-plane contact, partial carbon and partial monolayer contact and partial or complete multilayer contact.

In Figures 6.11 and 6.12 very different responses are observed for the two types (carbon and MXene) of surface morphology; also, a significant difference between the first and second cycle is observed when MXene flakes are contacted in the cell. The difference between consecutive cycles can be attributed to conditioning of the MXene surface during the initial cycle, which is often related to the effect of cycling on the  $\text{T}_x$  group environment.<sup>20,56-58</sup> Note that the previous literature does not provide a description at the molecular level of the MXene conditioning process; however, experimental evidence indicates that constant capacitance values are obtained only after one or a few cycles in the electrolyte of choice.<sup>18</sup> As observed in Figures 6.11 A and 6.12 A, this behaviour is not observed when only carbon is contacted, where the first and second cycle present an identical response. To minimise possible contributions from any surface conditioning process, only the second cycle of each point was used for further analysis.

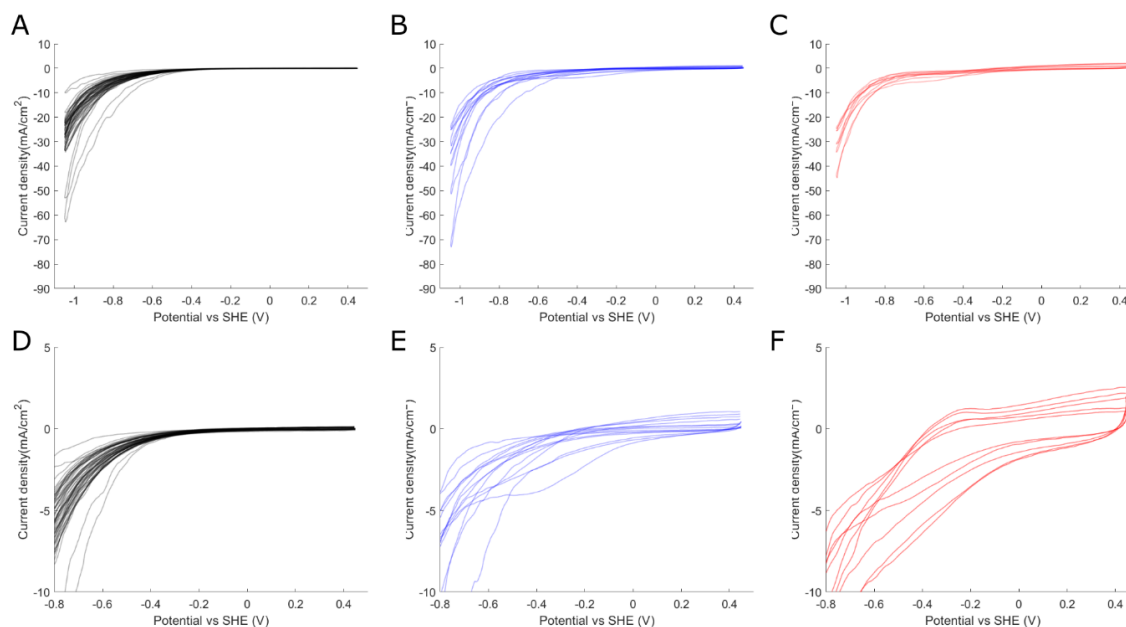
From the 2<sup>nd</sup> cycle voltammograms, Figure 6.12, two electrochemical regimes can be distinguished:

- Between +0.5 V and -0.5 V vs. Pd- $\text{H}_2$  (Pd- $\text{H}_2$  is +50 mV vs SHE) the voltammograms obtained over  $\text{Ti}_3\text{C}_2\text{T}_x$  flakes show the characteristic I-V curves of pseudocapacitive charging.<sup>18,20,59</sup> For droplet cells contacting partial carbon and partial monolayer surfaces, a capacitive charge is also observed but of lower magnitude. At this potential window, carbon exhibits a flat response, indicating a minor capacitive behaviour. Also, see Figure 6.13 A, where representative voltammograms on the carbon surface and on the basal plane of monolayer  $\text{Ti}_3\text{C}_2\text{T}_x$  flakes are overlapped to facilitate a comparison of their respective capacitive responses.
- Below -0.6 V vs. Pd- $\text{H}_2$  an exponential increase in current magnitude is observed on both  $\text{Ti}_3\text{C}_2\text{T}_x$  flakes and the carbon substrate, which is consistent with the onset of the hydrogen evolution reaction (HER).<sup>13,60</sup>

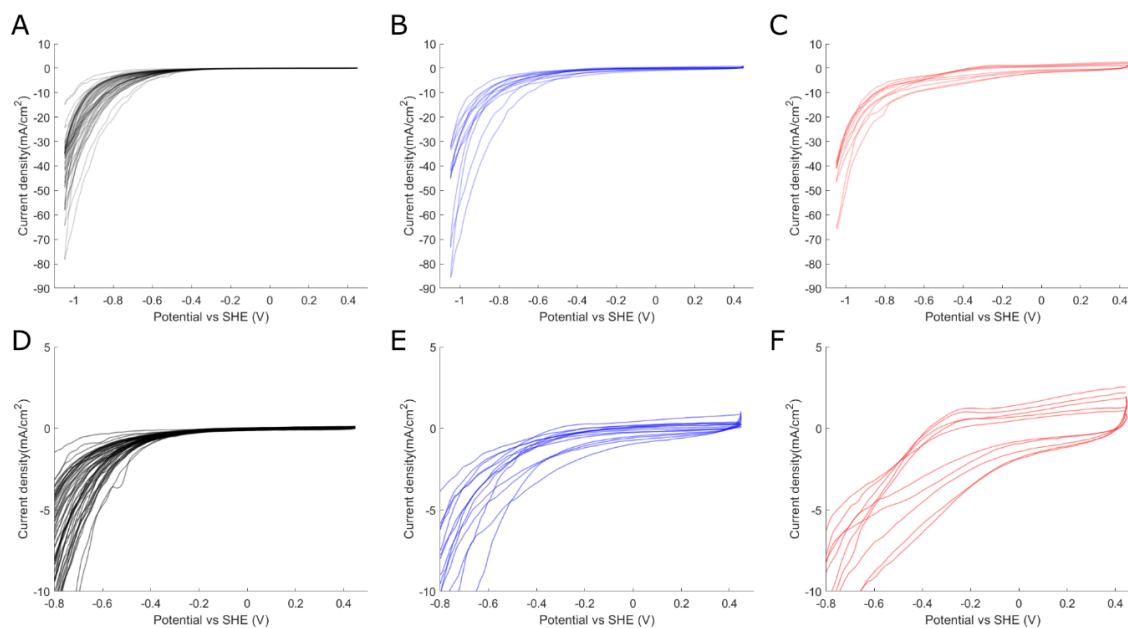
Therefore, the chosen potential window, + 0.5 V to – 1.0 V vs. Pd- $\text{H}_2$ , induced both pseudocapacitive and HER responses without inducing irreversible anodic oxidation, which occurs above + 0.7 V vs. Pd- $\text{H}_2$  (+ 0.75 V vs. SHE).<sup>59</sup>

Cycling into the HER regime should favour conditioning of the MXene surface by saturating terminal oxide groups with adsorbed protons.<sup>22</sup> Note here that in the case of macroscopic electrodes the evolution of gas can create mechanical instabilities that degrade or change the response over time. However, in the case of SECCM experiments, gas evolution takes place on a mono-/few-layer electrode and the gas can transport very rapidly to the droplet cell air interface, preventing bubble formation.<sup>61,62</sup> If gas bubble formation were to occur within the SECCM droplet cell, a discontinuity would be observed in the current trace of the voltammograms, because of the associated change in contact area and reactant mass transport. This has previously been observed when performing HER experiments with other 2D materials using SECCM,<sup>62</sup> but such behaviour was not observed here, indicating that bubble formation does not occur under our experimental conditions. The SECCM configuration, which only wets a very minor portion of the sample surface, prevents the “lift-off” of the MXene flake from the surface. The AFM and SEM shows that the MXene layers are intact on the carbon working electrode support and show no evidence of exfoliation. Therefore, the mechanical instability commonly observed in macroscale MXene electrodes,<sup>63</sup> is not a concern under the experimental conditions used here.

In summary, the MXene surface presents a characteristic capacitive response. Depending on the morphology of the MXene surface contacted or just between different points that contact the same morphology type (*i.e.* the monolayer of Figure 6.12 F) different capacitive current magnitudes are observed.



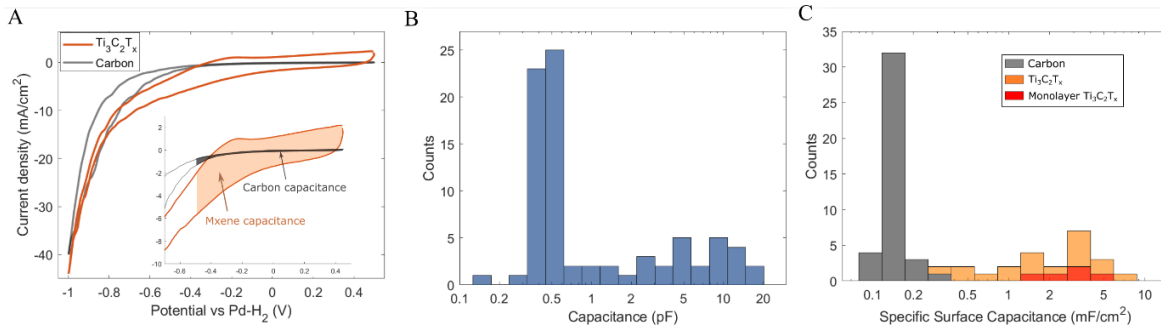
**Figure 6.11:** First loop of cyclic voltammograms on **A** Carbon sample points, **B** Mixed monolayer MXene and Carbon sample points, and **C** monolayer (basal-plane) MXene sample points. **D**, **E** and **F** are maximised plots of A, B and C, respectively.



**Figure 6.12:** Second loop of cyclic voltammograms on **A** Carbon sample points, **B** Mixed monolayer MXene and Carbon sample points, and **C** monolayer (basal-plane) MXene sample points. **D**, **E** and **F** are maximised plots of A, B and C, respectively.

#### 6.4.7 Observation of the capacitive response in subregions of $\text{Ti}_3\text{C}_2\text{T}_x$ flakes

To quantitatively compare the difference in the pseudocapacitive response for the different surface morphologies and between different sample points, the capacitance of each point was determined by integrating the charge between +0.5 V and -0.5 V, as illustrated in Figure 6.11 A. The distribution of the capacitance values obtained for all points of the SECCM grid ( $N = 80$ ) resulted in the histogram shown in Figure 6.13 B and suggests the presence of two distinct populations. To account for different contact areas, the capacitance was normalised by the geometric area to derive the specific surface capacitance at each point. Figure 6.13 C displays stacked histograms of the specific surface capacitance obtained at carbon contact points and at MXene flake contact points, with points contacting a monolayer basal-plane of  $\text{Ti}_3\text{C}_2\text{T}_x$ , exclusively, highlighted in red. The average surface capacitance obtained for carbon was  $0.15 \pm 0.04 \text{ mF/cm}^2$ , consistent with graphitic carbons in acidic electrolytes (up to  $0.35 \text{ mF/cm}^2$ ).<sup>64,65</sup> The average surface capacitance measured on monolayer  $\text{Ti}_3\text{C}_2\text{T}_x$  MXene sample points, exclusively, is  $2.8 \pm 1.0 \text{ mF/cm}^2$ , more than an order of magnitude larger than that of the carbon support. As shown in Figure 6.11 C, the remaining points in contact with  $\text{Ti}_3\text{C}_2\text{T}_x$  flakes present a distribution of specific surface capacitance, with values larger than the mean carbon specific surface capacitance. A detailed assignment of these points, shown in Figure 6.7, suggests that the broad distribution in specific surface capacitance is due to a wide range of flake morphologies (*e.g.* edge, multilayer).



**Figure 6.13:** Representative cyclic voltammograms on a carbon surface (black) and a single monolayer MXene flake (orange) at a scan rate of 0.5 V/s in 20 mM HClO<sub>4</sub>. **B.** Histogram of the capacitance values of each individual SECCM grid point observed on the SEM image (N = 80). **C.** Stacked histogram of the surface capacitance over the carbon surface (black, N = 40) and the MXene flake (orange, N =24), of which it is highlighted the once over basal plane of single layer Ti<sub>3</sub>C<sub>2</sub>T<sub>x</sub> (red, N = 5). Reproduced with permission from Brunet Cabré, M. *et al.*<sup>40</sup>.

The average surface capacitance values found for the monolayer Ti<sub>3</sub>C<sub>2</sub>T<sub>x</sub> are derived from a flat 2D surface (*i.e.*, the basal plane), and cannot be directly compared with the areal capacitance values (normalised by geometric area) of the three-dimensional electrodes reported in the literature. However, previous literature studies also reported specific gravimetric capacitance values for three-dimensional electrodes, as shown in Table 6.5. MXene capacitance values derived from different approaches are often compared using gravimetric capacitance metrics. For instance, in experimental work carried out using macroscopic electrodes, the capacitance is normalised by the mass of electrode material deposited over the geometric area contacted by the electrolyte.<sup>15,18,20,52,59,66-69</sup> Computational work also translates monolayer simulations of specific areal capacitance into gravimetric capacitances.<sup>15,20,22,25,26,70</sup>

The gravimetric capacitance can be calculated from the sample points that contact the monolayer basal plane exclusively, based on the known contact area of the SECCM measurement and the crystal structure of Ti<sub>3</sub>C<sub>2</sub>T<sub>x</sub> monolayers which consist of 12 unit cells/nm<sup>2</sup>.<sup>22</sup> Thus, the mass per unit area of the Ti<sub>3</sub>C<sub>2</sub>T<sub>x</sub> monolayers was calculated as:

$$m_i = A * \frac{1}{SSA_{1L}} \quad (\text{Eq.6.3})$$

where  $m_i$  is the mass of Ti<sub>3</sub>C<sub>2</sub>T<sub>x</sub> the droplet cell of point  $i$ ,  $A$  is the wetted area and  $SSA_{1L}$  is the specific surface area of a Ti<sub>3</sub>C<sub>2</sub>T<sub>x</sub> monolayer.  $SSA_{1L}$  was calculated from Ti<sub>3</sub>C<sub>2</sub>T<sub>x</sub> stoichiometry, molar mass and a surface termination, T<sub>x</sub>, assumed to consist of –OH groups. Thus:

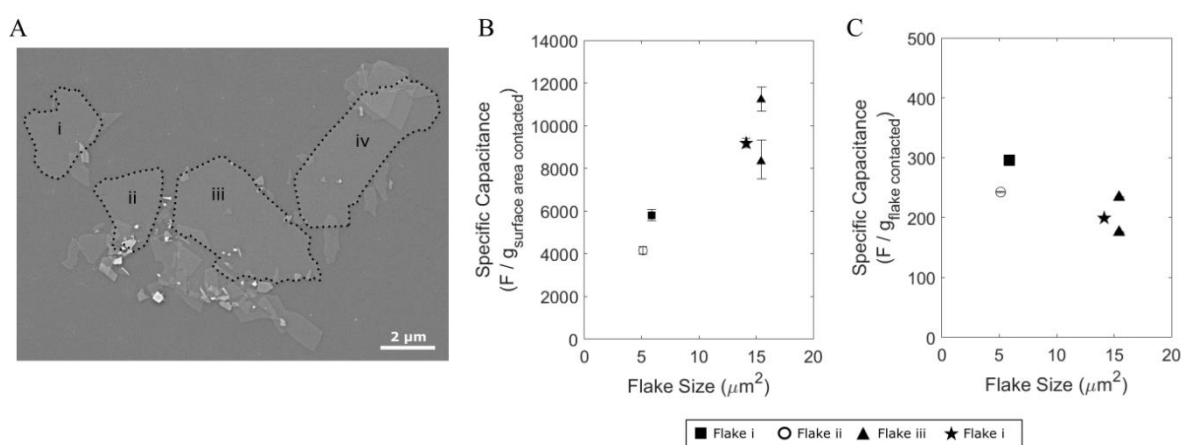
$$\frac{1}{SSA_{1L}} = \frac{\text{mass of } Ti_3C_2OH}{\mu m^2 \text{ of monolayer}} = \frac{12 \text{ unit cells}}{nm^2} \cdot \frac{10^6 nm^2}{1 \mu m^2} \cdot \frac{3 \cdot Ti_{MW} + 2 \cdot C_{MW} + 1 \cdot O_{MW} + 1 \cdot H_{MW}}{1 \text{ unit cell}} \cdot \frac{1}{N_A}$$

$$\frac{1}{SSA_{1L}} = 3.678 \cdot 10^{-15} \frac{g}{\mu m^2} \quad SSA_{1L-one \ side} = 271.9 \frac{m^2}{g}$$



The electrochemical area contacted in our measurements is  $0.31 \mu\text{m}^2$ , and therefore the mass of monolayer  $\text{Ti}_3\text{C}_2\text{T}_x$  contained in the  $0.31 \mu\text{m}^2$  area is  $1.15 \pm 0.10 \text{ fg}$ . We can normalize the capacitance values on monolayer points by this equivalent mass yielding gravimetric capacitances between 4000 - 12000 F/g for a monolayer basal plane. These values are remarkably high, one to two orders of magnitude greater than any previous theoretical prediction or measurement (see Table 6.5).<sup>66-68,71</sup> The pseudocapacitive charging is estimated to provide about  $0.4 e^-$  per unit cell per volt of storage when both sides of a monolayer are protonated.<sup>22,25,27</sup> A gravimetric capacitance of 12000 F/g would be equivalent to  $14.8 e^-$  per unit cell per volt, an unphysically large capacitance that suggests that the MXene monolayer area engaged in capacitive charging might be much larger than the area of the submicron droplet contact ( $0.31 \mu\text{m}^2$ ).

The SEM imaging, Figure 6.14 A, shows that the MXene sample consists of four separate monolayer flakes. A comparison of the basal plane pseudocapacitance values ( $N = 5$ ) obtained on the four flakes reveals differences, as shown in Figure 6.14 B, with a trend of increasing capacitance with increasing flake size. When the basal-plane capacitance values are normalised by the mass of the entire flake (see Table 6.4), the specific gravimetric capacitance values are found to be independent of the flake size and range between 180 and 300 F/g (see Figure 6.14 C). These estimates of gravimetric capacitance are in excellent agreement with values predicted by DFT simulations (*ca.* 230 F/g)<sup>22,25,26,70,72</sup> and previous experimental determinations (220 - 250 F/g).<sup>45,69</sup> Normalising the basal-plane capacitance values by the two-sided area of the entire monolayer flake, we obtain specific surface capacitance values of  $40 \pm 10 \mu\text{F}/\text{cm}^2$ , which is in agreement with the DFT prediction for  $\text{Ti}_3\text{C}_2\text{T}_x$  of  $45 \mu\text{F}/\text{cm}^2$ .<sup>70</sup> This suggests that the capacitance response arises from the entire MXene flake and is not confined to the contact area between the MXene basal plane and the SECCM-based electrochemical cell.



**Figure 6.14:** **A.** Electron micrograph of sample surface flakes larger than  $5 \mu\text{m}^2$  labelled. **B.** Specific gravimetric capacitance on monolayer  $\text{Ti}_3\text{C}_2\text{T}_x$  compared to the total area  $\text{Ti}_3\text{C}_2\text{T}_x$  flake, obtained by normalising the capacitance by the mass of MXene in electrochemical contact with the electrolyte. **C.** Specific gravimetric capacitance obtained by normalising the total mass of the monolayer flake. Reproduced with permission from Brunet Cabré, M. *et al.*<sup>40</sup>.

**Table 6.4:** Area of  $\text{Ti}_3\text{C}_2\text{T}_x$  flakes determined from SEM micrographs (see Figure 6.8 and Table 6.2) and the equivalent mass of each flake.

Flake label	Flake size ( $\mu\text{m}^2$ )	Flake Mass (fg)
(i)	$5.87 \pm 0.03$	21.5
(ii)	$5.13 \pm 0.03$	18.9
(iii)	$15.43 \pm 0.09$	56.8
(iv)	$14.14 \pm 0.04$	52.0

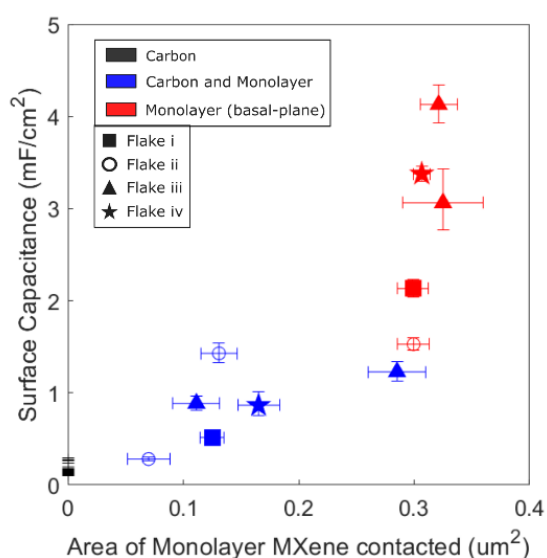
**Table 6.5:** Summary of the capacitance values reported in the literature for  $\text{Ti}_3\text{C}_2\text{T}_x$  electrodes.

	Specific gravimetric capacitance (F/g)	Specific surface area ( $\text{m}^2/\text{g}$ )	Specific surface capacitance ( $\text{mF}/\text{cm}^2$ )	Ref.	
$\text{Ti}_3\text{C}_2\text{T}_x$ film	231	16.2	1.43	71	
$\text{Ti}_3\text{C}_2\text{T}_x$ film	220	19.2	1.145	73	
$\text{Ti}_3\text{C}_2\text{T}_x$ /Ni foam film	350	32	1.093	67	
$\text{Ti}_3\text{C}_2\text{T}_x$ aerogel	438	108	0.406	71	
$\text{Ti}_3\text{C}_2\text{T}_x$ hydrogel	220	196	0.112	73	
3D printed $\text{Ti}_3\text{C}_2\text{T}_x$ aerogel	242	177	0.137	68	
Monolayer $\text{Ti}_3\text{C}_2\text{T}_x$	Electrochemically contacted surface area	$7700 \pm 2800$	271.9 (SSA <sub>1L-one side</sub> )	$2.8 \pm 1.0$	This work
	Flake surface area	$240 \pm 50$	543.9 (SSA <sub>1L-two sides</sub> )	$0.04 \pm 0.01$	

### 6.4.8 Implications on the pseudocapacitive mechanism of MXenes.

In acid electrolytes, the pseudocapacitance of MXenes is described as arising from proton intercalation/deintercalation accompanied by redox switching of the Ti centers and protonation/deprotonation of oxygen functional groups.<sup>3,21</sup> However, our samples consist of monolayer MXene on a carbon surface, and therefore ion intercalation would need to occur between the monolayer MXene and the underlying carbon surface. Furthermore, we conduct our electrochemical measurements by establishing electrochemical contact with only a fraction of the basal plane of the MXene, which leaves no clear pathway for the intercalation of ions between the MXene and the carbon substrate. Nonetheless, we appear to be measuring the pseudocapacitance response from the entire MXene flake, despite our experimental configuration only allowing ion transport to approximately 3% of the total MXene flake surface.

Ion intercalation might be possible when contacting the boundary between the flake edge and the carbon substrate, thus providing enhanced capacitive responses.<sup>20,24,66,74</sup> On such sample points, the SECCM-based electrochemical cell is in contact with the carbon substrate-monolayer MXene gap which could enable intercalation between the monolayer MXene and the carbon surface. However, as shown in Figure 6.15, the edge points show capacitance values per area that are smaller than those at monolayer basal-plane. This analysis suggests that the ion intercalation at the flake edges is unlikely to be responsible for the specific pseudocapacitive values shown in Figure 6.15.



**Figure 6.15:** Surface capacitance plotted against the area of the  $\text{Ti}_3\text{C}_2\text{T}_x$  monolayer contacted. Different symbols indicate which flake was contacted, while the colour code indicates surface type. Reproduced with permission from Brunet Cabré, M. *et al.*<sup>40</sup>.

## 6.5 Discussion

In the literature, capacitive  $I$ - $V$  curves obtained on macroscopic 3D electrodes are often deconvoluted into current contributions from both surface and bulk processes,<sup>18,29,33</sup> using a model described by Dunn *et al.*<sup>30</sup> Both surface and bulk processes are important for describing the MXene pseudocapacitive behaviour, and it is useful to differentiate between the timescales of the fast protonation kinetics of  $T_x$  groups (surface processes) and the contribution from the slower ion-intercalation (bulk processes).<sup>33</sup> The Dunn *et al.* model however only considers two possible charging processes and assumes that the transport of charged species, *i.e.* bulk processes, can be described as a one-dimensional linear diffusion process.<sup>48</sup> This is a limitation for the description of 3D hierarchical structures that display intercalation. Deconvolution can in principle be improved by including other transport mechanisms.<sup>31,32</sup> However, increasing the number of parameters makes the modelling complex and can potentially lead to non-unique solutions.<sup>33</sup>

The system studied here does not resemble any of the previous macroscale configurations used for MXene pseudocapacitance studies and enables measurement of discrete monolayer flakes without confounding effects that might arise from the 3D electrode architecture/organisation. Thus, enabling the unambiguous assignment of the observed charging behaviour to surface processes, going well beyond approaches that involve mathematical deconvolution with a multi-parameter model. The results of our study show that by establishing electrochemical contact with only a small portion (approx. 3 %) of the basal plane of a single monolayer MXene flake, the pseudocapacitive response observed is equivalent to that from the entire MXene flake. Assuming that pseudocapacitive behaviour in MXene monolayers is associated with protonation/deprotonation, our results suggest that protons are transported from/to the electrochemical cell over the entire MXene flake. Therefore, while our unique SECCM configuration isolates the surface processes and restricts ion-intercalation mechanisms, the proton transport effects are still found to dominate the capacitive response. Significantly, we conducted our measurements at 0.5 V/s, thus probing timescales where prior MXene descriptions stated that the response should be dominated by surface capacitive storage.<sup>33</sup> Our results, however, identify that proton transport is likely to be present even at very short timescales, where prior studies described the capacitive response of MXene as independent of the ion transport processes.

We speculate that the pseudocapacitive charging (*i.e.*  $-O \rightarrow -OH$  surface protonation) outside the wetted area arises from the surface transport of protons in a water adlayer on the MXene flake surface.<sup>47,49,52</sup> Although we cannot exclude other possible proton transport mechanisms, such as proton transfer between functional groups ( $-O$  and  $-OH$  groups), proton tunnelling through the MXene layer or proton conduction through structural defects in the MXene.<sup>56</sup> Our measurements were conducted without atmospheric control, (approx. humidity of  $47 \pm 4$  %RH, see Appendix

Figure A1 and Methods section 6.3), and it is likely that a thin water layer is present on the MXene surface that would facilitate proton transport. The AFM step-height profile of  $\text{Ti}_3\text{C}_2\text{T}_x$  flakes suggests the presence of water adsorbed on its surface and/or water trapped between the carbon substrate and the  $\text{Ti}_3\text{C}_2\text{T}_x$  flake (see Section 6.4.3). The timescale of the cyclic voltammograms obtained in this work is on the order of 1 s; assuming surface diffusion of protons in a thin water layer, this would suggest that diffusion coefficients  $>10^{-8} \text{ cm}^2 \text{ s}^{-1}$  would be needed to access a  $10 \mu\text{m}^2$  flake surface during the electrochemical measurements. This is not an unreasonable diffusion rate, based on studies of proton dynamics at hydrophilic surfaces that reveal high proton mobility/diffusivity via water-assisted and anhydrous mechanisms.<sup>24,74-76</sup>

Our results suggest that proton conduction on the MXene surface may contribute to the outstanding performance often observed in MXene-based supercapacitors, whereby even limited percolation contacts might be sufficient to achieve very high specific gravimetric capacitances. The proton transport across the MXene surface at diffusion coefficients  $>10^{-8} \text{ cm}^2 \text{ s}^{-1}$  would act as a complementary mechanism supporting the retention of capacitive behaviour observed at ultrafast charging/discharging rates ( $>1000\text{V/s}$ ) for three-dimensional networks.<sup>15</sup> Finally, these results suggest that MXene-based supercapacitors need to account for short time proton transport contributions, complementing the proton intercalation/deintercalation into MXene interlayer spaces.

## 6.6 Conclusion

MXenes exhibit excellent performance as electrochemical supercapacitors due to their high specific surface area, metallic-like conductivity, and pseudocapacitive response. The development of new super/pseudo-capacitor technology depends on a precise understanding of the physical nature of the electrochemical charge storage mechanism. However, there were no prior nano-electrochemical studies that evaluated the pseudocapacitive behaviour of monolayer MXene flakes.

Using SECCM, I performed electrochemical mappings over monolayer MXene ( $\text{Ti}_3\text{C}_2\text{T}_x$ ) flakes in acidic media with  $0.3 \mu\text{m}^2$  resolution. Coupling nanoscale electrochemical measurements with surface structure determinations allows to calculate the gravimetric capacitance of individual monolayer  $\text{Ti}_3\text{C}_2\text{T}_x$  flakes. The capacitance values shown in this chapter confirm that the edges of the flakes do not contribute to an enhanced capacitive response. More importantly, this approach revealed extraordinarily high gravimetric capacitance values, up to 40 times larger than previously reported for  $\text{Ti}_3\text{C}_2\text{T}_x$ , using macroscale electrodes. We suggest that thanks to the unique experimental configuration implemented in this work, for the first time it can be demonstrated that the capacitive response extends beyond the area of on monolayer  $\text{Ti}_3\text{C}_2\text{T}_x$  MXene wetted by the electrolyte.

## Authorship Statement

This chapter is an extended adaptation of the work presented in the publication:

*Isolation of pseudocapacitive surface processes at monolayer MXene flakes reveals delocalized charging mechanism*

Marc Brunet Cabré, Dahnan Spurling, Pietro Martinuz, Mariangela Longhi, Christian Schröder, Hugo Nolan, Valeria Nicolosi, Paula E. Colavita, Kim McKelvey \*

*Nature Communications*, 2023, 14, 374

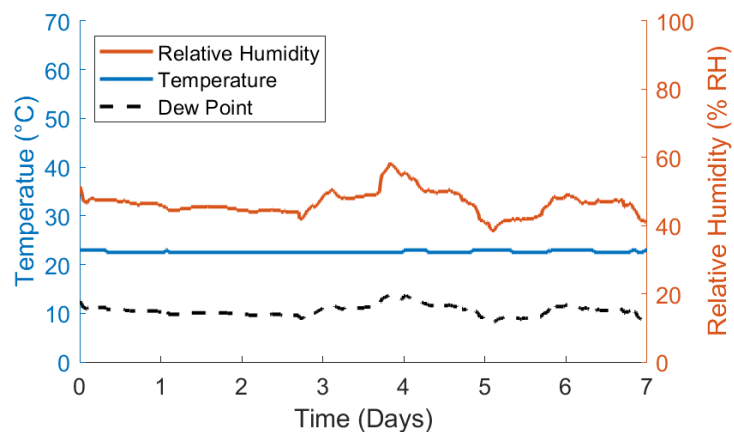
This publication is reproduced in the appendix section of the thesis.

Electrochemical experiments, morphological characterisation, data analysis and manuscript writing were carried out by the first author of the publication, M.B.C, as part of the PhD thesis presented here.

Co-authors D.S. manufacture the 2D MXenes and perform spectroscopical characterisation. P.M contributed to the optimization processes of sample preparation and the obtention of preliminary electrochemical experiments. C.S. and H.N. manufactured the carbon substrates. V.N. and M.L. provided guidance, logistics and facilities which were essential to carry out this project.

P.E.C. and K.M. led the experimental design for the acquisition of electrochemical data, provided guidance over data analysis and results discussion, and contributed to manuscript drafting and correction.

## Appendix



**Figure A1:** Ambient conditions inside the Faradaic cage where AFM and SECCM measurement were performed. Temperature (blue), humidity (orange) and dew point (black dotted line) recorded inside the faradic cage for 7 days. The temperature is very stable with a mean value of  $22.6 \pm 0.2$  °C. Humidity values oscillate between 40 – 60 % RH.



## References

- 1 Kalair, A., Abas, N., Saleem, M. S., Kalair, A. R. & Khan, N. Role of energy storage systems in energy transition from fossil fuels to renewables. *Energy Storage* **3** (2020). <https://doi.org/10.1002/est2.135>
- 2 Bard, A. J. & Faulkner, L. R. *Electrochemical methods: fundamentals and applications*. 2nd edn, (John Wiley & Sons, Inc., 2001).
- 3 Shao, Y. *et al.* Design and Mechanisms of Asymmetric Supercapacitors. *Chem. Rev.* **118**, 9233-9280 (2018). <https://doi.org/10.1021/acs.chemrev.8b00252>
- 4 Raza, W. *et al.* Recent advancements in supercapacitor technology. *Nano Energy* **52**, 441-473 (2018). <https://doi.org/10.1016/j.nanoen.2018.08.013>
- 5 Liu, T. Y., Zhang, F., Song, Y. & Li, Y. Revitalizing carbon supercapacitor electrodes with hierarchical porous structures. *J. Mater. Chem. A* **5**, 17705-17733 (2017). <https://doi.org/10.1039/c7ta05646j>
- 6 Pottathara, Y. B., Tiyyagura, H. R., Ahmad, Z. & Sadasivuni, K. K. Graphene Based Aerogels: Fundamentals and Applications as Supercapacitors. *J Energy Storage* **30** (2020). <https://doi.org/10.1016/j.est.2020.101549>
- 7 Fleischmann, S. *et al.* Pseudocapacitance: From Fundamental Understanding to High Power Energy Storage Materials. *Chem. Rev.* **120**, 6738-6782 (2020). <https://doi.org/10.1021/acs.chemrev.0c00170>
- 8 Costentin, C. & Saveant, J. M. Energy storage: pseudocapacitance in prospect. *Chem. Sci.* **10**, 5656-5666 (2019). <https://doi.org/10.1039/c9sc01662g>
- 9 Banda, H. *et al.* High-Capacitance Pseudocapacitors from Li<sup>+</sup> Ion Intercalation in Nonporous, Electrically Conductive 2D Coordination Polymers. *J. Am. Chem. Soc.* **143**, 2285-2292 (2021). <https://doi.org/10.1021/jacs.0c10849>
- 10 Bi, S. *et al.* Molecular understanding of charge storage and charging dynamics in supercapacitors with MOF electrodes and ionic liquid electrolytes. *Nat. Mater.* **19**, 552-558 (2020). <https://doi.org/10.1038/s41563-019-0598-7>
- 11 Wu, H. *et al.* Graphene based architectures for electrochemical capacitors. *Energy Storage Mater.* **5**, 8-32 (2016). <https://doi.org/10.1016/j.ensm.2016.05.003>
- 12 Nan, J. *et al.* Nanoengineering of 2D MXene-Based Materials for Energy Storage Applications. *Small* **17**, e1902085 (2021). <https://doi.org/10.1002/sml.201902085>
- 13 Nguyen, T. P. *et al.* MXenes: Applications in electrocatalytic, photocatalytic hydrogen evolution reaction and CO<sub>2</sub> reduction. *Molecular Catalysis* **486** (2020). <https://doi.org/10.1016/j.mcat.2020.110850>
- 14 Rozmysłowska, A. Colloidal Properties and Stability of 2D Ti<sub>3</sub>C<sub>2</sub> and Ti<sub>2</sub>C MXenes in Water. *Int. J. Electrochem*, 10837-10847 (2018). <https://doi.org/10.20964/2018.11.56>
- 15 Li, K. *et al.* 3D MXene Architectures for Efficient Energy Storage and Conversion. *Adv. Funct. Mater.* **30** (2020). <https://doi.org/10.1002/adfm.202000842>

- 16 Zhu, Q. Z., Li, J. P., Simon, P. & Xu, B. Two-dimensional MXenes for electrochemical capacitor applications: Progress, challenges and perspectives. *Energy Storage Mater.* **35**, 630-660 (2021). <https://doi.org/10.1016/j.ensm.2020.11.035>
- 17 Li, J., Wang, H. & Xiao, X. Intercalation in Two-Dimensional Transition Metal Carbides and Nitrides (MXenes) toward Electrochemical Capacitor and Beyond. *Energy Environ. Mater.* **3**, 306-322 (2020). <https://doi.org/10.1002/eem2.12090>
- 18 Lukatskaya, M. R. *et al.* Ultra-high-rate pseudocapacitive energy storage in two-dimensional transition metal carbides. *Nature Energy* **2** (2017). <https://doi.org/10.1038/nenergy.2017.105>
- 19 Mu, X. P. *et al.* Revealing the Pseudo-Intercalation Charge Storage Mechanism of MXenes in Acidic Electrolyte. *Adv. Funct. Mater.* **29** (2019). <https://doi.org/10.1002/adfm.201902953>
- 20 Shao, H. *et al.* Unraveling the Charge Storage Mechanism of  $Ti_3C_2T_x$  MXene Electrode in Acidic Electrolyte. *ACS Energy Lett.* **5**, 2873-2880 (2020). <https://doi.org/10.1021/acseenergylett.0c01290>
- 21 Hu, M. *et al.* Emerging 2D MXenes for supercapacitors: Status, challenges and prospects. *Chem. Soc. Rev.* **49**, 6666-6693 (2020). <https://doi.org/10.1039/d0cs00175a>
- 22 Zhan, C. *et al.* Understanding the MXene Pseudocapacitance. *J. Phys. Chem. Lett.* **9**, 1223-1228 (2018). <https://doi.org/10.1021/acs.jpcllett.8b00200>
- 23 Al-Temimy, A. *et al.* Spatially resolved X-ray absorption spectroscopy investigation of individual cation-intercalated multi-layered  $Ti_3C_2T_x$  MXene particles. *Appl. Surf. Sci.* **530** (2020). <https://doi.org/10.1016/j.apsusc.2020.147157>
- 24 Sun, Y. *et al.* Proton Redox and Transport in MXene-Confined Water. *ACS Appl. Mater. Interfaces* **12**, 763-770 (2020). <https://doi.org/10.1021/acsaem.9b18139>
- 25 Wang, L. *et al.* Origin of theoretical pseudocapacitance of two-dimensional supercapacitor electrodes  $Ti_3C_2T_2$  (T = bare, O, S). *J. Mater. Chem. A* **7**, 16231-16238 (2019). <https://doi.org/10.1039/c9ta03529j>
- 26 Ji, X. *et al.* Probing the electrochemical capacitance of MXene nanosheets for high-performance pseudocapacitors. *Phys. Chem. Chem. Phys.* **18**, 4460-4467 (2016). <https://doi.org/10.1039/c5cp07311a>
- 27 Goff, J. M., Vieira, F. M. D., Keilbart, N. D., Okada, Y. & Dabo, I. Predicting the Pseudocapacitive Windows for MXene Electrodes with Voltage-Dependent Cluster Expansion Models. *Acs Applied Energy Materials* **4**, 3151-3159 (2021). <https://doi.org/10.1021/acsaem.0c02910>
- 28 Maleski, K., Ren, C. E., Zhao, M. Q., Anasori, B. & Gogotsi, Y. Size-Dependent Physical and Electrochemical Properties of Two-Dimensional MXene Flakes. *ACS Appl. Mater. Interfaces* **10**, 24491-24498 (2018). <https://doi.org/10.1021/acsaem.8b04662>
- 29 Kim, H. S. *et al.* Oxygen vacancies enhance pseudocapacitive charge storage properties of  $MoO(3-x)$ . *Nat. Mater.* **16**, 454-460 (2017). <https://doi.org/10.1038/nmat4810>
- 30 Wang, J., Polleux, J., Lim, J. & Dunn, B. Pseudocapacitive contributions to electrochemical energy storage in  $TiO_2$  (anatase) nanoparticles. *J. Phys. Chem. C* **111**, 14925-14931 (2007). <https://doi.org/10.1021/jp074464w>

- 31 Dupont, M. F. & Donne, S. W. A Step Potential Electrochemical Spectroscopy Analysis of Electrochemical Capacitor Electrode Performance. *Electrochim. Acta* **167**, 268-277 (2015). <https://doi.org/10.1016/j.electacta.2015.03.137>
- 32 Gibson, A. J. & Donne, S. W. A step potential electrochemical spectroscopy (SPECS) investigation of anodically electrodeposited thin films of manganese dioxide. *J. Power Sources* **359**, 520-528 (2017). <https://doi.org/10.1016/j.jpowsour.2017.05.082>
- 33 Shao, H., Lin, Z. F., Xu, K., Taberna, P. L. & Simon, P. Electrochemical study of pseudocapacitive behavior of  $\text{Ti}_3\text{C}_2\text{T}_x$  MXene material in aqueous electrolytes. *Energy Storage Mater.* **18**, 456-461 (2019). <https://doi.org/10.1016/j.ensm.2018.12.017>
- 34 Ardizzone, S., Fregonara, G. & Trasatti, S. Inner and Outer Active Surface of RuO<sub>2</sub> Electrodes. *Electrochim. Acta* **35**, 263-267 (1990). [https://doi.org/10.1016/0013-4686\(90\)85068-X](https://doi.org/10.1016/0013-4686(90)85068-X)
- 35 Conway, B. & Kannangara, D. Zinc Oxidation and Redeposition Processes in Aqueous Alkali and Carbonate Solutions: I. pH and Carbonate Ion Effects in Film Formation and Dissolution. *J. Electrochem. Soc.* **134**, 894 (1987).
- 36 Ebejer, N. *et al.* Scanning electrochemical cell microscopy: a versatile technique for nanoscale electrochemistry and functional imaging. *Annu. Rev. Anal. Chem.* **6**, 329-351 (2013). <https://doi.org/10.1146/annurev-anchem-062012-092650>
- 37 Alhabeab, M. *et al.* Guidelines for Synthesis and Processing of Two-Dimensional Titanium Carbide ( $\text{Ti}_3\text{C}_2\text{T}_x$  MXene). *Chem. Mater.* **29**, 7633-7644 (2017). <https://doi.org/10.1021/acs.chemmater.7b02847>
- 38 Bentley, C. L. *et al.* Electrochemical maps and movies of the hydrogen evolution reaction on natural crystals of molybdenite ( $\text{MoS}_2$ ): basal vs. edge plane activity. *Chem. Sci.* **8**, 6583-6593 (2017). <https://doi.org/10.1039/c7sc02545a>
- 39 Brunet Cabré, M., Paiva, A. E., Velický, M., Colavita, P. E. & McKelvey, K. Electrochemical kinetics as a function of transition metal dichalcogenide thickness. *Electrochim. Acta* **393** (2021). <https://doi.org/10.1016/j.electacta.2021.139027>
- 40 Brunet Cabre, M. *et al.* Isolation of pseudocapacitive surface processes at monolayer MXene flakes reveals delocalized charging mechanism. *Nat. Commun.* **14**, 374 (2023). <https://doi.org/10.1038/s41467-023-35950-1>
- 41 Borghetti, M., Serpelloni, M., Sardini, E., Spurling, D. & Nicolosi, V. Temperature influence on  $\text{Ti}_3\text{C}_2\text{T}_x$  lines printed by aerosol jet printing. *Sens. Actuator A Phys.* **332**, 113185-113185 (2021). <https://doi.org/10.1016/j.sna.2021.113185>
- 42 Daviddi, E., Gonos, K. L., Colburn, A. W., Bentley, C. L. & Unwin, P. R. Scanning Electrochemical Cell Microscopy (SECCM) Chronopotentiometry: Development and Applications in Electroanalysis and Electrocatalysis. *Anal. Chem.* **91**, 9229-9237 (2019). <https://doi.org/10.1021/acs.analchem.9b02091>
- 43 Sarycheva, A. & Gogotsi, Y. Raman Spectroscopy Analysis of the Structure and Surface Chemistry of  $\text{Ti}_3\text{C}_2\text{T}_x$  MXene. *Chem. Mater.* **32**, 3480-3488 (2020). <https://doi.org/10.1021/acs.chemmater.0c00359>
- 44 Wang, X. *et al.* Atomic-scale recognition of surface structure and intercalation mechanism of  $\text{Ti}_3\text{C}_2\text{T}_x$ . *J. Am. Chem. Soc.* **137**, 2715-2721 (2015). <https://doi.org/10.1021/ja512820k>

- 45 Ghidui, M., Lukatskaya, M. R., Zhao, M. Q., Gogotsi, Y. & Barsoum, M. W. Conductive two-dimensional titanium carbide 'clay' with high volumetric capacitance. *Nature* **516**, 78-81 (2014). <https://doi.org/10.1038/nature13970>
- 46 Halim, J. *et al.* Transparent Conductive Two-Dimensional Titanium Carbide Epitaxial Thin Films. *Chem. Mater.* **26**, 2374-2381 (2014). <https://doi.org/10.1021/cm500641a>
- 47 Cai, M. *et al.* Ti<sub>3</sub>C<sub>2</sub>T<sub>x</sub>/PANI composites with tunable conductivity towards anticorrosion application. *Chem. Eng. J.* **410**, 128310-128310 (2021). <https://doi.org/10.1016/j.cej.2020.128310>
- 48 Lipatov, A. *et al.* Elastic properties of 2D Ti<sub>3</sub>C<sub>2</sub>T<sub>x</sub> MXene monolayers and bilayers. *Sci. Adv.* **4**, eaat0491 (2018). <https://doi.org/10.1126/sciadv.aat0491>
- 49 Lipatov, A. *et al.* Effect of Synthesis on Quality, Electronic Properties and Environmental Stability of Individual Monolayer Ti<sub>3</sub>C<sub>2</sub> MXene Flakes. *Adv. Electron. Mater.* **2** (2016). <https://doi.org/10.1002/aelm.201600255>
- 50 Miranda, A., Halim, J., Lorke, A. & Barsoum, M. W. Rendering Ti<sub>3</sub>C<sub>2</sub>T<sub>x</sub> (MXene) monolayers visible. *Mater. Res. Lett.* **5**, 322-328 (2017). <https://doi.org/10.1080/21663831.2017.1280707>
- 51 Shearer, C. J., Slattery, A. D., Stapleton, A. J., Shapter, J. G. & Gibson, C. T. Accurate thickness measurement of graphene. *Nanotechnology* **27**, 125704 (2016). <https://doi.org/10.1088/0957-4484/27/12/125704>
- 52 Mashtalir, O. *et al.* The effect of hydrazine intercalation on the structure and capacitance of 2D titanium carbide (MXene). *Nanoscale* **8**, 9128-9133 (2016). <https://doi.org/10.1039/c6nr01462c>
- 53 Ochedowski, O., Bussmann, B. K. & Schleberger, M. Graphene on mica - intercalated water trapped for life. *Sci. Rep.* **4**, 6003 (2014). <https://doi.org/10.1038/srep06003>
- 54 Coy Diaz, H., Addou, R. & Batzill, M. Interface properties of CVD grown graphene transferred onto MoS<sub>2</sub>(0001). *Nanoscale* **6**, 1071-1078 (2014). <https://doi.org/10.1039/c3nr03692h>
- 55 Zhang, C. J. *et al.* Additive-free MXene inks and direct printing of micro-supercapacitors. *Nat. Commun.* **10**, 1795 (2019). <https://doi.org/10.1038/s41467-019-09398-1>
- 56 Sang, X. *et al.* Atomic Defects in Monolayer Titanium Carbide (Ti<sub>3</sub>C<sub>2</sub>T<sub>x</sub>) MXene. *ACS Nano* **10**, 9193-9200 (2016). <https://doi.org/10.1021/acsnano.6b05240>
- 57 Halim, J. *et al.* X-ray photoelectron spectroscopy of select multi-layered transition metal carbides (MXenes). *Appl. Surf. Sci.* **362**, 406-417 (2016). <https://doi.org/10.1016/j.apsusc.2015.11.089>
- 58 Liu, F. *et al.* Preparation of Ti<sub>3</sub>C<sub>2</sub> and Ti<sub>2</sub>C MXenes by fluoride salts etching and methane adsorptive properties. *Appl. Surf. Sci.* **416**, 781-789 (2017). <https://doi.org/10.1016/j.apsusc.2017.04.239>
- 59 Tang, J. *et al.* Tuning the Electrochemical Performance of Titanium Carbide MXene by Controllable In Situ Anodic Oxidation. *Angew. Chem. Int. Ed. Engl.* **58**, 17849-17855 (2019). <https://doi.org/10.1002/anie.201911604>

- 60 Li, S. *et al.* Ultrathin MXene nanosheets with rich fluorine termination groups realizing efficient electrocatalytic hydrogen evolution. *Nano Energy* **47**, 512-518 (2018). <https://doi.org/10.1016/j.nanoen.2018.03.022>
- 61 Liu, Y. *et al.* Visualization and Quantification of Electrochemical H<sub>2</sub> Bubble Nucleation at Pt, Au, and MoS<sub>2</sub> Substrates. *ACS Sens.* **6**, 355-363 (2021). <https://doi.org/10.1021/acssensors.0c00913>
- 62 Liu, Y., Lu, X., Peng, Y. & Chen, Q. Electrochemical Visualization of Gas Bubbles on Superaerophobic Electrodes Using Scanning Electrochemical Cell Microscopy. *Anal. Chem.* **93**, 12337-12345 (2021). <https://doi.org/10.1021/acs.analchem.1c02099>
- 63 Orangi, J. & Beidaghi, M. A Review of the Effects of Electrode Fabrication and Assembly Processes on the Structure and Electrochemical Performance of 2D MXenes. *Adv. Funct. Mater.* **30** (2020). <https://doi.org/10.1002/adfm.202005305>
- 64 Laušević, Z., Apel, P. Y., Krstić, J. B. & Blonskaya, I. V. Porous carbon thin films for electrochemical capacitors. *Carbon* **64**, 456-463 (2013). <https://doi.org/10.1016/j.carbon.2013.07.098>
- 65 Ji, H. *et al.* Capacitance of carbon-based electrical double-layer capacitors. *Nat. Commun.* **5**, 3317 (2014). <https://doi.org/10.1038/ncomms4317>
- 66 Shpigel, N. *et al.* In Situ Monitoring of Gravimetric and Viscoelastic Changes in 2D Intercalation Electrodes. *ACS Energy Lett.* **2**, 1407-1415 (2017). <https://doi.org/10.1021/acsenergylett.7b00133>
- 67 Hu, M. *et al.* Self-assembled Ti<sub>3</sub>C<sub>2</sub>T<sub>x</sub> MXene film with high gravimetric capacitance. *Chem. Commun.* **51**, 13531-13533 (2015). <https://doi.org/10.1039/c5cc04722f>
- 68 Yang, W. *et al.* 3D Printing of Freestanding MXene Architectures for Current-Collector-Free Supercapacitors. *Adv. Mater.* **31**, e1902725 (2019). <https://doi.org/10.1002/adma.201902725>
- 69 Lukatskaya, M. R. *et al.* Probing the Mechanism of High Capacitance in 2D Titanium Carbide Using In Situ X-Ray Absorption Spectroscopy. *Adv. Energy Mater.* **5**, 2-5 (2015). <https://doi.org/10.1002/aenm.201500589>
- 70 Zhan, C. *et al.* Computational Screening of MXene Electrodes for Pseudocapacitive Energy Storage. *J. Phys. Chem. C* **123**, 315-321 (2019). <https://doi.org/10.1021/acs.jpcc.8b11608>
- 71 Wang, X. *et al.* 3D Ti<sub>3</sub>C<sub>2</sub>T<sub>x</sub> aerogels with enhanced surface area for high performance supercapacitors. *Nanoscale* **10**, 20828-20835 (2018). <https://doi.org/10.1039/c8nr06014b>
- 72 Ando, Y., Okubo, M., Yamada, A. & Otani, M. Capacitive versus Pseudocapacitive Storage in MXene. *Adv. Funct. Mater.* **30** (2020). <https://doi.org/10.1002/adfm.202000820>
- 73 Shang, T. X. *et al.* 3D Macroscopic Architectures from Self-Assembled MXene Hydrogels. *Adv. Funct. Mater.* **29** (2019). <https://doi.org/10.1002/adfm.201903960>
- 74 Gennis, R. B. Proton Dynamics at the Membrane Surface. *Biophys. J.* **110**, 1909-1911 (2016). <https://doi.org/10.1016/j.bpj.2016.04.001>

- 75 Herath, M. B., Creager, S. E., Kitaygorodskiy, A. & DesMarteau, D. D. Effect of perfluoroalkyl chain length on proton conduction in fluoroalkylated phosphonic, phosphinic, and sulfonic acids. *J. Phys. Chem. B* **114**, 14972-14976 (2010). <https://doi.org/10.1021/jp107190q>
- 76 Xu, L. & Jiang, D. E. Proton dynamics in water confined at the interface of the graphene-MXene heterostructure. *J. Chem. Phys.* **155**, 234707 (2021). <https://doi.org/10.1063/5.0066835>







# CHAPTER 7

---

Conclusion and Future work

---

## 7.1 Conclusions

The objective of this thesis is to employ advanced nano-electrochemical techniques, such as Scanning Electrochemical Cell Microscopy (SECCM), to explore 2D materials relevant for energy storage and conversion technologies. Additionally, this thesis endeavours to advance the development of nano-electrochemical characterisation techniques and methods.

In Chapter 3, I demonstrated single entity electrochemistry with microsecond temporal resolution by combining a custom transimpedance amplifier with a micropipette SECCM probe. The setup designed allowed for voltammetry and chronoamperometry measurements at a close distance to the current amplifier to minimise connections, input capacitance, and noise levels. Throughout Chapter 3 it is demonstrated the efficacy of the method developed, which could be further used to study other single-entity systems at high resolution bandwidth. For instance, energy conversion studies based on nanomaterial electrocatalysts can benefit from high bandwidth single entity level characterisation to unveil reaction dynamics from recording transient fluctuation in the electrochemical response.

The objective of Chapter 4 was to examine the correlation between the number of layers stacked in two-dimensional transition metal dichalcogenides (2D TMDCs) and the resultant electrochemical response. The findings of the study provided valuable insight into the significance of the band gap in determining the tunnelling barriers that dominate the electron transfer kinetics and the overall electrochemical response for the outer sphere redox species. The findings of the study have implications for the future use of 2D TMDCs in electrochemical systems, such as energy conversion devices. First, it was demonstrated that the way electrical contact is established with 2D TMDCs affects their electrochemical kinetics, which could potentially extend to other semiconductor 2D nanomaterials. The second key finding of the study is the electrochemical observation of a dependence between the number of stacked layers and the properties of electron transfer. Fewer number of layers provide thinner tunnelling barrier of height (few TMDCs stacked layers have larger band gap), while a larger number of stack layers provide thicker tunnelling barrier of smaller height (more TMDCs layers stacked have smaller band gap). Ultimately, the results of Chapter 4 provide information about how the morphology and structure of the 2D TMDCs affect the electrochemical response.

The analysis performed in Chapter 5 builds upon the dataset presented in Chapter 4. The focus of Chapter 5 is to examine the response of anomalous current response points, which were not identified as basal plane in Chapter 4. The results of this analysis highlight the significant impact that nanoscale defects can have on the electrochemical response of seemingly defect-free 2D materials. The study demonstrates that even small defects can greatly alter the overall response, emphasising the need for caution when interpreting electrocatalysis results on 2D TMDCs because

the dominant response may not stem from the material's intrinsic properties, but from the defects present. The defect-generated catalytic centres in 2D materials can be used to produce highly efficient electrocatalysts. Chapter 5 provides a method for the identification of these centres through electrochemical means.

MXenes, particularly  $\text{Ti}_3\text{C}_2\text{T}_x$ , are a 2D material of great interest for use as supercapacitors. To develop new energy storage technologies, it is crucial to have a deep understanding of their physiochemical nature, which was explored in Chapter 6. The examination of single flakes of MXene using SECCM revealed a pseudocapacitive response with delocalised charging, adding to other studies that highlight the dependence of structure and morphology on energy storage efficiency.

Among the different contributions in the study of nanomaterials for energy conversion and energy storage, this thesis broadens the research conducted using SECCM and its methodologies. Along the different chapters, a specific methodology had to be developed according to the experimental demands. SECCM, with over a decade of existence, has established its efficacy in the realm of nano-electrochemistry through numerous high cited publications. Nevertheless, the overall number of SECCM publications is still limited, and so, the methodologies reported are often bound to the specific experimental requirements. A search of the Web of Science database shows that there are only 118 publications related to SECCM (information obtained utilising term “SECCM” on “Topic” search on the 09/02/2023). Then, the four first-author publications produced in the course of this thesis represent more than 3% of the total publications ever conducted using SECCM. The adoption of SECCM technology is expanding as more research groups utilise it. Last year alone, in 2022, 26 articles related to SECCM were published, accounting for 22% of all SECCM publications since 2010. In addition, there has been an increasing commercial interest in SECCM, leading to the development of the first commercially available equipment in the past two years. During my Ph.D., as part of the Prof. McKelvey’s group, I was involved in testing and providing guidance for the development of the first commercial SECCM equipment produced by ParkSystems.

## 7.2 Future work

The previous section presented the thesis contribution and advances in relation to the current state of the art. This section discusses potential future steps for the various research topics covered.

In Chapter 3, the analysis of the noise levels of the custom TIAs revealed increased floor noise levels for higher-bandwidth TIAs. According to our collaborators who designed and manufactured the TIAs, the noise floor difference originates from a design flaw on the TIAs PCB board. The collaborators already corrected this issue and manufactured a new batch of current amplifiers. The experiments on single entities in Chapter 3 also showed that using a printed gold pad as the working electrode is not an effective solution. The printed pad does not guarantee a clean and pristine state of the working electrode surface. To address this problem, the next generation of TIAs has replaced the printed gold pad with a gold ball bond. Therefore, further work includes testing and analysing the performance of the next generation current amplifier by SECCM. The improved noise levels and electrode surface of the next generation TIAs should enable a wide range of single entity electrochemistry experiments, including the study of diffusion and adsorption of nanoparticles, time evolution of nanoscale phases or single bio-analyte, *e.g.* single enzyme, testing.

In Chapter 4 the relation between the number of TMDC stacked layers and electrochemical behaviour was studied using an outer sphere redox probe. However, in the field of energy conversion technologies, 2D TMDCs are frequently used as catalysts for inner sphere reactions, such as the hydrogen evolution reaction. Thus, it would be of great interest to also analyse the inner-sphere and/or catalytic reaction kinetic dependence with the number of TMDC layers. During the thesis, this measurement was attempted but coincided with the lockdown of the COVID-19 pandemic, which resulted in a delay of a few months. Unfortunately, after lockdown, it was not possible to ensure the pristine state of the samples, as they may have been degraded because of exposure to air for a period of months. To achieve an unambiguous isolation of the basal plane electrochemical response, as accomplished in Chapter 4, it is imperative to maintain strict control over the sample condition. Thus, the method implemented requires to precisely identify the points of contact with the pristine base plane and distinguish them from defective points. Future work includes using a fresh batch of 2D TMDC samples to employ the protocol developed in Chapter 4 to evaluate whether inner-sphere and/or electrocatalytic kinetics also display correlation with the number of TDMC stacked layers. It should be noted that the preparation of large-scale basal plane domains of 2D TMDCs on a conductive substrate is a challenging task, as outlined in Chapter 4, and there is no commercially available alternative.

Similarly, the study of kinetically enhanced defects on 2D TMDCs described in Chapter 5 was performed with outer-sphere redox probes. Therefore, future work could involve the electrochemical detection of inner-sphere kinetically enhanced defects on 2D TDMCs. Although a

fresh batch of 2D TMDC samples would ideally be required to ensure a pristine surface state, the degraded samples may still provide valuable information on the required methods, the defect presence, and the electrochemical response characteristics. Preliminary data obtained on the old TMDCs samples have shown that there are individual isolated points and multiple aligned points that display an enhanced hydrogen evolution reaction response. The electrochemical measurements have been complemented with AFM and TERS (tip enhanced Raman spectroscopy) characterisation, which allowed the observation of correlations between enhanced HER response and the presence of morphological features, such as 2D TMDC flake edges and cracks on the flakes. AFM and TERS also revealed that there are current enhance points that cannot be related to any apparent morphological defects, suggesting that there are multiple defects on MoS<sub>2</sub> that could act as catalytic centres for HER enhancement. These preliminary results indicate the applicability of the method developed in Chapter 5 for identifying electrochemically the presence of individual defects that act as electrocatalytic active centres.

Throughout the thesis, the importance of mass transfer processes in relation to the electrochemical response is emphasised, particularly in the context of quantitative determination of kinetic rates. Despite this emphasis, the impact of convective mass transport in SECCM was not considered and no literature discussing the relevance of such effects was found. In general, convective effects are often considered negligible in micro- nano-electrochemical systems due to the fast thermal equilibria offered by the microscale elements immersed in the electrolyte solution. Furthermore, in micro-nanoscale electrochemical systems, diffusive mass transport often plays a more dominant role in comparison to macroscale setups where convective effects are common. However, SECCM has a very different configuration of the different electrochemical elements compared to the traditional microelectrochemical system. First, in SECCM the components are not immersed in a common electrolyte solution, which leads to slower and more complex thermal equilibria. Second, it is expected that the tapered end of the SECCM probe restricts the hemispherical diffusion front to a give cone angle, which will be always smaller compared to the hemispherical diffusion front characteristic of microelectrodes. Third, and most notably, the droplet cell in SECCM is subject to evaporation of the electrolyte solvent, which can cause a flux of solvent toward the pipette aperture and result in thermal drift over the droplet cell and tapered end of the pipette. These differences might raise questions whether the assumption of negligible convection due to the fast thermal stability of microscale systems is applicable to SECCM configuration. Given the absence of literature addressing this topic, it would be of great interest to conduct a study to quantify the impact of convective mass transport on SECCM. The aim would be to determine if there are any conditions where convective transport in SECCM can/cannot be ignored by comparing its contribution to diffusive transport. With that aim, finite element simulations (FEMs) that incorporate both convective and diffusive transport can be implemented to achieve a first prediction. These simulations could then be verified through experimental SECCM studies.

In Chapter 6, the electrochemical response obtained on single MXene flakes indicates that the entire flake can become charged through contact with only a portion of it, but the mechanism behind this delocalised charging remains unclear. The findings of Chapter 6 raise many scientific questions that could be the foundation for future research, such as:

- How does the charging mechanism observed in the SECCM configuration compare to that seen in bulk ensemble electrochemical methods? Is the delocalised charging related to protonation/deprotonation of functional groups across the whole MXene flake surface? Are the oxidation states of Ti centre across the MXene flake affected, as occurs in conventional ensemble-based configurations? Is the charging state homogeneous across the MXene flake?
- How does proton transport (as a charge carrier) occur across the MXene surface? Are protons conducted and/or transported over the MXene surface? Does this relate to a layer of adsorbed water? Do MXene  $T_x$  groups and their protonation state have a role over charge carrier motion?
- If charging occurs at a distance, will a given charging state be retained after contact with the MXene flake is removed?

Further studies are required to answer these and many other interesting questions. Work proceeding from the results presented in Chapter 6 has already been defined with two complementary research lines. First, the combination of SECCM with spatially resolved spectroscopic characterisation using soft transmission X-ray microscopy (STXM) is being explored thanks to international collaboration. The aim of these measurements is to map the oxidation state of titanium across an MXene flake after conducting SECCM (*i.e.*, after only a subregion of the flake has been contacted). The SECCM and STXM combination should provide insight into the extent of the delocalised electrochemical behaviour. A second line of research aims to address the open questions of MXene charging by utilising electrochemical methods that can be performed with current facilities (such as SECCM). For instance, a relatively simple follow up measurement would include SECCM mapping alternating charging and discharging on consecutive points (*i.e.* applying an anodic and cathodic potential step in alternating points). Utilising this simple method would give an indication as to whether charging can be retained upon removing the electrochemical connection and whether charging and discharging can occur by contacting different locations on the flake.

Finally, future efforts can also be directed towards improving accessibility to single entity electrochemistry techniques. As a long-term user of SECCM, I would like to offer the following insight. At the beginning of my thesis, I acquired an understanding of the SECCM methods and because my thesis is devoted to this technique, over the course of four years I became proficient in its use. During my thesis, I had the opportunity to train six potential new users in the SECCM technique. I observed that for new users the learning curve for SECCM is steeper compared to that

of other more common electrochemical, microscopy, or spectroscopic techniques. This was observed even when the new users were trained on the commercially available and more user friendly SECCM equipment from ParkSystems, indicating that induction to a custom-made SECCM equipment would require an even longer learning process. The current state of development of SECCM instrumentation and methodology demands that the user carry out the methodologies with great precision, delicacy, and attention to detail. A crucial aspect of SECCM lies in the role of the user during the operation, who must continually evaluate the validity of the ongoing processes from monitoring the data in real time. This requires a comprehensive understanding of SECCM methods. However, it is unreasonable to expect a profound level of knowledge on SECCM methods from a novice user. As a result, new users often require several tutored sessions before they become (partially) independent. Given the limited number of SECCM users worldwide and its focus on fundamental electrochemical studies, the development of a more user-friendly SECCM technique would be beneficial. Additionally, there are limited number of publications that detail SECCM methodology in a manner that non-experts can easily follow and implement. This highlights the importance of taught methods and tutoring sessions as the primary means of transferring SECCM operation knowledge. However, this should not discourage efforts to make SECCM more accessible to a wider range of research groups. To provide easier access to SECCM and share the insights gained during my thesis, future work could involve publishing an introductory guide to single barrel SECCM methods. Chapter 2 of this thesis, which in some aspects contains an extended description of the SECCM methodology, was written to serve as the initial foundation for this guide.





# APPENDIX

---

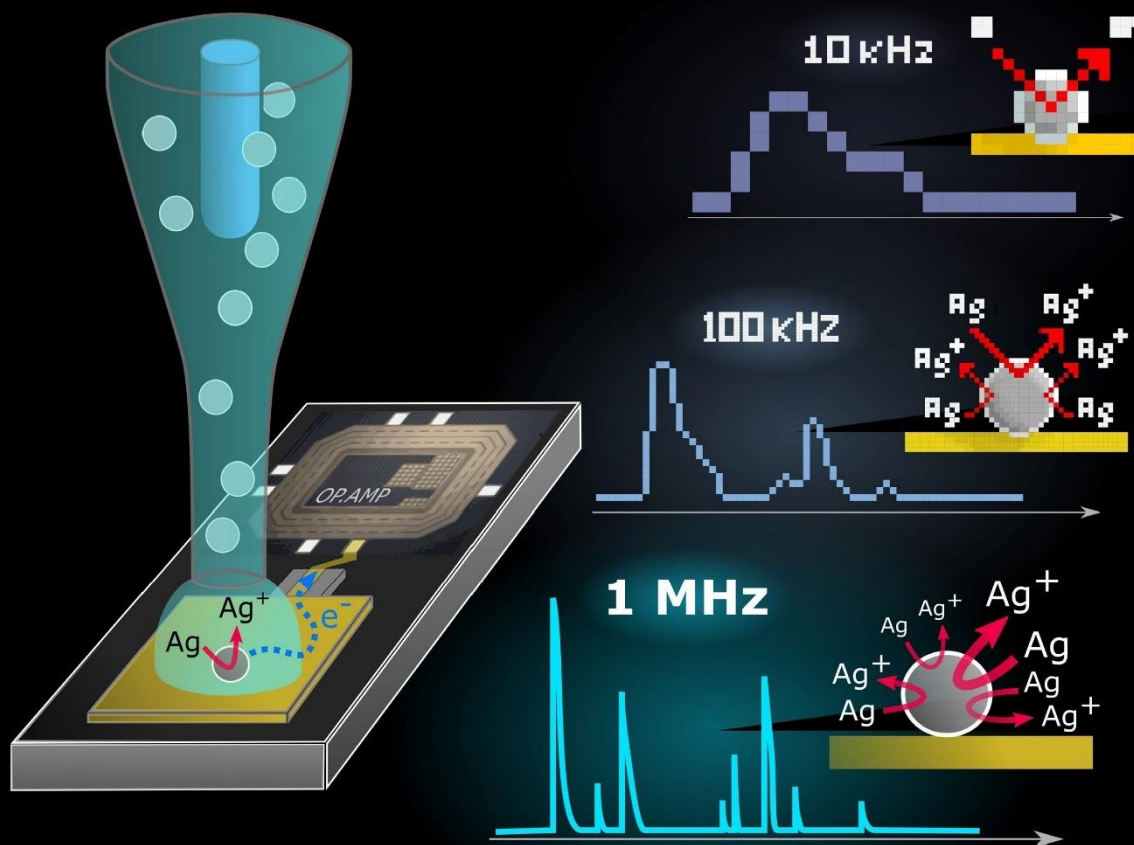
Published work

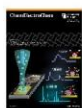
---

**Cover Feature:**

*M. Brunet Cabré et al.*

Microscale Electrochemical Cell on a Custom CMOS Transimpedance Amplifier  
for High Temporal Resolution Single Entity Electrochemistry





# Microscale Electrochemical Cell on a Custom CMOS Transimpedance Amplifier for High Temporal Resolution Single Entity Electrochemistry\*\*

Marc Brunet Cabré,<sup>[a]</sup> Denis Djekic,<sup>[b]</sup> Timothée Romano,<sup>[a]</sup> Nadim Hanna,<sup>[b]</sup> Jens Anders,<sup>[b]</sup> and Kim McKelvey\*<sup>[a, c]</sup>

Stochastic collision electrochemistry requires high-resolution and high-bandwidth current amplification due to the low magnitude and short duration of the current signals. However, increasing the current amplifier bandwidth leads to increased current noise levels, which in turn obscures the current signal generated from stochastic collision electrochemistry experiments. The key to minimizing current noise is an experimental configuration that minimizes the input capacitance to the

current amplifier. Here, we report a new strategy to minimize the input capacitance to a current amplifier by using a movable microscale electrochemical cell, formed at the end of a micropipette using a scanning electrochemical cell microscopy approach, to conduct electrochemical experiments in close proximity (~300 μm) to a transimpedance amplifier. We demonstrated this via electro-oxidation of single Ag nanoparticles detected at a bandwidth of 1 MHz.

## 1. Introduction

Measuring the electrochemical response from single entities, such as single nanoparticles, nanodroplets, enzymes, or cells, can provide fundamental insights into electrochemistry at the nanoscale as well as sample heterogeneity. Conventional ensemble-based electrochemical approaches average the electrochemical response over many entities and in doing so, obscure the effects of sample heterogeneity and the exact relationship between sample structure and electrochemical activity. The key to unravelling these relationships is the development of techniques to restrict electrochemical measurements to single electrochemically active entities. To date, this has been achieved most successfully using stochastic collision electrochemistry.<sup>[1–3]</sup>

In stochastic collision electrochemistry, the sample is dispersed as freely diffusing single entities in solution which collide with the surface of a micro or nanoscale electrode, making electrical contact and catalysing an electrochemical response.<sup>[1,4]</sup> By controlling sample concentration, individual collision events can be separated in time. This approach is also

known as nano-impact electrochemistry<sup>[5,6]</sup> or electrocatalytic amplification<sup>[7,8]</sup> depending on the nature of the electrochemical signal. Examples include hydrogen evolution measured at single Pt nanoparticles and clusters,<sup>[9]</sup> reduction and oxidation of single Ag nanoparticles,<sup>[10,11]</sup> H<sub>2</sub>O<sub>2</sub> oxidation measured on single IrO<sub>x</sub> nanoparticles,<sup>[12,13]</sup> single collisions of toluene-in-water emulsion droplets,<sup>[14]</sup> oxygen reduction at single enzymes,<sup>[15]</sup> or the collision of single red blood cells with an electrode surface.<sup>[16]</sup> The stochastic collision approach to single entity electrochemistry is simple to implement, high resolution, and high throughput. Over 10's of seconds the experimenter can measure 1000's of single entities, providing robust statistics while continuing to work at a single entity level.

However, in stochastic collision electrochemistry (and in nanoscale electrochemistry in general) current signals are on the femtoampere (fA) to picoampere (pA) scale. At these current scales, the response time of the current amplifier (i.e. its bandwidth) often limits the temporal resolution of the measurement.<sup>[17]</sup> The current bandwidth and amplifier scale are intimately linked, with efforts to increase the bandwidth introducing higher current noise, which obscures the target electrochemical signal. For instance, commercial current amplifiers operating with an amplification factor of 1 V/nA (1 GΩ) have bandwidths of 10 kHz–50 kHz, but when moving to a current amplification factor of 1 V/pA (1 TΩ) the bandwidth of the current amplifier can drop to just 1 Hz (for example with the DDPKA-300 from FEMTO).


In addition to generating currents on the fA to pA scale, collisions of a single entity with an electrode surface typically occur over a short duration, for example, the entire duration of an IrO<sub>x</sub> nanoparticle collision is less than 1 ms,<sup>[12,13]</sup> RuO<sub>x</sub> collisions occur over 300 μs,<sup>[18]</sup> and Ag nanoparticle oxidation collisions have a duration of 10's of milliseconds with many individual collision events during this time.<sup>[19]</sup> Thus, the current amplification scale needed for stochastic collision electrochem-

[a] M. Brunet Cabré, T. Romano, Dr. K. McKelvey  
School of Chemistry  
Trinity College Dublin  
Dublin, Ireland

[b] D. Djekic, N. Hanna, Prof. J. Anders  
Institute of Smart Sensors  
University of Stuttgart  
Keplerstraße 7, 70174 Stuttgart, Germany

[c] Dr. K. McKelvey  
School of Chemical and Physical Sciences  
Victoria University of Wellington  
Kelburn, Wellington 6012, New Zealand  
E-mail: kim.mckelvey@vuw.ac.nz

[\*\*] CMOS: Complementary metal–oxide–semiconductor

 Supporting information for this article is available on the WWW under <https://doi.org/10.1002/celec.202001083>

istry measurements can severely limit the temporal resolution and compromises the interpretation of the resulting current signal.

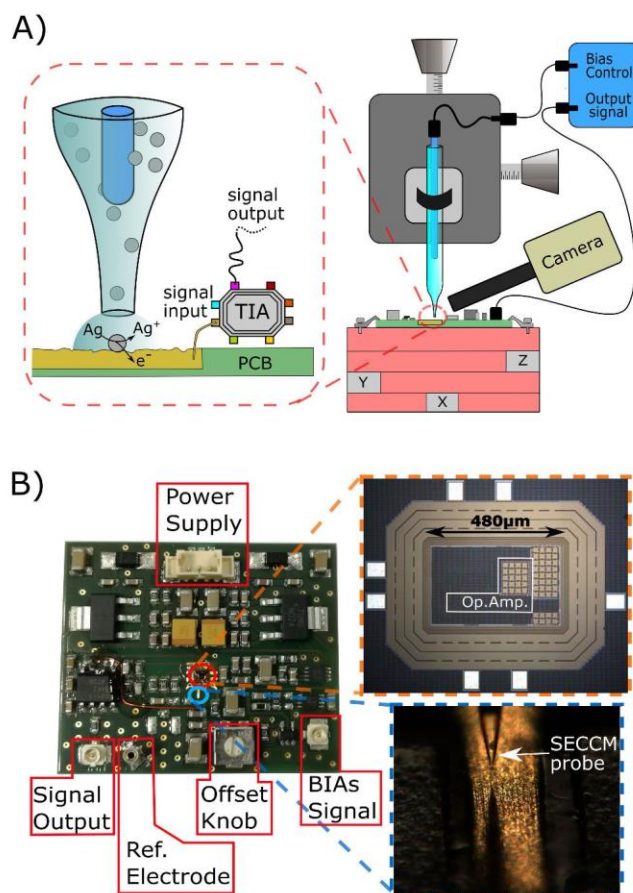
The key to achieving high bandwidth electrochemical measurements is to minimize the input capacitance to the current amplifier.<sup>[20,21]</sup> Input capacitance can depend on the parasitic capacitance of the connection cables, stray capacitances in the current amplifier, as well as capacitance from the electrochemical cell.<sup>[22]</sup> To reduce current noise levels custom current amplifiers have incorporated nanopores and electrodes into the current amplifier chip itself,<sup>[23]</sup> integrated large electrochemical cells onto the current amplifier,<sup>[20]</sup> or fabricated arrays of nanoscale electrodes on the current amplifier.<sup>[24]</sup> Here we report a new approach for conducting stochastic collision electrochemistry experiments at a high bandwidth extending from DC into the MHz range. We use a moveable microscale electrochemical cell (3  $\mu\text{m}$  in diameter) formed at the end of a glass micropipette, resulting in a setup that is similar to scanning electrochemical cell microscopy (SECCM),<sup>[25]</sup> to conduct electrochemical experiments with minimum stray capacitance at the input of the current amplifier. Using a moveable microscale electrochemical cell formed at the end of a glass micropipette allows us to perform the stochastic collision electrochemistry experiments on a gold trace of a printed circuit board, in very close proximity of the contact pad of a custom-designed transimpedance amplifier (TIA), as shown in Figure 1A and B. Thereby, input stray capacitance is minimized and current noise levels are improved.<sup>[26]</sup> In contrast to chip-integrated solutions, our approach does not require the integration of a defined working electrode and the associated sealing of the TIA and PCB surface away from the solution of the electrochemical experiment and can therefore in principle be used with any TIA design.

## 2. Results and Discussion

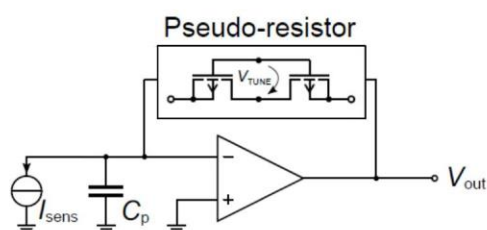
Minimizing current noise levels is critical for detecting the low current signals produced by nano-entities at high bandwidths, and, as discussed above, this requires reducing the input capacitance.<sup>[21]</sup> We have assessed the contribution of the double-layer capacitance at the microscale droplet/Au electrode interface to the overall TIAs noise response. The equivalent circuit for the TIA is shown in Figure 2.<sup>[27]</sup>

Three different TIA configurations, cf. Experimental Section, were used for microscale cells measurements, each with a different bandwidth (80 kHz, 250 kHz, 1 MHz) and always using a sampling frequency of 1 MHz, which is limited by the speed of the data acquisition card. The current noise levels of the TIAs were measured in open circuit (*i.e.* without the microscale electrochemical cell in contact with the Au contact), and the resulting current-time traces are shown in Figure SI1. The integrated RMS current noise in open circuit is 22.2 pA for the 80 kHz current amplifier, 88.8 pA current noise for the 250 kHz current amplifier, and 196 pA for the 1 MHz TIA.

Open circuit noise corresponds to the intrinsic device noise, while the closed-circuit noise, *i.e.* when the microscale electro-



**Figure 1.** A) Schematic of the micropipette-based microscale electrochemical cell measurement directly on the TIA. The PCB board, which contains the TIA, is mounted on a piezoelectric positioner and the micropipette probe is positioned over the working gold electrode. Magnified area represents a silver nanoparticle oxidation experiment on the gold electrode on the PCB board. B) Photo of the PCB board, with the main components labelled. Top-right magnification is a photo of the TIA chip. Bottom-right magnification is a photo of the gold electrode on the PCB with a micropipette positioned a few micrometres of its surface.



**Figure 2.** Equivalent circuit for the custom TIA with pseudo-resistor feedback, including the input capacitance ( $C_p$ ), input current source equivalent to adjacent electrode pad ( $I_{\text{elec}}$ ), internal pseudo-resistor with tuning circuit ( $V_{\text{tune}}$ ) and output voltage ( $V_{\text{out}}$ ).

chemical cell is in contact with the Au contact, is the noise level in operation conditions. Closed-circuit current noise contains contributions from the current amplifier and noise originating in the electrochemical cell, the latter including noise from the double layer capacitance at the droplet-electrode interface. The integrated RMS current noise in closed circuit is 22.9 pA for 80 kHz TIAs, 89.2 pA for 250 kHz TIAs, and 197 pA for 1 MHz

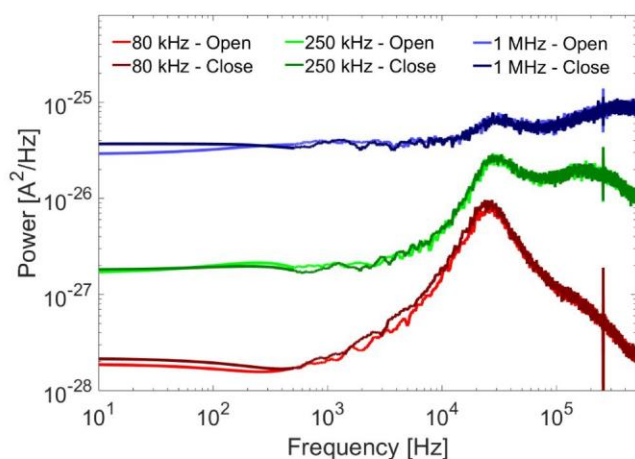
TIA. The difference in noise values obtained for open and close circuit is below 1 pA for all TIAs. The measurements in both open circuit and closed circuit were made without any faradaic current in 10 mM KCl solution. The relatively small increase in RMS noise upon contact of the microscale electrochemical cell indicates that the current noise is dominated by the intrinsic current noise of the current amplifier and not from the electrochemical cell.

The current noise depends on the input capacitance at the opamp input and can be described by Equation (1), for frequencies above the flicker noise dominated region.<sup>[28]</sup>

$$S_{\Delta I} \approx \frac{4kT}{R_{\text{tot}}} + \omega^2 C_p^2 S_{\Delta V} \quad (1)$$

Where  $S_{\Delta I}$  is the input-referred current noise power spectral density (PSD) ( $A^2/Hz$ ) at the TIA's output,  $R_{\text{tot}}$  is the total resistance of the pseudo-resistor feedback (250 M $\Omega$ ),  $k$  is the Boltzman Constant,  $T$  is temperature,  $\omega = 2\pi f$  is the working frequency (Rad/s),  $C_p$  is the input capacitance (F) and  $S_{\Delta V}$  is the intrinsic microchip opamp noise power spectral density ( $V^2/Hz$ ) which has been measured separately (See Figure SI2 for details). The term  $4kT/R_{\text{tot}}$  corresponds to the thermal noise for a resistive feedback TIA, while the  $\omega^2 C_p^2 S_{\Delta V}$  term describes the contribution of the opamp noise, which is shaped by the admittance of the parasitic input capacitance  $\omega C_p$ .

The input-referred current noise is obtained by Fourier analysis of the current traces, and the power spectral density (PSD) of the current traces is displayed in Figure 3 for 80 kHz, 250 kHz, and 1 MHz bandwidth TIAs in both open and close circuit. The curves shown in Figure 3 were smoothed by a third-order Savitzky-Golay filter with a frame length of 1001 points. The resulting filtered curves are representative of the input-referred noise variation, as shown in Figure SI3. The input-referred noise floor (<1 kHz) of 80 kHz TIA is  $2 \cdot 10^{-28} A^2/Hz$ , within the same regime of the expected thermal noise of an equivalent 250 M $\Omega$  resistor feedback amplifier ( $6 \cdot 58^{-29} A^2/Hz$ ). The noise floor increases for higher bandwidth settings due to added noise from the second stage of the amplifier.<sup>[27,28]</sup> Above



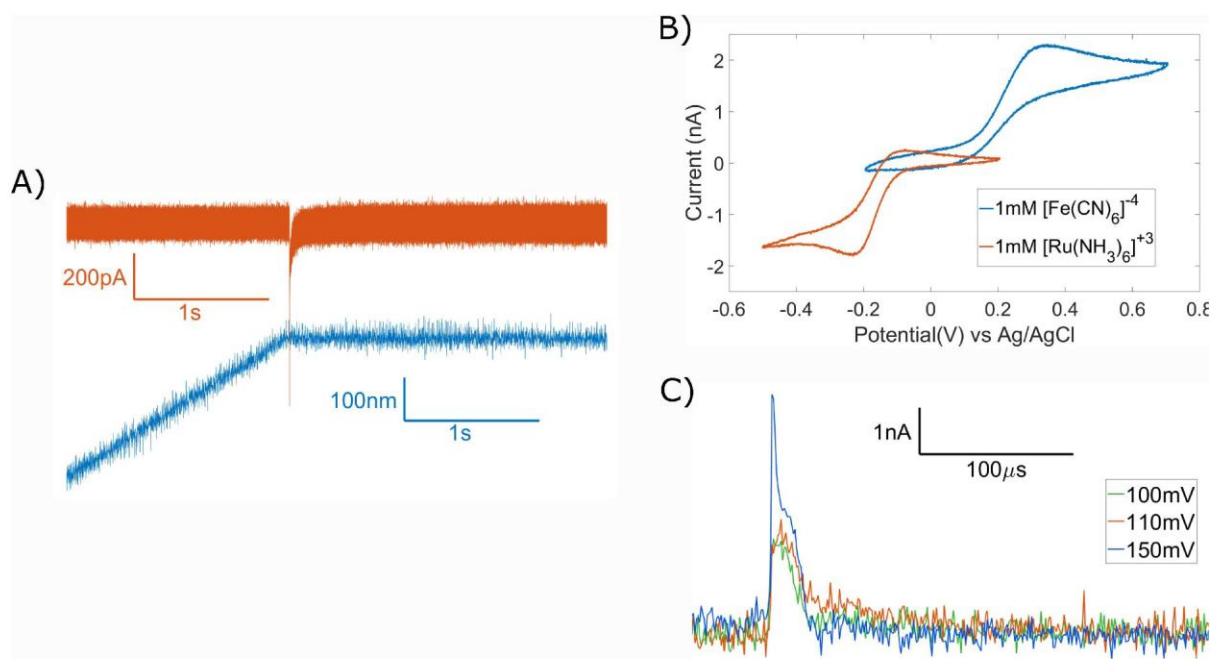
**Figure 3.** Input referred noise in open circuit and close circuit for the 80 kHz, 250 kHz, and 1 MHz TIA.

1 kHz, the input-referred noise is dominated by the capacitive opamp noise (second term of Equation 1) and a noise peak at 20 kHz, which originates from the parasitics of the pseudoresistor.

The square root of the input-referred noise PSD gives the current density (with units  $A/\sqrt{Hz}$ ) and is displayed in Figure SI4. The time-domain signals at the TIA output are corrupted by the integrated input-referred RMS noise multiplied by the effective TIA transimpedance, as is displayed in Figure SI5. The TIAs' output noise obtained are in good agreement (<0.1 pA difference) with the measured RMS noise, see Table SI1 for a comparison.

To calculate the input capacitance, Equation 1 is fitted to the filtered input-referred noise as shown in Figure SI6, where the noise is dominated by pseudoresistor and opamp noise (100 Hz to 5 kHz for 80 kHz TIA, 100 Hz to 10 kHz for 250 kHz TIA, and 100 Hz to 20 kHz for 1 MHz TIA). The input capacitance deduced from fitting is 11.7 pF for the open circuit and 13.7 pF for the closed circuit configuration on the 80 kHz TIA. The open-circuit input capacitance arises from circuitry, connections, and the electrode contact pad capacitance in the TIA design. Therefore, the difference of 2.0 pF for 80 kHz TIAs between closed and open circuit capacitance can be attributed to the electrochemical cell. Electrochemical cell capacitance depends on electrolyte, electrode material and area of electrode in contact with the solution. Therefore the cell capacitance contribution to the input capacitance is expected to be equal regardless of TIAs bandwidth. The electrochemical cell capacitance obtained from fitting of the input-referred noise of the 250 kHz and 1 MHz TIAs are both ca. 2.5 pF (details of the fitting results in Table SI2), although the fitting at 250 kHz and 1 MHz TIAs is less certain due to uneven input-referred noise, as shown in Figure SI6. The droplet diameter is approximately equal to pipette aperture (3.5  $\mu\text{m}$ ).<sup>[25]</sup> and therefore the capacitance per unit area is approximately 20  $\mu\text{F}/\text{cm}^2$  which is in agreement with the expected value for double-layer capacitance on an Au electrode in 10 mM KCl (between 15  $\mu\text{F}/\text{cm}^2$  to 40  $\mu\text{F}/\text{cm}^2$ ).<sup>[29]</sup> This suggests that the capacitance of the electrochemical cell is dominated by the double-layer capacitance of the working electrode. This also demonstrates that in our case the input capacitance, and therefore the current noise, is dominated by the TIA design and not by the electrochemical cell or the electrical double layer at the working electrode surface.

The formation of the electrochemical cell was achieved by landing the droplet at the end of the micropipette on the Au electrode surface, and this was detected via the double-layer formation current upon wetting of the electrode surface by the micropipette droplet. A typical current-time trace and the corresponding vertical position-time trace during a micropipette landing is shown in Figure 4A, indicating the ability to land a micro-scale electrochemical cell directly on an Au electrode next to a TIA input on a PCB. Note that no additional current noise was observed when the nanopipette was moving vertically towards the sample surface, compared to when the nanopipette was held still, indicating that the movement of the nanopipette does not add additional noise sources. To demon-



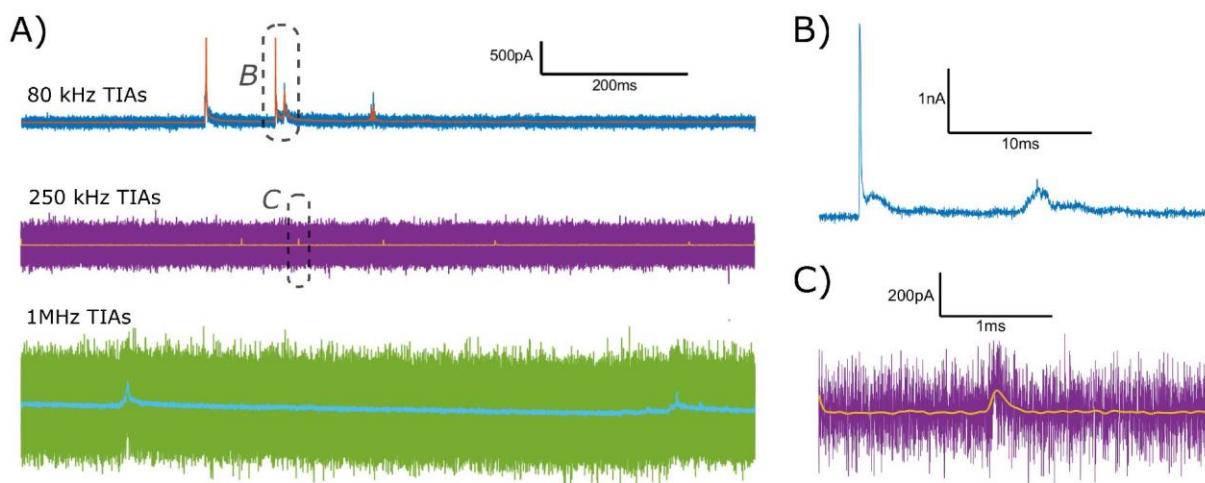
**Figure 4.** A) Concurrent current-time and vertical position-time traces recorded during the approach at 200 nm/s of a 3.5  $\mu\text{m}$  diameter micropipette probe to the Au electrode of an 80 kHz TIA at a potential of  $-0.5$  V vs Ag/AgCl. Upon detection of the double layer charging current the vertical movement of the probe was halted automatically via a control loop running of the FPGA-DAQ card. B) Cyclic voltammetry of conducted with a 400 nm probe on the Au electrode of an 80 kHz TIA with two different redox couples, 1 mM ferrocyanide and 1 mM RuHex, both in 20 mM KCl. C) Current signal response due to double layer formation upon contact of a 400 nm diameter probe droplet containing 10 mM KCl on a 1 MHz current amplifier at three different potentials (vs an Ag/AgCl reference electrode). Note the vertical movement of the probe is immediately halted on the detection of charging current, as demonstrated in part A.

strate the ability to conduct electrochemistry directly on the TIA electrode cyclic voltammetry measurements with 1 mM RuHex and 1 mM ferricyanide redox couples were conducted and the results are shown in Figure 4B. This demonstrates that we have a good contact between the micropipette droplet cell and can conduct electrochemical measurements within 300  $\mu\text{m}$  of the TIA circuit.

As an aside, in Figure 4C the current-time signal recorded for double-layer formation in 10 mM KCl solution upon the very initial contact between the probe droplet and the underlying Au electrode surface at different potentials is shown. Importantly, double layer formation occurs over a very short time period, estimated to be 50  $\mu\text{s}$  in 10 mM solution,<sup>[30]</sup> and therefore is very often obscured due to bandwidth limitations especially on the micro and nanoscales. Using a micropipette approach on a high bandwidth current amplifier enables the initial stages of double-layer formation (and any ion absorption processes that could occur on the initial contact of the solution with an electrode surface) to be measured with unprecedented resolution.

Single entity electrochemistry was demonstrated through the collision and oxidation of single 100 nm diameter Ag nanoparticles on the gold electrode (a process known as nano-impact oxidation). A solution containing freely diffusing Ag nanoparticles was loaded into the micropipette probes, and upon contact between the droplet with the Au electrode surface, the oxidation of the single nanoparticles could be observed when the electrode was held at a sufficiently oxidizing

potential (1 V vs Ag/AgCl). Ag nanoparticles undergo multipeak electro-oxidation, with multiple peaks attributed to Brownian motion of the Ag nanoparticles in solution,<sup>[31,32]</sup> although the exact nature of the multipeak behaviour is still under debate.<sup>[33]</sup> As expected, multiple short nA-scale current spikes were observed when the micropipette probe containing Ag nanoparticles were brought into contact with the Au electrode. Typical current-time traces which display the characteristic current spikes of Ag nanoparticle electro-oxidation on the three different TIA (80 kHz, 250 kHz and 1 MHz) are shown in Figure 5A. A filtered current-time trace is also included, filtered with a bilinear transformed Bessel filter with 10 kHz cut-off frequency and 5<sup>th</sup> order pole to preserve the amplitude responses, emulating a low bandwidth current amplifier response.<sup>[34,35]</sup> The oxidation of Ag nanoparticles on the three different current amplifiers show differences in spike shape and magnitude. We believe this is because Ag nanoparticle oxidation is very sensitive to surface state of the Au electrode and our electrodes have a relatively rough surface topography (see Figure S17 for an AFM image of the Au electrode surface). The Ag nanoparticle oxidation events were detected with the 80 kHz TIA approximately every 20 seconds which last 10's of milliseconds and are constituted by multiple peaks above 1 nA (as shown in Figure 5A and B). The integrated charge over the duration of a collision event is  $\sim 4$  pC, suggesting the single Ag nanoparticle is fully oxidized over the collision event (the theoretical charge for the full oxidation of a single spherical 100 nm diameter Ag nanoparticle is 4.9 pC). With the 250 kHz



**Figure 5.** A) Chronoamperometry of single Ag nanoparticle collision and oxidation for three different bandwidth TIA's (80 kHz, 250 kHz, 1 MHz). The current spikes observed correspond to nanoparticle impact and oxidation. Also is shown the 10 kHz Bessel-filtered signal. B) Magnification of chronoamperometry on 80 kHz TIA, the complex behaviour of the signal is attributed to multiple Ag nanoparticle collision/oxidation events. C) Magnification of chronoamperometry with 250 kHz TIA showing the current generated by a nano-impacts and partial oxidation of a single Ag nanoparticle.

TIA, Ag nanoparticle collision signals form a longer duration event with numerous smaller current spikes (as shown in Figure 5 A and C). In this case, the integrated charge ( $\sim 0.3$  pC) is smaller than the value expected from full nanoparticle oxidation, suggesting only a partial oxidation of the 100 nm diameter Ag nanoparticle. Finally, for the 1 MHz TIA, single long oxidation peaks are observed, with the integrated charge ( $\sim 3.2$  pC) indicating partial oxidation. Blank measurements (i.e. without nanoparticles) are displayed in Figure SI8 and show no current spikes.

### 3. Conclusions

These results demonstrate that using a micro or nanoscale electrochemical cell, defined at the end of a glass pipette, in close proximity of the TIA allows the detection of single nanoparticle electrochemistry with 1 MHz bandwidth. This approach greatly reduces the input stray capacitance of the TIA, which is the dominant capacitance (11.7 pF for the TIA vs. 2 pF for the electrochemical cell). Thereby, the integrated RMS current noise is greatly reduced, allowing for precision current measurements with increased temporal resolutions. In future work, we intend to further improve the design of our TIA and perform additional reductions of the input stray capacitance (as well as a reduction in Au electrode roughness) to allow for quantitative analysis of single entity electrochemistry via this approach.

### Experimental Section

A custom electrochemical scanning probe microscope (EC-SPM) was used to perform the localized microscale electrochemical cell measurements, shown in Figure 1A. Briefly, coarse positioning of the micropipette probe is achieved using manual micropositioners

(XYZ differential adjusters, Thorlabs), while fine displacement of the PCB board is achieved using a XYZ piezoelectric positioner stage (NanoCube P611.3 with LVPZT-Amplifier controller, Physik Instrumente). The EC-SPM is situated in a Faraday cage supported on an optics table. A field-programmable gate array (FPGA) data acquisition card (USB-7855R, National Instruments) running custom LabVIEW code (LabVIEW 2018, National Instruments) was used for data recording and piezoelectric positioner control.

A custom TIA, schematically shown in Figure 1 and whose details have previously been presented,<sup>[27]</sup> was used for the readout of the current signal. The TIA uses active pseudoresistor feedback that allows for large adjustable transimpedance values with minimum stray capacitance for maximum bandwidth. The TIA was fabricated using a commercial silicon-on-insulator (SOI) CMOS technology, which further minimizes stray capacitances and thereby maximizes the achievable bandwidth. The TIA was mounted as bare dies, i.e. without package, on a PCB (5 cm  $\times$  5 cm) that provides all required power supply and signal connections to the TIA chip, as shown in Figure 1B. The TIA's transimpedance value is adjustable via an external resistor on the PCB. A subsequent shelving filter is used to further extend the bandwidth by providing increased gain at high frequencies. Three different TIA settings with bandwidths of 80 kHz, 250 kHz and 1 MHz were used, while the last two feature the bandwidth extension circuit. The electrochemical experiments were performed on a gold trace situated 300  $\mu$ m from the TIA input on the PCB.

A hollow glass capillary pulled to a sharp point in a laser puller (P-2000, Sutter Instruments) was used to form a micropipette. The micropipette was filled with solution and a quasi-reference electrode inserted in the top end (an Ag/AgCl wire in this case) to form a movable microscale electrochemical cell for localized electrochemical measurements, as is used in SECCM measurements.<sup>[25,36–38]</sup> The micropipette tip was positioned within 10's of micrometres of the gold electrode with the help of an external optical camera (PL-B776U, Pixelink), as shown in Figure 1A. The micropipette tip was then approached vertically to the gold electrode surface using the piezoelectric positioners until the electrochemical cell formed between tip and surface. The contact with the gold electrode surface was detected via the capacitive current spike produced by the formation of the electrical double layer on the gold electrode surface. On measuring this signal, the

vertical movement of the pipette was stopped. After positioning of the probe on the electrode surface, either cyclic voltammetry or chronoamperometry experiments were performed. Details of chemicals and reagents available in supporting information S11.

The data algorithm for noise analysis is detailed in a flowchart diagram in supporting information S12.

## Acknowledgements

We acknowledge Trinity College Dublin for a PhD studentship for M.B.C. We acknowledge funding from the Center of Integrated Quantum Science and Technology (IQST).

## Conflict of Interest

The authors declare no conflict of interest.

**Keywords:** stochastic collision · electrochemistry · nanoparticles · SECCM · transimpedance amplifier

- [1] Y.-Y. Peng, R.-C. Qian, M. E. Hafez, Y.-T. Long, *ChemElectroChem* **2017**, *4*, 977–985.
- [2] T. J. Anderson, B. Zhang, *Acc. Chem. Res.* **2016**, *49*, 2625–2631.
- [3] F. T. Patrice, K. Qiu, Y.-L. Ying, Y.-T. Long, *Annu. Rev. Anal. Chem.* **2019**, *12*, 347–370.
- [4] C. Ma, W. Wu, L. Li, S. Wu, J. Zhang, Z. Chen, J.-J. Zhu, *Chem. Sci.* **2018**, *9*, 6167–6175.
- [5] E. Kätelhön, A. Feng, W. Cheng, S. Eloul, C. Batchelor-McAuley, R. G. Compton, *J. Phys. Chem. C* **2016**, *120*, 17029–17034.
- [6] W. Cheng, R. G. Compton, *TrAC Trends Anal. Chem.* **2014**, *58*, 79–89.
- [7] A. J. Bard, H. Zhou, S. J. Kwon, *Isr. J. Chem.* **2010**, *50*, 267–276.
- [8] T. M. Alligrant, R. Dasari, K. J. Stevenson, R. M. Crooks, *Langmuir* **2015**, *31*, 11724–11733.
- [9] J. Kim, J. E. Dick, A. J. Bard, *Acc. Chem. Res.* **2016**, *49*, 2587–2595.
- [10] R. Hao, Y. Fan, B. Zhang, *J. Electrochem. Soc.* **2016**, *163*, H3145–H3151.
- [11] K. McKelvey, D. A. Robinson, N. J. Vitti, M. A. Edwards, H. S. White, *Faraday Discuss.* **2018**, *210*, 189–200.
- [12] M. Zhou, Y. Yu, K. Hu, H. L. Xin, M. V. Mirkin, *Anal. Chem.* **2017**, *89*, 2880–2885.
- [13] S. J. Kwon, F.-R. F. Fan, A. J. Bard, *J. Am. Chem. Soc.* **2010**, *132*, 13165–13167.
- [14] B.-K. Kim, A. Boika, J. Kim, J. E. Dick, A. J. Bard, *J. Am. Chem. Soc.* **2014**, *136*, 4849–4852.
- [15] A. N. Sekretaryova, M. Yu. Vagin, A. P. F. Turner, M. Eriksson, *J. Am. Chem. Soc.* **2016**, *138*, 2504–2507.
- [16] T. L. T. Ho, N. T. T. Hoang, J. Lee, J. H. Park, B.-K. Kim, *Biosens. Bioelectron.* **2018**, *110*, 155–159.
- [17] S.-M. Lu, Y.-Y. Peng, Y.-L. Ying, Y.-T. Long, *Anal. Chem.* **2020**, *92*, 5621–5644.
- [18] M. Kang, D. Perry, Y.-R. Kim, A. W. Colburn, R. A. Lazenby, P. R. Unwin, *J. Am. Chem. Soc.* **2015**, *137*, 10902–10905.
- [19] F. Zhang, M. A. Edwards, R. Hao, H. S. White, B. Zhang, *J. Phys. Chem. C* **2017**, *121*, 23564–23573.
- [20] J. K. Rosenstein, M. Wanunu, C. A. Merchant, M. Drndic, K. L. Shepard, *Nat. Methods* **2012**, *9*, 487–492.
- [21] A. J. W. Hartel, S. Shekar, P. Ong, I. Schroeder, G. Thiel, K. L. Shepard, *Anal. Chim. Acta* **2019**, *1061*, 13–27.
- [22] R. L. Fraccari, M. Carminati, G. Piantanida, T. Leontidou, G. Ferrari, T. Albrecht, *Faraday Discuss.* **2016**, *193*, 459–470.
- [23] M. Carminati, G. Ferrari, A. P. Ivanov, T. Albrecht, M. Sampietro, *Anal. Int. Circ. Sig. Proc.* **2013**, *77*, 333–343.
- [24] S. G. Lemay, C. Laborde, C. Renault, A. Cossetti, L. Selmi, F. P. Widdershoven, *Acc. Chem. Res.* **2016**, *49*, 2355–2362.
- [25] N. Ebejer, A. G. Güell, S. C. S. Lai, K. McKelvey, M. E. Snowden, P. R. Unwin, *Annu. Rev. Anal. Chem.* **2013**, *6*, 329–351.
- [26] C. E. Arcadia, C. C. Reyes, J. K. Rosenstein, *ACS Nano* **2017**, *11*, 4907–4915.
- [27] D. Djekic, M. Ortmanns, G. Fantner, J. Anders, in *2016 IEEE International Symposium on Circuits and Systems (ISCAS)*, **2016**, pp. 842–845.
- [28] D. Djekic, G. Fantner, J. Behrends, K. Lips, M. Ortmanns, J. Anders, in *ESSCIRC 2017–43rd IEEE European Solid State Circuits Conference*, **2017**, pp. 79–82.
- [29] S. Srinivasan, in *Fuel Cells: From Fundamentals to Applications* (Ed.: S. Srinivasan), Springer US, Boston, MA, **2006**, pp. 27–92.
- [30] R. Morrow, D. R. McKenzie, M. M. M. Bilek, *J. Phys. D* **2006**, *39*, 937–943.
- [31] S. M. Oja, D. A. Robinson, N. J. Vitti, M. A. Edwards, Y. Liu, H. S. White, B. Zhang, *J. Am. Chem. Soc.* **2017**, *139*, 708–718.
- [32] D. A. Robinson, Y. Liu, M. A. Edwards, N. J. Vitti, S. M. Oja, B. Zhang, H. S. White, *J. Am. Chem. Soc.* **2017**, *139*, 16923–16931.
- [33] V. Sundaresan, J. W. Monaghan, K. A. Willets, *J. Phys. Chem. C* **2018**, *122*, 3138–3145.
- [34] J. Ustarroz, M. Kang, E. Bullions, P. R. Unwin, *Chem. Sci.* **2017**, *8*, 1841–1853.
- [35] D. A. Robinson, M. A. Edwards, H. Ren, H. S. White, *ChemElectroChem* **2018**, *5*, 3059–3067.
- [36] R. G. Mariano, K. McKelvey, H. S. White, M. W. Kanan, *Science* **2017**, *358*, 1187–1192.
- [37] B. D. B. Aaronson, J. C. Byers, A. W. Colburn, K. McKelvey, P. R. Unwin, *Anal. Chem.* **2015**, *87*, 4129–4133.
- [38] C. L. Bentley, M. Kang, P. R. Unwin, *Curr. Opin. Electrochem.* **2017**, *6*, 23–30.

Manuscript received: August 17, 2020  
 Revised manuscript received: September 21, 2020  
 Accepted manuscript online: September 27, 2020









# Electrochemical kinetics as a function of transition metal dichalcogenide thickness

Marc Brunet Cabré<sup>a</sup>, Aislan Esmeraldo Paiva<sup>a</sup>, Matěj Velický<sup>b,c,d</sup>, Paula E. Colavita<sup>a</sup>, Kim McKelvey<sup>a,e,\*</sup>

<sup>a</sup>School of Chemistry, Trinity College Dublin, Dublin 2, Ireland

<sup>b</sup>School of Physics and Astronomy, University of Manchester, Oxford Road, Manchester M13 9PL, United Kingdom

<sup>c</sup>Department of Chemistry and Chemical Biology, Cornell University, Ithaca, NY 14853, United States

<sup>d</sup>J. Heyrovský Institute of Physical Chemistry, Czech Academy of Sciences, Dolejškova 2155/3, Prague 182 23, Czech Republic

<sup>e</sup>School of Chemical and Physical Sciences, Victoria University of Wellington, Wellington 6012, New Zealand

## ARTICLE INFO

### Article history:

Received 6 May 2021

Revised 8 July 2021

Accepted 29 July 2021

Available online 6 August 2021

### Keywords:

TMDC

2D

Thickness dependence

Electron transfer

Tunneling

SECCM

## ABSTRACT

Two-dimensional transition metal dichalcogenides are used as electroactive materials for electrochemical and electrocatalytic applications. However, it remains unclear how transition metal dichalcogenide thickness influences the electrochemical response measured at its surface. We use scanning electrochemical cell microscopy to assess the electrochemical response of different thicknesses of bottom-contacted MoS<sub>2</sub>, MoSe<sub>2</sub>, WS<sub>2</sub>, and WSe<sub>2</sub> towards the simple outer-sphere redox couple [Ru(NH<sub>3</sub>)<sub>6</sub>]<sup>3+/2+</sup> with sub-micron spatial resolution. A detailed analysis, coupling mass transport and electrochemical kinetics, reveals that the electrochemical response can be described using an electron tunneling barrier, which scales with the band gap of the two-dimensional transition metal dichalcogenide. Our results suggest that interpretation of the electrochemical and electrocatalytic responses on transition metal dichalcogenide-covered electrodes should account for the through-layer electron transport kinetics.

© 2021 Elsevier Ltd. All rights reserved.

## 1. Introduction

The layered crystal structure of transition metal dichalcogenides (TMDCs) enables their mechanical exfoliation into mono- and few-layer two-dimensional (2D) sheets. 2D TMDCs have unique electronic, chemical, and mechanical properties [1], which have been harnessed in electronic, spintronic, photonic, and energy conversion technologies [2–6]. Of particular interest here is the use of 2D TMDCs as active materials for electrochemical and electrocatalytic applications [7–9]. Examples of 2D TMDCs used in electrochemical applications include electrode materials for Li-ion batteries [10], electrodes for supercapacitors [11,12], and electrocatalysts for the hydrogen evolution reaction (HER) [8, 13–16].

The electrochemical response of bulk TMDCs has previously been shown to differ significantly between two distinct surface types: the basal plane and the edge plane [17,18]. Outer-sphere redox mediators, such as hexammineruthenium [Ru(NH<sub>3</sub>)<sub>6</sub>]<sup>3+/2+</sup>, which we consider here, showed enhanced electron transfer kinetics

on the edge plane compared to the basal plane surfaces [17,18]. Similar enhancement of the HER kinetics on the edge planes of MoS<sub>2</sub> crystal compared to its basal plane has also been observed [19].

The preparation of TMDCs in their 2D form typically yields heterogeneous samples with a variable flake size and variable flake geometry. The number of TMDC layers stacked strongly affects the electronic structure and the electrochemistry of the stacked material [7,20,21]. Isolation and electrochemical investigation of specific TMDC thicknesses remain a significant challenge, primarily because it is difficult to prepare homogeneous mono- and few-layer flakes larger than tens of microns in lateral size. This challenge has recently been overcome by a gold-mediated exfoliation of TMDCs, capable of producing millimeter-to-centimeter sized monolayer flakes, combined with localized electrochemical methods [20,22,23].

Scanning electrochemical probe microscopy techniques are particularly well suited to isolate the electrochemical activity of nano- and micro- scale domains [20,24,25]. Scanning electrochemical cell microscopy (SECCM) allows electrochemical mapping with a spatial resolution of tens to hundreds of nanometers using a nanodroplet-electrochemical cell located at the end of a nanopipettes [26–28]. A

\* Corresponding author at: School of Chemical and Physical Sciences, Victoria University of Wellington, Wellington 6012, New Zealand  
E-mail address: [kim.mckelvey@vuw.ac.nz](mailto:kim.mckelvey@vuw.ac.nz) (K. McKelvey).

key advantage of a SECCM approach is the localized measurement at the area of interest, without electrochemical activation of the entire sample surface by its exposure to the electrolyte, as is the case in macroscale electrochemistry or scanning electrochemical microscopy. Furthermore, SECCM can be combined with complementary microscopy approaches, such as atomic force microscopy (AFM), to correlate the electrochemical activity with surface morphology. Unwin *et al.* have previously studied the electrocatalytic activity of bulk TMDCs using SECCM [29,30]. These studies investigated HER on the surface of top-contacted TMDCs ( $\text{MoS}_2$  and  $\text{WS}_2$ ), which showed an enhanced electrocatalytic activity at the edge plane compared to the basal plane. Takahashi *et al.* recently used SECCM with an impressive 20 nm resolution to characterize a few-layer  $\text{MoS}_2$ , as well as heterostructures of  $\text{MoS}_2$  and  $\text{WS}_2$ , confirming an increased HER activity at the edge planes of  $\text{MoS}_2$  but showing no significant differences in HER activity on different number of TMDCs layers [31].

We have previously measured the electrochemical and photoelectrochemical response of 2D  $\text{MoS}_2$  on an insulating substrate towards reduction of the  $[\text{Ru}(\text{NH}_3)_6]^{3+/2+}$  redox couple using a microdroplet electrochemical cell [32]. This showed the significant effect of the number of layers (comparing monolayer, 3–4 layers, 5–10 layers, and bulk) on the electrochemical response, which was also sensitive to illumination. However, the spatial resolution was limited to the size of the microdroplets (20–40  $\mu\text{m}$ ), which made measurements on individual layers challenging. In addition, the electrical contact to the  $\text{MoS}_2$  was made directly at the top layer (top-contacted), which we will show to be a key difference with respect to our current results.

The location of the electrical contact made to the 2D TMDCs strongly influences the electrochemical response we observe. In a top-contact configuration, the electrical contact is made to the top layer of the layered 2D material stack, usually using a conductive adhesive and a metallic wire. In this configuration, only lateral electron transport along the layers occurs due to the high in-plane electrical conductivity through the basal plane [33]. In a bottom-contact configuration, electrical contact is established through the supporting metallic substrate on which the 2D layers are immobilized. In this configuration, electron transport occurs between the metallic substrate and the top 2D layer, where the electrochemical reaction takes place. Therefore, in a bottom-contacted sample, the interlayer electron transport can influence the electrochemical response, as we observe in our studies here.

The HER response of monolayer (1L), bilayer (2L), and trilayer (3L)  $\text{MoS}_2$  in a bottom-contact configuration has recently been reported [25]; these results revealed that the electron transport between the conductive substrate and 2D TMDC could be the rate-limiting step in HER electrocatalysis. Another work on bottom-contacted  $\text{MoS}_2$  suggests that HER electrocatalysis relies on electron hopping between the  $\text{MoS}_2$  layers [21]. However, a recent report of HER on bottom-contacted  $\text{MoS}_2$  did not observe any significant dependence of the electrocatalytic response on the thickness [31]. Therefore, a clear scientific question arises about how do the layer thickness of TMDCs and the bottom-contact affect the electrochemical response [34]. HER is an inner sphere multistep reaction whose overall rate on TMDC electrodes is proposed to depend on chemical steps involving surface-adsorbate intermediates. Therefore, a well-defined outer-sphere redox couple, sensitive only to the density of electronic states, is better suited to assess the dependence of the electrochemical response on the number of TMDC layers.

To that end, we isolated the electrochemical response from the  $[\text{Ru}(\text{NH}_3)_6]^{3+/2+}$  outer-sphere redox couple on monolayer, bilayer, and trilayer  $\text{MoS}_2$ ,  $\text{MoSe}_2$ ,  $\text{WS}_2$ , and  $\text{WSe}_2$ , immobilized on an Au substrate. As shown in Fig. 1A, a Park Systems NX10 instrument was used to perform both optical characterization, determination

of surface morphology by AFM, and the SECCM measurements. We use a SECCM probe with ca. 800 nm spatial resolution to perform the electrochemical mapping, targeting TMDC layers of different thicknesses, as shown in Fig. 1B. The electrical bottom contact is established through the Au electrode substrate, as shown in Fig. 1C. The localized electrochemical response was then correlated with the surface morphology, characterized by optical microscopy and AFM. We used the Gerischer formalism of electron transfer coupled with the diffusional transport of  $[\text{Ru}(\text{NH}_3)_6]^{3+/2+}$  in the SECCM probe to simulate the electrochemical response. We extract the electron transfer kinetics of the  $[\text{Ru}(\text{NH}_3)_6]^{3+/2+}$  redox couple on the different TMDC thicknesses by fitting simulations to experimental data.

## 2. Experimental

Hexaammineruthenium (III) chloride ( $[\text{Ru}(\text{NH}_3)_6]\text{Cl}_3$ ) was purchased from JMC Corporation (South Korea). Potassium chloride (KCl,  $\geq 99.5\%$ ) was obtained from VWR Chemicals (USA). All chemicals were used as received. Distilled water with a resistivity of 18  $\text{M}\Omega\text{ cm}$  was used to prepare the solution of 10 mM KCl and 1.0 mM  $[\text{Ru}(\text{NH}_3)_6]^{3+}$ . All the procedures were carried out at room temperature.

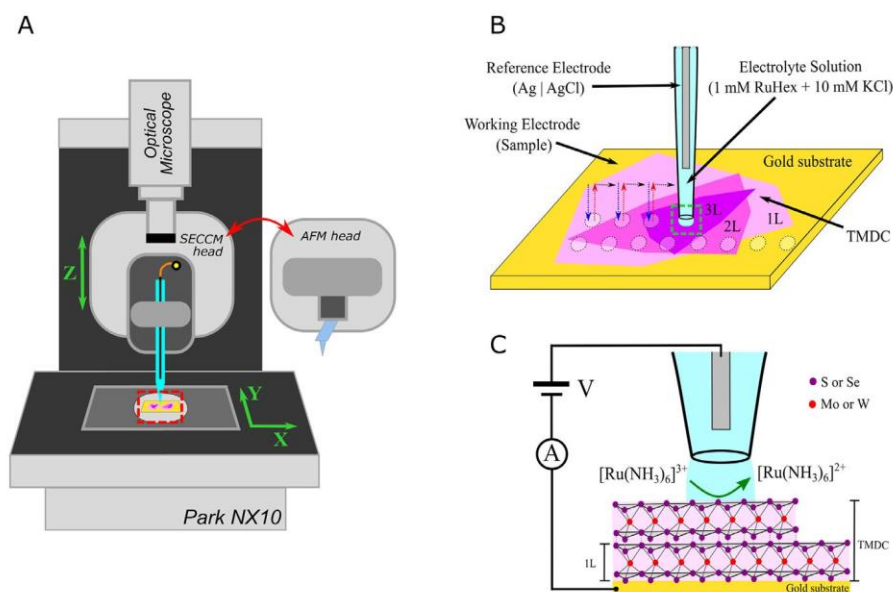
Samples of the transition metal dichalcogenides ( $\text{MX}_2$ , M = Mo or W and X = S or Se) were prepared via mechanical exfoliation of bulk crystals on Au substrates, as previously reported [20]. The bottom-contact electrical connection to the TMDCs was established via the gold substrate.

Optical, AFM, and SECCM measurements were acquired on a Park NX10 (Park Systems, South Korea). The AFM images were obtained in a non-contact mode (NCM) with a PPP-NCHR cantilever type (force constant = 42 N/m, resonance frequency = 330 kHz, Nanosensors).

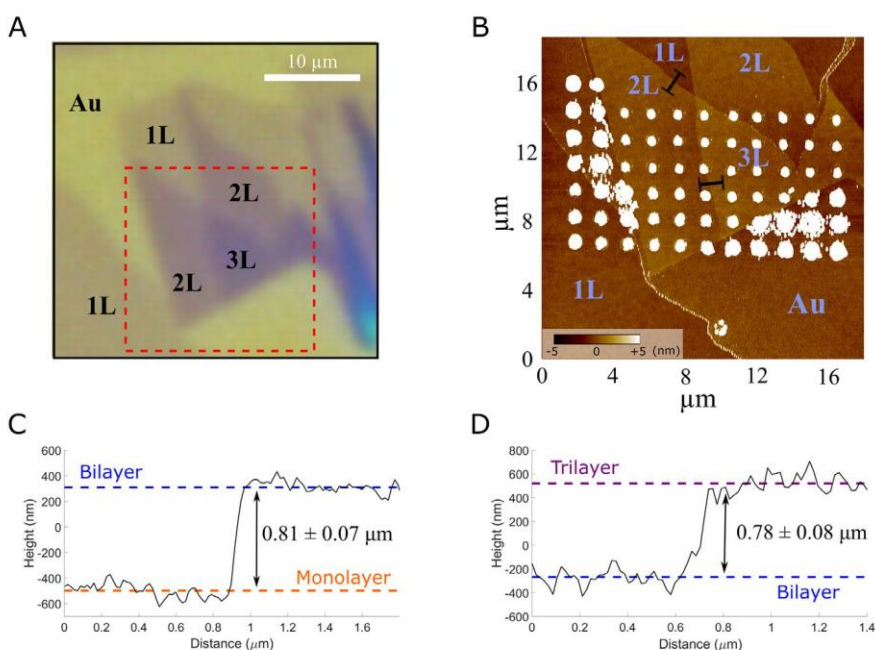
The SECCM probes were made of single-barreled nanopipettes with 300 – 600 nm aperture radius. The nanopipettes were fabricated from single-barreled borosilicate capillaries (1.5 mm O.D and 0.86 mm I.D., BF150-86-7.5, Sutter Instrument, USA) using a P-2000 laser puller (Sutter Instrument, USA). The nanopipette was filled with the solution of 1 mM  $[\text{Ru}(\text{NH}_3)_6]^{3+}$  in 10 mM KCl (sufficient supporting electrolyte for nanoscale electrochemical measurements [35]) using a pipette filler (MicroFil MF34G-5, World Precision Instruments, USA); prior to this, the electrolyte was filtered through a 0.45  $\mu\text{m}$  syringe filter (PTFE membrane, Fisher Scientific, USA). An Ag/AgCl reference electrode was inserted into the top end of the nanopipette.

The SECCM measurements were performed using the ParkSystem NX10 system. The SECCM probe was aligned to the sample area on the surface using the optics and LSVs were then recorded at a preprogrammed squared grid, with individual measurement spots spaced at 1.5  $\mu\text{m}$ . A hopping mode was used in which the probe was approached vertically towards the sample surface at a speed of 0.3  $\mu\text{m/s}$  and a potential of  $-0.8\text{ V}$  until contact between the nanopipette droplet and the surface was established. The contact was detected as the appearance of a double layer charging current and immediate  $[\text{Ru}(\text{NH}_3)_6]^{3+}$  reduction, with a threshold of 5 pA. At this point, the vertical movement of the probe was stopped immediately, and LSVs were recorded in the potential range of  $+0.2\text{ V}$  to  $-0.8\text{ V}$  at a speed of 1 V/s. After completing the measurement, the nanopipette was retracted and moved to the next sample point on the grid.

Simulations of the nanoelectrochemical cell at the end of the SECCM probe were performed in COMSOL Multiphysics (COMSOL 5.2, Sweden). See supplementary information (SI-4) for further details.



**Fig. 1.** (A) Schematic of the ParkSystems NX10 experimental setup, featuring an SECCM probe and an exchangeable AFM probe head (B) Schematic of the SECCM nanopipette probe mapping the electrochemical response of the TMDC surface. (C) Schematic of the nanodroplet-based electrochemical cell (located at the end of an SECCM probe), showing the electrochemical reaction taking place at TMDCs surface, the TMDC structure, and the electrical contact with the Au substrate.



**Fig. 2.** (A) Optical image of MoSe<sub>2</sub> crystals with differing number of layers. (B) AFM image of a region depicted by the red rectangle in part A. The AFM was taken after the SECCM measurements and therefore revealed the electrolyte residues at the areas of contact between the droplet and surface. (C) and (D) line profiles of 1L/2L and 2L/3L boundaries, respectively, taken from areas shown by black lines in (B). Step-height was calculated as the difference of the average terrace height (dashed colored lines).

### 3. Results and discussion

#### 3.1. TMDC thickness characterization

Mechanical exfoliation was used to isolate high-quality 2D flakes of MoS<sub>2</sub>, MoSe<sub>2</sub>, WS<sub>2</sub>, and WSe<sub>2</sub> on an Au substrate [20]. Regions of the Au substrate coated with TMDC flakes of a different number of layers could be distinguished optically, as shown for MoSe<sub>2</sub> in Fig. 2A. The optical contrast and color of the flakes change with the different number of layers of MoSe<sub>2</sub> [36]. Similar

results were obtained for MoS<sub>2</sub>, WS<sub>2</sub>, and WSe<sub>2</sub>, as reported in the Supporting Information (Figs. S1–S3).

The optical images were first used to locate surface regions containing various TMDCs thicknesses (1L–3L) prior to SECCM characterization. AFM was used to corroborate the layer assignment from the step-height profiles obtained after the SECCM measurement, as shown in Fig. 2B. Step-height profiles of 1L/2L and 2L/3L areas displayed in Fig. 2C and 2D yield monolayer thickness of ca. 0.81 nm and 0.78 nm, in agreement with previous monolayer MoS<sub>2</sub> estimates from AFM (~0.85 nm) [37]. The step-height from

Au to 1L could not be clearly determined due to the roughness of the gold surface. AFM step-height profiles for the MoS<sub>2</sub>, MoSe<sub>2</sub>, and WSe<sub>2</sub> samples are displayed in Figure S1 - S3. The measured layer thicknesses agree with previous studies of different TMDCs and support our optical analysis [20,38-40].

### 3.2. Local electrochemical measurements

SECCM imaging was carried out using a single-barreled nanopipette probe of approximately 800 nm diameter. An Ag/AgCl wire immersed in the electrolyte solution was used as a reference electrode. Linear sweep voltammograms (LSVs) for the reduction of [Ru(NH<sub>3</sub>)<sub>6</sub>]<sup>3+</sup> to [Ru(NH<sub>3</sub>)<sub>6</sub>]<sup>2+</sup> were obtained at a regular grid of sample points spaced at 1.5 μm intervals on all four TMDC materials (MoS<sub>2</sub>, MoSe<sub>2</sub>, WS<sub>2</sub>, WSe<sub>2</sub>); multiple measurements were carried out on each surface type (Au, 1L, 2L, and 3L). The AFM images shown in Fig. 2B, which were obtained after the SECCM measurements, reveal salt residues left at points of contact between the SECCM droplet and the surface after water evaporation.

The droplet/surface contact area was estimated from the AFM images by measuring the diameter of the droplet residue; these values are summarized in Figure S4. The droplet size is determined by the pipette aperture, with a small variability expected due to the nature of the pipette pulling process. A new pipette was used for each experiment, thus, the average droplet size was slightly different for each of the TMDC materials investigated and estimated to be 0.81 ± 0.05 μm, 0.73 ± 0.05 μm and 0.80 ± 0.09 μm for MoSe<sub>2</sub>, WS<sub>2</sub>, and WSe<sub>2</sub>, respectively, as shown in Figure S4. The average droplet size of MoS<sub>2</sub> was found to be considerably larger at approximately 1.30 ± 0.11 μm in diameter. The larger droplet size observed on MoS<sub>2</sub> is due to a larger pipette aperture for this experiment (determined from the diffusion-limited current on MoS<sub>2</sub>, see Section SI-6). The droplet size displayed only a narrow dispersion with the TMDC thickness, as seen in Fig. S4 histograms, while the variance observed is consistent with the wetting behaviour of TMDCs surfaces after exposure to air [41,42]. Grid points sampled on bare gold surfaces (see MoSe<sub>2</sub> and WSe<sub>2</sub> samples in Figs. S6-S7) exhibited the largest droplet contact size, which can be attributed to the higher hydrophilicity of Au in comparison to TMDC [42,43].

The salt residues were used to assign each LSV to a specific surface type: bare gold, 1L, 2L, 3L, and layer boundaries. Fig. 3A shows an AFM image of a WS<sub>2</sub> sample recorded after the SECCM measurements, where the sampled areas are color-coded to reflect the corresponding surface type, as identified by optical microscopy and AFM. The same protocol was used for the assignment of LSV curves of MoSe<sub>2</sub> and WSe<sub>2</sub>, as shown in Figs. S6 and S7. The relative spacing (1.5 μm) of the SECCM point grid was identical for all four TMDCs. Due to the greater wetting on MoS<sub>2</sub>, a larger fraction of the sample became covered by salt residues, which rendered the AFM analysis of the surface type unreliable. We therefore employed optical microscopy to assign the surface type as detailed in Fig. S8.

The above procedure resulted in multiple LSV curves obtained at each surface type (Au, 1L, 2L, and 3L), thus generating a representative dataset for further analysis. Both AFM and optical microscopy indicate that several LSVs measurements were obtained at boundaries between different layer thicknesses (such as Au-1L, 1L-2L, Au-2L, 1L-3L boundaries). However, the dearth of data from the boundaries prevents us from drawing any strong conclusions and we leave the analysis of these types of measurement to future work. The AFM imaging also revealed various forms of defects and surface irregularities, such as cracks in the 2D flakes and defects in the underlying Au substrate, as shown in Figs. S5-S7. As these defects are likely to affect the electrochemical response, the corresponding LSVs curves were also discounted from the analysis of

the electrochemical response as a function of the TMDC thickness, details on the excluded points are given in Table S1.

The TMDC thickness (1L, 2L, 3L) for each point used in our LSV analysis is displayed in Fig. 3B for WS<sub>2</sub> and in Figure S6 - S8 for MoSe<sub>2</sub>, WSe<sub>2</sub>, and MoS<sub>2</sub>. The LSVs corresponding to 1L, 2L, and 3L WS<sub>2</sub> are shown as black traces in Fig. 3C, 3D, and 3E, respectively, while the LSVs on MoS<sub>2</sub>, MoSe<sub>2</sub>, and WSe<sub>2</sub> are shown in the Figures S9-S12. Figures S9 - S12 also show every LSV measurement on TMDCs (including the measurements at defect sites) and LSV measurements once sites with defects have been excluded. Both LSV datasets show the dependence of the electrochemical behavior on the TMDC layer thickness. However, the LSVs collected at the defect sites are noticeably different to those at the pristine basal plane and resemble the Au surface response (Fig. S16). The defective areas generally show faster apparent kinetics. One therefore expects macroscopic measurements over both the pristine and defective areas would also yield enhanced kinetics, subject to the defect density.

### 3.3. Electrochemical kinetics

The LSVs in Fig. 3C-3E show that the [Ru(NH<sub>3</sub>)<sub>6</sub>]<sup>3+</sup> reduction is more facile on thinner WS<sub>2</sub>; similar trends are observed for the other three TMDC materials (Figs. S10-S12). To quantify the observed electrochemical response, a finite element simulation implemented by COMSOL Multiphysics was used to describe the transient diffusional transport of [Ru(NH<sub>3</sub>)<sub>6</sub>]<sup>3+/2+</sup> in the SECCM probe (details in Section SI-5) and the electron transfer kinetics at the sample surface. The geometry of each SECCM probe used, such as the droplet contact area and pipette aperture, were derived from AFM imaging and limiting current calculations, respectively (see Section SI-2 and SI-6).

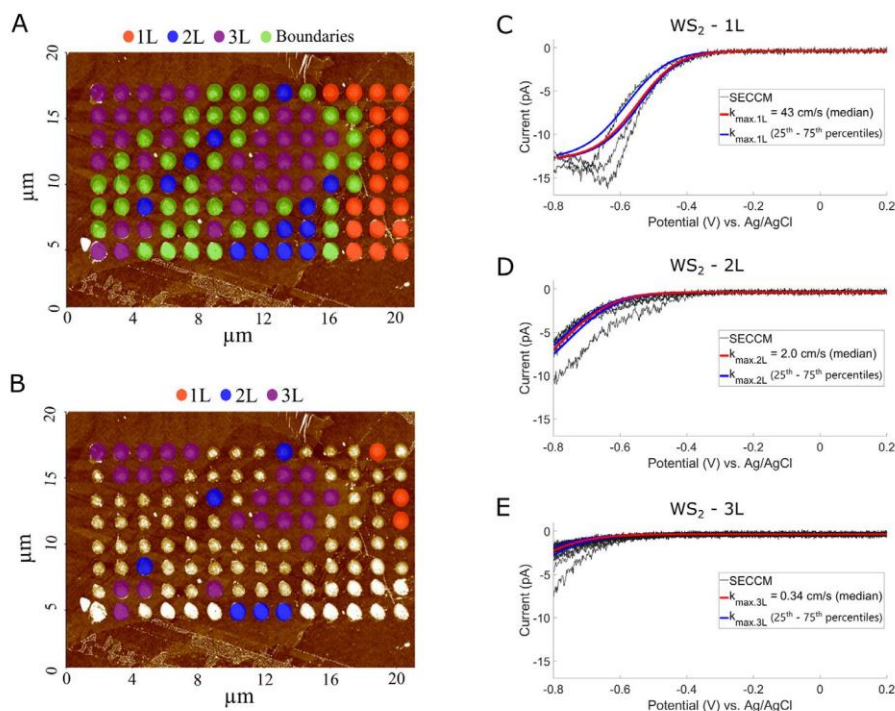
The simulated rate of heterogeneous electron transport (HET) was described by a Gerischer formalism. As theoretically predicted by Feldberg [44] and recently verified experimentally [45], for an ultramicroelectrode with slow kinetics a significant difference exists between the HET rate constant value calculated from the Butler-Volmer and Marcus-Hush/Gerischer formalism. In the Gerischer formalism, the kinetics of HET can be described by considering the overlap between isoenergetic electronic states of the electrode and the redox species in solution (electronic coupling in the Marcus-Hush formalism). Therefore, the kinetics of cathodic electron transfer ( $k_{cat}$ ) is given by the overlap between isoenergetic occupied states at the electrode ( $f(E)_{occupied}$ ) and empty electron acceptor states in the solution ( $W_{ox}$ ) [46]. Likewise, the anodic kinetics ( $k_{an}$ ) is determined by the overlap of isoenergetic filled electron donor states ( $W_{red}$ ) in the solution and unoccupied states in the electrode ( $f(E)_{unoccupied}$ ). Therefore, the cathodic and anodic kinetic rates can be written as:

$$k_{cat} = k_{max} \cdot \int_{-\infty}^{\infty} W_{ox}(E) \cdot f(E)_{occupied} \partial E \quad (1)$$

$$k_{an} = k_{max} \cdot \int_{-\infty}^{\infty} W_{red}(E) \cdot f(E)_{unoccupied} \partial E \quad (2)$$

where the integration parameter  $E$  is the electron energy (in eV), and the prefactor,  $k_{max}$ , is the maximum rate of electron transfer [46]. The solution states ( $W_{ox}$  and  $W_{red}$ ) are described by normalized Gaussian distributions and the electrode states ( $f(E)_{occupied}$  and  $f(E)_{unoccupied}$ ) are described by normalized Fermi-Dirac distributions for free electrons in a metal, see supplementary information (SI-7) for more details.

The overlap integrals for anodic and cathodic processes, as described in Eqs. (1) and (2), were calculated by numerical integration, obtaining two waveforms (for anodic and cathodic processes), which describe the ratio of the overlap of the reacting



**Fig. 3.** (A) Color-coded surface-type assignment in the AFM image showing the SECCM grid on WS<sub>2</sub>. (B) Color-coded surface-type assignment in the same AFM image, excluding measurements at defects and boundaries. (C), (D) and (E) LSVs of [Ru(NH<sub>3</sub>)<sub>6</sub>]<sup>3+</sup> reduction on 1L, 2L, and 3L from the points shown in B (black traces). Simulated response corresponding to the median  $k_{max}$  fitted in red and simulated response corresponding to 25th and 75th percentiles of  $k_{max}$  fitting in blue. Dataset formed by 3, 6 and 23 fitted LSVs with  $k_{max}$  values for 1L, 2L and 3L respectively.

redox species as a function of the applied potential. The waveforms, displayed in Figure S15, range between 0 and 1 and assume a metallic electrode with flat DOS and reorganization energy ( $\lambda$ ) for [Ru(NH<sub>3</sub>)<sub>6</sub>]<sup>3+/2+</sup> of 1 eV [45,47,48]. Thus, the total current can be expressed as:

$$i = i_{an} - i_{cat} \quad (3)$$

$$i_{an} = nF \cdot C_{red} \cdot k_{an} = nF \cdot C_{red} \cdot k_{max} \cdot \int W_{red}(E) \cdot f(E)_{unoccupied} \partial E \quad (4)$$

$$i_{cat} = nF \cdot C_{ox} \cdot k_{cat} = nF \cdot C_{ox} \cdot k_{max} \cdot \int W_{ox}(E) \cdot f(E)_{occupied} \partial E \quad (5)$$

where  $n = 1$  is the number of electrons in the reaction,  $F$  is Faraday's constant,  $C_{red}$  is the concentration of [Ru(NH<sub>3</sub>)<sub>6</sub>]<sup>2+</sup> at the electrode surface, and  $C_{ox}$  is the concentration of [Ru(NH<sub>3</sub>)<sub>6</sub>]<sup>3+</sup> at the electrode surface.

The simulated LSVs were matched to the experimental data recorded on different TMDC thicknesses by using only  $k_{max}$  as the fitting parameter, with  $E_0'$  set to -0.29 V as determined on a bare gold electrode in SI-8. At the bare gold surface,  $k_{max,Au}$  was determined to be at least  $2 \times 10^4$  cm/s, as shown in Figure S16B. Note that  $k_{max}$  values greater than  $2 \times 10^4$  cm/s yielded simulated LSV curves that were no longer distinguishable (Figure S16C). Our  $k_{max,Au}$  value is close to the pre-exponential frequency factor for the adiabatic heterogeneous electron transfer dominated by the reorganization energy predicted by the Marcus-Hush theory ( $10^4$ – $10^5$  cm/s) [49,50] and also to the experimentally determined value ( $1.1 \times 10^5$  cm/s) obtained for [Ru(NH<sub>3</sub>)<sub>6</sub>]<sup>3+/2+</sup> on bare gold [51].

Matching simulation to each individual experimental LSV over the kinetic region (up to the 1/3 of the diffusion-limited current) by adjusting  $k_{max}$  allows us to estimate the apparent  $k_{max}$  on the

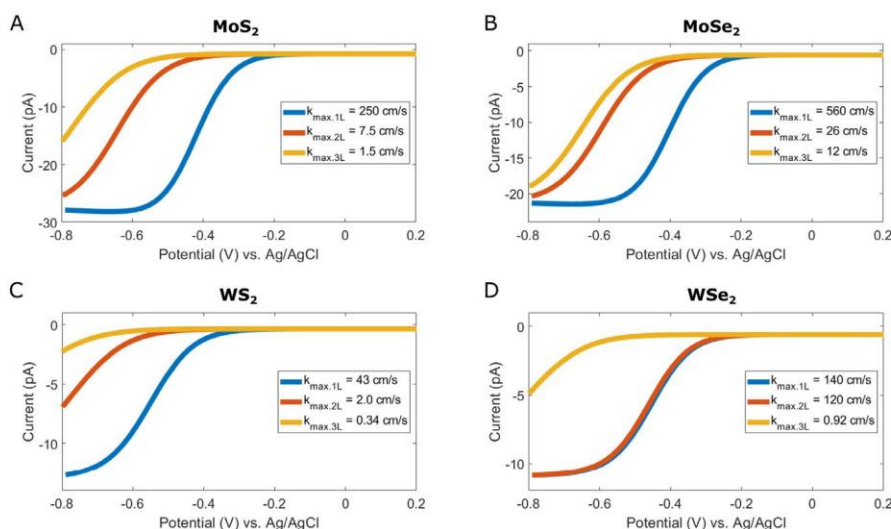
different layers ( $k_{max,nL}$  for  $nL$ ), as shown in Fig. 3C–3E for WS<sub>2</sub>. The median  $k_{max,nL}$  on MoS<sub>2</sub>, MoSe<sub>2</sub>, and WSe<sub>2</sub> surfaces are shown in Figs. S17–S19. The [Ru(NH<sub>3</sub>)<sub>6</sub>]<sup>3+</sup> reduction kinetics slows down with the increasing number of layers, as shown in Fig. 4. This observation agrees with previous work on the HER at 2D TMDC electrodes [21]. The median  $k_{max,nL}$  values extracted for all four studied materials, MoS<sub>2</sub>, WS<sub>2</sub>, MoSe<sub>2</sub>, and WSe<sub>2</sub>, are summarized in Table 1 and plotted versus the layer number in Fig. 5A.

The responses on all four materials are similar and indicate a decrease in  $k_{max}$  with an increase in layer thickness, as shown in Fig. 5A, except for  $k_{max,2L}$  for WSe<sub>2</sub>, which is significantly larger compared to the other TMDCs studied, although it remains unclear why this is the case. According to the Gerischer model for heterogeneous electron transfer, the prefactor  $k_{max}$  scales with the electronic transmission coefficient, which represents the probability of the electron transfer. An electron tunneling barrier arising from the TMDC material itself would reduce the transmission coefficient, and so  $k_{max}$ , as the number of layers increases. Previously an electron tunneling barrier model has been used to evaluate photocurrents obtained for 2D MoS<sub>2</sub> in a bottom-contact configuration [52], and has also been used to assess the HER kinetics on mono and few-layer MoS<sub>2</sub> [21]. Therefore, assuming that tunneling is the dominant process leading to a decrease in  $k_{max}$ , the  $k_{max,nL}$  corresponding to  $nL$  TMDC can be described as:

$$k_{max,nL} = k_{max,Au} \cdot \exp(-\beta \cdot h \cdot n) \quad (6)$$

where  $\beta$  is the tunneling decay constant,  $h$  is the thickness of the TMDCs layer ( $h = 6.15$  Å for MoS<sub>2</sub>, 6.47 Å for MoSe<sub>2</sub>, 6.16 Å for WS<sub>2</sub> and 7.00 Å for WSe<sub>2</sub>) [7],  $n$  is the number of TMDCs layers. Diagram of tunneling barrier can be found in Figure S22.

The  $\beta$  values for [Ru(NH<sub>3</sub>)<sub>6</sub>]<sup>3+</sup> reduction on different layer stacks for MoS<sub>2</sub>, MoSe<sub>2</sub>, WS<sub>2</sub>, and WSe<sub>2</sub> obtained from Eq. (6) are reported in Table 1. The four different TMDCs have tunneling decay constants in the range 1.0 – 0.4 Å<sup>-1</sup>, which vary significantly depending on total thickness. Our  $\beta$  values are consistent for 2D



**Fig. 4.** Simulated LSVs with median  $k_{max,nL}$  extracted from fitting recorded LSVs on 1L, 2L, and 3L of (A) MoS<sub>2</sub>(B) MoSe<sub>2</sub>(C) WS<sub>2</sub> and (D) WSe<sub>2</sub>. Each TMDC displayed a different limiting current according to variation of the observed droplet size, which explains the varying scale of the y-axes.

**Table 1**

Median prefactor,  $k_{max}$ , and tunneling decay constant,  $\beta$ , evolution with the number of TMDCs layers.

	$k_{max,1L}$ (cm/s)	$k_{max,2L}$ (cm/s)	$k_{max,3L}$ (cm/s)	$\beta_{Au-1L}$ ( $\text{\AA}^{-1}$ )	$\beta_{Au-2L}$ ( $\text{\AA}^{-1}$ )	$\beta_{Au-3L}$ ( $\text{\AA}^{-1}$ )
MoS <sub>2</sub>	250	7.5	1.5	0.71	0.64	0.52
MoSe <sub>2</sub>	560	26	12	0.55	0.51	0.38
WS <sub>2</sub>	43	2.0	0.34	1.00	0.75	0.59
WSe <sub>2</sub>	140	120	0.92	0.71	0.36	0.48

TMDCs, which have previously been estimated to have tunneling decay constants of  $0.512 \text{ \AA}^{-1}$  [53].

The data in Table 1 show that the tunneling decay constant,  $\beta$ , decreases with increasing numbers of layers for all four TMDCs. However,  $k_{max,nL}$  values do not follow an exponential decay with increased layer thickness as we might expect if each additional layer added an identical electron tunneling barrier, as shown in Fig. 5A. Instead, the kinetics is faster for a larger number of layers than would be predicted by a tunneling model with a constant  $\beta$ .

The electronic band structure of TMDCs depends on the number of stacked layers [54–56]. The band gap of MoS<sub>2</sub>, MoSe<sub>2</sub>, WS<sub>2</sub>, and WSe<sub>2</sub> increases with the decreasing layer number (<5L) due to strong quantum confinement in thin layers [56,57]. The larger band gap of thinner layers should therefore lead to an increase in the tunneling barrier height, and therefore larger tunneling decay constants ( $\beta$ ). Conversely, the smaller band gap of thicker layers should lead to smaller tunneling decay constants. Diagrams of tunneling barriers presented Fig. S22 illustrate changes of tunneling barrier with number of layers stacked. Indeed, the derived tunneling decay constants listed in Table 1 agree with this trend.

The  $\beta_{Au-nL}$  values describe n-layers of TMDCs acting as a single tunneling barrier, thus  $\beta_{Au-nL}$  can be compared with the band gaps reported for  $n$  layers of TMDCs (also displayed in Table S5) [7]. From Table S5, we observe a correlation between  $\beta_{Au-nL}$  values and band gap on the different layer thickness of TMDCs. For instance, of the TMDCs we studied, WS<sub>2</sub> has the largest band gap and WS<sub>2</sub> also showed the largest tunneling decay constant,  $\beta_{Au-nL}$ , values. Likewise, of the materials we considered, MoSe<sub>2</sub> has the smallest band gap and also shows the smallest  $\beta_{Au-nL}$  values. In fact, we observe a strong correlation between the band gap values sourced from literature and our measured tunneling decay constant,  $\beta_{Au-nL}$ , values, as shown in Fig. 5B. Our findings are supported by recent work by Lee *et al.*, who experimentally determined the tun-

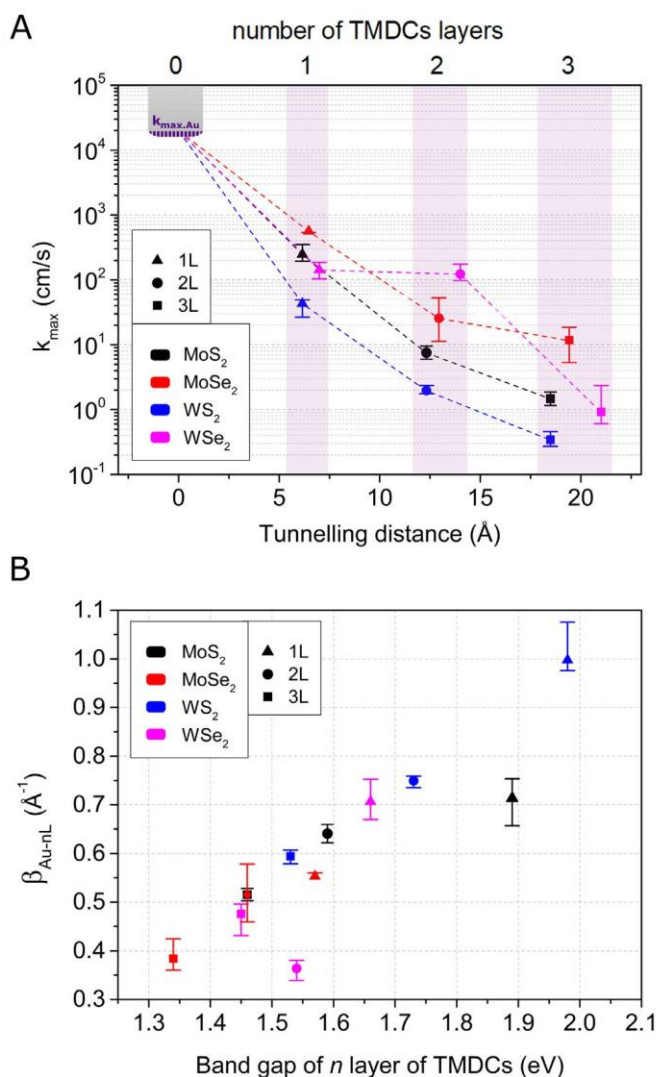
neling barrier height on the different number of layers (1–5L) of MoS<sub>2</sub> on gold using conducting AFM [58]. The barrier height maximum is observed at 1L, then decreases and stabilizes at >5L, in good agreement with values reported in Table 1 obtained using an outer-sphere redox probe.

The electrochemical response on a few-layer 2D TMDCs, in a bottom-contacted configuration, depends on the electron transport process through the TMDC layers. This electron transport is strongly influenced by the electronic structure of the 2D TMDCs, with larger band gaps resulting in a larger decrease in  $k_{max}$  with each additional layer, and therefore a higher electron tunneling barrier. However, 2D TMDCs with a fewer number of stacked layers show faster electron transport kinetics due to a narrower tunneling barrier, despite having a larger tunneling decay constant. As a consequence, bottom-contacted TMDC samples with a heterogeneous number of stacked layers will produce an electrochemical response dominated by the monolayer activity at lower overpotentials but with increasing activity of thicker layers at higher overpotentials (assuming there is no diffusional overlap). Our findings suggest that the electrochemical response of TMDC electrode surfaces is profoundly affected by the mode of contact established on electrodes. This has implications for the interpretation of electrochemical and, importantly, electrocatalytic experiments at TMDC nanoarchitectures. Through-layer or within-layer electron transport must be considered when interpreting the performance of TMDC materials in the HER or other reactions of relevance to advanced electrochemical applications.

#### 4. Conclusions

SECCM has been used to quantify the effect of the number of stacked layers of 2D TMDCs (MoS<sub>2</sub>, MoSe<sub>2</sub>, WS<sub>2</sub>, WSe<sub>2</sub>) on the electrochemical response of the  $[\text{Ru}(\text{NH}_3)_6]^{3+/2+}$  redox couple. Combining SECCM and AFM allowed us to precisely determine the





**Fig. 5.** (A)  $k_{max}$  values determined from fitting simulation to experimental data for different layer thickness. Solid points correspond to each  $k_{max}$  value and dashed lines are displayed to guide the eye. Error bar correspond to  $k_{max}$  values for 25th and 75th percentiles. (B)  $\beta_{Au-nL}$  values plotted against band gap for 1-, 2-, and 3-layer MoS<sub>2</sub>, MoSe<sub>2</sub>, WS<sub>2</sub>, and WSe<sub>2</sub> [7]. Error bar correspond to  $\beta_{Au-nL}$  derived from  $k_{max}$  values for 25th and 75th percentiles. Note some surface types have a limited dataset points and percentile might not be representative of distribution, see Table S1.

exact nature of the underlying 2D material at each sample point, and to quantify the electrochemical response on the different numbers of layers. There is a significant difference in the electrochemical response on the different numbers of stacked layers, with more facile kinetics observed on thinner stacks of all four materials.

The kinetic dependence was assessed by comparison with a finite element simulation that coupled the diffusional mass transport of [Ru(NH<sub>3</sub>)<sub>6</sub>]<sup>3+/2+</sup> in the nanopipette probe with the Gerischer description of the electrochemical kinetics. We quantified the rate of electron transfer on a different number of stacked layers of four TMDCs by fitting a simulated response to the experimentally measured LSVs by only varying the maximum kinetic rate,  $k_{max}$ . MoS<sub>2</sub>, MoSe<sub>2</sub>, WS<sub>2</sub>, and WSe<sub>2</sub> all show a decrease in the electron transfer rate constant as the number of layers increases.

Trends in the electron transfer rates were described by considering an electron tunneling barrier arising from the TMDC itself. This allowed us to extract the apparent tunneling decay constants,  $\beta$ , which range over 1.0–0.4 Å<sup>-1</sup> across all TMDC materials tested;

these values are consistent with those reported for tunneling decay constants of 2D TMDCs by other groups [53,58].

We observe that the prefactor,  $k_{max}$ , decays more slowly than we would expect if each additional layer added an identical electron tunneling barrier. Thus, the previously reported tunneling barrier model for HER on a few-layer MoS<sub>2</sub>, where tunneling decay constant was unaffected by the number of TMDCs layers [21], is insufficient to explain our experimental data. The correlation observed between band gap and tunneling decay constant suggest that non-exponential decay of rate constants is due to a change in the electronic properties of the tunneling barrier, resulting from band gap changes as a function of the number of stacked layers of TMDCs. Therefore, the variation on the electronic structure of the 2D material affects the electron transport to such an extent that we can observe the effect in our electrochemical measurements.

### Declaration of Competing Interest

The authors declare that they have no known competing financial interests or personal relationships that could have appeared to influence the work reported in this paper.

### Credit authorship contribution statement

**Marc Brunet Cabré:** Investigation, Data curation, Formal analysis, Visualization, Writing – original draft, Writing – review & editing. **Aislan Esmeraldo Paiva:** Investigation, Writing – original draft. **Matěj Velický:** Conceptualization, Resources, Writing – original draft, Writing – review & editing. **Paula E. Colavita:** Writing – review & editing, Supervision. **Kim McKelvey:** Conceptualization, Resources, Writing – original draft, Writing – review & editing, Supervision.

### Acknowledgment

We acknowledge parkAFM for loan of the NX10 AFM instrument. M.B. acknowledges the School of Chemistry, Trinity College Dublin for funding of his PhD.

### Supplementary materials

Supplementary material associated with this article can be found, in the online version, at [doi:10.1016/j.electacta.2021.139027](https://doi.org/10.1016/j.electacta.2021.139027).

### References

- [1] S. Manzeli, D. Ovchinnikov, D. Pasquier, O.V. Yazyev, A. Kis, 2D transition metal dichalcogenides, *Nat. Rev. Mater.* 2 (2017) 17033–17048, doi:10.1038/natrevmats.2017.33.
- [2] Q.H. Wang, K. Kalantar-Zadeh, A. Kis, J.N. Coleman, M.S. Strano, Electronics and optoelectronics of two-dimensional transition metal dichalcogenides, *Nat. Nanotechnol.* 7 (2012) 699–712, doi:10.1038/nnano.2012.193.
- [3] W. Choi, N. Choudhary, G.H. Han, J. Park, D. Akinwande, Y.H. Lee, Recent development of two-dimensional transition metal dichalcogenides and their applications, *Mater. Today* 20 (2017) 116–130, doi:10.1016/j.mattod.2016.10.002.
- [4] E. Pomerantseva, F. Bonaccorso, X. Feng, Y. Cui, Y. Gogotsi, Energy storage: the future enabled by nanomaterials, *Science* 366 (2019) 969, doi:10.1126/science.aan8285.
- [5] M. Ahmadi, O. Zabihi, S. Jeon, M. Yoonessi, A. Dasari, S. Ramakrishna, M.J. Naeb, 2D transition metal dichalcogenide nanomaterials: advances, opportunities, and challenges in multi-functional polymer nanocomposites, *Mater. Chem. A* 8 (2020) 845–883 8, doi:10.1039/C9TA10130F.
- [6] Z. Wei, B. Li, C. Xia, Y. Cui, J. He, J.B. Xia, J. Li, Various structures of 2D transition-metal dichalcogenides and their applications, *Small Methods* 2 (2018) 1800094, doi:10.1002/smt.201800094.
- [7] M. Velický, P.S. Toth, From two-dimensional materials to their heterostructures: an electrochemist's perspective, *Appl. Mater. Today* 8 (2017) 68–103, doi:10.1016/j.apmt.2017.05.003.
- [8] X. Chia, A.Y.S. Eng, A. Ambrosi, S.M. Tan, M. Pumera, Electrochemistry of nanostructured layered transition-metal dichalcogenides, *Chem. Rev.* 115 (2015) 11941–11966, doi:10.1021/acs.chemrev.5b00287.

- [9] M. Chhowalla, H.S. Shin, G. Eda, L.J. Li, K.P. Loh, H. Zhang, The chemistry of two-dimensional layered transition metal dichalcogenide nanosheets, *Nat. Chem.* 5 (2013) 263–275, doi:10.1038/nchem.1589.
- [10] T. Stephenson, Z. Li, B. Olsen, D. Mitlin, Lithium ion battery applications of molybdenum disulfide (MoS<sub>2</sub>) nanocomposites, *Energy Environ. Sci.* 7 (2014) 209–231, doi:10.1039/C3EE42591F.
- [11] S. Ratha, C.S. Rout, Supercapacitor electrodes based on layered tungsten disulfide-reduced graphene oxide hybrids synthesized by a facile hydrothermal method, *ACS Appl. Mater. Interfaces* 5 (2013) 11427–11433, doi:10.1021/am403663f.
- [12] E.G.S. Firmiano, A.C. Rabelo, C.J. Dalmaschio, A.N. Pinheiro, E.C. Pereira, W.H. Schreiner, E.R. Leite, Supercapacitor electrodes obtained by directly bonding 2D MoS<sub>2</sub> on reduced graphene oxide, *Adv. Energy Mater.* 4 (2014) 1301380, doi:10.1002/aenm.201301380.
- [13] Z. Zhu, H. Yin, C.T. He, M. Al-Mamun, P. Liu, L. Jiang, Y. Zhao, Y. Wang, H.G. Yang, Z. Tang, D. Wang, X.M. Chen, H. Zhao, Ultrathin transition metal dichalcogenide/3D metal hydroxide hybridized nanosheets to enhance hydrogen evolution activity, *Adv. Mater.* 30 (2018) 1–7, doi:10.1002/adma.201801171.
- [14] Q. Fu, J. Han, X. Wang, P. Xu, T. Yao, J. Zhong, W. Zhong, S. Liu, T. Gao, Z. Zhang, L. Xu, B. Song, 2D transition metal dichalcogenides: design, modulation, and challenges in electrocatalysis, *Adv. Mater.* 33 (2020) 1907818, doi:10.1002/adma.201907818.
- [15] L. Lin, P. Sherrill, Y. Liu, W. Lei, S. Zhang, H. Zhang, G.G. Wallace, J. Chen, Engineered 2D transition metal dichalcogenides—a vision of viable hydrogen evolution reaction catalysis, *Adv. Energy Mater.* 10 (2020) 1903870, doi:10.1002/aenm.201903870.
- [16] Q. Lu, Y. Yu, Q. Ma, B. Chen, H. Zhang, 2D transition-metal-dichalcogenide-nanosheet-based composites for photocatalytic and electrocatalytic hydrogen evolution reactions, *Adv. Mater.* 28 (2016) 1917–1933, doi:10.1002/adma.201503270.
- [17] S.M. Tan, A. Ambrosi, Z. Sofer, Š. Huber, D. Sedmidubský, M. Pumera, Pristine basal- and edge-plane-oriented molybdenite MoS<sub>2</sub> exhibiting highly anisotropic properties, *Chem. Eur. J.* 21 (2015) 7170–7178, doi:10.1002/chem.201500435.
- [18] M. Velický, M.A. Bissett, P.S. Toth, H.V. Patten, S.D. Worrall, A.N.J. Rodgers, E.W. Hill, I.A. Kinloch, K.S. Novoselov, T. Georgiou, L. Britnell, R.A.W. Dryfe, Electron transfer kinetics on natural crystals of MoS<sub>2</sub> and graphite, *Phys. Chem. Chem. Phys.* 17 (2015) 17844–17853, doi:10.1039/C5CP02490K.
- [19] T.F. Jaramillo, K.P. Jørgensen, J. Bonde, J.H. Nielsen, S. Hørch, I. Chorkendorff, Identification of active edge sites for electrochemical H<sub>2</sub> evolution from MoS<sub>2</sub> nanocatalysts, *Science* 317 (2007) 100–102, doi:10.1126/science.1141483.
- [20] M. Velický, G.E. Donnelly, W.R. Hendren, S. McFarland, D. Scullion, W.J.I. Debenetti, G.C. Correa, Y. Han, A.J. Wain, M.A. Hines, D.A. Muller, K.S. Novoselov, H.D. Abruna, R.M. Bowman, E.J.G. Santos, F. Huang, Mechanism of gold-assisted exfoliation of centimeter-sized transition-metal dichalcogenide monolayers, *ACS Nano* 12 (2018) 10463–10472, doi:10.1021/acsnano.8b06101.
- [21] Y. Yu, S.Y. Huang, Y. Li, S.N. Steinmann, W. Yang, L. Cao, Layer-dependent electrocatalysis of MoS<sub>2</sub> for hydrogen evolution, *Nano Lett.* 14 (2014) 553–558, doi:10.1021/nl403620g.
- [22] S.B. Desai, S.R. Madhupathy, M. Amani, D. Kiriya, M. Hettick, M. Tosun, Y. Zhou, M. Dubey, J.W. Ager, D. Chrzan, A. Javey, Gold-mediated exfoliation of ultralarge optoelectronically-perfect monolayers, *Adv. Mater.* 28 (2016) 4053–4058, doi:10.1002/adma.201506171.
- [23] G.A. Magda, J. Pető, G. Dobrik, C. Hwang, L.P. Biró, L. Tapasztó, Exfoliation of large-area transition metal chalcogenide single layers, *Sci. Rep.* 5 (2015) 14714, doi:10.1038/srep14714.
- [24] C.L. Bentley, M. Kang, P.R. Unwin, Nanoscale surface structure–activity in electrochemistry and electrocatalysis, *J. Am. Chem. Soc.* 141 (2019) 2179–2193, doi:10.1021/jacs.8b09828.
- [25] C.L. Bentley, J. Edmondson, G.N. Meloni, D. Perry, V. Shkirskiy, P.R. Unwin, Nanoscale electrochemical mapping, *Anal. Chem.* 91 (2019) 84–108, doi:10.1021/acs.analchem.8b05235.
- [26] M.E. Snowden, A.G. Güell, S.C.S. Lai, K. McKelvey, N. Ebejer, M.A. O'Connell, A.W. Colburn, P.R. Unwin, Scanning electrochemical cell microscopy: theory and experiment for quantitative high resolution spatially-resolved voltammetry and simultaneous ion-conductance measurements, *Anal. Chem.* 84 (2012) 2483–2491, doi:10.1021/ac203195h.
- [27] N. Ebejer, A.G. Güell, S.C.S. Lai, K. McKelvey, M.E. Snowden, P.R. Unwin, Scanning electrochemical cell microscopy: a versatile technique for nanoscale electrochemistry and functional imaging, *Ann. Rev. Anal. Chem.* 6 (2013) 329–351, doi:10.1146/annurev-anchem-062012-092650.
- [28] N. Ebejer, M. Schnippering, A.W. Colburn, M.A. Edwards, P.R. Unwin, Localized high resolution electrochemistry and multifunctional imaging: scanning electrochemical cell microscopy, *Anal. Chem.* 82 (2010) 9141–9145, doi:10.1021/ac102191u.
- [29] C.L. Bentley, M. Kang, F.M. Maddar, F. Li, M. Walker, J. Zhang, P.R. Unwin, Electrochemical maps and movies of the hydrogen evolution reaction on natural crystals of molybdenite (MoS<sub>2</sub>): basal vs. edge plane activity, *Chem. Sci.* 8 (2017) 6583–6593, doi:10.1039/C7SC02545A.
- [30] B. Tao, P.R. Unwin, C.L. Bentley, Nanoscale variations in the electrocatalytic activity of layered transition-metal dichalcogenides, *J. Phys. Chem. C* 124 (2020) 789–798, doi:10.1021/acs.jpcc.9b10279.
- [31] Y. Takahashi, Y. Kobayashi, Z. Wang, Y. Ito, M. Ota, H. Ida, A. Kumatani, K. Miyazawa, T. Fujita, H. Shiku, Y.E. Korchev, Y. Miyata, T. Fukuma, M. Chen, T. Matsue, High-resolution electrochemical mapping of the hydrogen evolution reaction on transition-metal dichalcogenide nanosheets, *Angew. Chemie Int. Ed.* 59 (2020) 3601–3608, doi:10.1002/ange.201912863.
- [32] M. Velický, M.A. Bissett, C.R. Woods, P.S. Toth, T. Georgiou, I.A. Kinloch, K.S. Novoselov, R.A.W. Dryfe, Photoelectrochemistry of pristine mono- and few-layer MoS<sub>2</sub>, *Nano Lett.* 16 (2016) 2023–2032, doi:10.1021/acs.nanolett.5b05317.
- [33] W. Liao, S. Zhao, F. Li, C. Wang, Y. Ge, H. Wang, S. Wang, H. Zhang, Interface engineering of two-dimensional transition metal dichalcogenides towards next-generation electronic devices: recent advances and challenges, *Nanoscale Horiz* 5 (2020) 787, doi:10.1039/C9NH00743A.
- [34] J.C. McGlynn, T. Dankwort, L. Kienle, N.A.G. Bandeira, J.P. Fraser, E.K. Gibson, I. Cascallana-Matías, K. Kamarás, M.D. Symes, H.N. Miras, A.Y. Ganin, The rapid electrochemical activation of MoTe<sub>2</sub> for the hydrogen evolution reaction, *Nat. Commun.* 10 (2019) 4916, doi:10.1038/s41467-019-12831-0.
- [35] X. Li, C. Batchelor-McAuley, E. Laborda, R.G. Compton, Aqueous voltammetry in the near absence of electrolyte, *Chem. Eur. J.* 23 (2017) 15222–15226, doi:10.1002/chem.201703525.
- [36] N.S. Taghavi, P. Gant, P. Huang, I. Niehues, R. Schmidt, S.M. Vasconcellos, R. Bratschitsch, M. García-Hernández, R. Frisenda, A. Castellanos-Gomez, Thickness determination of MoS<sub>2</sub>, MoSe<sub>2</sub>, WS<sub>2</sub> and WSe<sub>2</sub> on transparent stamps used for deterministic transfer of 2D materials, *Nano Res* 12 (2019) 1691–1695, doi:10.1007/s12274-019-2424-6.
- [37] J.C. Shaw, H. Zhou, Y. Chen, N.O. Weiss, Y. Liu, Y. Huang, X. Duan, Chemical vapor deposition growth of monolayer MoSe<sub>2</sub> nanosheets, *Nano Res* 7 (2014) 511–517, doi:10.1007/s12274-014-0417-z.
- [38] J. Park, M.S. Kim, E. Cha, J. Kim, W. Choi, Synthesis of uniform single layer WS<sub>2</sub> for tunable photoluminescence, *Sci. Rep.* 7 (2017) 16121, doi:10.1038/s41598-017-16251-2.
- [39] B. Liu, M. Fathi, L. Chen, A. Abbas, Y. Ma, C. Zhou, Chemical vapor deposition growth of monolayer WSe<sub>2</sub> with tunable device characteristics and growth mechanism study, *ACS Nano* 9 (2015) 6119–6127, doi:10.1021/acsnano.5b01301.
- [40] Y. Zhang, H. Li, H. Wang, R. Liu, S.L. Zhang, Z.J. Qiu, On valence-band splitting in layered MoS<sub>2</sub>, *ACS Nano* 9 (2015) 8514–8519, doi:10.1021/acsnano.5b03505.
- [41] P.K. Chow, E. Singh, B.C. Viana, J. Gao, J. Luo, J. Li, Z. Lin, A.L. Elías, Y. Shi, Z. Wang, M. Terrones, N. Koratkar, Wetting of mono and few-layered WS<sub>2</sub> and MoS<sub>2</sub> films supported on Si/SiO<sub>2</sub> substrates, *ACS Nano* 9 (2015) 3023–3031, doi:10.1021/nn5072073.
- [42] A. Kozbial, G. Gong, H. Liu, L. Li, Understanding the intrinsic water wettability of molybdenum disulfide (MoS<sub>2</sub>), *Langmuir* 31 (2015) 8429–8435, doi:10.1021/acs.langmuir.5b02057.
- [43] T. Smith, The hydrophilic nature of a clean gold surface, *J. Colloid Interface Sci.* 78 (1980) 51–55, doi:10.1016/0021-9797(80)90348-3.
- [44] S.W. Feldberg, Implications of Marcus–hush theory for steady-state heterogeneous electron transfer at an inlaid disk electrode, *Anal. Chem.* 82 (2010) 5176–5183, doi:10.1021/ac1004162.
- [45] M. Velický, S. Hu, C.R. Woods, P.S. Tóth, V. Zólyomi, A.K. Geim, H.D. Abruña, K.S. Novoselov, R.A.W. Dryfe, Electron Tunneling through boron nitride confirms Marcus–hush theory predictions for ultramicroelectrodes, *ACS Nano* 14 (2020) 993–1002, doi:10.1021/acsnano.9b08308.
- [46] R. Memming, *Semiconductor Electrochemistry*, Wiley-VCH Verlag GmbH & Co.KG, 2015, p 127–244 (Second Edition), 10.1023/A:1025744525621
- [47] W.J. Royea, T.W. Hamann, B.S. Brunschwig, N.S.A. Lewis, A comparison between interfacial electron-transfer rate constants at metallic and graphite electrodes, *J. Phys. Chem. B* 110 (2006) 19433–19442, doi:10.1021/jp062141e.
- [48] S. Ghosh, S. Hammes-Schiffer, Calculation of electrochemical reorganization energies for redox molecules at self-assembled monolayer modified electrodes, *J. Phys. Chem. Lett.* 6 (1–5) (2015), doi:10.1021/jz5023784.
- [49] J.T. Hupp, M.J. Weaver, Experimental estimate of the electron-tunneling distance for some outer-sphere electrochemical reactions, *J. Phys. Chem.* 88 (1984) 1463, doi:10.1021/j150652a004.
- [50] Z.D. He, Y.X. Chen, E. Santos, W. Schmickler, The pre-exponential factor in electrochemistry, *Angew. Chem. Int. Ed.* 57 (2018) 7948–7956, doi:10.1002/anie.201800130.
- [51] A.M. Becka, C. Miller, Electrochemistry at  $\omega$ -hydroxy thiol coated electrodes. 3. Voltage independence of the electron tunneling barrier and measurements of redox kinetics at large overpotentials, *J. Phys. Chem.* 96 (1992) 2657–2668, doi:10.1021/j100185a049.
- [52] Y. Son, Q.H. Wang, J.A. Paulson, C.J. Shih, A.G. Rajan, K. Tvrđy, S. Kim, B. Alfeeli, R.D. Braatz, M.S. Strano, Layer number dependence of MoS<sub>2</sub> photoconductivity using photocurrent spectral atomic force microscopic imaging, *ACS Nano* 9 (2015) 2843–2855, doi:10.1021/nn506924j.
- [53] K. Datta, Q.D.M. Khosru, Simulation of thin-TFETs using transition metal dichalcogenides: effect of material parameters, gate dielectric on electrostatic device performance, *J. Comput. Electron.* 16 (2017) 228–239, doi:10.1007/s10825-017-0978-7.
- [54] K.C. Wang, T.K. Stanev, D. Valencia, J. Charles, A. Henning, V.K. Sangwan, A. Lahiri, D. Mejia, P. Sarangapani, M. Povolotskiy, A. Afzaljan, J. Maassen, G. Klimeck, M.C. Hersam, L.J. Lauhon, N.P. Stern, T. Kubis, Control of interlayer physics in 2H transition metal dichalcogenides, *J. Appl. Phys.* 122 (2017) 224302, doi:10.1063/1.5005958.
- [55] J.H. Park, S. Vishwanath, X. Liu, H. Zhou, S.M. Eichfeld, S.K. Fullerton-Shirey, J.A. Robinson, R.M. Feenstra, J. Furdyna, D. Jena, H.G. Xing, A.C. Kummel, Scanning tunneling microscopy and spectroscopy of air exposure effects on molecular beam epitaxy grown WSe<sub>2</sub> monolayers and bilayers, *ACS Nano* 10 (2016) 4258–4267, doi:10.1021/acsnano.5b07698.

- [56] D.J. Trainer, A.V. Putilov, C. Giorgio, T. Saari, B. Wang, M. Wolak, R.U. Chandrasena, C. Lane, T.R. Chang, H.T. Jeng, H. Lin, F. Kronast, A.X. Gray, X. Xi, J. Nieminen, A. Bansil, M. Iavarone, Inter-layer coupling induced valence band edge shift in mono- to few-layer MoS<sub>2</sub>, *Sci. Rep.* 7 (2017) 40559, doi:[10.1038/srep40559](https://doi.org/10.1038/srep40559).
- [57] W.S. Yun, S.W. Han, S.C. Hong, I.G. Kim, J.D. Lee, Thickness and strain effects on electronic structures of transition metal dichalcogenides: 2H-MX<sub>2</sub> semiconductors (M = Mo, W; X = S, Se, Te), *Phys. Rev. B* 85 (2012) 033305, doi:[10.1103/PhysRevB.85.033305](https://doi.org/10.1103/PhysRevB.85.033305).
- [58] H. Lee, S. Deshmukh, J. Wen, V.C. Costa, J.S. Schuder, M. Sanchez, A.S. Ichimura, E. Pop, B. Wang, A.K.M. Newaz, Layer-dependent interfacial transport and optoelectrical properties of MoS<sub>2</sub> on ultraflat metals, *ACS Appl. Mater. Interfaces* 11 (2019) 31543–31550, doi:[10.1021/acsami.9b09868](https://doi.org/10.1021/acsami.9b09868).



# Electrochemical Detection of Isolated Nanoscale Defects in 2D Transition Metal Dichalcogenides

Marc Brunet Cabré, Aislan Esmeraldo Paiva, Matěj Velický, Paula E. Colavita, and Kim McKelvey\*



Cite This: *J. Phys. Chem. C* 2022, 126, 11636–11641



Read Online

ACCESS |



Metrics & More

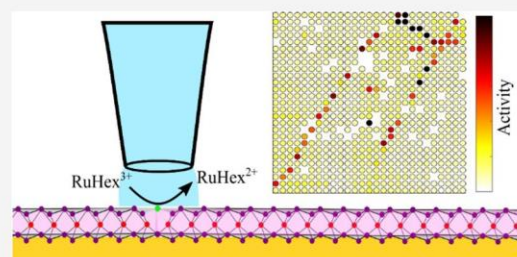


Article Recommendations



Supporting Information

**ABSTRACT:** We show that nanometer and sub-nanometer scale defects in two-dimensional transition metal dichalcogenides can be detected electrochemically using scanning electrochemical cell microscopy (SECCM). We detect isolated anomalous electrochemical responses for the hexaammineruthenium ( $[\text{Ru}(\text{NH}_3)_6]^{3+/2+}$ ) redox couple on mono-, bi-, and trilayer regions of mechanically exfoliated  $\text{MoS}_2$ . These anomalous sample points display faster electrochemical kinetics, with a diffusion-limited current plateau, compared to the surrounding sample points. The analysis of the electrochemical current suggests that the defects are equivalent to disk-shaped defects with radii of tens of nanometers, or to one-dimensional defects with nanometer to sub-nanometer widths. These results demonstrate that we can effectively isolate and electrochemically amplify the response from individual defects on a sample surface using SECCM, revealing features below the optical diffraction limit that would normally require high-resolution electron microscopy or scanning tunneling microscopy to detect.



## INTRODUCTION

Electrochemically active surfaces, including two-dimensional (2D) transition metal dichalcogenides (TMDCs) that we consider here,<sup>1–3</sup> present a variety of nanoscale surface morphological features such as vacancies, adatoms, grain boundaries, and impurities.<sup>4</sup> The presence of such morphological features strongly influences the physicochemical properties of the surface and subsequently the electrochemical response.<sup>5</sup> Characterization of the electrochemical response of defects can therefore be helpful to understand electrochemical performance. The collective average responses originating from these features are usually detected via photoemission spectroscopy,<sup>6</sup> Raman spectroscopy,<sup>7</sup> or photoluminescence.<sup>7</sup> However, mapping of individual defects on a surface at the nanoscale requires high-resolution transmission electron microscopy (TEM)<sup>8</sup> or scanning tunneling microscopy (STM).<sup>9</sup>

Electrochemical scanning probe microscopy techniques typically demand complementary microscopy maps such as atomic force microscopy, electron microscopy, or optical microscopy to correlate the morphological features on surfaces with the electrochemical response. This approach was applied to 2D materials in our previous work<sup>10,11</sup> and other studies of 2D materials.<sup>12–17</sup> It is somewhat limiting to correlate electrochemical response with complementary microscopy maps as it restricts the assignments to features that only require relatively large spatial resolution to be identified. Atomic-size features still require the use of techniques such as TEM or STM that are challenging to interface with electrochemical methods.<sup>4</sup> However, electrochemistry is unique in that mass transport effects can amplify the size of

the spatial region that is affected by a point-like change in the electrode surface. In classical electrochemical methods, this had been demonstrated, e.g., by Amatore et al., when discussing the effect of pin-hole defects on the waveform at SAM-modified electrodes;<sup>18</sup> it is clear that, in electrochemistry, the interplay between the timescale used for potential steps/steps and the size of a diffusion front can be leveraged to increase the characteristic length scale of the observed effects. The recent development of the scanning electrochemical cell microscopy (SECCM) technique offers a unique tool for the study of mass transport-controlled electrochemical processes that allow an analysis of the effect of individual defects,<sup>19</sup> as shown by excellent studies on pinholes in passivating layers<sup>20</sup> or defects in graphene on copper.<sup>12</sup>

In this work, we explore how to detect the presence of individual defects with enhanced electrochemical kinetics in 2D materials using an SECCM approach.<sup>21–23</sup> We show that it is possible to identify defects with enhanced electrochemical kinetics with a characteristic size ranging from a few angstroms to a few nanometers scale in  $\text{MoS}_2$ . These defects are too small to be easily mapped via optical or even atomic force microscopy and would normally require TEM or STM approaches for their identification. To the best of our

Received: March 9, 2022

Revised: June 24, 2022

Published: July 7, 2022



knowledge, our work is the first to report mapping of defects with enhanced kinetics with high spatial resolution coupled to analysis/modeling of their size and shape based on diffusion-limited currents. Our approach is complementary but highly novel with respect to prior reports by other groups such as Unwin and co-workers,<sup>12,24</sup> and Payne and Mauzeroll.<sup>20</sup> The small contact area (approx.  $1 \mu\text{m}^2$ ) offered by SECCM combined with mass transport effects can amplify the characteristic length scale of these defects in the current response. This means that SECCM is thus uniquely sensitive to the presence of otherwise hidden sub-nanometer defects with enhanced kinetics at the material's surface and reveals nanometer scale defects in 2D TMDCs that otherwise would remain hidden.

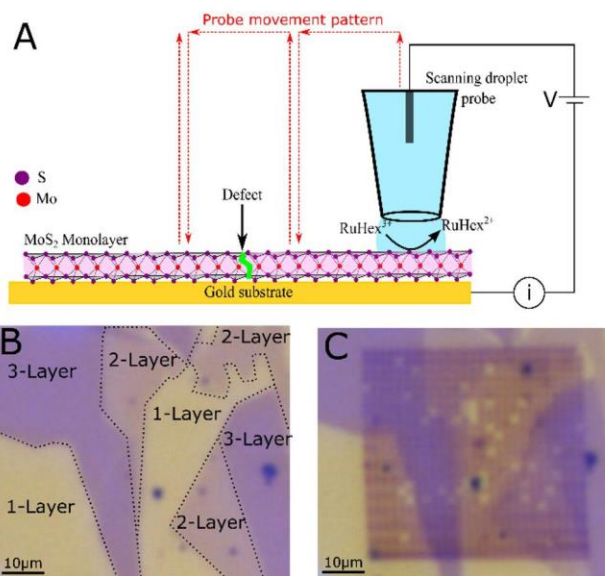
## EXPERIMENTAL SECTION

MoS<sub>2</sub>, MoSe<sub>2</sub>, and WSe<sub>2</sub> samples were prepared on Au electrode surfaces by mechanical exfoliation from bulk crystals.<sup>25</sup> Electrical contact with the sample was established via the underlying Au. Optical and SECCM measurements were made using a Park NX10 instrument (Park Systems, South Korea). The SECCM tips were fabricated from glass capillaries (1.5 mm O.D. and 0.86 mm I.D., BF150-86-7.5, Sutter Instruments, USA) using a P-2000 laser puller (Sutter Instrument, USA) to form a 640 nm radius single-barreled nanopipette. SECCM tips were filled with 1.0 mM [Ru(NH<sub>3</sub>)<sub>6</sub>]Cl<sub>3</sub> (JMC Corporation, South Korea) in 10 mM KCl (VWR Chemicals, USA). A chloridized Ag wire was used as an Ag/AgCl quasi-reference counter electrode and was inserted into the top end of the nanopipette. SECCM measurements were made at an array of equally spaced points (1.5  $\mu\text{m}$  apart) in a hopping mode. Upon contact between the nanodroplet at the end of the SECCM tip, a linear sweep voltammogram (LSV) of the one electron reduction of [Ru(NH<sub>3</sub>)<sub>6</sub>]<sup>3+</sup> (RuHex<sup>3+</sup>) to [Ru(NH<sub>3</sub>)<sub>6</sub>]<sup>2+</sup> (RuHex<sup>2+</sup>) was conducted at the sample surface with fast sweep rates ranging from 0.2 to 1 V s<sup>-1</sup>. All potentials are reported vs the Ag/AgCl quasi-reference counter electrode.

## RESULTS AND DISCUSSION

A 640 nm radius single-barreled nanopipette was used to map the one electron reduction of RuHex<sup>3+</sup> to RuHex<sup>2+</sup> on the MoS<sub>2</sub> surface using a hopping mode SECCM, as illustrated in Figure 1A. Optical images of the MoS<sub>2</sub> sample in the region of the SECCM mapping are shown in Figure 1B,C before and after SECCM experiments, respectively. The region of interest contains mono-, bi-, and trilayer MoS<sub>2</sub> immobilized on the underlying Au electrode surface, as determined by optical microscopy displayed in Figure 1B.<sup>26</sup> The MoS<sub>2</sub> layers appear to be continuous in the optical images. In our recent publication, we reported voltammetric analysis obtained on MoS<sub>2</sub> and other 2D TMDCs, showing how the electrochemical kinetics of the RuHex<sup>3+/2+</sup> couple depends on the number of 2D TMDC layers and, ultimately, the band gap of the 2D TMDC layer.<sup>10</sup> In this work, we examine the electrochemical responses at individual sample points and identify nanoscale defects at the sample surface.

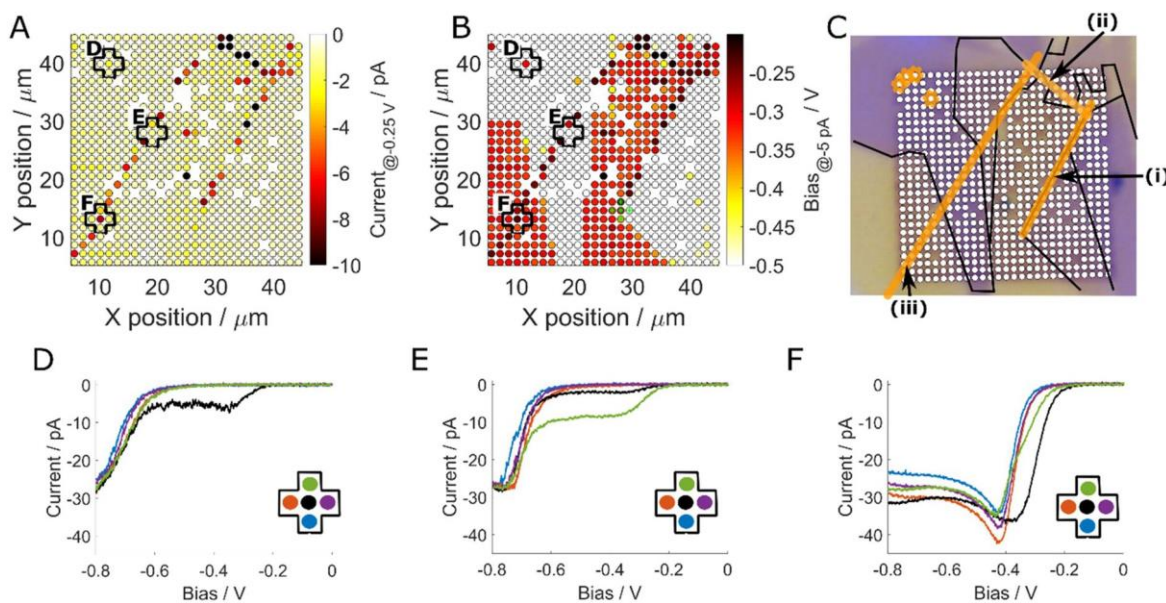
Figure 2A shows a map of the current obtained at -0.25 V from LSV curves measured at each position/pixel in the probed array; the -0.25 V bias is sufficient to drive RuHex<sup>3+</sup> reduction at metallic Au surfaces but insufficient to observe reduction at most MoS<sub>2</sub> surfaces, as we reported in our



**Figure 1.** (A) Schematic of the SECCM experimental configuration in which we use a 640 nm radius single-barreled nanopipette filled with 1 mM RuHex<sup>3+</sup> and 10 mM KCl electrolyte solution to conduct a series of LSVs over the sample surface (which is either mono-, bi-, or trilayer MoS<sub>2</sub>) in an SECCM configuration. The probe movement pattern during the hopping mode scanning is shown in red. We apply a bias (V) between the quasi-reference counter electrode inside the SECCM droplet probe and the Au-supported MoS<sub>2</sub> sample and measure the current through the sample surface. (B) Optical image of the sample surface before SECCM measurements, with the regions of different MoS<sub>2</sub> thicknesses labeled. (C) Optical image of the sample surface after the SECCM experiments, showing the salt deposits left over from the SECCM imaging, which were used to assign the MoS<sub>2</sub> thickness (monolayer, bilayer, and trilayer) for each LSV measurement. Note at some sample points the SECCM droplet did not contact the sample surface due to early activation of the automatic feedback loop prior to the droplet contact with the sample surface, therefore leaving no salt deposits, which can be seen as bright spots in the optical image.

previous publication<sup>10</sup> and is shown in Supporting Information Figure S1. Figure 2A shows certain sample points (shown in orange/red/black) that display current magnitudes that are significantly larger than those observed at the surrounding pixels (shown in yellow/white). Figure 2B shows a map of the applied bias required to observe a current of -5 pA at each pixel, which indicates that the points identified in Figure 2A are also prominent in this constant current map and require lower biases to drive the same current than neighboring pixels. In Section S5, it is detailed by the current threshold of -5 pA was chosen because it provides sufficient contrast for visualizing the defective points.

Figure 2A,B identifies positions that yield deviations in current/bias relative to the surrounding sample points; these are highlighted and overlapped with the optical image in Figure 2C. Several of these positions/pixels are aligned along MoS<sub>2</sub> edges, such as those labeled (i) and (ii) in Figure 2C. Therefore, MoS<sub>2</sub> edges appear to be associated with anomalous electrochemical responses, although not all edges show anomalous responses. However, it is not always the case that the anomalous electrochemical responses are associated with MoS<sub>2</sub> edges. For instance, the line of anomalous electrochemical responses labeled (iii) in Figure 2C is not associated



**Figure 2.** (A) Map of electrochemical response for  $\text{RuHex}^{3+}$  reduction showing the current measured at a bias of  $-0.25$  V, sufficient to drive  $\text{RuHex}^{3+}$  reduction on Au but not on a  $\text{MoS}_2$  surface. The LSV responses at the sample points within regions D–F as shown in part D–F, respectively. (B) Map of the electrochemical response showing the bias required to maintain a constant current of  $-5$  pA. The LSV responses at the sample points within regions D–F as shown in part D–F, respectively. (C) Composite optical image showing the alignment of the defect features on the surfaces. (D–F) LSV response at sample regions D–F shown in part A and B, respectively. Sweep rate used  $1 \text{ V s}^{-1}$ .

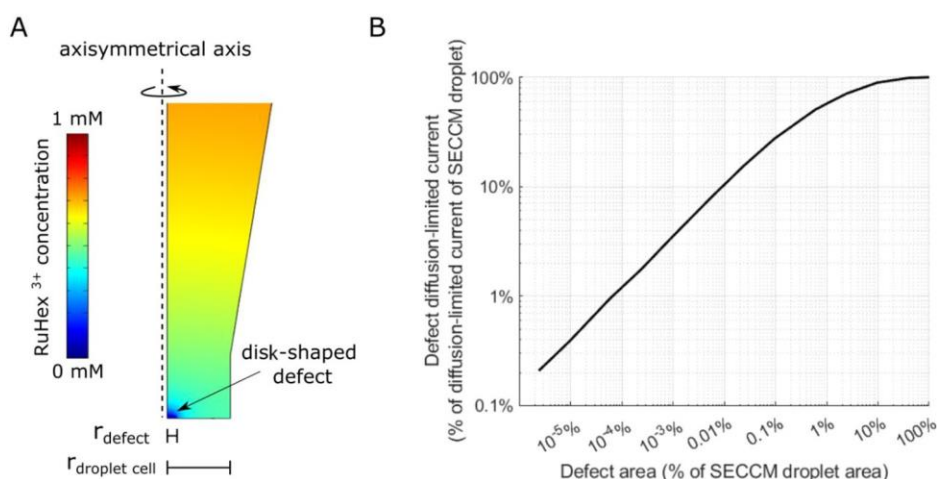
with a  $\text{MoS}_2$  edge. The anomalous sample points that are not associated with a  $\text{MoS}_2$  edge suggest that other defects, e.g., dislocation, grain boundaries, or even physical cracks in  $\text{MoS}_2$  are at the origin of their responses. Finally, we also observe sample points with enhanced electrochemical currents that are isolated and do not belong to a line of anomalous sample points, such as the point labeled D in Figure 2A,B. These anomalous sample points suggest that the electrochemical response is associated with point defects in the  $\text{MoS}_2$  sample surface. Additional SECCM maps on  $\text{MoS}_2$ ,  $\text{MoSe}_2$ , and  $\text{WSe}_2$  are shown in Figures S8–S11. Anomalous points were observed on all samples, indicating that defects are commonly detected on mechanically exfoliated 2D TMDCs.

Figure 2D–F shows the LSV responses measured in three regions, labeled D–F of panel 2A and 2B, respectively; the LSVs of all 728 sample points are shown in Supporting Information Figures S2–S7. Figure 2D shows the electrochemical response on trilayer  $\text{MoS}_2$ ; this position is not part of a line of anomalous sample points. A significantly enhanced electrochemical response for  $\text{RuHex}^{3+}$  reduction is observed at one point in Figure 2D relative to that of the surrounding sample points: a current plateau at approximately  $-5.5$  pA between  $-0.35$  and  $-0.7$  V, while biases less negative than  $-0.7$  V are insufficient to drive  $\text{RuHex}^{3+}$  reduction on trilayer  $\text{MoS}_2$ . The next two sample regions, whose LSVs are shown in Figure 2E,F, lie along the lines of anomalous sample points (iii): region E is located on trilayer  $\text{MoS}_2$ , while region F is located on monolayer  $\text{MoS}_2$ . Note that two of the sample points in Figure 2E show anomalous electrochemical behavior.

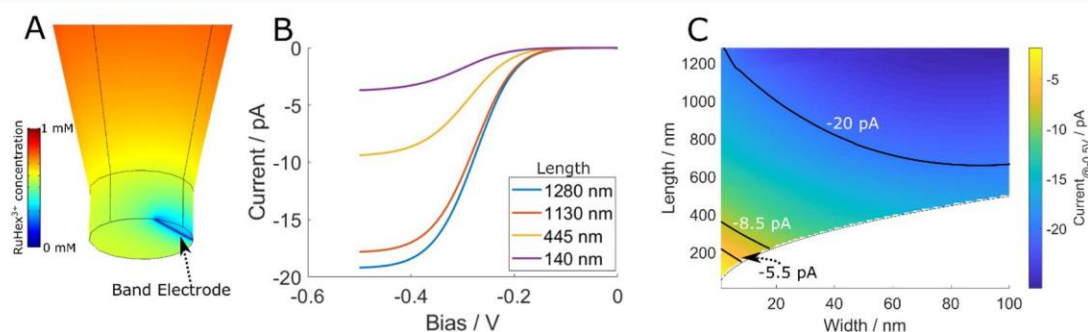
The onset biases for  $\text{RuHex}^{3+}$  reduction that we observe at the anomalous sample points are identical to those observed on an Au electrode surface (see Supporting Information Figure S1). This suggests that the enhanced electrochemical kinetics for the  $\text{RuHex}^{3+/2+}$  redox couple on the anomalous sample points is equivalent and indistinguishable to that on a metallic Au surface.<sup>27,28</sup>

We observe a plateau in the reductive current at approximately  $-27$  pA in all the LSVs when applying a bias sufficient to drive the reduction of  $\text{RuHex}^{3+}$  ( $< -0.8$  V on trilayer,  $< -0.7$  V on bilayer,  $< -0.4$  V on monolayer, and  $< -0.25$  V on Au, see Supporting Information Figure S1), due to the diffusion-limited transport of  $\text{RuHex}^{3+}$  to the  $\text{MoS}_2$  surface. In an SECCM configuration, the magnitude of diffusion-limited current at higher overpotentials depends on the concentration of  $\text{RuHex}^{3+}$ , the diffusion coefficient, the contact area between the SECCM nanodroplet, and the sample surface, as well as the geometry of the SECCM probe.<sup>22</sup> The current plateau at the defect points shown in Figure 2D,E is observed at much lower biases (ca.  $-0.25$  V), which is consistent with the electrochemical response for  $\text{RuHex}^{3+}$  reduction on a sufficiently metallic surface. However, the current plateaus are all below the  $-27$  pA observed at higher overpotentials, namely,  $-5.5$  pA for the point in Figure 2D, and  $-8.5$  and  $-2$  pA for the points in Figure 2E. In Figure 2F, the anomalous sample point, in black, shows a response at a much lower bias, but does not display a lower current plateau. In all LSVs (Figure 2D–F) at higher biases the current then obtains the  $-27$  pA diffusion-limited current. This suggests that a small portion of the nanodroplet contact area is exposed to a surface defect with enhanced kinetics. Note that the observation of a current plateau of smaller magnitude than expected based on droplet cell size indicates that the diffusion layer associated with the defect site must be smaller than the one resulting from the total contacted area of the  $\text{MoS}_2$  surface. Importantly, larger defects will lead to plateau currents that approach the maximum limiting current.

The current plateaus on the kinetically enhanced defects that we observe in Figure 2D–F can be assessed by calculating the size of the equivalent disk-shaped site in the  $\text{MoS}_2$  surface which could give rise to such a diffusion-limited current. We do not consider the mass transport limitations imposed by the SECCM droplet configuration in our analysis, which is a good



**Figure 3.** (A) Simulated axisymmetric two-dimensional concentration profile of  $\text{RuHex}^{3+}$  at a disk-shaped defect. (B) Relationship between size of a planar circular defect and the resulting diffusion-limited current, compared to the size and diffusion-limited current of the entire SECCM droplet.



**Figure 4.** (A) Simulated three-dimensional concentration profile of  $\text{RuHex}^{3+}$  at a band electrode with a 1 nm width offset from the center of the 640 nm radius SECCM droplet (with a band electrode length of 798 nm). (B) Simulated LSV responses at a 1 nm wide band electrode transecting the 640 nm radius SECCM droplet with different lengths at a bias of  $-0.5$  V. (C) Map of the limiting current at  $-0.5$  V for different widths and lengths of the band electrode in a 640 nm radius SECCM droplet. The contours indicate the combination of the band width and length which give rise to currents of  $-20$ ,  $-8.5$ , and  $-5.5$  pA, respectively. The lower limit of the electrode length is visible as the curve separating the white area from the rest of the map. This limit is defined as the entire band electrode width at its center point being just contained within the disk of the SECCM droplet.

approximation for defects much smaller than the SECCM droplet. In this case the diffusion-limited current  $i$  can be described by<sup>29</sup>

$$i = 4nrDFc \quad (1)$$

here  $n$  is the number of electrons transferred in the reaction ( $n = 1$  for the  $\text{RuHex}^{3+/2+}$  redox couple),  $r$  is the equivalent radius of the defect,  $D = 8.4 \times 10^{-6} \text{ cm}^2 \text{ s}^{-1}$  is the diffusion coefficient of  $\text{RuHex}^{3+}$ ,<sup>30</sup>  $F = 96,485 \text{ C mol}^{-1}$  is Faraday's constant, and  $c = 1 \text{ mM}$  is the bulk solution concentration of  $\text{RuHex}^{3+}$ . Using eq 1, we determine that a diffusion-limited current of  $-5.5$  pA observed in Figure 2D is equivalent to a defect with a radius of 17 nm. Likewise, the diffusion-limited currents of  $-8.5$  and  $-2$  pA in Figure 2E correspond to defects with radii of 26 and 6 nm, respectively. The defect in Figure 2F gives a diffusion-limited current plateau that is the same magnitude as  $\text{RuHex}^{3+}$  reduction on the entire contacted  $\text{MoS}_2$  surface, suggesting that this defect is  $>83$  nm in radius. This simple analysis suggests that the anomalous electrochemical responses that we observe can be generated by nanoscale kinetically enhanced defects in the  $\text{MoS}_2$  surface. The percentage of the defect area with respect to the SECCM droplet contact area ranges from 0.01% (6 nm defect) to 0.16%

(26 nm defect) and their estimated sizes are well below the diffraction limit and therefore impossible to detect optically.

The relationship between the defect area in the SECCM droplet and the relative diffusion-limited current as simulated by finite element methods, as shown in the scheme of Figure 3A and further details in Supporting Information Section S4. The result of the simulations is displayed in Figure 3B highlighting that defects only need to be present in a small fraction of the surface to give a large and measurable electrochemical response. Similar relationships to the one in Figure 3B are obtained regardless of the absolute droplet area, as shown in Figure S13. However, by changing the pipette aperture (i.e., changing droplet size), a defect of a given size will result in a different limiting current relative to the maximum value expected. Therefore, it is possible to optimize droplet size by modifying the pipette aperture to achieve the best contrast for the detection of differently sized defects. We have included a graph, Figure S14, showing the absolute diffusion limiting current expected for each size of nanoscale defect and pipette aperture used, which can be used to select the size of the droplet needed for optimum detection of differently sized defects.



The anomalous sample points that are arranged in lines (see Figure 2C) might more accurately be described by linear defects in the MoS<sub>2</sub> sample surface (such as dislocations, grain boundaries, or cracks). The electrochemical response of a linear defect that traverses through the SECCM droplet can be approximated by a band electrode with a width  $w$  that traverses the SECCM droplet for a length  $L$ . We simulated the time-dependent current response for band electrodes of different widths, which transverse the SECCM droplet during an LSV at 1 V/s, see Supporting Information Section S4 for computational details. A typical simulated concentration profile at a 1 nm wide band electrode, which is offset from the center of the SECCM droplet, is shown in Figure 4A. The simulated response for a 1 nm wide band electrode traversing the SECCM droplet with different offsets from the center and, thus, with correspondingly different electrochemically active lengths, is shown in Figure 4B. The simulations highlight that the length of the band electrode has a large influence on the observed response. Although in the case of our measurements, there is uncertainty on the exact length of the line defect traversing the SECCM droplet, simulating a range of different band electrode sizes allows us to construct a map of all possible width-length combinations that can give rise to a given current plateau, as shown in Figure 4C. A current plateau of  $-8.5$  pA in a linear defect, as observed in Figure 2E, could be obtained only with an electrode band width of less than 20 nm. Likewise, a current plateau of  $-2$  pA would require an electrode band width of less than 1 nm (which is the minimum band width which we simulated). This simple analysis suggests that linear defects could be on the scale of single-nanometer or a few atoms wide.

The analysis implemented in this work aims to provide an estimate of the electrochemical response of kinetically enhanced defects on 2D TMDCs using an SECCM approach. The conventional diffusion-based voltammetric theory used here has limitations when considering nanoscale electrochemical interfaces,<sup>31</sup> namely, for electrode radii smaller than 5 nm, the electron transfer kinetics manifested might be different compared to macroscale electrodes.<sup>32,33</sup> Still, this diffusion-based theory has been used to describe electrochemical response down to single atoms.<sup>34,35</sup> Our simulation results highlight that nanoscale defects, which represent a minor portion of the contacted area (<0.01%), have a major impact on the electrochemical response. Note that the defect size calculations are based on the diffusion limiting current value, which depend on diffusion properties along the SECCM probe and not the electron transfer kinetics of the defects. Therefore, the special conditions of small wetting areas and mass transport offered by SECCM allow detection of nanoscale electrochemically enhanced domains, which are not easily detectable with other characterization techniques compatible with electrochemical analysis.

## CONCLUSIONS

SECCM mapping of the electrochemical reduction of [Ru(NH<sub>3</sub>)<sub>6</sub>]<sup>3+</sup> on a 2D MoS<sub>2</sub> sample with a 640 nm radius probe has allowed us to identify defects in mono-, bi-, and trilayer MoS<sub>2</sub>. These defects give rise to electrochemical responses, which are equivalent to disk-shaped defects with radii of tens of nanometers in size, or to band electrodes of nanometer to sub-nanometer widths. Our results highlight that an SECCM-based approach can isolate and amplify the electrochemical response from surface features orders of magnitude smaller than the

SECCM probe, enabling us to detect features electrochemically that are well below the diffraction limit and therefore impossible to detect optically.

Importantly, our results also highlight the impact of nanoscale defects on the overall observed electrochemical response on seemingly defect-free 2D materials. Only a very small defect needs to be present to dominate the electrochemical response of the entire surface area. This suggests that one must be careful in the interpretation of electrocatalysis results on 2D TMDC materials, where the dominant response may not be the intrinsic electrocatalytic response of the material but the electrocatalytic response of the defects present in the material. On the other hand, our results also underline that one only needs to introduce a very low density of defects into our sample surface to effectively alter the electrocatalytic properties.

## ASSOCIATED CONTENT

### Supporting Information

The Supporting Information is available free of charge at <https://pubs.acs.org/doi/10.1021/acs.jpcc.2c01656>.

Typical RuHex<sup>2+/3+</sup> responses on Au, monolayer, bilayer, and trilayer MoS<sub>2</sub> surfaces, raw data of all LSVs, and simulation details (PDF)

## AUTHOR INFORMATION

### Corresponding Author

Kim McKelvey – School of Chemistry, Trinity College Dublin, Dublin 2, Ireland; MacDiarmid Institute for Advanced Materials and Nanotechnology, School of Chemical and Physical Sciences, Victoria University of Wellington, Wellington 6012, New Zealand; [orcid.org/0000-0002-0686-6898](https://orcid.org/0000-0002-0686-6898); Phone: +64 4 463 5957; Email: [kim.mckelvey@vu.ac.nz](mailto:kim.mckelvey@vu.ac.nz)

### Authors

Marc Brunet Cabré – School of Chemistry, Trinity College Dublin, Dublin 2, Ireland

Aislan Esmeraldo Paiva – School of Chemistry, Trinity College Dublin, Dublin 2, Ireland; [orcid.org/0000-0003-2231-0360](https://orcid.org/0000-0003-2231-0360)

Matěj Velický – J. Heyrovský Institute of Physical Chemistry, Czech Academy of Sciences, 182 23 Prague 8, Czech Republic; [orcid.org/0000-0003-4230-3811](https://orcid.org/0000-0003-4230-3811)

Paula E. Colavita – School of Chemistry, Trinity College Dublin, Dublin 2, Ireland; [orcid.org/0000-0003-1008-2874](https://orcid.org/0000-0003-1008-2874)

Complete contact information is available at: <https://pubs.acs.org/doi/10.1021/acs.jpcc.2c01656>

### Notes

The authors declare no competing financial interest.

## ACKNOWLEDGMENTS

We acknowledge Park Systems for loaning the Park NX10 instrument. M.B.C. acknowledges the School of Chemistry, Trinity College Dublin for PhD funding. M.V. acknowledges the support of the Lumina Quaeruntur Fellowship No. LQ200402201 by the Czech Academy of Sciences.

## REFERENCES

- (1) Wang, Q. H.; Kalantar-Zadeh, K.; Kis, A.; Coleman, J. N.; Strano, M. S. *Nat. Nanotechnol.* **2012**, *7*, 699–712.
- (2) Choi, W.; Choudhary, N.; Han, G. H.; Park, J.; Akinande, D.; Lee, Y. H. *Mater. Today* **2017**, *20*, 116–130.
- (3) Wei, Z.; Li, B.; Xia, C.; Cui, Y.; He, J.; Xia, J.-B.; Li, J. *Small Methods* **2018**, *2*, No. 1800094.
- (4) Hu, Z.; Wu, Z.; Han, C.; He, J.; Ni, Z.; Chen, W. *Chem. Soc. Rev.* **2018**, *47*, 3100–3128.
- (5) Sun, T.; Zhang, G.; Xu, D.; Lian, X.; Li, H.; Chen, W.; Su, C. *Mater. Today Energy* **2019**, *12*, 215–238.
- (6) Syari'Ati, A.; Kumar, S.; Zahid, A.; Ali El Yumin, A.; Ye, J.; Rudolf, P. *Chem. Commun.* **2019**, *55*, 10384–10387.
- (7) Chee, S. S.; Lee, W. J.; Jo, Y. R.; Cho, M. K.; Chun, D. W.; Baik, H.; Kim, B. J.; Yoon, M. H.; Lee, K.; Ham, M. H. *Adv. Funct. Mater.* **2020**, *30*, No. 1908147.
- (8) Aryeetey, F.; Ignatova, T.; Aravamudhan, S. *RSC Adv.* **2020**, *10*, 22996–23001.
- (9) Vancsó, P.; Magda, G. Z.; Peto, J.; Noh, J. Y.; Kim, Y. S.; Háng, C.; Biró, L. P.; Tapasztó, L. *Sci. Rep.* **2016**, *6*, 29726.
- (10) Brunet Cabré, M.; Paiva, A. E.; Velický, M.; Colavita, P. E.; McKelvey, K. *Electrochim. Acta* **2021**, *393*, No. 139027.
- (11) Velický, M.; Bissett, M. A.; Toth, P. S.; Patten, H. V.; Worrall, S. D.; Rodgers, A. N. J.; Hill, E. W.; Kinloch, I. A.; Novoselov, K. S.; Georgiou, T.; et al. *Phys. Chem. Chem. Phys.* **2015**, *17*, 17844–17853.
- (12) Liu, D.-Q.; Kang, M.; Perry, D.; Chen, C.-H.; West, G.; Xia, X.; Chaudhuri, S.; Laker, Z. P. L.; Wilson, N. R.; Meloni, G. N.; Melander, M. M.; et al. *Nat. Commun.* **2021**, *12*, 7110.
- (13) Güell, A. G.; Ebejer, N.; Snowden, M. E.; McKelvey, K.; Macpherson, J. V.; Unwin, P. R. *Proc. Natl. Acad. Sci. U. S. A.* **2012**, *109*, 11487–11492.
- (14) Takahashi, Y.; Kobayashi, Y.; Wang, Z.; Ito, Y.; Ota, M.; Ida, H.; Kumatani, A.; Miyazawa, K.; Fujita, T.; Shiku, H.; et al. *Angew. Chem., Int. Ed.* **2020**, *59*, 3601–3608.
- (15) Zhong, J.-H.; Zhang, J.; Jin, X.; Liu, J.-Y.; Li, Q.; Li, M.-H.; Cai, W.; Wu, D.-Y.; Zhan, D.; Ren, B. *J. Am. Chem. Soc.* **2014**, *136*, 16609–16617.
- (16) Bentley, C. L.; Agoston, R.; Tao, B.; Walker, M.; Xu, X.; O'Mullane, A. P.; Unwin, P. R. *ACS Appl. Mater. Interfaces* **2020**, *12*, 44307–44316.
- (17) Hill, J. W.; Hill, C. M. *Nano Lett.* **2019**, *19*, 5710–5716.
- (18) Amatore, C.; Saveant, J. M.; Tessier, D. *J. Electroanal. Chem. Interfacial Electrochem.* **1983**, *147*, 39–51.
- (19) Williams, C. G.; Edwards, M. A.; Colley, A. L.; Macpherson, J. V.; Unwin, P. R. *Anal. Chem.* **2009**, *81*, 2486–2495.
- (20) Payne, N. A.; Mauzeroll, J. *ChemElectroChem* **2019**, *6*, 5439–5445.
- (21) Ebejer, N.; Güell, A. G.; Lai, S. C. S.; McKelvey, K.; Snowden, M. E.; Unwin, P. R. *Annu. Rev. Anal. Chem.* **2013**, *6*, 329–351.
- (22) Snowden, M. E.; Güell, A. G.; Lai, S. C. S.; McKelvey, K.; Ebejer, N.; O'Connell, M. A.; Colburn, A. W.; Unwin, P. R. *Anal. Chem.* **2012**, *84*, 2483–2491.
- (23) Chen, C.; Jacobse, L.; McKelvey, K.; Lai, S. C. S.; Koper, M. T. M. M.; Unwin, P. R. *Anal. Chem.* **2015**, *87*, 5782–5789.
- (24) Bentley, C. L.; Kang, M.; Maddar, F. M.; Li, F.; Walker, M.; Zhang, J.; Unwin, P. R. *Chem. Sci.* **2017**, *8*, 6583–6593.
- (25) Velický, M.; Donnelly, G. E.; Hendren, W. R.; McFarland, S.; Scullion, D.; Debenedetti, W. J. I.; Correa, G. C.; Han, Y.; Wain, A. J.; Hines, M. A.; et al. *ACS Nano* **2018**, *12*, 10463–10472.
- (26) Taghavi, N. S.; Gant, P.; Huang, P.; Niehues, I.; Schmidt, R.; Michaelis de Vasconcellos, S.; Bratschitsch, R.; García-Hernández, M.; Frisenda, R.; Castellanos-Gomez, A. *Nano Res.* **2019**, *12*, 1691–1695.
- (27) Van Der Zande, A. M.; Huang, P. Y.; Chenet, D. A.; Berkelbach, T. C.; You, Y.; Lee, G. H.; Heinz, T. F.; Reichman, D. R.; Muller, D. A.; Hone, J. C. *Nat. Mater.* **2013**, *12*, 554–561.
- (28) Dong, S.; Wang, Z. *Electrocatalysis* **2018**, *9*, 744–751.
- (29) Bard, A. J.; Faulkner, L. R. *Electrochemical Methods: Fundamentals and applications*, 2nd ed.; John Wiley & Sons: New York, 2001.
- (30) Wang, Y.; Limon-Petersen, J. G.; Compton, R. G. *J. Electroanal. Chem.* **2011**, *652*, 13–17.
- (31) Yu, S.; Yu, L.; Zhixiu, L.; Lu, X.; Aili, W.; Shengli, C. *J. Phys. Chem. C* **2009**, *113*, 9878–9883.
- (32) Feldberg, S. W. *Anal. Chem.* **2010**, *82*, 5176–5183.
- (33) Liu, Y.; Chen, S. J. *J. Phys. Chem. C* **2012**, *116*, 13594–13602.
- (34) Agyekum, I.; Nimley, C.; Yang, C.; Sun, P. *J. Phys. Chem. C* **2010**, *114*, 14970–14974.
- (35) Zhou, M.; Bao, S.; Bard, A. J. *J. Am. Chem. Soc.* **2019**, *141*, 7327–7332.

## Recommended by ACS

High-Frequency Sheet Conductance of Nanolayered WS<sub>2</sub> Crystals for Two-Dimensional Nanodevices

Stan E.T. ter Huurne, Jaime Gómez Rivas, et al.

OCTOBER 13, 2022  
ACS APPLIED NANO MATERIALS

READ

## Tip-Mediated Bandgap Tuning for Monolayer Transition Metal Dichalcogenides

Meng-Kai Lin, Chun-Liang Lin, et al.

AUGUST 29, 2022  
ACS NANO

READ

Role of Defects in the Transport Properties and Photoresponse of a Silicon–MoS<sub>2</sub> Mixed-Dimensional Van der Waals Heterostructure

Vrinda Narayanan P. Atikur Rahman, et al.

DECEMBER 15, 2022  
ACS APPLIED ELECTRONIC MATERIALS

READ

Atomic-Level Dynamics of Point Vacancies and the Induced Stretched Defects in 2D Monolayer PtSe<sub>2</sub>

Jun Chen, Jamie H. Warner, et al.

APRIL 07, 2022  
NANO LETTERS

READ

Get More Suggestions &gt;





# Isolation of pseudocapacitive surface processes at monolayer MXene flakes reveals delocalized charging mechanism

Received: 13 July 2022

Accepted: 10 January 2023

Published online: 23 January 2023

Check for updates

Marc Brunet Cabré<sup>1</sup>, Dahnan Spurling<sup>1</sup>, Pietro Martinuz<sup>1,2</sup>, Mariangela Longhi<sup>2</sup>, Christian Schröder<sup>1</sup>, Hugo Nolan<sup>1</sup>, Valeria Nicolosi<sup>1</sup>, Paula E. Colavita<sup>1</sup> & Kim McKelvey<sup>1,3</sup>✉

Pseudocapacitive charge storage in  $\text{Ti}_3\text{C}_2\text{T}_x$  MXenes in acid electrolytes is typically described as involving proton intercalation/deintercalation accompanied by redox switching of the Ti centres and protonation/deprotonation of oxygen functional groups. Here we conduct nanoscale electrochemical measurements in a unique experimental configuration, restricting the electrochemical contact area to a small subregion ( $0.3 \mu\text{m}^2$ ) of a monolayer  $\text{Ti}_3\text{C}_2\text{T}_x$  flake. In this unique configuration, proton intercalation into interlayer spaces is not possible, and surface processes are isolated from the bulk processes, characteristic of macroscale electrodes. Analysis of the pseudocapacitive response of differently sized MXene flakes indicates that entire MXene flakes are charged through electrochemical contact of only a small basal plane subregion, corresponding to as little as 3% of the flake surface area. Our observation of pseudocapacitive charging outside the electrochemical contact area is suggestive of a fast transport of protons mechanism across the MXene surface.

The transition to a low-carbon economy based on renewable energy requires the development of energy storage technologies. Supercapacitors, characterized by both high-power density and high-energy density, bridge the gap between rechargeable batteries and more traditional parallel-plate capacitors<sup>1</sup>. The development of new supercapacitor technology depends on the development of new materials, and this is supported by the precise understanding of the physical nature of the electrochemical charge storage mechanism<sup>2–4</sup>.

MXenes are two-dimensional materials from the family of transition metal carbides, nitrides, and carbon-nitrides with the structure  $\text{M}_{n+1}\text{X}_n\text{T}_x$  ( $n=1,2,3$ )<sup>5</sup>. Among other applications<sup>6</sup>, MXenes exhibit excellent performance as supercapacitors due to their high specific surface area, metallic-like conductivity, and pseudocapacitive response<sup>7</sup>. Titanium carbide MXenes ( $\text{Ti}_3\text{C}_2\text{T}_x$ ) can be obtained by facile exfoliation, display high stability and allow several electrode

architectures, with specific gravimetric capacitances about  $250 \text{ F/g}$ <sup>8</sup>. The origin of charge storage in acidic media is fast ion intercalation into interlayer spaces coupled with the change in the oxidation state of the Ti and protonation of the oxygen functional groups ( $\text{T}_x \rightarrow -\text{O}$  to  $-\text{OH}$ )<sup>9–13</sup>. Macroscale MXene electrodes, however, are complex 3D networks of individual MXene flakes, which affect ion transport from the electrolyte throughout the material network. As a result, on macroscale electrodes we can distinguish surface processes, which involve fast protonation of surface sites exposed to electrolyte and occur at shorter timescales, and bulk processes, which involve ion conduction and intercalation processes through the 3D network and occur at longer timescales<sup>14</sup>.

In this study, we quantify the intrinsic electrochemical pseudocapacitive response of monolayer  $\text{Ti}_3\text{C}_2\text{T}_x$  MXene by isolating the capacitive response on  $0.3 \mu\text{m}^2$  regions of monolayer  $\text{Ti}_3\text{C}_2\text{T}_x$  MXene

<sup>1</sup>School of Chemistry, Trinity College Dublin, Dublin 2, Ireland. <sup>2</sup>Università degli Studi di Milano, Dipartimento di Chimica, Via Golgi 19, 20133 Milano, Italy. <sup>3</sup>MacDiarmid Institute for Advanced Materials and Nanotechnology, School of Chemical and Physical Sciences, Victoria University of Wellington, Wellington 6012, New Zealand. ✉e-mail: [kim.mckelvey@vuw.ac.nz](mailto:kim.mckelvey@vuw.ac.nz)

flakes immobilized on a carbon supporting electrode using scanning electrochemical cell microscopy (SECCM)<sup>15</sup>, as shown in Fig. 1. In our nanoscale SECCM configuration the bulk effects, that might arise from the macroscale 3D electrode, are eliminated and so any contributions from ion-intercalation processes. Therefore, the SECCM configuration allows us to isolate surface dependent processes that contribute to MXene pseudocapacitive response. Using a SECCM approach we measure cyclic voltammograms on a regular grid of sample points spaced  $1.80\ \mu\text{m}$  apart on a region of monolayer  $\text{Ti}_3\text{C}_2\text{T}_x$  flakes. Cyclic voltammograms are acquired on both  $\text{Ti}_3\text{C}_2\text{T}_x$  flakes and the surrounding carbon substrate, allowing us to compare the response on different flakes, different parts of the same flake, and control sample points of the carbon substrate.

## Results

### $\text{Ti}_3\text{C}_2\text{T}_x$ flake characterization

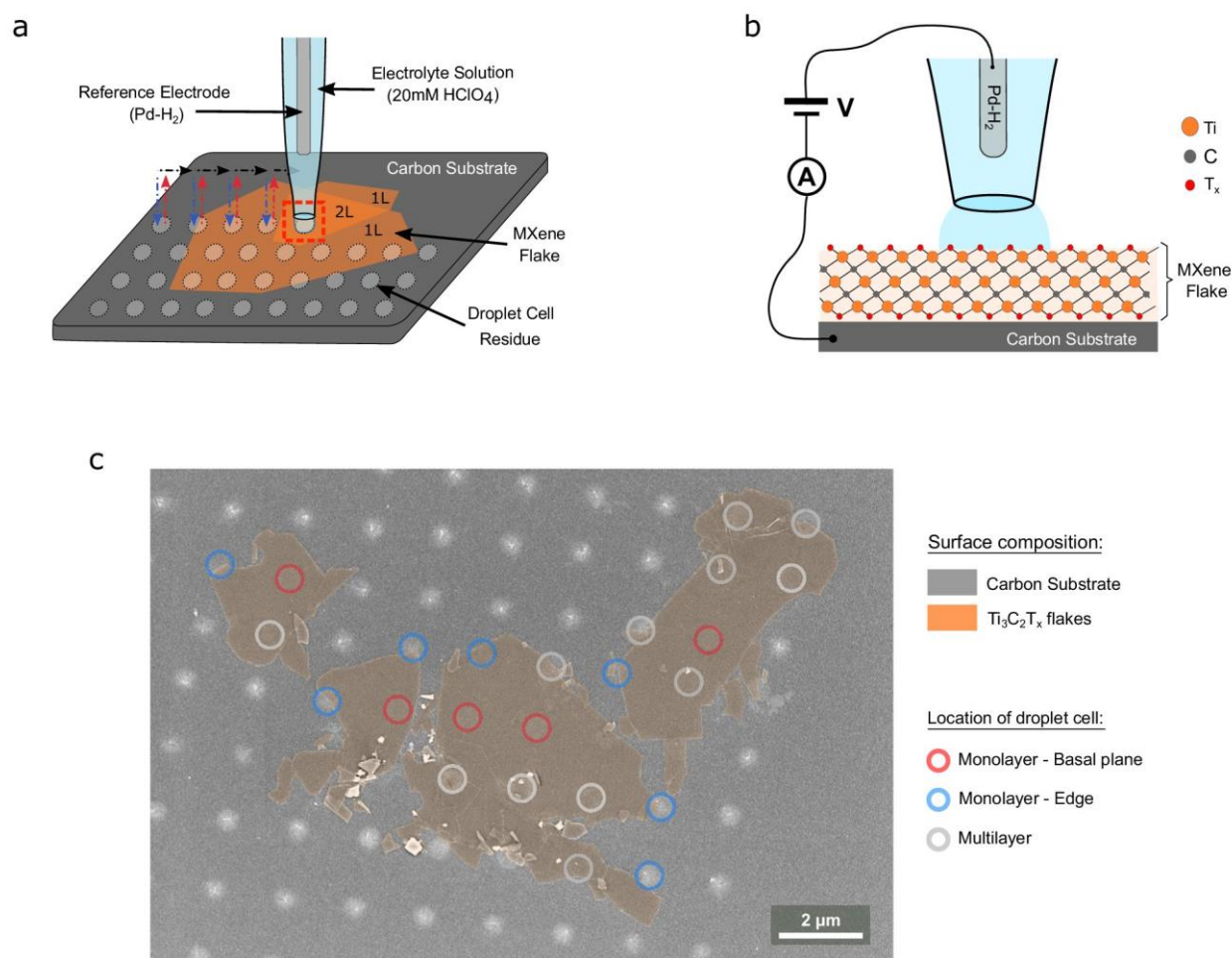
A stock dispersion of  $\text{Ti}_3\text{C}_2\text{T}_x$  flakes was obtained by liquid exfoliation of MAX phase ( $\text{Ti}_3\text{AlC}_2$ ). Freestanding films were prepared via vacuum filtration using stock  $\text{Ti}_3\text{C}_2\text{T}_x$  dispersions (28 mg/ml) on which EDX, Raman, and XRD characterization were performed. Supplementary Figs. 1–3 show the XRD, EDX, and Raman spectra, which are consistent with those of  $\text{Ti}_3\text{C}_2\text{T}_x$ .

$\text{Ti}_3\text{C}_2\text{T}_x$  flakes were drop cast on a carbon surface, and isolated flakes were selected for electrochemical characterization using an SECCM approach. The morphology of individual  $\text{Ti}_3\text{C}_2\text{T}_x$  flakes was determined by a combination of atomic force microscopy (AFM) and scanning electron microscopy (SEM), which indicates that the flakes are monolayer (see Supplementary Note 1).

### Localized electrochemical measurements on $\text{Ti}_3\text{C}_2\text{T}_x$ flakes

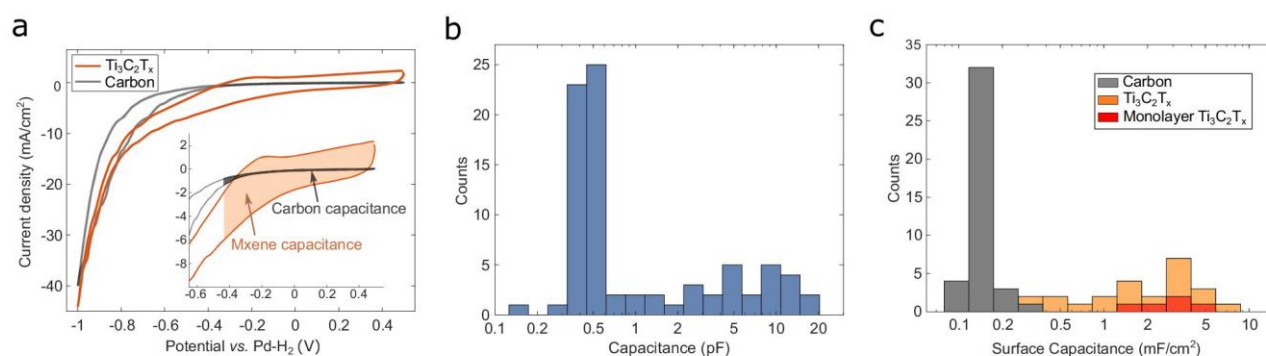
On our isolated  $\text{Ti}_3\text{C}_2\text{T}_x$  flakes the backscattered SEM images show the electrolyte residues remaining after SECCM measurements with a total of 80 points identified (see Supplementary Fig. 7A). From the 80 sample points 64 points presented a well-defined circular geometry which allowed us to determine the electrochemical surface area (i.e., the geometric contact area defined by the SECCM droplet on the sample surface), which was found to be  $0.31 \pm 0.03\ \mu\text{m}^2$  (see Supplementary Fig. 8). As shown in Fig. 1c, a total of 24 points were found to partially or completely contact the MXene flake; of these, 5 were unambiguously located on the basal plane of monolayer  $\text{Ti}_3\text{C}_2\text{T}_x$ , 40 points were identified as contacting the carbon substrate exclusively (see Supplementary Note 2 for further details).

Representative voltammograms on the carbon surface and on the basal plane of monolayer  $\text{Ti}_3\text{C}_2\text{T}_x$  flakes are shown in Fig. 2a. All ana-



**Fig. 1 | Experimental configuration used to isolate monolayer MXene pseudocapacitive responses.** **a** Schematic of the SECCM configuration for measuring monolayer  $\text{Ti}_3\text{C}_2\text{T}_x$  flakes immobilized on a carbon supporting electrode surface. SECCM-based cyclic voltammogram measurements were conducted in a hopping mode, with the probe movement pattern shown in coloured arrows (blue approach, red retract, black move to next measurement position). **b** Schematic of

end of SECCM probe, highlighting the nanoscale electrochemical droplet cell at the end of the SECCM probe and the two-electrode electrochemical cell configuration. **c** Electron micrograph of sample surface containing monolayer MXene immobilized on a carbon surface after SECCM measurements, with each SECCM sample location highlighted according to the surface composition.



**Fig. 2 | Capacitive response on monolayer MXene flakes and surrounding carbon substrate.** **a** Representative cyclic voltammograms over a carbon surface (black) and a single monolayer MXene flake (orange) at scan rate of 0.5 V/s in 20 mM HClO<sub>4</sub>. **b** Histogram of the capacitance at each individual SECCM grid point

observed on the SEM image ( $N=80$ ). **c** Stacked histogram of the surface capacitance over carbon surface (black,  $N=40$ ) and MXene flake (orange,  $N=24$ ), of which the basal plane of single layer  $\text{Ti}_3\text{C}_2\text{T}_x$  points are highlighted (red,  $N=5$ ).

lyses were carried out based on the second cycle of the CV response and all cyclic voltammograms obtained on carbon and  $\text{Ti}_3\text{C}_2\text{T}_x$  can be found in Supplementary Note 2. Between +0.5 and -0.5 V vs Pd-H<sub>2</sub> (Pd-H<sub>2</sub> is +50 mV vs SHE) the voltammograms obtained over  $\text{Ti}_3\text{C}_2\text{T}_x$  flakes, displayed in Fig. 2 and Supplementary Fig. 10, show the characteristic  $i$ - $V$  curves of pseudocapacitive charging in acidic media<sup>10,16,17</sup>. Below -0.6 V vs Pd-H<sub>2</sub> an exponential increase in the current magnitude is observed vs applied potential on both  $\text{Ti}_3\text{C}_2\text{T}_x$  flakes and the carbon substrate, which is consistent with the onset of the hydrogen evolution reaction (HER)<sup>6,18</sup>.

The potential window, -1 to 0.5 V vs Pd-H<sub>2</sub>, was chosen to induce pseudo-capacitive and HER responses without inducing irreversible anodic oxidation, which occurs above +0.7 V vs Pd-H<sub>2</sub> (+0.75 V vs. SHE)<sup>17</sup>. We cycled into the HER response region to condition the MXene surface by saturating terminal oxide groups with adsorbed protons<sup>12</sup>. The first cycle over each point of the SECCM is considered as a conditioning step<sup>10</sup>, and the capacitance response is determined from the second cycle.

Mechanical instability issues are common of macroscale MXene electrodes when placed under electrolyte<sup>19</sup>. The SECCM configuration, which only wets a very minor portion of the sample surface, prevents MXene flakes from lifting off from the surface. The SECCM droplet cell ensures rapid gas transport to the liquid-air interface to prevent bubble formation during hydrogen evolution<sup>20,21</sup>. The AFM and SEM, show that the MXene layers are intact on the carbon working electrode support and show no evidence of exfoliation.

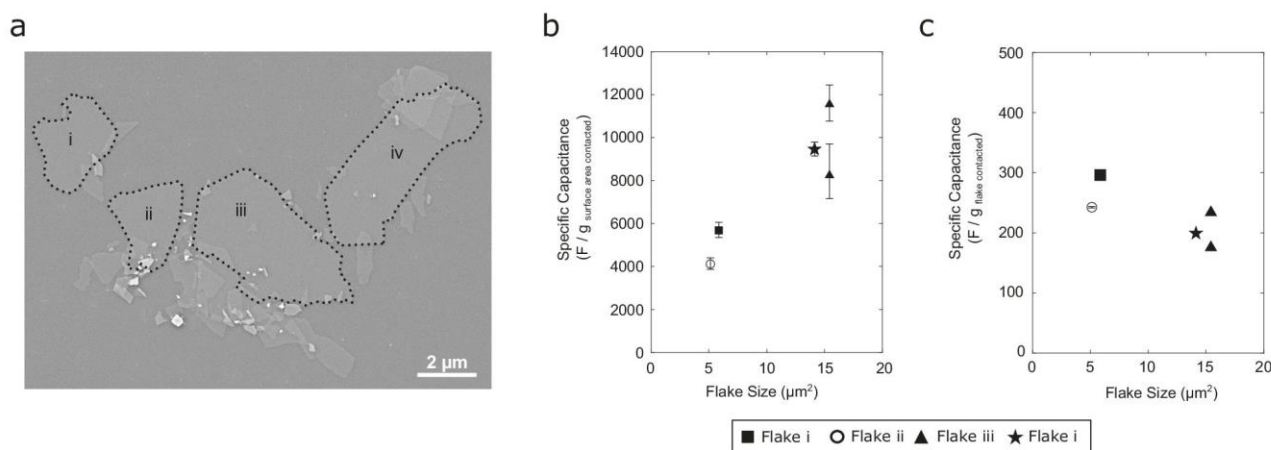
### Observation of capacitive responses on subregions of $\text{Ti}_3\text{C}_2\text{T}_x$ flakes

The capacitance was determined by integrating the charge between +0.5 and -0.5 V vs Pd-H<sub>2</sub>, as illustrated in Fig. 2a. A histogram of the capacitance values obtained for all SECCM grid points ( $N=80$ ) is displayed in Fig. 2b and suggests the presence of two distinct populations. To account for different contact areas, the capacitance was normalized by the geometric area to derive the specific surface capacitance at each point. Furthermore, the location of each SECCM grid point, determined from the electrolyte residues in SEM images, allowed us to correlate the capacitance at each point to the morphology of the surface contacted, i.e., only carbon contact ( $N=40$ ) and partial/complete  $\text{Ti}_3\text{C}_2\text{T}_x$  flake contact ( $N=24$ ). Figure 2c displays stacked histograms of the specific surface capacitance obtained at carbon contact points and at MXene flake contact points, with points contacting a monolayer basal-plane of  $\text{Ti}_3\text{C}_2\text{T}_x$  exclusively highlighted in red (see Supplementary Note 2). The average surface capacitance obtained for carbon was  $0.15 \pm 0.04$  mF/cm<sup>2</sup>, consistent with graphitic carbons in acidic electrolytes (up to 0.35 mF/cm<sup>2</sup>)<sup>22,23</sup>. The average

surface capacitance measured on monolayer  $\text{Ti}_3\text{C}_2\text{T}_x$  MXene sample points, exclusively, is  $2.8 \pm 1.0$  mF/cm<sup>2</sup>, more than an order of magnitude larger than that of the carbon support. As shown in Fig. 2c, the remaining points in contact with  $\text{Ti}_3\text{C}_2\text{T}_x$  flakes present a distribution of specific surface capacitance, with values larger than the mean carbon specific surface capacitance. A detailed assignment of these points, shown in Supplementary Fig. 7, suggests that the broad distribution in specific surface capacitance is due to a wide range of flake morphologies (e.g., edge, multilayer).

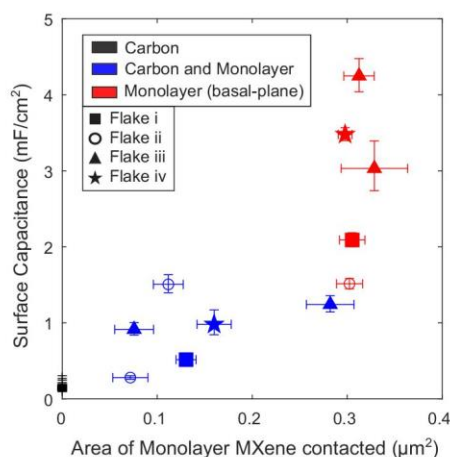
MXene capacitive values derived from different approaches are often compared using gravimetric capacitance metrics. For instance, in experimental work carried out using macroscopic electrodes the capacitance is normalized by the mass of electrode material deposited over the geometric area contacted by the electrolyte<sup>8,10,16,17,24-28</sup>. Computational work translates monolayer simulations of specific areal capacitance into gravimetric capacitances<sup>8,10,12,29-31</sup>. In our SECCM experiments, we measure directly the electrochemical contacted area (see Supplementary Fig. 8). Assuming the crystalline structure of  $\text{Ti}_3\text{C}_2\text{T}_x$ , we can calculate the specific surface area of a monolayer single sided flake,  $\text{SSA}_{\text{1L-one side}}$ , as 272 m<sup>2</sup> g<sup>-1</sup> (see calculation details in Supplementary Note 3). Then, the equivalent mass of MXene contacted can be determined from the experimentally measured contact area. The electrochemical contacted area in our measurements is 0.31 μm<sup>2</sup>, and therefore the mass of monolayer  $\text{Ti}_3\text{C}_2\text{T}_x$  contained in the 0.31 μm<sup>2</sup> area is  $1.15 \pm 0.10$  fg. We can normalize the capacitance values on monolayer points by this equivalent mass, yielding gravimetric capacitances between 4000 and 12,000 F/g for a monolayer basal plane. These values are remarkably high, one to two orders of magnitude greater than any previous theoretical prediction or measurement (see Supplementary Table 5)<sup>24-26,32,33</sup>. The  $\text{Ti}_3\text{C}_2\text{T}_x$  pseudocapacitive charging is estimated to provide about 0.4 e<sup>-</sup> per unit cell per volt of storage when both sides of a monolayer are protonated<sup>12,29,34</sup>. A gravimetric capacitance of 12,000 F/g would be equivalent to 14.8 e<sup>-</sup> per unit cell per volt, an unphysically large capacitance that suggests that the MXene monolayer area engaged in capacitive charging is much larger than the area of the submicron droplet contact (0.31 μm<sup>2</sup>).

SEM imaging shows that the MXene sample consists of four separate monolayer flakes (Fig. 3A). A comparison of the basal plane pseudocapacitance values ( $N=5$ ) obtained on the four flakes reveals differences, as shown in Fig. 3b, with a trend of increasing capacitance with increasing flake size. When the basal-plane capacitance values are normalized by the mass of the entire flake (see Supplementary Table 3), the specific gravimetric capacitance values are found to be independent of flake size and range between 180 and 300 F/g (see Fig. 3c). These estimates of gravimetric capacitance are in



**Fig. 3 | Monolayer MXene capacitive response dependence on flake size.** **a** Electron micrograph of sample surface with flakes larger than  $5 \mu\text{m}^2$  labelled. **b** Specific gravimetric capacitance on monolayer  $\text{Ti}_3\text{C}_2\text{T}_x$  compared to the total area  $\text{Ti}_3\text{C}_2\text{T}_x$  flake, obtained by normalizing capacitance by the mass of MXene in

electrochemical contact with electrolyte. **c** Specific gravimetric capacitance obtained by normalizing by the total mass of the monolayer flake. Error bars represent the standard deviation from determination of **b** MXene mass contacted and **c** MXene flake mass.



**Fig. 4 | Capacitance on edge and basal plane of monolayer MXene flakes.** Surface capacitance plotted against the area of  $\text{Ti}_3\text{C}_2\text{T}_x$  monolayer contacted. Different symbols indicate which flake was contacted, while colour code indicated surface type. Data shows the mean and error bars represent the standard deviation.

excellent agreement with values predicted by DFT simulations (*ca.*  $230 \text{ F/g}$ )<sup>12,29–31,34,35</sup> and previous experimental determinations ( $220\text{--}250 \text{ F/g}$ )<sup>27,36</sup>. Normalizing the basal-plane capacitance values by the two-sided area of the entire monolayer flake, we obtain specific surface capacitance values of  $40 \pm 10 \mu\text{F/cm}^2$ , which agrees with DFT prediction for  $\text{Ti}_3\text{C}_2\text{T}_x$  of  $45 \mu\text{F/cm}^2$ <sup>27</sup>. This suggests that the capacitance response arises from the entire MXene flake and is not confined to the contact area between the MXene basal plane and our SECCM-based electrochemical cell.

#### Implications for MXene pseudocapacitive mechanism

In acid electrolytes the pseudocapacitance of MXenes is described as arising from proton intercalation/deintercalation accompanied by redox switching of the Ti centres and protonation/deprotonation of oxygen functional groups<sup>4,11</sup>. However, our samples consist of monolayer MXene on a carbon surface, and therefore ion intercalation would need to occur between the monolayer MXene and the underlying carbon surface. Further, we conduct our electrochemical measurements by establishing electrochemical contact with only a fraction of the basal plane of the MXene, which leaves no clear pathway for

intercalation of ions between the MXene and the carbon substrate. Nonetheless, we appear to be measuring the pseudocapacitance response from the entire MXene flake, despite our experimental configuration only allowing ion transport to approximately 3% of the total MXene flake surface.

Ion intercalation might be possible when contacting the boundary between the flake edge and the carbon substrate, and this could potentially provide an enhanced capacitive response<sup>10,24,37,38</sup>. On such sample points, the SECCM-based electrochemical cell is in contact with the carbon substrate-monolayer MXene gap, which could enable intercalation between the monolayer MXene and the supporting carbon surface. However, as shown in Fig. 4, edge points show a capacitance value per area of MXene contacted that is smaller than that at basal-plane monolayer points. This analysis suggests that ion intercalation at flake edges is not likely to be responsible for the specific pseudocapacitive values shown in Fig. 3.

#### Discussion

In literature, capacitive  $I\text{--}V$  curves obtained on macroscopic 3D electrodes are often deconvoluted into current contributions from both surface and bulk processes<sup>14,16,39</sup>, using a model described by Dunn et al.<sup>40</sup>. Both surface and bulk processes are important for describing the MXene pseudocapacitive behaviour, and it is useful to differentiate between the timescales of the fast protonation kinetics of  $\text{T}_x$  groups (surface processes) and the contribution from the slower ion-intercalation (bulk processes)<sup>14</sup>. The Dunn et al. model however only considers two possible charging processes and assumes that the transport of charged species, *i.e.*, bulk processes, can be described as a one-dimensional linear diffusion process<sup>40</sup>. This is a limitation for the description of 3D hierarchical structures that display intercalation. Deconvolution can in principle be improved by including other transport mechanisms<sup>41,42</sup>. However, increasing the number of parameters makes the modelling complex and can potentially lead to non-unique solutions<sup>14</sup>.

The system studied here does not resemble any of the previous macroscale configurations used for MXene pseudocapacitance studies and enables measurement of discrete monolayer flakes without confounding effects that might arise from the 3D electrode architecture/organization. This enables the unambiguous assignment of the observed charging behaviour to surface processes, going well beyond approaches that involve mathematical deconvolution with a multi-parameter model. The results of our study show that by establishing electrochemical contact with only a small portion (approx. 3%) of basal



plane of a single monolayer MXene flake, the pseudocapacitive response observed is equivalent to that from the entire MXene flake. Assuming that pseudocapacitive behaviour in MXene monolayers is associated with protonation/deprotonation, our results suggest that protons are transported from/to the electrochemical cell over the entire MXene flake. Therefore, while our unique SECCM configuration isolates the surface processes and restricts ion-intercalation mechanisms, the proton transport effects are still found to dominate the capacitive response. Significantly, we conduct our measurements at 0.5 V/s, thus probing timescales where prior MXene descriptions stated that the response should be dominated by surface capacitive storage. Our results, however, identify that proton transport is likely to be present even at those very short timescales, where the MXene capacitive response is often thought to be independent of ion transport processes.

We speculate that the pseudocapacitive charging (i.e.,  $-O \rightarrow -OH$  surface protonation) outside the wetted area arises from the surface diffusion of protons in a water adlayer on the MXene flake surface<sup>28,43,44</sup>. Although we cannot exclude other possible proton transport mechanisms, such as proton transfer between functional groups ( $-O$  and  $-OH$  groups), proton tunnelling through the MXene layer or proton conduction through structural defects in the MXene<sup>45</sup>. Our measurements were conducted without atmospheric control (approx. humidity of  $47 \pm 4$  %RH, see Supplementary Note 4), and it is likely that a thin water layer is present on the MXene surface that would facilitate proton transport. The AFM step-height profile of  $Ti_3C_2T_x$  flakes suggests the presence of water adsorbed on its surface and/or water trapped between the carbon substrate and the  $Ti_3C_2T_x$  flake (see Supplementary Note 1). The timescale of the cyclic voltammograms obtained in this work is on the order of 1 s; assuming surface diffusion of protons in a thin water layer, this would suggest that diffusion coefficients  $>10^{-8}$   $cm^2 s^{-1}$  would be needed to access a  $10 \mu m^2$  flake surface during the electrochemical measurements. This is not an unreasonable diffusion rate, based on studies of proton dynamics at hydrophilic surfaces that reveal high proton mobility/diffusivity via water-assisted and anhydrous mechanisms<sup>37,38,46–48</sup>.

The proton transport across the MXene surface at diffusion coefficients  $>10^{-8}$   $cm^2 s^{-1}$  would act as a complementary mechanism supporting the retention of capacitive behaviour observed at ultrafast charging/discharging rates ( $>1000$  V/s) for engineered three-dimensional networks<sup>8,16</sup>. Whereby, even limited percolation contacts might be sufficient to achieve very high specific gravimetric capacitances. Finally, these results suggest that MXene-based supercapacitors need to account for short time proton transport contributions, complementing the proton intercalation/deintercalation into MXene interlayer spaces.

## Methods

### Chemicals

Perchloric Acid ( $HClO_4$ , Fluka Analytical, 67–72%) was used as supplied by the manufacturer. All solutions were made with distilled Millipore water with a high resistivity of 18 M $\Omega$  cm. All procedures were carried out at room temperature.

### Preparation of carbon substrates

Carbon substrates were synthesized on  $SiO_2/Si$  wafers substrates via sputtering deposition followed by graphitization under inert atmosphere.  $SiO_2/Si$  wafers (300 nm thermal oxide) were first cleaned with piranha solution (3:1  $H_2SO_4/H_2O_2$  CAUTION: Piranha solution is a strong oxidant which may react explosively with organic solvents and must always be used in a fumehood), then rinsed with Millipore water and dried under nitrogen prior to sputter deposition. Deposition was carried out as previously reported<sup>48</sup>; briefly, amorphous carbon thin films were deposited in a dc-magnetron sputtering chamber (Torr

international, Inc.) using a graphite target at a base pressure  $<2 \times 10^{-6}$  mbar for 40 min using Ar as deposition gas (50 sccm,  $1-2 \times 10^{-2}$  mbar). Films were subsequently graphitized at 900 °C in a tube furnace (Carbolite Gero) under  $N_2$  flow for 60 min, yielding  $73 \pm 3$  nm thick carbon electrodes.

### Preparation of $Ti_3C_2T_x$ stock solution

20 ml of 9 M HCl (Sigma) was added in a PTFE vented vessel containing 1.6 g of LiF powder (Sigma). To allow dissolution of LiF powder, the solution was stirred at 400 rpm for 10 min while the vessel was placed in a 35 °C oil bath. Keeping the vessel in the oil bath while stirring the solution, a total of 1 g of MAX  $Ti_3AlC_2$  phase (Carbon-Ukraine Ltd.) was added to the solution in small fractions, allowing the temperature to stabilize between additions and minimizing overheating of the solution. To achieve a complete etching of the MAX phase, the solution was kept at 35 °C and stirred at 400 rpm for 24 h. After this time, the solution was diluted with deionized water and centrifuged for 5 min at  $2800 \times g$  (5000 rpm). The supernatant was discarded, the sediment was redispersed in deionized water and centrifuged again for 5 min at  $2800 \times g$  (5000 rpm). This process was repeated until the solution was at pH 6. The solution was then vortexed for 30 min to ensure delamination of multilayer  $Ti_3C_2T_x$  flakes into monolayer  $Ti_3C_2T_x$  flakes. After vortexing the solution was centrifuged for 30 min at  $250 \times g$  (1500 rpm), and the supernatant which contained the monolayer flakes was collected. A final centrifugation step for 1 hour at  $2800 \times g$  (5000 rpm) was used to concentrate the monolayer flakes in the sediment, which was redispersed to obtain a stock solution of  $Ti_3C_2T_x$  flakes of 4 g/ml. The  $Ti_3C_2T_x$  synthesis method described here was previously reported<sup>49</sup>.

### Preparation of monolayer MXene flakes supported on carbon electrodes

The stock solution was further diluted with distilled water down to 10  $\mu g/ml$ . The  $Ti_3C_2T_x$  stock and aliquots were bubbled with argon to degas the solution and the flask was filled with argon to store solution in an inert atmosphere. 2  $\mu l$  of diluted solution were drop-cast onto carbon substrates within 24 h of obtaining the stock solution. The sample was left to dry overnight in air, obtaining regions within the drop-cast area with single MXene flakes on the carbon substrate, which established the bottom-contact connection. Electrochemical measurements were carried out within 1 day.

### Instruments

Optical, AFM, and SECCM measurements of monolayer MXene flakes supported on carbon electrodes were acquired on a Park NX10 (Park Systems, South Korea). The AFM images were obtained in a non-contact mode (NCM) with a PPP-NCHR cantilever type (force constant = 42 N/m, resonance frequency = 330 kHz, Nanosensors). AFM and SECCM measurements were done in a room with temperature control. The temperature and humidity inside the SECCM and AFM Faraday cage were recorded for 7 days (see Supplementary Note 4), with a mean temperature of  $22.6 \pm 0.2$  °C and relative humidity between 40 and 60 %RH. SEM images were acquired with a ZEISS Ultra Plus field-emission SEM with the secondary electron detectors, SE2 and In-Lens, at acceleration voltage of 3 kV. Energy dispersive X-ray spectroscopy (EDX) was performed on Zeiss Ultra Plus field-emission SEM at an acceleration voltage of 10 keV with a 20 mm<sup>2</sup> Oxford Inca EDX detector. X-ray diffraction (XRD) was obtained using the powder diffractometer Bruker D8 Discovery, in  $\theta/2\theta$  configuration and range of 3–75° at 2°  $min^{-1}$ . Raman spectroscopy measurements were acquired using a WITec Alpha 300R with a 633 nm He-Ne laser source and 1800 lines/mm grating. The structural characterization measurements (EDX, Raman, and XRD) were performed on as-synthesized  $Ti_3C_2T_x$  thin film produced by vacuum filtration.

### Probe preparation

SECCM probes were single-barrelled nanopipettes with approximately 400 nm aperture radius. The nanopipettes were fabricated from single-barrelled borosilicate capillaries (1.5 mm O.D and 0.86 mm I.D., BF150-86-7.5, Sutter Instrument, USA) using a P-2000 laser puller (Sutter Instrument, USA). Using a pipette filler (MicroFil MF34G-5, World Precision Instruments, USA) the nanopipette was filled with 20 mM HClO<sub>4</sub> electrolyte. A Pd-H<sub>2</sub> quasi reference counter electrode (QRCE) was inserted at the top end of the pipette; prior to this, a Palladium wire (0.25 mm diameter, 5 cm long, PD005130, Goodfellow, UK) was biased at -3 V vs. a Pt counter electrode in 20 mM HClO<sub>4</sub> solution for 15 min to yield the Pd-H<sub>2</sub> quasi reference electrode<sup>50,51</sup>. Pd-H<sub>2</sub> QRCE was calibrated against the standard calomel electrode (SCE) after the SECCM scan with a value of -191 mV, which corresponds to a potential of +50 mV vs Standard Hydrogen Electrode (SHE).

### Scanning protocol

Electrochemical SECCM measurements were performed over a sample region where monolayer Ti<sub>3</sub>C<sub>2</sub>T<sub>x</sub> flakes were immobilized, as identified using optical microscopy (see Supplementary Fig. 4). SECCM imaging was carried out on a regular grid of sample points spaced 1.8 μm apart. At each SECCM sample point two cyclic voltammograms were measured between +0.5 and -1 V vs. Pd-H<sub>2</sub> at a scan rate of 0.5 V/s. Cyclic voltammograms were acquired over both Ti<sub>3</sub>C<sub>2</sub>T<sub>x</sub> flakes and the surrounding carbon substrate, as we can see from the salt residues shown in Fig. 1c. A hopping mode was used in which the probe was approached vertically towards the sample surface at a speed of 0.2 μm/s and a potential of -0.5 V was held until contact between the nanopipette droplet and the surface was established. The contact was detected as the appearance of a double layer charging current, which exceed a defined absolute threshold current of 3.0 pA. After approach, the potential was changed to +0.5 V and after a holding time of 2.0 s, two voltammetry cycles were recorded; then the pipette was retracted and moved to the next sample point of the pre-defined grid. Note, SECCM scans leave droplet residues on the surface, and when using HClO<sub>4</sub>, the droplet cell residues were smaller than using H<sub>2</sub>SO<sub>4</sub>. The resulting small morphological features enabled AFM scanning to resolve the monolayer and bilayer MXene flake steps in the sample region.

### Data availability

The authors declare that all data supporting the finding could be found in the manuscript and supporting information. Raw datasets obtained from electrochemical and morphological characterization are available anytime upon request to the corresponding author.

### References

1. Kalair, A., Abas, N., Saleem, M. S., Kalair, A. R. & Khan, N. Role of energy storage systems in energy transition from fossil fuels to renewables. *Energy Storage* **3**, e135 (2021).
2. Fleischmann, S. et al. Pseudocapacitance: from fundamental understanding to high power energy storage materials. *Chem. Rev.* **120**, 6738–6782 (2020).
3. Costentin, C. & Savéant, J. M. Energy storage: pseudocapacitance in prospect. *Chem. Sci.* **10**, 5656–5666 (2019).
4. Shao, Y. et al. Design and mechanisms of asymmetric supercapacitors. *Chem. Rev.* **118**, 9233–9280 (2018).
5. Nan, J. et al. Nanoengineering of 2D MXene-based materials for energy storage applications. *Small* **17**, 1902085 (2021).
6. Nguyen, T. P. et al. MXenes: applications in electrocatalytic, photocatalytic hydrogen evolution reaction and CO<sub>2</sub> reduction. *Mol. Catal.* **486**, 110850 (2020).
7. Zhu, Q., Li, J., Simon, P. & Xu, B. Two-dimensional MXenes for electrochemical capacitor applications: progress, challenges, and perspectives. *Energy Stor. Mater.* **35**, 630–660 (2021).
8. Li, K. et al. 3D MXene architectures for efficient energy storage and conversion. *Adv. Funct. Mater.* **30**, 2000842 (2020).
9. Mu, X. et al. Revealing the pseudo-intercalation charge storage mechanism of MXenes in acidic electrolyte. *Adv. Funct. Mater.* **29**, 1902953 (2019).
10. Shao, H. et al. Unraveling the charge storage mechanism of Ti<sub>3</sub>C<sub>2</sub>T<sub>x</sub> mxene electrode in acidic electrolyte. *ACS Energy Lett.* **5**, 2873–2880 (2020).
11. Hu, M. et al. Emerging 2D MXenes for supercapacitors: status, challenges, and prospects. *Chem. Soc. Rev.* **49**, 6666–6693 (2020).
12. Zhan, C. et al. Understanding the MXene pseudocapacitance. *J. Phys. Chem. Lett.* **9**, 1223–1228 (2018).
13. Al-Temimy, A. et al. Enhancement of Ti<sub>3</sub>C<sub>2</sub> MXene pseudocapacitance after urea intercalation studied by soft X-ray absorption spectroscopy. *J. Phys. Chem. C* **124**, 5079–5086 (2020).
14. Shao, H., Lin, Z., Xu, K., Taberna, P. L. & Simon, P. Electrochemical study of pseudocapacitive behavior of Ti<sub>3</sub>C<sub>2</sub>T<sub>x</sub> MXene material in aqueous electrolytes. *Energy Stor. Mater.* **18**, 456–461 (2019).
15. Güell, A. G., Lai, S. C. S., McKelvey, K., Snowden, M. E. & Unwin, P. R. Scanning electrochemical cell microscopy: a versatile technique for nanoscale electrochemistry and functional imaging. *Annu. Rev. Anal. Chem.* **6**, 329–351 (2013).
16. Lukatskaya, M. R. et al. Ultra-high-rate pseudocapacitive energy storage in two-dimensional transition metal carbides. *Nat. Energy* **6**, 17105 (2017).
17. Tang, J. et al. Tuning the electrochemical performance of titanium carbide MXene by controllable in situ anodic oxidation. *Angew. Chem. Int. Ed.* **58**, 17849–17855 (2019).
18. Li, S. et al. Ultrathin MXene nanosheets with rich fluorine termination groups realizing efficient electrocatalytic hydrogen evolution. *Nano Energy* **47**, 512–518 (2018).
19. Orangi, J. & Beidaghi, M. A review of the effects of electrode fabrication and assembly processes on the structure and electrochemical performance of 2D MXenes. *Adv. Funct. Mater.* **30**, 2005305 (2020).
20. Liu, Y. et al. Visualization and quantification of electrochemical H<sub>2</sub> bubble nucleation at Pt, Au, and MoS<sub>2</sub> substrates. *ACS Sens.* **6**, 355–363 (2021).
21. Liu, Y., Lu, X., Peng, Y. & Chen, Q. Electrochemical visualization of gas bubbles on superaerophobic electrodes using scanning electrochemical cell microscopy. *Anal. Chem.* **93**, 12337–12345 (2021).
22. Laušević, Z., Apel, P. Y., Krstić, J. B. & Blonskaya, I. V. Porous carbon thin films for electrochemical capacitors. *Carbon* **64**, 456–463 (2013).
23. Ji, H. et al. Capacitance of carbon-based electrical double-layer capacitors. *Nat. Commun.* **5**, 3317 (2014).
24. Shpigel, N. et al. In situ monitoring of gravimetric and viscoelastic changes in 2D intercalation electrodes. *ACS Energy Lett.* **2**, 1407–1415 (2017).
25. Hu, M. et al. Self-assembled Ti<sub>3</sub>C<sub>2</sub>T<sub>x</sub> MXene film with high gravimetric capacitance. *ChemComm* **51**, 13531–13533 (2015).
26. Yang, W. et al. 3D printing of freestanding MXene architectures for current-collector-free supercapacitors. *Adv. Mater.* **31**, 1902725 (2019).
27. Lukatskaya, M. R. et al. Probing the mechanism of high capacitance in 2D titanium carbide using in situ X-ray absorption spectroscopy. *Adv. Energy Mater.* **5**, 2–5 (2015).
28. Mashtalir, O. et al. The effect of hydrazine intercalation on the structure and capacitance of 2D titanium carbide (MXene). *Nanoscale* **8**, 9128–9133 (2016).
29. Wang, L. et al. Origin of theoretical pseudocapacitance of two-dimensional supercapacitor electrodes Ti<sub>3</sub>C<sub>2</sub>T<sub>2</sub> (T = bare, O, S). *J. Mater. Chem. A* **7**, 16231–16238 (2019).
30. Zhan, C. et al. Computational screening of MXene electrodes for pseudocapacitive energy storage. *J. Phys. Chem. C* **123**, 315–321 (2019).

31. Ji, X. et al. Probing the electrochemical capacitance of MXene nanosheets for high-performance pseudocapacitors. *Phys. Chem. Chem. Phys.* **18**, 4460–4467 (2016).
32. Wang, X. et al. 3D Ti<sub>3</sub>C<sub>2</sub>T<sub>x</sub>: X aerogels with enhanced surface area for high performance supercapacitors. *Nanoscale* **10**, 20828–20835 (2018).
33. Shang, T. et al. 3D macroscopic architectures from self-assembled MXene hydrogels. *Adv. Funct. Mater.* **29**, 1903960 (2019).
34. Goff, J. M., Marques Dos Santos Vieira, F., Keilbart, N. D., Okada, Y. & Dabo, I. Predicting the pseudocapacitive windows for MXene electrodes with voltage-dependent cluster expansion models. *ACS Appl. Energy Mater.* **4**, 3151–3159 (2021).
35. Ando, Y., Okubo, M., Yamada, A. & Otani, M. Capacitive versus pseudocapacitive storage in MXene. *Adv. Funct. Mater.* **30**, 2000820 (2020).
36. Ghidui, M., Lukatskaya, M. R., Zhao, M. Q., Gogotsi, Y. & Barsoum, M. W. Conductive two-dimensional titanium carbide 'clay' with high volumetric capacitance. *Nature* **516**, 78–81 (2015).
37. Sun, Y. et al. Proton redox and transport in MXene-confined water. *ACS Appl. Mater. Interfaces* **12**, 763–770 (2020).
38. Gennis, R. B. Proton dynamics at the membrane surface. *Biophys. J.* **110**, 1909–1911 (2016).
39. Kim, H. S. et al. Oxygen vacancies enhance pseudocapacitive charge storage properties of MoO<sub>3-x</sub>. *Nat. Mater.* **16**, 454–462 (2017).
40. Wang, J., Polleux, J., Lim, J. & Dunn, B. Pseudocapacitive contributions to electrochemical energy storage in TiO<sub>2</sub> (anatase) nanoparticles. *J. Phys. Chem. C* **111**, 14925–14931 (2007).
41. Dupont, M. F. & Donne, S. W. A step potential electrochemical spectroscopy analysis of electrochemical capacitor electrode performance. *Electrochim. Acta* **167**, 268–277 (2015).
42. Gibson, A. J. & Donne, S. W. A step potential electrochemical spectroscopy (SPES) investigation of anodically electrodeposited thin films of manganese dioxide. *J. Power Sources* **359**, 520–528 (2017).
43. Cai, M. et al. Ti<sub>3</sub>C<sub>2</sub>T<sub>x</sub>/PANI composites with tunable conductivity towards anticorrosion application. *Chem. Eng. J.* **410**, 128310 (2021).
44. Lipatov, A. et al. Effect of synthesis on quality, electronic properties and environmental stability of individual monolayer Ti<sub>3</sub>C<sub>2</sub> MXene flakes. *Adv. Electron. Mater.* **2**, 1600255 (2016).
45. Sang, X. et al. Atomic defects in monolayer titanium carbide (Ti<sub>3</sub>C<sub>2</sub>T<sub>x</sub>) MXene. *ACS Nano* **10**, 9193–9200 (2016).
46. Xu, L. & Jiang, D. E. Proton dynamics in water confined at the interface of the graphene–MXene heterostructure. *J. Chem. Phys.* **155**, 234707 (2021).
47. Herath, M. B., Creager, S. E., Kitaygorodskiy, A. & Desmarreau, D. D. Effect of perfluoroalkyl chain length on proton conduction in fluoroalkylated phosphonic, phosphinic, and sulfonic acids. *J. Phys. Chem. B* **114**, 14972–14976 (2010).
48. Cullen, R. J. et al. Spontaneous grafting of nitrophenyl groups on amorphous carbon thin films: a structure-reactivity investigation. *Chem. Mater.* **24**, 1031–1040 (2012).
49. Borghetti, M., Serpelloni, M., Sardini, E., Spurling, D. & Nicolosi, V. Temperature influence on Ti<sub>3</sub>C<sub>2</sub>T<sub>x</sub> lines printed by aerosol jet printing. *Sens. Actuators A: Phys.* **332**, 113185 (2021).
50. Daviddi, E., Gonos, K. L., Colburn, A. W., Bentley, C. L. & Unwin, P. R. Scanning electrochemical cell microscopy (SECCM) chronopotentiometry: development and applications in electroanalysis and electrocatalysis. *Anal. Chem.* **91**, 9229–9237 (2019).
51. Bentley, C. L. & Unwin, P. R. Nanoscale electrochemical movies and synchronous topographical mapping of electrocatalytic materials. *Faraday Discuss* **210**, 365–379 (2018).

## Acknowledgements

We acknowledge Park Systems for loan of a Park NX10 instrument. M.B. acknowledges the School of Chemistry, Trinity College Dublin for PhD funding. This project has received funding from the European Union's Horizon 2020 research and innovation programme under the Marie Skłodowska-Curie Grant Agreement No. 713567 (EDGE-Project HECAT4H2), received by H.N. The results of this publication reflect only the authors' view and the Commission is not responsible for any use that may be made of the information it contains. This publication has also emanated in part from research conducted with the financial support of Science Foundation Ireland under Grant No. 19/FFP/6761, received by P.E.C. Authors thank the support of European Research Council (ERC) CoG, 3D2DPrint (GA 681544), received by V.N. K.M. acknowledges the support of the MacDiarmid Institute for Advanced Materials and Nanotechnology. P.M. acknowledges Erasmus Traineeship Project. SEM imaging was carried out at the Advanced Microscopy Laboratory (AML) at the AMBER Research Centre, Trinity College Dublin, Ireland.

## Author contributions

M.B.C. and P.M. performed SECCM experiments and optimized sample preparation. D.S. designed the exfoliation process and manufactured the MXene flakes. M.B.C. and D.S. performed physical characterization by AFM and SEM. C.S. and H.N. designed and manufactured carbon substrates. K.M., P.E.C., V.N., and M.L. conceived and designed the project. M.B.C., K.M., and P.E.C. analyzed the data and wrote the manuscript.

## Competing interests

The authors declare no competing interests.

## Additional information

**Supplementary information** The online version contains supplementary material available at <https://doi.org/10.1038/s41467-023-35950-1>.

**Correspondence** and requests for materials should be addressed to Kim McKelvey.

**Peer review information** *Nature Communications* thanks Manyala Ncholu and the other, anonymous, reviewer(s) for their contribution to the peer review of this work. Peer reviewer reports are available.

**Reprints and permissions information** is available at <http://www.nature.com/reprints>

**Publisher's note** Springer Nature remains neutral with regard to jurisdictional claims in published maps and institutional affiliations.

**Open Access** This article is licensed under a Creative Commons Attribution 4.0 International License, which permits use, sharing, adaptation, distribution and reproduction in any medium or format, as long as you give appropriate credit to the original author(s) and the source, provide a link to the Creative Commons license, and indicate if changes were made. The images or other third party material in this article are included in the article's Creative Commons license, unless indicated otherwise in a credit line to the material. If material is not included in the article's Creative Commons license and your intended use is not permitted by statutory regulation or exceeds the permitted use, you will need to obtain permission directly from the copyright holder. To view a copy of this license, visit <http://creativecommons.org/licenses/by/4.0/>.

© The Author(s) 2023



